FAILURE ANALYSIS OF COMPONENTS AT HIGH TEMPERATURES

by

Vassilios Dimopulos, BSc (Eng), MSc (Eng), DIC

A thesis submitted for the degree of

Doctor of Philosophy

of the

University of London

March 1988

Imperial College of Science & Technology

Department of Mechanical Engineering

London SW7 2BX

ABSTRACT

The safety analysis and the life time prediction of high temperature components have to take into account a number of failure mechanisms. Depending on the loading conditions and the type of environment, a defect at high temperatures may grow by creep, corrosion and fatigue mechanisms.

The aim of this thesis is to study the crack propagation in a number of different materials, at high temperatures, and to examine the validity and limitations of fracture mechanics concepts. The materials tested were two low alloy steels, namely a 1/2%Cr1/2%Mo1/4%V steel (1/2CMV) and a 21/4%Cr1%Mo steel (21/4CM), two nickel base superalloys designated AP1 and 800H, and, a type 304H stainless steel.

The tests were carried out in air under static and cyclic loading at temperatures sufficient to give creep deformation and to simulate thermal fatigue. Mainly compact tension specimens were used. For the cyclic tests it was possible to divide the total crack growth into two components: cycle dependent and time dependent propagation.

Both Linear Elastic Fracture Mechanics (L.E.F.M.) and Non Linear Elastic Fracture Mechanics concepts have been applied to interpret the results, including the stress intensity factor K and, the line integral C*. Within certain limits of validity, these parameters can describe the behaviour of crack growth, for different materials, independent of geometry and loading conditions, so that, the results from laboratory tests can be transferred to real structures for lifetime predictions or safety analysis.

For an understanding of the crack tip deformation behaviour numerical methods such as Finite Element (F.E.) and Boundary Integral Equation (B.I.E.) methods, are needed to simulate the experiments, so that characteristic parameters such as K and C* can be then obtained for practical components.

Using F.E. and B.I.E. analysis, the stress distributions, stress intensity factor K, and, the C* line integral, were calculated for a material deforming in secondary creep according to the Norton creep law, for a number of different specimen geometries.

The practical case of crack growth in a rotating turbine disc is also considered to illustrate how the principles developed can be employed to predict components lifetimes.

Two models have been developed. A stationary crack model which predicts stress redistribution from short times to long times, and, a model which predicts crack growth rates using the C* line integral and the remaining ductility in the crack tip damage process zone.

For static and low frequency tests (≤ 0.1 Hz in general) where intergranular creep processes dominate, good correlations were obtained between the crack growth rate and the C* line integral when calculated from the experimental displacement rates. At high frequencies where transgranular fatigue processes control, it is demonstrated that, the crack growth per cycle can be described by the Paris law and that, the influence of load ratio can be accounted for by crack closure caused by fracture surface roughness, oxidation and plastic strain developed at the crack tip. At intermediate frequencies good correlations can be obtained if a cumulative damage law is assumed.

To my mother

ACKNOWLEDGEMENTS

I wish to express my sincerest thanks to my supervisors, Dr G.A. Webster and Dr R.T. Fenner, for their invaluable help, encouragement and guidance throughout the course of this project.

I would like also to thank Dr K.M. Nikbin for his many fruitful arguments on scientific method, the staff at the computer centre, and, the technical staff in particular Mr. D.K. Willis and Mr. O. Pathak. Special thanks are due to my research colleagues for their advice and suggestions and to Mr. S. Bakeas for his moral support throughout.

This work was made possible with the financial support of the The Ministry of Defence, to whom the author is grateful.

Finally, I wish to acknowledge the debt I owe to my parents, who, in every way, made this possible.

CONTENTS

		PAGE
Title Page		1
Abstract		2
Dedication		4
Acknowledgements		5
Contents		6
Nomenclature		13
CHAPTER 1:	GENERAL INTRODUCTION	18
CHAPTER 2:	MICROMECHANISMS OF FRACTURE AND CREEP DEFORMATION	21
2.1	Introduction	21
2.2	Micromechanisms of Fracture	21
2.2.1	Fracture of the ideal strength	21
2.2.2	Cleavage and brittle intergranular fracture	22
2.2.3	Ductile fracture at low temperature	22
2.2.4	Transgranular creep fracture	23
2.2.5	Intergranular creep-controlled fracture	23
2.2.6	Pure diffusional fracture	23
2.2.7	Rupture	24
2.3	The Creep Phenomenon	24
2.3.1	General shape of a Creep curve	24
2.3.2	Stress dependence of the steady state creep rate	25
2.3.3	Effect of temperature	26
2.3.4	Empirical formulas for the rupture time in the creep regime	27
	Figures 2.1 to 2.5	28

		PAGE
CHAPTER 3:	CONTINUUM DAMAGE MECHANICS	31
3.1	Introduction	31
3.2	Phenomenological relations	31
3.3	Mechanistic models	33
	Table 3.1	36
	Figures 3.1 to 3.5	37
CHAPTER 4 :	REVIEW OF FRACTURE MECHANICS CONCEPTS	40
4.1	Introduction	40
4.2	Linear Elastic Fracture Mechanics	41
4.2.1	The stress intensity factor (K)	41
4.2.2	The energy release rate (G)	42
4.2.3	Limitations of L.E.F.M.	43
4.3	Non Linear Elastic Fracture Mechanics	45
4.3.1	Introduction	45
4.3.2	The J integral	45
	Figures 4.1 to 4.6	49
CHAPTER 5 :	APPLICATION OF FRACTURE MECHANICS TO TIME DEPENDENT MATERIALS.	53
5.1	Introduction	53
5.2	Steady state conditions	53
5.2.1	The C* Integral	53
5.3	Non steady state conditions	57
5.3.1	Introduction	57
5.3.2	The C(t) Integral	57
5.3.3	Characteristic times to steady state conditions	59
5.3.4	Generalised material behaviour	61

		PAGE
5.3.5	Stress redistribution at the crack tip	62
5.3.6	The C_t parameter	63
5.4	The asymptotic stress and strain fields near the tip of a growing crack	67
5.4.1	Steady state behaviour	67
5.4.2	Transient behaviour	69
5.5	A theoretical model for predicting crack growth rates	72
5.5.1	Influence of state of stress	74
5.6	Link of fracture mechanics with damage mechanics	75
5.6.1	Prediction of crack growth rates	77
5.7	The reference stress concept	78
5.8	Parameters to characterise creep crack growth	80
	Figures 5.1 to 5.15	84
CHAPTER 6:	METHODS OF RETRIEVING C*	96
6.1	Experimental methods	96
6.2	Numerical methods for estimating crack growth parameters	98
6.3	The finite element method	99
6.3.1	Introduction	99
6.3.2	Mathematical analysis	100
	(a) Elastic analysis	100
	(b) Non-Linear problems	105
6.4	The Boundary Integral Equation (Boundary Element) method	107
6.4.1	Introduction	107
6.4.2	Mathematical analysis	109
	(a) Elastic analysis	109
	(b) Elasto-plastic analysis	112
6.5	Numerical astimates of C*	117

		PAGE
6.6	Reference stress approach for estimating C*	118
	Table 6.1	121
	Figures 6.1 to 6.7	123
CHAPTER 7:	INFLUENCE OF FATIGUE	128
7.1	Fatigue as a microstructural phenomenon	128
	7.1.1 Introduction	128
	7.1.2 Fracture mechanics approach to fatigue crack growth	129
	7.1.3 Crack closure in fatigue crack growth	130
7.2	Creep-Fatigue interaction	131
	7.2.1 Introduction	131
	7.2.2 Temperature effects	132
	7.2.3 Environmental effects	132
7.3	Frequency and waveform effects	133
	7.3.1 Introduction	133
	7.3.2 Slow cycling without rapid load variations	133
	7.3.3 Slow cycling with rapid load variations	134
	7.3.4 Rapid balanced cycling	135
	7.3.5 Rapid unbalanced cycling	135
7.4	A model for Creep-Fatigue interaction	136
	Figures 7.1 to 7.6	138
CHAPTER 8:	EXPERIMENTAL INVESTIGATIONS	143
8.1	Introduction	143
8.2	Materials: Composition and heat-treatment	143
8.3	Specimen geometry and dimentions	144
8.4	Description of the apparatus	145
8.5	Measurement methods	148

PAGE

8.5.1 Crack length measurements 148

8.5.2 Calibration of the crack length potential drop 150

8.5.3 Temperature calibration 151

8.5.4 Displacement and load calibration 152

8.6 Experimental procedure 152

8.7 Static crack growth tests 154

8.8 Cyclic crack growth tests 155

Tables 8.1 to 8.10 158

Figures 8.1 to 8.22 169

Appendix 8A 191

CHAPTER 9: THE FINITE ELEMENT AND BOUNDARY INTEGRAL EQUATION PROGRAMS, AND, NUMERICAL RESULTS 193

9.1 Description of the Finite Element program 193

9.1.1 Relationship between stress and strain 193

9.1.2 Iterative procedure 193

9.1.3 Convergence to solution 194

9.1.4 Numerical determination of C* 195

9.2 The Finite Element mesh generation 197

9.2.1 Input data for the Finite Element mesh generation routine 198

9.2.2 Modelling the crack tip 199

9.3 Description of the Boundary Integral Equation program 200

9.3.1 Solution peocedure 200

9.3.2 Convergence criteria 202

9.3.3 Boundary Integral Equation mesh generation 203

9.4 Numerical results and discussion 205

9.4.1 Geometries 205

9.4.2 Numerical results for the standard compact tension

PAGE

geometry 205

(a) Finite Element analysis 205

(b) Boundary Integral Equation analysis 206

9.4.3 Finite Element analysis of compact tension specimens containing blunt holes 207

(a) Crack initiation 207

(b) Crack propagation 209

9.4.4 Numerical results for the rotating disc geometry 214

(a) Finite Element analysis 214

(b) Boundary Integral Equation analysis 217

Figures 9.1 to 9.70 221

Appendix 9A 284

CHAPTER 10: ANALYSIS FOR, AND THE INTERPRETATION OF, THE EXPERIMENTAL DATA 288

10.1 Introduction 288

10.2 Stress redistribution model 290

10.2.1 r* positions for the compact tension geometry 293

10.3 Characterisation of creep crack growth 294

10.4 Rate data evaluation 297

10.5 Effect of crack growth on the measured displacement rate 299

10.6 Static crack growth of the 800H material 300

10.6.1 Introduction 300

10.6.2 800H results and discussion 301

10.7 Initial transient crack growth behaviour 302

10.7.1 Introduction 302

10.7.2 Remaining ductility model 303

10.8 Influence of aging on crack growth in type 304H stainless steel 307

PAGE

10.8.1 Introduction 307

10.8.2 Results and discussion 307

10.9 R-ratio and frequency effects on crack growth rates for cyclic tests 310

10.9.1 Introduction 310

10.9.2 Results and discussion 310

(a) R-ratio effects at low frequencies 314

(b) R-ratio effects at high frequencies 316

(c) Low frequency crack growth correlation in terms of C^*_{exp} 317

10.10 Constant displacement tests 319

10.10.1 Introduction 319

10.10.2 Displacement controlled tests results and discussion 320

10.11 HR-zone sizes due to growing crack 323

Tables 10.1 and 10.2 325

Figures 10.1 to 10.38 326

Appendix 10A 366

CHAPTER 11: GENERAL DISCUSSIONS, CONCLUSIONS AND RECOMMENDATIONS 368

11.1 General discussion and conclusions chapter 9 369

11.2 General discussion and conclusions chapter 10 371

11.2.1 Static constant load tests 371

11.2.2 Cyclic constant load range tests 373

11.2.3 Constant displacement tests 374

11.3 Recommendations for further work 376

References 377

Published work Abstracts 387

NOMENCLATURE.

The notation is also defined when it first appears in the text. For reference purposes , the important symbols are listed below.

Roman Symbols.

A		: area.
B	B_n	: thickness; gross, net section.
B		: constant in work-hardening law.
C		: constant in secondary creep law.
C*		: path-independent creep contour integral.
C_N	C_n	: non-linear plastic compliance; non-linear creep compliance.
[D]		: element elastic property matrix.
E	E'	: Young's modulus, effective modulus.
F		: non-dimensional function associated with C*.
[F]		: applied force matrix.
G	G_c	: strain energy release rate; critical.
H , H'		: non-dimensional functions associated with C_t.
I_n		: amplitude function.
J		: path-independent non-linear elastic contour integral.
K	K_c	: stress intensity factor; critical.
[K]		: overall stiffness matrix.
N		: number of load cycles.
P	P_L P_{LC}	: load; limit; cracked body limit load.
Q		: activation energy for creep.
R		: load ratio.
R		: gas constant.
T	T_m	: temperature; melting.

T_i	: traction vector.
U	: energy rate potential.
U*	: creep energy rate potential.
V	: volume
W	: width of body.
W	: strain energy density.
W *	: strain energy rate density.
a a_o Δa	: crack length; initial; increment.
a_{eff}	: effective crack length.
da/dt da/dN	: crack growth rate; growth rate per cycle.
[k]	: element stiffness matrix.
l	: void spacing
m	: yield load ratio.
n	:creep stress index.
q_i	: structural parameter.
[r]	: equivalent force vector.
r	: radial distance from crack tip.
r_p r_{cr} r_c	: Plastic zone size; creep zone size; damage zone size.
t t_1	: time ; time for stress redistribution.
t_R	: time to rupture
$\dot{u}$ $\dot{v}$	: displacement rates (x,y)
x	: cartesian coordinate.
y	: cartesian coordinate.

Greek Symbols.

Γ	: closed anticlockwise path encircling the crack tip.
Δ $\dot{\Delta}$	: load point displacement; rate.
[Δ]	: overall displacement matrix.

Φ : experimental exponent in crack growth rate correlations.

Ω Ω_i Ω_R : damage function; initial; final.

α : coefficient of expansion.

$[\delta]$: element displacement vector.

$[\varepsilon]$: two-dimensional strain vector.

ε $\dot{\varepsilon}$: strain; strain rate.

ε_s $\dot{\varepsilon}_s$: secondary creep; rate.

ε_e ε'_{ij} : equivalent strain; deviatoric strain.

ε^{el} ε^{cr} : elastic strain; creep strain.

η : damage coefficient.

θ : angular parameter.

λ : grain size.

ν : rupture coefficient.

ν : poisson's ratio.

ρ : density.

σ σ_o : stress; stress coefficient.

σ_y : yield stress.

σ_e σ'_{ij} : equivalent stress; deviatoric stress.

σ_R : reference stress.

τ : non-dimensional time.

ω ω_i ω_R : damage; initial; final.

ω : angular velocity.

Symbols for B.I.E analysis.

C_{ij} : second-order free-term coefficient tensor for displacements.

D_{kij} : third order displacement tensor for stresses.

H : plastic modulus.

P		: variable or load point on boundary or surface of body.
Q		: field point on boundary or surface of body.
S		: domain of a two dimensional body.
S_{kij}		: third-order traction tensor for stresses.
T_{ij}		: second-order traction tensor for displacements.
U_{ij}		: second-order displacement tensor for displacements.
$d\varepsilon_{ij}$		: total strain increment.
$d\varepsilon^e_{ij}$		: elastic strain increment.
$d\varepsilon^p_{ij}$		: plastic strain increment.
$d\sigma_{ij}$		: stress increment.
f_i	$\dot{f}_i$	: body force; rate.
n_i		: unit normal vector at a boundary point.
p		: variable or load point in interior of body.
q		: field point in interior of body.
r		: distance between variable and field points.
s		: boundary of two-dimensional body.
s_η		: boundary of a small circle of radius η.
t_i	$\dot{t}_i$	: traction; rate.
u_i	$\dot{u}_i$	: displacement; rate.
$\underset{\sim}{\dot{z}}$		: vector consisting of nodal unknowns.
Σ_{kij}	$\dot{\Sigma}_{kij}$	: third-order stress tensors for displacements.
Σ_{ijkh}	$\dot{\Sigma}_{ijkh}$	: fourth-order stress tensors for stresses.
δ_{ij}		: kronecher delta.
ε_{ij}	$\dot{\varepsilon}_{ij}$	: total strain; rate
ε^e_{ij}	$\dot{\varepsilon}^e_{ij}$	: elastic strain; rate.
ε^p_{ij}	$\dot{\varepsilon}^p_{ij}$	: plastic strain; rate.
ε^e_{eq}		: equivalent elastic strain .
ε^p_{eq}	$\dot{\varepsilon}^p_{eq}$	: equivalent plastic strain; rate.

η : radius of small circle.

μ : shear modulus.

v : poisson's ratio or effective poisson's ratio.

ξ_1 ξ_2 ξ_3 : intrinsic coordinates.

σ_{ij} $\dot{\sigma}_{ij}$: stress; rate

σ_{eq} : equivalent stress.

CHAPTER 1

GENERAL INTRODUCTION

In the aircraft, electric power generation and chemical industries there are industrial plants containing metal components operating at high temperatures. Premature failure of the components can have catastrophic results and must be avoided. On the other hand unnecessary shutdowns of a plant can prove very costly. So it is important that the usable life of a component can be predicted so that a satisfactory economic and safe compromise can be reached.

The study of failure modes under conditions which simulate actual service conditions is complicated by many experimental difficulties. Therefore the common approach is to investigate the effect of a limited number of variables on failure with the goal of eventual incorporation of the results into a fundamental model, which will include the important variables (and their interaction) governing failure in service.

One type of failure of the components is due to the propagation of crack-like defects. Defects may have arisen during manufacture so they are present when the component enters service, or they can be produced during service in regions of local imperfections in the material structure, or in regions of high stress concentration.

Crack growth studies are of particular importance where the failure of a component results from the propagation of a single crack. Such failure is likely to occur if there is a localization of strain due to the presence of bending moment, thermal gradients, geometric discontinuities or sharp defects produced during service.

At high temperatures there are many factors which will cause a crack to propagate including creep, cyclic stress, temperature, and aggressive environments. For example during the operation of a turbine the rotor blades are subjected to the simultaneous action of centrifugal and vibration mechanical loading and thermal fatigue. The aggressive gaseous environment can also cause a defect to grow in size. So the conditions under which different components operate make the unfortunate combination

of fatigue, creep and environment unavoidable.

The construction of steam turbines, used in the electric power generation, as well, as the construction of steam generation plants, is in general based on low alloy steels. Nickel base superalloys are used extensively in gas turbine engines used in the aircraft industry, for the construction of discs, turbine blades and vanes.

The integrity of welded components operating at high temperatures is of major importance in both fossil fuel and nuclear power plant. A problem associated with welds in industrial components is the problem of the Heat Affected Zone (H.A.Z.) cracking. The H.A.Z. cracking is a result of the precipitation of alloy carbides, which raise the creep strength of the matrix but leave the grain boundary area weak and the material relatively brittle (Myers and Price (1977), Ellis et. al. (1982)).

The main attention in this thesis is a description of crack growth in terms of fracture mechanics concepts. In fracture mechanics the component containing the crack can be viewed as a continuum, and external loading parameters can be used to characterize the crack growth. However a fracture model has been developed which characterizes crack growth, by means of the local damage zone at the crack tip.

The aim of this thesis is to investigate the contribution of some of the factors that can affect the problem of crack growth at high temperatures, under a range of conditions. For this purpose combined experimental, analytical and numerical methods are applied to a range of materials of practical interest.

Tests have been carried in air under static and cyclic conditions and under conditions to simulate thermal fatigue. Characterising parameters to correlate the crack growth data have been evaluated using experimental, Finite Element (F.E.) and Boundary Integral Equation (B.I.E.) methods. Models have been derived so that the correlating parameters can be used to predict crack growth rates.

The experimental evaluation of the characterising parameters requires the measurement of the response of the material during crack growth. This response can be

very complex as there are a number of different factors that can affect it.

If the response of the material during crack growth can be predicted using numerical methods and, or, analytical models then the results from laboratory specimens can be used to predict crack growth rates in practical situations and so the usable life of industrial components.

CHAPTER 2

MICROMECHANISMS OF FRACTURE AND CREEP DEFORMATION

2.1 INTRODUCTION

When a cylindrical bar of a crystalline solid is pulled in tension, it may fail in one of several ways. It may for example, fail by excessive deformation, cleavage or brittle intergranular fracture. At high temperatures, creep processes may intervene.

When a material is subjected to a stress state other than simple tension (for example the stress state at the tip of a propagating crack), the ranges of dominance of the individual mechanisms are shifted by this altered stress-state but the mechanisms themselves do not change. The particular mechanism determines whether the material is tough or brittle, or how fast (under given loading conditions) a fatigue crack propagates through it (Ashby and Tomkins (1979)).

Only monotonic loading is considered in this chapter. Cyclic loading and fatigue failures are examined later in chapter 7.

2.2 MICROMECHANISMS OF FRACTURE

2.2.1 FRACTURE OF THE IDEAL STRENGTH

The stress which will overcome the interatomic forces in a perfect crystal, causing it to separate on a plane normal to the stress axis, defines its upper limiting strength. (The ideal strength appears as a horizontal line coincident with the top of the diagram in fig. 2.1). Calculations by Kelly et. al. (1967) and Macmillan (1972) are in general agreement that an adequate level of accuracy for the ideal strength is:

$$\sigma_{ideal} = \left[\frac{2 E \gamma_s}{\pi b} \right]^{1/2} \frac{E}{10} \qquad (2.1)$$

where γ_s is the surface free energy, E is Young's Modulus and b is the atomic size. Fracture occurs when the maximum principal stress exceeds σ_{ideal}.

2.2.2 CLEAVAGE AND BRITTLE INTERGRANULAR FRACTURE

Almost all crystalline solids fail by cleavage if the temperature is sufficiently low, certain f.c.c. metals and their alloys appear to be the only exceptions. Cleavage can be (see figure 2.2): a) Due to a pre-existing crack "cleavage 1". The failure is almost brittle, and well below general yield. b) Due to a crack nucleated by slip or twinning, below general yield " cleavage 2" (Gandi and Ashby (1979)), this failure is almost brittle and c) we can have cleavage after general yield, with plastic strains 1-10% preceding fracture. Here plasticity is sufficient to blunt small pre-existing cracks (Gandi and Ashby (1979)). General plasticity or grain boundary sliding then nucleates a larger boundary crack or causes a pre-existing crack to grow in a stable manner, until its increased length, coupled with the higher stress caused by work-hardening, cause it to propagate unstably as a cleavage crack. This is referred to as "cleavage 3". Cleavage failure is a transgranular failure (see figure 2.3a).

The same type of failures can be possible but with separation along grain boundaries (figure 2.3a). This type of failure is refer to as "Brittle intergranular fracture (1,2 or 3)" (see figure 2.2).

If there is a delicate balance between the stress required to cause a crack to propagate by cleavage and that required to cause brittle separation along grain boundaries, the crack path can switch from one mode of failure to another.

2.2.3 DUCTILE FRACTURE AT LOW TEMPERATURE

When polycrystalline solids do not cleave they may fail in a ductile, transgranular way. Holes nucleate at inclusions, further plasticity makes them grow, and when they are large enough, or when the specimen itself becomes mechanically unstable, they coalesce, and the material fractures (Brown and Embury (1973), Goods and Brown (1979)).

Ductile fracture usually follows a transgranular path (figure 2.3b). But if the density of inclusions, or of pre-existing holes is higher on grain boundaries than it is

within the grains, then the fracture path may follow the boundaries, giving a fibrous, or ductile intergranular fracture as it is sketched in figure 2.3b. The region of dominance of this mechanism may be seen in figure 2.2.

At temperatures above 0.3 T_m metals creep. Several fracture mechanisms now appear.

2.2.4 TRANSGRANULAR CREEP FRACTURE

Transgranular creep fracture is merely the adaptation to the creep regime of low-temperature ductile fracture. Holes nucleate at inclusions within the grains and grow as the material creeps, until they coalesce to give a transgranular fracture path (see figure 2.3d). Although the stages of fracture are parallel to those described for ductile fracture their progress is modified, because, since the material is creeping, the stress within it tends to be lower than before (see figure 2.2) and nucleation may thereby postponed to larger strains. Also the strain-rate dependence of creep can stabilize flow and thereby postpone the coalescence of voids.

2.2.5 INTERGRANULAR CREEP-CONTROLLED FRACTURE

At lower stresses and larger times-to-fracture, a transition from transgranular to intergranular fracture is observed (see figure 2.2). Within this new regime, grain boundaries slide, wedge-cracks or voids grow on boundaries lying roughly normal to the tensile axis (see figure 2.3c). The fracture is controlled by power law creep (Crossman and Ashby (1975)).

2.2.6 PURE DIFFUSIONAL FRACTURE

When the temperature is high to permit diffusion and the stress so low that power law creep is negligible, holes on grain boundaries in stressed solids can grow by diffusion (Raj and Ashby (1975)). During diffusion matter flows out of the holes and deposits onto the boundary causing the grains on either side to move apart.

2.2.7 RUPTURE.

If no other fracture mechanism intervenes, a material pulled in tension ultimately becomes mechanically unstable. Deformation becomes localised and continues until the cross-section has gone to zero (see figure 2.3e), when the material is said to rupture (Burke and Nix (1975)). Rupture involves large reductions of area, and it can be thought at the tensile failure mode which appears when all other modes are suppressed. It requires that the nucleation of internal voids is suppressed, or if they nucleate, that they do not coalesce. It is commonly observed at high temperatures $>0.6T_m$ when dynamic recovery recrystallisation suppresses void nucleation.

Fig. 2.2 shows a fracture-mechanism map for tungsten tested in tension where all the mechanisms mentioned above are possible.

2.3 THE CREEP PHENOMENON

2.3.1 GENERAL SHAPE OF THE CREEP CURVE

Creep is a time-dependent deformation of a solid. The deformation characteristics of creep may be shown by strain-time curves plotted at constant temperature and load.

The most general shape of creep curve is shown in figure 2.4. Immediately upon loading, there is an elastic (plus, possibly an instantaneous plastic) strain and then three main regions. The first region is known as the primary creep region. This is a region of decreasing creep rate caused by work hardening, i.e. dislocation motion becomes more difficult. The second region is known as the secondary creep region. This is a region of constant creep rate, where the rate of work hardening is balanced by the rate of recovery. The third region known as the tertiary creep region is associated with a period of accelerated creep rate which ends in failure.

The general relationship between stress σ and creep strain ε is:

$$\varepsilon = \sum_{i=1}^{i=3} C_i \sigma^{n_i} F_i(t) \qquad (2.2)$$

Equation (2.2) holds for all stages of creep. C_i and n_i are material constants and $F_i(t)$ is a function of time. The values of C_i, n_i, $F_i(t)$ are different for the different stages of creep. A simple relationship between stress σ and creep strain ε is:

$$\varepsilon = \sum_{i=1}^{i=3} C_i \sigma^{n_i} t^{m_i} \qquad (2.3)$$

where $m_i < 1$ for primary creep, $m_i = 1$ for secondary creep and $m_i > 1$ for tertiary creep.

The cause of fracture is directly related to the growth and coalescence of cavities which were initiated in the secondary region. The tertiary creep is associated with necking cracking and overaging (metallurgical instability).

In general isolated cavities start to form in the material during the secondary creep stage and then they become oriented normal to the maximum principal tensile stress axis. When this happens tertiary creep takes over and the cavities link together to form microcracks with result the final failure.

Creep strength is sensitive to grain size, alloying additions, grain boundary precipitates and heat treatment. Larger grains are usually stronger but more brittle.

2.3.2 STRESS DEPENDENCE OF THE STEADY STATE CREEP RATE

Under most circumstances, the secondary creep rate, $\dot{\varepsilon}_s$, is proportional to a power of the stress σ. The relationship is generally attributed to Norton (1929) and has the form:

$$\dot{\varepsilon}_s = C \sigma^n \qquad (2.4)$$

where C and n are material constants independent of stress. Various workers, as summarized by Garofalo (1965), have concluded that for annealed metals and alloys, n ranges from 1 to 7, but n values as high as 20 are not uncommon in engineering alloys.

However there is experimental evidence that suggests a stronger dependence (for example exponential) under conditions of high stress and temperature. Some

investigators have interpreted this effect as a stress dependence on the creep exponent n, or more simply and generally as "power law breakdown" (Finnie and Heller (1959), Garofalo (1965)).

A hyperbolic-sine stress dependence of the form:

$$\dot{\varepsilon}_s = C\left[\sinh(\sigma/\sigma_0)\right]^n \qquad (2.5)$$

has been proposed by Finnie and Heller and Garofalo which reduces at low stresses to a power law creep and at high stresses to an exponential law. Constitutive relations for hyperbolic-sine law creep are given by Bassani (1983). However little work has been done based on this model.

In summarizing various stress functions, Penny and Marriot (1971) conclude that, due to its simplicity in applications equation (2.4) is to be preferred, whilst equation (2.5) should be used in predicting long term creep from high stress data. However given the large extent of scatter found in the creep data (2.4) will always give a good approximation.

2.3.3 EFFECT OF TEMPERATURE

Although creep deformation does occur at low temperatures, for most practical purposes it is of little significance between the absolute zero in temperature and 0.3 T_m. Creep deformation is a thermally-activated process controlled by the Arrhenius equation:

$$\dot{\varepsilon} = A\exp(-Q/RT) \qquad (2.6)$$

where Q is the activation energy for creep, T the absolute temperature, R the gas constant and A is a constant which is a function of stress. Thus increasing temperature as it can be seen from (2.6) produces an exponential increase in creep rate.

Garofalo (1965) denotes the activation energy in (2.6) as ΔH_i, this being the activation energy for the controlling creep process. He states that the quantity normally determined is not ΔH_i, but ΔH_c which is the apparent activation energy. The difficulty in determining ΔH_i is due to the complexity of the creep process, which often involves

several mechanisms operating simultaneously. Even when it is possible to establish the dominating mechanism, it is still difficult to determine ΔH_i because the exact function, giving dependence of creep rate on temperature and stress is not usually known for sufficiently wide ranges in each of these variables. So the activation energy generally referred to as Q in (2.6), should, accurately, be equivalent to ΔH_c, or apparent activation energy, used by Garofalo.

Above temperatures of about $0.5T_m$ the activation energy for creep of most pure metals are very close to the activation energies for atomic self diffusion. For alloys, creep activation energies usually equal the activation energy for diffusion of one of the elements (Garofalo (1965)). The effect of increasing temperature and stress on creep strain is shown schematically in figure 2.5.

2.3.4 EMPIRICAL FORMULAS FOR THE RUPTURE TIME IN THE CREEP REGIME.

There are several empirical formulas in use which describe the dependence of the rupture time on stress and temperature. These formulas include the Dorn parameter (Orr, Sherby and Dorn (1954)), and, the Larson-Miller parameter (Larson and Miller (1952)). Orr, Sherby and Dorn (1954) suggest that the rupture time t_R, stress σ and the temperature T are related by

$$\theta(\sigma) = t_R \exp(-Q/RT) \qquad (2.7)$$

Similar in principle but different in its functional form is the approach of Larson and Miller (1952) who assume the following relation between lifetime stress and temperature

$$P(\sigma) = (20 + \log t_R)\, T / 1000 \qquad (2.8)$$

where t_R is in hours and T is the absolute temperature. The Larson-Miller parameter $P(\sigma)$, is widely used to characterise the rupture behaviour of engineering materials.

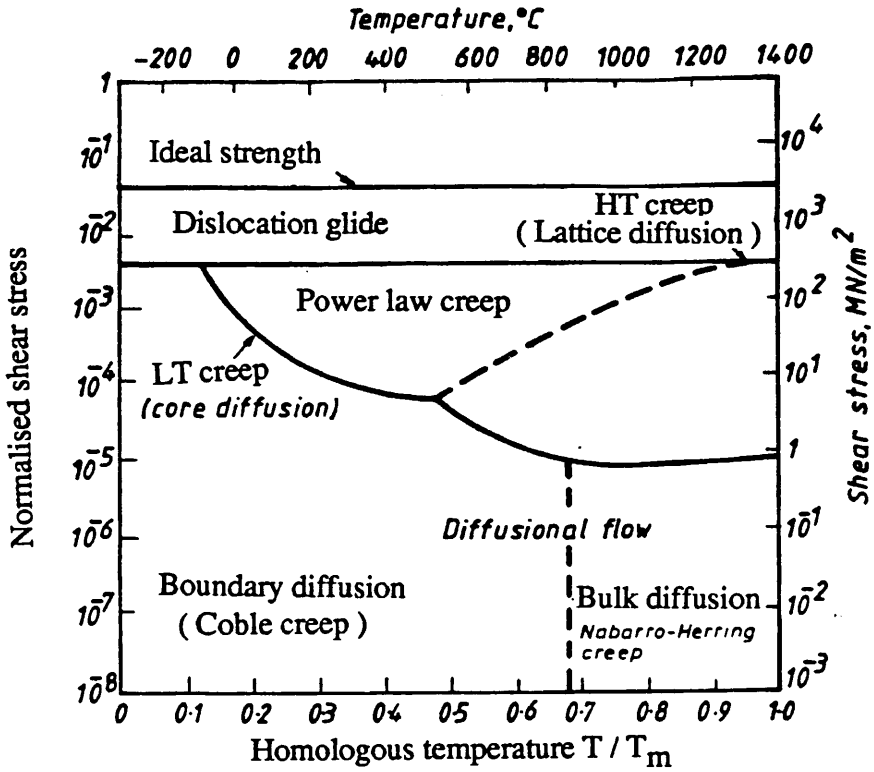


Figure 2.1 Deformation mechanism map for Nickel with a grain size of 1mm

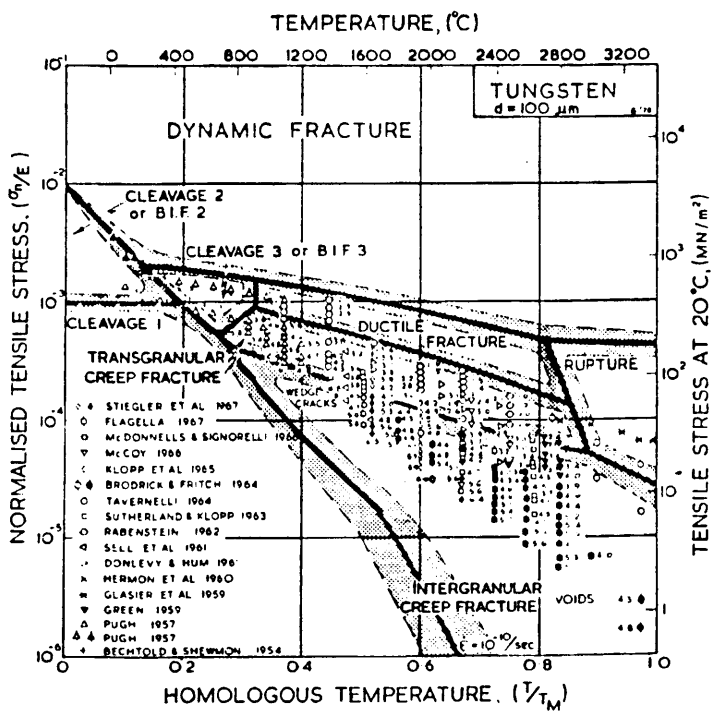


Figure 2.2 A fracture mechanism map for tungsten tested in tension with a grain size of 100μm. (Ashby 1977).

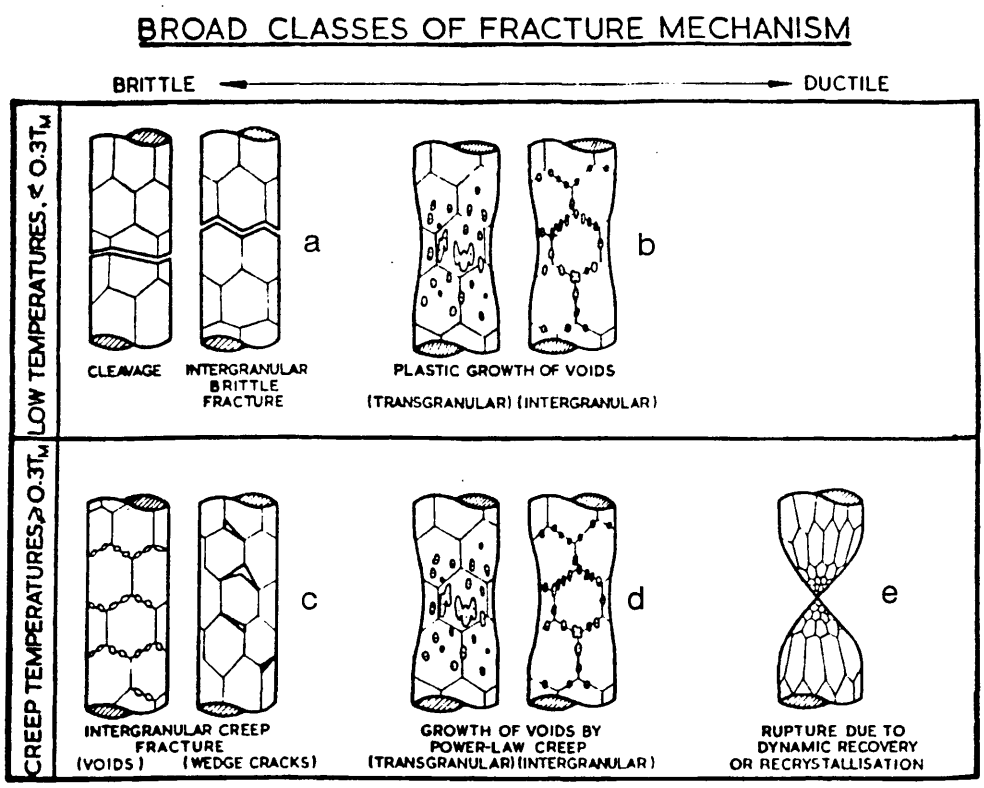


Figure 2.3 Classification of fracture mechanisms.

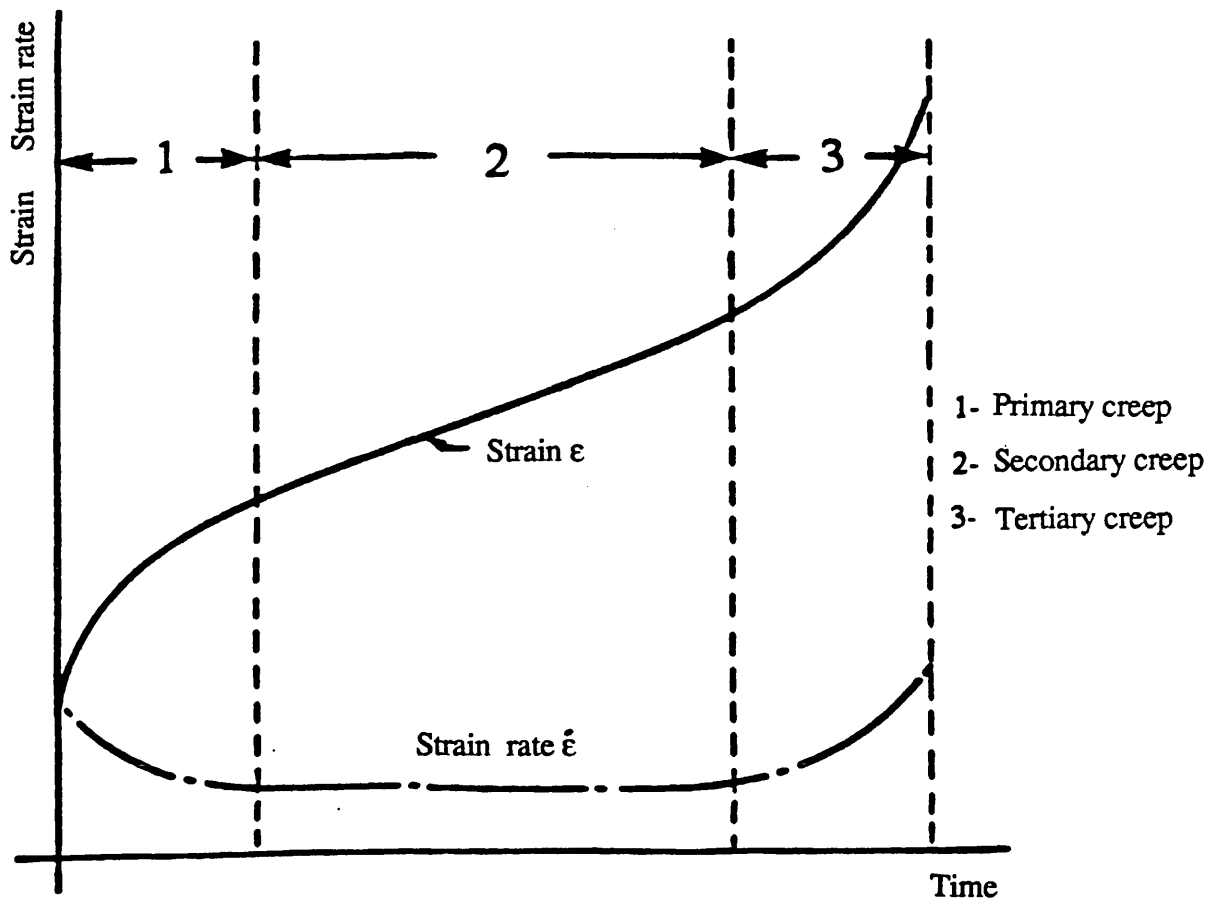


Figure 2.4 A typical creep curve.

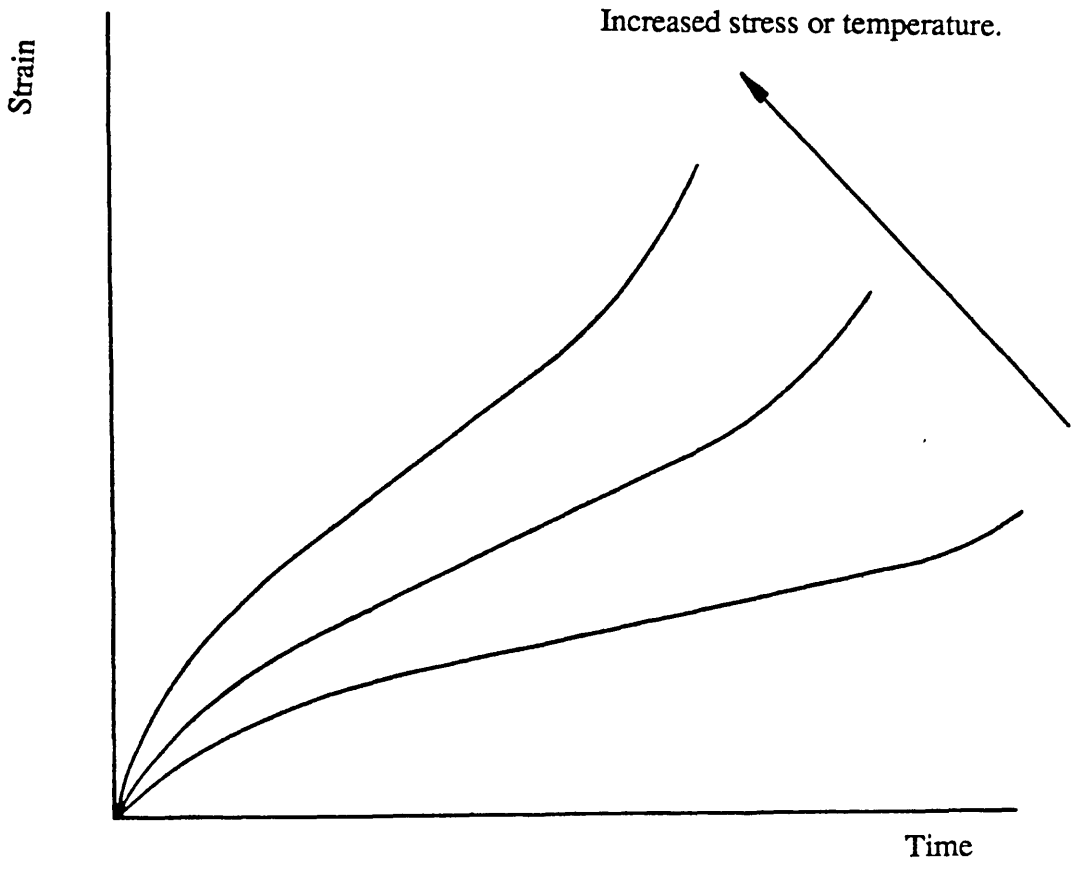


Figure 2.5 Effect of increased stress or temperature on the shape of the typical creep curve (strain on loading omitted)

CHAPTER 3

CONTINUUM DAMAGE MECHANICS

3.1 INTRODUCTION

Continuum damage mechanics models the creep failure mechanism by describing failure by a local rupture process. When a solid deforms at high temperatures holes or cracks may nucleate and propagate inside the solid. Its grain size may increase because of grain growth or decrease because of dynamic recrystallisation. Precipitates within it may coarsen or dissolve, or the microstructure may, in some other way be altered. All these changes are referred to as creep damage. The damage usually accelerates the creep-rate which in turn accelerates the rate of damage until the specimen or component fails. The tertiary part of a uniaxial creep curve is a direct result of the coupling of creep-rate and damage-development. Voids can grow by grain-boundary diffusion, by surface diffusion, by power law creep, and by any combination of these.

3.2 PHENOMENOLOGICAL RELATIONS.

Kachanov (1958), Rabotnov (1969) and Lerckie and Hayhurst (1974), have developed creep-damage mechanics as a continuum approach to the analysis of creep fracture.

A very general assumption permitting formulation of the constitutive equations of creep is that the creep rate at a given instant is determined by the stress, the temperature, and the structural state of the material, the last being defined by a certain number of structural parameters q_i .

$$\dot{\varepsilon} = \frac{d\varepsilon}{dt} = f(\sigma, T, q_i) \qquad (3.1)$$

The rate of change of these structural parameters should be described by a system of kinetic equations:

$$\dot{q}_i = g(\sigma, T, q_i) \qquad (3.2)$$

One of these parameters denoted as ω, is a state variable used as a measure of the deterioration or damage in the material. It may be represented by the fractional loss in area due to voiding as

$$\omega = 1 - \frac{A_R}{A_o} \qquad (3.2a)$$

where A_R is the area after some damage and A_o the initial area. The value of ω increases monotonicaly from zero in initially damage free material to unity at failure. Assuming that ω is a single structural parameter that describes the behaviour of the body up to the moment that rupture occurs the creep equations become:

$$\dot{\omega} = \frac{d\omega}{dt} = g(\sigma, T, \omega) \qquad (3.3)$$

$$\dot{\varepsilon} = \frac{d\varepsilon}{dt} = f(\sigma, T, \omega) \qquad (3.4)$$

Rabotnov (1969) suggested power law expressions for the functions g ( ) and f ( ) under uniaxial creep to give:

$$\dot{\omega} / \dot{\omega}_o = (\sigma/\sigma_o)^{\nu} (1/(1-\omega))^{\eta} \qquad (3.5)$$

$$\dot{\varepsilon} / \dot{\varepsilon}_o = (\sigma/\sigma_o)^{n} (1/(1-\omega))^{n} \qquad (3.6)$$

where $\dot{\varepsilon}_o$, $\dot{\omega}_o$, σ_o, n, ν, η are material constants. When the material is undamaged, ω=0, and equation (3.6) reduces to Norton's law. Rupture will occur when ω=1. Using this condition, integration of (3.5) gives a relation between the rupture time t_R and the applied stress σ as:

$$t_R = \frac{1}{\dot{\omega}_o (1+\eta)} \left[\frac{\sigma_o}{\sigma} \right]^{\nu} \qquad (3.6a)$$

Integration of (3.5) and (3.6) for constant stress yields:

$$\varepsilon = \varepsilon_R \left[1 - (1-\tau)^{1/\lambda} \right] \qquad (3.6b)$$

$$\omega = 1 - \left[1 - \tau \right]^{1/(\eta+1)} \qquad (3.6c)$$

where $\tau = t/t_R$, $\lambda = (\eta + 1)/(\eta + 1 - n)$, and ε_R is the rupture strain given by:

$$\varepsilon_R = \dot{\varepsilon}_o \left[\frac{\sigma}{\sigma_o} \right]^n t_R \lambda \qquad (3.6d)$$

The form of tertiary creep curve that results from this approach is shown in figure 3.1.

3.3 MECHANISTIC MODELS

In the phenomenological approach, the precise nature of the damage is not specified. In the mechanistic approaches, the individual voids are identified and models are proposed to describe their growth.

One such model was suggested by Edward and Ashby (1979) and has been extended by Cocks and Ashby (1980, 1982b). This model will be examined in detail.

Figure 3.2 considers an isolated cylindrical element of diameter 2l (the void spacing) and height λ (the grain size) centred on a grain-boundary void of diameter 2a. The damage fraction is then:

$$\omega = (a/l)^2 \qquad (3.7)$$

Using bounding theorems Cocks and Ashby (1980) demonstrated that the axial creep rate in a uniaxial tension specimen containing this void is given by:

$$\dot{\varepsilon} / \dot{\varepsilon}_o \leq (\sigma/\sigma_o)^n \left[1 + \frac{2a}{\lambda} \left(\frac{1}{(1-\omega)^n} - 1 \right) \right] \qquad (3.8)$$

When applied to the composite cylinder of figure 3.4, the result is intuitively obvious. The section A of the cylinder creeps at a rate

$$\dot{\varepsilon} / \dot{\varepsilon}_o = (\sigma/\sigma_o)^n \qquad (3.9)$$

while the remaining section B, constituting a fraction $2a/\lambda$ of the cylinder, creeps faster

(by a factor $1/(1-\omega)^n$ because the stress acting on it is larger, by a factor $1/(1-\omega)$).

If the defect-free material deforms in secondary creep according to (3.9) it can be shown from simple geometry, by relating the change of volume of the cylinder with the rate of growth of the area fraction of voids, that the damage rate can be expressed as:

$$\dot{\omega}/\dot{\varepsilon}_0 = (\sigma/\sigma_0)^n \left[\frac{1}{(1-\omega)^n} - (1-\omega) \right] \qquad (3.10)$$

Smith and Webster (1985) extended the analysis to non-spherical defects, for voids having the shape of oblate ellipsoids, as illustrated in figure 3.3.
Using the same bounding conditions equation (3.8) can be written for an oblate ellipsoid (figure 3.3) as:

$$\dot{\varepsilon} / \dot{\varepsilon}_0 \leq (\sigma/\sigma_0)^n \left[1 + \frac{2\alpha a}{\lambda} \left(\frac{1}{(1-\omega)^n} - 1 \right) \right] \qquad (3.11)$$

As with the phenomenological rate equations integrating (3.10) and (3.11) the damage is given by:

$$\omega = 1 - \left[1 - \Omega_R^{1-\tau} \, \Omega_i^{1-\tau} \right]^{\frac{1}{n+1}} \qquad (3.12)$$

where $\Omega_R = 1 - (1-\omega_R)^{n+1}$, $\Omega_i = 1 - (1-\omega_i)^{n+1}$, $\tau = t/t_R$ and

$$t_R = \frac{1}{\left[\dot{\varepsilon}_0 (\sigma/\sigma_0)^n \right]^{n+1}} \ln\left(\frac{\Omega_R}{\Omega_i}\right) \qquad (3.13)$$

ω_R and ω_i refer to the final and initial values of the void size.

The strain is given by:

$$\varepsilon = \dot{\varepsilon}_0 (\sigma/\sigma_0)^n t_R \left[\tau' + \frac{2l}{\lambda} \sum \right] \qquad (3.14)$$

where

$$\sum = \int_0^{\tau'} \left[\frac{\sqrt{\omega}}{(1-\omega)^n} - \sqrt{\omega} \right] d\tau \qquad (3.15)$$

and ω has to be substituted from:

$$\dot{\varepsilon} / \dot{\varepsilon}_0 = (\sigma / \sigma_0)^n (1 / (1 - \omega))^n$$

The phenomenological and the mechanistic models require a knowledge of a number of material parameters to completely identify the material behaviour. These are tabulated in table 3.1 for each case.

A comparison of the growth of damage using the phenomenological and mechanistic expression can been made, if (3.6c) is re-established for $\omega=\omega_i$ at $t_i=0$ as:

$$\omega = 1 - (1 - \omega_i) \left[1 - \tau \right]^{1/(\eta+1)} \qquad (3.16)$$

The comparison of the growth of damage using the phenomenological and the mechanistic expressions (equations (3.16) and (3.12) respectively) is shown in figure 3.5, for $n=\nu=\eta$, and $\omega_i = 0.01$. Both models show similar behaviour at the final stages of damage accumulation but the phenomenological model predicts faster initial rate.

Typical failure ductilities can range from 0.001 for creep brittle materials (1/2CMV steel) to 0.45 for creep ductile materials (21/4CM steel)

A link between the damage and fracture mechanics is possible, and will be discussed in chapter 5.

TABLE 3.1

List of parameters required for uniaxial creep damage models

Phenomenological	Mechanistic
n	n
σ_o	σ_o
$\dot{\varepsilon}_o$	$\dot{\varepsilon}_o$
$\dot{\omega}_o$	ω_i
ν	ω_R
ε_R	t_i
t_R	t_R
	$2l / L$

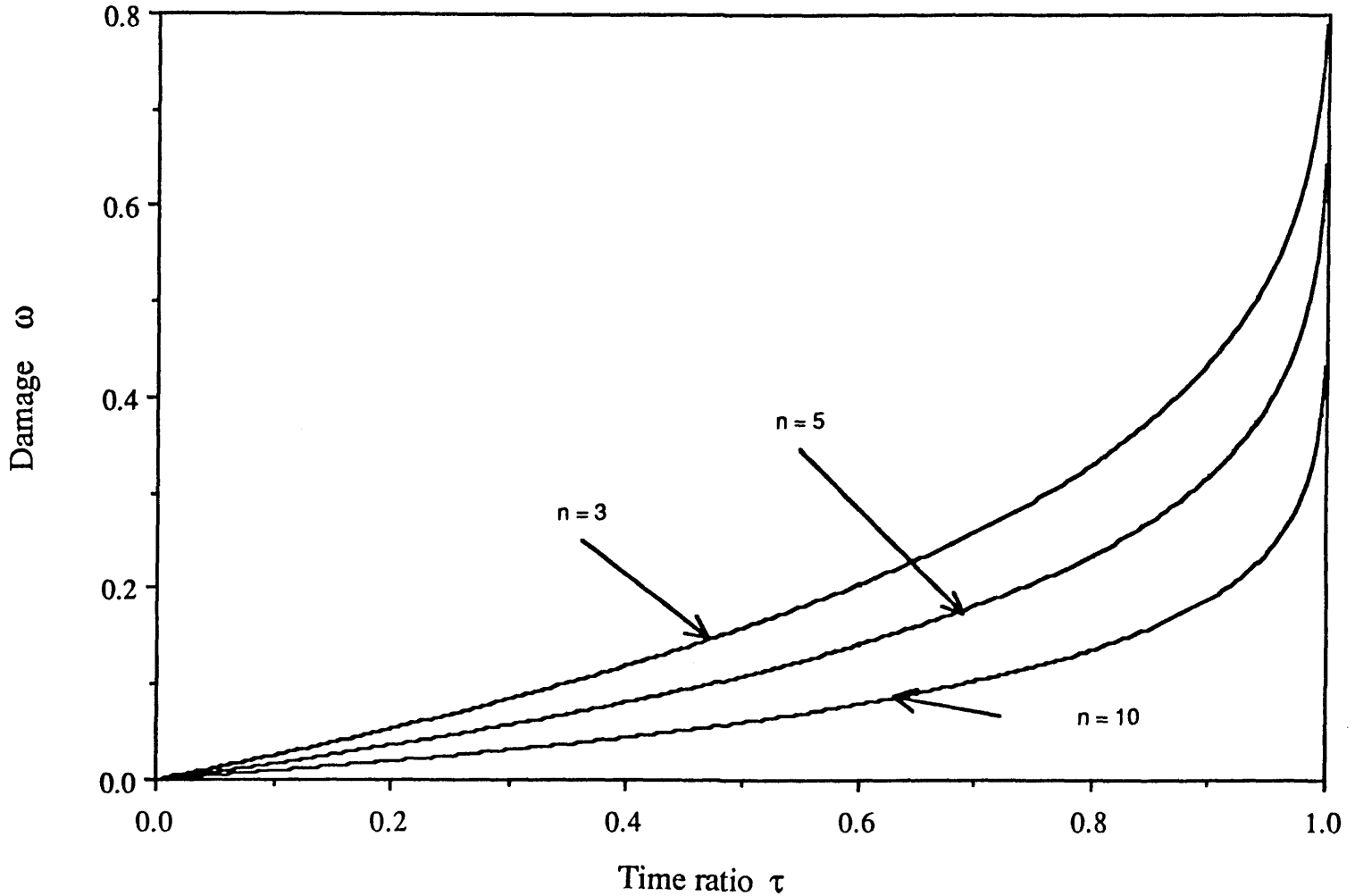


Figure 3.1 Damage variable as a function of the time ratio τ

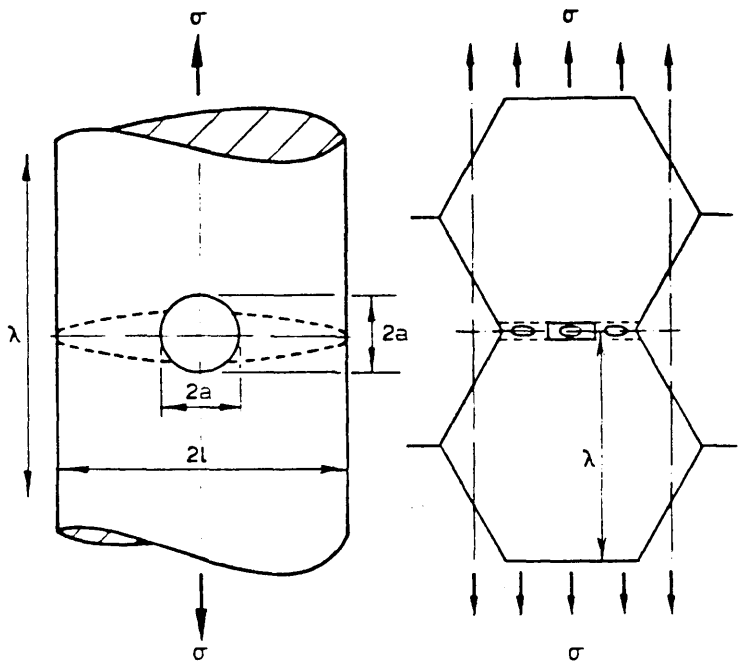


Figure 3.2 Schematic arrangement of grain boundary spherical voids.

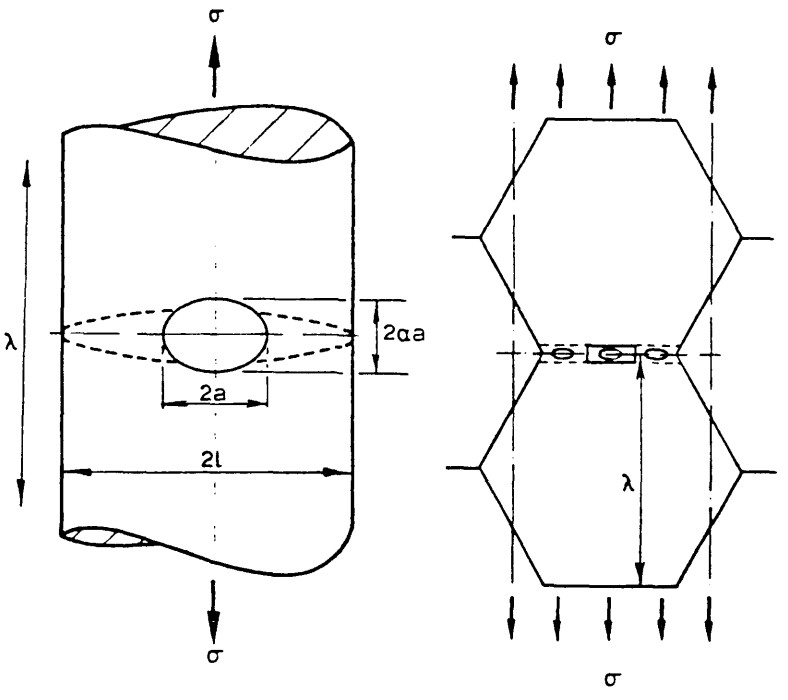


Figure 3.3 Schematic arrangement of grain boundary ellipsoidal voids.

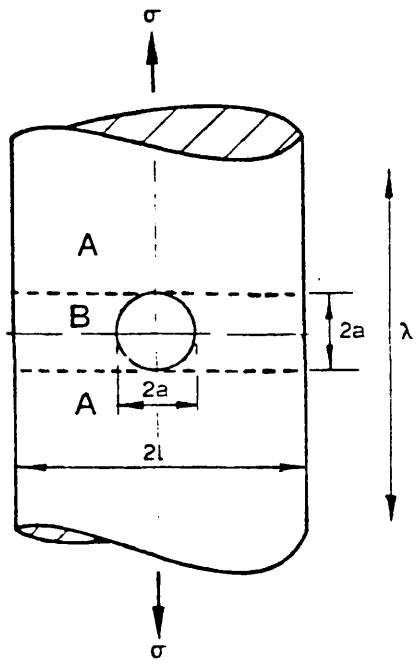


Figure 3.4 Composite cylinder used to evaluate bound on void growth rate.

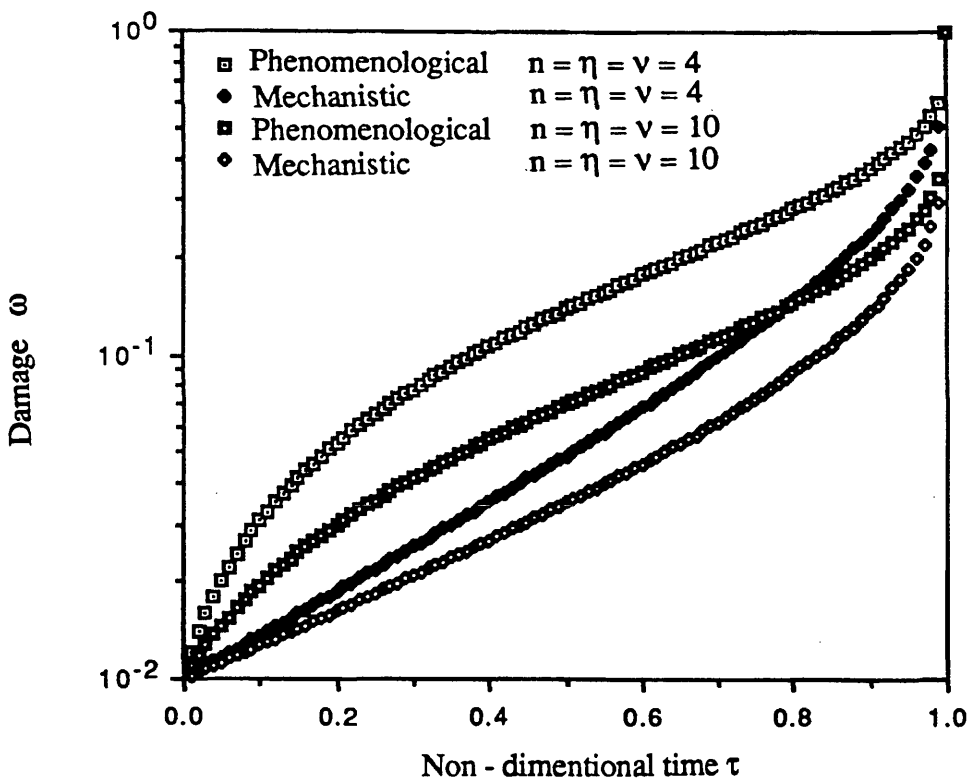


Figure 3.5 Comparison of the evolution of damage as a function of the time ratio $\tau = t / t_R$ for the phenomenological and mechanistic models.

CHAPTER 4

REVIEW OF FRACTURE MECHANICS CONCEPTS

4.1 INTRODUCTION

Fracture mechanics describes the fracture of material in terms of the laws of applied mechanics and the macroscopic properties of the material. It provides a quantitative treatment, which relates fracture strength to the applied load and structural geometry of a component containing defects.

Commonly the defect is replaced by an equivalent crack, so that the fracture strength can be assessed in terms of stress-strain conditions at the crack tip. Fracture mechanics then assumes that the influences of applied load upon crack extension can be represented in terms of certain parameters (usually only one) which characterize the stress-strain intensity near the crack tip.

Adjacent to the crack tip lies a region where damage accumulates. This region is termed the fracture process zone. The relevant continuum mechanics parameter to describe the crack tip behaviour will depend on the extent of deformation that occurs with cracking.

Linear Elastic Fracture Mechanics (L.E.F.M.) concepts will be relevant in cases where no plastic deformation is present, but it can also be used in cases where the degree of deformation is severely restricted with respect to the absolute size of the crack and component geometry.

Non Linear Elastic Fracture Mechanics concepts will be relevant in cases where extensive deformation and plasticity occur.

4.2 LINEAR ELASTIC FRACTURE MECHANICS

Linear elastic fracture mechanics (L.E.F.M.) is an approach to studying fracture based entirely on linear elastic theory. Attention will be restricted to through thickness cracks and the opening mode or Mode 1 of crack extension, which is associated with local displacements in which the crack surfaces move directly apart (figure (4.1a)), since these are the situations which have been examined most extensively at elevated temperatures.

Also Mode 1 crack growth is of most practical relevance as it takes place more easily than the forward sliding mode, Mode 2, and the parallel shear mode, Mode 3, (figures (4.1b) and (4.1c)).

4.2.1 THE STRESS INTENSITY FACTOR (K)

Consider a through thickness crack of length 2a (figure 4.2) subjected to a remote stress applied perpendicular to the crack plane.

The stresses at co-ordinates (r , θ) ahead of the crack tip are given by:

$$\sigma_{xx} = \frac{K}{\sqrt{2\pi r}} \cos\frac{\theta}{2}\left[1 - \sin\frac{\theta}{2}\sin\frac{3\theta}{2} + \ldots\ldots\ldots \right] \qquad (4.1)$$

$$\sigma_{yy} = \frac{K}{\sqrt{2\pi r}} \cos\frac{\theta}{2}\left[1 + \sin\frac{\theta}{2}\sin\frac{3\theta}{2} + \ldots\ldots\ldots \right] \qquad (4.2)$$

$$\sigma_{xy} = \frac{K}{\sqrt{2\pi r}} \cos\frac{\theta}{2}\left[\sin\frac{\theta}{2}\cos\frac{3\theta}{2} + \ldots\ldots\ldots \right] \qquad (4.3)$$

Equations (4.1) to (4.3) hold for stresses local to the crack tip.

Also $\sigma_{zz} = \nu (\sigma_{xx} + \sigma_{yy})$ for plane strain conditions (thick sections) and $\sigma_{zz} = 0$ for plane stress conditions (thin sections).

The parameter K, which defines the magnitude of the singularity at the crack tip for all stress components, is called the stress intensity factor. For an infinite plate with central crack 2a and applied stress remote from the crack σ it is found that :

$$K = \sigma\sqrt{\pi a} \qquad (4.4)$$

In general $$K = Y \sigma \sqrt{a} \qquad (4.5)$$

where Y is a non-dimensional factor, a function of the component geometry, and can be obtained for a selection of common test-piece geometries from reference handbooks, (e.g. Tada et. al. (1973), Rooke and Cartwright (1976)).

4.2.2 THE ENERGY RELEASE RATE (G)

An alternative approach by Griffith is in terms of the energy release rate G, where G is the energy required in extending a crack over a unit area.

Consider a body of thickness B containing an edge crack of length a (figure 4.2a). In figure 4.3 line OA represents the elastic load P versus load point displacement Δ. If at A the crack is allowed to extend by da, a line AA' will be traced. The line OA' will then represent the elastic load P versus load point displacement Δ for a crack of length a + da. Thus the shaded area dU is the energy available to extent the crack by an amount da. So G becomes:

$$G = \frac{dU}{B\,da} \qquad (4.6)$$

or if the compliance is defined as

$$c = \Delta / P \qquad (4.7)$$

then:

$$G = \frac{P^2}{2B}\,\frac{dc}{da} \qquad (4.8)$$

For crack extension at constant load P, G becomes:

$$G = \frac{P}{2B}\,\frac{d\Delta}{da} \qquad (4.9)$$

and for crack extension at constant displacement :

$$G = -\,\frac{\Delta}{2B}\,\frac{dP}{da} \qquad (4.10)$$

Irwin (1957) showed that for an infinite plate:

$$G = \frac{\sigma^2 \pi a}{E} \qquad (4.11) \qquad \text{for plane stress and}$$

$$G = \frac{\sigma^2 (1 - \nu^2) \pi a}{E} \qquad (4.12) \qquad \text{for plane strain.}$$

so that :

$$K^2 = E G \qquad (4.13) \qquad \text{for plane stress and}$$

$$K^2 = \frac{E G}{1 - \nu^2} \qquad (4.14) \qquad \text{for plane strain}$$

Thus G may also be used to characterize the elastic stress distribution around a crack tip. In the Griffith theory it is postulated that fracture takes place when K or G reach their corresponding critical values K_c or G_c respectively.

4.2.3 LIMITATIONS OF L.E.F.M.

According to the elastic field equations (4.1) to (4.3) infinitely high stresses exist at the crack tip. This, of, course, is inconsistent with the behaviour of real materials which tend to exhibit a yield stress beyond which they deform plastically. So there is always a plastic zone ahead of a crack tip. This fact, however, does not invalidate the methods of L.E.F.M. provided the extent of plasticity is small compared with the characteristic geometric dimension of the crack. Modifications of the L.E.F.M. analysis have been suggested to account for the size of the small plastic zone and several procedures have been proposed. They basically involve the "repositioning" of the crack tip. Irwin (1960) argued that the effect of the plastic zone is to make the crack to behave as if it were longer than its physical size. He suggested an effective crack length given by

$$a_{eff} = a + r_p \qquad (4.15)$$

where r_p is the plastic zone size, a measure of the extent of yielding ahead of the crack tip. It is given by:

$$r_p = \frac{1}{2\pi}\left[\frac{K}{\sigma_y}\right]^2 \qquad \text{for plane stress} \qquad (4.16a)$$

$$r_p = \frac{1}{6\pi}\left[\frac{K}{\sigma_y}\right]^2 \qquad \text{for plane strain} \qquad (4.16b)$$

where σ_y is the yield stress.

The accuracy of (4.16a) and (4.16b) depends on the yield criterion used, material work hardening characteristics and the value of Poisson's ratio. Although approximated as circular, the plastic zone is in fact dumb - bell shaped. Figure 4.4 shows the details of the crack repositioning to account for the crack tip plastic zone.

The application of these plastic zones becomes questionable if the spread of plasticity is extensive relative to the crack size. An elasto-plastic analysis would have to be employed then. The current testing standard for the determination of K_c (ASTM E399-74) requires that the thickness and the uncracked ligament of the test specimen should both exceed $2.5\,(K_c/\sigma_y)^2$. This means that, with Irwin's approximation, equation (4.15), the radius of the plastic zone r_p, may not exceed 2% of the specimen thickness or uncracked ligament.

4.3 NON LINEAR ELASTIC FRACTURE MECHANICS.

4.3.1 INTRODUCTION.

In practice because of plasticity and/or creep, the stresses local to the crack tip will be modified from those calculated assuming linear elastic behaviour. The case in the absence of creep deformation is considered first. For substantial plastic deformation K (and G) will cease to describe adequately the stresses local to the crack tip. In those circumstances it is necessary to resort to non-linear fracture mechanics concepts.

4.3.2 THE J INTEGRAL.

Consider an arbitrary contour Γ surrounding a crack tip in a two dimensional body of unit thickness (figure 4.5). The contour starts from the lower flat notch surface and finishes on the upper flat notch surface.

Rice (1968a) defined the J contour integral around Γ for a crack aligned in the x-direction to be:

$$J = \int_{\Gamma} W\,dy - T_i \frac{\partial u_i}{\partial x}\,ds \qquad (4.17)$$

where W is the strain energy density and is given by:

$$W = \int \sigma_{ij}\,d\varepsilon_{ij} \qquad (4.18)$$

where σ_{ij} and ε_{ij} are the stress and strain tensors respectively, T_i is the traction vector normal to Γ, u_i is the displacement vector and ds is the increment of distance along Γ.

Using Green's theorem it can be shown that J evaluated around a closed loop surrounding a crack is zero. Thus J is path independent.

The J concept can be used to characterize the stress state ahead of the crack tip in the same way as G for linear elasticity, but is strictly valid only for non linear elastic material. Although no proof exists for the path independence of J for materials following the more realistic incremental theory of plasticity, the fact that can be readily

evaluated both experimentally and numerically makes a critical J value an attractive elastoplastic fracture criterion (see, for example, Begley and Landes (1972)).

Rice and Rosengren (1968) and Hutchinson (1968) have shown that the J integral can be considered to be a measure of the stress and strain singularities at the crack tip in a power law hardening material. This type of singularity is referred to as the HRR singularity.

If the material constitutive relation can be written as:

$$\frac{\varepsilon}{\varepsilon_y} = \left[\frac{\sigma}{\sigma_y} \right]^N \qquad (4.19)$$

in simple tension, this may be generalized for a multiaxial stress state by the expression:

$$\frac{\varepsilon_{ij}}{\varepsilon_y} = \frac{3}{2} \left[\frac{\sigma_e}{\sigma_o} \right]^{N-1} \frac{\sigma_{ij}'}{\sigma_y} \qquad (4.20)$$

where the equivalent stress σ_e is given by:

$$\sigma_e^2 = \frac{3}{2} \sigma_{ij}' \sigma_{ij}' \qquad (4.21)$$

and the deviatoric stress by :

$$\sigma_{ij}' = \sigma_{ij} - \frac{1}{3} \sigma_{kk} \delta_{ik} \qquad (4.22)$$

The stress and strain fields at co-ordinates (r , θ) ahead of a stationary crack for a material obeying power law hardening are given by :

$$\frac{\sigma_{ij}}{\sigma_y} = \left[\frac{J}{I_N \sigma_y \varepsilon_y r} \right]^{\frac{1}{N+1}} \tilde{\sigma}_{ij} (\theta , N) \qquad (4.23)$$

$$\frac{\varepsilon_{ij}}{\varepsilon_y} = \left[\frac{J}{I_N \sigma_y \varepsilon_y r} \right]^{\frac{1}{N+1}} \tilde{\varepsilon}_{ij} (\theta , N) \qquad (4.24)$$

where $\tilde{\sigma}_{ij}$ (θ, N) and $\tilde{\varepsilon}_{ij}$ (θ, N) are non dimensional functions, chosen so that $\tilde{\sigma}_e$(θ, N) and $\tilde{\varepsilon}_e$(θ, N) have a maximum value of unity, and they have been plotted by Hutchinson (1968), for various N from 3 to 13 and for plane stress and plane strain conditions.The

factor I_N, has been tabulated by Hutchinson (1968) and is given approximately by McKlintock (1977) as:

$$I_N = 10.3\,(0.13 + 1/N)^{1/2} - 4.8/N \qquad (4.25)$$

for plane strain conditions.

Rice (1968b) showed that J can be obtained from the load displacement diagram of a cracked body in the same way as G.

Following the same arguments as for G from figure 4.6 :

$$J = \frac{dU}{Bda} \qquad (4.26)$$

where dU is the shaded area in figure 4.6. It may be shown using Ilyushin's theorem (Ilyushin (1946)) that for a power law hardening material, the stress/deformation relation will take the same form for all points in the body. The stress/displacement relation can then be written as :

$$\Delta = C_N P^N \qquad (4.27)$$

where C_N can be regarded as the plastic compliance of the cracked body, and will depend in general on crack length.

By differentiating (4.27) and substituting in (4.26) it may be shown that:

$$J = \frac{P^{N+1}}{(N+1)B}\,\frac{dC_N}{da} \qquad (4.28)$$

This equation is valid for any path AA'. For crack extension at constant load this reduces to:

$$J = \frac{P}{(N+1)B}\,\frac{d\Delta}{da} \qquad (4.29)$$

and for crack extension at constant displacement:

$$J = -\frac{N\Delta}{(N+1)B}\,\frac{dP}{da} \qquad (4.30)$$

When N=1 these equations reduce to the corresponding elastic equations. So in the case of linear elastic materials :

$$J = G = K^2/E' \qquad (4.31)$$

where $E' = E$ (4.32) for plane stress conditions

and $E' = E / (1 - \nu^2)$ (4.33) for plane strain conditions

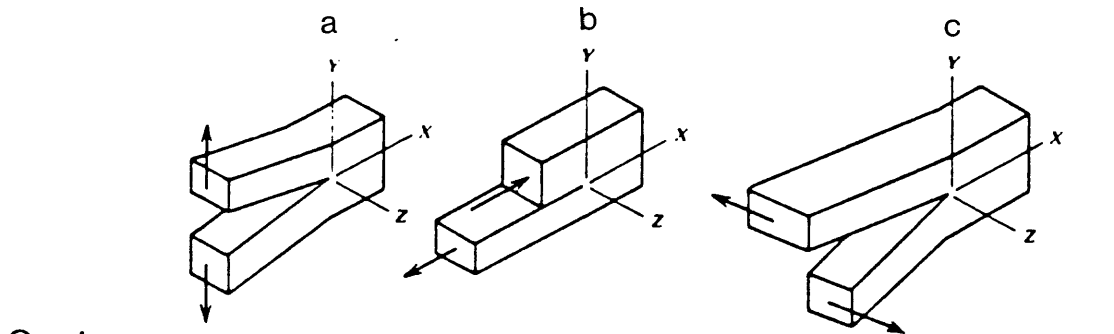


Figure 4.1 The three modes of failure.

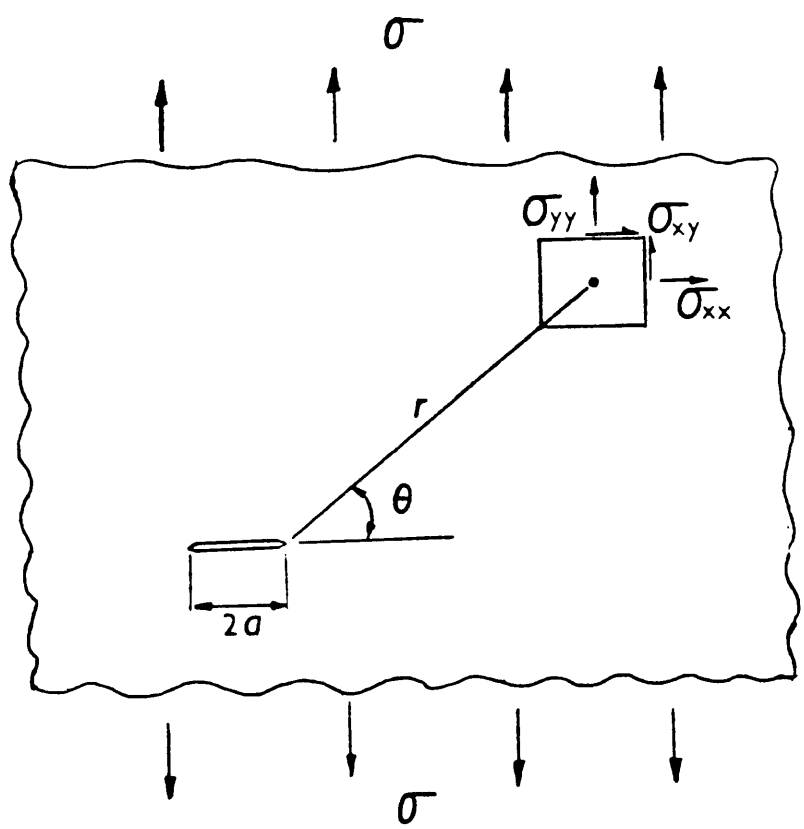


Figure 4.2 Stress distribution ahead of a crack tip.

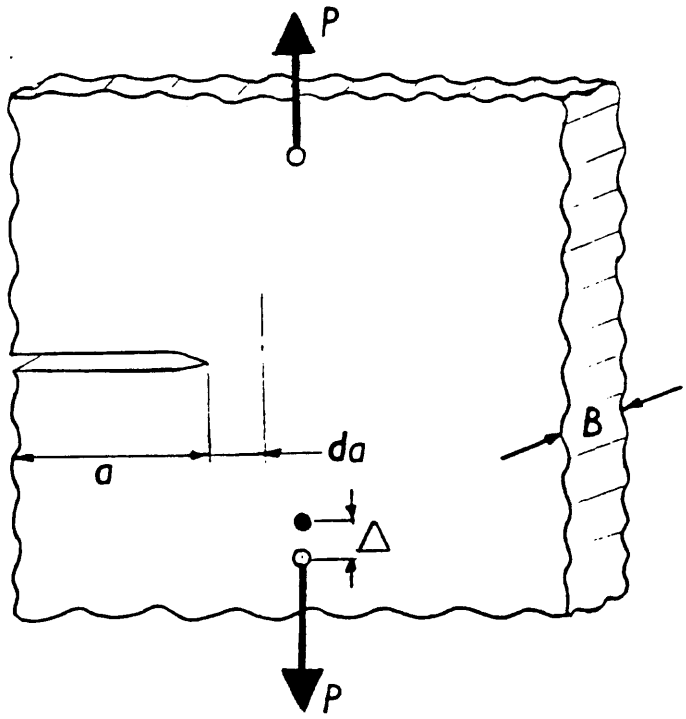


Figure 4.2a Loading of a cracked body.

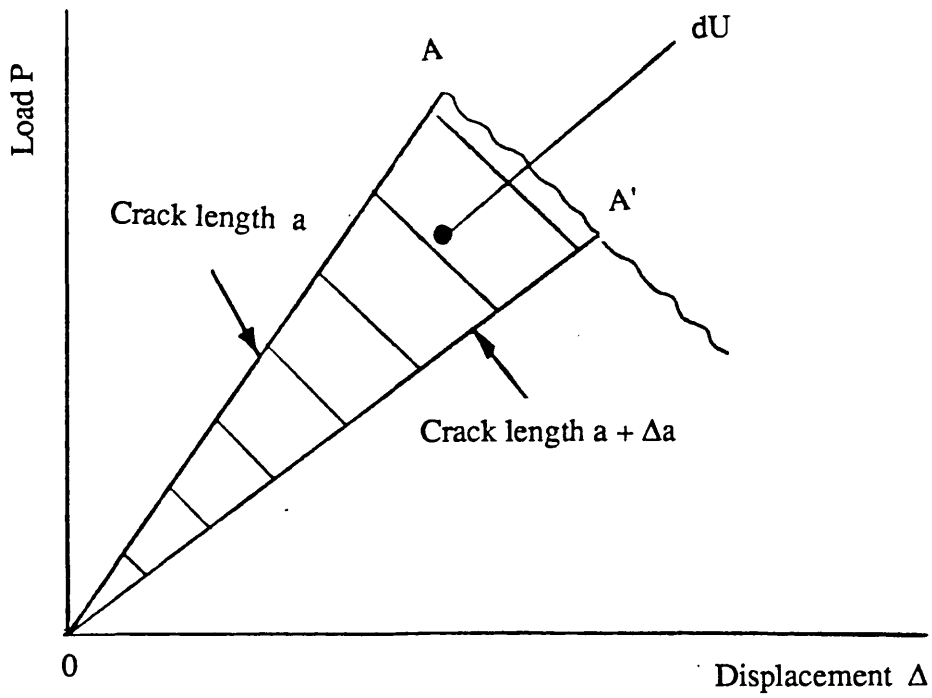


Figure 4.3 Elastic loading curves for crack lengths a and a+Δa under constant loading conditions.

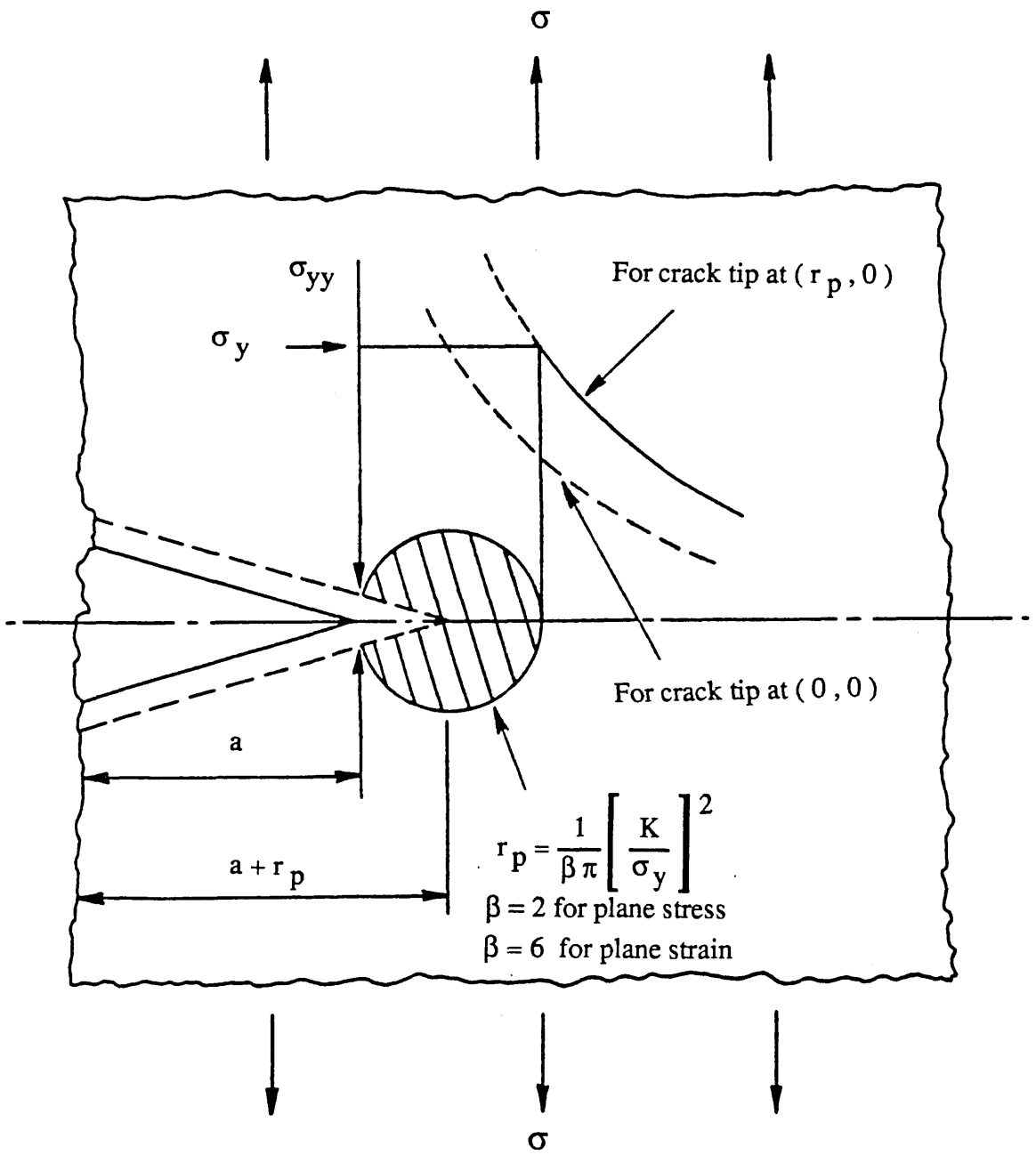


Figure 4.4 Details of crack border re-positioning to account for crack tip plastic zone.

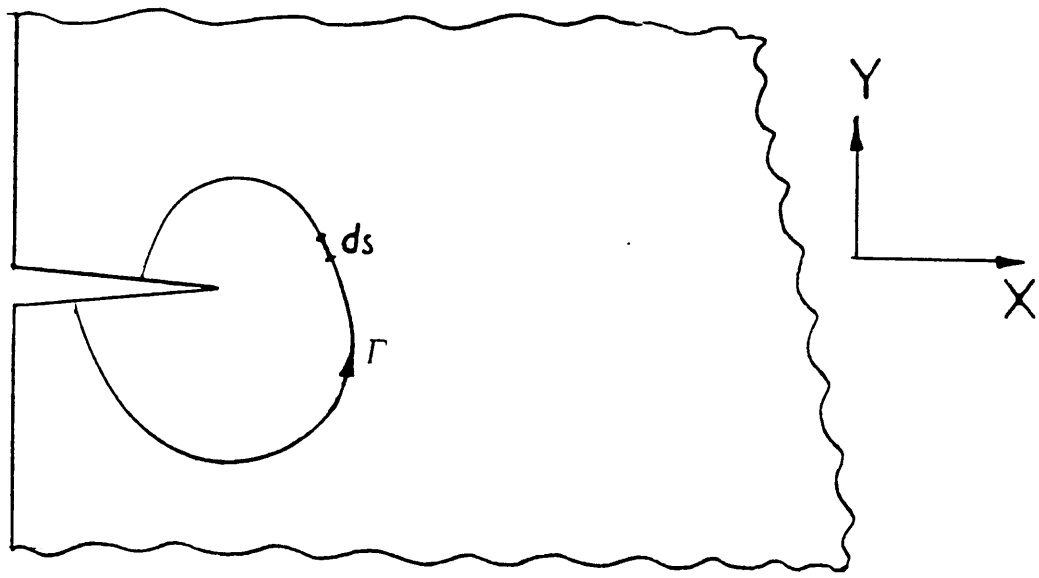


Figure 4.5 Arbitrary contour around a crack tip.

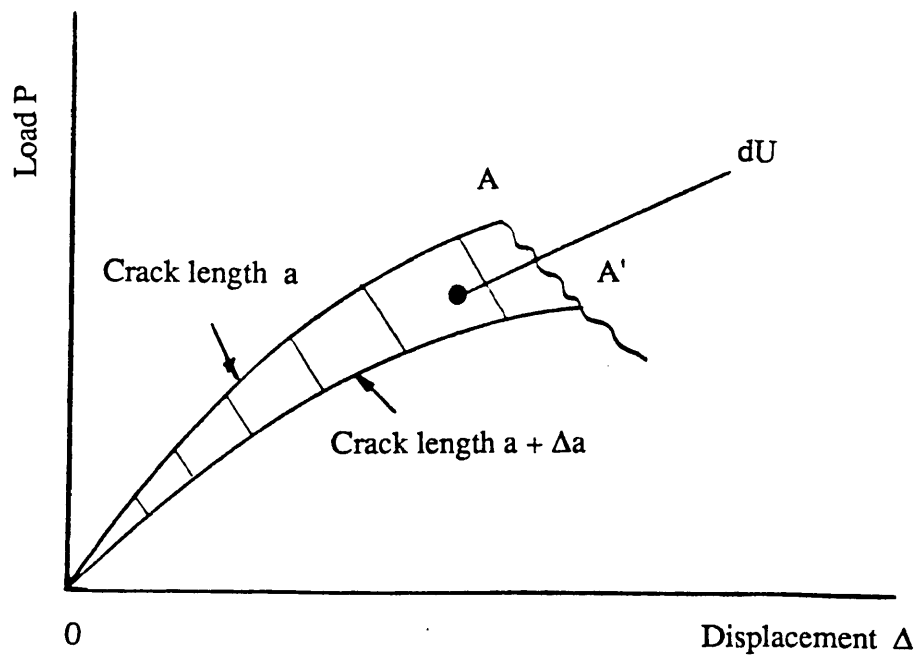


Figure 4.6 Load-displacement diagram for a power-law hardening material

CHAPTER 5

APPLICATION OF FRACTURE MECHANICS TO TIME DEPENDENT MATERIALS

5.1 INTRODUCTION

At high temperatures, particularly when $T > 0.5\ T_m$, where T is absolute temperature and T_m the melting temperature, creep effects become significant. Creep has the same effect as plasticity in modifying the initial elastic stress distribution. Immediately on loading, in the absence of plastic deformation, the stress distribution at the crack tip will be elastic and described by K. For creep "brittle" circumstances where little deformation accompanies fracture, the stress distribution will remain virtually unaltered by creep and K will continue to characterize the stresses around the crack. However, when substantial creep deformation accompanies fracture, stress redistribution will occur at the crack tip and K (or G) will cease to characterise the stress distribution in the region of the crack tip, necessitating the development of non linear parameters.

5.2 STEADY STATE CONDITIONS

5.2.1 THE C* INTEGRAL

For a material deforming under secondary creep, the Norton's uniaxial creep law is:

$$\frac{\dot{\varepsilon}}{\dot{\varepsilon}_0} = \left[\frac{\sigma}{\sigma_0}\right]^n \qquad (5.1)$$

where $\dot{\varepsilon}_0$ and σ_0 are reference strain rate and stress respectively and n is a material constant. The equivalent constitutive equation for a multiaxial stress state is given by:

$$\frac{\dot{\varepsilon}_{ij}}{\dot{\varepsilon}_0} = \frac{3}{2}\left[\frac{\sigma_e}{\sigma_0}\right]^{n-1}\frac{\sigma'_{ij}}{\sigma_0} \qquad (5.2)$$

where σ_e is the equivalent stress and σ'_{ij} the deviatoric stress tensor.

The secondary creep law is similar to the work hardening law for non-linear materials i.e. equation (4.19). Equilibrium and compatibility conditions dictate that if N=n the stress distribution at the crack tip in two identically loaded components, one deforming plastically according to (4.19) and the other creeping according to (5.1) will be the same. The only difference will be that a load P applied to the former will result in a displacement whereas it will cause a displacement rate in the latter.

By analogy with the work hardening case, it is possible to define a contour energy rate line integral C* which characterises the state of stress at the crack tip in creeping materials, in the same way that J does for the work hardening case.

C* (also known as J*) was independently proposed by Landes and Begley (1974) and Nikbin et. al. (1976). By comparison with equation (4.17) and for a contour Γ surrounding a crack tip in a 2D body of unit thickness, the C* parameter for a crack aligned in the x-direction, is a path independent energy rate integral given by:

$$C^* = \int_\Gamma W_s^* \, dy - T_i \frac{\partial \dot{u}_i}{\partial x} \, ds \qquad (5.3)$$

As illustrated in figure 4.5, Γ is the line contour taken from the lower crack surface to the upper crack surface.

$$W_s^* = \int \sigma_{ij} \, d\dot{\varepsilon}_{ij} \qquad (5.4)$$

is the strain energy rate density associated with point stress σ_{ij} and strain rate $\dot{\varepsilon}_{ij}$, T_i is the traction vector defined by the outward normal n_j along Γ, $T_i=\sigma_{ij}\, n_j$. The displacement rate vector is denoted by $\dot{u}_i$ and s is the arc length along the contour. C* is simply a modification of the J contour integral where strains and displacements ε_{ij} and u_{ij}, are replaced by their rates $\dot{\varepsilon}_{ij}$ and $\dot{u}_{ij}$.

For materials undergoing steady state or secondary creep deformation Golman and Hutchinson (1975) have shown that C* characterises the stress and strain rates in the vicinity of the crack tip as :

$$\frac{\sigma_{ij}}{\sigma_o} = \left[\frac{C^*}{I_n \sigma_o \dot{\varepsilon}_o r} \right]^{\frac{1}{n+1}} \tilde{\sigma}_{ij} (\theta, n) \qquad (5.5)$$

$$\frac{\dot{\varepsilon}_{ij}}{\dot{\varepsilon}_o} = \left[\frac{C^*}{I_n \sigma_o \dot{\varepsilon}_o r} \right]^{\frac{n}{n+1}} \tilde{\dot{\varepsilon}}_{ij} (\theta, n) \qquad (5.6)$$

where (r,θ) is the polar co-ordinate system centred at the crack tip and $\tilde{\sigma}_{ij}$ and $\tilde{\dot{\varepsilon}}_{ij}$ are non dimentional functions varying in the same way as $\tilde{\sigma}_{ij}$ and $\tilde{\varepsilon}_{ij}$ for plasticity. The factor I_n is analogous to I_N with N=n.

$$I_n = 10.3 \, (0.13 + 1 / n)^{1/2} - 4.8 / n \qquad (5.7)$$

for plane strain conditions. C* can be defined as the power difference between two identically loaded bodies having incrementally differing crack lengths. Consider figure 5.1 which shows creep displacement rate plotted as a function of load, for a body containing a crack of length a and then a crack of length $a+\Delta a$. For a body of thickness B, C* can be obtained from the shaded area dU* as:

$$C^* = \frac{dU^*}{B da} \qquad (5.8)$$

where U* is the energy dissipation rate, and is defined as:

$$U^* = \int_0^{\dot{u}} P \, d\dot{u} \qquad (5.9)$$

By analogy to plasticity using Ilyushin's theorem, for a material obeying the secondary creep law equation (5.1), we may write:

$$\dot{\Delta} = C_n P^n \qquad (5.10)$$

where C_n is a measure of the creep compliance of the body. Following the same

procedure as in plasticity it can be shown that:

$$C^* = \frac{P^{n+1}}{(n+1)B} \frac{dC_n}{da} \qquad (5.11)$$

Equation (5.11) may be rewritten as :

$$C^* = \frac{P\dot{\Delta}}{BW} \left[\frac{W}{n+1} \frac{1}{C_n} \frac{dC_n}{da} \right] \qquad (5.12)$$

where W is the width of the body. The term in the square brackets is non-dimentional. Expressing this factor as F, (5.12) gives:

$$C^* = \frac{P\dot{\Delta}}{BW} F \qquad (5.13)$$

For crack extension at constant load :

$$C^* = \frac{P\dot{\Delta}}{BW} \left[\frac{W}{n+1} \frac{1}{\dot{\Delta}} \frac{d\dot{\Delta}}{da} \right] \qquad (5.14)$$

and for crack extension at constant displacement rate:

$$C^* = \frac{P\dot{\Delta}}{BW} \left[-\frac{n}{n+1} \frac{W}{P} \frac{dP}{da} \right] \qquad (5.15)$$

Expressions (5.13) to (5.15) are particularly suitable for experimental determination of C*, since it will enable C* to be obtained from the experimental measurements of the displacement rates at the loading pins.

Is is important to note that the application of the C* parameter to correlate crack growth, assumes that, the material is following a steady-state creep law as expressed by equation (5.1). This assumes that all the transient effects as well, as elastic and short time plasticity effects can be ignored. Since the C* parameter is expressed as path independent line integral, this assumption must apply not only to the crack tip area, but to each point in the structure being analysed.

5.3 NON STEADY STATE CONDITIONS

5.3.1 INTRODUCTION

The C* integral fully characterizes creep crack growth for nonlinear viscous materials, i.e. it assumes that the elastic deformation is negligible compared to creep deformation.

However when a load is applied to a cracked specimen at t=0, the instantaneous response of an elastic/non-linear viscous material to load application is purely elastic and the crack tip field at time t=0 has the inverse - square root singular field given by equations (4.1) to (4.3). As time progresses the creep strains, which increase continuously, become exceedingly large compared to the elastic strains, which remain bounded. Then the stress field behaves as if the material is purely non - linearly viscous. The stress field again becomes time independent and is given by equation (5.5). The crack field is now the HRR field with C* being path independent and determining the severity of the HRR - singularity. It many practical situations the time required to establish steady state conditions, may be significant compared to the life of the component, necessitating the study of stress distributions around stationary cracks under non - steady or transient conditions.

5.3.2 THE C(t) INTEGRAL

At any time t the total strain rate for an elastic / non-linear viscous material it will be given by :

$$\dot{\varepsilon}_{ij} = \dot{\varepsilon}_{ij}^{el} + \dot{\varepsilon}_{ij}^{cr} \qquad (5.15a)$$

For a multiaxial stress state the elastic strain rate will be given by:

$$\dot{\varepsilon}_{ij}^{el} = \frac{(1+\nu)}{E}\dot{\sigma}_{ij} - \frac{\nu}{E}\dot{\sigma}_{kk}\,\delta_{ij} \qquad (5.16)$$

where δ_{ij} is the unit tensor and $\dot{\sigma}_{kk}$ is the trace of the stress rate tensor given by:

$$\dot{\sigma}_{kk} = \dot{\sigma}_{11} + \dot{\sigma}_{22} + \dot{\sigma}_{33} \qquad (5.17)$$

and the creep strain rate is given by :

$$\frac{\dot{\varepsilon}_{ij}}{\dot{\varepsilon}_0} = \frac{3}{2}\left[\frac{\sigma_e}{\sigma_0}\right]^{n-1}\frac{\sigma'_{ij}}{\sigma_0} \qquad (5.2)$$

where σ_e is the equivalent stress and σ'_{ij} the deviatoric stress tensor.

In uniaxial tension (5.15a) can be written as:

$$\dot{\varepsilon}_{ij} = \frac{\dot{\sigma}}{E} + \dot{\varepsilon}_0\left[\frac{\sigma}{\sigma_0}\right]^n \qquad (5.18)$$

It comprises elastic behaviour in response to load application, and viscous creep at the long - time limit.

At any time t > 0, very near the crack tip, and with n > 1, the elastic strain rates can be neglected compared to the creep rates because the stress is unbounded near the crack tip, and therefore the creep rate ($\propto \sigma^n$) has with n > 1 a stronger singularity than does the elastic strain rate ($\propto \dot{\sigma}$). As a consequence, the asymptotic fields at t > 0 are determined by power-law viscous creep alone, and must therefore be characterized by the HRR type fields as:

$$\frac{\sigma_{ij}}{\sigma_0} = \left[\frac{C(t)}{I_n \sigma_0 \dot{\varepsilon}_0 r}\right]^{\frac{1}{n+1}} \tilde{\sigma}_{ij}(\theta, n) \qquad (5.20)$$

$$\frac{\dot{\varepsilon}_{ij}}{\dot{\varepsilon}_0} = \left[\frac{C(t)}{I_n \sigma_0 \dot{\varepsilon}_0 r}\right]^{\frac{n}{n+1}} \tilde{\dot{\varepsilon}}_{ij}(\theta, n) \qquad (5.21)$$

where (r,θ) is the polar co-ordinate system centred at the crack tip and $\tilde{\sigma}_{ij}$ and $\tilde{\dot{\varepsilon}}_{ij}$ are non dimentional functions as defined in (5.5) and (5.6).

The functional form of C(t) generally remain undetermined by the asymptotic analysis, but at the long time limit C(t) must approach its steady state value C*.

Using similarity solutions in the small - scale creep or short time limit, Riedel

and Rice (1980) have shown that the crack tip field in the short time limit is:

$$\frac{\sigma_{ij}}{\sigma_o} = \left[\frac{K^2 (1-\nu^2)/E}{(n+1) I_n \sigma_o \dot{\varepsilon}_o r t} \right]^{\frac{1}{n+1}} \tilde{\sigma}_{ij} (\theta, n) \qquad (5.22)$$

Comparing (5.22) with (5.20), C(t) for small scale creep is :

$$C(t) = \frac{K^2 (1-\nu^2)}{(n+1) E t} \qquad (5.23)$$

Equations (5.22) and (5.23) are valid for plane strain conditions. For plane stress $(1-\nu^2)$ must be replaced by 1.

Since the time in equation (5.22) appears in the denominator, it describes a decreasing crack - tip stress field as expected.

For small scale plasticity, since $J=K^2(1-\nu^2)/E$ for plane strain and $J=K^2/E$ for plane stress, C(t) may be written as:

$$C(t) = \frac{J}{(n+1)t} \qquad (5.24)$$

5.3.3 CHARACTERISTIC TIMES TO STEADY STATE CONDITIONS

C* is related to the amplitude of the near tip singular field by:

$$A(t \rightarrow \infty) = \left[\frac{C^*}{I_n \dot{\varepsilon}_o \sigma_o} \right]^{\frac{1}{n+1}} \qquad (5.25)$$

According to equation (5.25) C* is the loading parameter that determines the near tip singular field, if the whole specimen creeps extensively.

For small scale yielding the amplitude of the singularity, assuming approximate path independence for J, is given by Riedel and Rice (1980) as:

$$A(t) = \left[\frac{K^2 (1-\nu^2)/E}{(n+1) I_n \sigma_o \dot{\varepsilon}_o t} \right]^{\frac{1}{n+1}} \qquad (5.26)$$

By equating the small scale creep singularity of equation (5.26) with the steady state singularity of equation (5.25) and solving for t, a characteristic time for the transition from small scale yielding to extensive creep can be estimated as:

$$t_1 = \frac{K^2 (1 - \nu^2)}{(n+1) C^* E} \qquad (5.27)$$

Equation (5.27) is valid for plane strain conditions. For plane stress $(1-\nu^2)$ must be replaced by 1.

Small scale creep prevails if the time is sufficiently small compared with the characteristic time t_1. For small scale plasticity

$$t_1 = \frac{J}{(n+1) C^*} \qquad (5.28)$$

The condition for the extensive creep limit to be valid, is that the creep strain rates are much larger compared with the elastic strain rates everywhere in the body. This starts to be fulfilled at the transition time t_1. Riedel and Rice (1980) suggest that there is not a big gap between the validity of the small - scale creep and the extensive creep case, but if a higher degree of accuracy is required it must be noted that the limiting cases are separated by a period of time where neither of them is accurate enough. However Ehlers and Riedel (1981) found that very good approximation to Ehlers (1981) finite element results for compact tension, three point bend, centre cracked plate in tension, and, double edge cracked plate in tension specimens, can be obtained in the whole range from short to long times by simply adding the small scale yielding equation (5.24) with the steady state value C* to give

$$C(t) = \frac{J}{(n+1)t} + C^* \qquad (5.29)$$

Substitution of (5.28) into (5.29) gives

$$C(t) = (1 + t_1 / t) C^* \qquad (5.29a)$$

which reduces to C (t) equation (5.24) in the short time limit and to C* for long times.

Figure 5.2 shows the finite element results of Ehlers (1981) compared to the

approximate formula (5.29a)

5.3.4 GENERALISED MATERIAL BEHAVIOUR

Riedel (1981) has analysed the stress fields developed near a stationary crack tip in a creeping material, with the uni-axial behaviour given by

$$\dot{\varepsilon} = \frac{\dot{\sigma}}{E} + B_0 \sigma^{(1/N)-1} + B_1 \sigma^{n_1} \varepsilon^{-p_1} + B_2 \sigma^{n_2} + B_3 \sigma^{n_3} \varepsilon^{p_3} \qquad (5.30)$$

The above relation incorporates elastic deformation, power law hardening, and, primary, secondary and tertiary creep.

Riedel (1981) shows that for a material obeying the uni-axial law

$$\dot{\varepsilon} = A \sigma^n \varepsilon^{-p} \qquad (5.31)$$

a path independent integral C^*_h (analogous to C*) can be defined which correlates the near tip stress field to the applied load for primary or tertiary creep. Equation (5.31) describes primary creep if $p > 0$. Tertiary creep is described if $p < 0$. The HRR stress field near the crack tip is given by a relation similar to (5.5) as

$$\sigma_{ij}(r,\theta,t) = \left[\frac{C^*_h}{(A(1+p))^{1/(1+p)} I_m r}\right]^{\frac{1}{m+1}} \tilde{\sigma}_{ij}(\theta, m) \qquad (5.32)$$

where $m=n/(1+p)$, I_m is the same as I_N with $m=N$ and $\tilde{\sigma}_{ij}(\theta,m)$ is normalised such that the maximum value of $\tilde{\sigma}_e(\theta,m)$ is equal to unity.

Using similarity solutions in the small-scale creep or short time limit and assuming approximate path independence of the J-integral the near tip stress field can be obtained by substituting C^*_h in (5.32) by:

$$C^*_h = \frac{K^2(1-\nu^2)/E}{((m+1)t)^{1/(1+p)}} \qquad (5.33)$$

The characteristic time for the transition from small-scale creep to extensive creep by equating the near-tip stress field of the short time limit and the long time limit is

given as:

$$t_1 = \frac{1}{m+1}\left[\frac{K^2(1-\nu^2)}{EC^*_h}\right]^{1+p} \qquad (5.34)$$

for plane strain. For plane stress $(1-\nu^2)$ must be replaced by 1. Riedel (1981) also considers growth of a primary /tertiary creep zone in a fully plastic body and growth of a secondary creep zone in a structure exhibiting gross primary creep. Similar expressions to equations (5.32), (5.33) and (5.34), are derived.

5.3.5 STRESS REDISTRIBUTION AT THE CRACK TIP

Figure (5.3) considers the elastic and creep stress distributions ahead of a crack tip. If the maximum effective stress is considered, the elastic stress distribution is:

$$\sigma = \frac{K}{(2\pi r)^{1/2}} \qquad (5.35)$$

and the steady state creep stress distribution is:

$$\sigma = \left[\frac{C^*}{I_n(\dot{\varepsilon}_0/\sigma_0^n)r}\right]^{\frac{1}{n+1}} \qquad (5.36)$$

On loading the stress distribution is elastic and after sufficient time t, assuming the crack is stationary, it will relax to its creep stress distribution. A stress σ^* can be defined at distance r^* from the crack tip, where the elastic and creep stress have the same magnitude. By equating (5.35) and (5.36) and solving for $r=r^*$, using $\dot{\varepsilon}=\dot{\varepsilon}_0(\sigma/\sigma_0)^n = C\,\sigma^n$:

$$r^* = \left[\frac{K^2}{2\pi}\right]^{\frac{n+1}{n-1}}\left[\frac{I_n C}{C^*}\right]^{\frac{1}{n-1}} \qquad (5.37)$$

the elastic strain at $r = r^*$ is given by:

$$\varepsilon^{el} = \frac{K}{E(2\pi r^*)^{1/2}} \qquad (5.38)$$

and the creep strain by:

$$\varepsilon^{cr} = C\left[\frac{C^*}{I_n C r^*}\right]^{\frac{n}{n+1}} t \qquad (5.39)$$

It is proposed that redistribution is sufficiently complete at a time t_w which gives $\varepsilon^{el}=\varepsilon^{cr}$. Equating (5.38) and (5.39) and solving for $t = t_w$:

$$t_w = \left[\frac{K^2}{2\pi r^*}\right]^{1/2 - n/2} \frac{1}{EC} \qquad (5.40)$$

and by substituting r* from (5.37)

$$t_w = \frac{I_n}{2\pi}\frac{K^2}{EC^*} \qquad (5.41)$$

Equation (5.41) is valid for plane stress. For plane strain :

$$t_w = \frac{I_n}{2\pi}\frac{K^2(1-\nu^2)}{EC} \qquad (5.42)$$

where the factor I_n , has been tabulated by Hutchinson (1968) for both plane stress and plane strain conditions. In general :

$$t_w = \frac{I_n}{2\pi}\frac{G}{C^*} \qquad (5.43)$$

compared to Riedel and Rice (1980) :

$$t_1 = \frac{1}{(n+1)}\frac{G}{C^*}$$

In general $t_w > t_1$. Figure 5.4 shows the ratio of t_w/t_1 as a function of n.

5.3.6 THE C_t PARAMETER.

Consider several identical pairs of cracked specimens. Within each pair one specimen has a crack length a, and the other has an incrementally differing crack length a+Δa. The specimens of each pair are loaded to various load levels P_1 , P_2 , ... , P_i ....e.t.c. at elevated temperatures, and the load-line deflection as a function of time is recorded as in figure 5.5. The load-line deflection due to creep is Δ_c. It is assumed that

no crack extension occurs in any of the specimens and that the instantaneous response is linear inelastic.

First the limit of small scale creep is considered. At a fixed time t, the load versus the creep deflection rate, $\dot{\Delta}_c$ behaviour is plotted for all these specimens, as shown in figure 5.6. By varying the time several of these plots can be generated. The area between the P - $\dot{\Delta}_c$ curves for specimens of crack lengths a and a + Δa is called ΔU^*_t, where t denotes constant time. ΔU^*_t represents the difference in the energy rates supplied to two cracked bodies with identical creep deformation histories as they are loaded to different load or deflection rate levels.

Saxena (1986) defines the C_t parameter as:

$$C_t = -\frac{1}{B}\frac{\partial U^*_t}{\partial a} \qquad (5.44)$$

where B is the specimen thickness. As $t \rightarrow \infty$, $C_t = C^*$ by definition, as under steady state conditions $\partial U^*_t / \partial a = \partial U^* / \partial a$.

For a material deforming according to uniaxial law :

$$\dot{\varepsilon} = \frac{\dot{\sigma}}{E} + C\,\sigma^n$$

where E is the Young's modulus, and C and n are material constants describing the material's secondary stage creep behaviour, the stress, and strain rate ahead of the crack tip at $t \rightarrow 0$ are given by :

$$\sigma \propto \left[\frac{K^2}{CEr\,t}\right]^{\frac{1}{n+1}} \qquad (5.45)$$

$$\dot{\varepsilon} \propto \left[\frac{K^2}{CEr\,t}\right]^{\frac{n}{n+1}} \qquad (5.46)$$

In small scale creep the creep zone r_{cr} is defined as the region around the crack tip where the creep strains exceed the elastic strains. Riedel and Rice (1980) give the size of the creep zone as:

$$r_{cr} = \alpha \frac{K^2}{(ECt)^{2/(n-1)}} \qquad (5.47)$$

$$\text{where } \alpha = \frac{1}{2\pi}\left[\frac{(n+1)^2}{2n\alpha_n^{n+1}}\right]^{\frac{2}{n-1}} \qquad (5.47a)$$

where α_n^{n+1} is a factor with a value of about 0.69 for n values between 3 and 10.

If Δ is the load line deflection due to a crack, $a_{eff} = a + r_{cr}$, and Δ_o the load line deflection due to a crack a, then

$$\Delta_o = c(a)P$$

$$\Delta = c(a + r_{cr})P$$

So at any time t, the additional load line deflection due to creep is given by:

$$\Delta_c = \Delta - \Delta_o = [c(a + r_{cr}) - c(a)]P \quad \text{or}$$

$$\Delta_c = \Delta - \Delta_o = P\frac{dc}{da} r_{cr} \qquad (5.48)$$

where P is the applied load Δ_o is the elastic deflection, Δ the total deflection and c the elastic compliance. From the relationship between K and G Irwin and Kies (1952) shown that :

$$\frac{dc}{da} = \frac{2BK^2}{EP^2}(1-\nu^2) \qquad (5.49)$$

Substituting (5.47) and (5.49) into (5.48) and differentiating with respect to t

$$\dot{\Delta}_c = \frac{4\alpha(1-\nu^2)}{E(n-1)}(P/B)^3 \frac{H^4}{W^2} t^{3-n/(n-1)} (EC)^{2/(n-1)} \qquad (5.50)$$

where $H=H(a/W)=(K/P)BW^{1/2}$. This formula holds for plane strain. For plane stress $(1-\nu^2)$ must be replaced by 1.

From the definition of C_t and following a similar procedure as for C* in 5.2.1 it can be deduced that for small scale creep :

$$C_t = \frac{P\dot{\Delta}_c}{BW}\frac{H'}{H} \qquad (5.51)$$

where H'=dH/d(a/W). Substituting (5.50) into (5.51), the C_t parameter for small scale creep is given by :

$$(C_t)_{ssc} = \frac{4\alpha(1-\nu^2)}{E(n-1)} \frac{K^4}{W} (EC)^{2/(n-1)} t^{-(n-3)/(n-1)} \frac{H'}{H} \quad (5.52)$$

where ssc stands for small scale creep. Motivated by the successful correlations made by Ehlers and Riedel (1981), for the estimation of transient solutions of the C(t) parameter by just adding the two asymptotic limits for $t \to \infty$ and $t \to 0$, the following equation for estimating C_t was proposed by Saxena and Liaw (1986):

$$C_t = (C_t)_{ssc} + C^* \quad (5.53)$$

Bassani, Hawk and Saxena (1986) suggest that the transition time from small scale to extensive creep, that can be found by equating $(C_t)_{ssc}$ with C* must closely approximate the Riedel and Rice (1980) transition time t_1. An interpolation formula for C_t from small scale to extensive creep similar to that of C(t) equation (5.29) can be then derived.

$$C_t = C^* \left[\left[\frac{t_1}{t} \right]^{\frac{n-3}{n-1}} + 1 \right] \quad (5.54)$$

which is in good agreement with finite element results by the same authors. The extend of small scale creep or transient conditions may be examined by using a parameter τ defined as:

$$\tau = \frac{C^*}{C_t} \quad (5.55)$$

For steady state $C_t = C^*$ so $\tau \to 1$. When highly transient conditions exist $\tau << 1$. Figure 5.7 shows the ratio of $C(t)/C_t$ plotted versus the non-dimensional time t/t_1. For short times when $t/t_1 < 1$, $C(t) > C_t$; for long times the reverse is true.

5.4 THE ASYMPTOTIC STRESS AND STRAIN FIELDS NEAR THE TIP OF A GROWING CRACK

5.4.1 STEADY STATE BEHAVIOUR

The analyses of crack growth presented in 5.2 and 5.3 assume that the near tip field is either the elastic singular field or an HRR-type singular field. Hui and Riedel (1981) shown that a different type of asymptotic field develops at the crack tip of a growing crack, and that the nature of the asymptotic stress and strain field near the tip changes abruptly at n=3.

Consider the uniaxial creep law:

$$\dot{\varepsilon} = \frac{\dot{\sigma}}{E} + C\sigma^n$$

For n > 3 the stress and strain singular fields are:

$$\sigma_{ij} = \alpha_n \left[\frac{\dot{a}(t)}{C\ E\ r} \right]^{\frac{1}{n-1}} \hat{\sigma}_{ij}(\theta, n) \qquad (5.56)$$

and

$$\varepsilon_{ij} = \frac{\alpha_n}{E} \left[\frac{\dot{a}(t)}{C\ E\ r} \right]^{\frac{1}{n-1}} \hat{\varepsilon}_{ij}(\theta, n) \qquad (5.57)$$

where $\hat{\sigma}_{ij}$, $\hat{\varepsilon}_{ij}$ and the dimensionless factor α_n are given by Hui and Riedel (1981), and, $\dot{a}(t)$ is the crack growth rate at time t. The asymptotic fields described by (5.56) and (5.57) have remarkable properties. Stress and strain are entirely independent of the applied load. Only the material parameters and the current crack growth rate, but not growth rates at prior times, nor the applied load determine the asymptotic fields. Of course this independence of load and prior history cannot hold for the remote fields. The field given by (5.56) and (5.57) is referred to as the HR field.

For $n < 3$ the stress field is dominated by the elastic strain rates and has an

inverse square root singularity, i.e. $\sigma \propto r^{-1/2}$. The amplitude of the near tip fields depends on the applied load and the crack growth rate.

Hui and Riedel deduced that steady state crack growth, within the confines of small scale yielding is only possible for $n > 3$.

Chang Popelar and Staab (1987) have extended the theory to primary creep for a material obeying the uniaxial relationship:

$$\dot{\varepsilon} = \frac{\dot{\sigma}}{E} + C \sigma^n \varepsilon_{cr}^{-p} \qquad (5.58)$$

where ε_{cr} is the creep contribution to the total strain and $p > 0$. The asymptotic fields at the tip of a growing crack abruptly change at $n-p=3$. For $n-p>3$ the stress and strain singular field is:

$$\sigma_{ij} = \alpha_n \left[\frac{\dot{a}(t)}{C E^{p+1} r} \right]^{\frac{1}{n-p-1}} \hat{\sigma}_{ij}(\theta, n, p) \qquad (5.59)$$

$$\varepsilon_{ij} = \frac{\alpha_n}{E} \left[\frac{\dot{a}(t)}{C E^{p+1} r} \right]^{\frac{1}{n-p-1}} \hat{\varepsilon}_{ij}(\theta, n, p) \qquad (5.60)$$

where $\hat{\sigma}_{ij}$, $\hat{\varepsilon}_{ij}$ and α_n are given by Chang Popelar and Staab. When $p=0$ i.e. for secondary creep, equations reduce to (5.56) and (5.57). As for the secondary creep case, only material parameters and the current crack growth rate, but not growth rates at prior times nor the applied load, determine the asymptotic fields. For $n-p< 3$ steady state crack propagation is not possible.

The fields given by (5.59) and (5.60) are universal for all geometries and loadings. Consequently, it is not permissible to appeal to the dominance of these fields and to invoke a fracture criterion based only upon these fields. To do so would lead to the physically unattainable conclusion that the crack speed is independent of the specimen geometry and the applied loading. Hence, the fracture process must also

depend upon the accumulated damage that occurs outside the zone of validity of the asymptotic fields.

5.4.2 TRANSIENT BEHAVIOUR

When a crack starts growing from a stationary position interesting features are introduced into the problem. For a stationary crack, under small scale creep (ssc) conditions constrained creep causes the crack tip stresses to relax in proportion to $t^{-1/(n+1)}$ (equation (5.22)). Even during crack growth, in regions where the creep strains dominate the elastic ones ssc constraint causes stress relaxation. On the other hand, the effect of the crack growth is to elevate the stresses near the crack tip due to an elastic response. The asymptotic field near the crack tip is the HR field (equation 5.56) in which the elastic and creep strain rates are of the same order of magnitude.

Hawk and Bassani (1986) proposed the following evolution for the transient crack-tip fields under ssc conditions. At time t=0, the crack tip field is simply the elastic K field and the crack begins to extend. A short time after, there exists a HR field very close to the crack tip, where the creep strain rate ($\dot{\varepsilon}^{cr}$) and the elastic strain rate ($\dot{\varepsilon}^{el}$) are of the same order, surrounded by the HRR field where $(\dot{\varepsilon}^{cr})>>(\dot{\varepsilon}^{el})$, which in turn is surrounded by the K field as figure 5.8 indicates.

A matching of the transient crack tip-fields for power-law creep is most easily visualized on a log-log plot of effective stress vs distance ahead of the crack tip as on figure 5.9. The K, HRR and HR fields appear as straight line segments with slopes of -1/2 for the K field, -1/(n+1) for the HRR field, and -1/(n-1) for the HR field, so that for n>3 the K field has the steepest slope, followed by the HR field and then the HRR field. For constant crack growth rate and K, the asymptotic HR and K field lines are fixed while the HRR field descends with time as indicated by the dashed lines on the plot at times $t_1< t_2< t_3<t_R$. It was suggested by McClintock and Bassani (1981) and verified by finite element analysis by Hawk and Bassani (1986) that each stress field

dominates in regions bounded by intersections with adjacent fields; with increasing r these fields appear in order HR, HRR, and K. For the time t_2 the asymptotic matching of stress is designated by the bold line in figure 5.9.

The region of dominance of the HR field has been estimated by Wu et. al. (1986), from the intersection of the effective stresses of the HR field and the HRR field as:

$$R_{HR,HRR} = C_1 \left[\frac{t}{K^2} \right]^{\frac{n-1}{2}} \dot{a}^{(n+1)/2} \qquad (5.61)$$

where C_1 is an angular function of θ.

Differentiation of (5.61) shows that the rate of increase of the HR zone is proportional to $t^{(n-3)/2}$, whereas differentiation of (5.47) shows that, the rate of increase of the creep zone or the region of dominance of the HRR field is proportional to $t^{-(n-3)/(n-1)}$. This means that the HR field grows faster than the HRR field. If small scale yielding persists, the region of dominance of the HRR field will eventually go to zero. The time when this happens is an important reference time and it will be denoted as t_R. Stress relaxation persist until $t = t_R$. From that time on the solution corresponds to a steady state solution with the HR field surrounded by the K field. Wu et.al. (1986) estimate t_R as :

$$t_R = b_1 \left[\frac{K^2}{\dot{a}} \right]^{\frac{n-1}{n-3}} \qquad (5.62)$$

where b_1 is given by Wu et. al. and is a function of the material properties and type of loading only. At this time the HR, HRR, and K effective stresses intersect at a single point ahead of the crack.

When $t > t_R$ the HRR field disappears and the region of dominance of the HR field is estimated from the intersection of the effective stresses of the HR field and the K field as:

$$R_{HR,K} = C_3 \left[\frac{K^{n-1}}{\dot{a}} \right]^{2(n-3)} \qquad (5.63)$$

where C_3 is an angular function of θ.

Two cases of interest, where ssc is expected to satisfied are:

(1) $t/t_R << 1$ and $t/t_1 << 1$.

(2) $t_R << t_1$.

where t_1 is the Riedel and Rice (1980) transition time.

Condition (1) states that for small enough time, ssc is always valid. Creep relaxation is important in this case. The parameter that characterizes the crack tip fields is C(t) and is proportional to K^2/t. But if (1) is satisfied only, extensive creep can still occur if $t_R >> t_1$. So condition (2) must be enforced. In other words condition (2) guarantees that ssc prevails. It is therefore a condition of a steady state crack growth with the K zone surrounding the HR zone. If (2) is not satisfied (e.g. $t_1 << _R$) then it is possible that extensive creep may occur before this steady state can be reached. In this case, if $t_1 < t < t_R$ the elastic far field boundary condition is therefore the C* field.

For this case i.e. when $t_1 < t < t_R$, and in the special case of a suddenly growing crack with constant crack growth rate $\dot{a}_o$, it is possible to find an approximate expression for the stresses, that is valid for all t >0. This is because C(t) for the case of a stationary crack under step loading is well approximated by Riedel and Wagner (1981) as :

$$C(t) = C^* (1 + t_1 / t) \qquad (5.63a)$$

A formula which interpolates the near tip stresses for short times ($t < t_1$), and long times ($t > t_1$) is given by Hui and Wu (1986) as:

$$\sigma_{ij} = \alpha_n \left[\frac{\dot{a}_o}{C E r} \right]^{\frac{1}{n-1}} \hat{\sigma}_{ij}(\theta, n) + \left[\frac{C(t)}{C I_n r} \right]^{\frac{1}{n+1}} \tilde{\sigma}_{ij}(\theta, n) \qquad (5.64)$$

where all parameters have been defined in equations (5.20) and (5.56). Note that when

$\dot{a}_o=0$ (ie.when the crack is stationary) equation (5.64) reduces to stationary crack equation (5.20).

Even though the above analysis is for constant K and crack growth rate, it is expected that for reasonably slow variations in K and crack growth rate, the asymptotic solution is a good approximation to the exact solution.

5.5 A THEORETICAL MODEL FOR PREDICTING CRACK GROWTH RATES

Nikbin and Webster (1982), Cocks and Ashby (1982c) and Nikbin et. al. (1983) have postulated a process zone ahead of the crack tip in which creep damage accumulates. By using this model Nikbin et. al. (1983) have developed the following expression for crack growth rate, for a material obeying (5.1)

$$\dot{a} = (n+1)\frac{\dot{\varepsilon}_o}{\varepsilon^*_f}\left[\frac{C^*}{I_n \sigma_o \dot{\varepsilon}_o}\right]^{\frac{n}{n+1}} r_c^{1/(n+1)} \qquad (5.65)$$

where r_c is the size of the process zone and ε^*_f is the creep ductility of the material appropriate to the state of stress at the crack tip. In most practical situations n>>1, and since r_c is raised to a small fractional power relative insensitivity to the size of the damage zone is predicted. Most experimental evidence (Nikbin (1976), Smith (1983)) indicates correlation of cracking rate of the form

$$\dot{a} \propto (C^*)^{\Phi} \qquad (5.66)$$

Comparison of (5.65) and (5.66) reveals them to be of the same form if $\Phi=n/(n+1)$. The experimental observations of Φ being a fraction close to unity provides support of this model since n>>1. Substitution of the appropriate values for the parameters in (5.65) for a selection of low alloy steels and an aluminium alloy has indicated that equation (5.65) can be approximated, to within a factor of about two for these materials by (Nikbin et. al. (1983))

$$\dot{a} = \frac{300}{\varepsilon^*_f} (C^*)^{0.85} \qquad (5.67)$$

where $\dot{a}$ is in millimeters per hour with ε^*_f as a percentage and C* in units of megajoules per square meter per hour. It is clear from this expression, therefore, that the creep ductility is the most important material parameter governing susceptibility of the material to creep crack propagation at a given value of C*. A decrease in ductility will cause an increase in cracking rate and vise versa.

In deriving (5.65) Nikbin et. al. (1983) assumed that secondary creep deformation dominated and that the creep ductility was not influenced by the applied stress. In general an element of material will undergo, primary, secondary, and, tertiary creep as it traverses the process zone. To allow for these effects Nikbin et . al. (1984) define an average creep strain rate $\dot{\varepsilon}_A$ for a failure strain ε_f and rupture time t_R as:

$$\dot{\varepsilon}_A = \frac{\varepsilon_f}{t_R} \qquad (5.68)$$

which enables (5.1) to be written as

$$\frac{\dot{\varepsilon}_A}{\dot{\varepsilon}_0} = \left[\frac{\sigma}{\sigma_0} \right]^n \qquad (5.69)$$

where the constants n and σ_0 are obtained from rupture data rather than secondary creep properties. For a typical rupture plot illustrated in figure 5.10

$$t_R = \frac{D}{\sigma^\nu} \qquad (5.70)$$

where D and ν are material constants. Substitution of (5.69) and (5.70) into (5.68) results in:

$$\varepsilon_f = \dot{\varepsilon}_0 D \frac{\sigma^{n-\nu}}{\sigma_0^n} \qquad (5.71)$$

Equation (5.71) expresses the stress sensitivity of the creep ductility. Since ε_f usually decreases with decrease in stress, n is usually greater than ν. When $n=\nu$, a

constant creep strain at failure is predicted. By letting the creep ductility be ε_{fo} at stress σ_o, (5.71) becomes.

$$\varepsilon_{fo} = \dot{\varepsilon}_o \frac{D}{\sigma_o^{\nu}} \qquad (5.72)$$

By substituting (5.72) into (5.69), Nikbin et. al. (1984) deduced that the crack growth rate may be predicted from:

$$\dot{a} = \left[\frac{n+1}{n+1-\nu}\right] \frac{\dot{\varepsilon}_o}{\varepsilon^*_{fo}} \left[\frac{C^*}{I_n \sigma_o \dot{\varepsilon}_o}\right]^{\frac{\nu}{n+1}} r_c^{(n+1-\nu)/(n+1)} \qquad (5.73)$$

where ε^*_{fo} is the creep ductility appropriate to the state of stress at the crack tip. When ductility is independent of stress $n=\nu$ and (5.73) and (5.65) become identical if $\varepsilon^*_{fo}=\varepsilon^*_f$.

5.5.1 INFLUENCE OF STATE OF STRESS

The term ε^*_{fo} was defined as being the creep ductility appropriate to the state of stress at the crack tip, whereas ε_{fo} was taken as the uniaxial creep ductility. State of stress effects may be incorporated in (5.73) by allowing for the influence of hydrostatic tension on the void growth mechanism. Several models are available. Rice and Tracey (1969) for example developed an expression for rigid plastic deformation ($n=\infty$) which gives

$$\varepsilon^*_{fo} = \frac{1.64\,\varepsilon_{fo}}{\exp(3\sigma_m / 2\sigma_e)} \qquad (5.74)$$

Cocks and Ashby (1980) used a creep model to obtain

$$\varepsilon^*_{fo} = \frac{\sinh\left[\frac{2}{3}\left[\frac{n-1/2}{n+1/2}\right]\right]}{\sinh\left[2\left[\frac{n-1/2}{n+1/2}\right]\frac{\sigma_m}{\sigma_e}\right]}\,\varepsilon_{fo} \qquad (5.75)$$

where σ_e is the equivalent stress and σ_m is the hydrostatic tensile stress ahead of the crack tip. The dependence of the term $\varepsilon_{fo}/\varepsilon^*_{fo}$ on the ratio σ_m/σ_e has been investigated by Nikbin et. al. (1984) and is shown in figure 5.11. Both (5.74) and (5.75) indicate similar treads. The ratio increases with an increase in σ_m/σ_e, suggesting a marked increase in ductility with increase in triaxiality. For n>>1 (5.75) predicts the biggest effect. For plane stress loading ε^*_{fo} can be expected to be close to ε_{fo}. For plane strain conditions an indication of the influence of state of stress can be obtained by considering the stresses associated with a Prandtl field for which σ_m/σ_e=2.4. Figure 5.11 shows that for this stress field $\varepsilon_{fo}/\varepsilon^*_{fo}$ ranges between 25 and 80 depending upon the model assumed. Nikbin et. al. (1984) chose to use an average value of $\varepsilon_{fo}/\varepsilon^*_{fo}$=50 under plane strain conditions. It is apparent that state of stress significantly affects the creep ductility.

5.6 LINK OF FRACTURE MECHANICS WITH DAMAGE MECHANICS

Smith and Webster (1985) incorporated damage mechanics concepts into a fracture mechanics interpretation of the creep crack growth by extending the method of evaluating C* for a structure containing a single crack, to a structure containing a uniform distribution of microcracks.

For a single crack C* can be obtained from the load P against load-point displacement rate $\dot{\Delta}$ diagram as explained in section 5.2. So for a crack of area A_c :

$$C^* = - \frac{\partial U^*}{\partial A_c} \qquad (5.76)$$

where ∂U^* is the change in the creep energy dissipation rate for a crack extension ∂A_c.

For a body deforming according to secondary creep law equation (5.1), it can be shown following the same procedure as in section 5.2 that, for constant load

$$C^* = \frac{P}{n+1} \frac{d\dot{\Delta}}{dA_c} \qquad (5.77)$$

This expression can be extended to multiple cracking by considering a tensile bar of length L and cross - sectional area A subjected to load P.

Let the sample contain a uniform distribution of grain-boundary cracks separated axially by the grain size λ as shown in figure 5.12. If A_c is the total area cracked, then the fraction ω of the cross - section which is cracked is :

$$\omega = \frac{\lambda A_c}{LA} \qquad (5.78)$$

Since the deformation along the gauge length is uniform the load-point displacement rate can be expressed as :

$$\dot{\Delta} = \dot{\varepsilon} L \qquad (5.79)$$

If for simplicity small strains are considered differentiating (5.78) and (5.79) and substituting into (5.77)

$$C^* = \frac{\sigma \lambda}{n+1} \frac{d\dot{\varepsilon}}{d\omega} \qquad (5.80)$$

where σ=P/A, is the stress applied to the bar. This equation is the appropriate expression for evaluating C* in the presence of multiple cracking.

Using (5.80), Smith and Webster (1985), obtained estimates of C* for the phenomenological and mechanistic models. However the phenomenological model, gives the physically unrealistic result of a finite value for C* in the limit of zero damage, where C* must reduce to zero since no singularity is present. So only the mechanistic model will be considered.

In this model the void spacing can be expressed as a fraction of the grain size as:

$$2l = \beta \lambda \qquad (5.81)$$

Then equation (3.8) of mechanistic damage accumulation becomes:

$$\frac{\dot{\varepsilon}}{\varepsilon_0} = \left[\frac{\sigma}{\sigma_0}\right]^n \left[1 + \alpha\beta\sqrt{\omega}\left[\frac{1}{(1-\omega)^n} - 1\right]\right] \qquad (5.82)$$

Differentiation of this equation and substitution into (5.80) gives

$$C^* = \sigma_o \dot{\varepsilon}_o \left[\frac{\sigma}{\sigma_o}\right]^{n+1} \alpha \beta \lambda \frac{h(\omega)}{n+1} \qquad (5.83)$$

where

$$h(\omega) = \frac{1}{2\sqrt{\omega(1-\omega)^n}} + \frac{n\sqrt{\omega}}{(1-\omega)^{n+1}} - \frac{1}{2\sqrt{\omega}} \qquad (5.84)$$

In figure 5.13 the non dimensional form of C* is plotted versus ω for different n values. At a given value of ω, C* increases with increasing n but similar trends are apparent for each value of n. The curve rises rapidly as complete fracture is approached at ω=1. However when $\omega \rightarrow 0$, C* also tends to zero as will be expected for the undamaged material.

5.6.1 PREDICTION OF CRACK GROWTH RATES

The mechanistic model is only to be considered, since the phenomenological model gives unrealistic values for C* for small values of ω. Equation (3.7) relating the damage fraction ω with the radius a of the voids and the distance 2l separating them,was:

$$\omega = (a/l)^2$$

Differentiating with respect to time and substituting l from (5.81)

$$\dot{a} = \frac{\beta \lambda}{4} \frac{\dot{\omega}}{\sqrt{\omega}} \qquad (5.85)$$

substitution in (3.10) gives:

$$\dot{a} = \frac{\beta \lambda}{4} \frac{\dot{\varepsilon}_o}{\sqrt{\omega}} \left[\frac{\sigma}{\sigma_o}\right]^n \left[\frac{1}{(1-\omega)^n} - (1-\omega)\right] \qquad (5.86)$$

The non dimentional form of $\dot{a}$ is plotted versus ω in figure 5.14.

It is not possible to eliminate ω from (5.86) and (5.83) to get an explicit relationship between $\dot{a}$ and C*, for any value of ω. However explicit relationships

may be obtained for $\omega<<1$ and $\omega\rightarrow 1$.

For $\omega<<1$

$$\frac{\dot{a}}{\dot{\varepsilon}_0 \beta \lambda} \approx \frac{(n+1)^2}{6n} \frac{\sigma_0}{\sigma} \frac{C^*}{\sigma_0 \dot{\varepsilon}_0 \alpha \beta \lambda} \qquad (5.87)$$

and for $\omega\rightarrow 1$:

$$\frac{\dot{a}}{\dot{\varepsilon}_0 \beta \lambda} \approx \frac{1}{4} \left[\frac{n+1}{n}\right]^{n/(n+1)} \left[\frac{C^*}{\sigma_0 \dot{\varepsilon}_0 \alpha \beta \lambda}\right]^{n/(n+1)} \qquad (5.88)$$

Equations (5.87) and (5.88) show that, at small damage ratio a stress-ratio effect is expected, but as fracture is approached this disappears. Similarly, as β and λ can approximately be canceled from each side of both equations, individual crack growth rates are not sensitive to void spacing or grain size. For $\omega<<1$ proportionality is predicted between $\dot{a}$ and C^* whereas as $\omega\rightarrow 1$, $\dot{a}$ becomes proportional to $C^{*\,n/(n+1)}$ which is in agreement with experimental observations. The growth rate for a given distribution is in inverse proportion to α at $\omega<<1$ and almost inverse proportion for $\omega\rightarrow 1$. So the void growth rate is much dependent on the void shape. As α decreases the voids become more disc-shaped and cracked like. So as expected the crack growth increases as a smaller C^* is required to cause a flatter defect to spread.

5.7 THE REFERENCE STRESS CONCEPT

In a cracked body as the creep exponent n increases the net section stress distribution will degenerate to a reference stress (at $n = \infty$). Therefore according to the deformation mode, and, particular test conditions the use of a particular value of the stress index n should ideally describe the rate of stress relaxation.

Mackenzie (1968) and Anderson (1980) found from calculations that there is a point in the body where the stress is approximately constant for all values of the stress index n. This point is called the skeletal point, and, the reference stress can be defined to be equivalent to the stress at that point. Al-Faddagh et. al. (1982) found that there is a

skeletal point for circumferentially notched bars. The conventional method of obtaining the reference stress is to obtain stress distributions for two different values of n, but this technique is difficult for complicated structures. Mariott (1970) indicates that the upper limit of the exact reference stress arising from Sim's (1968) work is :

$$\sigma_R \leq \frac{P}{P_L} \sigma_y \qquad (5.89)$$

where P_L is the limit load of the structure. This upper bound reference stress can, however, predict deformations which are well in excess of the exact deformation (Anderson (1980)).

In essence this reference stress describes only the creep deformation in a particular geometry and it can be used to predict creep life only, but for materials of high creep index n it is assumed that the stress distribution and the stress conditions are very similar for a cracked and an uncracked body, when their particular reference stress values are the same.

An extension of the upper limit for the exact reference stress for a cracked geometry is discussed by Haigh and Richards (1974). The limit load P_L of a cracked geometry, may be written on terms of the yield ratio m. Haigh and Richards (1974) define the term m as a ratio given by

$$m = \frac{\text{Collapse load of a cracked geometry}}{\text{Collapse load of the same uncracked geometry}} = \frac{P_{LC}}{P_L} \qquad (5.89a)$$

The reference stress for the cracked geometry is given by substituting P_L by P_{LC} in (5.89) to give

$$\sigma_R \leq \frac{P}{P_{LC}} \sigma_y = \frac{P}{m P_L} \sigma_y \qquad (5.90)$$

Haigh and Richards (1974) give m for the compact tension geometry as

$$(1 - a/W) = 1.26 (2m + m^2)^{1/2} - m \qquad (5.91)$$

for plane strain conditions, and

$$m^2 + 2m (1 + a/W) = (1 - a/W)^2 \qquad (5.92)$$

for plane stress conditions.

5.8 PARAMETERS TO CHARACTERISE CREEP CRACK GROWTH.

Several field parameters have been proposed for characterising the creep crack growth rate behaviour of metals. These parameters include, the stress intensity K, the contour integral J, the reference stress, and, the energy rate line integral C*.

For materials which exhibit low creep ductility, the loading conditions may be not sufficient to cause extensive creep deformation, so that small scale creep conditions may predominate at the crack tip. Hence, stress relaxation at the crack tip is limited to a region, which is much smaller compared to the K zone size. For high crack growth rates, as explained in section 5.4, there is the possibility that a zone of stress relaxation does not exists at the crack tip. Under these circumstances K will characterise the crack growth rate behaviour. Sadananda and Shahinian (1978) suggest good correlation of the crack growth rate with K using a relationship of the form:

$$\dot{a} = A K^{m} \qquad (5.93)$$

where A and m are material constants. Siverns and Price (1973), Floreen (1975) and Dimopulos et. al. (1986) have correlated their results using (5.93) with some success.

For ductile materials where there is substantial creep deformation the singularity at the crack tip will be lost so K losses significance. Correlating parameters that can be used in these situations are the net section stress, and, the reference stress. The reference stress concept has been discussed in section 5.7. The net section stress is the applied load divided by the uncracked area, parallel to the crack. For geometries that do not have bending component in the uncracked ligament, the net section stress is the same as the reference stress. It must be said however that, these terms are essentially parameters for estimating the overall deformation rate of the uncracked ligament, which fails by net section rupture. They do not describe a crack propagation process, or the magnitudes of stress, strain or strain rate, in the crack tip region, and therefore are not

strictly applicable. Nevertheless, attempts have been made using the following empirical expression:

$$\dot{a} = H \sigma_R^p \qquad (5.94)$$

where σ_R can be the reference stress or the net section stress, H and p are material constants. Harrison and Sandor (1971) reported modest correlation between the crack growth rate and the net section stress in a Cr-Mo-V steel using centre crack tension specimens only. However better correlation was achieved than that with K. Ellison and Walton (1974) using various specimen geometries reported lack of correlation between da/dt and the net section stress. Haigh (1975) shows that, over a range of crack lengths, for which crack growth rates are generally determined in several geometries, notably single edge notch tension (SENT) and centre cracked plate (CCP) specimens, similar correlations will obtained using either the reference stress or K.

The problem of defining what is "creep brittle" and what is "creep ductile" behaviour, in terms of crack growth for steady load conditions, is of particular importance. Harper (1976) and Ellison and Harper (1978), postulate three distinct regimes of creep fracture.They illustrate the various regimes by considering the competing processes of stress redistribution and damage accumulation at, and ahead of, the crack tip. Figure 5.15 shows the relevant crack tip stress σ (e.g. either maximum principal or maximum shear) normalised with the reference stress σ_R, and damage accumulation represented by a general parameter D normalised with the critical value for local rupture D_c. The ratios σ/σ_R, D/D_c are plotted against a time axis.

For brittle materials damage, be it crack like or otherwise, reaches a critical value for local rupture before substantial stress relaxation (figure 5.15a). In the absence of plastic deformation the stress and strain fields ahead of the crack tip are predominantly elastic and not an HRR type due to creep deformation. It is possible, therefore, that under these circumstances, crack growth rates may correlate with the stress intensity factor, K.

In ductile materials and where restraint is low, the reverse occurs. The crack tip stress relaxes rapidly to the net section stress before appreciable local damage accumulation (figure 5.15b). The problem then becomes one of general creep deformation and rupture, and the reference stress may be used to predict failure time and deformation rates.

However even for the ductile material, when deformation is constrained, a third intermediate form of behaviour is apparent, in which it is assumed that the stress redistribution precedes local rupture but that the relaxed value of the crack tip stress is much higher than the reference stress (figure 5.15c). This resulting failure may be termed "quasi brittle" since crack propagation is considered to be largely a crack tip event. The quasi brittle situation with a ductile material is essentially a constraint effect, caused by both the existence of a sharp crack and sufficient component size. The probable manner in which behaviour will be altered by either crack tip radius or specimen thickness is shown in figures 5.15d and 5.15e. Increasing crack - tip radius whilst keeping thickness constant, will reduce the initial stress elevation, causing slower damage accumulation, and thus effectively enhancing ductility. Decreasing thickness has the same effect: although the initial crack tip elevation may be unaltered, the rate of relaxation is very much higher.

Indications are that the C* line integral will characterize stress-strain conditions in this regime. Nikbin (1976) conducting tests on various specimen geometries shows that good correlation is obtained using the relationship:

$$\dot{a} = D C^{*\Phi} \qquad (5.95)$$

where D, Φ are material constants. Landes and Begley (1974) and Harper (1976), show also satisfactory correlations using (5.95). Smith and Webster (1981) obtained good correlations using both CT and DCB specimens of 1CMV steel at 565° C using (5.95), but neither K or σ_R provided an adequate correlation. Recent results by Nikbin et. al. (1984), Nikbin et. al. (1986) and Dimopulos et. al. (1986), show good correlation

using (5.95). The major problem confronting experiments in using C* is its evaluation. Both numerical and experimental techniques can be used to determine C*. These techniques will be reviewed in detail in chapter 6.

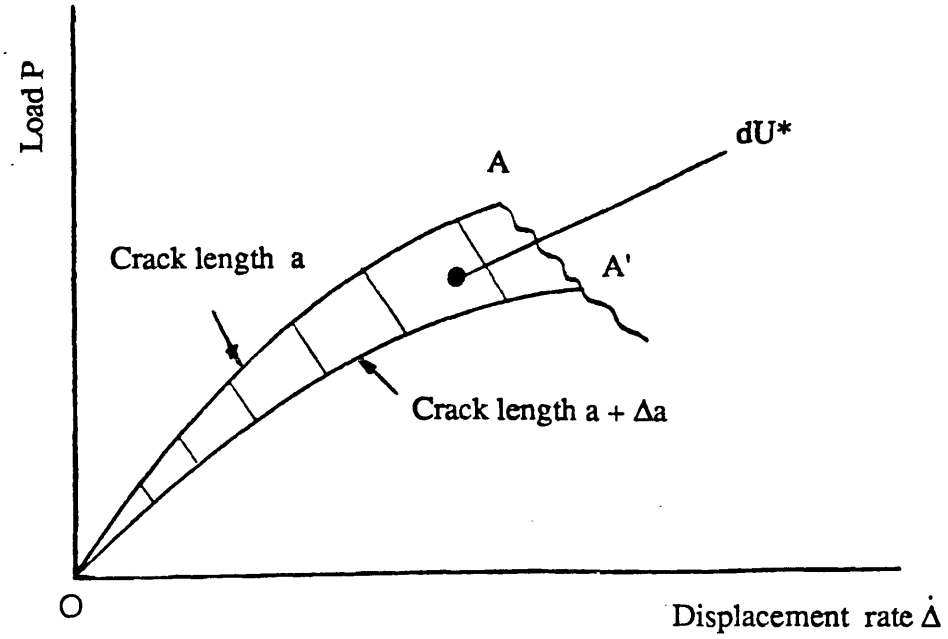


Figure 5.1 Load-displacement rate diagram for a material obeying the Norton's secondary creep law.

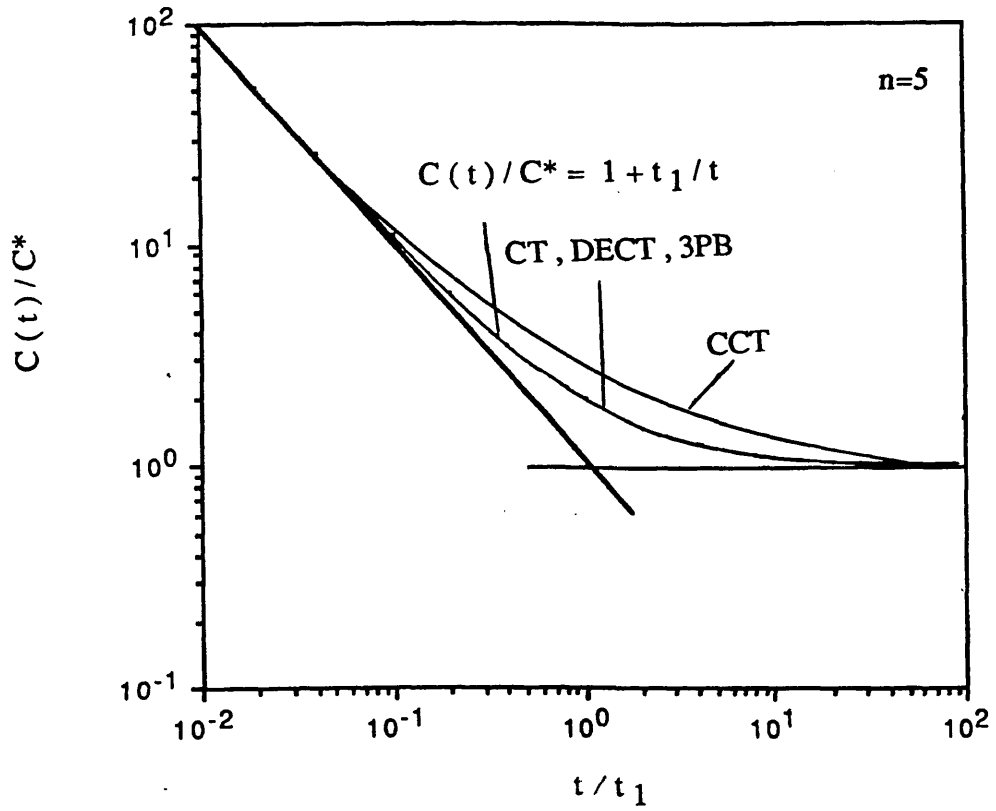


Figure 5.2 From Ehlers and Riedel (1981). Finite Element results of Ehlers (1981) compared to the approximate formula $C(t)/C^* = 1 + t_1/t$.

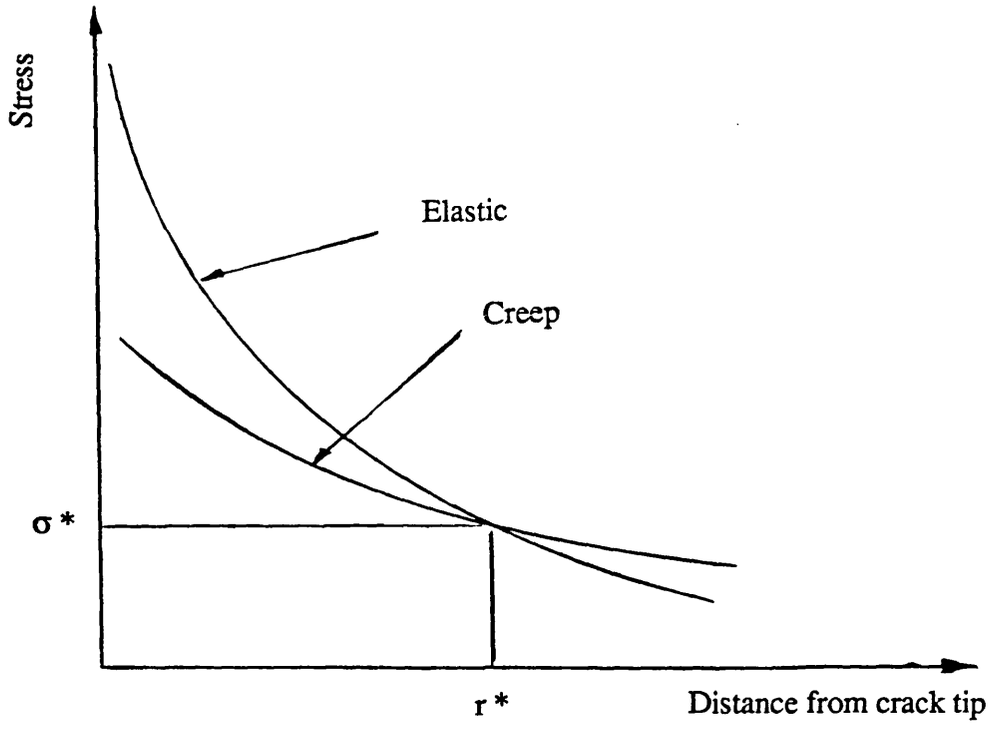


Figure 5.3 Elastic and steady state creep stress distribution ahead of a crack tip.

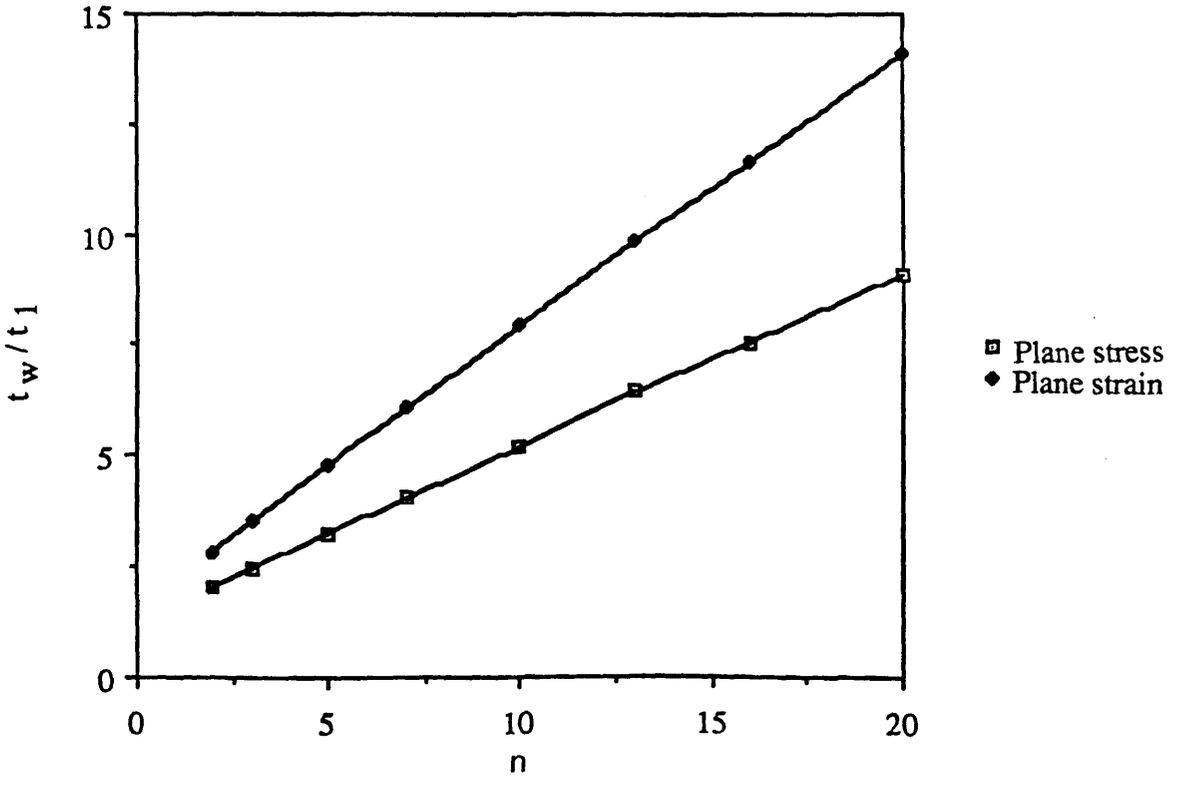


Figure 5.4 t_w / t_1 as a function of the creep exponent n for plane strain and plane stress conditions

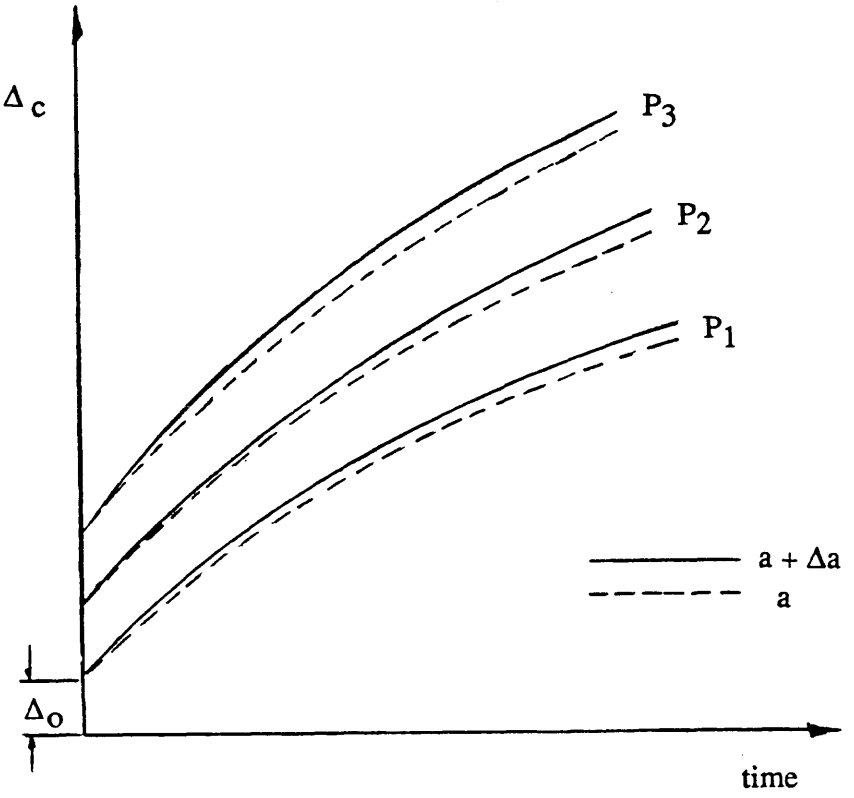


Figure 5.5 Load- line deflection Δ_c, as a function of time for bodies of crack lengths a and a + Δa at various load levels.

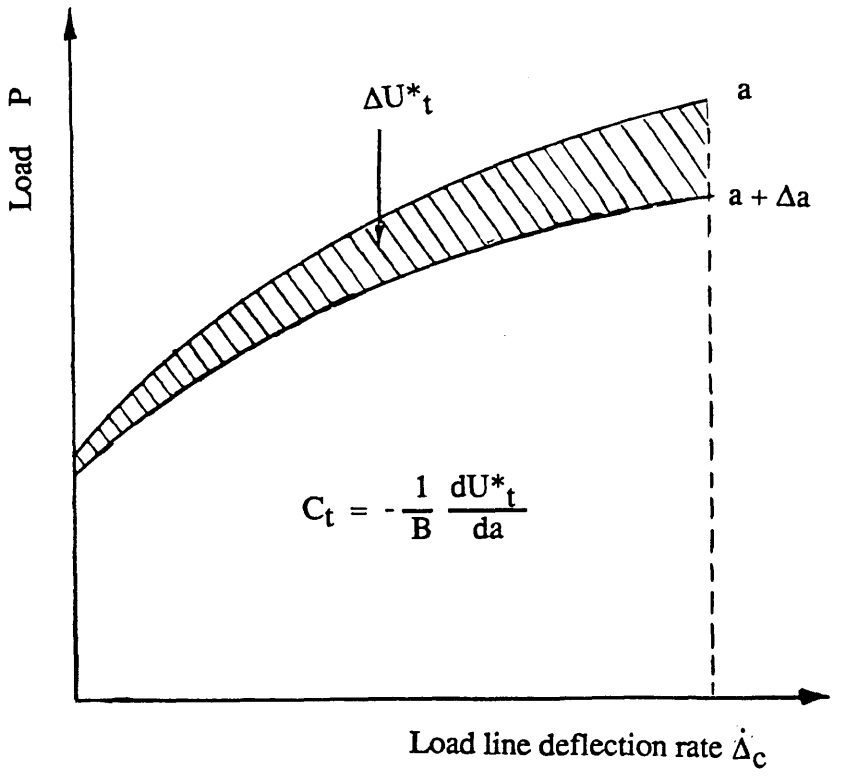


Figure 5.6 The definition of C_t parameter.

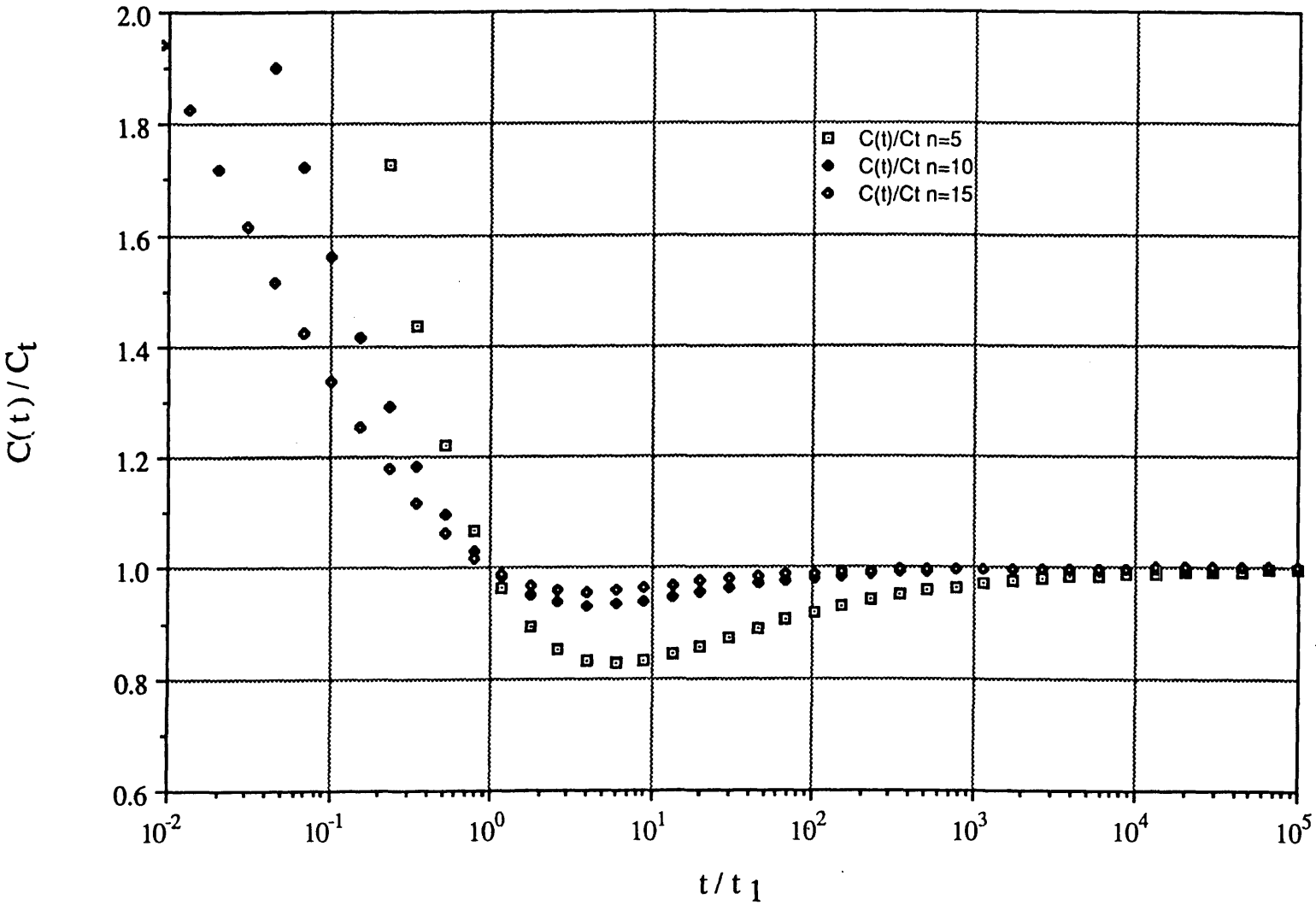


Figure 5.7 Relationship between C(t) and C_t for short and long times for various values of n.

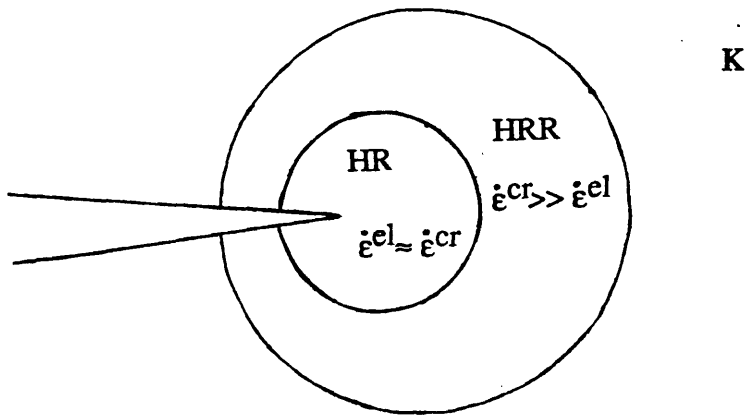


Figure 5.8 Schematic figure showing the different regions of dominance of the asymptotic stress fields near the tip of a growing crack under transient crack growth conditions

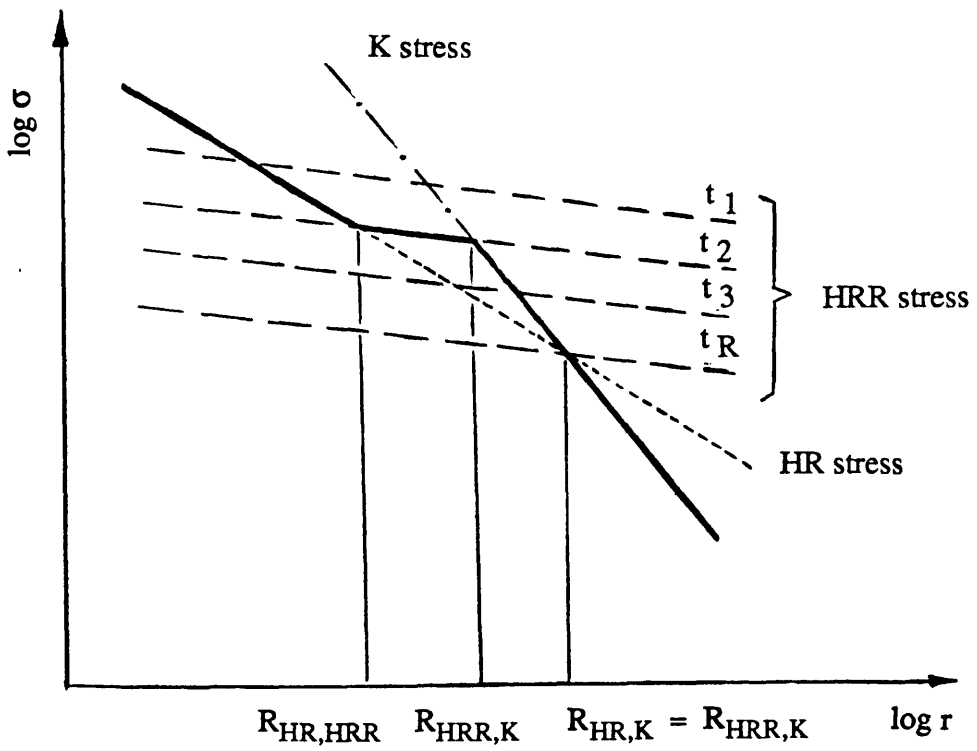


Figure 5.9 From Hawk and Bassani (1986) . Log- log plot of effective stress vs distance ahead of crack based on matching of singular crack-tip stress fields under transient crack growth conditions.

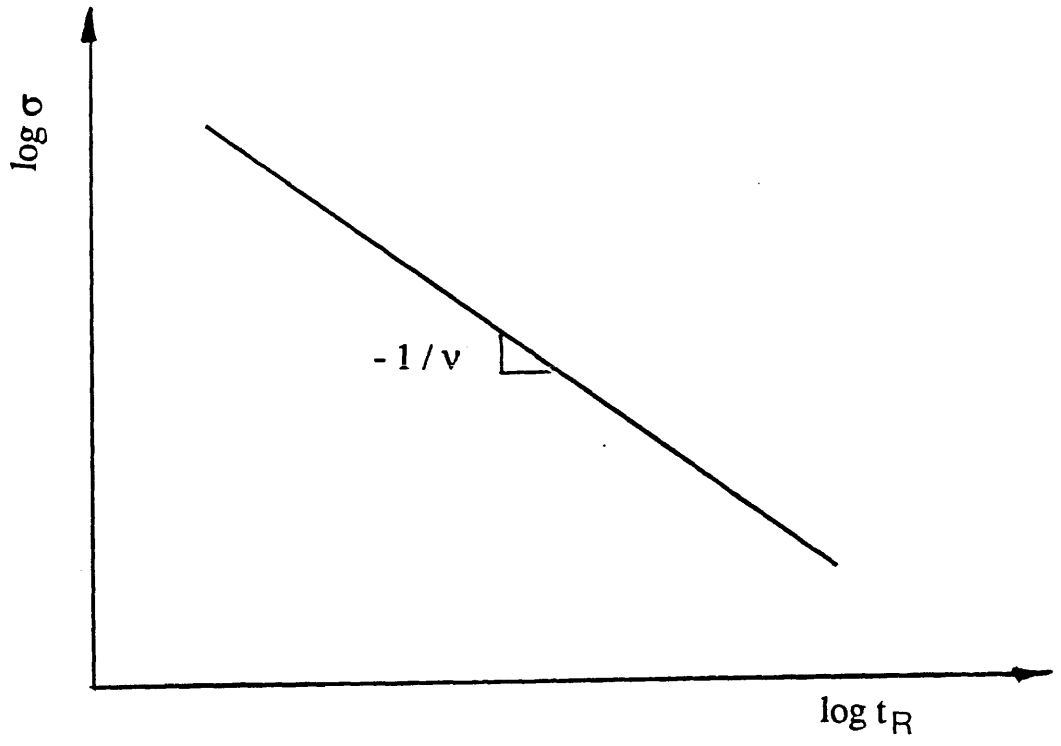


Figure 5.10 Typical stress rupture plot.

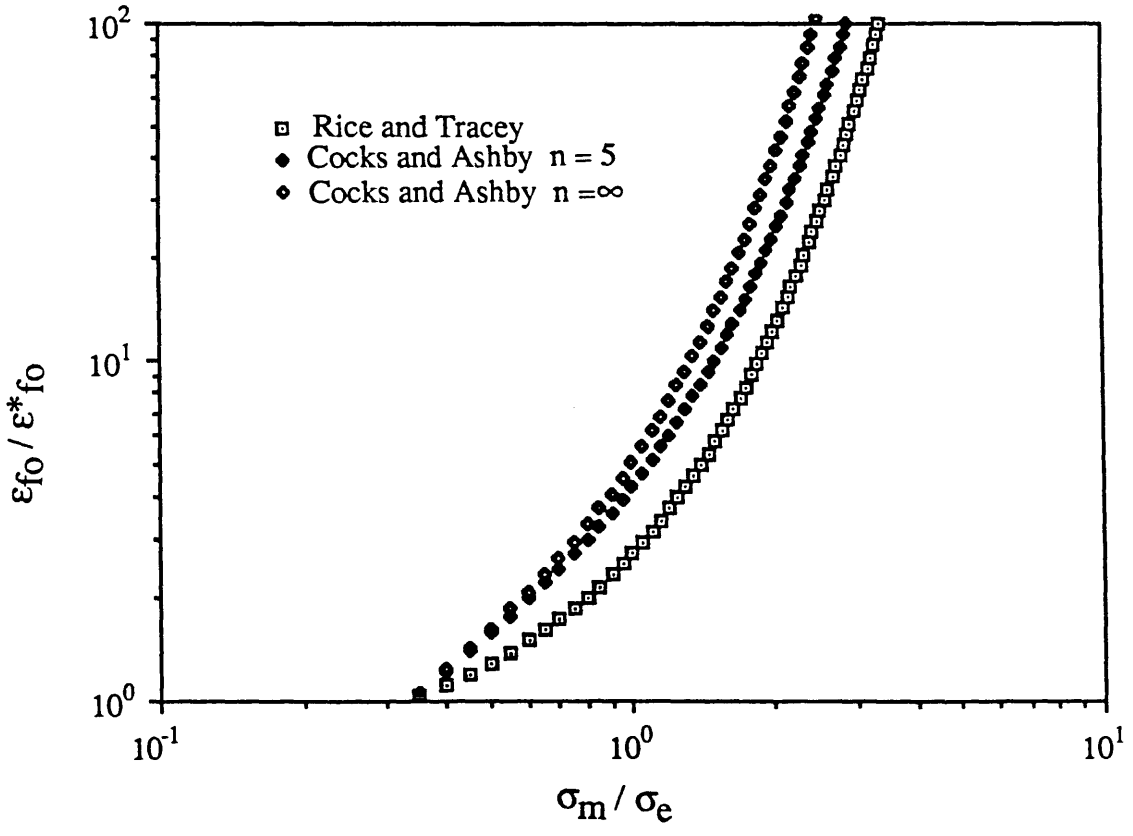


Figure 5.11 Influence of state of stress on creep failure strain.

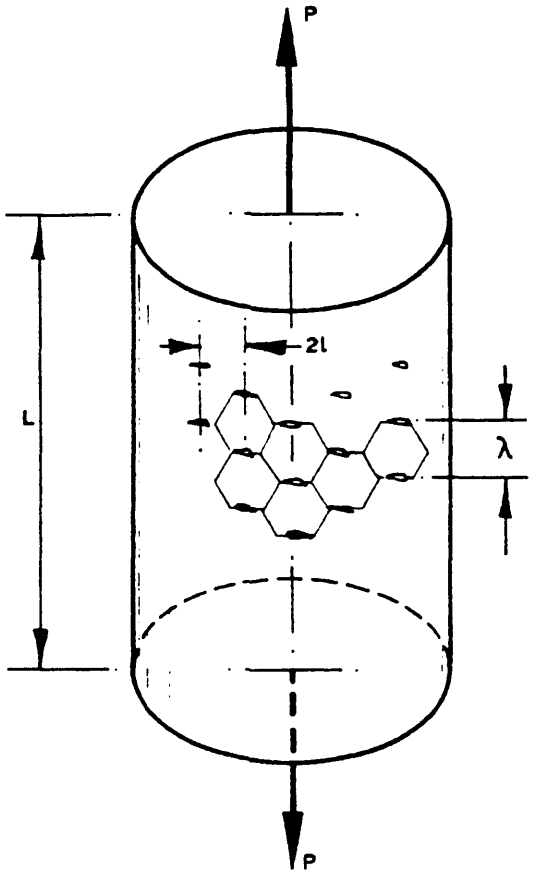


Figure 5.12 Distribution of grain boundary voids in uniaxial creep specimen.

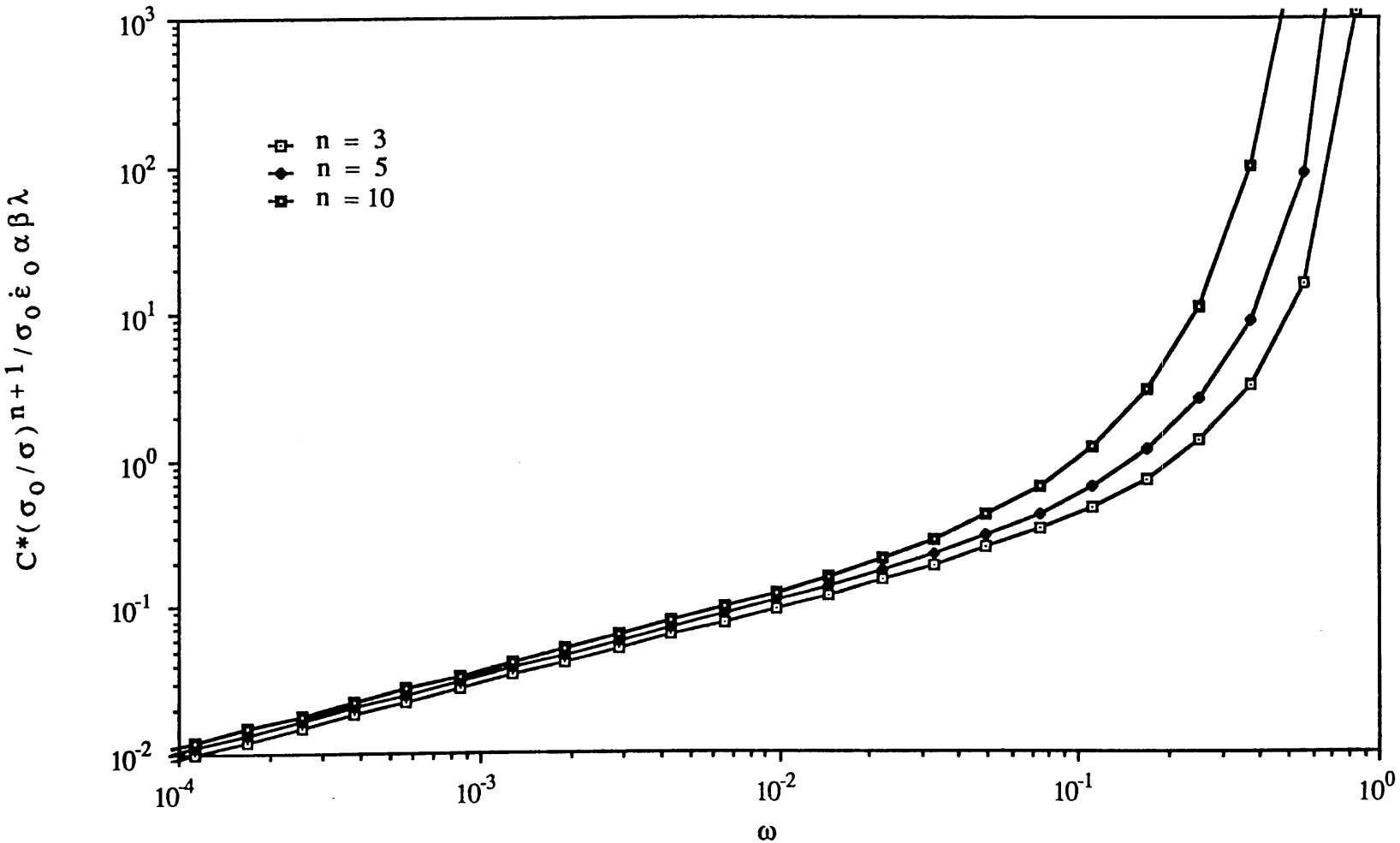


Figure 5.13 Dependence of dimensionless form of C* on void fraction ω for mechanistic damage accumulation model. (from Smith and Webster (1985))

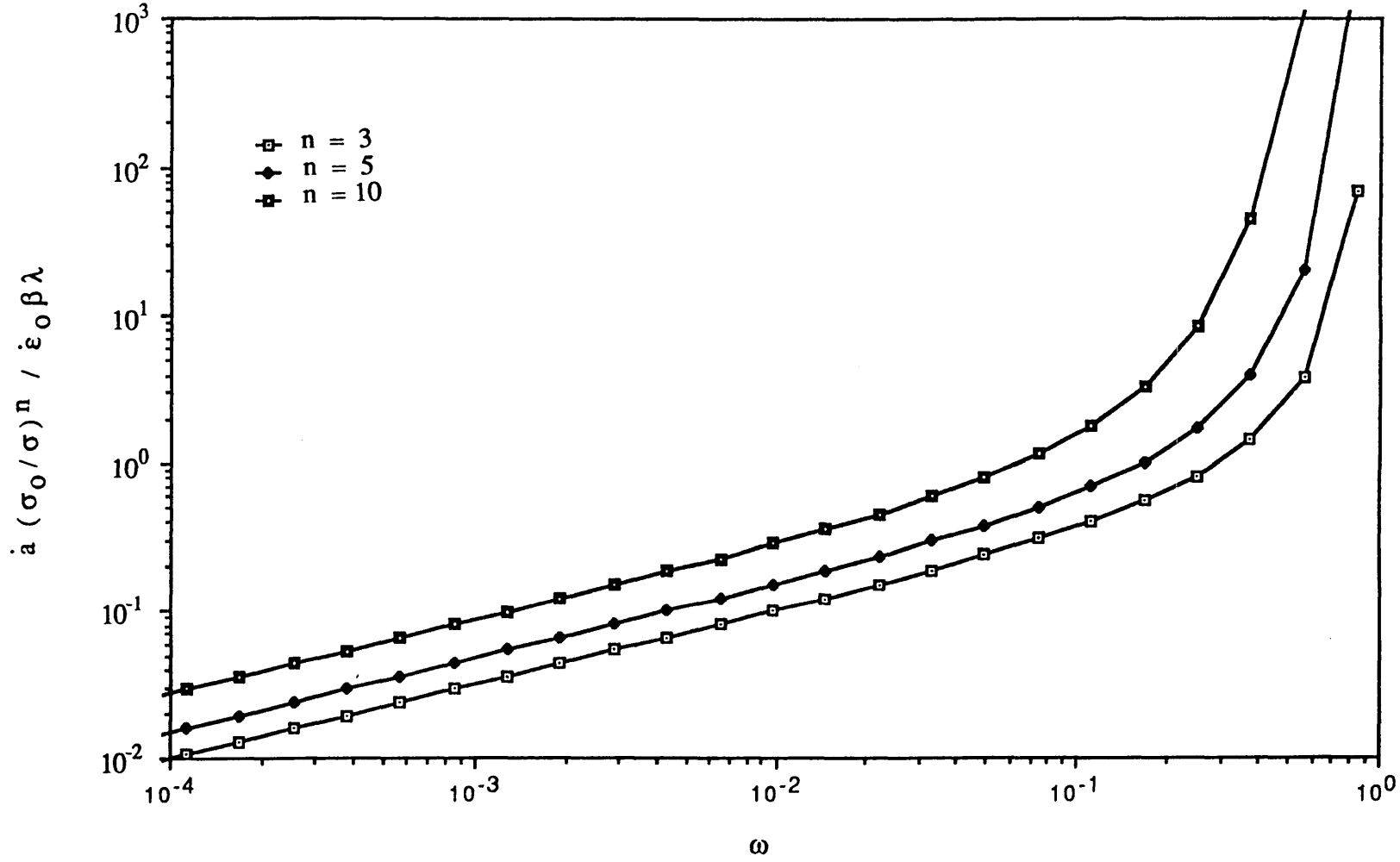
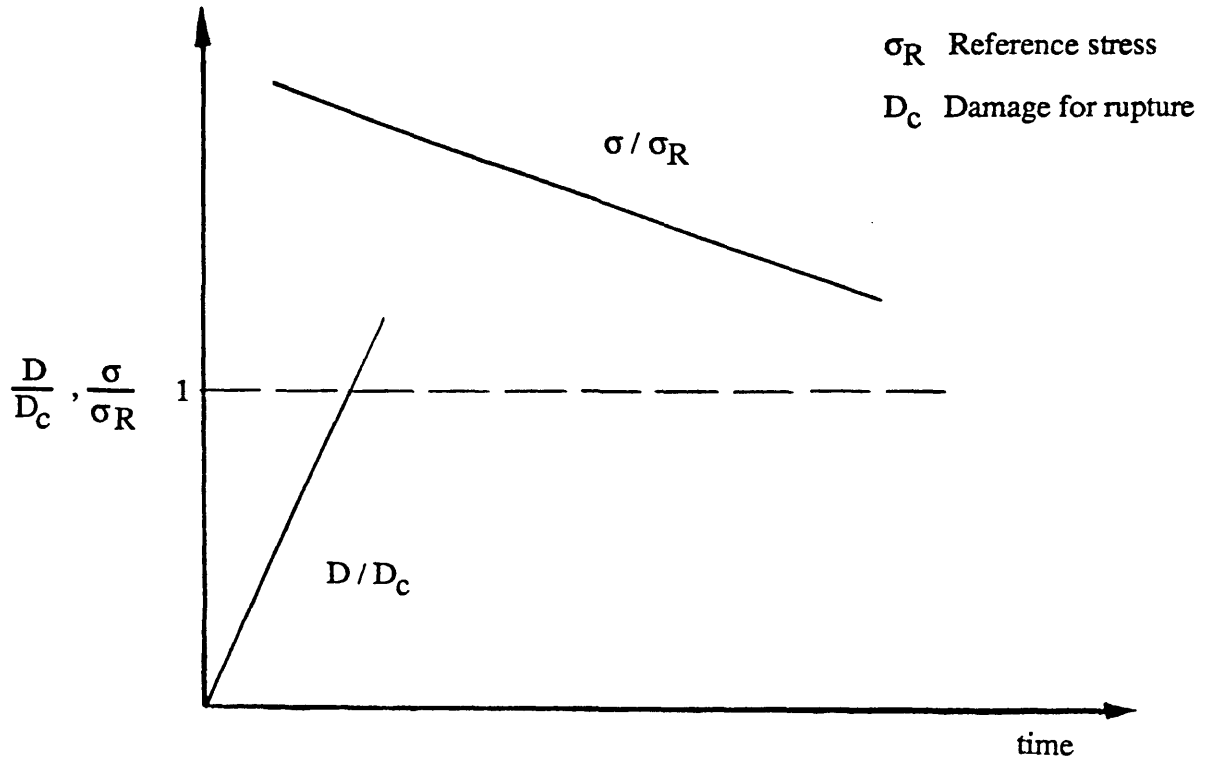
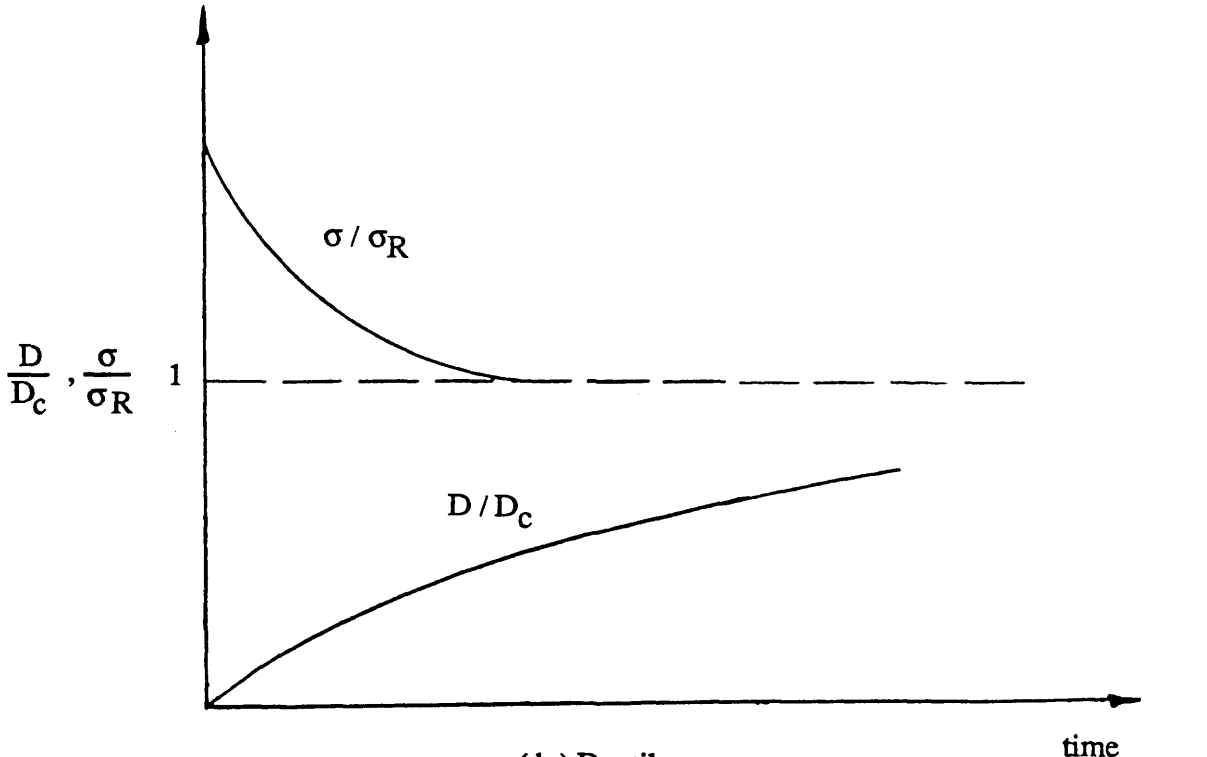


Figure 5.14 Relationship between void growth rate $\dot{a}$ and area fraction ω for mechanistic damage accumulation model. (from Smith and Webster (1985))

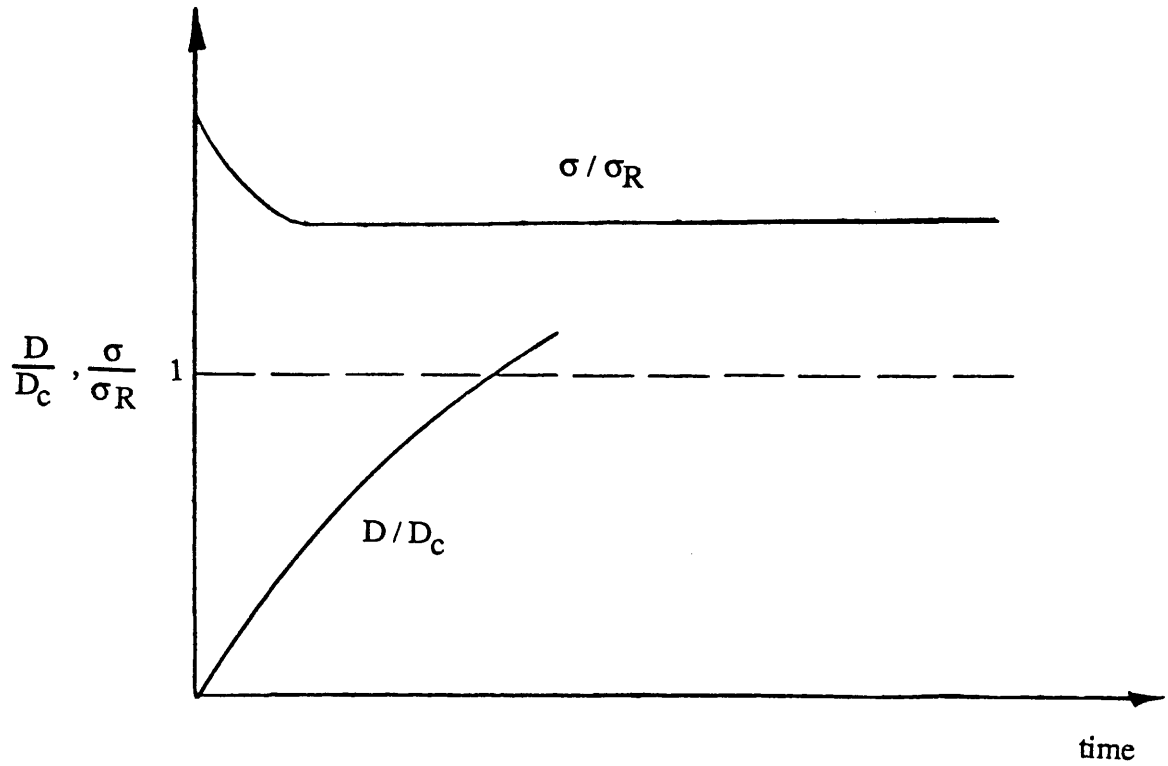


(a) Brittle

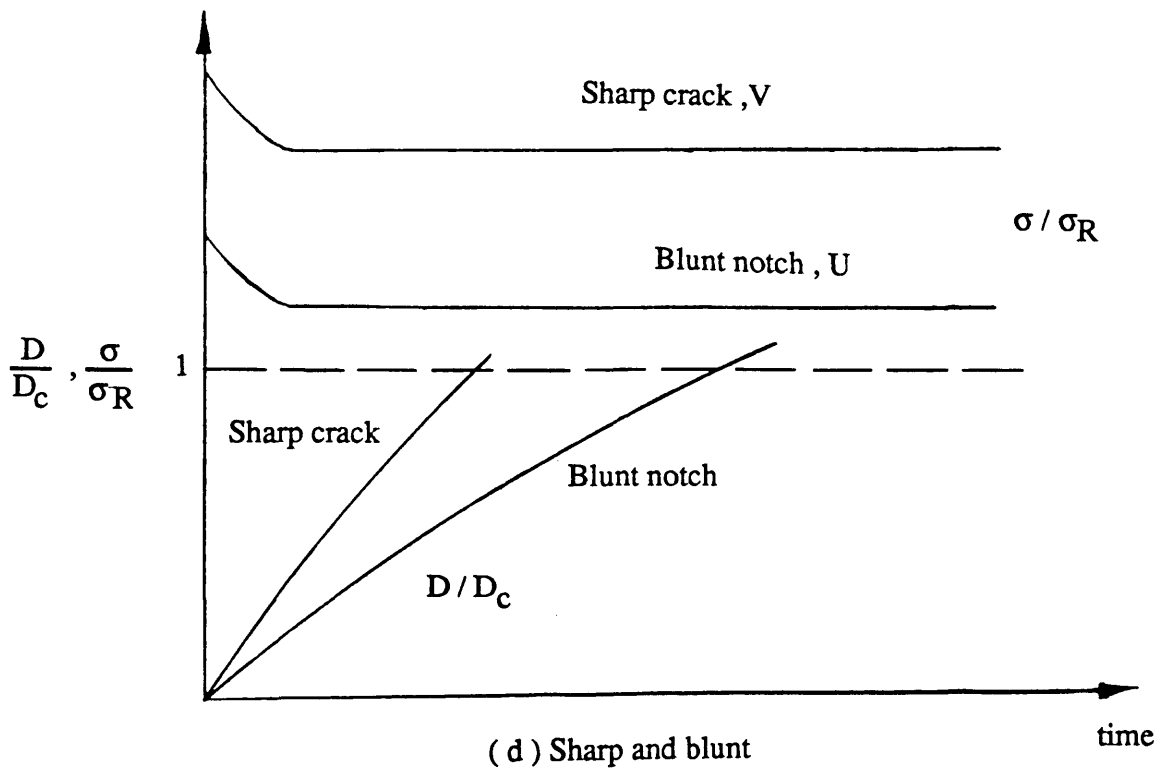


(b) Ductile

Figure 5.15 From Ellison and Harper (1978). Schematic representation of regimes of creep ductility (a) Brittle (b) Ductile .



(c) Quasi-brittle



(d) Sharp and blunt

Figure 5.15 (continued) Schematic representation of regimes of creep ductility

(c) Quasi-brittle (d) Sharp and blunt

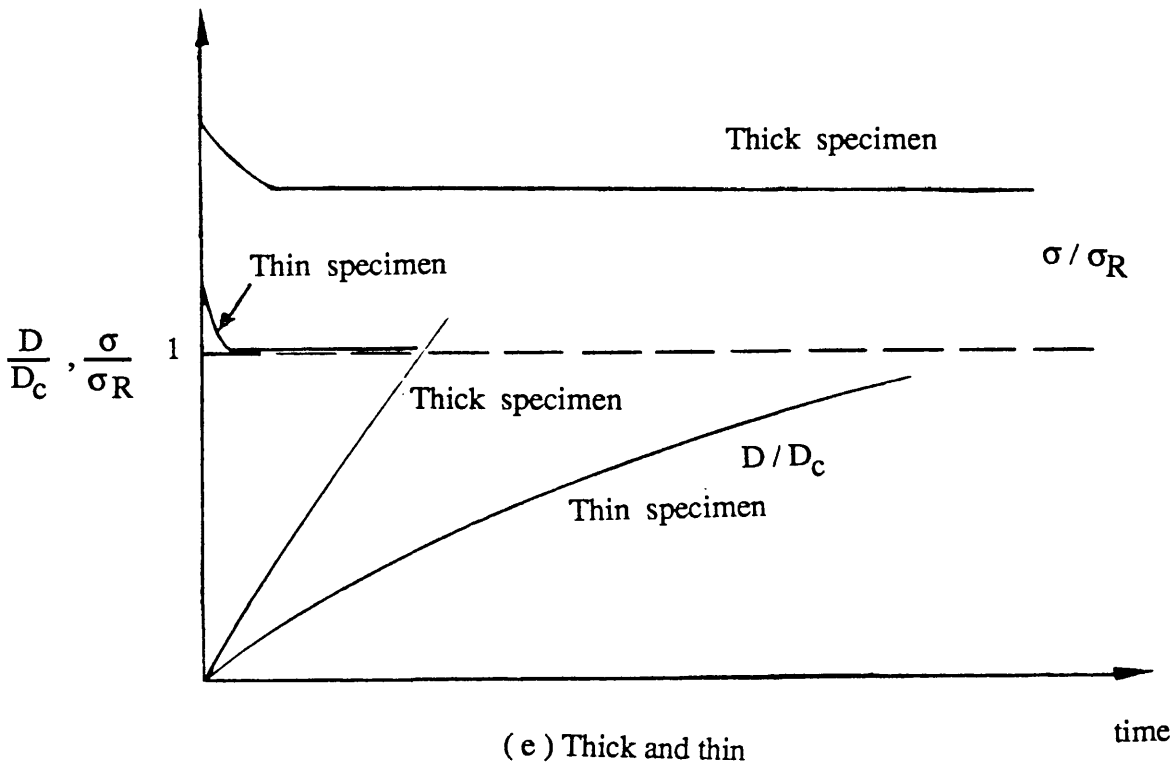


Figure 5.15 (continued) Schematic representation of regimes of creep ductility

(e) Thick and thin

CHAPTER 6

METHODS OF RETRIEVING C*

6.1 EXPERIMENTAL METHODS

The experimental methods of retrieving C* are based in equations (5.12) to (5.15) . Equation (5.13) was :

$$C^* = \frac{P\dot{\Delta}}{B\,W}\,F$$

Approximate procedures of calculating F, are based on the experimental observation that n>>1 for most metals. In this circumstance limit analysis techniques can be applied to express P as a fraction of the plastic collapse load of the cracked body P_{LC} (Haigh and Richards (1974)). Provided the proportionality factor is only weakly dependent on crack length, it is possible to write (Smith and Webster (1981), Harper and Ellison (1977)).

$$\frac{1}{P}\frac{dP}{da} \approx \frac{1}{P_{LC}}\frac{dP_{LC}}{da} \qquad (6.1)$$

So that from equation (5.15):

$$F \approx \left[\frac{-n}{n+1}\frac{W}{P_{LC}}\frac{dP_{LC}}{da}\right] \qquad (6.2)$$

Substitution of (6.2) into (5.13) allows approximate estimates of C* to be obtained, for a range of values of n and specimen configurations, provided appropriate limit load solutions are available. Equation (5.13) is written in a convenient form for obtaining C* from experimental data, when the precise creep behaviour of the material is not known, provided that the load line displacement Δ is measured throughout the test, as a function of the crack length, and that, the dependence of the crack length on F is also available. Then by subtracting the elastic displacements from the total

recorded, the creep displacement rate $\dot{\Delta}$ can be obtained and hence C*. Estimates of the non-dimensional factor F are given in the literature, as a function of a/W for a number of specimens (for example Smith and Webster (1983), Haigh and Richards (1974), Merkle and Corten (1974). For the CT geometry which is the geometry mainly used in this thesis, the non dimensional factor F determined from collapse solutions is given by Haigh and Richards (1974), (figure 6.1) as :

$$F = \frac{\frac{-n}{n+1}\left[\frac{5.404}{r}\frac{a}{W} - 1.702\right]}{\left[0.851\, r - \left[1 + 1.702\frac{a}{W}\right]\right]} \qquad (6.3)$$

$$\text{where } r = \left[3.732 + 6.350\left[\frac{a}{W}\right]^2\right]^{1/2}$$

In general (Smith and Webster (1983)) the non dimensional factor F has been found to be dependent on specimen geometry and crack length, but to be relatively insensitive to creep stress index n.

If side grooves are introduced it is necessary to replace the gross thickness B, by the net thickness between the side grooves B_n so that (5.13) becomes :

$$C^* = \frac{P\dot{\Delta}}{B_n W} F \qquad (6.4)$$

6.2 NUMERICAL METHODS FOR ESTIMATING CRACK GROWTH PARAMETERS

Most practical engineering problems are impossible to solve by conventional analytical method, in which exact mathematical expressions are obtained for the required variables such as displacements and stresses. In the past such problems were simplified, to a point where an analytical solution could be obtained which, it was hoped bore some resemblance to the solution of the real problem. Because of the uncertainties involved in such a procedure large factors of safety were used.

The advent of high speed digital computers has led to the emergence of many numerical techniques for scientific analysis. Using numerical analysis is possible to solve problems of real engineering interest, for which analytical solutions do not exist, with relative ease. In the field of solid mechanics, the degree of confidence in the numerical solutions, has resulted in allowing higher working stresses in engineering components and structures.

Two of the most successful numerical methods in the analysis of stresses in solid components are, the Finite Element method (F.E.) and the Boundary Integral Equation method. (B.I.E). The F.E. method may be described as a domain method because the distributions of the variables are obtained at a finite number of discrete points over the entire region of the body. In boundary methods, one of which is the B.I.E. method, the primary results are the distributions of the variables on the boundary of the solution domain only, again defined in terms of values at a finite number of points.

One method over the other has advantages and disadvantages, depending upon the type of problem.

The F.E. and B.I.E. methods are reviewed in sections 6.3 and 6.4 respectively. In section 6.5 the F.E. results of Kumar et. al. (1981) are presented.

6.3 THE FINITE ELEMENT METHOD

6.3.1 INTRODUCTION

The finite element method is widely used by engineers, particularly for the stress analysis of solid components. An analytical description of the method is given by Fenner (1975). The main features of the method are summarized below.

(a) The physical systems, such as structures, solid or fluid continua are divided into small sub-regions or elements. Each element is essentially a simple unit, the behaviour of which can be analysed. The term "finite element" stems from the fact that the physical system is modelled by a finite number of elements.

(b) The elements can be triangular, rectangular etc. The analysis used in this thesis uses constant strain triangular elements. The corners of the element are known as nodes. Two adjacent elements will have one common side i.e. two common nodes. The displacements of the nodes are the unknowns of the problem.

(c) Polynomial functions are used to relate the displacement of a point to its position in the element. For the case where linear functions are used the displacements vary linearly throughout the element and the elements are called "constant strain" elements.

(d) Boundary conditions are applied to simulate prescribed surface tractions, and, restrains applied to some of the displacements.

(e) The displacements may be related to strains and hence to stresses via the properties of the continuum.

(f) By applying the condition of equilibrium the displacements, and hence the stresses and strains may be obtained.

6.3.2 MATHEMATICAL ANALYSIS

(a) ELASTIC ANALYSIS

The formulation used in the finite element analysis, is for two-dimensional problems of the biharmonic plane stress or plane strain, using constant strain triangles (CST) as the finite elements. All the elements and nodal points are numbered. The typical element is shown in figure 6.2. The element is numbered m and its nodes i , j, k .

The cartesian co-ordinates X and Y are the global co-ordinates for the solution domain. The solution domain has unit thickness in Z- direction. The dimensions of the element can be expressed in terms of the lengths $a_i, a_j, a_k, b_i, b_j, b_k$, as shown in figure 6.2. These may be obtained from the co-ordinates of the nodal points as:

$$\begin{aligned} a_i &= X_j - X_k & b_i &= Y_j - Y_k \\ a_j &= X_k - X_i & b_j &= Y_k - Y_i \\ a_k &= X_i - X_j & b_k &= Y_i - Y_j \end{aligned} \qquad (6.5)$$

The area of the elements can be then calculated as :

$$\Delta_m = 1/2\,(a_k b_j - a_j b_k) \qquad (6.6)$$

For CST elements the displacements at the nodal points are given by :

$$\begin{aligned} u(x,y) &= C_1 + C_2 x + C_3 y \\ v(x,y) &= C_4 + C_5 x + C_6 y \end{aligned} \qquad (6.7)$$

where C_1 to C_6 are constant for a particular element and

$$C_1 = u_i$$

$$C_4 = v_i$$

and C_2, C_3, C_5, C_6 can be found from:

$$\begin{bmatrix} C_2 & C_5 \\ C_3 & C_6 \end{bmatrix} = \frac{1}{2\Delta_m} \begin{bmatrix} b_i & b_j & b_k \\ a_i & a_j & a_k \end{bmatrix} \begin{bmatrix} u_i & v_i \\ u_j & v_j \\ u_k & v_k \end{bmatrix} \qquad (6.8)$$

The displacements of a typical element are schematically shown in figure 6.3.

Now from definition:

$$\varepsilon_{xx} = \frac{du}{dx} \quad , \quad \varepsilon_{yy} = \frac{dv}{dy} \quad , \quad \varepsilon_{xy} = \varepsilon_{yx} = \frac{du}{dy} + \frac{dv}{dx} \qquad (6.9)$$

or in matrix form:

$$[\varepsilon] = \begin{bmatrix} \varepsilon_{xx} \\ \varepsilon_{yy} \\ \varepsilon_{xy} \end{bmatrix} = \begin{bmatrix} du/dx \\ dv/dy \\ du/dy + dv/dx \end{bmatrix} = \begin{bmatrix} C_2 \\ C_6 \\ C_3 + C_5 \end{bmatrix} = \frac{1}{2\Delta_m} B \begin{bmatrix} \delta_i \\ \delta_j \\ \delta_k \end{bmatrix} \qquad (6.9a)$$

where

$$B = \begin{bmatrix} b_i & 0 & b_j & 0 & b_k & 0 \\ 0 & a_i & 0 & a_j & 0 & a_k \\ a_i & b_i & a_j & b_j & a_k & b_k \end{bmatrix} \qquad (6.9b)$$

and

$$\delta_i = \begin{bmatrix} u_i \\ v_i \end{bmatrix} \qquad (6.9c)$$

The strains and therefore the corresponding stresses are constant over each element. Their effects can be expressed in terms of equivalent forces acting at the midpoints of the sides of the elements. A further transformation allows the forces acting at the mid points of the sides, to be replaced by an equivalent set acting at the nodes. For equilibrium it can be proved that:

$$U_i = 1/2 (\sigma_{xx} b_i + \sigma_{xy} a_i) \qquad (6.10)$$

Similar expressions can be obtained for the other nodes to give:

$$\begin{bmatrix} R_i \\ R_j \\ R_k \end{bmatrix} = \frac{1}{2} B^T \begin{bmatrix} \sigma_{xx} \\ \sigma_{yy} \\ \sigma_{xy} \end{bmatrix} \qquad \text{where } R_i = \begin{bmatrix} U_i \\ V_i \end{bmatrix} \qquad (6.10a)$$

For a homogeneous isotropic and linearly elastic material the constitutive equations are:

$$\varepsilon_{xx} = \frac{1}{E}\left[\sigma_{xx} - \nu(\sigma_{yy} + \sigma_{zz}) \right] + \alpha \Delta T \qquad (6.11a)$$

$$\varepsilon_{yy} = \frac{1}{E}\left[\sigma_{yy} - \nu(\sigma_{zz} + \sigma_{xx}) \right] + \alpha \Delta T \qquad (6.11b)$$

$$\varepsilon_{zz} = \frac{1}{E}\left[\sigma_{zz} - \nu(\sigma_{xx} + \sigma_{yy}) \right] + \alpha \Delta T \qquad (6.11c)$$

$$\varepsilon_{xy} = \frac{\sigma_{xy}}{G} = \frac{2(1+\nu)}{E}\sigma_{xy} \qquad (6.11d)$$

$$\varepsilon_{yz} = \frac{\sigma_{yz}}{G} = \frac{2(1+\nu)}{E}\sigma_{yz} \qquad (6.11e)$$

$$\varepsilon_{zx} = \frac{\sigma_{zx}}{G} = \frac{2(1+\nu)}{E}\sigma_{zx} \qquad (6.11f)$$

where α is the coefficient of expansion. For plane stress $\sigma_{zz} = 0$. So the constitutive relations in matrix form can be written as:

$$\begin{bmatrix} \varepsilon_{xx} \\ \varepsilon_{yy} \\ \varepsilon_{xy} \end{bmatrix} = \frac{1}{E}\begin{bmatrix} -1 & -\nu & 0 \\ -\nu & 1 & 0 \\ 0 & 0 & 2(1+\nu) \end{bmatrix}\begin{bmatrix} \sigma_{xx} \\ \sigma_{yy} \\ \sigma_{xy} \end{bmatrix} + \alpha \Delta T \begin{bmatrix} 1 \\ 1 \\ 0 \end{bmatrix} \qquad (6.12)$$

For plane strain $\varepsilon_{zz}=0$ or $\sigma_{zz}=\nu(\sigma_{xx}+\sigma_{yy}) - E\alpha\Delta T$. Substituting for σ_{zz} into expressions for ε_{xx} , ε_{yy} and ε_{xy} , the constitutive equations in matrix form can be obtained as :

$$\begin{bmatrix} \varepsilon_{xx} \\ \varepsilon_{yy} \\ \varepsilon_{xy} \end{bmatrix} = \frac{1}{E^*}\begin{bmatrix} -1 & -\nu^* & 0 \\ -\nu^* & 1 & 0 \\ 0 & 0 & 2(1+\nu^*) \end{bmatrix}\begin{bmatrix} \sigma_{xx} \\ \sigma_{yy} \\ \sigma_{xy} \end{bmatrix} + \alpha^* \Delta T \begin{bmatrix} 1 \\ 1 \\ 0 \end{bmatrix} \qquad (6.13)$$

where $E^*=E/(1-\nu^2)$, $\nu^*=\nu/(1-\nu)$ and $\alpha^*=(1+\nu)\alpha$. So analysis is the same as for plane stress, and only the material properties need to be modified.

Inverting (6.13)

$$[\sigma] = [D]\left[[\varepsilon] - [\varepsilon_T] \right] \qquad (6.14a)$$

where:

$$\left[\varepsilon_T\right] = \alpha^* \Delta T \begin{bmatrix} 1 \\ 1 \\ 0 \end{bmatrix} \qquad (6.14b) \text{ and}$$

$$\left[D\right] = \frac{E^*}{1-\nu^{*2}} \begin{bmatrix} 1 & \nu^* & 0 \\ \nu^* & 1 & 0 \\ 0 & 0 & 1/2(1-\nu^*) \end{bmatrix} \qquad (6.14c)$$

Equations (6.14a) to (6.14c) hold for plane stress and plane strain but for plane stress:

$$E^* = E \ , \ \nu^* = \nu \text{ and } \alpha^* = \alpha$$

and for plane strain:

$$E^* = E/(1-\nu^2) \ , \ \nu^* = \nu/(1-\nu) \text{ and } \alpha^* = (1+\nu)\alpha$$

It must be noted here that for plane strain :

$$\frac{E^*}{1-\nu^{*2}} = \frac{E(1-\nu)}{(1+\nu)(1-2\nu)}$$

which becomes infinity when $\nu = 1/2$. So the present F.E. analysis is unsuitable for plane strain when $\nu = 1/2$.

Substituting (6.9a) and (6.10a) into (6.12)

$$\begin{bmatrix} R_i \\ R_j \\ R_k \end{bmatrix} = \frac{1}{4\Delta_m} \left[B\right]^T \left[D\right]\left[B\right] \begin{bmatrix} \delta_i \\ \delta_j \\ \delta_k \end{bmatrix} - \frac{1}{2}\left[B\right]^T\left[D\right]\varepsilon_T$$

$$\text{or } \left[R\right]_m = \left[k\right]_m \left[\delta\right]_m - \left[\Theta\right]_m \qquad (6.15)$$

where the element stiffness matrix is given by:

$$\left[k\right]_m = \frac{1}{4\Delta_m}\left[B\right]^T\left[D\right]\left[B\right] = \begin{bmatrix} k_{11} & k_{12} & k_{13} \\ k_{21} & k_{22} & k_{23} \\ k_{31} & k_{32} & k_{33} \end{bmatrix}_m \qquad (6.16)$$

where m is the element number. Each of the coefficients is a 2x2 submatrix which can be expressed as:

$$[k]_{rs} = \begin{bmatrix} k_{xx} & k_{xy} \\ k_{yx} & k_{yy} \end{bmatrix}_{rs} \qquad (6.17)$$

Now the condition for equilibrium may be expressed as:

$$\sum \begin{bmatrix} \text{externally applied} \\ \text{forces at nodes} \end{bmatrix} = \sum \begin{bmatrix} \text{forces on the elements} \\ \text{at these nodes} \end{bmatrix}$$

For equilibrium at a node i

$$[F]_i + \sum [G]_i^{(m)} = \sum [R]_i^{(m)} \qquad (6.18)$$

$$[F]_i = \begin{bmatrix} F_x \\ F_y \end{bmatrix}_i$$

$[F]_i$ represents the forces applied externally at the node i of an element. $[G]_i^{(m)}$ and, $[R]_i^{(m)}$, represent the body forces and the internal forces applied to the elements. The summations in (6.18) are performed for the elements which have point i as a node. The set of equations for equilibrium at all the nodes can be expressed as :

$$[F]^* = [K][\delta] = \sum [k_m][\delta_m] \qquad (6.19)$$

where $[F]^* = [F] + [G] + [\Theta]$

represents the externally applied forces modified for body force and thermal forces.

The $[k_m]$ are element stiffness matrices, which are assembled to form the overall stiffness matrix [K]. Solution of the overall linear equations, which is equivalent of inverting the matrix, yields to nodal points displacements and hence stresses. An important consequence of using constant strain triangular (CST) finite elements is that the method of solution can be either a direct elimination type technique, or, an iterative procedure such as Gauss-Seidel. The latter is particularly useful when dealing with non linear problems.

(b) NON - LINEAR PROBLEMS

Non-linearities in material behaviour, such as creep and plastic deformation, which cause the effective elastic properties E and ν to vary with time or the local state of strain can be dealt with in different ways.

For creep deformation one way is to solve a series of linear problems corresponding to small increments of time. An advantage of this method is that solutions are not only obtained at the final time but at a number of intermediate times too. However there is the disadvantage that if the time increment is too large the computed solutions will diverge from their true values, and on the other hand if the time increment is very small, the amount of computing required becomes excessive as a large number of linear equations in the form of equation (6.19) are required.

Another approach, and the one which is used here, is to treat the elastic properties as variables, thereby making the [D] matrix for each element its stiffness matrix, and the overall stiffness matrix into variables. Thus (6.19) is no longer linear. Nevertheless, it can be solved using the Gauss-Seidel method, provided the elastic properties and stiffness matrices are up-dated during the iterative process. Although the amount of computing involved in a typical non-linear problem is more than that required for the corresponding linear solution, it is generally only greater by a factor of 2 to 4, so more economical than the incremental time step approach, and it is generally much easier to ensure correct convergence of the solution. On the other hand the intermediate solutions associated with the incremental approach are of no value.

The constitutive equation for secondary creep law is

$$\bar{\varepsilon} = C \bar{\sigma}^n \qquad (6.20)$$

Therefore the strain at time t is given by

$$\bar{\varepsilon} = C \bar{\sigma}^n t \qquad (6.20a)$$

which may be inverted to give

$$\bar{\sigma} = \left[\frac{\bar{\varepsilon}}{C_t} \right]^{1/n} \qquad (6.20b)$$

An apparent or effective modulus, E', can be defined as

$$E' = \frac{\bar{\sigma}}{\bar{\varepsilon}} \qquad (6.20c)$$

Substituting (6.20b) into (6.20c) gives

$$E' = \frac{1}{\bar{\varepsilon}} \left[\frac{\bar{\varepsilon}}{C_t} \right]^{1/n} = E_o \left[\frac{\bar{\varepsilon}}{\bar{\varepsilon}_o} \right]^{1/n - 1} \qquad (6.20d)$$

where E_o is the effective modulus at some reference strain $\bar{\varepsilon}_o$. Setting n=1 gives a constant modulus $E'=E_o$, whereas for $n>1$, E' will be a function of the strain.

The procedure of determining C* from the finite element solution is discussed in detail in section 9.1.

6.4 THE BOUNDARY INTEGRAL EQUATION (BOUNDARY ELEMENT) METHOD

6.4.1 INTRODUCTION

The Boundary Integral Equation (B.I.E.) or Boundary Element method is a powerful procedure for the solution of boundary value problems in many branches of engineering. In boundary methods, the primary results are the distributions of the variables on the boundary of the solution domain only. In the B.I.E. method, the partial differential equations, governing the physical process throughout the solution domain, are transformed into integral equations applied in the boundary alone. It is also called Boundary Element Method (B.E.M.) since only the boundary is discretized into elements.

The important feature of the B.I.E. method is that instead of attempting to find an approximate solution for the governing differential equation throughout the solution domain, as in domain (eg. F.E.) methods, the equation is converted into an integral form, often involving only integrals over the boundary of the domain. Consequently only the boundary has to be discretized in order to carry out integrations.

So the dimensionality of the problem is reduced by one. A three dimensional, volume problem, becomes a two dimensional one, while a two dimensional problem involves only one-dimensional line integrations. Because the interior of the solution domain is not discretized, there is much less approximation involved in representing the solution variables, and rapid variations of, for example stresses and displacements can be resolved very accurately.

The interior of the body is effectively modelled by superimposed fundamental solutions, each of which is an exact solution of the partial differential equations. It is therefore, to be expected that the B.I.E. method can model interior behaviour more effectively than domain methods, which involve both boundary and interior discretization and approximation. Having obtained all the boundary displacements and

tractions, it is a straight forward matter to calculate interior values at the desired point, although each calculation involves a summation of fundamental solutions associated with the boundary values. Numerical analysis with the B.I.E. method has shown that it possesses a higher degree of resolution of stresses and strains than the F.E. method, which may be attributed to the fact that no domain discretization is needed, and hence no further approximations in the behaviour of the body are introduced. This important feature has made the B.I.E. method a very attractive numerical tool for elastostatics, particularly linear elastic fracture mechanics.

When applied to non-linear problems, one of the advantages of the B.I.E. method is lost, in that some integration over the interior of the solution domain is necessary. Nevertheless, it is still not necessary to solve for values of, say, displacements and tractions at interior points. Also, internal integration is only required for non-linear regions of the domain, such as plastic regions in an elastic-plastic problem.

The B.I.E. method is not without its drawbacks. Although the coefficient matrix associated with the final set of equations is smaller than in the F.E. method, it is fully populated and non-symmetric. The method loses its appeal in problems with large surface-to-volume ratio or where the displacements or stresses at many interior points are required.

As with domain methods, B.I.E. treatments of non-linear analysis generally require repeated analyses to arrive at the required solutions.

6.4.2. MATHEMATICAL ANALYSIS

(a) ELASTIC ANALYSIS.

For a homogeneous, isotropic two dimensional body the governing differential equations for linear elasticity are the equilibrium equations:

$$\sigma_{ij,j} + f_i = 0 \qquad (6.21a)$$

The kinematic equations, for small strains and displacements, are:

$$\varepsilon_{ij} = \frac{1}{2}(u_{i,j} + u_{j,i}) \qquad (6.21b)$$

and the constitutive equations (generalized Hooke's law)

$$\sigma_{ij} = 2\mu\varepsilon_{ij} + \delta_{ij}\frac{2\mu\nu^*}{1-2\nu^*}\varepsilon_{kk} \qquad (6.22)$$

where i, j, k take the range 1, 2 and

$$\nu^* = \nu \qquad \text{in plane stress}$$

$$\nu^* = \frac{\nu}{1+\nu} \qquad \text{in plane strain} \qquad (6.22a)$$

u_i is the displacement vector, f_i represents the body force vector, and μ is the shear modulus given by:

$$\mu = \frac{E}{2(1+\nu)} \qquad (6.23)$$

The above equations can be combined to yield the Navier equations for the displacement:

$$u_{i,jj} + \frac{1}{1-2\nu^*}u_{j,ji} = -\frac{f_i}{\mu} \qquad (6.24)$$

In all subsequent analysis relating to two dimensional problems the (*) will dropped and the effective Poisson's ratio as defined by (6.22a) will be employed.

By utilising Helmholtz's theorem, which states that a vector field can be written in terms of its scalar and vector potentials, it can be derived (see Lee (1983)), that

the particular solution to the equivalent of Kelvin's problem in two dimensions is:

$$U_{ij}(p,q) = -\frac{1}{8\pi(1-\nu)\mu}\{\delta_{ij}(3-4\nu)\ln r - r_{,i}r_{,j}\} \qquad (6.24a)$$

$$T_{ij}(p,Q) = -\frac{1-2\nu}{4\pi(1-\nu)}\frac{1}{r}\{(\delta_{ij}+\frac{2}{1-2\nu}r_{,i}r_{,j})\frac{\partial r}{\partial n} - r_{,i}n_j + r_{,j}n_i\} \qquad (6.24b)$$

where U_{ij} and T_{ij} are the second order displacement and traction vectors in the j direction at the field point Q or q due to an orthogonal unit load at the variable point p in the i direction, r is the distance between the variable and field points, and n_i is the component in the i direction of the unit normal at Q.

Betti's reciprocal theorem in two dimensions for a domain S with boundary s is given by :

$$\int_s t_i^* u_i \, ds + \int_S f_i^* u_i \, dS = \int_s t_i u_i^* \, ds + \int_S f_i u_i^* \, dS \qquad (6.25)$$

By utilizing Kelvin's point load solution as the starred field, and by remembering to exclude a small circle of radius η with boundary $s_\eta(p)$ and area $S_\eta(p)$ centred at point p (see figure 6.4), due to the singular nature of the solution, Kelvin's fundamental solution in the above theorem yields:

$$\int_{s+s_\eta(p)} T_{ij}(p,Q)\,u_j(Q)\,ds_Q = \int_{s+s_\eta(p)} U_{ij}(p,Q)\,t_j(Q)\,ds_Q + \int_{S-S_\eta(p)} U_{ij}(p,q)\,f_j(Q)\,dS_q \qquad (6.26)$$

Note that the upper and lower case letters of the variable point, p, and the field point, q, refer to points on the boundary and the interior, respectively.

Taking the above equation to a limit as η approaches zero results in an integral equation, known as Somigliana's identity which relates the displacements at an interior point, p to the displacements and tractions on the boundary (see Lee (1983)).

$$u_i(p) = -\int_S T_{ij}(p,Q)\,u_j(Q)\,ds_Q + \int_S U_{ij}(p,Q)\,t_j(Q)\,ds_Q + \int_S U_{ij}(p,q)\,f_j(q)\,dS_q \qquad (6.27)$$

As p approaches the boundary point P, the integrals need to be determined in the limit over the main boundary of the body and that part of the boundary of a small circular region of radius η with boundary $s_\eta(P)$ and area $S_\eta(P)$ centred at the point P which is not contained inside the domain of the body (see figure 6.5)

$$u_i(P) = -\int_{s+s_\eta(p)} T_{ij}(P,Q)\,u_j(Q)\,ds_Q + \int_{s+s_\eta(p)} U_{ij}(P,Q)\,t_j(Q)\,ds_Q + \int_{S+S_\eta(P)} U_{ij}(P,q)\,f_j(q)\,dS_q \qquad (6.28)$$

Finally, in the limit, the boundary integral equation is obtained as (see Remzi (1981)).

$$C_{ij}(P)\,u_j(P) = -\int_S T_{ij}(P,Q)\,u_j(Q)\,ds_Q + \int_S U_{ij}(P,Q)\,t_j(Q)\,ds_Q + \int_S U_{ij}(P,q)\,f_j(q)\,dS_q \qquad (6.29)$$

where

$$C_{ij}(P) = \delta_{ij} + \lim_{\eta\to 0} \int_{s_\eta(P)} T_{ij}(P,Q)\,ds_Q \qquad (6.30)$$

When P possesses a unique tangent, it can be shown that

$$\lim_{\eta\to 0} \int_{s_\eta(P)} T_{ij}(P,Q)\,ds_Q = -\frac{1}{2}\delta_{ij} \qquad (6.31)$$

Also the stresses and strains at the interior points are given by:

$$\sigma_{ij}(p) = -\int_S S_{kij}(p,Q)\,u_k(Q)\,ds_Q + \int_S D_{kij}(p,Q)\,t_k(Q)\,ds_Q + \int_S D_{kij}(p,q)\,f_k(q)\,dS_q \qquad (6.32)$$

where the third order tensors $D_{kij}(p,Q)$ and $S_{kij}(p,Q)$ are given by:

$$D_{kij}(p,Q) = \frac{1}{4\pi(1-\nu)}\frac{1}{r}\{(1-2\nu)(\delta_{jk}r_{,i} + \delta_{ik}r_{,j} - \delta_{ij}r_{,k}) + 2r_{,i}r_{,j}r_{,k}\} \qquad (6.33)$$

and

$$S_{kij}(p,Q) = \frac{\mu}{2\pi(1-\nu)}\frac{1}{r^2}\{2[\nu(\delta_{jk}r_{,i} + \delta_{ik}r_{,j}) + (1-2\nu)\delta_{ij}r_{,k} - 4r_{,i}r_{,j}r_{,k}]\frac{\partial r}{\partial n} + [(1-2\nu)\delta_{jk} + 2\nu\, r_{,j}r_{,k}]n_i + [(1-2\nu)\delta_{ik} + 2\nu\, r_{,i}r_{,k}]n_j - [(1-4\nu)\delta_{ij} - 2(1-2\nu)r_{,i}r_{,j}]n_k\}$$

The stresses at the boundary can then be derived from the limiting form of equation (6.32) as p is taken to the boundary point P or, alternatively, from the local tractions and displacement gradient in the tangential direction (see Lee (1983)).

(b) ELASTO-PLASTIC ANALYSIS

Consider a two dimentional homogeneous, isotropic body undergoing time-independent plastic deformation. The elastic stress-strain equations, the total strain-displacement relations and the equations of equilibrium then apply in rate form.

$$\dot{\sigma}_{ij,j} + \dot{f}_i = 0 \qquad (6.35)$$

$$\dot{\varepsilon}_{ij} = \frac{1}{2}(\dot{u}_{i,j} + \dot{u}_{j,i}) \qquad (6.36)$$

$$\dot{\sigma}_{ij} = 2\mu\dot{\varepsilon}^e_{ij} + \delta_{ij}\frac{2\mu\nu}{1-2\nu}\dot{\varepsilon}^e_{k\,k} + \delta_{ij}\frac{2\mu\nu}{1-2\nu}\dot{\varepsilon}^p_{kk} \qquad (6.37)$$

for plane strain, and

$$\dot{\sigma}_{ij} = 2\mu \dot{\varepsilon}^{e}_{ij} + \delta_{ij} \frac{2\mu\nu}{1-2\nu} \dot{\varepsilon}^{e}_{k\,k} \qquad (6.38)$$

for plane stress, where the effective value of the Poisson's ratio as defined in (6.22a) has to be used. The stress rates are also given by:

$$\dot{\sigma}_{ij} = 2\mu \dot{\varepsilon}_{ij} + \delta_{ij} \frac{2\mu\nu}{1-2\nu} \dot{\varepsilon}_{kk} - 2\mu \dot{\varepsilon}^{p}_{ij} \qquad (6.39)$$

for plane strain and

$$\dot{\sigma}_{ij} = 2\mu \dot{\varepsilon}_{ij} + \delta_{ij} \frac{2\mu\nu}{1-2\nu} \dot{\varepsilon}_{kk} - 2\mu \dot{\varepsilon}^{p}_{ij} - \delta_{ij} \frac{2\mu\nu}{1-2\nu} \dot{\varepsilon}^{p}_{kk} \qquad (6.40)$$

for plane stress.

The above equations can be combined to yield the Navier equations for the displacement rates.

$$\dot{u}_{i,jj} + \frac{1}{1-2\nu} \dot{u}_{j,ji} = -\frac{\dot{f}_i}{\mu} + 2\dot{\varepsilon}^{p}_{ij,j} \qquad (6.41)$$

for plane strain and

$$\dot{u}_{i,jj} + \frac{1}{1-2\nu} \dot{u}_{j,ji} = -\frac{\dot{f}_i}{\mu} + 2\dot{\varepsilon}^{p}_{ij,j} + \frac{2\nu}{1-2\nu} \dot{\varepsilon}^{p}_{jj,i} \qquad (6.42)$$

for plane stress. Where $\dot{\varepsilon}^{e}_{ij}$, and, $\dot{\varepsilon}^{p}_{ij}$, are the elastic and plastic components of the total strain rate

$$\dot{\varepsilon}_{ij} = \dot{\varepsilon}^{e}_{ij} + \dot{\varepsilon}^{p}_{ij} \qquad (6.43)$$

The plastic strain rate for a material obeying the Von Mises yield criterion is:

$$\dot{\varepsilon}^{p}_{ij} = \frac{9}{4} \frac{S_{ij} S_{kl} \dot{\sigma}_{kl}}{H \sigma^{2}_{eq}} \qquad (6.44)$$

$$\dot{\varepsilon}^{p}_{ij} = \frac{3}{2} \frac{S_{ij} S_{kl} \dot{\varepsilon}_{kl}}{\{1 + (H/3\mu)\} \sigma^{2}_{eq}} \qquad (6.45)$$

where S_{ij} is the deviatoric stress tensor, $\dot{\sigma}_{kl}$ is the stress rate tensor, σ_{eq} is the equivalent stress, $\dot{\varepsilon}_{ij}$ is the total stain rate, and H is the plastic modulus.

The effect of plastic flow can be treated by modifying the techniques used in linear elastostatics. There are three different ways of dealing with the plastic terms in the Navier rate equations. One way is to treat derivatives of the plastic strain rates as a kind of body force. The underlying aim is to enable the Navier rate equations to be expressed in a form which bears some resemblance to the elastostatic equations. Alternatively, the plastic strain rates may be considered as initial strain rates, so that by invoking Betti's reciprocal theorem and modifying it to include the plastic work terms, the plastic work terms, the pseudoboundary integral equation for the initial strain approach is obtained for plane strain and plane stress (see Lee (1983))

$$C_{ki}(P)\dot{u}_i(P) = -\int_S T_{ki}(P,Q)\,\dot{u}_i(Q)\,ds_Q$$

$$+\int_S U_{ki}(P,Q)\,\dot{t}_i(q)\,ds_Q + \int_S U_{ki}(P,q)\,\dot{f}_i(q)\,dS_q$$

$$+\int_S \{\Sigma_{kij}(P,q) + \bar{\Sigma}_{kij}(P,q)\}\,\dot{\varepsilon}^p_{ij}(q)\,dS_q \qquad (6.46)$$

Here $\dot{t}_i$ is the traction rate, U_{ij} and T_{ij} are the second order displacements and traction tensors in the j direction at the field point Q or q due to an orthogonal unit load at the variable point P or p in the i direction . As before capital letters are used to indicate that the point concerned lies on the boundary s. Σ_{kij} denotes the third order tensor for the stress at the field point due to an orthogonal unit load at the variable point in the k direction. These tensors can be derived from the fundamental solution to Kelvin's problem in two dimensions. U_{ij} and T_{ij} are given by (6.24a) and (6.24b), and

$$\Sigma_{kij}(p,q) = -\frac{1}{4\pi(1-\nu)}\frac{1}{r}\{(1-2\nu)$$

$$(\delta_{jk}r_{,i} + \delta_{ik}r_{,j} - \delta_{ij}r_{,k}) + 2r_{,i}r_{,j}r_{,k}\} \qquad (6.47)$$

The free term tensor C_{ij} is given by (6.30) and the auxiliary tensor, $\bar{\Sigma}_{kij}$ (from plastic

strain terms in the out of plane direction), is given by

$$\bar{\Sigma}_{kij}(p,q) = \frac{\nu}{2\pi(1-\nu)}\,\delta_{ij}\,\frac{r,_k}{r} \qquad (6.48)$$

for plane strain and is zero for plane stress. The integral expression of the total strain rates at an interior point can be derived by differentiating the corresponding identity for the displacement rate. The singularity of Σ_{kij} and $\bar{\Sigma}_{kij}$ is of order one less than the dimensionality of the problem, so, convected differentiation of the related domain integral has to be employed (see Lee (1983)). Thus

$$\begin{aligned}\dot{\varepsilon}_{kh} = &-\int_S S_{ikh}(p,Q)\,\dot{u}_i(Q)\,ds_Q + \int_S D_{ikh}(p,Q)\,\dot{t}_i(Q)\,ds_Q \\ &+ \int_S D_{ikh}(p,q)\,\dot{f}_i(q)\,ds_q \\ &+ \int_S \{\Sigma_{ijkh}(p,q) + \bar{\Sigma}_{ijkh}(p,q)\}\,\dot{\varepsilon}^p_{ij}(q)\,ds_q \\ &+ k_1\,\dot{\varepsilon}^p_{kh}(p) + k_2\,\delta_{kh}\,\dot{\varepsilon}^p_{mm}(p)\end{aligned} \qquad (6.49)$$

where

$$D_{kij}(p,Q) = \frac{1}{8\pi(1-\nu)\mu}\,\frac{1}{r}\,\{(1-2\nu)(\delta_{jk}\,r,_i + \delta_{ik}\,r,_j - \delta_{ij}\,r,_k) + 2\,r,_i\,r,_j\,r,_k\} \qquad (6.50)$$

$$\begin{aligned}S_{kij}(p,Q) = &\frac{1}{4\pi(1-\nu)}\,\frac{1}{r^2}\,\{2[\nu(\delta_{jk}\,r,_i + \delta_{ik}\,r,_j) + \delta_{ij}\,r,_k - 4\,r,_i\,r,_j\,r,_k]\frac{\partial r}{\partial n} + [(1-2\nu)\,\delta_{jk} + 2\nu\,r,_j\,r,_k]\,n_i \\ &+ [(1-2\nu)\,\delta_{ik} + 2\nu\,r,_i\,r,_k]\,n_j - [(1-2\nu)(\delta_{ij} - 2\,r,_i\,r,_j]\,n_k\}\end{aligned} \qquad (6.51)$$

$$\Sigma_{ijkh}(p,q) = -\frac{1}{4\pi(1-\nu)}\frac{1}{r^2}\{2(1-2\nu)\delta_{ij}r,_k r,_h + 2\delta_{kh}r,_i r,_j$$

$$-8r,_i r,_j r,_k r,_h + 2\nu[\delta_{jh}r,_i r,_k + \delta_{jk}r,_i r,_h$$

$$+\delta_{ih}r,_j r,_k + \delta_{ik}r,_j r,_h]$$

$$+(1-2\nu)(\delta_{jk}\delta_{ih} + \delta_{ik}\delta_{jh} - \delta_{ij}\delta_{kh})\} \qquad (6.52)$$

$$\bar{\Sigma}_{ijkh}(p,q) = -\frac{\nu}{4\pi(1-\nu)}\frac{1}{r^2}\delta_{ij}(\delta_{kh} - 2r,_k r,_h) \qquad (6.53)$$

for plane strain and is zero for plane stress.

$$k_1 = \frac{3-4\nu}{4(1-\nu)} \qquad (6.54)$$

$$k_2 = -\frac{1}{8(1-\nu)} \quad \text{for plane strain} \quad k_2 = -\frac{1-4\nu}{8(1-\nu)} \quad \text{for plane stress} \qquad (6.55)$$

Similar expressions for the stress rates at interior points can be obtained by substituting (6.49) into the stress-strain relations

Another approach, although not considered here, consists of expressing the plastic strains rates in terms of the initial stress rates, instead of utilizing initial or plastic strain rates (see for example Lee (1983)).

6.5 NUMERICAL ESTIMATES OF C*

Goldman and Hutchinson (1975) and Shih and Hutchinson (1976) shown that for a non-linear incompressible or fully plastic material characterized by the uniaxial law :

$$\frac{\varepsilon}{\varepsilon_0} = \left[\frac{\sigma}{\sigma_0}\right]^N \qquad (6.56)$$

the fracture parameters such as the J integral, the mouth opening displacement δ and the remote load point displacement due to the crack Δ, are scalable and the normalized quantities are functions of the crack length to specimen width ratio a/W and the strain hardening parameter N. By analogy in the steady state creep (secondary creep) regime described by

$$\frac{\dot{\varepsilon}}{\dot{\varepsilon}_0} = \left[\frac{\sigma}{\sigma_0}\right]^n \qquad (6.57)$$

the parameters C* mouth opening displacement rate $\dot{\delta}$ and load line displacement rate $\dot{\Delta}$, are also scalable and can be determined using the fully plastic solutions.

Kumar et. al. (1981) give fully plastic F.E. solutions of J, δ, and, Δ for a number of geometries, a/W and strain hardening parameter N in normalised form.

For the CT geometry, which was the geometry mainly used in this thesis, and by substituting N=n by analogy between creep and power law hardening behaviour Kumar et. al. give C* and $\dot{\Delta}$ as:

$$C^* = \sigma_0 \dot{\varepsilon}_0 \, c h_1(a/W, n) \left[\frac{P}{P_0}\right]^{n+1} \qquad (6.58)$$

$$\dot{\Delta} = \dot{\varepsilon}_0 \, a h_3(a/W) \left[\frac{P}{P_0}\right]^n \qquad (6.59)$$

where P is the load per unit thickness and c=W-a is the uncracked ligament. P_0 is the limit load per unit thickness and is given by

$$P_0 = 1.455 \, \eta \, c \, \sigma_0 \qquad \text{for plane stress} \qquad (6.60)$$

$$P_0 = 1.072 \, \eta \, c \, \sigma_0 \qquad \text{for plane strain} \qquad (6.61)$$

where η is defined as

$$\eta = \left[\left[\frac{2a}{c} \right]^2 + 2 \left[\frac{2a}{c} \right] + 2 \right]^{1/2} - \left[\frac{2a}{c} + 1 \right] \qquad (6.62)$$

h_1 and h_3 in (6.58) and (6.59) are functions of a/W and n alone. Thus knowing the steady state creep properties, the load P and the crack length a, C* and $\dot{\Delta}$, can easily be determined.

Values of h_1 and h_3, are tabulated by Kumar et. al. for a number of common specimen geometries, such as CCP, SEN, DEN e.t.c., both for plane stress and plane strain conditions. The calculated values of h_1 and h_3 for the compact tension specimen are presented in table 6.1 for both plane stress and plane strain conditions, and, for a/W= 0.25, 0.375, 0.500, 0.625, 0.750 and $\rightarrow$1 and for n = 1, 2, 3, 5, 7, 10, 13, 16 and 20. h_1 for plane stress and plane strain is shown as a function of a/W for various values of n in figures 6.6 and 6.7 respectively.

6.6 REFERENCE STRESS APPROACH FOR ESTIMATING C*

By writing

$$\sigma_r = \frac{P \sigma_o}{P_o} \qquad (6.63)$$

equation (6.58) may be written in terms of σ_r and the corresponding creep strain rate $\dot{\varepsilon}_r$ derived from (6.57) as

$$C^* = \sigma_r \dot{\varepsilon}_r c\, h_1 (a/W, n) \qquad (6.64)$$

Here σ_r is a normalizing stress and should not be confused with the reference stress, based on limit analysis, as the normalizing load P_o can be chosen for convenience when normalizing the F.E. results and need not be the limit load. In fact if a different normalizing load P'_o is chosen and the corresponding normalizing stress is $\sigma'_r = P\sigma_o / P'_o$ then (6.64) becomes.

$$C^* = \sigma'_r \dot{\varepsilon}'_r c\, h'_1 (a/W, n) \qquad (6.65)$$

where $$h'_1(a/W, n) = h_1(a/W, n)\,(P'_o/P_o)^{n+1} \qquad (6.66)$$

Ainsworth (1987) has shown that for any geometry and crack length (at least those for which the fully plastic or steady state creep solutions are known) it is possible to select a P'_o so that the variation of h'_1 with n is negligible, so that the approximation can be made

$$h'_1(a/W, n) = h'_1(a/W, n=1) \qquad (6.67)$$

Now n=1 in (6.57) is equivalent to an elastic solution if strain rate is replaced by strain and ε_o/σ_o is set equal to 1/E'. Correspondently (6.65) is a result for J which in the elastic limit is K^2/E'. Thus

$$\frac{K^2}{E'} = \sigma'_r \left[\frac{\sigma'_r}{E'}\right] h'_1(a/W, n=1)\,c \qquad (6.68)$$

Solving for h'_1 and substituting in (6.65)

$$C^* = \sigma'_r \dot{\varepsilon}'_r \left[\frac{K}{\sigma'_r}\right]^2 \qquad (6.69)$$

Ainsworth has shown that the particular choice of P'_o, which makes equation (6.67) a good approximation, is close to the limit load P_L. In addition P_L is lower than P'_o by about 5%. This means that the reference stress

$$\sigma_R = \frac{P\sigma_o}{P_L(\sigma_o)} \qquad (6.70)$$

is higher by about 5% than the normalizing stress in (6.69). Thus replacing the stress in equation (6.69) by the reference stress will lead to conservative estimates of C*, although the conservatism would not be great. The reference stress estimate of C* is then

$$C^* = \sigma_R \dot{\varepsilon}_R \left[\frac{K}{\sigma_R}\right]^2 \qquad (6.71)$$

$$\sigma_R = \frac{P\sigma_y}{P_L(\sigma_y)} \qquad (6.72)$$

Here σ_o has been replaced by σ_y, the notation for yield stress. Of course the reference stress is independent of σ_y as the limit load P_L is directly proportional to σ_y.

Ainsworth has used (6.71) with success for a C - Mn weld metal.

The reference stress method has the advantage that it can be used for geometries, were the fully plastic solutions (or steady state creep solutions) are not known, so that expensive numerical solutions for determining C* can be avoided.

TABLE 6.1a

h_1 FOR THE PLANE STRESS COMPACT TENSION SPECIMEN

a / W	n = 1	n = 2	n = 3	n = 5	n = 7	n = 10	n = 13	n = 16	n = 20
0.250	1.609	1.464	1.284	1.060	0.903	0.729	0.601	0.511	0.395
0.375	1.552	1.249	1.047	0.801	0.647	0.484	0.377	0.284	0.220
0.500	1.398	1.084	0.901	0.686	0.558	0.436	0.356	0.298	0.238
0.625	1.274	1.031	0.875	0.695	0.593	0.494	0.423	0.370	0.310
0.750	1.234	0.977	0.833	0.683	0.598	0.506	0.431	0.373	0.314
$\rightarrow 1$	1.133	1.010	0.775	0.680	0.650	0.620	0.490	0.470	0.420

TABLE 6.1b

h_1 FOR THE PLANE STRAIN COMPACT TENSION SPECIMEN

a / W	n = 1	n = 2	n = 3	n = 5	n = 7	n = 10	n = 13	n = 16	n = 20
0.250	2.227	2.048	1.783	1.475	1.334	1.248	1.258	1.325	1.566
0.375	2.148	1.716	1.392	0.970	0.693	0.443	0.276	0.176	0.098
0.500	1.935	1.509	1.242	0.919	0.685	0.461	0.314	0.216	0.132
0.625	1.763	1.449	1.237	0.974	0.752	0.602	0.459	0.347	0.248
0.750	1.709	1.424	1.263	1.033	0.864	0.717	0.575	0.448	0.345
$\rightarrow 1$	1.568	1.450	1.350	1.180	1.080	0.950	0.850	0.730	0.630

TABLE 6.1c

h_3 FOR THE PLANE STRESS COMPACT TENSION SPECIMEN

a / W	n = 1	n = 2	n = 3	n = 5	n = 7	n = 10	n = 13	n = 16	n = 20
0.250	9.670	7.996	7.205	5.944	5.000	3.945	3.191	2.591	2.023
0.375	7.800	5.734	4.615	3.253	2.475	1.765	1.330	0.990	0.746
0.500	6.288	4.149	3.107	2.087	1.590	1.181	0.938	0.774	0.614
0.625	5.419	3.375	2.536	1.804	1.468	1.176	0.988	0.853	0.710
0.750	4.767	2.922	2.242	1.657	1.379	1.116	0.936	0.800	0.666
→ 1	4.231	2.829	1.930	1.524	1.387	1.274	0.985	0.933	0.824

TABLE 6.1d

h_3 FOR THE PLANE STRAIN COMPACT TENSION SPECIMEN

a / W	n = 1	n = 2	n = 3	n = 5	n = 7	n = 10	n = 13	n = 16	n = 20
0.250	9.852	8.506	8.170	7.774	7.706	7.942	8.517	9.371	10.887
0.375	7.944	5.760	4.643	3.103	2.139	1.292	0.793	0.494	0.266
0.500	6.406	4.268	3.157	2.024	1.413	0.888	0.585	0.393	0.236
0.625	5.521	3.431	2.583	1.787	1.373	1.000	0.746	0.568	0.368
0.750	4.857	3.048	2.456	1.807	1.450	1.114	0.869	0.686	0.514
→ 1	4.310	2.990	2.474	1.946	1.697	1.436	1.258	1.066	0.909

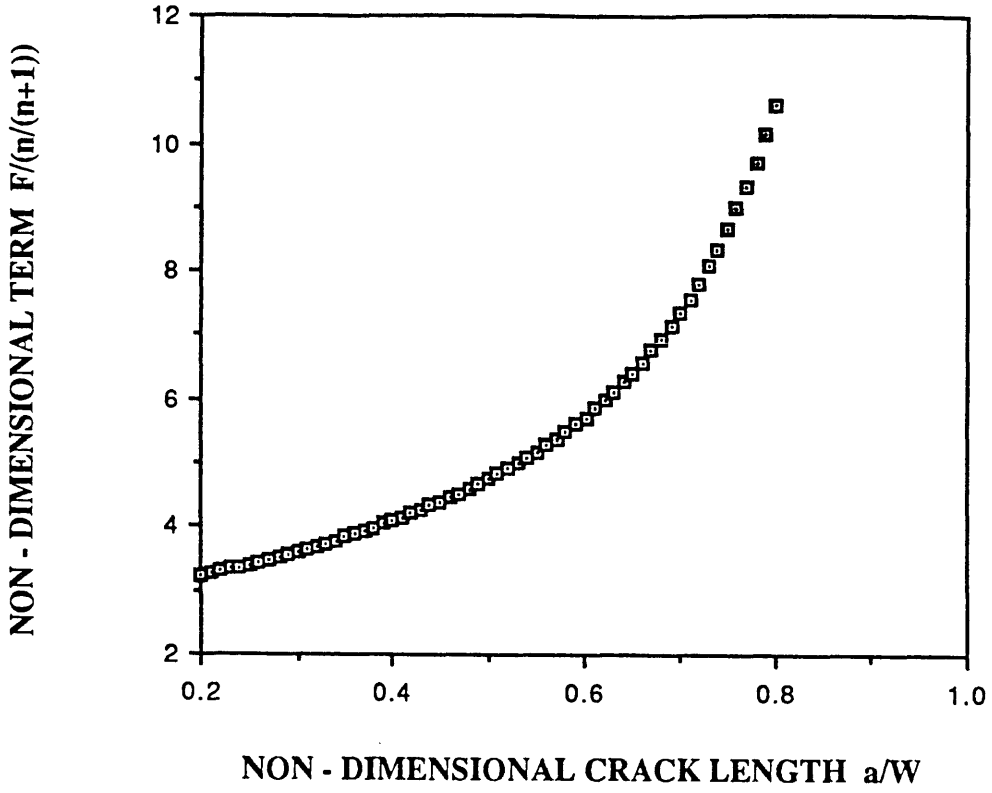


Figure 6.1 Collapse load solution for F/ (n / (n + 1)) for CT geometry.

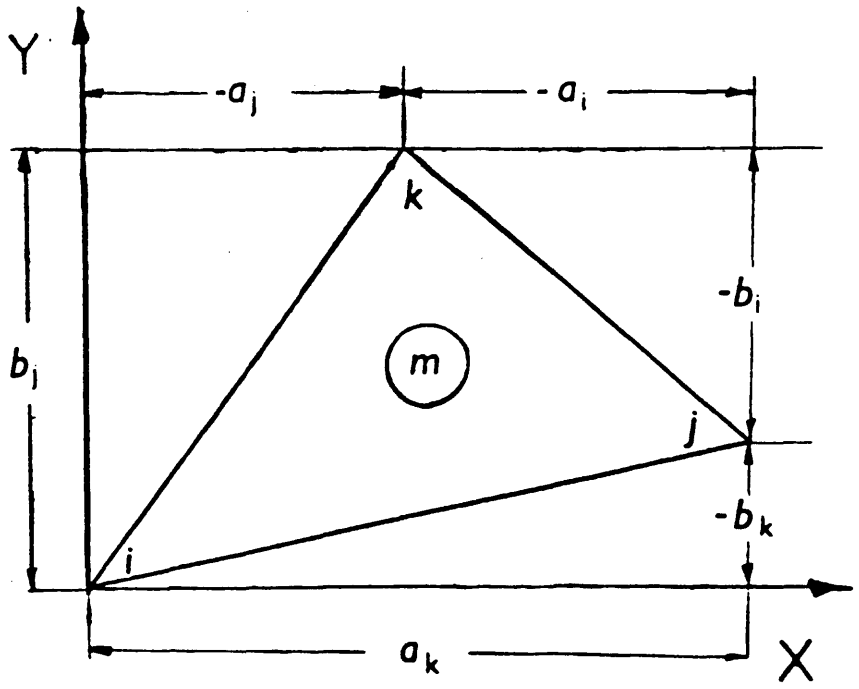


Figure 6.2 Angles and lengths of sides of a typical triangular element.

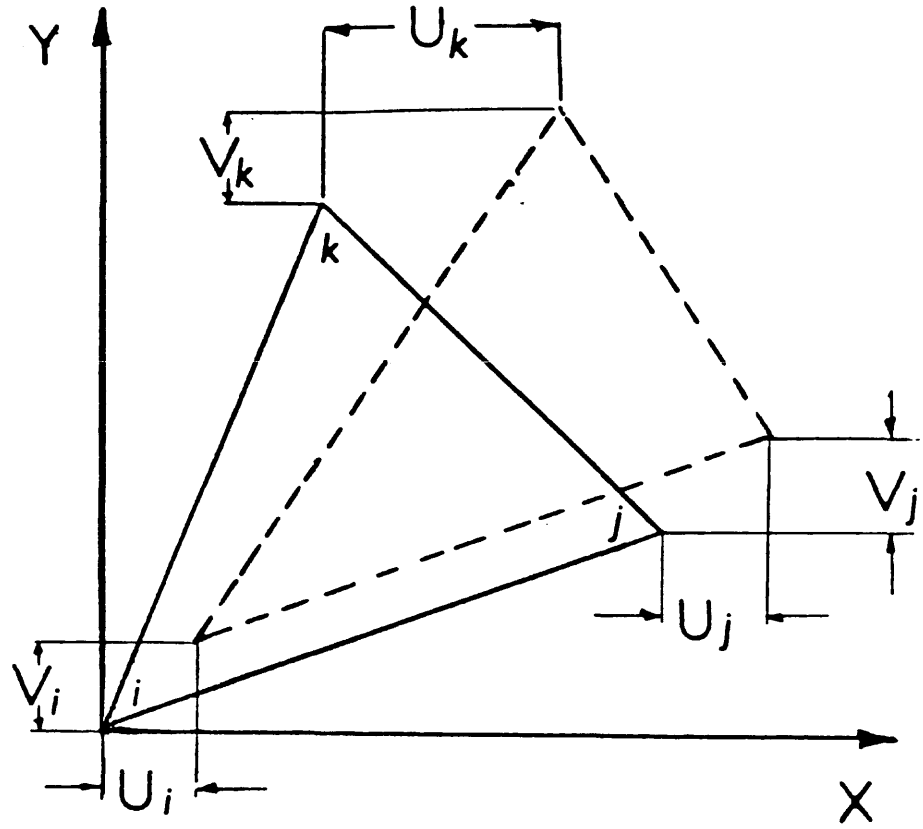


Figure 6.3 Displacements of a typical element.

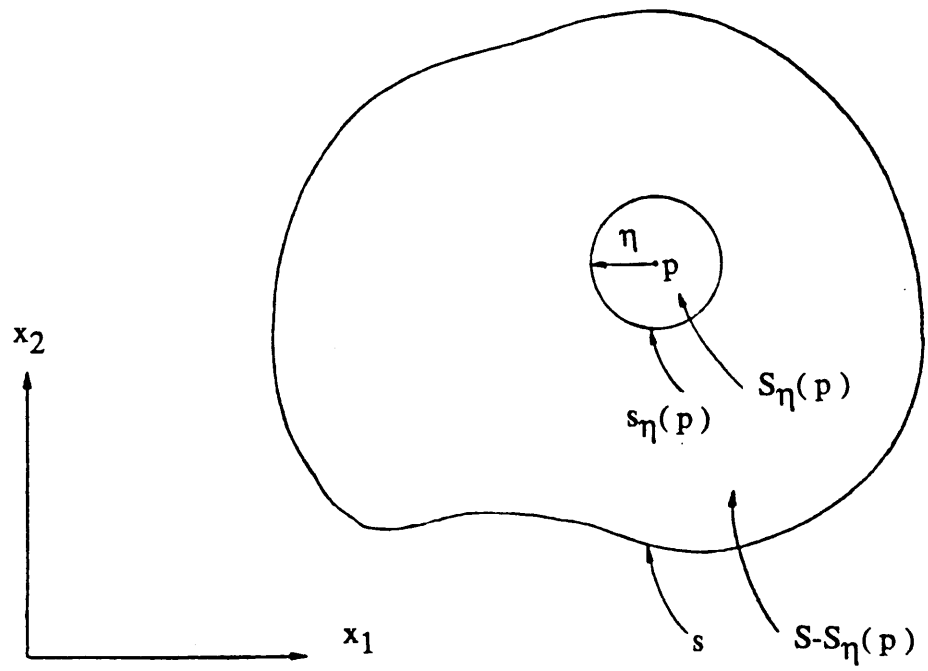


Figure 6.4 Exclusion of a small circular region of radius η from the domain S

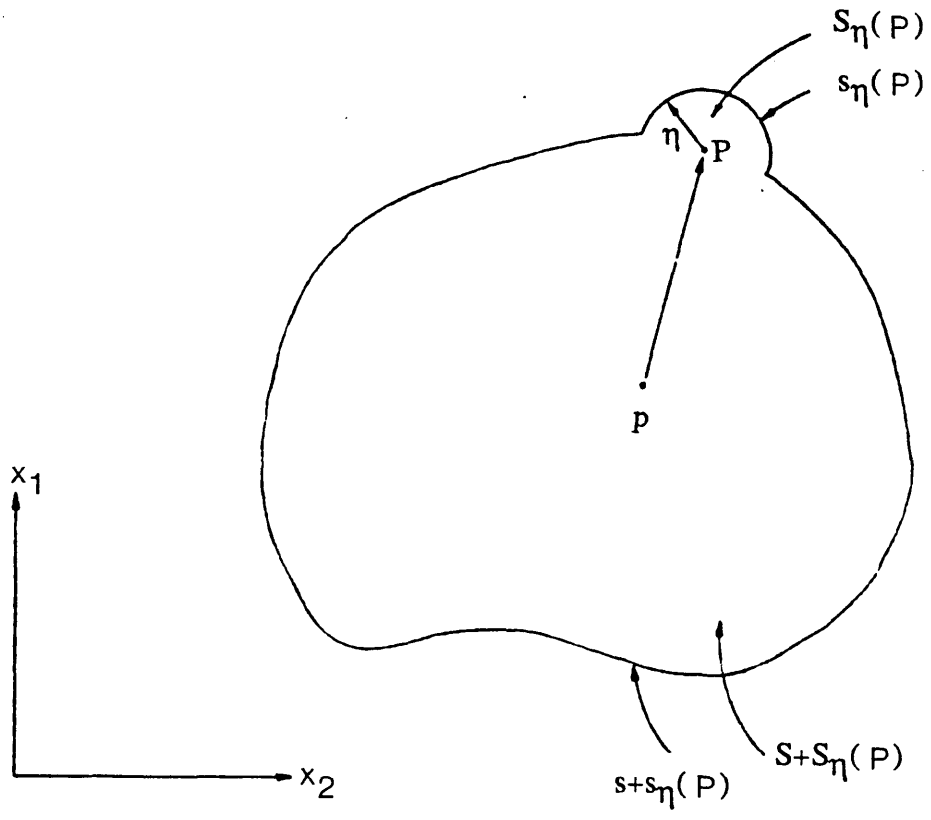


Figure 6.5 Taking the interior point p to the boundary point P.

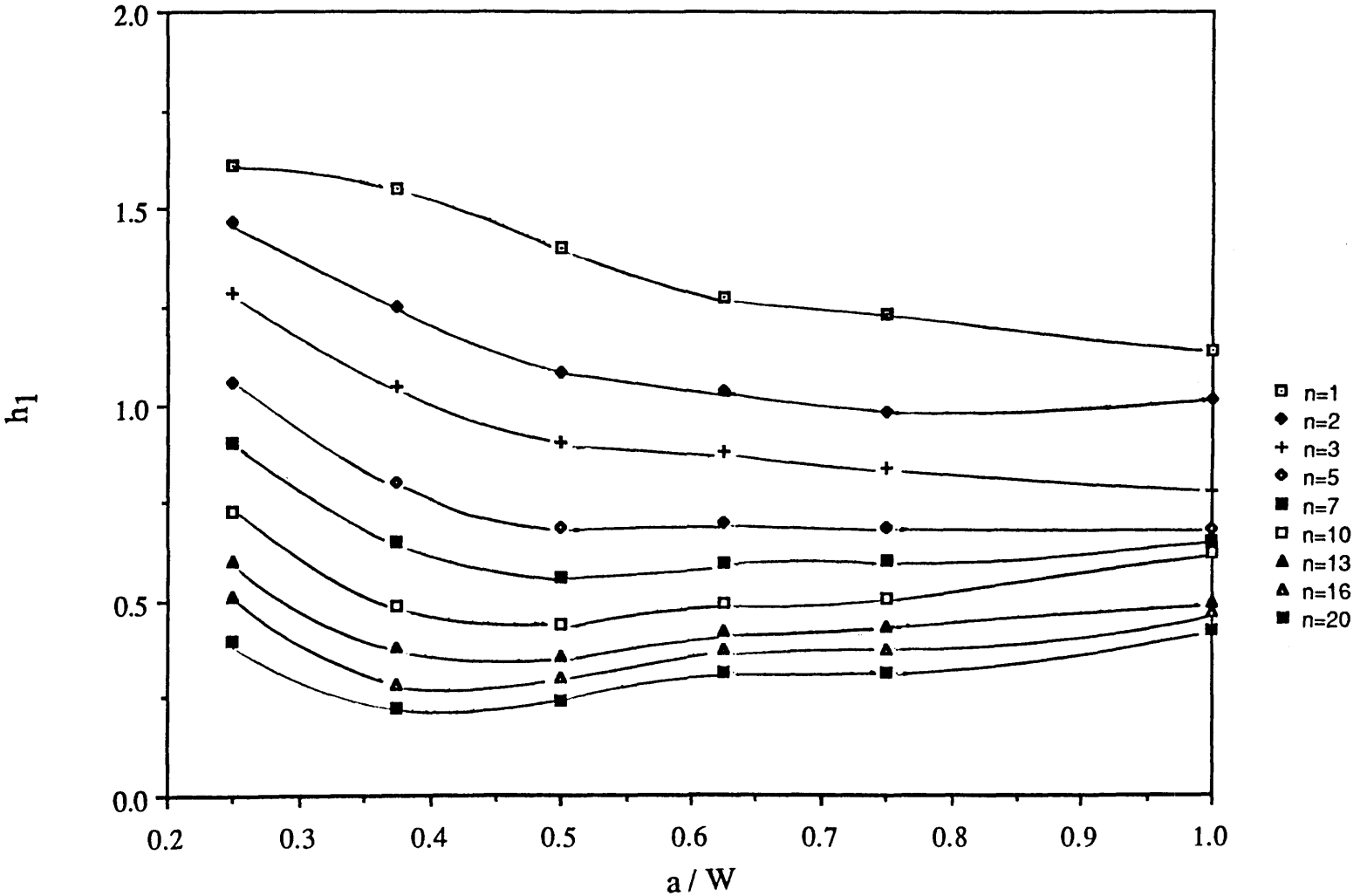


Figure 6.6 h_1 as a function of a / W for Plane Stress Compact Tension specimen

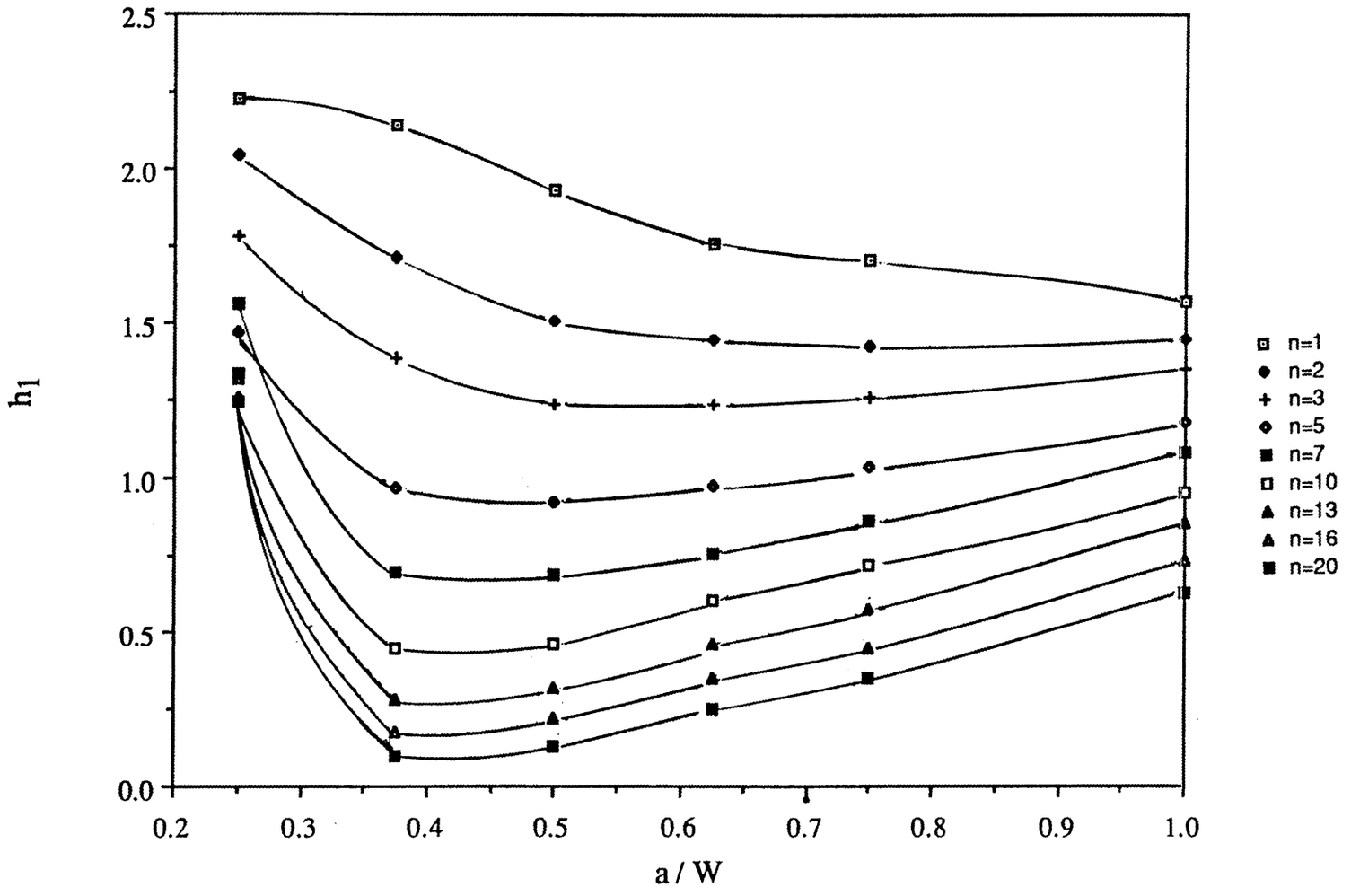


Figure 6.7 h_1 as a function of a / W for Plane Strain Compact Tension specimen

CHAPTER 7.

INFLUENCE OF FATIGUE

7.1 FATIGUE AS A MICROSTRUCTURAL PHENOMENON

7.1.1 INTRODUCTION

Fatigue is the progressive localised permanent structural change that occurs in a material subjected to repeated or fluctuating loads at stresses having a maximum value less than the tensile strength of the material. Fatigue may result in cracks or fracture after a sufficient number of fluctuations.

Fatigue fractures are caused by the simultaneous action of cyclic stress, tensile stress and plastic strain. If any one of these three is not present, fatigue cracking will not initiate and propagate. The cyclic stress starts the crack; the tensile stress propagates it. Compressive stress will not cause fatigue.

The process of fatigue may be considered as consisting of three stages (see figure 7.1).

(1) Initiation fatigue damage leading to crack initiation (stage 1).

(2) Crack propagation until the remaining uncracked ligament becomes too weak to carry the loads imposed (stage 2).

(3) Final, sudden fracture of the remaining ligament (stage 3).

The three progressive stages of fatigue fracture are shown in figure 7.1 as a relationship between the crack growth per cycle da/dN, and the stress intensity range $\Delta K=K_{max}-K_{min}$.

In stage 1 crack growth cracks are initiated by localised slip. This process is shear-stress controlled so that cracking occurs on planes at about 45° to the axis of principal normal stress. A crack, once initiated, may continue to grow, presumably by slip processes, on planes of high shear stress for a substantial life fraction. In this stage there are large effects of the microstructure, mean stress and environment.

Increasing the crack growth rate, the micro crack growth of stage 1 changes to

macro crack growth of stage 2, represented by the linear portion of growth rate curve in figure 7.1. During this stage for specimens undergoing tension-tension loading cycles, cracks propagate by plastic blunting of the crack tip during the part of the cycle that the load is increased and resharpening of the crack during the part of the cycle where the load is decreasing. This repetitive combination of blunting and resharpening processes causes the formation of transgranular ductile striations on the fractured surfaces. This mechanism was studied in great detail by Laird (1967) and it is illustrated in figure 7.2. Each load excursion is responsible for each striation and the striation spacing is influenced by both the maximum value and the range of values of the applied load and is consequently a function of both the maximum value and the range of values of the stress intensity factor. Generally ductile striation formation becomes more pronounced and the striation spacing increases with increasing ΔK level. In this region the influence of microstructure, mean stress, material thickness and environment, is not significant. (Suresh et. al. (1981)).

At higher growth rates, where K_{max} approaches K_C, static or monotonic fracture modes such as cleavage cracking, intergranular separation and fibrous fracture occur in addition to striation growth, resulting in a marked sensitivity of propagation rates to both micro-structure and mean stress. This mode of failure is represented by stage 3 on figure 7.1.

7.1.2 FRACTURE MECHANICS APPROACH TO FATIGUE CRACK GROWTH

Since fatigue crack extension would occur in the highly stressed region at the crack tip, it is reasonable to assume that for an elastic material, the intensity of crack tip stress field as represented by K is one of the factors that will control the rate of crack extension. Other factors may be the loading frequency, environmental conditions, temperature and mean stress.

Extensive work has been carried out on fatigue crack growth in the past years

both analytically and experimentally, and various continuum mechanics models for fatigue crack growth have been proposed (Forman et. al (1967), Walker (1970), Williams (1977)).

For the stage 2 cracking, which is the region of interest in this thesis, most studies confirmed that the fatigue crack growth rate da/dN is primarily controlled by the stress intensity range ΔK through the well known Paris equation (Paris and Erdogan (1963))

$$\frac{da}{dN} = C \Delta K^m \qquad (7.1)$$

where m is a material dependent constant usually between 2 and 4 when cycling is taking place at room temperature, and the proportionality factor C being sensitive to the minimum to maximum load ratio R (Elber (1971), Schijve (1979)). An increase in R usually produces an increase in da/dN.

7.1.3. CRACK CLOSURE IN FATIGUE CRACK GROWTH.

Crack closure was first popularized by Elber (1971) and it was considered to arise from the fact that during fatigue crack growth, material is plastically strained at the crack tip, and due to the restraint of surrounding elastic material on the residual stretch, some closure at the crack tip occurs at positive loads during the fatigue cycle. This concept is termed as plasticity induced crack closure and has proved to be extremely effective in explaining many aspects of fatigue crack propagation behaviour including the influence of R ratio (Elber (1971).

Other mechanisms of crack closure that they have been proposed, are based on the role of crack flank corrosion deposits (Ritchie et. al. (1980), Stewart (1980) and Suresh et. al. (1981), and fracture surface roughness (Suresh et. al. (1981)). A schematic illustration of the mechanisms of fatigue closure is shown in figure 7.3.

The first of these mechanisms is so called oxide-induced crack closure. It arises from the fact that when oxide deposits, formed on freshly exposed surfaces at the

crack tip due to environmental conditions, reach a thickness comparable to crack tip opening displacements, the crack can become effectively wedged-closed at stress intensities above K_{min}.

The second mechanism, termed roughness-induced crack closure, arises in situations where the size-scale of the surface roughness is comparable to crack tip opening displacements.

An effective stress intensity range may be defined as:

$$\Delta K_{eff} = K_{max} - K_{cl} \qquad (7.2)$$

where K_{cl} is the stress intensity where the crack closes.

In high temperatures both oxide-induced crack closure and roughness-induced crack closure will be enhanced, so that ΔK_{eff} will be a fraction of ΔK, with this fraction becoming smaller as K_{min} decreases or as R decreases.

7.2 CREEP - FATIGUE INTERACTION

7.2.1 INTRODUCTION.

Fatigue crack growth at elevated temperatures is a complicated problem since widespread creep, in addition to elastic deformation can accompany crack extension, and since the micromechanisms of crack growth comprise grain boundary cavitation, the striation mechanism and corrosive effects. At room temperature the micromechanism by which a fatigue crack advances, is usually the striation mechanism, which results from the irreversible cyclic opening and closing of the crack tip. At elevated temperatures, fatigue may depend on the number of cycles as well, as on the loading frequency (Winstone et. al. (1985), Dimopulos et. al. (1986)). Since considerable creep deformation, often accompanies crack extension, the stress intensity factor will not always correlate the crack growth rates.

A great variety of micromechanisms has been reported to be responsible for crack extension under high temperature fatigue conditions, with the most common ones,

the striation mechanism at high loading frequencies and intergranular creep growth at low frequencies (Dimopulos et. al. (1986), Ellison and Harper (1978), Sadananda and Shahinian (1981), Winstone et. al. (1985), Smith (1983)).

Since elevated-temperature fatigue testing is rather time consuming and expensive, estimates of the performance of a specific material of engineering interest are very useful.

7.2.2 TEMPERATURE EFFECTS

At a given applied stress, an increase in temperature reduces the number of cycles to failure. Often the reduction in failure life, is accompanied by a transition from transgranular to intergranular cracking (Wells et. al. (1971)). The mechanical strength, including the fatigue strength, of materials usually decline with an increasing temperature.

7.2.3 ENVIRONMENTAL EFFECTS

Air may have a pronounced influence on fatigue even at room temperature. At elevated temperatures the environmental effects are more significant with oxidation being a main concern. When the frequency is lowered there is more time not only for creep but also for oxidation or other surface reactions.

Although there is still an argument about whether the environmental effects or creep effects, decisively influence the fatigue crack growth at elevated temperatures, it is believed that both of them can strongly effect crack growth in appropriate circumstances. Both the environmental and creep effects are time dependent, and is difficult to distinguish between them, in the actual performance of a machine component.

Strain enhanced oxide formation near the crack tip can have an advantageous or deleterious effect on crack propagation. Vacuum rewelding upon crack closure, oxide bridging and oxide filling preventing compression resharpening may decrease the crack growth rate. Oxide wedging at the crack tip, and oxide formation and subsequent

rupturing may increase the crack growth rate (Suresh and Ritchie (1982), Suresh et. al. (1981)).

7.3 FREQUENCY AND WAVEFORM EFFECTS

7.3.1 INTRODUCTION.

Crack tip stress and strain fields and crack growth under creep-fatigue have been extensively studied by Riedel (1983). Under steady load conditions the characteristic time :

$$t_1 = \frac{G}{(n+1)C^*}$$

characterizes the transition from short time K controlled to the long time C* controlled limit. Corresponding Riedel (1983) proposes a characteristic frequency

$$\omega_1 \approx 1 / t_1 \qquad (7.3)$$

to distinguish between slow cyclic where C* will be applicable and fast cyclic where ΔK will be applicable. It must be stressed here that ω_1 characterizes the transition from creep dominated to elastically dominated overall specimen behaviour, and it has nothing to do with the transition from the cavitation to the striation mechanism which will, in general occur at another characteristic frequency.

The types of cycle that have been considered are, slow cyclic without rapid load variations, slow cyclic with rapid load variations, rapid balanced cycling, and, rapid unbalanced cycling (figures 7.4, 7.5, 7.6)

7.3.2 SLOW CYCLING WITHOUT RAPID LOAD VARIATIONS.

This type of cycle is schematically shown in figure 7.4. When the cycle rise time, t_r, is much greater than the characteristic time, t_1, the crack tip stress and strain fields and the crack growth behaviour are governed by C*.

For tension - tension type loading no crack growth by the striation mechanism

would be predicted since then no cyclic opening and closing of the crack tip occurs in the limit of slow cycling. In this limiting case, crack growth is purely time-controlled, rather than cycle-controlled. If the load varies cyclically in time such that $C^* = C^*_{max} f(\omega t)$, then the following expression for the crack growth rate is valid :

$$\frac{da}{dN} \propto \frac{C^{*\,n/(n+1)}_{max}}{\omega} \int_0^{2\pi} \left[f(\tau) \right]^{n/(n+1)} d\tau \qquad (7.4)$$

7.3.3 SLOW CYCLING WITH RAPID LOAD VARIATIONS.

This type of cycle is schematically shown in figure 7.5. When the cycle rise time $t_r << t_1$, which may occur in square or trapezoidal loading waveforms, the near crack tip stress field will exhibit a peak at the end of the rise time.

The magnitude of the stress peak is a function of ΔK and the rate of loading. If the load is kept constant long enough after the load step, the specimen arrives at a steady state of extensive creep, so that C* governs the long term behaviour.

For loading in proportion to a power β of the time ($P \propto t^{\beta}$), the characteristic time t_1 for the transition from the short to long time limit is given by:

$$t_1 = \frac{1 + 2\beta n}{n + 1} \frac{G}{C^*} \qquad (7.5)$$

For step loading, β=0, the above expression reduces to the Riedel and Rice (1980), transition time (equation 5.27).

At low applied stress levels, the peaks in the crack tip stress field may significantly enhance cavity nucleation thereby accelerating the crack growth rate markedly compared with sustained loading.

Also rapid opening of the crack tip during stress peaks may rupture stable oxide layer which cover the crack tip, allowing the environment to react more easily with the metal and cause an acceleration in crack growth rates.

7.3.4. RAPID BALANCED CYCLING.

This type of cycle is schematically shown in figure 7.6. For balanced cycling no creep strain is accumulated over long times in a proportional stress field. Under this conditions the near tip HRR field must have the form.

$$\sigma_{ij} = s(\omega t)\left[\frac{\Delta K^2 \omega (1-\nu^2)}{I_n E C r}\right] \tilde{\sigma}_{ij}(\theta, n) \qquad (7.6)$$

for plane strain. For plane stress $(1-\nu^2)$ must be replaced by 1 in (7.6). ω is the loading frequency, $s(\omega t)$ is a function of n and the wave shape and the rest of the parameters have been defined in the equations for the HRR fields.

Riedel (1983) showed that $s(\omega t)$ reaches a steady cyclic state very quickly. The curves for the second and all following cycles are indistinguishable, and even the first cycle deviates only in its initial parts, since it starts from the steady state that is free from any internal stresses. The field described by equation (7.6) is valid as long as the creep zones that grow and shrink cyclically around the crack tip are small enough compared with the specimen dimensions.

The smallness of the creep zone is ensured by large enough loading frequencies according to :

$$\omega \geq \omega_1 = \frac{\pi}{t_1} = \frac{\pi (n+1) C^*}{(1+2\beta n) G} \qquad (7.7)$$

$\beta=0$ for step loading, $\beta=1$ for triangular loading and $0<\beta<1$ for sine loading. For frequencies $\omega > \omega_1$ the stress field is determined by the stress intensity factor K.

7.3.5 RAPID UNBALANCED CYCLING

In the case of rapid unbalanced cycling a time-independent stress is superimposed on the cyclic stressing. The time dependent near tip fields are determined by the stress intensity factor if the cyclic frequency is large enough to satisfy:

$$\omega >> \omega_1 = \frac{AE}{a^{(n-1)/(2(n+1))}\,\Delta K}\left[\frac{C^*}{A}\right]^{n/(n+1)} \qquad (7.8)$$

Above this frequency provided that the micromechanism of crack growth responds primarily to cyclic straining (like probably the striation mechanism), crack growth rates should correlate with ΔK.

The magnitude of the time independent superimposed stress can be characterised by C^* if the mean load is large compared with the load range i.e. for R ratios close to 1. Otherwise no analytic expression for the time independent component has been found. Assuming that the crack growth occurs by the striation mechanism :

$$\frac{da}{dN} \propto \frac{(\Delta K)^{2n/(n+1)}}{\omega^{1/(n+1)}} \int_0^{\pi} [\, s(\omega t) \,]^n \, d(\omega t) \qquad (7.9)$$

where the numerical value of the time integral depends on the waveshape.

In general the case or rapid unbalanced cycling has not been solved satisfactorily.The rapidly varying component of the near tip stress field is probably identical to that of the rapid balanced cycling, but the behaviour of the superimposed slowly creep component cannot be determined easily.

If fatigue crack growth occurs by the alternating slip mechanism, the rapid cyclic component will play a dominant role, but the creep component may play at least a secondary role by reducing the amount of crack closure and thus accelerating crack growth. If grain boundary cavitation is the relevant micromechanism, the creep component will be of primary importance.

7.4 A MODEL FOR CREEP - FATIGUE INTERACTION

In 7.3 it was explained that when load is cycled at elevated temperatures three potential fracture mechanisms may be involved in propagating the crack.

(1) Fatigue failure, when the extend of cavitation is small or negligible

(2) Creep-fatigue interaction failure, when there is interaction between the fatigue crack and the internal cavitation

(3) Creep failure if cavity development takes place significantly faster than

fatigue crack growth process.

The speed at which a crack will propagate, will in general depend upon the mechanism of failure.

For the case where the creep and fatigue crack growths are both significant, the use of empirical models becomes necessary. Winstone et. al. (1985) and Dimopulos et. al. (1986) have found good correlation assuming linear superposition of the creep and fatigue damage, when the two processes act together, by expressing the total crack growth per cycle as:

$$\frac{da}{dN} = \left[\frac{da}{dN}\right]_c + \left[\frac{da}{dN}\right]_f \qquad (7.10)$$

where the subscripts "c" and "f" refer to the creep and fatigue components respectively.

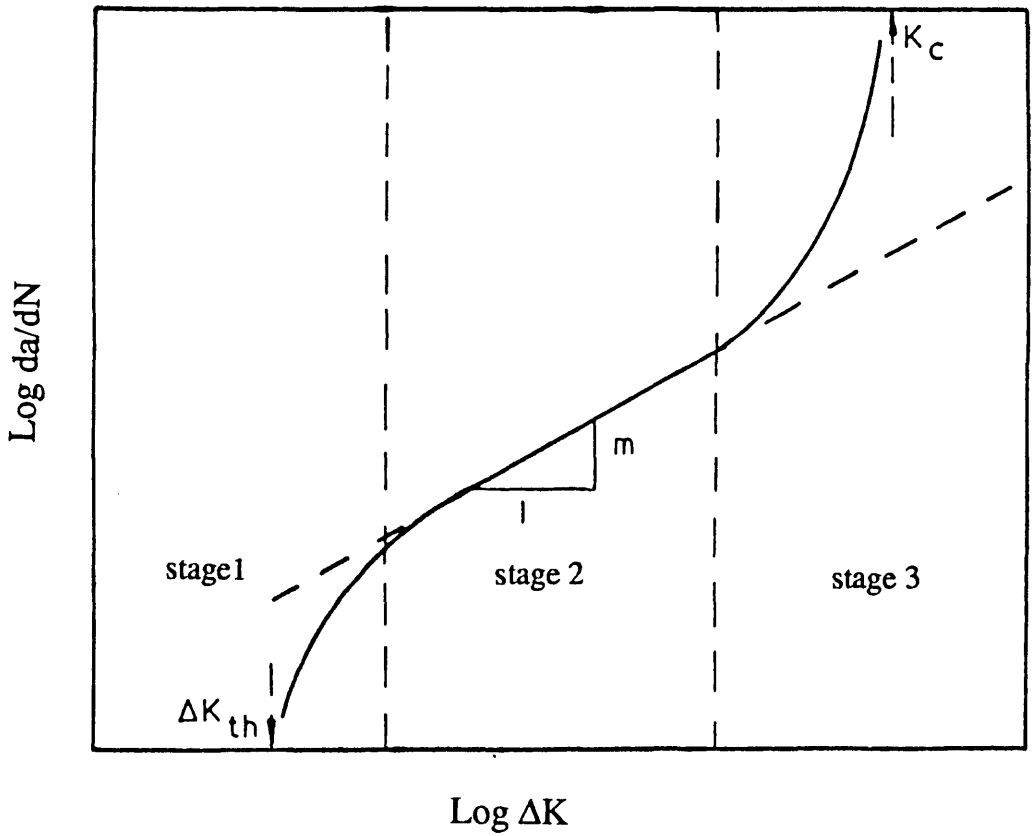


Figure 7.1 A typical fatigue curve

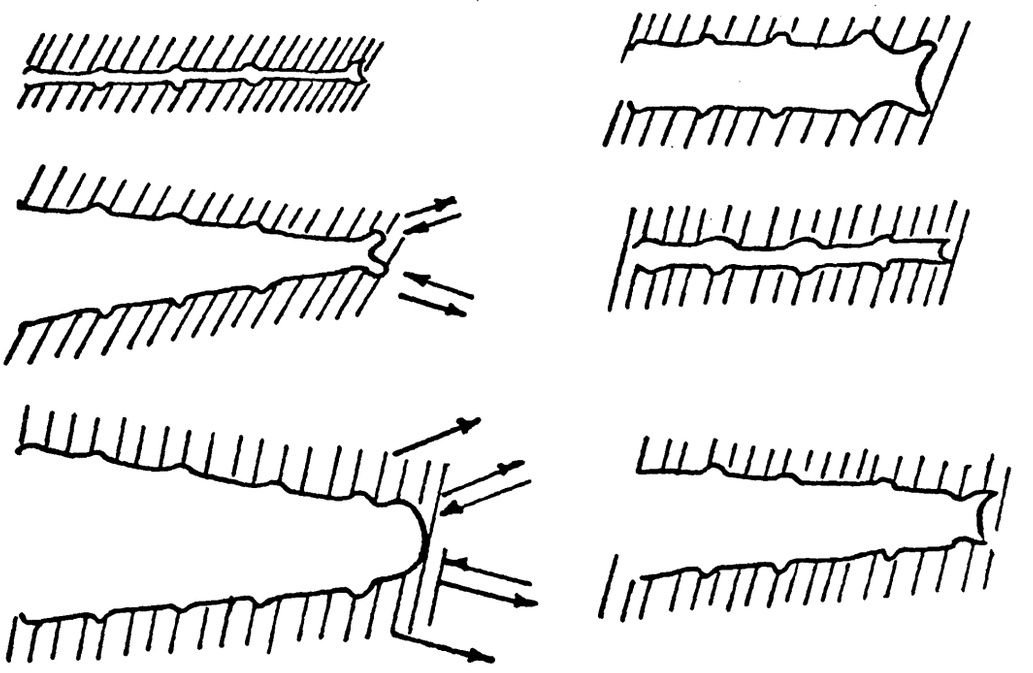


Figure 7.2a Diagrammatic representation of striation formation blunting process.

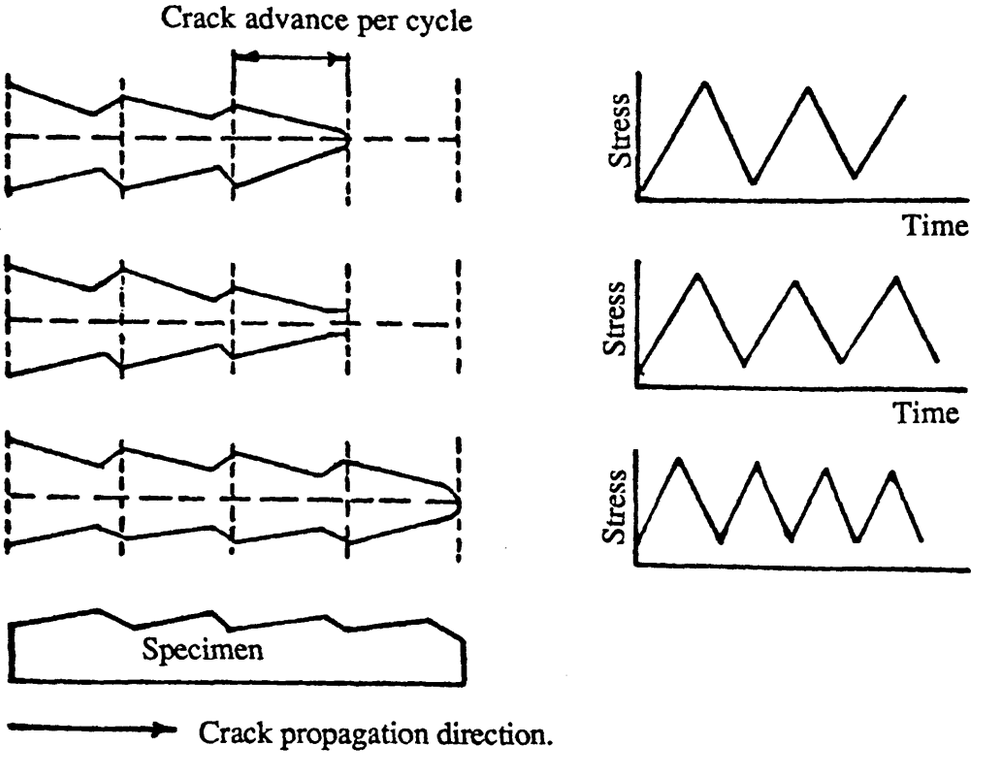


Figure 7.2b Diagrammatic representation of the formation of striations

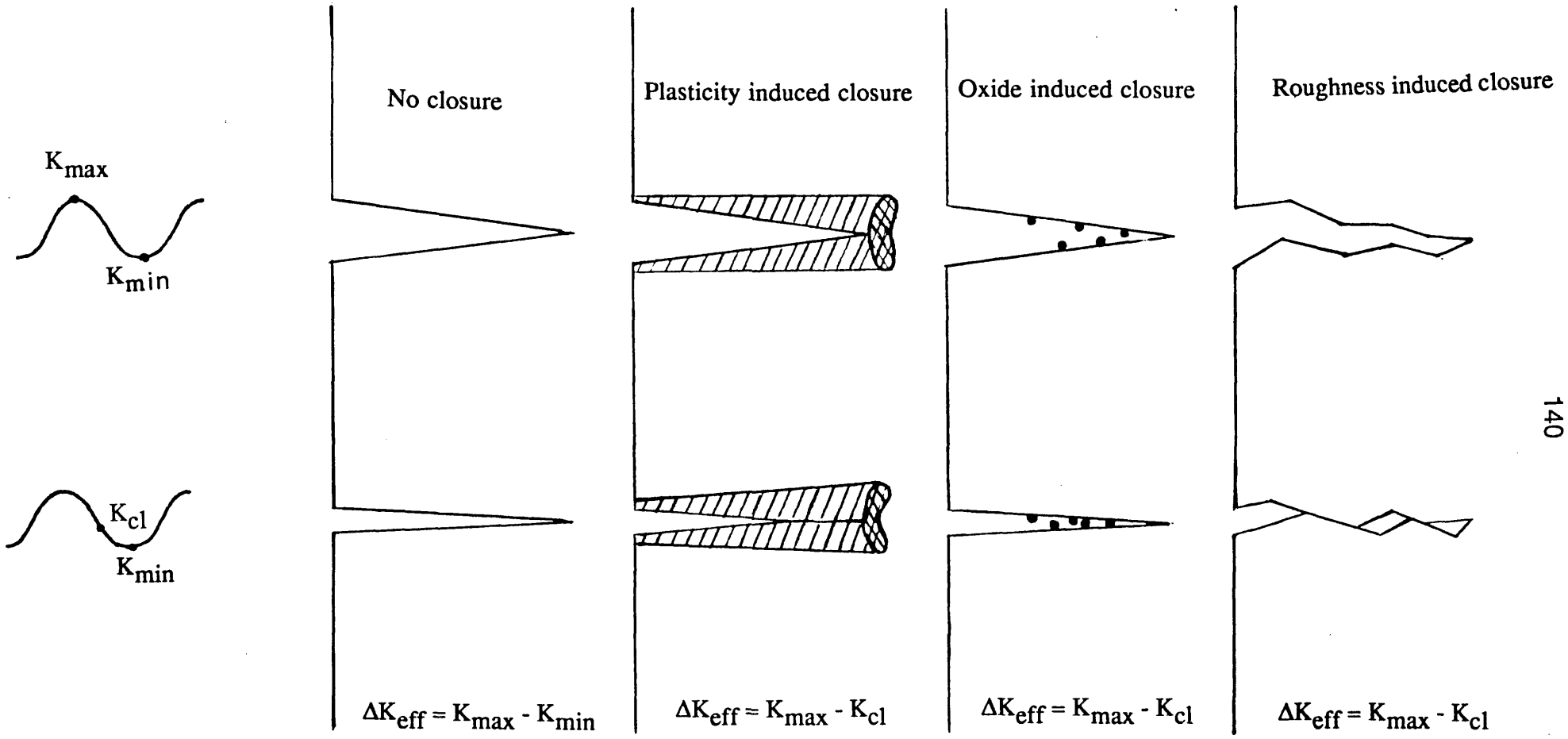


Figure 7.3 Schematic illustration of possible mechanisms of fatigue crack closure.

ΔK_{eff} is the effective stress intensity range , given by $K_{max} - K_{cl}$.

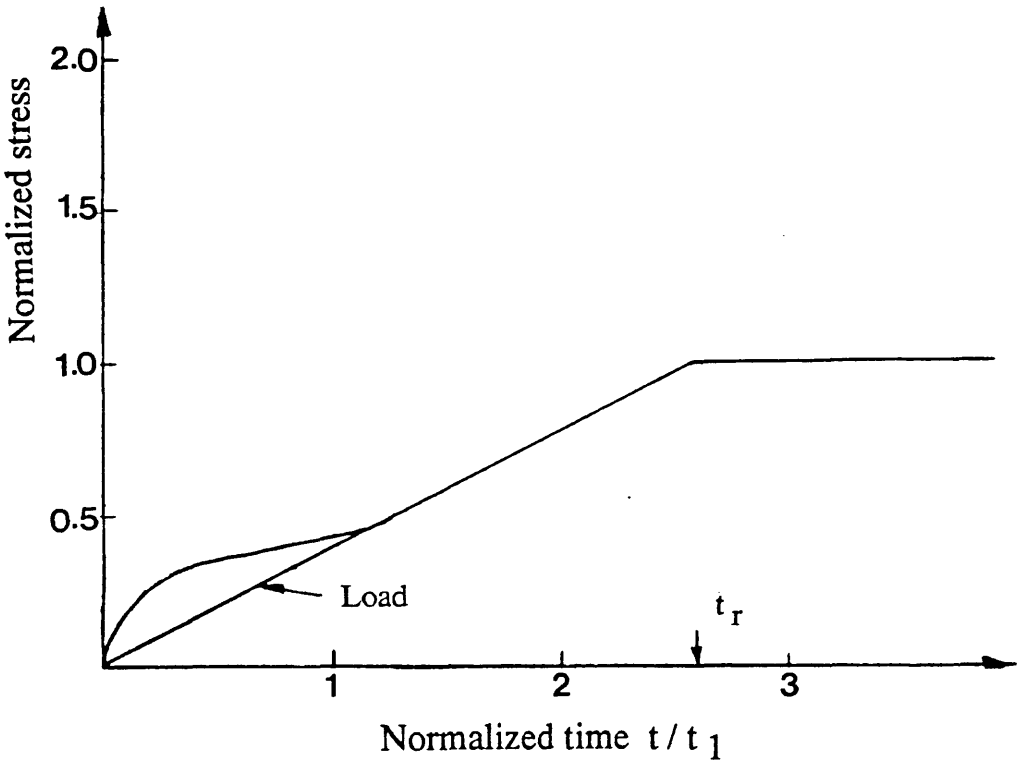


Figure 7.4 Crack tip stress in response to a slow linear load increase followed by a hold time

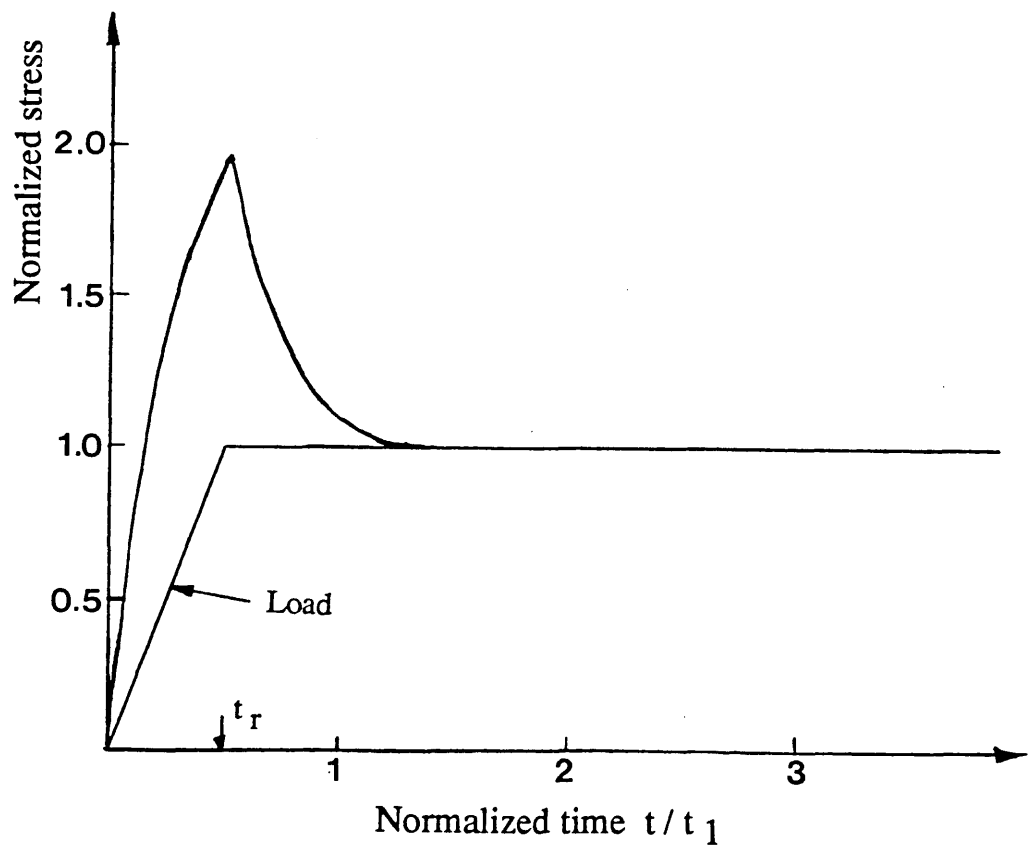


Figure 7.5 Crack tip stress in response to a fast linear load increase followed by a hold time

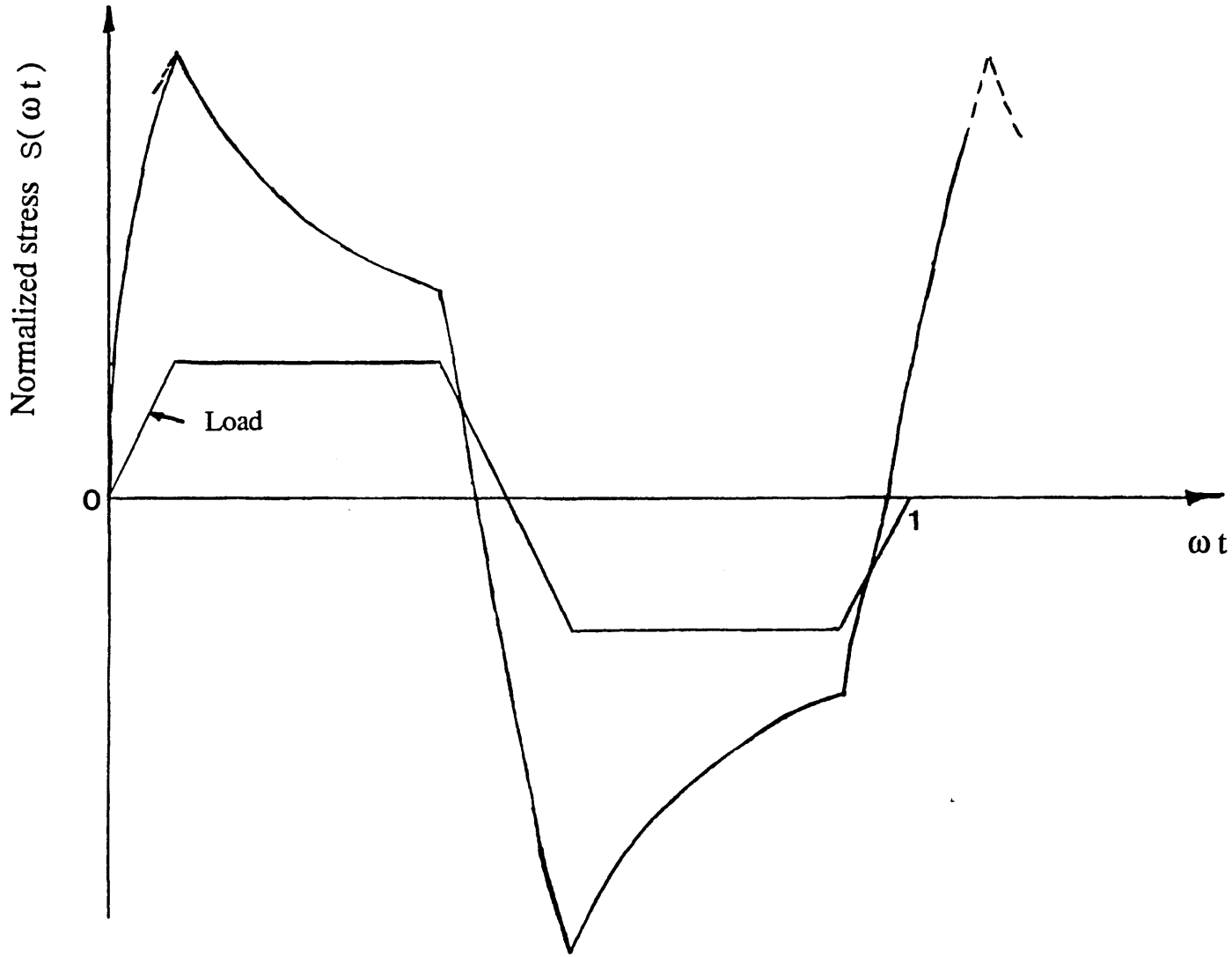


Figure 7.6 Crack tip stress for rapid cycling. Solid lines: first loading cycle ; dashed lines : all following cycles.

CHAPTER 8

EXPERIMENTAL INVESTIGATIONS

8.1 INTRODUCTION

This chapter describes the experimental investigations carried out, to study several features of crack growth at elevated temperatures. The experimental work was divided into static crack growth tests and cyclic crack growth tests. The static tests have been conducted under constant load and constant displacement, and, the cyclic between fixed load and fixed displacement ranges. The main variables that have been examined are minimum to maximum load ratio and frequency. The deterioration in material properties that occurs with aging, and, the subsequent sensitivity to cracking is also examined.

8.2 MATERIALS : COMPOSITION AND HEAT - TREATMENT

The materials used were two low alloy steels, namely a 1/2%Cr 1/2%Mo 1/4%V steel (1/2CMV) and a 21/4%Cr 1%Mo steel (21/4CM), two nickel base superalloys designated AP1 and 800H, and, a type 304H stainless steel.

The 1/2CMV material was heat-treated to represent brittle stress relieved heat affected zone material, with a tempered bainite microstructure and grain size of between 250 and 350μm. The 21/4CM steel was heat treated to simulate ductile parent plate with a mixed bainite/ferrite microstructure and grain size between 8 and 33μm. The former material was tested at 565° C and the latter at 538° C. At these temperatures the 1/2CMV steel had a uni-axial creep ductility in the range 0.1 to 5% and the 21/4CM steel a creep failure strain of 45%. The compositions heat treatment and tensile properties of the 1/2CMV and 21/4CM steels are given in tables 8.1 and 8.2 respectively.

The nickel base superalloy which is designated AP1, was received in the form of a hot isostatically pressed billet which had been heat-treated to produce a

microstructure containing approximately 40 vol % of γ' phase dispersed in a γ-nickel solution matrix and a grain size of 60μm. It was tested at a temperature of 700° C. At this temperature it had a uni-axial ductility of about 15%. The nickel base superalloy which is designated 800H, was received in the form of a plate and had a grain size of about 40μm. It was tested at a temperature of 800° C and at this temperature it had a uni-axial ductility of about 50%. The compositions and tensile properties of the AP1 and 800H steels are given in tables 8.5 and 8.4 respectively.

The 304H virgin (new) stainless steel unaged material was supplied by Exxon Research and Engineering company as a slab 11/2" thick by 10" wide and 14" long, and, the 304H stainless steel aged material was received from the Welding Institute. The aged material was taken from a component which had been in service for 15 years at temperatures in the range 690 to 725° C. The grain size of both the aged and the unaged material was about 500μm. The materials were tested at 760° C and at that temperature the unaged material had a uni-axial ductility of 50% whereas the aged had a uni-axial ductility of 25%. The composition and tensile properties of the 304H stainless steel are given in table 8.3.

8.3 SPECIMEN GEOMETRY AND DIMENSIONS

The geometry used for all experimental investigations is the compact tension geometry. Figure 8.1 shows the dimensions on the standard ASTM compact specimen. The specimen dimensions for the 800H superalloy and the 304H stainless steel are given in tables 8.7 and 8.6 respectively. Insufficient 304H aged material was available to make monobloc specimens, so a sandwich construction was employed with aged material electron beam welded between two layers of unaged material as illustrated in figure 8.10. The crack was then propagated through the aged material. The height H of the aged material is given in table 8.6. All 1/2CMV specimens had dimensions; width W=50mm and thickness B=25mm. Sidegrooves were introduced to give a net thickness of B_n=18mm. The 21/4CM steel specimens had dimensions; width W=50mm thickness

B=25mm and net thickness B_n=10mm. The AP1 superalloy specimens had dimensions; W=62.5mm and B=25mm (thick specimens) or B=12.5mm (thin specimens). Sidegrooves were not introduced in the AP1 superalloy specimens.

8.4 DESCRIPTION OF THE APPARATUS

An illustration of the equipment used for the steady load crack growth is shown in figure 8.2. The creep deformation equipment consisted of a standard rig with a 10:1 lever ratio loading arm and, two sets of Nimonic 80A pull rods and shackles.

The two pull-rods were connected to the shackles via ball-bearings, in order to ensure that the pull-rods and therefore the specimen remained vertical throughout the test. The furnaces used to heat the specimens were rectangular in design and opened vertically in the middle, as shown in figure 8.3. Each half of the furnace was fitted with a horizontal window so that the specimens could be observed. The furnace temperature was measured by using two chromel-alumel thermocouples attached to the ends of the specimen, and, the temperature was kept constant to within $\pm 1^{o}$ C using a three-zone temperature controller.

To measure the vertical load line displacement extensometer equipment similar to that used by Nikbin (1976) and Smith (1983) were used. Figures 8.3 and 8.4 show the arrangement of the extensometry. A set of two Nimonic extensometer legs was attached to each shackle and the legs passed down through a set of plates (perspex or aluminium), thus allowing extension to be measured at the load line.

For low frequency cyclic tests, the static load rig was modified as shown in figure 8.5. It consisted of a motor driving through a gear box, and, two screw jacks, all fitted into a tubular frame. A platform to lift the weights on and of the test ring loading train, was fixed to the screw jacks. The speed and the direction of the motor was controlled via a transformer, elecromechanical timers and mercury switches. To limit the movement of the loading platform, microswitches, set at suitable positions were used. The equipment allowed trapezoidal waveform loading tests to be conducted for

frequencies up to 10^{-3} Hertz.

For constant load range tests conducted at higher frequencies, and, for all the tests were the displacement between the loading pins was kept constant (static or cyclic), a servo-hydraulic high temperature facility was used.

The servo-hydraulic equipment was a Mayes model ESHF 100 kN and a Mayes ESHF 250 kN, machines with facilities for cyclic testing using various waveforms, and also with facilities of constant load range loading or constant transducer displacement range loading. A general layout of the ESHF 100 kN rig is shown in figure 8.6. A rectangular furnace of the same type described earlier, was supported within the loading frame using an adjustable platform. For specimen loading (except AP1 testing), pull-rods and shackles of a similar construction to that used for the static load crack growth tests, were used. The details of the pull rods and extensometry are shown in figure 8.4.

For the AP1 testing the loading frame was quite different. The extensometer legs were attached to the shackles as above but now the bottom pull-rod was rigidly fixed to the machine and in order to allow flexibility in the loading system, and, that the specimen remained vertical throughout the test, the top pull-rod was connected to the machine through a universal joint. The pull rods were made from Nimonic 80A material. A different set of shackles had to be used for the AP1 material because, the set used for crack propagation in the other materials was not capable of withstanding the loads used for crack propagation in the AP1 superalloy.

For automatic crack length measurement, direct current potential drop (DC) systems and an alternating potential drop (AC) system were used.

For the steady load and low frequency tests on the low alloy steels, 800H Incoloy and 304H stainless steel a single 60A Coutant, Model ASA 5000, power pack provided a series supply to the specimens, as shown in figure 8.7. To ensure proper electrical insulation of the crack growth test specimens, for the use with the (DC) potential drop system, the pull rod assembly was fitted with insulating bushes in the

upper and lower halves of loading trains on each of the crack growth test rigs. To make certain that the power pack operated as a constant current device, the resistance of the overall circuit, including specimens, was designed such that it was approximately one tenth of the power pack sensing lead resistance. To provide a low resistance circuit, heavy duty, multicore, cable was used for the current supply, external to the furnaces, to the specimens. For the current leads inside the furnaces, brass strip was used.

To measure the output voltage across the crack growth specimens, screened soft iron was used. The output voltage across the specimens was found to be, for a 30 to 40 Ampere current input, of the order of millivolts. To provide an improved signal, direct current amplifiers were used, designed to give long term stability and low junction resistance.

For the automatic crack length measurements on tests conducted in the servo-hydraulic test rigs and for all materials, except AP1, a (DC) potential drop system manufactured by Mayes was used. The load train in these rigs was fitted with insulating bushes and, the input and output currents in the cracked specimens were similar as above. Direct current amplifiers similar as above were used to improve the output signal. For the specimens made from the AP1 superalloy an alternating current (AC) potential drop system had to be used, since the output of the (DC) system was erratic for this material. For the current leads inside the furnace a stainless steel wire 1.5 mm thick was used. The (AC) system used is shown in figure 8.8. To measure the output voltage across the crack growth specimens, soft iron wire was used of the same type as for the (DC) system. The output voltage was typically of the order of millivolts. Two stable low noise (AC) amplifiers were used to improve the signal.

8.5 MEASUREMENT METHODS

8.5.1 CRACK LENGTH MEASUREMENTS

Two methods were used for measuring the position of the crack in the plane perpendicular to the loading. An optical method and a potential drop method.

With the optical method the crack growth was measured using a telescope mounted on a shaft attached to the platform (figure 8.9). The crack reflection was viewed through windows using two side mirrors clamped at an angle of 45° to either side of the furnace. The crack length was measured from the loading line at convinient time intervals. The AP1 superalloy and the 304H stainless steel didn't present any problem but testing of the 1/2CMV, 21/4CM and the 800H Incoloy at 565° C 538° C and 800° C respectively presented a problem of oxidation which completely obscured the view of the crack.

Nikbin (1976) testing the 1/2CMV steel at 565° C found that by coating the surface of the specimen with a high temperature paint having the trade-name Delta-Guard 130 prevented the surface oxide forming. With this method the specimen was sand blasted and degreased using trichoroethylene, and then a thin layer of Delta-Guard 130 was applied using a pencil brash.

At test temperature of 565° C for the 1/2 CMV and 538° C for the 21/4CM steels Delta-Guard 130 forms a brilliant white matt surface which adheres extremely well to the specimen surface. At 800° C i.e the test temperature for the 800H the Delta-Guard 130 is much darker than at 565° C and 538° C, but at least it stops surface oxide forming, so visual observation of the crack is much easier. When the surface of the specimen, beneath the paint cracked, the brittle paint also fractured.

By shining a strong white light into the painted surface and observing the surface through the telescope and the mirror, as shown in figure 8.9 the ruptured paint showed as a dark hair-like crack, contrasting with the matt white background of the paint. With this method crack extensions of the order of 0.1mm can be detected readily,

but the reliability of precisely locating the crack tip by this means is probably no better than ±0.5mm. An advantage of this method is that the crack extention is obtained readily, as no calibration is required. However it has the disadvantage of being manual and having to depend upon the operator's skill, and a reliable indication of average crack length will only be obtained if the crack front is relatively straight through the thickness of the specimen. A way of encouraging straight fronted cracks is to increase through thickness constraint by introducing side grooves as shown in figure 8.10. If these are not provided as extensive creep deformation takes place, crack tunneling is often obtained. Bowed cracks may not only cause unreliable estimates of crack propagation rates, but also lead to inaccurate estimates of the appropriate fracture mechanics characterising parameters, as these depend on crack length.

The second method, for crack length measurement, was a potential drop method. This method is described extensively in the literature (see, for example Klintworth (1977), Klintworth and Webster (1979).

In all these methods a constant current is passed through the specimen and the change in potential between two points either side of the crack plane monitored as the crack extends. The positions of the current supply and potential measuring leads are chosen to optimise the system (Klintworth and Webster (1979)). Either a direct current (DC) or an alternating current (AC) can be used. Each has its attractions for particular applications. Substantially smaller currents are in general needed in the AC method compared with those needed in the DC method. However, in the AC method, the current is concentrated mainly on the surface of the specimen, and therefore the surface length of the crack is measured. Nevertheless, it has been shown that the AC method provides an accurate method of automatically measuring crack lengths (Klintworth (1981)). With this method it is essential to twist both the current and potential sensing leads together and bring them perpendicular from the specimen surface to minimize inductive pick-up as this would affect the calibration.

The direct current (DC) method requires large currents to obtain a minimum current density for an acceptable level of accuracy in the output voltage. The output voltage is more susceptible to electrical noise than its AC counterpart so capacitors may have to be used. The DC system results in a uniform current density through the test-piece thickness. It therefore effectively responds to crack area and will give an indication of the average crack length. Klintworth (1981) conducted a comparison between the two electrical methods, and it was found that although the two systems gave comparable results, the DC system was more reliable over large periods even though the DC output was prone to more electrical noise. It was found that with the AC system, the slightest movement of the monitoring leads produced large changes in the output voltage, probably due to the production of eddy currents in the monitoring leads, as they moved in the fluctuating magnetic field in the vicinity of the specimen surface. This effect did not occur in the DC system. So a DC system was decided to be used for monitoring the crack growth. It was found however that for the AP1 superalloy, the output voltage using a DC system gave unreliable results, so the AC system had to be employed for this material.

8.5.2 CALIBRATION OF THE CRACK LENGTH POTENTIAL DROP

To obtain accurate measurements of crack length from the potential drop output accurate calibration curves have to be obtained. Calibrations can be obtained using experimental, analogue or numerical techniques.

Smith (1983) made a comparison of these methods for the CT geometry taking the effect of side grooves into account. He found that complete agreement is not obtained and he concluded that the most reliable calibration is the experimental. In the experimental method, a calibration test specimen was saw-cut to a particular crack length. The current leads were then fixed to the specimen via screws and the monitoring leads spot-welded to the specimen. The specimen and leads were then positioned in the test rig loading frame, the specimen heated to the correct temperature, the current applied

and the corresponding voltage drop across the monitoring leads measured. The above method was then repeated for various crack lengths. A calibration curve can be constructed in terms of the normalised voltage V/V_i and the normalised crack length a/W. Smith (1983) found that side-grooving affects the calibration curve, so different calibration curves are needed for different side-grooving.

For the CT geometry Klintworth and Webster (1979) suggest current monitoring positions to give an optimised calibration curve. But it was found however, that the optimised lead positions were unsuitable for the experimental set-up used. The shackles of the loading pull-rods interfered with the input leads. Furthermore, when placing the specimen in the shackles, the spot-welded monitoring leads were easily broken. To overcome these problems the specimen pin-holes were machined further away from the crack plane and the current monitoring leads were positioned in more convinient places. The experimental calibration was then conducted for the CT geometry with side-grooves.

Although the normalised calibration curve V/V_i versus a/W, is a characteristic curve for a particular specimen geometry, together with the current and monitoring lead positions, it was found from tests conducted on apparently identical specimen geometries with identical current and monitoring lead positions, that the initial measured voltage was not the same. Normalizing subsequent measured voltage changes due to crack length did not, therefore, produce repeatable calibration curves.

However with the use of optical readings taken during the crack growth tests, a calibration curve for each test could be found by shifting the original experimental calibration along the V/V_i axis to match the observed results.

8.5.3 TEMPERATURE CALIBRATION.

The furnaces were calibrated using a dummy specimen, fitted with thermocouples along the crack plane. An approximate temperature distribution along the horizontal length of the furnace was obtained and the furnace controller dial settings were

noted and used as a guide for setting up the furnaces and specimens for crack growth testing.

The correct temperature distribution for each specimen was achieved at the time of testing.

8.5.4 DISPLACEMENT AND LOAD CALIBRATION

The displacement transducers were calibrated prior to testing of all crack growth specimens. The transducer was placed in an assembly consisting of a drum-type micrometer held in a frame, into which the transducer was fixed. A calibration curve of transducer output voltage and micrometer setting was then drawn. In all cases the calibration curve was a straight line.

The load calibration of the servo-hydraulic machines, was done by a technician from the manufactures of the equipment, W. H. Mayes Limited. During the period of crack growth testing on the servo-hydraulic rigs the load calibration did not alter.

8.6 EXPERIMENTAL PROCEDURE

Each specimen was first fatigue cracked at the desired initial crack length according to ASTM standard E647-78T, at room temperature. In the cases were side grooves were introduced to the specimens, they were introduced after fatigue cracking to avoid bowing of the crack during fatigue (see appendix 8A). Then the low alloy steel and the 800H specimens, were lightly sand blasted and degreased as explained in 8.5.1. The chrome-alumel thermocouples as well as the PD monitoring leads were then fixed to the specimen, as described in 8.5.2. The current leads were then fixed to the specimen via screws, or in the case of API welded into the specimen.

Then where necessary, the specimen was coated with a high temperature paint as explained in section 8.5.1, and they were marked on both sides at intervals of 0.5 inches, since the vernier on the telescope mounting was marked in fractions of an inch.

The specimen was then placed into the appropriate test rig, and the displacement extensometry fitted. High temperature grease was used on the necessary joints. In the cases that the servo-hydraulic test rigs were used, the specimens were fitted into position by operating the machine in displacement control. The rig was then placed into stand-by load on completion of setting up.

The thermocouples and the PD system were then tested to ensure that the correct response was obtained. In particular, the response of loose or bad earth connections was checked.

The furnace was then closed, the specimen heated to the required temperature and, held at the testing temperature for about 16 hours before testing, so that a uniform temperature distribution was achieved.

For the tests performed in the creep test machines, the loading of the specimen was performed manually. The loading rate was kept to within one minute for the full load in all cases. For the tests performed in the servo-hydraulic machines, the machine was transferred from stand-by load into load control for the constant load range tests and to strain (or transducer) control for the constant transducer displacement range tests, and the load set to the required mean level. Then the desired frequency and load amplitude were set on the signal generator module and then switched to the operating mode. Some adjustments were necessary to obtain the correct frequency and load amplitude required.

Once the load had been applied, the initial optical crack reading, the PD voltage, and, the transducer displacement readings were taken. Subsequent data values for the PD, transducer displacement, load, and, temperature, were collected on y-t recorders. Optical readings were initially taken at short intervals and at convinient times thereafter depending on the rate of crack growth.

8.7 STATIC CRACK GROWTH TESTS

Static crack growth tests were performed on the 800H superalloy and the 304H stainless steel (both aged and unaged material) under constant load conditions. The static crack growth behaviour of the 1/2CMV and 21/4CM steels has been studied in detail by Smith (1983), and that of the AP1 superalloy by Nikbin (1986). All tests were carried out in the dead load creep machines described earlier.

Although all the static load tests tended to fail in a catastrophic manner, the amount of stable crack growth could be discerned from a change in the fracture surface appearance of colour. The sudden failure of the specimen and subsequent shutdown of the furnace in a relatively short time, ensured that the surfaces exposed due to unstable crack growth, did not accumulate a large amount of high temperature oxide. The surfaces which had been exposed due to slow crack growth for lengthy periods could easily be identified, thus allowing the amount of slow crack growth to be measured directly.

The resultant values of crack length obtained from the PD system and the calibration curve approximately agreed with the final crack length measured from the fractured specimens. Thus the results obtained from the use of the PD system were considered reliable. On the other hand the optical readings can not be considered reliable as high oxidation and/or excessive deformation, prevented reliable optical readings to be obtained for the 800H and the 304H materials.

Specimen graphs of crack growth against time are simultaneously shown with the graph of the transducer displacement versus time, in figures 8.11 to 8.13. In this way, the extent of loading pin displacement in relation to the amount of crack growth can be compared. In all constant load static tests the crack growth and displacement both accelerated rapidly with crack advance and time. This is expected as when the load is kept constant, there is a rapid increase in the stress intensity factor K with the crack length for the compact tension specimen.

8.8 CYCLIC CRACK GROWTH TESTS

Cyclic crack growth tests, under both constant load range and constant displacement range, were mainly performed on the 1/2CMV steel the 21/4CM steel and the AP1 superalloy. However two constant displacement range tests were performed on the aged 304H stainless steel.

In the constant load range tests on the 1/2CMV steel the 21/4CM steel and the AP1 superalloy, the variation of the loading frequency and the cyclic to mean load ratio (R - ratio) are considered. The test conditions are presented in tables 8.8, 8.9 and 8.10 respectively.

For each material crack growth experiments have been conducted over a range of R values from 0.1 to 0.8 and frequencies between 10^{-4} and 10 Hz. The waveshape employed was sinusoidal for frequencies of 0.1 Hz and greater and square-wave shape for lower frequencies. The high frequency tests ($\geq$ 0.01 Hz) were carried out in the servo-hydraulic machines, and the low frequency tests in creep machines which had been modified to allow slow load cycling as described earlier in this chapter. The test conditions were chosen to give crack growth per cycle da/dN in the range 10^{-5} to 1mm/cycle. In most instances stable crack propagation over a distance of approximately 10 to 15mm was obtained.

Specimen graphs of crack growth against time are simultaneously shown with the graph of the transducer displacement versus time, in figures 8.14 to 8.16. In this way, the extent of loading pin displacement in relation to the amount of crack growth can be compared. As in the constant load static tests, the crack growth and displacement both accelerated rapidly with crack advance and time.

The constant displacement range tests were mainly conducted on the AP1 superalloy over a range of R values from 0.1 to 0.7 and frequencies between 10^{-3} and 1 Hz. The present loading system was not capable of constant displacement range

loading at frequencies greater than 1Hz. The tests are presented in table 8.10.

A limited number of constant displacement range tests has been conducted on other materials. Both the 1/2CMV steel and the 21/4CM steel have been tested at a frequency of 10^{-3} Hz and R=0.8. Two constant displacement range tests have been conducted on the 304H stainless steel aged material at a frequency of 10^{-3} Hz and R=0. In one of these tests the effect of elastic follow-up was simulated by keeping the displacement range of the fatigue machine constant instead of the displacement range of the loading pins.

All constant displacement range tests were conducted in the servo-hydraulic machines. The constant displacement tests represent more closely the conditions often experienced in low cycle fatigue and thermal fatigue situations.

The behaviour exhibited by the 21/4CM steel is shown in figure 8.17 and that of 304H stainless steel aged material in figures 8.18 and 8.19. Both materials show a rapid decay in load, and a corresponding decrease in the crack growth rate, as elastic recovery is exchanged for creep deformation. Eventually the load drops to such a low value that creep deformation and cracking eventually cease. However it was found that if the initial load is regenerated and cycling is continued cracking can be reactivated and the whole process repeated. It was also found that more crack growth is observed with elastic follow-up than without (figures 8.18 and 8.19).

The behaviour exhibited by the1/2CMV steel is shown in figure 8.20. Similar behaviour to the 21/4CM steel and 304H stainless steel is observed. However the load relaxation was slower and the crack extension greater. Only 0.4mm of crack extension was observed in the 21/4CM and 0.5mm in the 304H stainless steel before cracking ceased, whereas about 5mm was measured in the 1/2CMV steel. Specimen graphs of the AP1 material behaviour are shown in figures 8.21 and 8.22. It was observed that in general the load relaxation was linear resulting in a constant crack growth rate, and, the crack extension was enough for the specimen to fail.

The PD system, as pointed out earlier was used to measure the change in the

crack length during the cyclic crack growth tests, like in the static tests. The optical readings can be considered reliable only for the AP1 superalloy, the 1/2CMV steel and for the high frequency 21/4CM steel tests, as deformation was very small and the crack tip could be clearly and accurately observed. For the low frequency 21/4CM steel and 304H stainless steel tests, excessive deformation prevented reliable optical readings being obtained.

The change in the measured specimen displacement due to the change in load, can also be used as a means of measuring the change in the crack length (Webster (1981)). However it was found that especially for tests involving small load amplitudes the change in compliance with crack length could not be measured accurately. This technique was, therefore, for the majority of tests, an unsuitable means of measuring the change in crack length.

TABLE 8.1 COMPOSITION HEAT TREATMENT AND TENSILE PROPERTIES OF THE 1/2CMV STEEL.

(a) Material Composition (in percentages).

C	Cr	Mo	V	Mn	Al	Ce	Fe
0.08	0.42	0.69	0.33	0.31	0.005	0.025	Balance

(b) Heat Treatment.

1) 0.5 hour at 1250° C.

2) Oil quenched at room temperature.

3) Tempered, 24 hours at 680° C.

4) Air cooled.

(c) Tensile Properties .

Properties at 20° C

Young's Modulus, E = 216 GPa

Yield Stress, σ_y = 657 MPa

Tensile Strength = 749 MPa

Failure Strain = 4.2 %

Properties at 565° C

Young's Modulus, E = 176 GPa

Yield Stress, σ_y = 580 MPa

Tensile Strength = 708 MPa

Failure Strain = 5.6 %

TABLE 8.2 COMPOSITION HEAT TREATMENT AND TENSILE PROPERTIES OF THE 2¼CM STEEL.

(a) Material Composition (in percentages).

C	Si	Mn	S	P	Ni	Cr	Mo
0.12	0.34	0.59	0.005	0.015	0.19	2.4	1.00
Al	Zr	Ti	Cu	Sn	Fe		
0.02	0.01	0.034	0.07	0.01	Balance		

(b) Heat Treatment.

1) Anneal, 15 hours soak at 960° C.

2) Furnace cooled.

3) Normalise, 12 hours soak at 960° C.

4) Fan assisted cooling

5) Temper, 12 hours soak at 700° C.

6) Furnace cooled.

7) Stress relieved, 36 hours soak at 690° C.

8) Furnace cooled.

(c) Tensile Properties .

20° C		538° C	
Young's Modulus,	E = 194 GPa	Young's Modulus,	E = 152 GPa
0.02% Proof Stress	= 403 MPa	0.02% Proof Stress	= 169MPa
Tensile Strength	= 573 MPa	Tensile Strength	= 352 MPa
Failure Strain	= 25 %	Failure Strain	= 28 %

TABLE 8.3 COMPOSITION AND TENSILE PROPERTIES OF THE 304H STAINLESS STEEL

The new material was supplied as annealed plate to ASTM Standard A 240 - 80B.

(a) Material Composition (in percentages).

NEW MATERIAL

C	P	S	Si	N	Mn	Cr	Ni	Fe
0.061	0.027	0.015	0.500	0.055	1.74	18.55	8.49	Balance

AGED MATERIAL

C	P	S	Si	N	Mn	Cr	Ni	Mo	V	Fe
0.052	0.009	0.011	0.45	0.023	0.98	17.5	9.6	0.21	0.034	Balance

(b) Tensile Properties at 20° C. for the new material.

Young's Modulus,	E = 205 GPa
0.02% Proof Stress	= 267MPa
Tensile Strength	= 573 MPa
Elongation	=60%
Reduction in Area	=71%
Hardness	= 150 Brinell

TABLE 8.4 COMPOSITION AND TENSILE PROPERTIES OF THE 800H SUPERALLOY.

(a) Material Composition (in percentages).

C	Si	Mn	P	S	Cr	Ni	Al	Ti	Fe
0.07	0.46	0.68	0.020	0.004	20.26	31.11	0.34	0.31	Balance

(b) Tensile Properties at 20° C. (Manufacturer's data)

Young's Modulus,	E = 250 GPa
0.02% Proof Stress	= 250 MPa
Tensile Strength	= 573 MPa
Reduction in Area	= 26%
Elongation	= 74%

TABLE 8.5 COMPOSITION AND TENSILE PROPERTIES OF THE AP1 SUPERALLOY

(a) Material Composition (in percentages).

Cr	Co	Mo	Ti	Al	Zr	C	Ni
14.8	16.9	5.04	3.52	3.98	0.044	0.022	Balance

(b) Heat Treatment.

(1) 4 hours at 1100° C.

(2) Air Cooled.

(3) 24 hours at 650° C.

(4) Air Cooled.

(5) 4 hours at 760° C.

(6) Air Cooled.

(c) Tensile Properties.

	20° C	535° C	650° C	760° C
0.2% Proof Stress (Mpa)	1042	970	949	856
Tensile Strength (Mpa)	1450	1332	1333	1088
Elongation (%)	25	18.5	19.6	23.9
Reduction in Area (%)	25	21	23	26
Hardness (VPN)	360			

TABLE 8.6 DIMENSIONS OF THE 304H SS SPECIMENS.

Specimen No.	Material	Thickness B (mm)	Net Thickness B_n (mm)	Aged Layer Height H (mm)
EX1	New	18.0	12.6	_
EX2	New	25.0	10.0	_
EX3	New	25.0	10.0	_
EX5	New	25.0	10.0	_
EX7	New	18.0	12.6	_
EX8	New	18.0	12.6	_
EX9	New	14.0	10.0	_
EX10	New	14.0	10.0	_
EXW4	Aged	14.0	10.0	25.0
EXW7	Aged	14.0	10.0	15.0
EXW8	Aged	14.0	10.0	14.0
EXW9	Aged	14.0	10.0	15.0
EXW10	Aged	14.0	10.0	18.0
EXW11	Aged	14.0	10.0	18.0
EXW13	Aged	14.0	10.0	18.0

For further specimen dimensions see figure 8.10

All specimens except EXW11 and EXW13 were tested under static, constant load, conditions. EXW11 was tested under constant displacement range conditions at R=0, and, F = 10^{-3} Hz. EXW13 was tested under constant displacement range to simulate elastic follow-up at R=0, and, F=10^{-3}

TABLE 8.7 DIMENSIONS OF THE 800H SPECIMENS.

Specimen No.	Thickness B (mm)	Net Thickness B_n (mm)	Width W (mm)
A64	25	20	50
A66	25	20	50
A76	25	20	50
A77	25	20	50
A89	20	16	40
G208	12.5	10	25
G209	12.5	10	25

All specimens were tested under static, constant load, conditions.

TABLE 8.8 LIST OF TESTS CONDUCTED ON THE 1/2CMV MATERIAL.

(1) Costant Load Range Tests.

R = 0.1 F = 10^{-2} Hz

R = 0.1 F = 10^{-1} Hz

R = 0.1 F = 1 Hz

R = 0.1 F = 10 Hz

R = 0.5 F = 10^{-2} Hz

R = 0.5 F = 10^{-1} Hz

R = 0.5 F = 1 Hz

R = 0.5 F = 10 Hz

R = 0.8 F = 10^{-4} Hz

R = 0.8 F = 10^{-3} Hz

R = 0.8 F = 10^{-1} Hz

R = 0.8 F = 10 Hz

(2) Costant Displacement Range Tests.

R = 0.8 F = 10^{-3} Hz

TABLE 8.9 LIST OF TESTS CONDUCTED ON THE 2¼CM MATERIAL.

(1) Costant Load Range Tests.

R = 0.1 F = 10^{-3} Hz

R = 0.1 F = 10^{-1} Hz

R = 0.1 F = 10 Hz

R = 0.8 F = 10^{-3} Hz

R = 0.8 F = 10^{-2} Hz

R = 0.8 F = 1 Hz

R = 0.8 F = 10 Hz

(2) Costant Displacement Range Tests.

R = 0.8 F = 10^{-3} Hz

TABLE 8.10 LIST OF TESTS CONDUCTED ON THE AP1 MATERIAL.

(1) Costant Load Range Tests.

All tests were conducted on 25mm thick specimens.

R = 0.1 F = 10^{-3} Hz

R = 0.1 F = 10^{-2} Hz

R = 0.1 F = 10^{-1} Hz

R = 0.1 F = 10 Hz

R = 0.5 F = 10^{-3} Hz

R = 0.5 F = 10^{-1} Hz

R = 0.5 F = 10 Hz

R = 0.7 F = 10^{-3} Hz

R = 0.7 F = 10^{-2} Hz

R = 0.7 F = 10^{-1} Hz

R = 0.7 F = 1 Hz

R = 0.7 F = 10 Hz

(2) Costant Displacement Range Tests.

(a) Tests conducted on 25mm thick specimens.

R = 0.1 F = 10^{-3} Hz

R = 0.1 F = 10^{-2} Hz

R = 0.1 F = 10^{-1} Hz

R = 0.1 F = 1 Hz

R = 0.7 F = 10^{-3} Hz

R = 0.7 F = 10^{-2} Hz

R = 0.7 F = 1 Hz

R = 1 F = 0 Hz (static)

(b) Tests conducted on 12.5mm thick specimens.

R = 0.1 F = 10^{-3} Hz

R = 0.1 F = 10^{-2} Hz

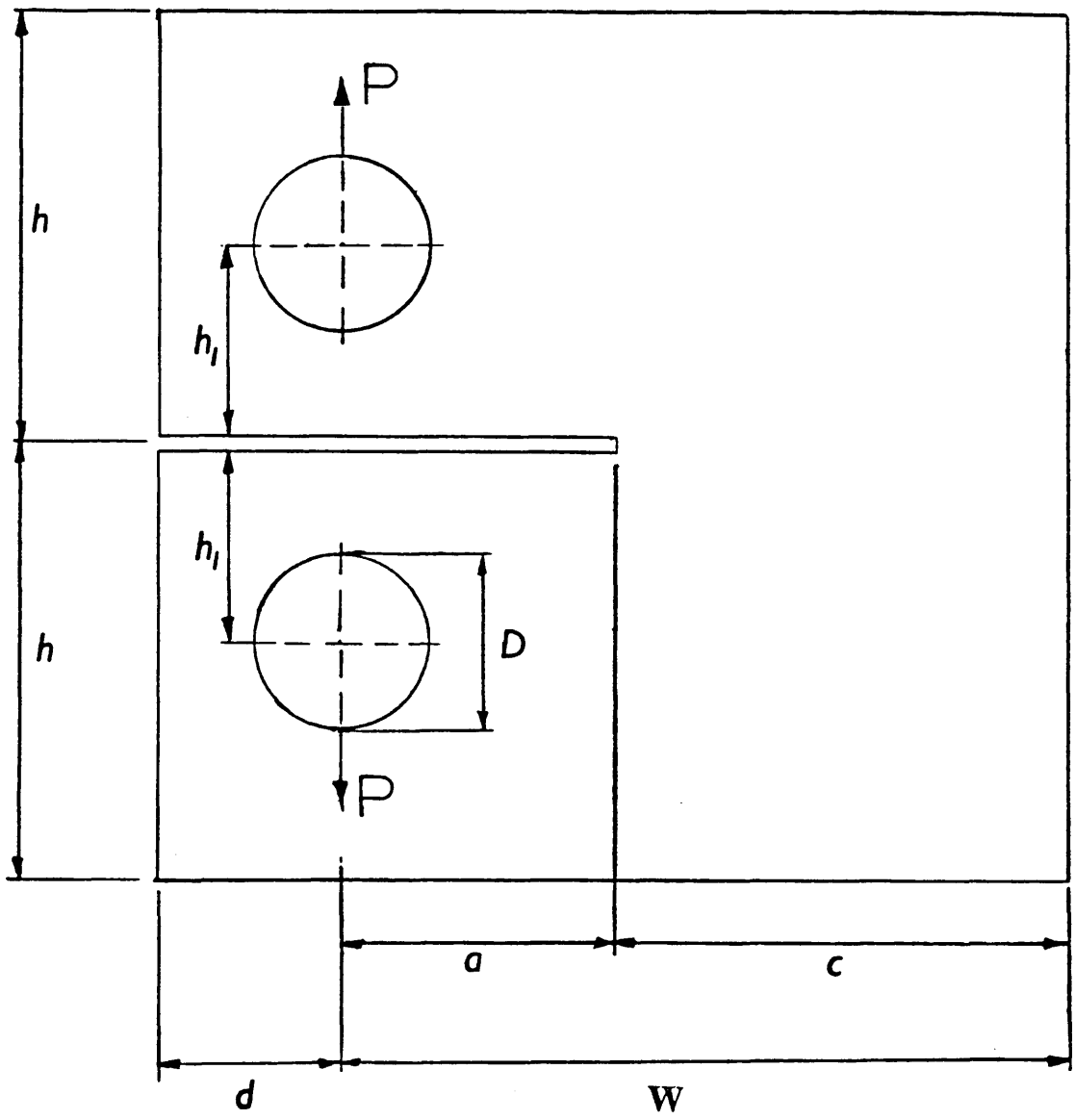
R = 0.1 F = 10^{-1} Hz

R = 0.1 F = 1 Hz

R = 0.7 F = 10^{-3} Hz

R = 0.7 F = 10^{-1} Hz

R = 1 F = 0 Hz (static)



h = 0.6 W

h_1= 0.275 W

D = 0.25 W

d = 0.25 W

B = 0.5 W

B : Thickness

Figure 8.1 Geometry of standard ASTM Compact Tension specimen

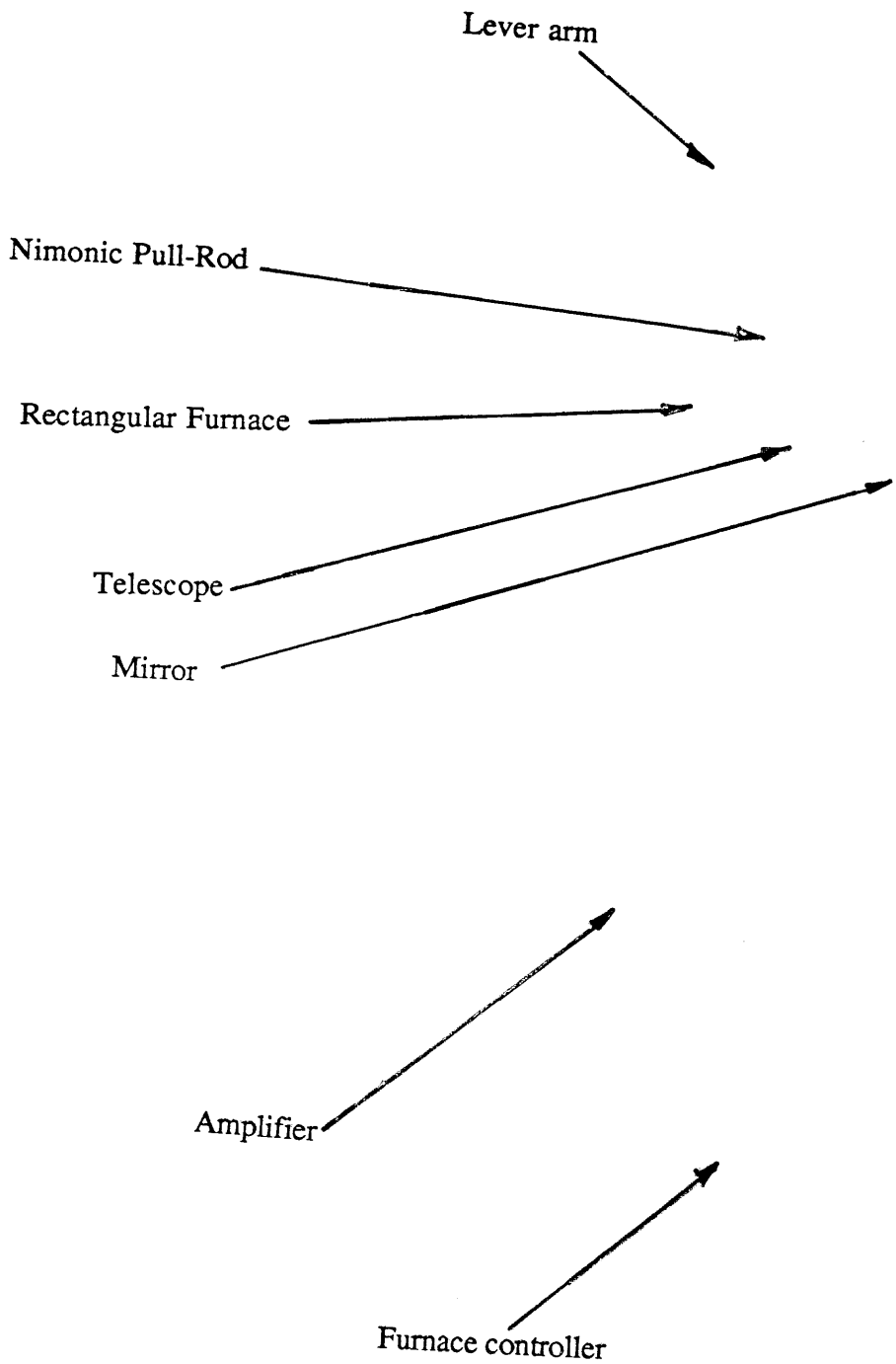


Figure 8.2 Steady load crack growth equipment.

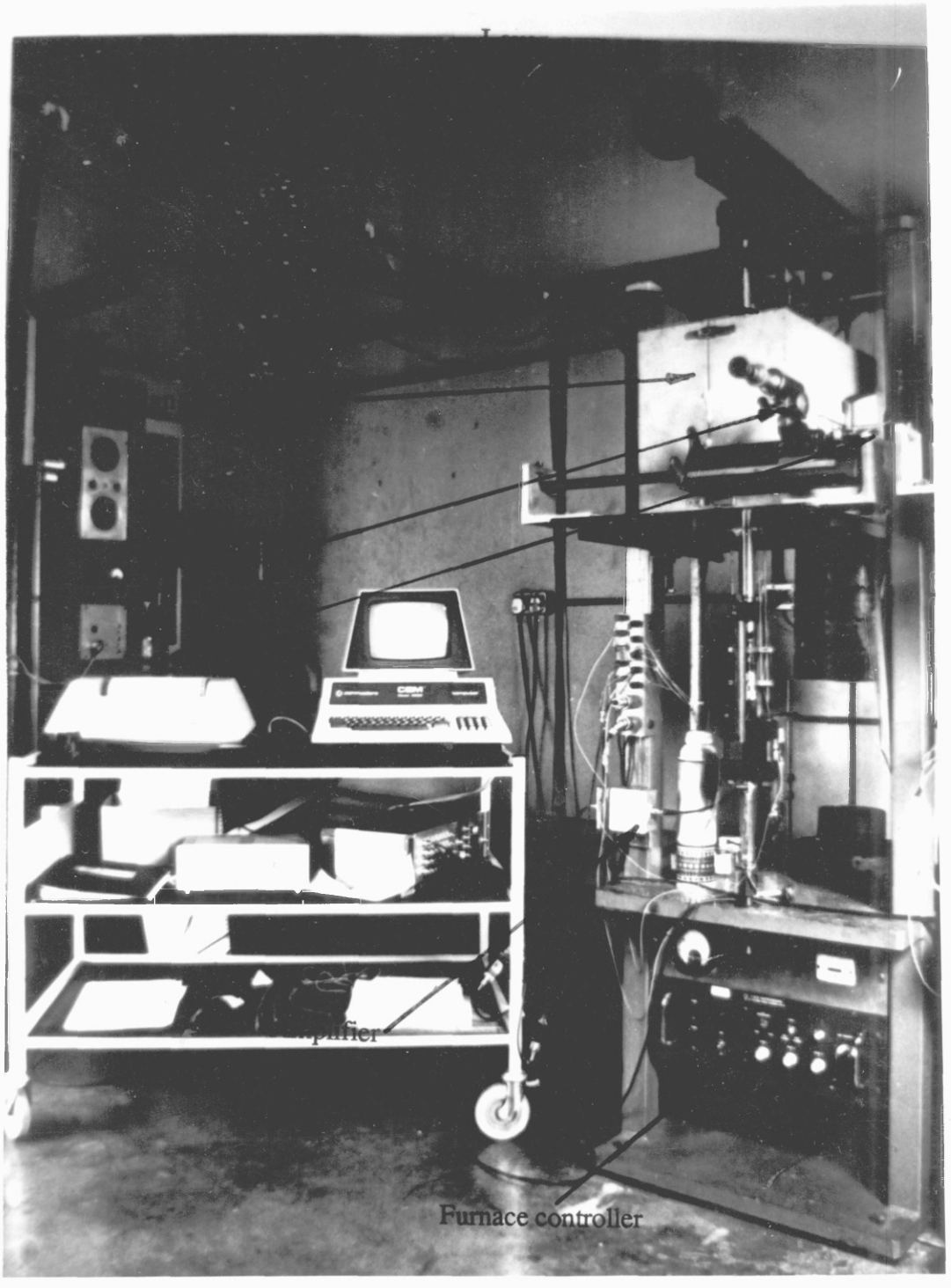


Figure 8.2 Steady load crack growth equipment.

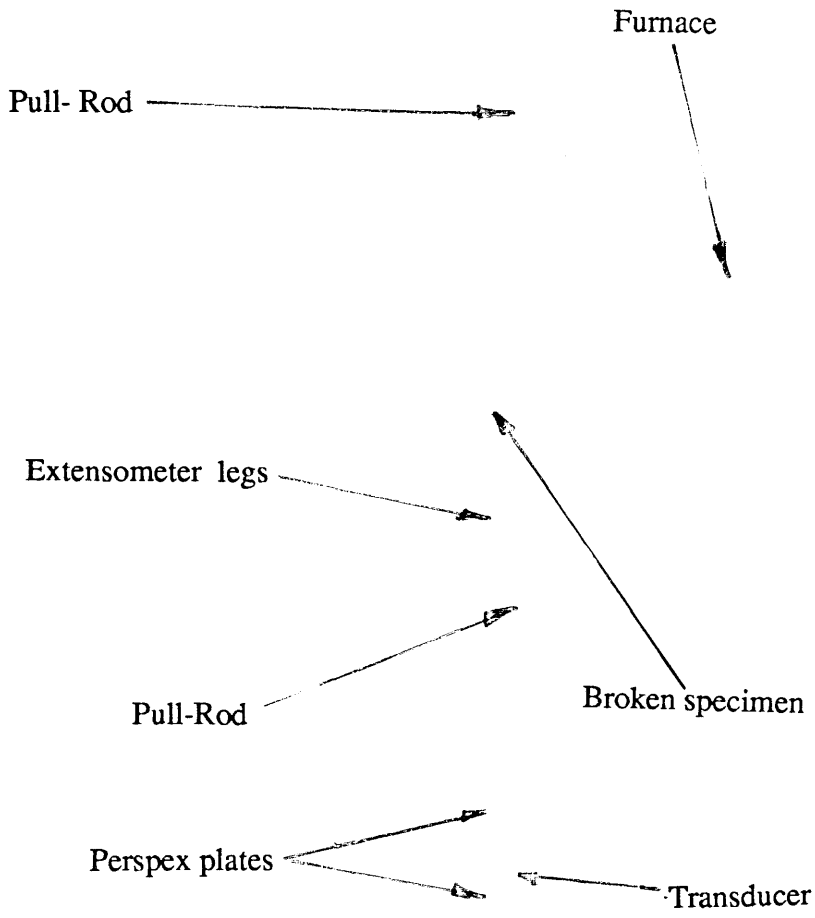


Figure 8.3 Arrangement of crack growth specimen and extensometer equipment in the servo-hydraulic test rig.

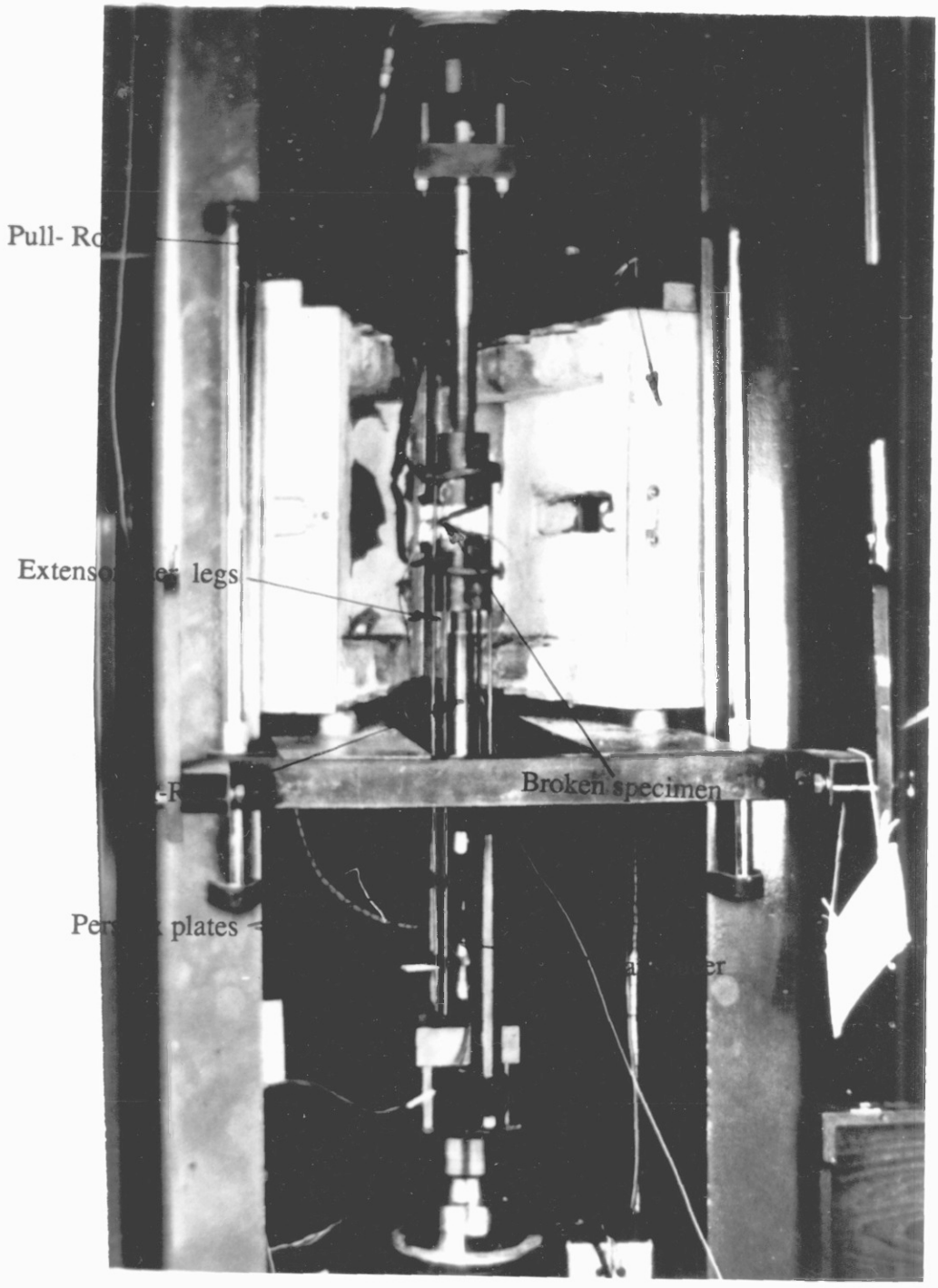


Figure 8.3 Arrangement of crack growth specimen and extensometer equipment in the servo-hydraulic test rig.

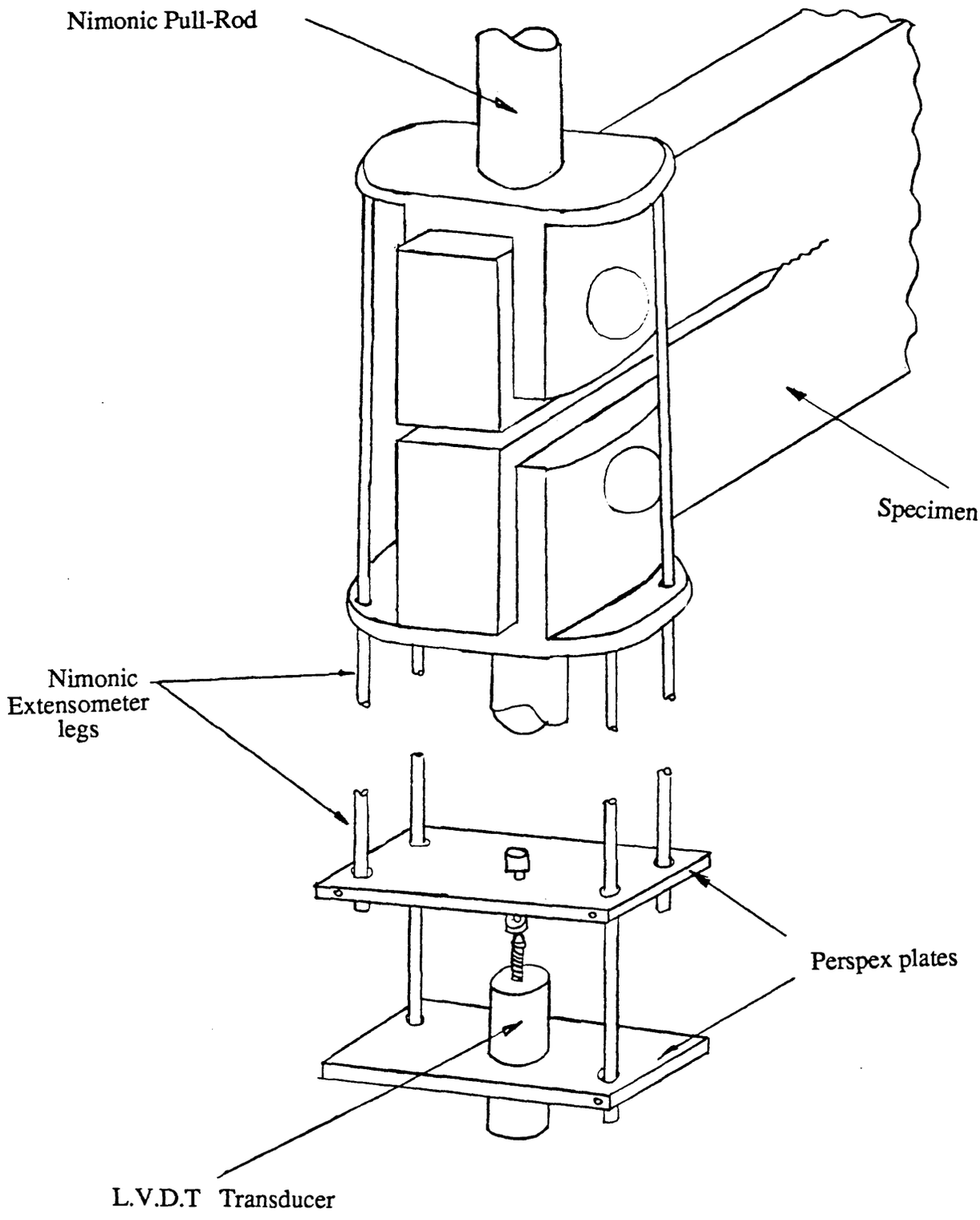


Figure 8.4 Arrangement of extensometry to measure load line displacements

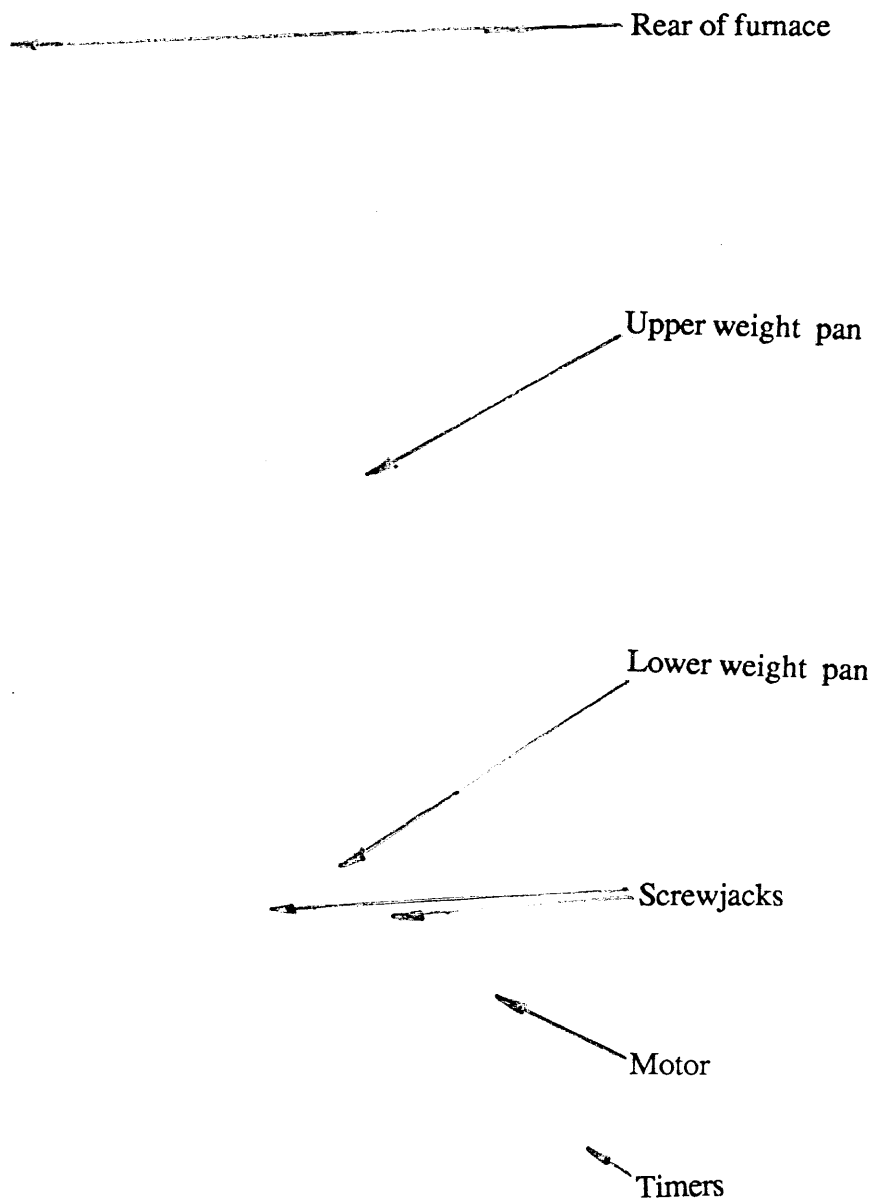


Figure 8.5 Low frequency load cycling equipment at rear of steady load crack growth rig.

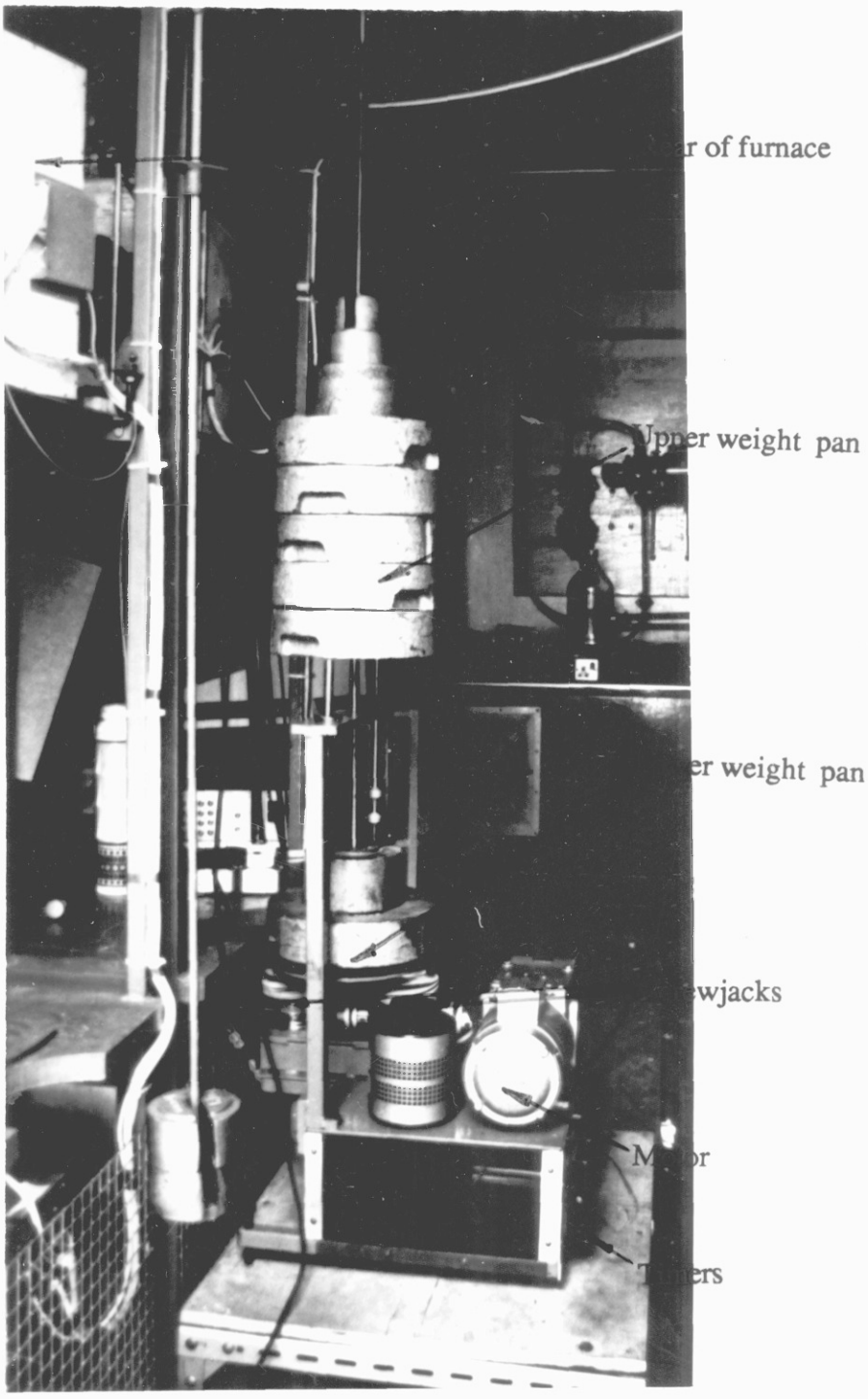


Figure 8.5 Low frequency load cycling equipment at rear of steady load crack growth rig.

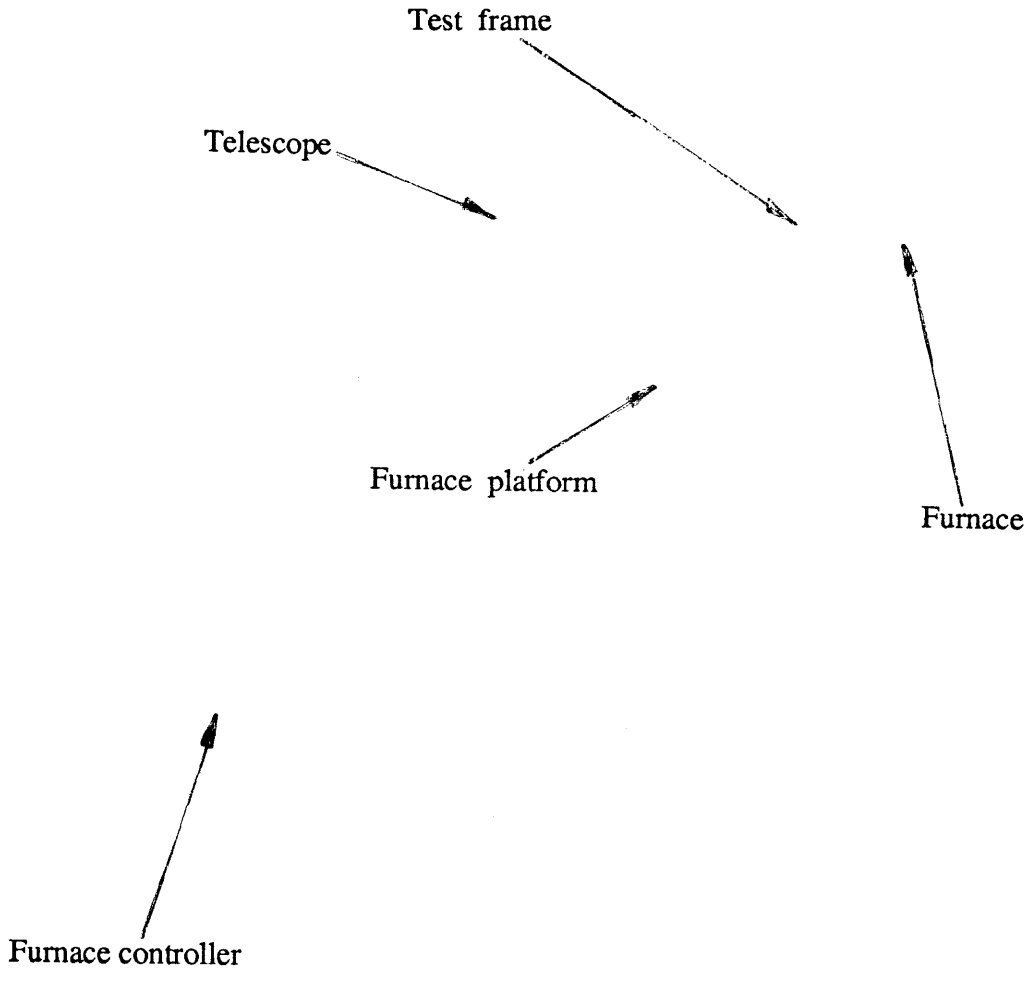


Figure 8.6 Arrangement of servo-hydraulic test rig.

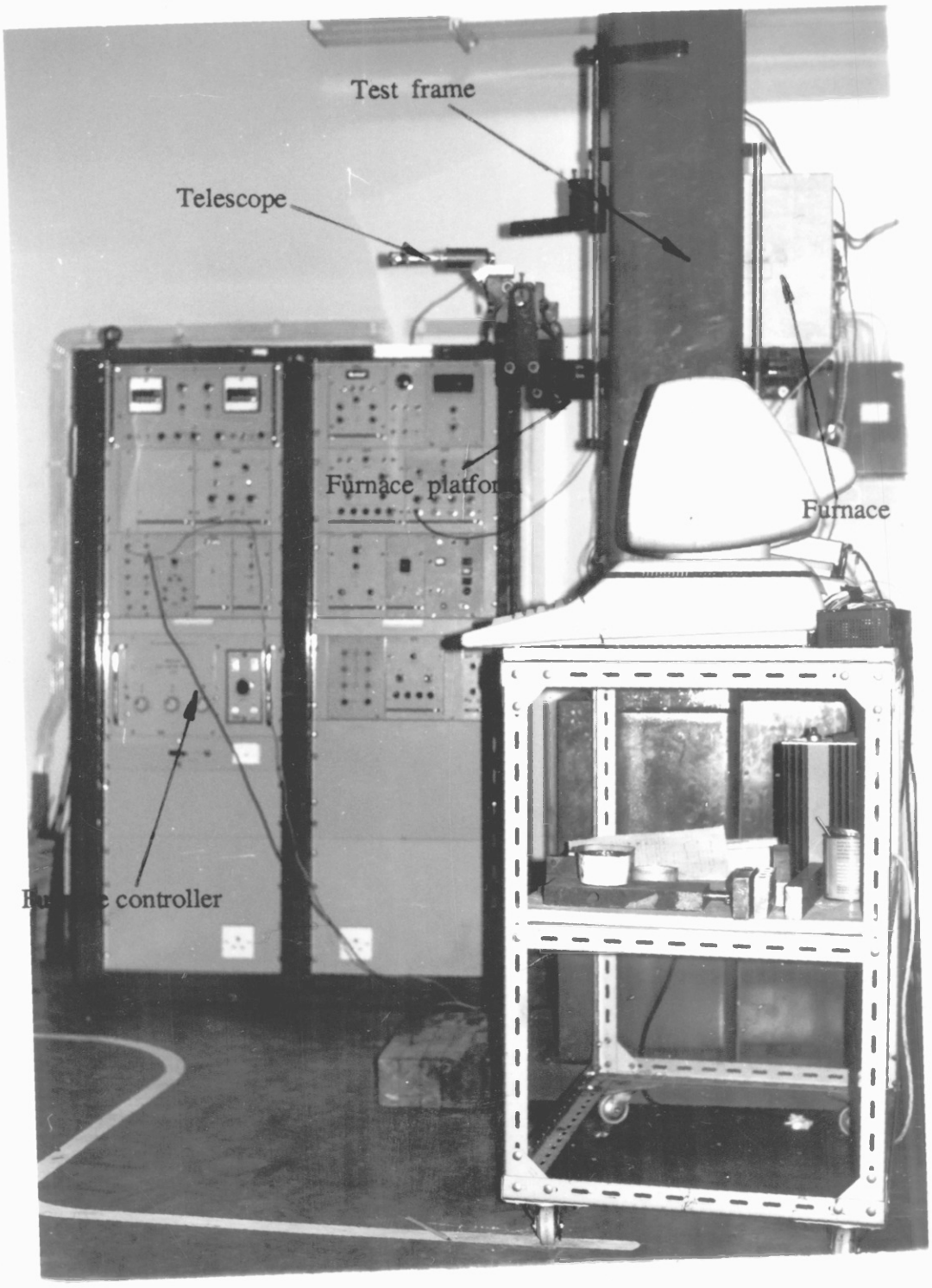


Figure 8.6 Arrangement of servo-hydraulic test rig.

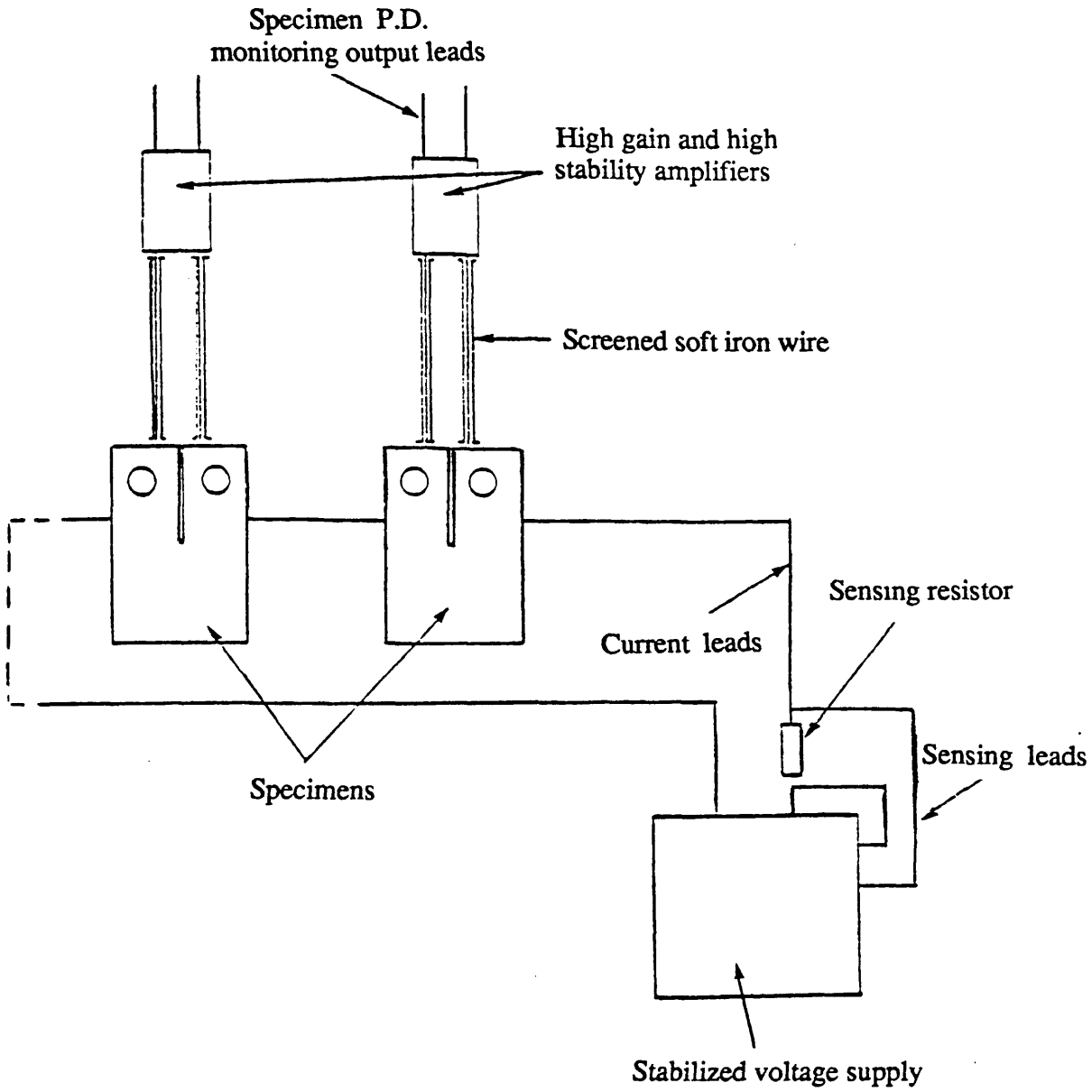


Figure 8.7 Arrangement of direct current potential drop equipment for crack length measurement.

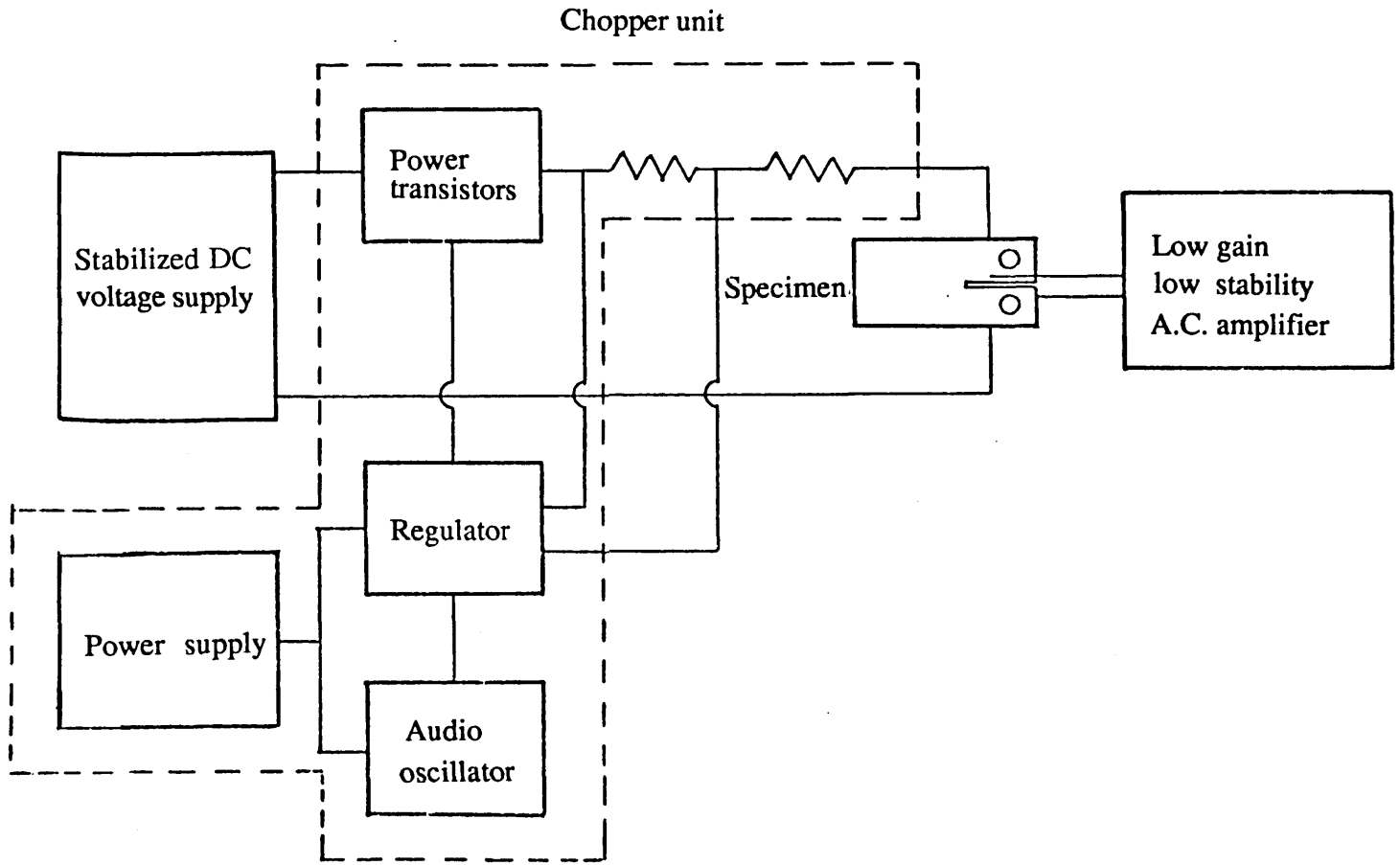


Figure 8.8 Arrangement of alternating current potential drop equipment for crack length measurement.

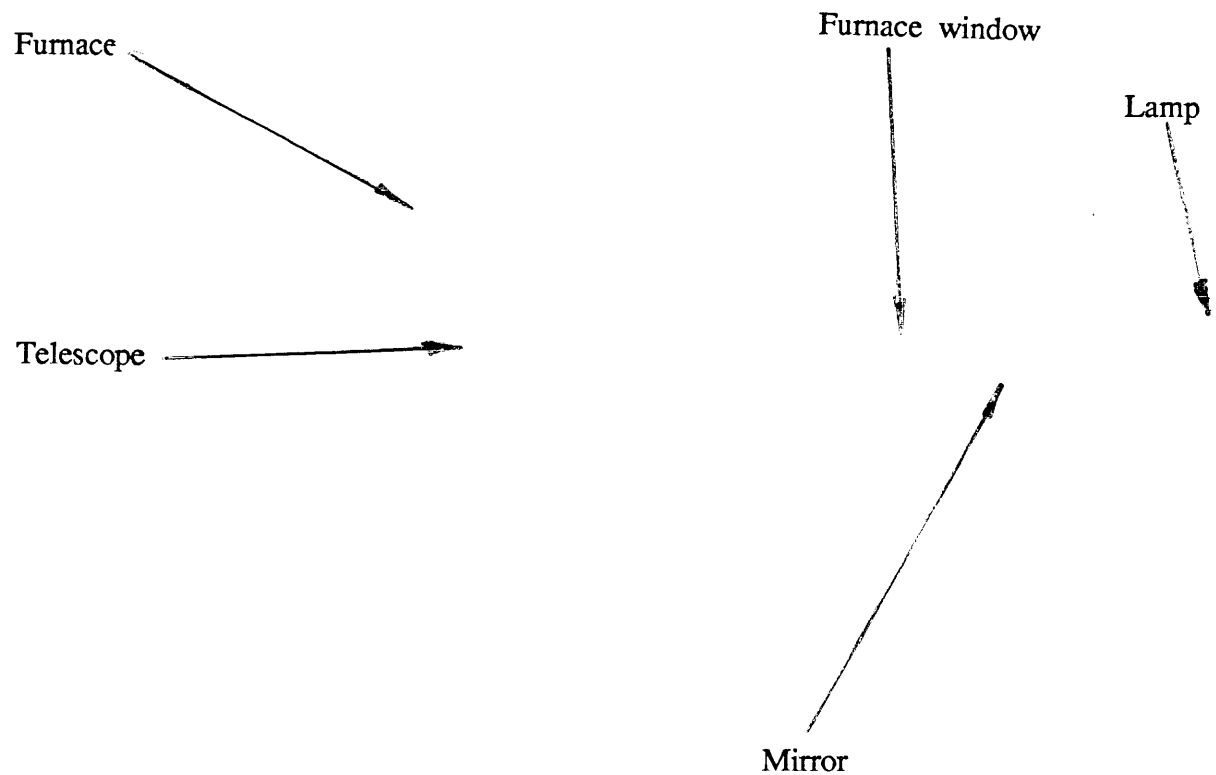
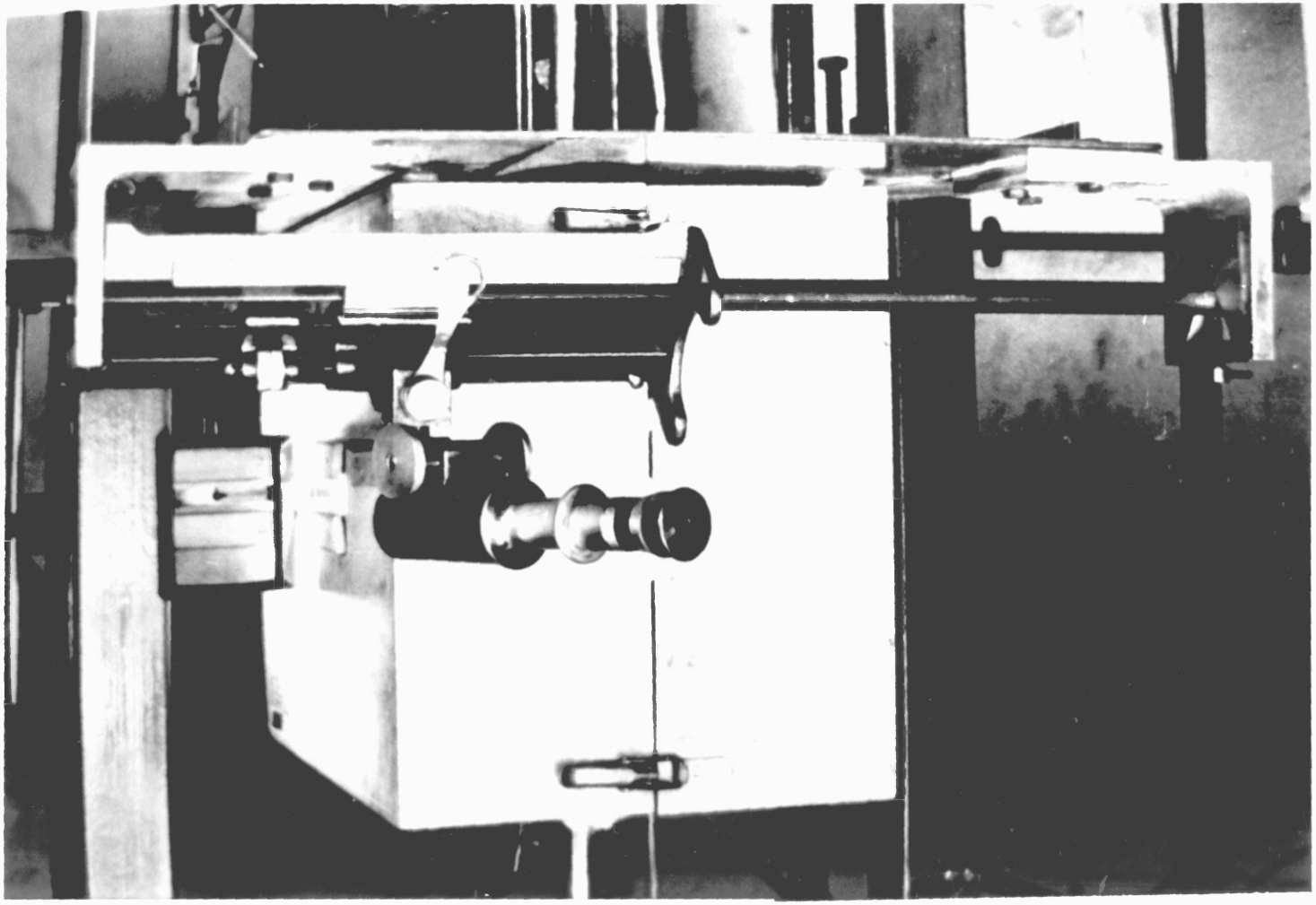
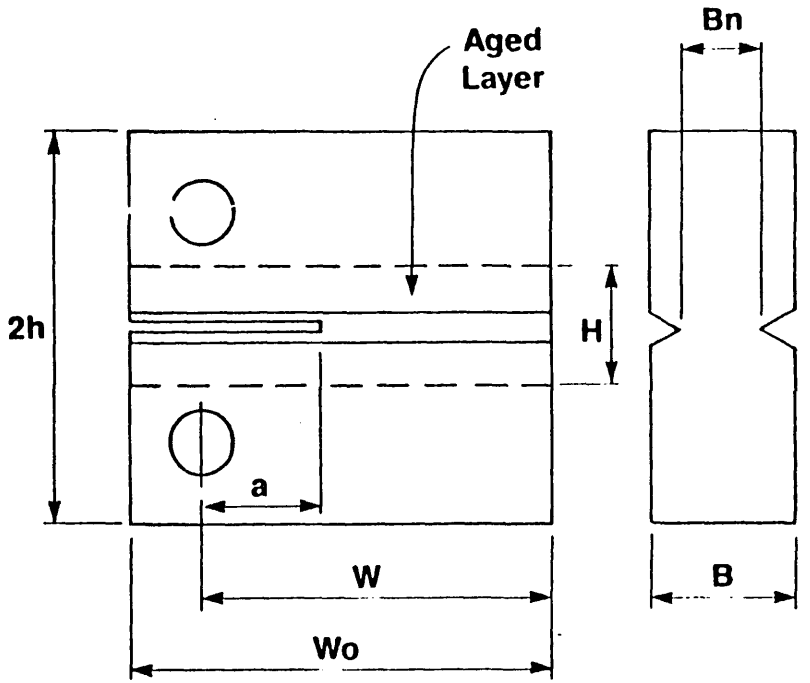


Figure 8.9 Arrangement of telescope and mirror.





CT SPECIMEN

Specimen Dimensions (mm)

		NEW	AGED
W	=	50.0	41.6
W_o	=	62.5	52.0
h	=	31.0	25.0
H	=	—	14.0–25.0
a/w (after precrack)	≅	0.40	0.38

		SIDEGROOVES		
		DEEP	SHALLOW	
B	=	25.0,	18.0	14.0
Bn	=	10.0,	12.6	10.0

Figure 8.10 Dimensions of compact tension test specimens used in the 304H material creep crack growth tests.

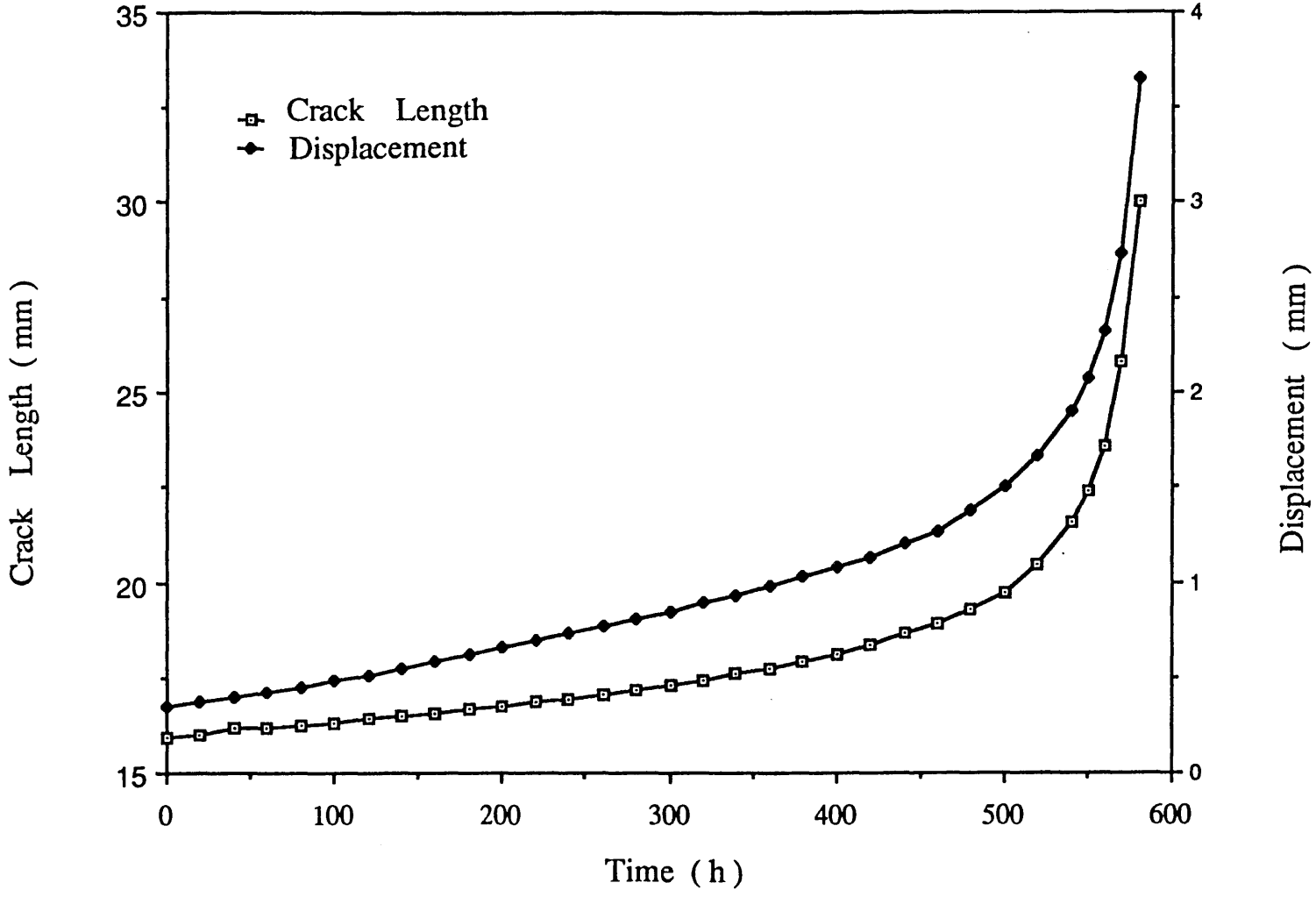


Figure 8.11 Crack growth and displacement versus time for 304H aged stainless steel , for constant load and 760° C.

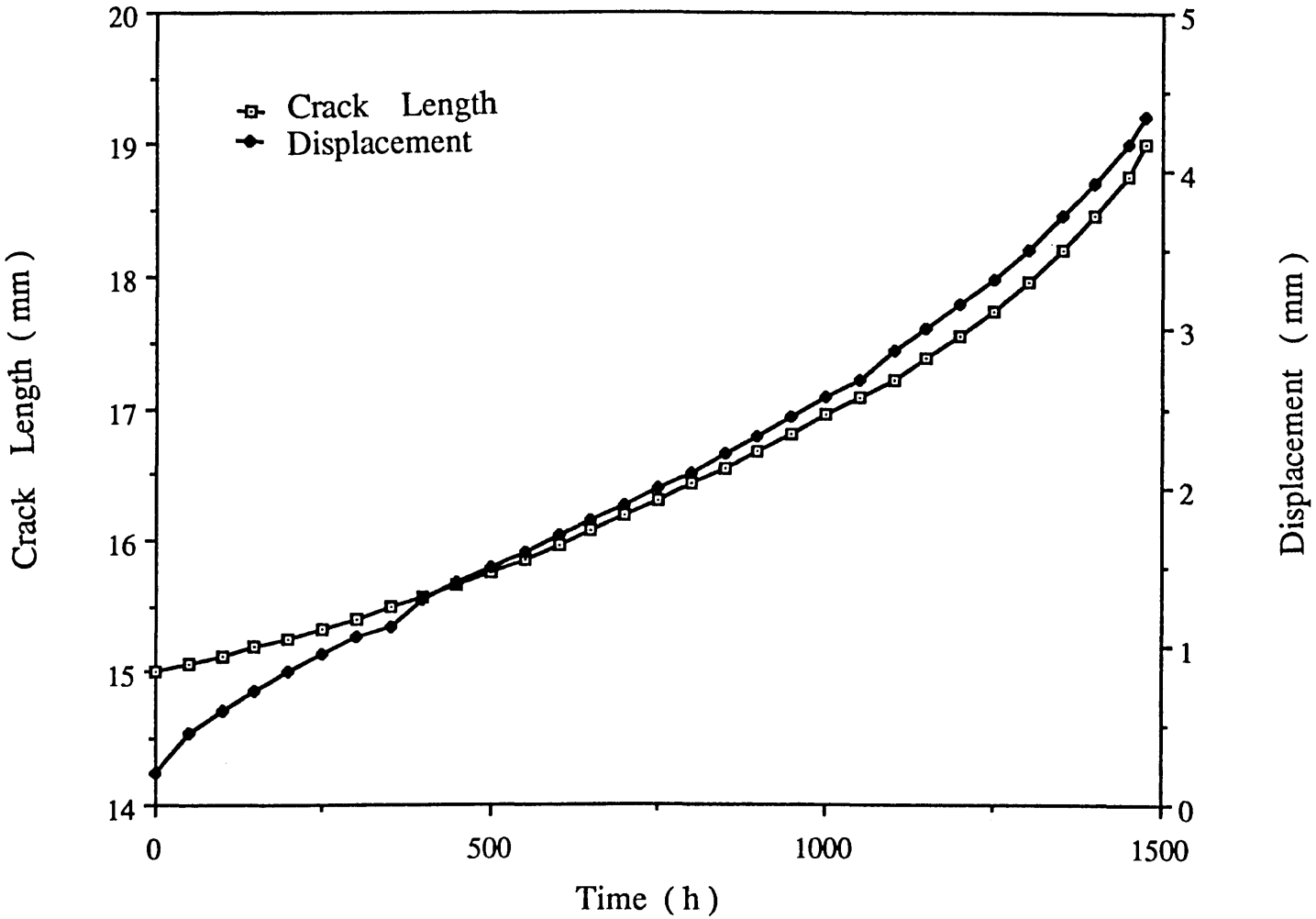


Figure 8.12 Crack growth and displacement versus time for 304H new stainless steel , for constant load and 760° C.

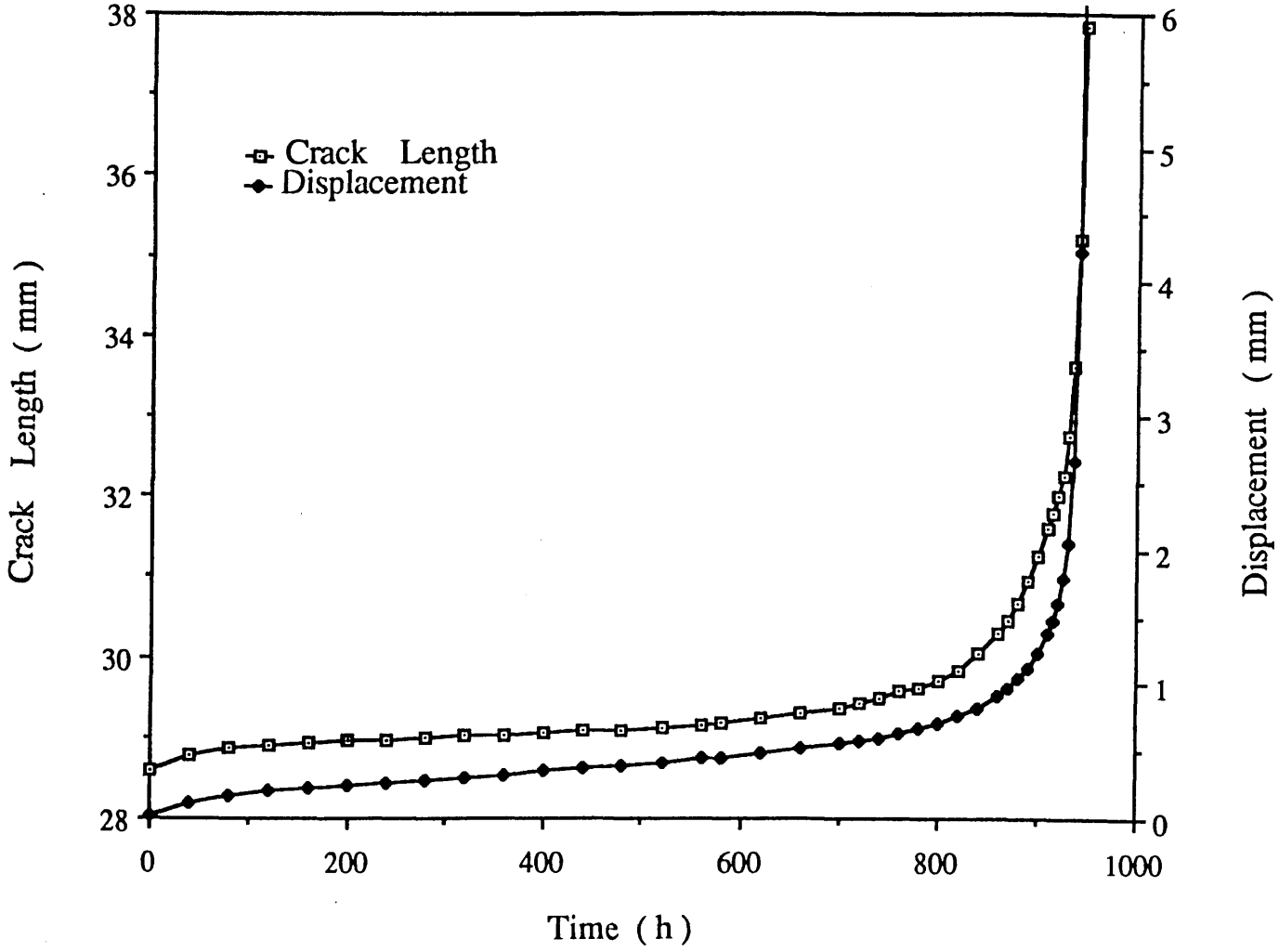


Figure 8.13 Crack growth and displacement versus time for 800H superalloy, for constant load and 800° C.

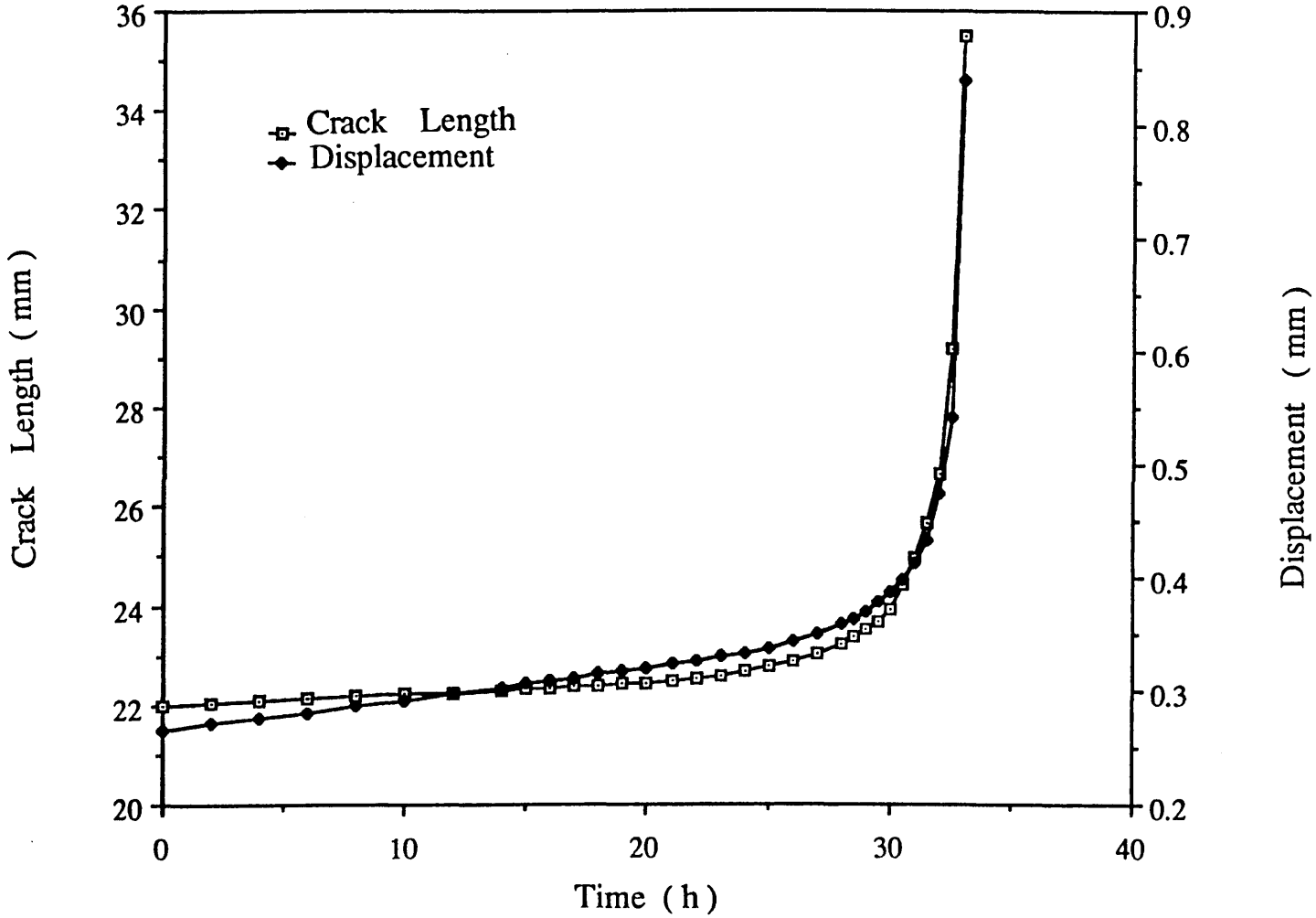


Figure 8.14 Crack growth and displacement versus time for 1/2 CMV steel , for constant load amplitude cycling at R=0.1 , f = 0.1Hz and 565° C.

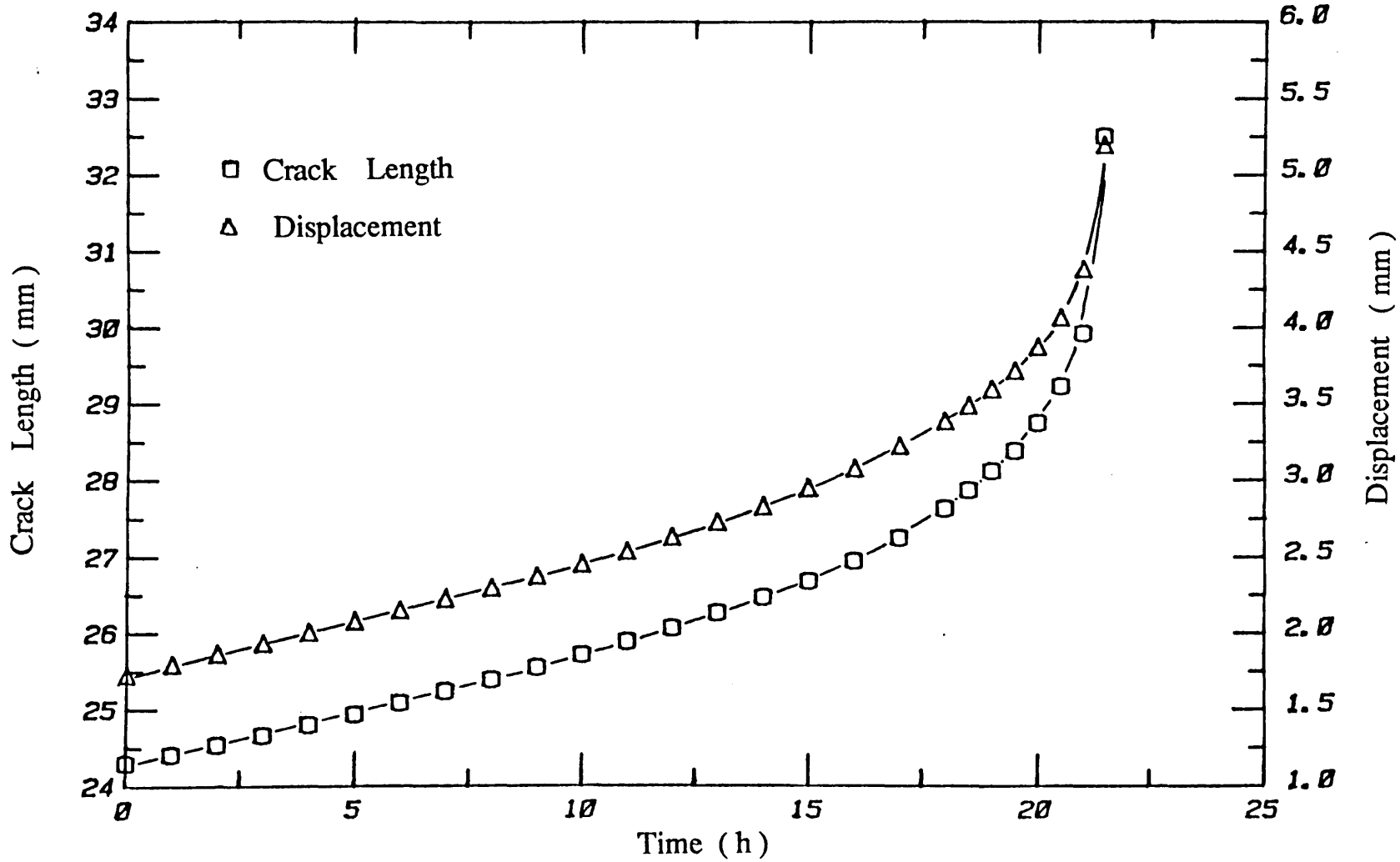


Figure 8.15 Crack growth and displacement versus time for 21/4 CM steel , for constant load amplitude cycling at R=0.8 , f = 10Hz and 538° C.

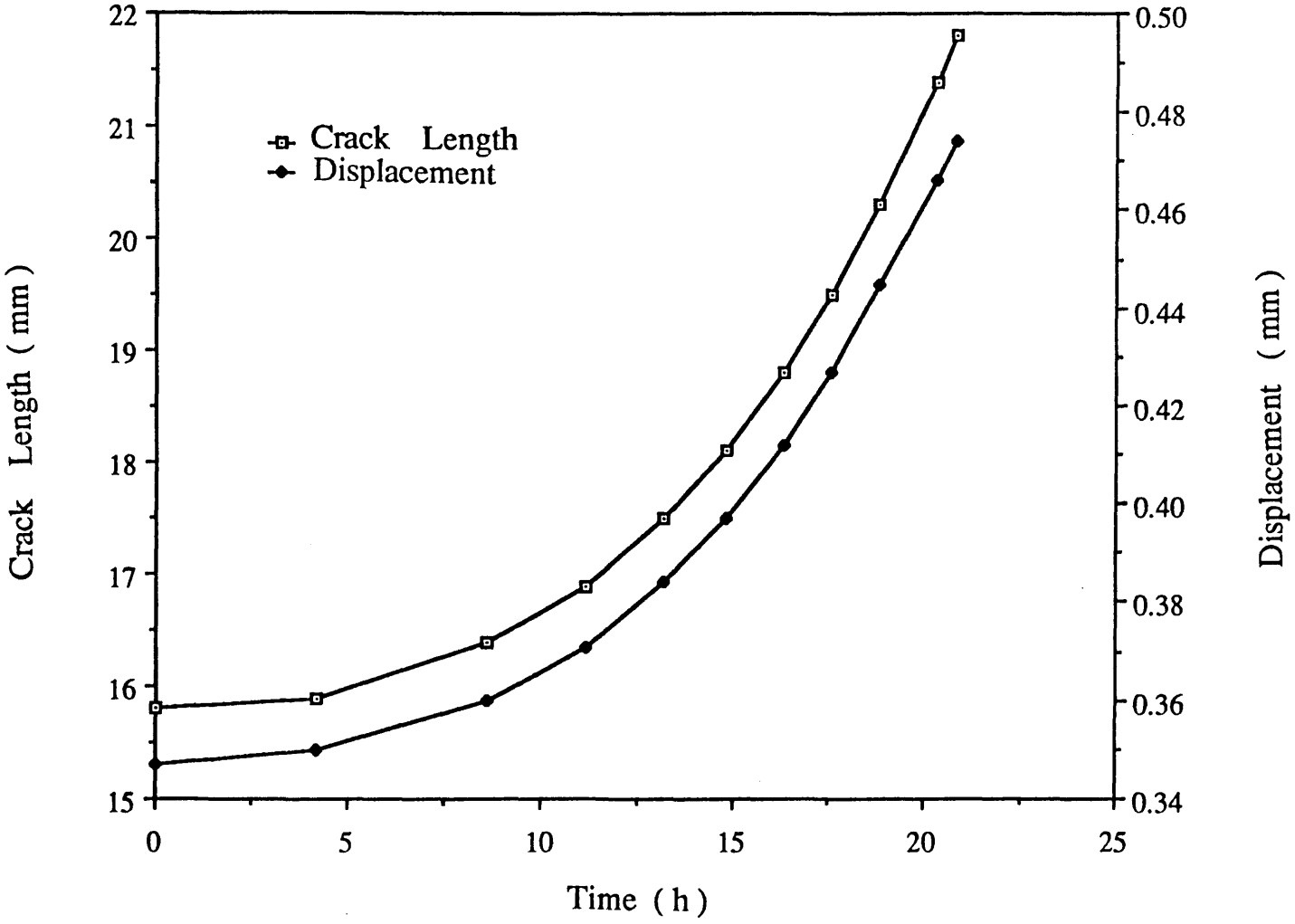


Figure 8.16 Crack growth and displacement versus time for AP1 superalloy , for constant load amplitude cycling at R=0.1 , f = 10Hz and 700° C.

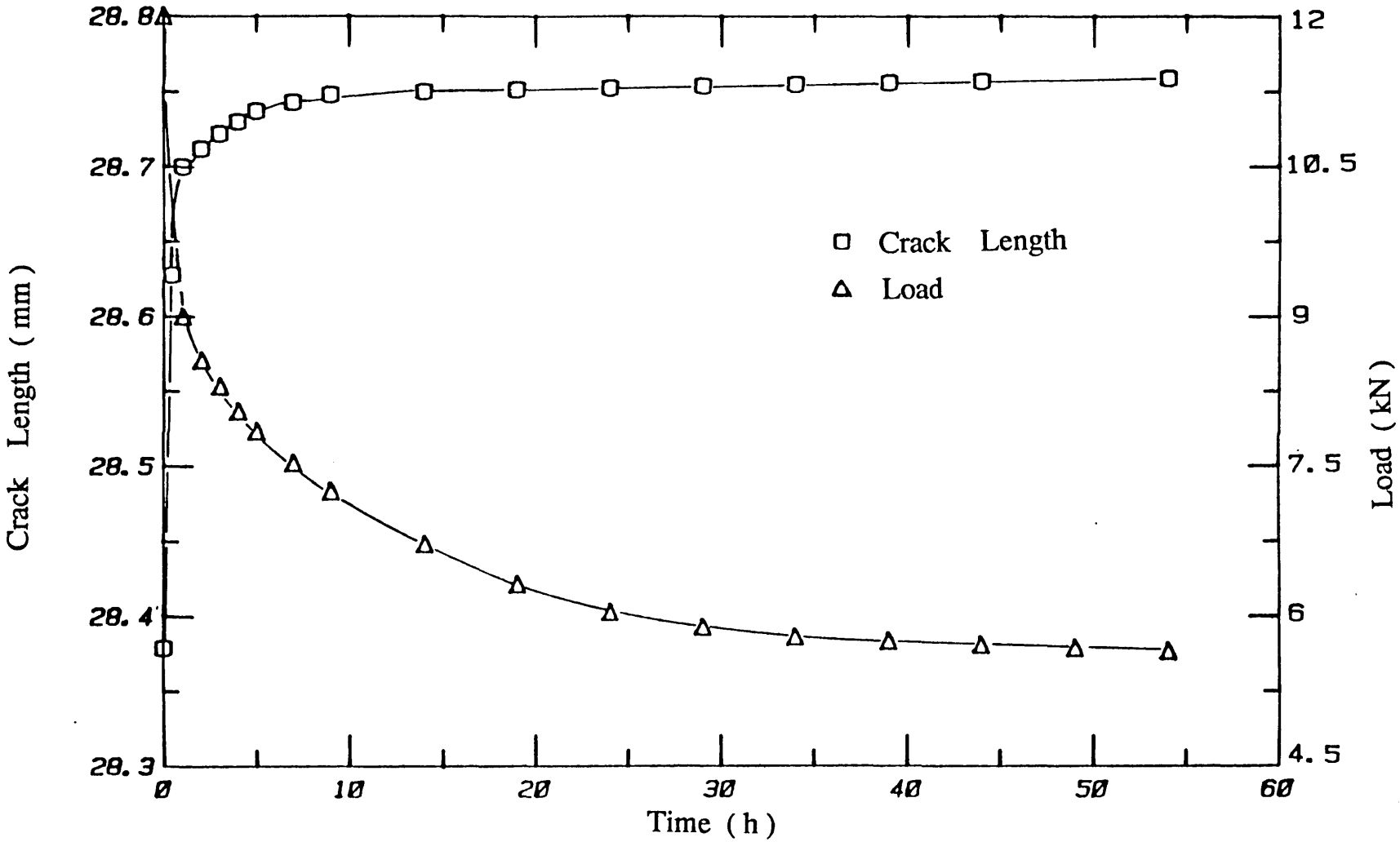


Figure 8.17 Crack growth and load relaxation for 21/4 CM steel , for constant displacement amplitude cycling at R=0.8 , f = 0.001 Hz and 538° C.

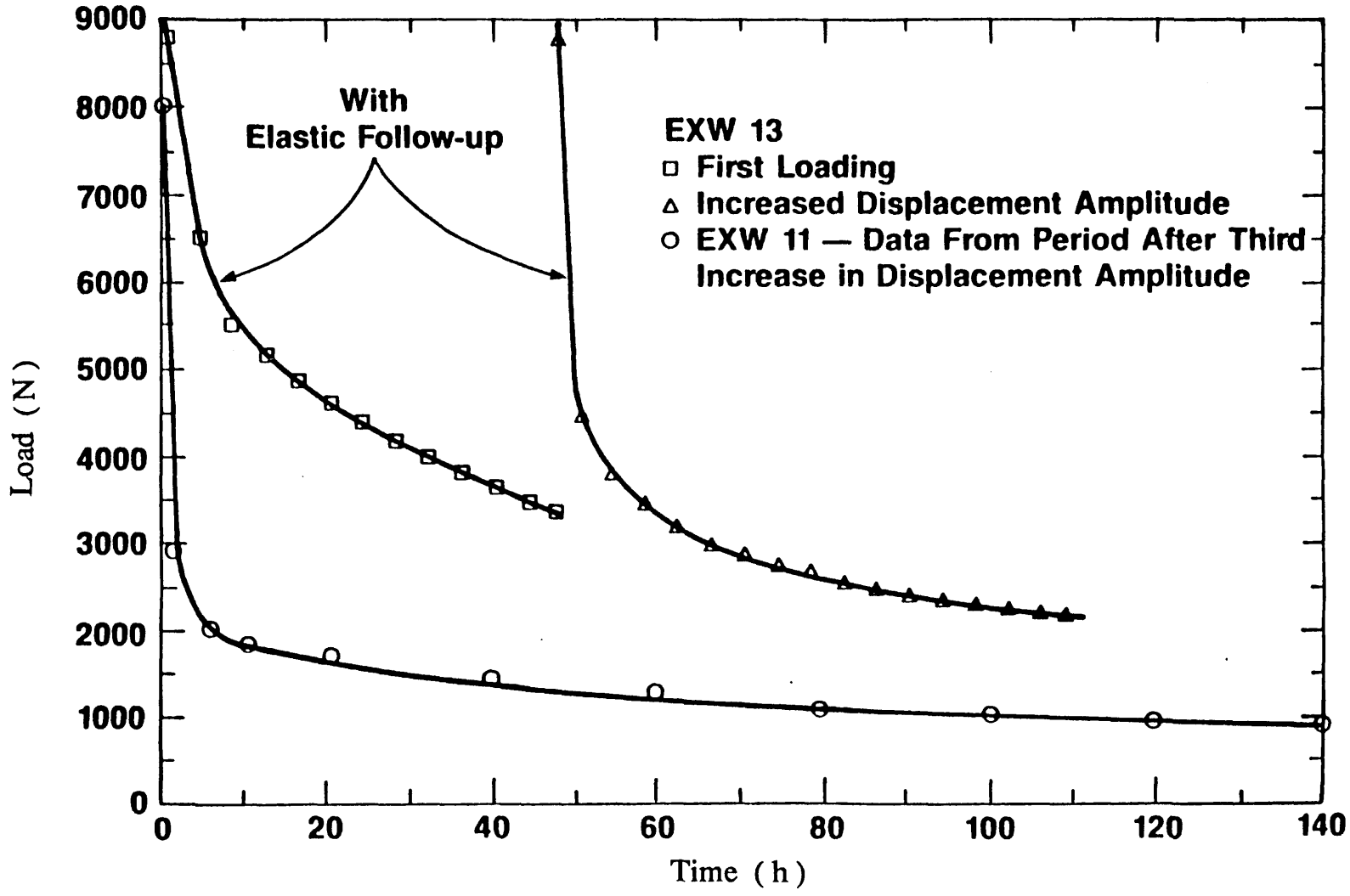


Figure 8.18 Load relaxation for 304H stainless steel , for constant displacement amplitude cycling at $R = 0$, $f = 0.001$ Hz and 760° C.

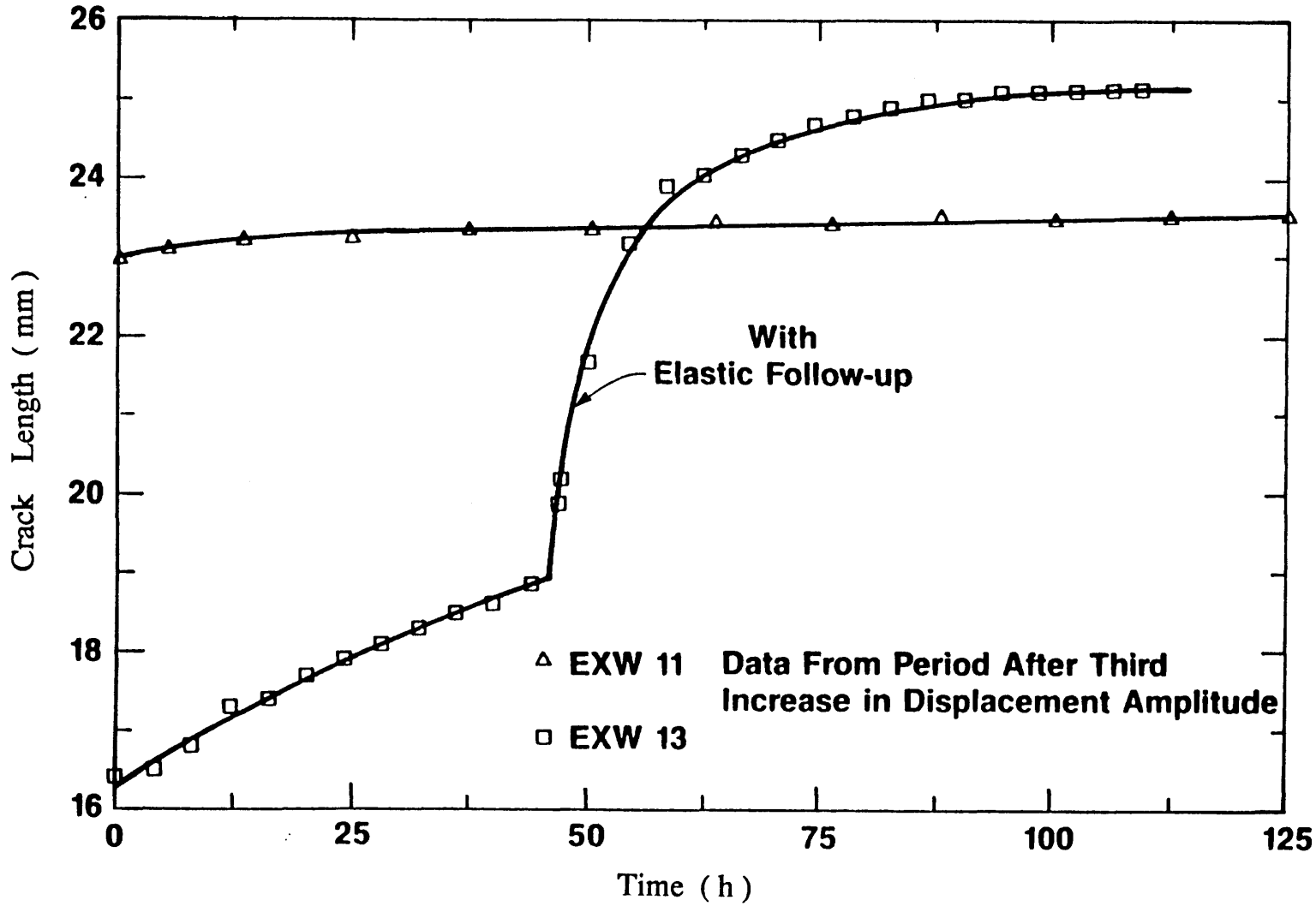


Figure 8.19 Crack growth for 304H stainless steel , for constant displacement amplitude cycling at R = 0 , f = 0.001 Hz and 760° C.

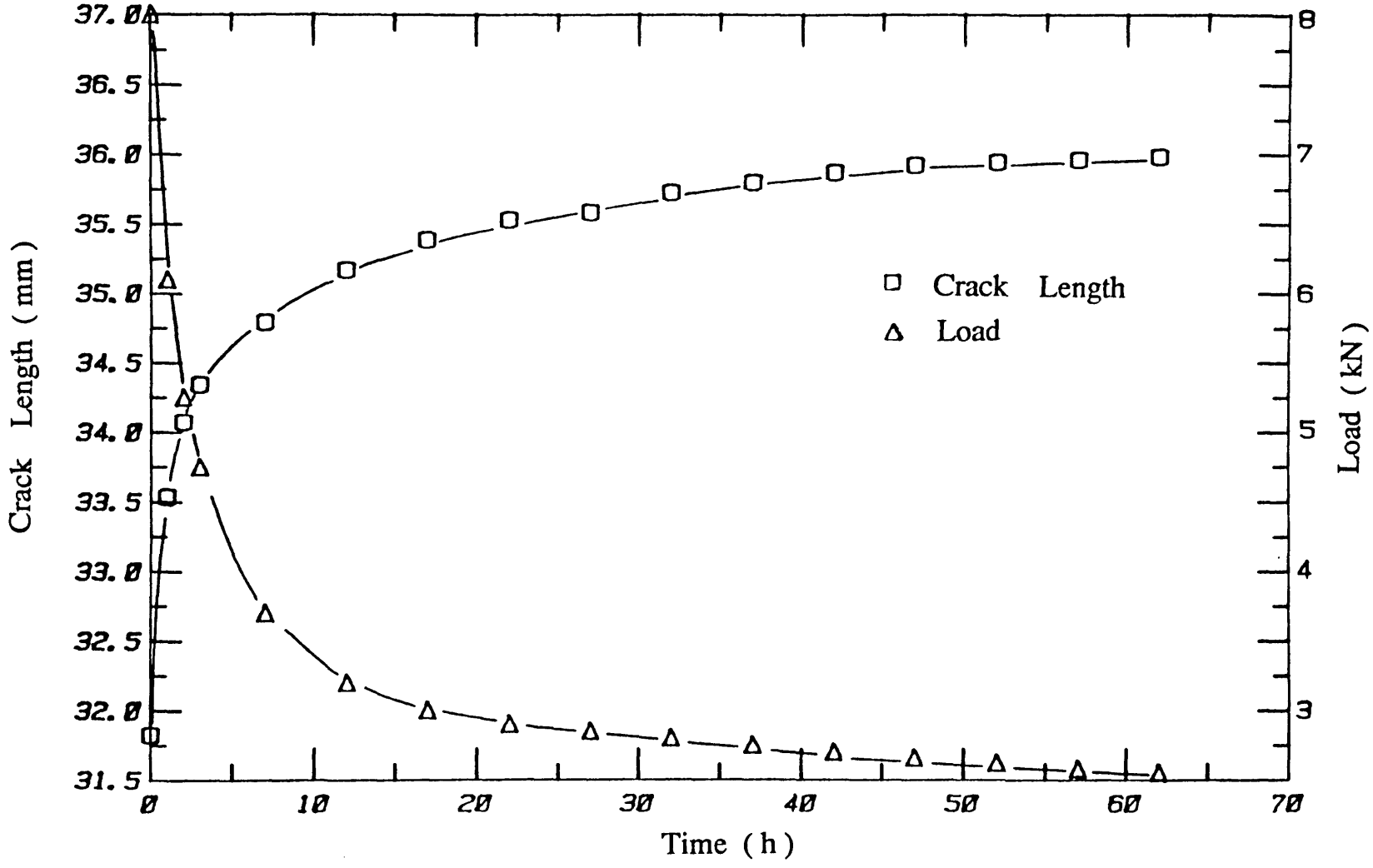


Figure 8.20 Crack growth and load relaxation for 1/2CMV steel , for constant displacement amplitude cycling at R=0.8 , f = 0.001 Hz and 565° C.

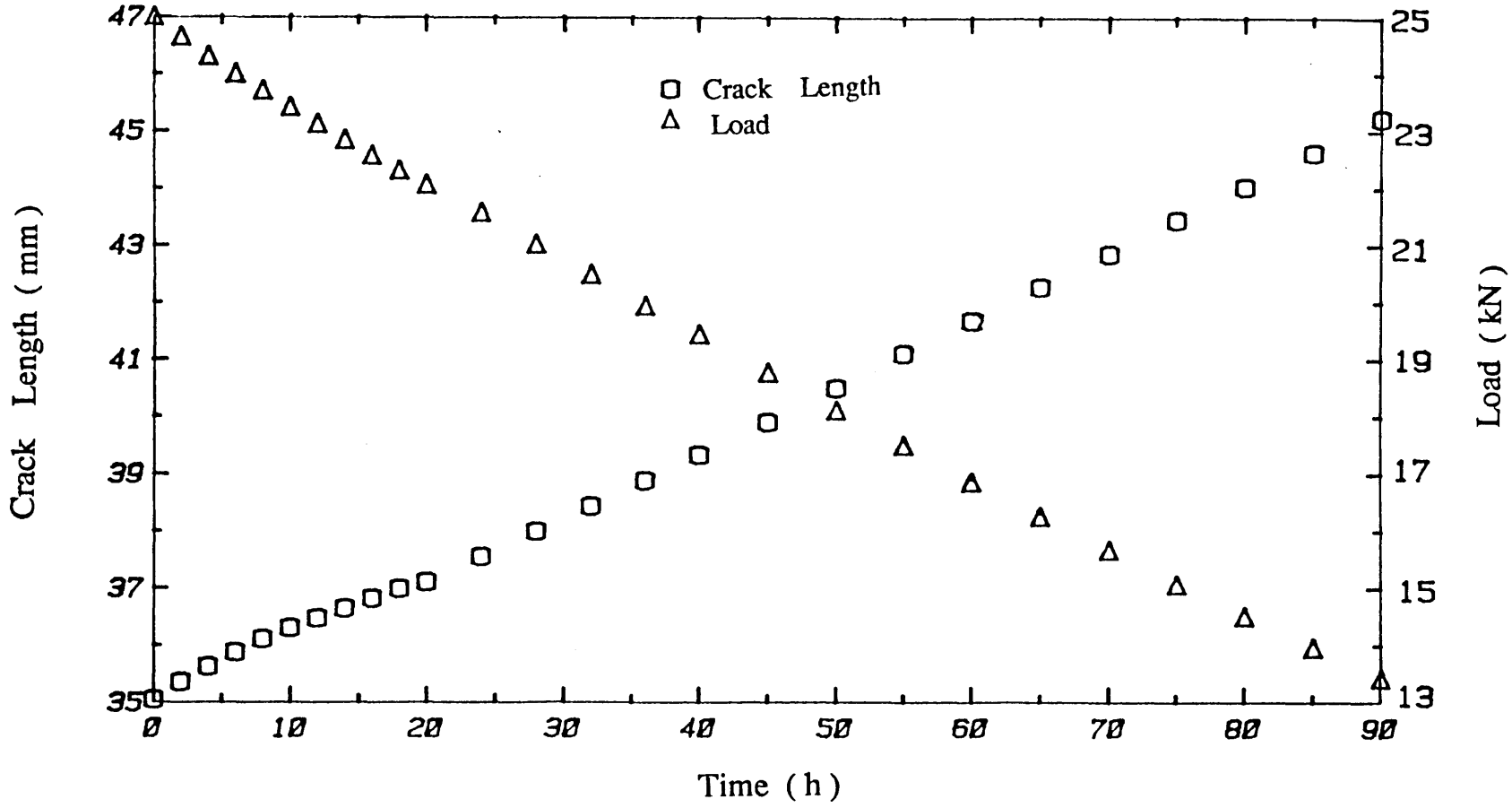


Figure 8.21 Crack growth and load relaxation for AP1 superalloy , for constant displacement amplitude cycling at R=0.7 , f = 0.1 Hz and 700° C.

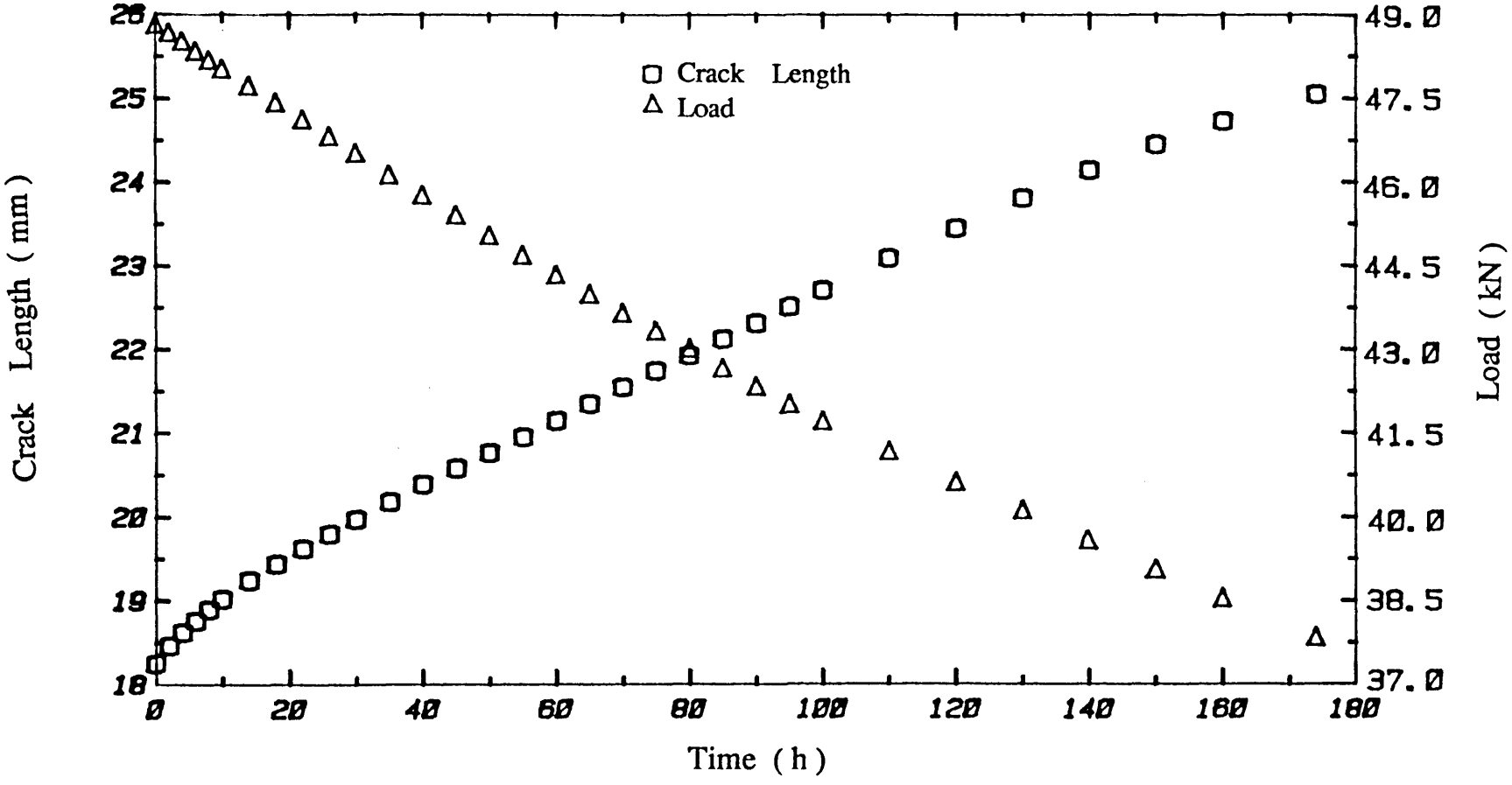


Figure 8.22 Crack growth and load relaxation for AP1 superalloy , for constant displacement amplitude cycling at R=0.7 , f = 0.01 Hz and 700° C.

APPENDIX 8A

EFFECT OF SIDEGROOVING ON THE C* DISTRIBUTION IN THE CRACK FRONT

Delorenzi and Shih (1983), did an elasto-plastic analytical comparison of a standard and a sidegrooved CT specimen with 25% sidegrooves. Both specimens were analysed using 3-D finite element techniques in the elastic regime as well, as under small scale and large scale yielding conditions, for a value of the strain hardening parameter N=10. The large scale yielding results can be used as steady state creep results if N is replaced with n, and the displacements replaced with their rates.

In the case of the standard CT specimen, the energy release rate in the elastic regime is about 1.7 times greater at the centre than at the side. In the large yielding regime, the energy release rate is 6.2 times higher at the centre than in the side. This non uniform distribution clearly indicates that even for moderate amounts of creep deformation, a critical value for the energy release rate or C* integral, will be reached at the centre, long before the sides or edge of the specimen. This suggests that the crack will propagate at the centre faster than in the edge of the specimen resulting in a tunneling mode of crack propagation, with the sides of the specimen finally failing in shear.

The side-grooved specimen has a more uniform distribution of the energy release rate. The elastic distribution peaked at the side grooves, but this peak decreases for increasing creep deformation and drops below the value at the centre for very large deformations. For moderate amounts of creep deformation the overall variation is very uniform. So for the side-grooved specimen the energy release rate would therefore reach the critical value almost simultaneously all along the crack front, and thereby promote a uniform crack front.

These numerical results are in agreement with the tests made on CT specimens in this thesis. For the static and low frequency creep tests conducted on the AP1

superalloy, where side-grooves were not introduced, there was significant tunneling, but for the remaining materials, where side grooves were introduced there was not significant tunneling.

CHAPTER 9

THE FINITE ELEMENT AND BOUNDARY INTEGRAL EQUATION PROGRAMS, AND, NUMERICAL RESULTS

9.1 DESCRIPTION OF THE FINITE ELEMENT PROGRAM

For a full descriptive see Al-Faddagh (1983). The main points of the program are.

9.1.1 RELATIONSHIP BETWEEN STRESS AND STRAIN

The constitutive equation used is the non-linear hardening law

$$\varepsilon = B\,\sigma^{N} \qquad (9.1)$$

Since this law is very similar to the secondary creep law

$$\dot{\varepsilon}_c = C\,\sigma^{n} \qquad (9.2)$$

the program can be used to solve both steady state creep and fully plastic problems. The only difference is that for the creep case the strains calculated from the F.E. analysis must be read as strain rates. An effective modulus is defined for the material as explained in section 6.3.2(b) as

$$E' = E_0 \left[\frac{\bar{\varepsilon}}{\bar{\varepsilon}_0} \right]^{\frac{1}{n}-1} \qquad (9.3)$$

Note that when $n=1$, $E'=E_0$ so that the program can be used for linear analysis too. This feature was used to calculate the stress intensity factors of the specimens considered. For values of $n > 1$, E' is a function of the local state of strain so it varies from point to point.

9.1.2 ITERATIVE PROCEDURE

For a material with non-linear elastic properties, i.e. for a material where the stiffness is a function of the displacement

$$[F] = [K][\Delta]$$

but $$[K] = [K(\Delta)] \qquad (9.4)$$

The elastic property matrix [D] is now a function of the strain and hence the displacement. Several techniques may be used to solve the non-linear problems, namely

(i) incremental.

(ii) iterative, either tangent or secant stiffness.

(iii) initial strain, coupled with either an incremental or iterative procedure.

(iv) initial stress.

Full description of the methods is given by Desai and Abel (1972). Al-Faddagh (1983) compared the incremental and secant-stiffness iterative methods and chose the latter to solve the non-linear equations in the F.E. program.

The secant-stiffness iterative method proceeds directly to the steady state solution as illustrated in figure 9.1. First a constant stiffness is employed to obtain a temporary solution, using the Gauss-Seidel iterative method, each step being known as inner iteration. Then this solution is used to modify the stiffness for each element i.e. to find a temporary value for the effective modulus of each element. The new stiffness is used to obtain another temporary solution which is used, in turn, to find another stiffness. The same procedure is repeated until convergence has occurred to a prescribed tolerance. Each step to make up the non-linear analysis is known as outer iteration.

9.1.3 CONVERGENCE TO SOLUTION

Each time the stiffness is modified it can cause a large change in the solution. So the temporary solution does not need to converge to a fine tolerance, because this accuracy will be lost in the next iteration. So it is needed to have either a coarse tolerance between outer iterations and fine tolerance only at the last outer iteration or, as it was selected in the present F.E. program, a prescribed number of inner iterations for every outer iteration.

The F.E. program has the following definition for convergence. The number

of inner iterations for every outer iteration is either the number of iterations required to the prescribed tolerance or, a maximum number of iterations whatever is achieved first. The program has converged if only one inner iteration is required for convergence of the temporary solution. Convergence of the solution occurs when a value known as displacement vector is less than the prescribed tolerance. The displacement vector is defined as

$$\frac{\sum_{n=1}^{i}\left[\,|\delta u_i|+|\delta v_i|\,\right]}{\sum_{n=1}^{i}\left[\,|u_i|+|v_i|\,\right]} \qquad (9.5)$$

where u_i and v_i are the nodal displacements of the node i and δu_i, δv_i the changes in these displacements between successive iterations.

It should be noted that it is necessary using the present finite element program, to specify sufficient boundary conditions to preclude rigid body motion. If only force boundary conditions are specified then even though the external forces are in equilibrium the displacements are indeterminate, and attempts to solve such a problem will result in failure.

9.1.4 NUMERICAL DETERMINATION OF C*

When convergence has occurred, the data identifying the nodes around the contour paths and the elements that surround the nodes are read into the program. The strains and hence the stresses from the known displacements, at each node on the path are then calculated, and, the data for each node are written to a data file which is made available to subroutine CONTOUR. The method for determining C* from the available data is as follows.

Hayes (1970) rewrote the second term in equation (4.17) to give the following expression for J.

$$J = \int_{\Gamma} \left[W - \sigma_{xx} \frac{du}{dx} - \sigma_{xy} \frac{dv}{dx} \right] dy$$

$$+ \int_{\Gamma} \left[\sigma_{yy} \frac{dv}{dx} + \sigma_{xy} \frac{du}{dx} \right] dx \qquad (9.6)$$

where W is the strain energy density given by (4.18). In analogy to J and following the same arguments as in section 5.2.1 for the definition of the C* integral, equation (5.3) may be written as

$$C^* = \int_{\Gamma} \left[W^*_s - \sigma_{xx} \frac{d\dot{u}}{dx} - \sigma_{xy} \frac{d\dot{v}}{dx} \right] dy$$

$$+ \int_{\Gamma} \left[\sigma_{yy} \frac{d\dot{v}}{dx} + \sigma_{xy} \frac{d\dot{u}}{dx} \right] dx \qquad (9.7)$$

where W^*_s the strain energy rate can be expressed for two dimensional problems as

$$W^*_s = \frac{n}{n+1} (\sigma_{xx} \dot{\varepsilon}_{xx} + \sigma_{yy} \dot{\varepsilon}_{yy} + \sigma_{xy} \dot{\varepsilon}_{xy}) \qquad (9.7a)$$

Equations (9.7) and (9.7a) may be used to calculate C* from the nodal data supplied by the finite element analysis. The path used to evaluate the integral is taken from node to node around the crack tip. Values for the required parameters as well as the coordinates of the nodes are provided by the finite element analysis. If $p + 1$ nodes are used to define a contour path then equation (9.7) may be written as

$$C^* = \sum_{1}^{p} \left[W^*_s - \sigma_{xx} \dot{\varepsilon}_{xx} - \sigma_{xy} \frac{d\dot{v}}{dx} \right] \delta y$$

$$+ \sum_{1}^{p} \left[\sigma_{yy} \frac{d\dot{v}}{dx} + \sigma_{xy} \dot{\varepsilon}_{xx} \right] \delta x \qquad (9.8)$$

as from definition $\dot{\varepsilon}_{xx} = \frac{d\dot{u}}{dx}$

In equation (9.8) $dx = x_i - x_{i+1}$, and, $dy = y_i - y_{i+1}$, where suffices i, i+1 refer to the nodes i and i+1 of a line segment along the contour path. Many

different paths may be used for estimating C*, so the path independence on C* may be determined.

A self explanatory flowchart of the finite element program is shown in figure 9.2.

9.2 THE FINITE ELEMENT MESH GENERATION

A major source of errors when running finite element programs is incorrect element data. The preparation of the element data can be a time consuming task too. However programs are available that can automatically generate the element data required. The mission of a mesh generation program is to locate the node points within a region and then subdivide the region into elements.

The mesh generation program used in the present research was reported by Segerlind (1976). This program uses a group of eight-node quadrilateral regions to define the body under consideration. It is capable of modeling two-dimentional domains that are composed of rectangles and triangles having second order curved boundaries. The only region available is the quadratic quadrilateral. However this region is quite versatile, and it can be used as rectangle, general quadrilateral or as a triangle as shown in figure 9.3. Two sides of the quadrilateral are used to define one side of a triangular region. The eight nodes that define the region are numbered as in figure 9.4. Node 1 is always at location $\xi=\eta=-1$ and the other nodes are numbered in a counterclockwise way. Five functions are performed when each quadrilateral region is considered.

(1) The number of rows and columns of nodes are defined according to input data.

(2) A check is made to determine whether any of the boundary nodes have been numbered previously. If the check is positive, the nodes on the labeled boundary are given values identical to the previous ones.

(3) The nodes are numbered in a sequence that starts at $\xi=-1$, $\eta=+1$ and proceeds from left to right ($\xi=-1$, $\xi=+1$) and from top to bottom ($\eta=+1$, $\eta=-1$).

All previously numbered nodes are skipped.

(4) All nodes on the boundaries are stored for future reference when considering regions that are adjacent to the region under consideration.

(5) The region is subdivided into triangular elements, and each element is numbered.

The region is subdivided into elements by considering four nodes that form a quadrilateral such as the area in figure 9.5. The length of the two diagonals are calculated and compared. Then the elementary quadrilateral is subdivided into triangular elements using the shortest diagonal. A body or domain can be modelled using several quadrilateral regions connected to each other along one or more sides. The possibility of a common boundary between two regions requires that certain information be provided, to ensure that the nodes on the this common boundary have the same numbers regardless of which region is being considered. Identical numbers are assured by what is called the "connectivity data". The connectivity data convey to the computer how the region under consideration is connected to the other regions. For a single region the connectivity data consist of four numbers one for each side. Each number is the number of the region connected to a particular side. The sides of the quadrilateral region are labeled as shown in figure 9.4, side 1 is between nodes 1 and 3 side 2 between nodes 3 and 5 and so-forth.

9.2.1 INPUT DATA FOR THE FINITE ELEMENT MESH GENERATION ROUTINE

The input data for GRIDAX can be subdivided into five classifications. A title card, a parameter card, the x and y coordinates of the defining nodes for the quadrilateral regions, the connectivity data, and the region data.

(1) The title card is a descriptive statement that is printed on the top of the pages of output for identification purposes.

(2) The parameter card contains four pieces of information.

INGR = The number of regions

INBP = The number of boundary points

IPCH is a punch option for saving the element data in a file

MOUT is a write option for outputting the element data

(3) The coordinate data card. The x and y coordinates are read separately. All the x coordinates are input first and then all the y coordinates.

(4) The connectivity data card. The card contains the numbers of the regions that are connected to the four sides of the region.

(5) The region data card. Here care must be taken so that the quadrilaterals with a common side have the same number of columns in the common side.

9.2.2 MODELLING THE CRACK TIP.

Due to the presence of an infinitely sharp crack very steep stress and strain gradients are produced in the region near the crack tip. In order to produce an accurate model using constant strain triangles as the finite elements, it is necessary to refine the size of the elements near the crack tip.

It is possible to vary the size of the elements by placing nodes 2,4,6,8 in figure 9.6 at some point other than the midpoint of the side. For example, if very fine elements near node 1 of the quadrilateral region are required, this can be achieved by placing nodes 2 and 8 nearer to node 1 than to nodes 3 and 7 (see figure 9.6) However these mid side nodes must remain within the interval

$$-1/2 < \xi < 1/2 \quad \text{or} \quad -1/2 < \eta < 1/2$$

Chan et al. (1970) studied the effect of element size in the accuracy of the finite element analysis in cracked bodies and their results show an indication of the element size required around the crack tip, and throughout the rest of the body. They concluded that the finer the crack tip elements, the more accurate the solution is. However the computational cost increases when finer elements are used, so to avoid

high computational costs, the mesh refinement must be just sufficient for the accuracy required. The meshes used in this study were not very fine, because of the intention to calculate contour integrals rather than the stress intensity factor K. C* and J are path independent, so they may be calculated along paths which are away from the crack tip, i.e. in regions where the stress and strain fields are more accurately known (Hyde et. al. (1983)).

9.3 DESCRIPTION OF THE BOUNDARY INTEGRAL EQUATION PROGRAM

The formulation used in the present B.I.E. program was presented in section 6.4. For a full descriptive of the program see Lee (1983). The main points of the program are.

9.3.1 SOLUTION PROCEDURE

The solution procedure employed in the analysis can be best described by means of flowcharts. The program may be conveniently divided into four sections. The program organization for the first two sections is depicted by the flowchart in figure 9.7. The first section is solely concerned with the input of data and the subsequent processing and checking of the data. Thus, the subroutine DATA requires the specification of the type of the problem to be solved (that is, with or without body forces and/or temperature conditions, plane strain or plane stress). The input of material properties and other relevant data such as the number of integration points is also performed here. It also controls the subroutines for the input of data defining the geometry of the problem, namely, the cartesian/polar coordinates of the boundary and interior nodes, and the number of nodes belonging to the individual boundary and interior elements. BCOND is next responsible for the specification of the various types of boundary conditions, after which BPOC processes and checks the prescribed conditions to ensure that a problem

with a unique solution has been posed.

The second section primarily determines the initial elastic solution to the problem and prepares the elastoplastic solution procedure. SET and SIZE are first used to initialise the arrays that are needed for the accumulation of data, and to compute the optimum sizes of the matrices which are utilized for the transmission of the data between the central memory and the mass storage files. MAT1 next sets up the elastic integral equations and obtains the coefficient matrix and the elastic second member after the application of the imposed boundary conditions. The out-of-core solver in SOLVE is then employed to provide the elastic solution of the problem. Following the calculation of the elastic stresses at the boundary and interior nodes by STRESS1 and STRESS2, the level of loading required to initiate yielding is determined in YIELD. This subroutine also sets the sizes of subsequent load-steps and scales down the initial elastic solution to the values at the onset of yielding which are next printed by RESULT1.

Before the incremental part of the solution procedure is implemented in INCREM, all the matrices arising from the elastoplastic equations need to be evaluated. This is the responsibility of MATRIX which calls a group of subroutines that are located in the third section of the program. After the load-step has been applied by INCREM, the iterative procedure commences in ITERATE. This latter subroutine basically controls the program flow through the various subroutines belonging in the fourth section. If the iterations are successful, the converged elastoplastic results are printed out by RESULT2. Before proceeding to the next load step, LOAD conducts a check on the number of iterations for the current step and if it exceeds a predetermined value, the sizes of the subsequent steps are suitably reduced. Execution is halted after full loading conditions have been reached, unless an analysis of unloading or cyclic loading is required. In the latter case, appropriate sign changes in the boundary conditions are made in RESIGN and control thereafter reverts to YIELD where the new reyield load is computed. The whole elastoplastic solution process is then repeated as many times as necessary.

Figure 9.8 shows a self-explanatory flowchart for the evaluation of the matrices which are utilized repetitively during the iterations. Note that MAT4 may be alternatively used to set up the matrix for the calculation of strain rates instead of stress rates. With the exception of the calling subroutine MATRIX, all the subroutines that are listed have been placed in the third section of the program.

The subroutines involved in the iteration loop are given in Figure 9.9. The roles of the individual subroutines in this fourth section of the program are clearly defined in the flowchart.

9.3.2 CONVERGENCE CRITERIA

To ensure that a prescribed standard of accuracy is attained before the iterations are terminated, it is necessary to provide some tests in the iterative procedure. Four criteria have been incorporated in the algorithm and can be used jointly or separately. These criteria concern the vector $\dot{\underset{\sim}{z}}$ of the primary unknowns of the problem and the plastic strain rates $\dot{\underset{\sim}{\varepsilon}}^{p}_{ij}$ which act as the secondary unknowns. The four criteria are:

(i) Norm of changes in $\dot{\underset{\sim}{z}}$. At each iteration, the changes $\Delta\dot{\underset{\sim}{z}}$ are calculated from the current and previous values of $\dot{\underset{\sim}{z}}$ and the results are assumed to have converged if the norm defined as

$$|| \Delta\dot{\underset{\sim}{z}} || = \Delta\dot{\underset{\sim}{z}} \cdot \Delta\dot{\underset{\sim}{z}} \qquad (9.9)$$

is less than either a specified absolute value or a specified percentage in the norm of $\dot{\underset{\sim}{z}}$.

(ii) Norm changes in $\dot{\underset{\sim}{\varepsilon}}^{p}$. In a similar manner, the norm of the changes $\Delta\dot{\underset{\sim}{\varepsilon}}^{p}$ is computed from

$$|| \Delta\dot{\underset{\sim}{\varepsilon}}^{p} || = \Delta\dot{\underset{\sim}{\varepsilon}}^{p} \cdot \Delta\dot{\underset{\sim}{\varepsilon}}^{p} \qquad (9.10)$$

and compared with a specified absolute value or a specified percentage of the norm of $\dot{\underset{\sim}{\varepsilon}}^{p}$.

(iii) Magnitude of changes in $\dot{\underset{\sim}{z}}$. With this criterion the absolute value of the

largest term in $\Delta\underset{\sim}{\dot{z}}$ or the largest percentage change in the individual terms of $\underset{\sim}{\dot{z}}$ is found and compared with a value specified a priori.

(iv) Magnitude of changes in $\underset{\sim}{\dot{\varepsilon}}^p$. In this case, the absolute value of the largest term in $\Delta\underset{\sim}{\dot{\varepsilon}}^p$ or the largest percentage change in the individual terms of $\underset{\sim}{\dot{\varepsilon}}^p$ is checked with a specified value to determine whether convergence has been achieved.

While absolute changes are sometimes used in the criteria, it is evidently simpler to employ percentage changes because the value which is prescribed for comparison purposes does not depend on the units of the problem. Typical values for percentage changes lie between 0.001% and 0.01% for the first two criteria and between 0.1% and 1% for the last two.

9.3.3 BOUNDARY INTEGRAL EQUATION MESH GENERATION.

All B.I.E. meshes were generated manually. However the work involved in a B.I.E. mesh generation was less than the work needed for the mesh generation of the corresponding F.E. mesh, even when a mesh generation routine is used for the generation of the F.E. mesh. In the present formulation three types of elements were used. The boundary is divided into three-noded line elements (figure 9.10), and the discretised part of the interior is represented by eight-noded quadrilaterals and six-noded triangles as illustrated in figure 9.11.

For a boundary element, the geometry is defined in terms of quadratic shape functions of an intrinsic coordinate, ξ, which varies from -1 to +1 along the element. If $x_i(\xi)$ denote the Cartesian coordinates of a point on such an element, then

$$x_i(\xi) = M^c(\xi)\, x_i^c \quad ; \; c = 1 \text{ to } 3 \qquad (9.11)$$

where $M^c(\xi)$ are the shape functions, and x_i^c are the Cartesian coordinates of the cth node.

For quadrilateral elements the geometry is governed by quadratic shape functions $N^f(\xi)$ of two intrinsic coordinates, ξ_1 and ξ_2, both which vary from -1 to +1. Thus

$$x_i(\xi) = N^f(\xi)\, x_i^f \quad ; f = 1 \text{ to } 8 \qquad (9.12)$$

When triangular elements are used, the geometry is expressed by quadratic shape functions of three intrinsic coordinates, ξ_1, ξ_2 and ξ_3, all of which vary from 0 to +1 over each element, and

$$x_i(\xi) = N^f(\xi)\, x_i^f \quad ; f = 1 \text{ to } 6 \qquad (9.13)$$

Only two of the intrinsic coordinates can be considered as dependent of each other, and the third is found from the following relation

$$\xi_1 + \xi_2 + \xi_3 = 0 \qquad (9.14)$$

It should be noted here (see Lee (1983)), that with the present method, the perpendicular distance between the variable point p of the interior and the nearest boundary element should preferably not be less than half of the length of the same boundary element, otherwise this may result in inaccurate estimates of the field parameters evaluated at that point.

9.4 NUMERICAL RESULTS AND DISCUSSION

9.4.1 GEOMETRIES

To check the accuracy of the numerical results, the F.E.and B.I.E. procedures were first applied to a standard compact tension specimen containing a crack of relative length a /W=0.5, and comparisons made with other calculations in the literature by Kumar et al. (1981).

Having establish the accuracy of the numerical procedures, calculations were performed for cracks emanating from blunt holes to represent behaviour adjacent to a stress concentration. A compact tension specimen was adapted for comparison with experimental data already available on this test-piece geometry (Morzeria (1979)).

Further calculations have been made for a rotating disc containing a central hole only, and, for a disc containing a central hole and six satellite holes, equally spaced around a constant radius.

9.4.2 NUMERICAL RESULTS FOR THE STANDARD COMPACT TENSION SPECIMEN

(a) FINITE ELEMENT ANALYSIS

Figure 9.12 shows the finite element mesh employed for the analysis, on the standard compact tension specimen containing a relative crack length of a/W=0.5. For simplicity the pin hole was not included in the mesh design. Newman (1974) has investigated the effect of the pin hole on K. He found that for n=1 the effect is negligible for $a/W \geq 0.4$. For non linear materials ($n \geq 3$) and under fully plastic or creep conditions the deformation concentrates along the uncracked ligament. Thus it may be argued that for $n \geq 3$ the effect of the pin hole is negligible. Because of the symmetry of the compact tension specimen it is only necessary to model half of it. The missing half can be simulated by applying suitable boundary conditions.

The creep contour integral C*, has been calculated for different paths as shown in figure 9.13, for n = 1, 3, 5, 7, 10 and for both plane stress and plane strain conditions. The solutions were obtained with load P = 800 N/mm thickness, W=50mm, σ_0=500Mpa and $\dot{\varepsilon}_0$=1/h. The results are shown in figures 9.15 to 9.24. Excluding the shortest and longest paths (figure 9.13), path independence to within about ±2% is demonstrated. Also in these figures comparisons have been made with other calculations in the literature by Kumar et al. (1981). Considering the relative course mesh employed in the present analysis acceptable agreement is observed.

(b) BOUNDARY INTEGRAL EQUATION ANALYSIS.

Figure 9.14 shows the B.I.E. mesh employed for the analysis, on the standard compact tension specimen containing a relative crack length of a / W = 0.5. As for the F.E. analysis, because of the symmetry only half of the specimen is modeled and the missing half is simulated by applying suitable boundary conditions. Fully plastic (or steady state creep) solutions can't be obtained as the present program is suitable for elastic and elasto-plastic analysis, so direct comparison with the finite element method is only possible for the elastic (n=1) case.

Solutions for the C* contour integral are shown in figures 9.15 and 9.20 for plane stress and plane strain situations respectively. Values intermediate between those of Kumar et. al. (1981) and the finite element predictions were obtained. Excluding the shortest path, path independence to within about ±0.2% is demonstrated.

Although both the F.E. and the B.I.E procedures are mainly used throughout this thesis to obtain estimates of the creep contour integral C*, estimates of the stress intensity factor K can also be obtained from the n=1 solution, if stain rate is replaced by strain and ε_0/σ_0 is set equal to 1/E. Then the result will be an estimate for J instead of C* which in the elastic limit is K^2/E'.

9.4.3 FINITE ELEMENT ANALYSIS OF COMPACT TENSION SPECIMENS CONTAINING BLUNT HOLES

Having tested the accuracy of the finite element procedure in obtaining estimates of the creep contour integral C* (and the stress intensity factor K) the procedure was next applied on compact tension specimens containing blunt holes of the 1/2CMV material. Both crack initiation from the hole, and subsequent crack propagation in terms of the C* creep contour integral and the stress intensity factor were investigated, and, comparisons made with experimental data (Morzeria (1979)).

Holes sizes of 0, 3, 4, 6 and 9 mm in diameter in a compact specimen of width W=50 mm were considered. The holes were positioned to allow a crack to initiate at a value of a/W=0.31. The specimen and hole dimensions as well as the position of the holes were so chosen, so that direct comparison with Morzeria's (1979) experimental results can be made. The finite element meshes that have been developed for a crack close to the hole are shown in figures 9.25 to 9.29. A new mesh distribution had to be employed for cracks further away. These are shown in figures 9.30 to 9.34.

Application of the Nikbin et. al. (1983) crack growth model to the experimental 1/2CMV compact tension data (see figure 10.34), demonstrates that the data are closer to plane stress, than to plane strain conditions. Plane stress conditions were assumed in all the numerical analyses.

(a) CRACK INITIATION.

Crack initiation is first considered. Stress distributions in the uncracked ligament have been obtained for both the elastic n=1 (t = 0) and the steady state creep case ($t \rightarrow \infty$). The values of the creep stress exponent n and σ_o chosen for the analysis are given by Nikbin (1976) as, n=10, and, σ_o= 500Mpa for $\dot{\varepsilon}_o$=1/hr. A load of 11.12kN was applied with B=6.5mm and W=50mm, so that direct comparison can be made with the experimental data (Morzeria (1979).

Figure 9.35 shows the elastic σ_{yy} stress distribution ahead of the hole root

for all different hole diameters. It is evident that the maximum stress is always at the hole root for all different hole diameters, and that the relative magnitude of the maximum decreases with increasing hole diameter, indicating that the stress concentration at the hole root decreases with increasing hole diameter.

Figure 9.36 shows the steady state creep σ_{yy} stress distribution for all different hole diameters up to a distance of 10 mm ahead of the hole root. It is noted that the maximum stress migrates away from the hole root, as a function of the hole diameter. A bigger hole diameter causes the position of the maximum stress to move further away from the hole root. Similar results were obtained by Al-Faddagh et. al. (1982) and Hayhurst et.al. (1977) for the steady state stress distribution across the throat of a BS V-notch in a round bar. It is also noted that the magnitude of the maximum stress as well as the magnitude of the stress at the hole root increases with decreasing hole diameter, indicating as for the elastic case, that the stress concentration at the hole root decreases with increasing hole diameter. However the relative magnitude of the steady state creep stress is much smaller than the corresponding magnitude of the elastic stress, indicating significant stress relaxation. The full stress distribution across the uncracked ligament is shown in figure 9.37. It may be deduced that after a distance of about 8 mm from the hole root the effect of the hole size on stress distribution is negligible.

The time for crack initiation may be estimated from the stress near the hole root. Figure 9.38 shows a column of material just ahead of the hole root. If stress redistribution is complete then the column of material will deform according to

$$\frac{\dot{\varepsilon}}{\dot{\varepsilon}_0} = \left[\frac{\sigma}{\sigma_0}\right]^n \qquad (9.15)$$

or

$$\frac{d\varepsilon}{dt} = \dot{\varepsilon}_0 \left[\frac{\sigma}{\sigma_0}\right]^n \qquad (9.16)$$

integrating with respect to time, it may be proved that

$$t = \frac{\varepsilon}{\frac{\dot{\varepsilon}_0}{\sigma_0^n}\sigma^n} \qquad (9.17)$$

Rupture of the column and so crack initiation will occur when the ductility ε^*_f of the material is exhausted, where ε^*_f is defined in section 5.5, so that the time for crack initiation will be given by

$$t_i = \frac{\varepsilon_f^*}{\frac{\dot{\varepsilon}_0}{\sigma_0^n}\sigma^n} \qquad (9.18)$$

The crack initiation times were estimated by considering the stress magnitude at a distance 500μm from the hole root (which is between 1.5 to 2 times the grain size of the 1/2CMV steel, and the region over which damage accumulation prior to crack propagation was observed (Morzeria (1979))). The estimated crack initiation times are compared in figure 9.39 with the experimental crack initiation Morzeria (1979) results. The analytical crack initiation times were calculated using $\varepsilon^*_f = 0.2\%$ which is in the range of the measured creep ductility of the 1/2CMV steel, $0.1\% \leq \varepsilon^*_f \leq 5\%$ given by Nikbin et. al. (1984). Considering the experimental scatter, very good agreement is observed, indicating the adequacy of the procedure employed.

(b) CRACK PROPAGATION

Values of C* for n=1 and plane stress conditions, have been obtained from contour integrals performed around a crack of 0mm to 6.25mm long extending from each hole size, for a load of 800kN/m thickness of sample, σ_0=500Mpa and $\dot{\varepsilon}_0$=1/hr. The results are shown in figure 9.40. Also included in this figure are estimates of C* for a sample containing no hole. Local to the hole surface (a/W=0.31) C* rises rapidly from zero to join the calibration curve for the standard compact tension specimen without the hole. The effect is most pronounced for the larger hole radius. Typically the value of C* has approached within 5% of that for the sample without the hole by the time the crack

has reached a distance of the hole radius away from the hole.

Special care must be taken when choosing contours were the C* integral is to be evaluated. It is important to note that equations (4.17) and (5.3) which give the definition of J and C* contour integrals, are only valid for problems with crack faces that are traction-free and parallel to the x-coordinate axis. A more general expression, for equation, (5.3) say, is thus obtained by writing (see for example Wilson and Yu (1979))

$$C^* = \int_{\Gamma+s} W^*_s \, dy - T_i \frac{\partial \dot{u}_i}{\partial x} \, ds \qquad (9.19)$$

where s is the path along the crack face joining the points where Γ meets the crack faces to the crack tip (unticlockwise path E to G in figure 9.41). So evaluation of C* in contours like AB-BC-CD-DE in figure 9.41 must be avoided, because due to the presence of the hole it will lead to inaccurate predictions of C*. The effect of the hole may be taken into account if the contour is extended so that C* is evaluated in contours like AB-BC-CD-DE-EF-FG in figure 9.41. However the predictions of the stresses, strains and in general all the parameters needed for the evaluation of C* are much less accurate at a free surface, than in the interior. Hilton (1977) has suggested that the F.E. method would require special treatment of the free surface region of the crack. Raju and Newman (1979) progressively refined their mesh at the free surface and found rapid variations which were highly localised in a boundary layer near the free surface. So evaluation of C* using a contour which includes surface nodes will result in inaccurate estimates and should be avoided. To avoid the problems associated with contours which include free surface nodes, contours similar to AB-BC-CG in figure 9.41 were used.

An important characteristic feature of the fully plastic (or steady state creep) solutions is that they are scalable. For a material where the strain is related to the stress in uniaxial tension by

$$\frac{\varepsilon}{\varepsilon_0} = \left[\frac{\sigma}{\sigma_0} \right]^N \qquad (9.20)$$

Goldman and Hutchinson (1975) shown, from the simple dependence of the field

quantities on the applied load or displacement, that the J-integral has the following form

$$\frac{J}{\sigma_0 \varepsilon_0 a} = \left[\frac{P}{P_0}\right]^{N+1} \hat{J}^p (a/W, N) \qquad (9.21)$$

Superscript p denotes fully plastic quantity, and the dimensionless quantity $\hat{J}^p$ is a function only of a/W and n. P_0 is a function of a/W and is directly proportional to σ_0. So for a constant a/W and N it can be deduced that

$$J \propto \frac{\varepsilon_0}{\sigma_0^N} P^{N+1} \qquad (9.22)$$

Following the same arguments as in section 5.2.1, for the definition of C* in analogy to J, then for a material deforming under secondary creep according to Norton's uniaxial creep law

$$\frac{\dot{\varepsilon}}{\dot{\varepsilon}_0} = \left[\frac{\sigma}{\sigma_0}\right]^n \qquad (9.23)$$

then in analogy to equation (9.22)

$$C^* \propto \frac{\dot{\varepsilon}_0}{\sigma_0^n} P^{n+1} \qquad (9.24)$$

So the results shown in figure 9.40 can be scaled for other loads and values of σ_0 and $\dot{\varepsilon}_0$. Estimates of the stress intensity factor K can be obtained from the n=1 C* solution as explained in section 9.4.2(b).

The crack growth rate for the 1/2CMV steel can be correlated with the stress intensity factor K if a relationship of the form

$$\frac{da}{dt} = A K^8 \qquad (9.25)$$

is assumed (Dimopulos et.al.(1986) and chapter 10 of the present thesis).

From equation (9.25) it can be deduced that when the data are correlated in terms of the stress intensity K, the relative crack growth rate, for a specimen where the crack starts to propagate from a blunt notch (a hole in the present case), and, a specimen having a sharp notch, will be given by

$$\frac{(da/dt)_{d=i}}{(da/dt)_{d=0}} = \left[\frac{K_{d=i}}{K_{d=0}}\right]^8 \qquad (9.26)$$

where subscript "d" denotes diameter, and, in the present analysis i =3, 4, 6 and 9mm.

Figure 9.42 shows the relative crack growth rate as a function of the starter hole diameter at a distance of 0.5mm ahead of the crack tip. Also shown in this figure are the experimental Morzeria (1979), initial crack growth rates. Good agreement between the experimental and predicted crack growth rates is observed at a distance 0.5mm ahead of the hole root. Summarizing this result with the results for crack initiation, good prediction of the crack initiation and subsequent initial crack propagation rates can be achieved for this material, if the crack is considered to be initiated when the ductility at a distance 0.5 mm from the crack tip is exhausted and subsequent crack propagation from this position is correlated with the stress intensity K. Figure 9.42a shows the analytical evolution of the crack as a function of the time after crack initiation, for the different hole diameters. The crack is assumed to start to propagate at a distance 0.5mm from the hole root. It has been assumed that the crack propagates according to equation (9.25). The numerical value of A in (9.25) has been taken for the 1/2CMV steel as $A=3*10^{-61}$ with da/dt in mm/h and K in MPa$\sqrt{m}$ (Smith (1983)). A load of 11.12kN was applied, and, the thickness B and width W were assumed to be 6.5mm and 50mm respectively. Unfortunately Morzeria (1979) was able to compare only the initial crack growth rates, so comparison of the subsequent experimental and analytical crack growth rates can not be made.

Values of C* for n=10 and plane stress conditions, have been obtained from contour integrals performed around a crack of 0mm to 3.5mm long extending from each hole size for a load of 800kN/m thickness of sample, σ_0=500Mpa and $\dot{\varepsilon}_0$=1/hr. The results are shown in figure 9.43. Also included in this figure are estimates of C* for a sample containing no hole. Results similar to the n=1 case are obtained. For the specimens containing the hole, C* is initially less than the corresponding value for the sample without the hole, which is most pronounced for the larger hole radius, but

eventually all the solutions merge to the same value for cracks of sufficient length from the hole. Comparison of figures 9.40 and 9.43 shows that the solutions merge at a shorter distance from the crack tip for n=10 than they merge for the n=1 elastic case, indicating that the effect of the hole is less significant for the steady state creep case than it is for the elastic case. Using equation (9.24) the results shown in figure 9.43 can be scaled for other loads and values of σ_o and $\dot{\varepsilon}_o$.

Nikbin et. al. (1983) shown that the creep crack growth rate can be correlated with the C* creep contour integral if a relationship of the form

$$\frac{da}{dt} = D\, C^{*\, n/(n+1)} \qquad (9.27)$$

is assumed. For the 1/2CMV steel n=10 so

$$\frac{da}{dt} = D\, C^{*\, 0.91} \qquad (9.28)$$

From equation (9.28) it can be deduced that when the data are correlated in terms of the C* creep contour integral, the relative crack growth rate, for a specimen where the crack starts to propagate from a blunt notch, and, a specimen having a sharp notch, will be given by

$$\frac{(da/dt)_{d=i}}{(da/dt)_{d=0}} = \left[\frac{C^*_{d=i}}{C^*_{d=0}}\right]^{0.91} \qquad (9.29)$$

Figure 9.44 shows the relative crack growth rate as a function of the starter hole diameter at 0.5mm ahead of the crack tip. Also shown in this figure are the experimental Morzeria (1979), initial crack growth rates. It is noticed that the initial predicted crack growth rates at the bigger hole diameters are bigger than the experimental results. This is due to that the stress redistribution times being very long and the stresses not having relaxed enough for the crack growth rates to be correlated with C*.

In general it may be expected that crack tip notch profile will affect the incubation time, crack growth rate and the final time to rupture measured. The 1/2CMV steel exhibits limited creep ductility. Consequently little stress redistribution due to creep will be possible and the elastic stress concentration will not be relaxed. A high sensitivity

to hole diameter may therefore be anticipated. For more ductile materials where substantial creep deformation is possible relaxation of the high local stress will take place and the effects due to a hole may be less critical. However superimposed fatigue loading may continually regenerate the elastic stresses and cause both ductile and brittle materials to be sensitive to notch dimensions under creep/fatigue loading.

9.4.4 NUMERICAL RESULTS FOR THE ROTATING DISC GEOMETRY

(a) FINITE ELEMENT ANALYSIS

The finite element computer program, was next modified to incorporate centrifugal loading. The same solution procedure that it was used for the compact tension specimens of going directly from an elastic to a steady state creep solution has been maintained. To test the accuracy of the solution procedure plane strain loading was assumed so that the numerical results can be directly compared with existing analytical results.

Figure 9.46 shows the steady state creep stress distributions obtained for a stress exponent n= 1,3, 5, 7 and 10 compared with analytical estimates for an example of a rotating disc containing a central hole only. The mesh employed for this analysis is shown in figure 9.45. The inner radius of the disc was chosen to be 27mm and the outer 130mm. Using symmetry and suitable boundary conditions it is necessary to model only 1/12 of the disc. Plane strain loading was assumed with $\rho\omega^2/B=7800MN/m^5$, corresponding to a density $\rho=7800$ kg/m^3, an angular speed of rotation $\omega=100$rad/s and disc thickness B=10mm. The satisfactory agreement observed confirms the adequacy of the procedure adopted. Rotating turbine discs are thin and in general more likely to be under plane stress conditions. So all subsequent calculations assume plane stress conditions. However no analytical plane stress solutions exist for a rotating disc, so the comparison between the analytical and finite element results had to be made for plane

strain conditions. It is expected that the present finite element program is more accurate for plane stress conditions than it is for plane strain conditions as explained in section 6.3.2

Further calculations have been made for a rotating disc containing six satellite holes as illustrated in figure 9.47. The steady state creep stress distributions, for plane stress conditions, along a radius vector through a satellite hole diameter AB in the absence of a crack are shown in figure 9.48 for values of n= 1, 3, 5, 7 and 10. The corresponding relative stress concentration factors F at A and B are indicated in figure 9.49 where

$$F = \frac{\text{Creep stress concentration factor}}{\text{Elastic stress concentration factor}} \qquad (9.30)$$

At both locations the value of F increases approximately linearly with 1/n as was observed by Al-Faddagh et.al. (1982) for a circumferential notch in a tensile bar. It should also be noted that the maximum hoop stress migrates away from point A at the in-board radius of the satellite hole towards the disc bore indicating that in this circumstance failure would be expected to initiate away from the satellite hole. For elastic loading the hoop stress at A exceeds that at B. The same holds for values of the creep index n = 3,5 but for $n \geq 7$ the steady creep stress at B exceeds that at A.

Calculations of the creep contour integral C* for cracks of different lengths emanating from A at a satellite hole are presented in figures 9.51, 9.52, 9.53 and 9.54, for n=1,3,5, and 10 respectively. The calculations have been performed for $\dot{\varepsilon}_o=1/h$, $\sigma_o=500MPa$ and $\rho\omega^2/B=7800MN/m^5$. Figure 9.50 shows the finite element mesh employed for the evaluation of the C* creep contour integral extending 0 mm to 7mm from the hole. The mesh dimensions were the same as those of figure 9.47. For longer cracks the mesh shown in figure 9.47 was employed. Results similar to those obtained for the compact tension geometry are observed. A rapid increase in C* for short crack lengths close to the satellite hole is apparent which is most pronounced for high values of n, indicating that the effect of the hole becomes less significant for increasing n.

To study the effect of the hole on the C* creep contour integral the hole was replaced by a sharp crack. Special care must be taken for the mesh design of this geometry as both crack tips need to be modeled. Figure 9.55 shows the finite element mesh employed for this analysis. In the analysis the crack is assumed to extend from point A, and the crack at B to remain stationary, so that direct comparison can be made with the estimates of C* for cracks emanating from the satellite hole at point A (figure 9.50). Calculations of the creep contour integral C* for cracks of different lengths emanating from A are presented in figures 9.56, 9.57, 9.58 and 9.59 for n=1,3,5, and 10 respectively. Also included in this figure are the calculations of the C* integral at point B. It is evident that the magnitude of the C* contour integral is always bigger for the crack emanating from the point A than it is at point B, so that the crack growth rate for a crack aligned in the radial direction of a rotating disc, is always going to be greater in the direction towards the bore than towards the outer radius. In figures 9.56 to 9.59 the C* estimates of the sharp crack are compared with the C* estimates for cracks emanating from blunt holes. These results may be approximately compared with the case of the crack emanating from a circular hole in a compact tension specimen (figures 9.40 and 9.43). Similar trends are obtained although the hole retains an influence on C* even to large crack extensions. This is due to that, unlike in the case of the compact tension specimen, the loading of the rotating disc with the satellite holes, is different to the loading of the rotating disc without the satellite holes, as the latter will have more mass. It is expected that the influence on C* is most pronounced for high values of n, as C* is proportional to P^{n+1} (equation 9.24). This is clearly shown in figures 9.56 to 9.59.

The analytical evolution of the crack for the elastic case, for both the disc which contains the sharp crack and the disc which contains the blunt hole is shown in figure 9.56a as a function of the time. It has been assumed that the crack starts to propagate at a distance 0.5mm from point A, with the crack at B remaining stationary.The AP1 superalloy properties have been assumed. For the AP1 superalloy crack growth rate can be described in terms of K by (see section 10.9.2)

$$\frac{da}{dt} = A K^{2.5} \qquad (9.30a)$$

with A having a numerical value (taken from figure 10.24) of $A=8.39*10^{-21}$ with da/dt in mm/h and K in Pa$\sqrt{m}$. The loading assumed was $\rho\omega^2/B=7800MN/m^5$, corresponding to a density $\rho=7800$ kg/m^3, an angular speed of rotation $\omega=100$rad/s and disc thickness B=10mm. It is observed that the time needed for the same crack extension is significantly smaller for the disc containing the sharp crack as expected.

The analytical evolution of the crack for the steady state creep case, for both the disc which contains the sharp crack and the disc which contains the blunt hole is shown in figure 9.59a as a function of the non-dimentional time τ, for n= 3, 5, 10. τ has been defined as t/t_c, were t_c is the time taken for the crack to grow 7mm from point A in the disc containing the sharp crack (figure 9.55) with the crack at B remaining stationary. It has been assumed that the crack starts to propagate at a distance 0.5mm from point A, according to equation (9.27). It is observed that the time needed for the same crack extension is smaller in the disc containing the sharp crack as expected. If the discs had the same loading then, the effect of the hole on the non-dimentional time τ is expected to be less significant with increasing n. However because as explained above the mass of the two discs differs and hence the loading, and $C^* \propto P^{n+1}$, da/dt will be proportional to P^n (using 9.27), and hence the effect of the hole on τ will increase with increasing n. This is reflected on figure 9.59a where for the same crack extension, τ for n=3 is bigger than τ for n=5, but they are both smaller than τ for n=10.

(b) BOUNDARY INTEGRAL EQUATION ANALYSIS

It has not been possible to obtain a steady state creep solution with this method, as the present B.I.E. program is only suitable for elastic, and, elastic-plastic analysis. Instead elastic-plastic calculations have been performed to represent elastic-creep behaviour. The constitutive equation used for the Boundary Integral Equation analysis is given by the relation

$$\varepsilon = \frac{\sigma}{E} \qquad \text{for } \sigma < \sigma_y$$

$$\varepsilon = \frac{\sigma}{E} + \left[\frac{\sigma}{\sigma_{op}}\right]^N - \left[\frac{\sigma_y}{\sigma_{op}}\right]^N \qquad \text{for } \sigma > \sigma_y \qquad (9.31)$$

where E is the elastic modulus, σ_{op} a normalising stress, σ_y is yield stress and N is the power-law hardening exponent of plastic deformation.

Advantage was taken of the symmetry and as in the finite element case only 1/12 of the disc was modelled. The meshes used for the B.I.E. analysis are shown in figures 9.60, 9.61 and 9.61a. The mesh dimensions are the same as those of figure 9.47. No singularity elements were placed at the crack tip, therefore, in order to be able to represent rapid variations of the stress around the crack tip, very fine meshes were employed around the crack tip region. As for the interior domain, the extent of the discretisation is dependent on the size of the yield zones at the final loading conditions. For moderate yielding, only the region around the crack tip needs to be modelled. However, in the present investigation, large scale yielding solutions were required, and therefore the whole interior domain was modelled.

An elastic solution was conducted first, until the load at first yield was reached, and thereafter an elasto-plastic analysis was made for each additional load increment. Because the plastic strains are increasing in proportion to P^N were P is the load and N the power law hardening exponent, the load increment was successively reduced as the load level become higher, so that a sufficient level of accuracy was maintained.

The value of J was determined numerically along each of four different rectangular paths. It was found that at relatively low loads, the values of J evaluated along each of these paths were constant with respect to each other, to within the limits of numerical error. With increasing plastic deformation, the calculated values of J, for a given load level, began to deviate from one another, but at load levels were the whole

specimen had yielded, the deviations were observed to decrease. This is demonstrated in figure 9.62, where the ratio of the value of J obtained for the second path over the value of J obtained for the fourth path, is plotted versus the load level, for a value of the power law hardening exponent N=3. This indicates that the deviations, are more likely to be due to that the contour paths are crossing the elastic-plastic interface, rather than any inaccuracies in the solution procedure.

For the path nearest to the crack tip large deviations were observed as the load increased. The most likely reason is that the path is very close to the crack tip, and the present elements in this region cannot provide the required asymptotic behaviour.

Direct correspondence of the elastic-creep behaviour

$$\varepsilon = \frac{\sigma}{E} + \left[\frac{\sigma}{\sigma_0} \right]^n \dot{\varepsilon}_0 \, t \qquad (9.32)$$

with the elastic-plastic behaviour (equation (9.31)) is possible, if σ_0, $\dot{\varepsilon}_0$ and n represent the creep properties of the disc material and time can be calculated from (see appendix 9A).

$$t = \frac{1}{n+1} \left[\frac{P_1}{P_2} \right]^{n-1} \qquad (9.33)$$

where P_1 is the load applied to the elastic-plastic disc and P_2 is that applied to the elastic-creeping disc to give the same ratio of plastic to elastic strain and creep to elastic strain rate. The stresses σ_2 in the elastic-creeping disc at time t are given by

$$\sigma_2 = \sigma_1 \left[\frac{P_2}{P_1} \right] \qquad (9.34)$$

where σ_1 is the corresponding stress in the elastic-plastic disc. Consequently stress redistribution with increasing time is achieved by progressive increments of load from the elastic-plastic calculations using equations (9.33) and (9.34).

A comparison of the BIE and FE elastic stress distributions across a radius vector through a satellite hole for an uncracked disc is shown in figure 9.63. Close correspondence is achieved. The form of the stress redistribution that takes place with

increasing plastic (creep) strain for n=3 is presented in figure 9.64 for σ_o=1060MPa (to represent the AP1 superalloy), σ_{op}=1060MPa, σ_y=55MPa and E=200GN/m^2. The value of σ_y was chosen for computational convenience.

Estimates of C* for different contours as indicated in figure 9.60, have been determined for different values of n and time, using the B.I.E. procedure. A check was first made that agreement was achieved with the elastic solution. This is shown in figure 9.51. Essentially the procedure involves calculating the elastic-plastic contour integral J and then converting J to C(t) from (see appendix 9A)

$$C(t)=\left[\frac{P_2}{P_1}\right]^{n+1} J \qquad (9.35)$$

provided σ_o= σ_{op} and both ε_o and $\dot{\varepsilon}_o$ have a magnitude of 1. When the dimensions of $\dot{\varepsilon}_o$ are 1/h, C(t) will have the dimensions of J divided by hours.

The predictions obtained for J and C(t) for a crack length of 7mm from point A, for n=3, 5 and 10 are presented in figures 9.65 to 9.70. The value of σ_y was chosen for computational convenience. For n=3 σ_y was taken to equal 55MPa , for n=5 165MPa, and, for n=10 325MPa. σ_o was chosen to equal 1060MPa with $\dot{\varepsilon}_o$=1/h, σ_{op}=1060MPa with ε_o=1, and E=200GN/m^2. Whilst stress redistribution is taking place there is an approximately linear decay on logarithmic scales in C(t) with time. At long times asymptotic approach to the FE steady state solution C* is obtained.

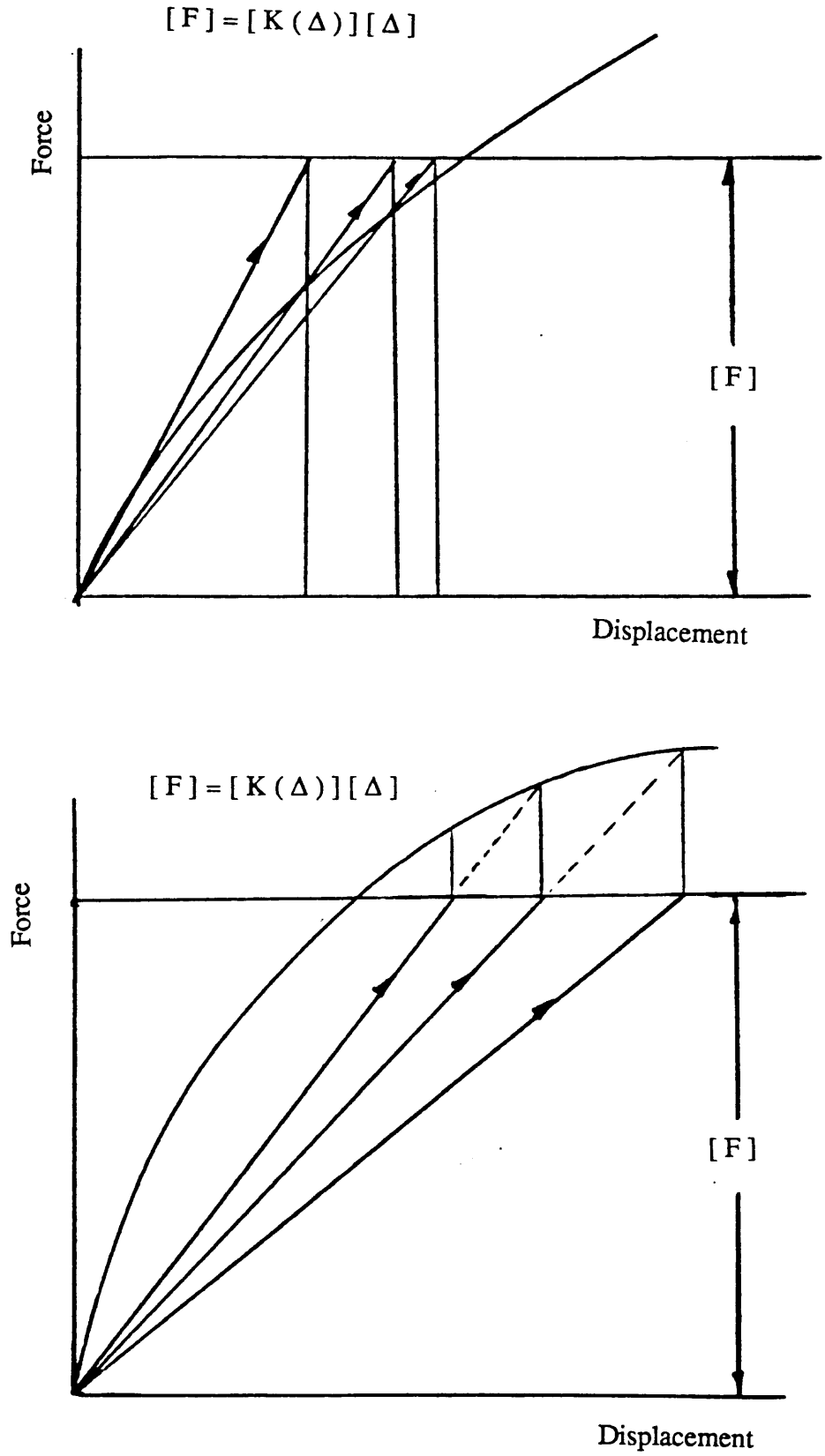


Figure 9.1 Secant - stiffness iterative method.

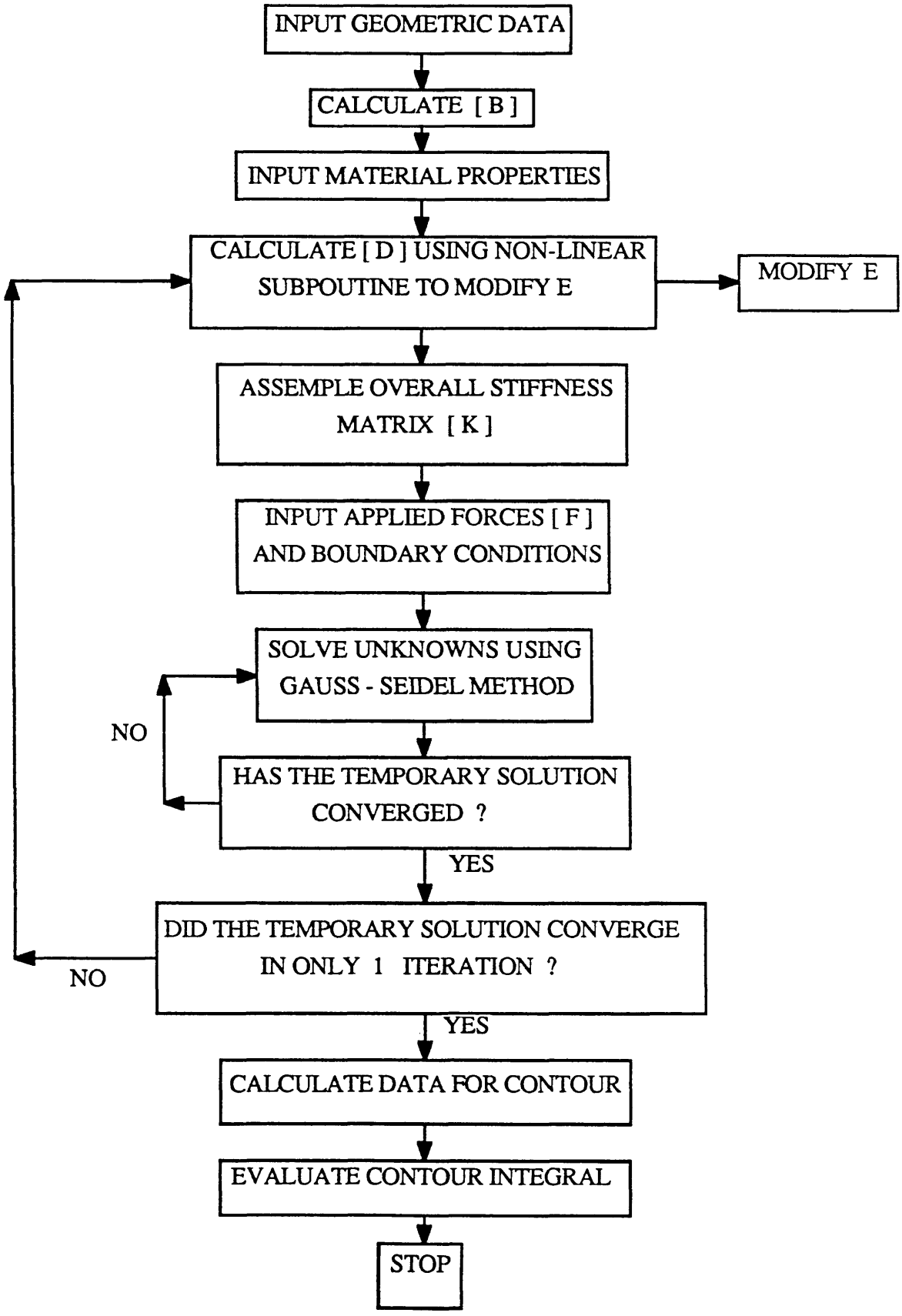


Figure 9.2 Flowchart showing the procedure in the finite element program.

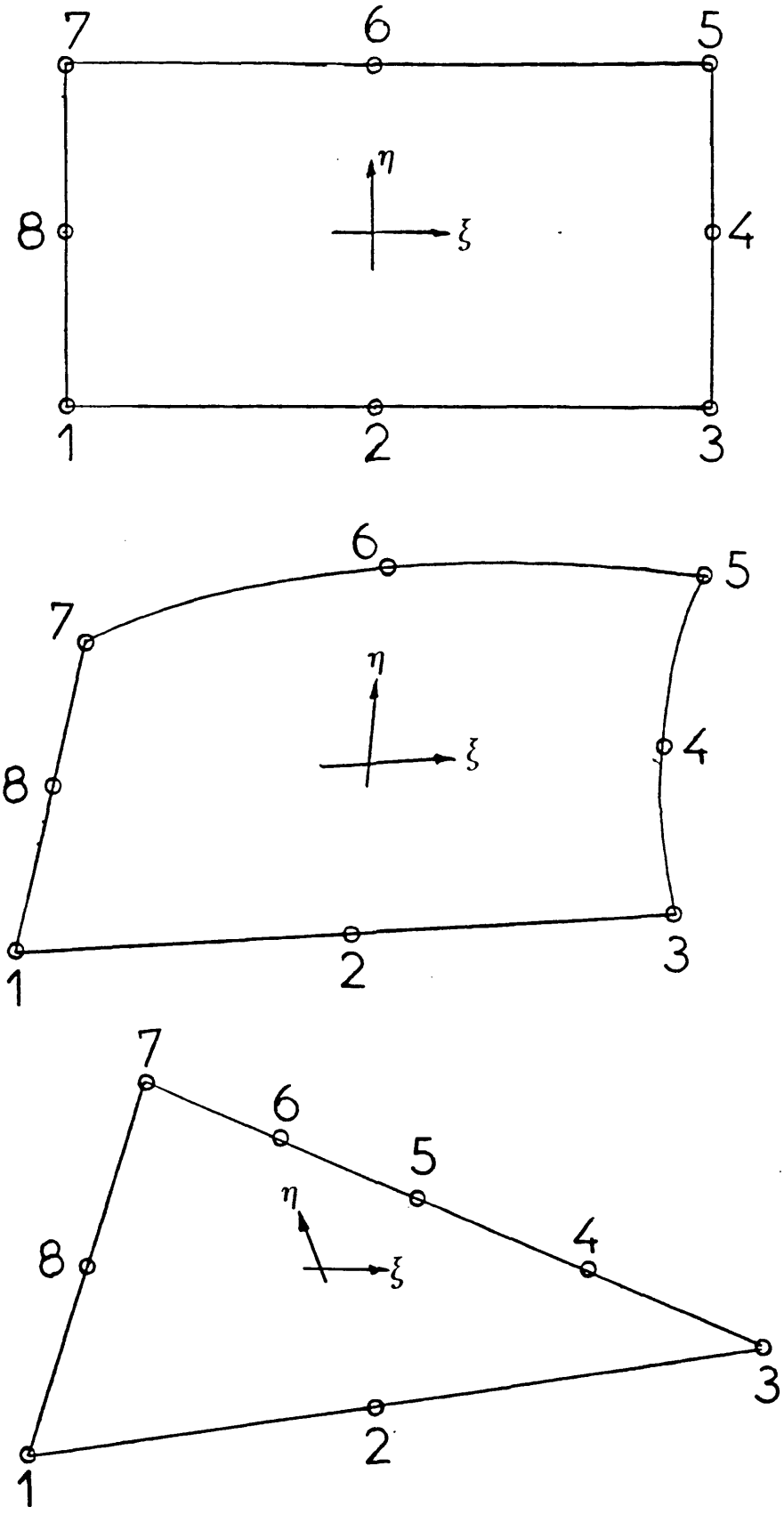


Figure 9.3 Possible regions of a quadrilateral.

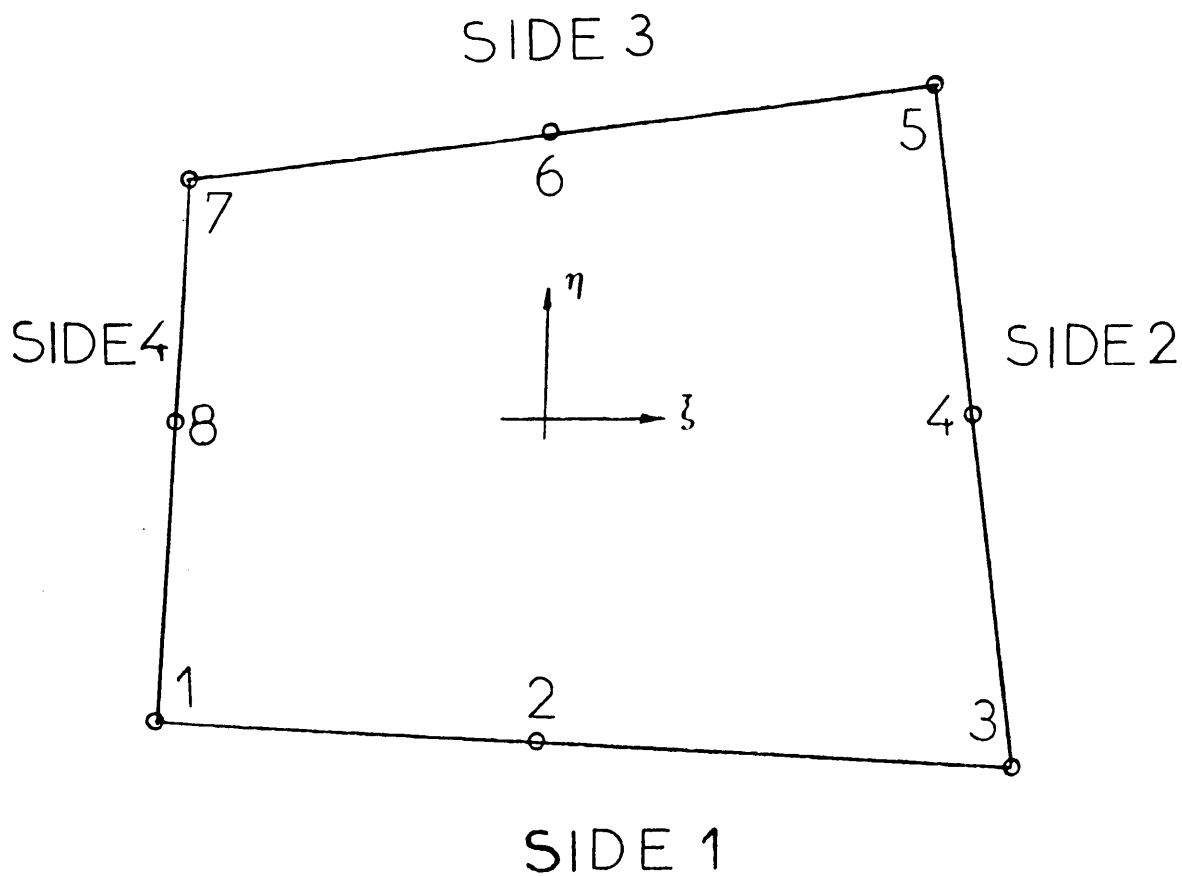


Figure 9.4 The sides of a quadrilateral region.

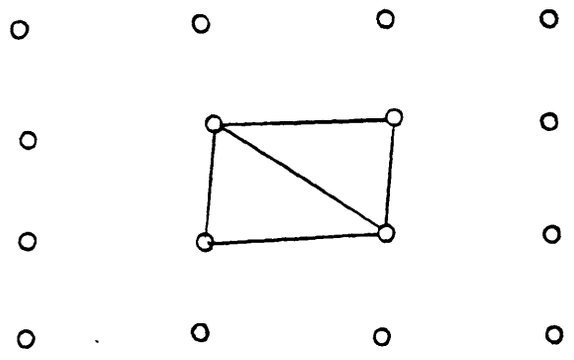


Figure 9.5 A set of four nodes divided into two triangular elements.

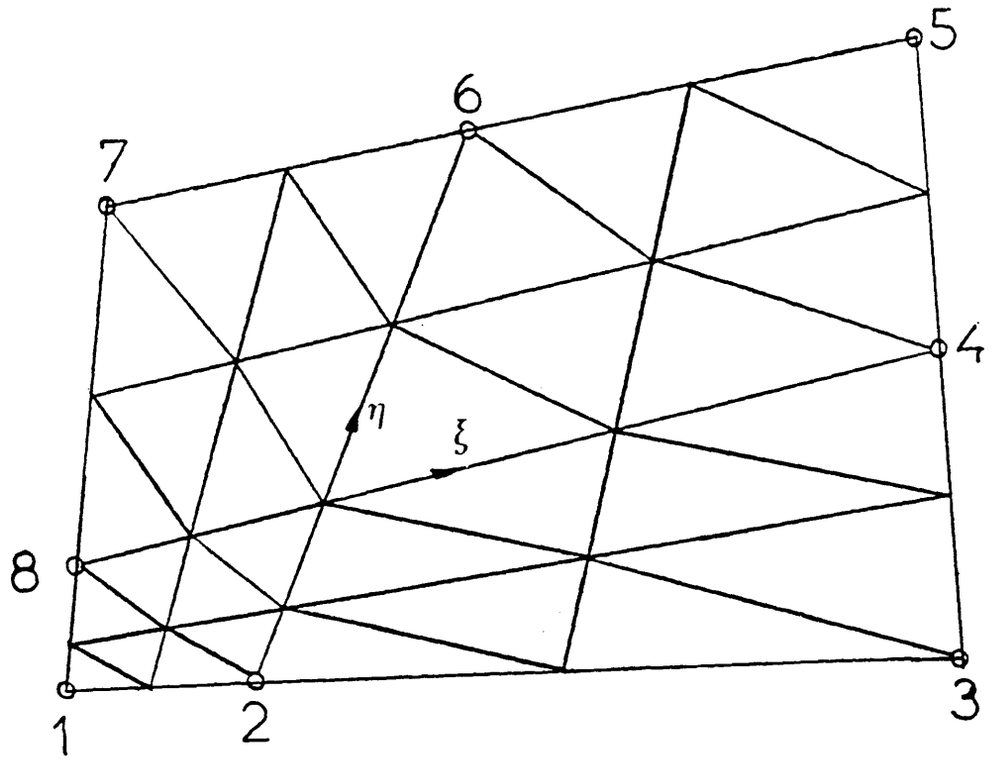
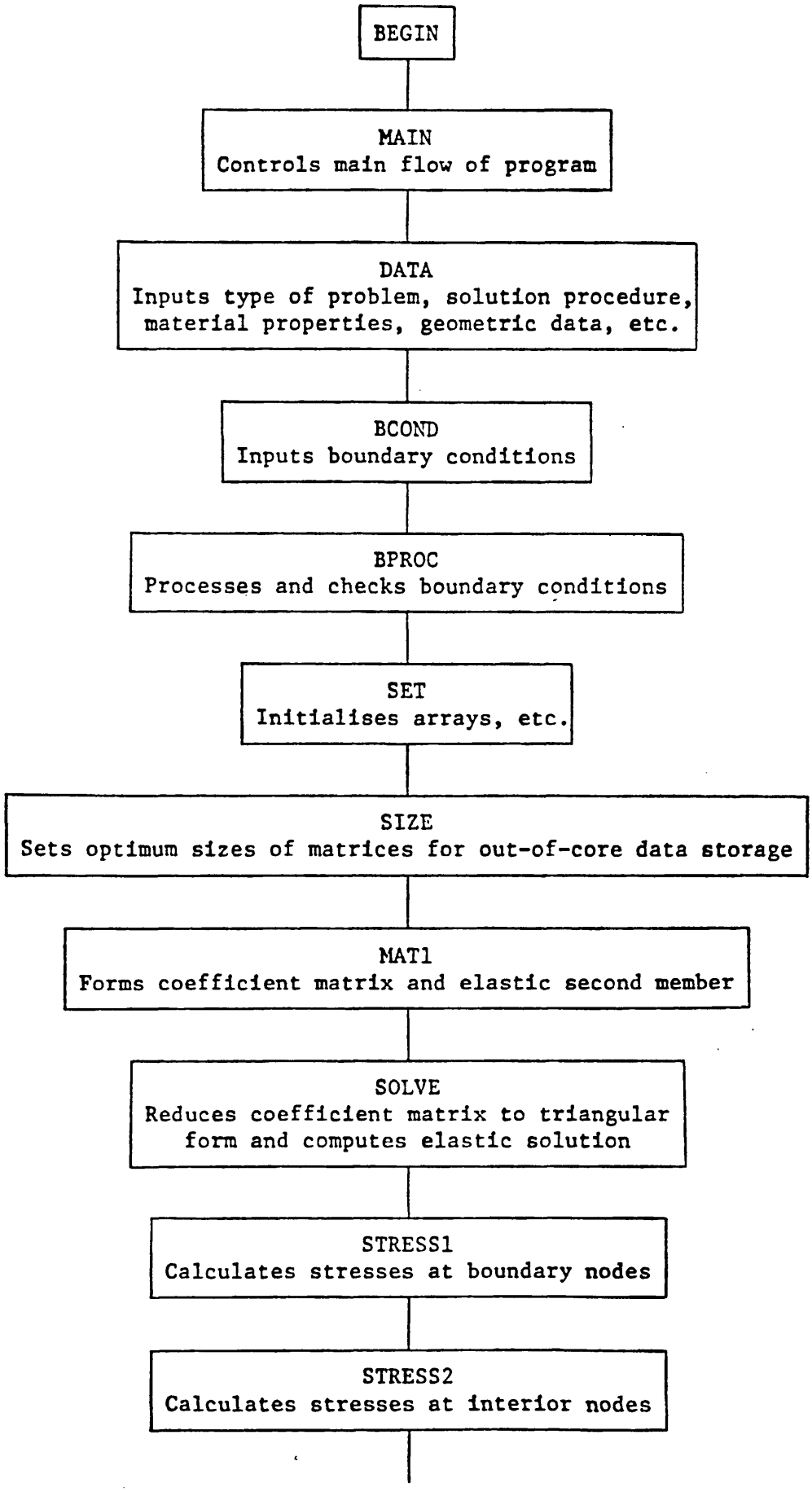


Figure 9.6 A region with a change in element size.


BEGIN
MAIN
Controls main flow of program
DATA
Inputs type of problem, solution procedure, material properties, geometric data, etc.
BCOND
Inputs boundary conditions
BPROC
Processes and checks boundary conditions
SET
Initialises arrays, etc.
SIZE
Sets optimum sizes of matrices for out-of-core data storage
MAT1
Forms coefficient matrix and elastic second member
SOLVE
Reduces coefficient matrix to triangular form and computes elastic solution
STRESS1
Calculates stresses at boundary nodes
STRESS2
Calculates stresses at interior nodes

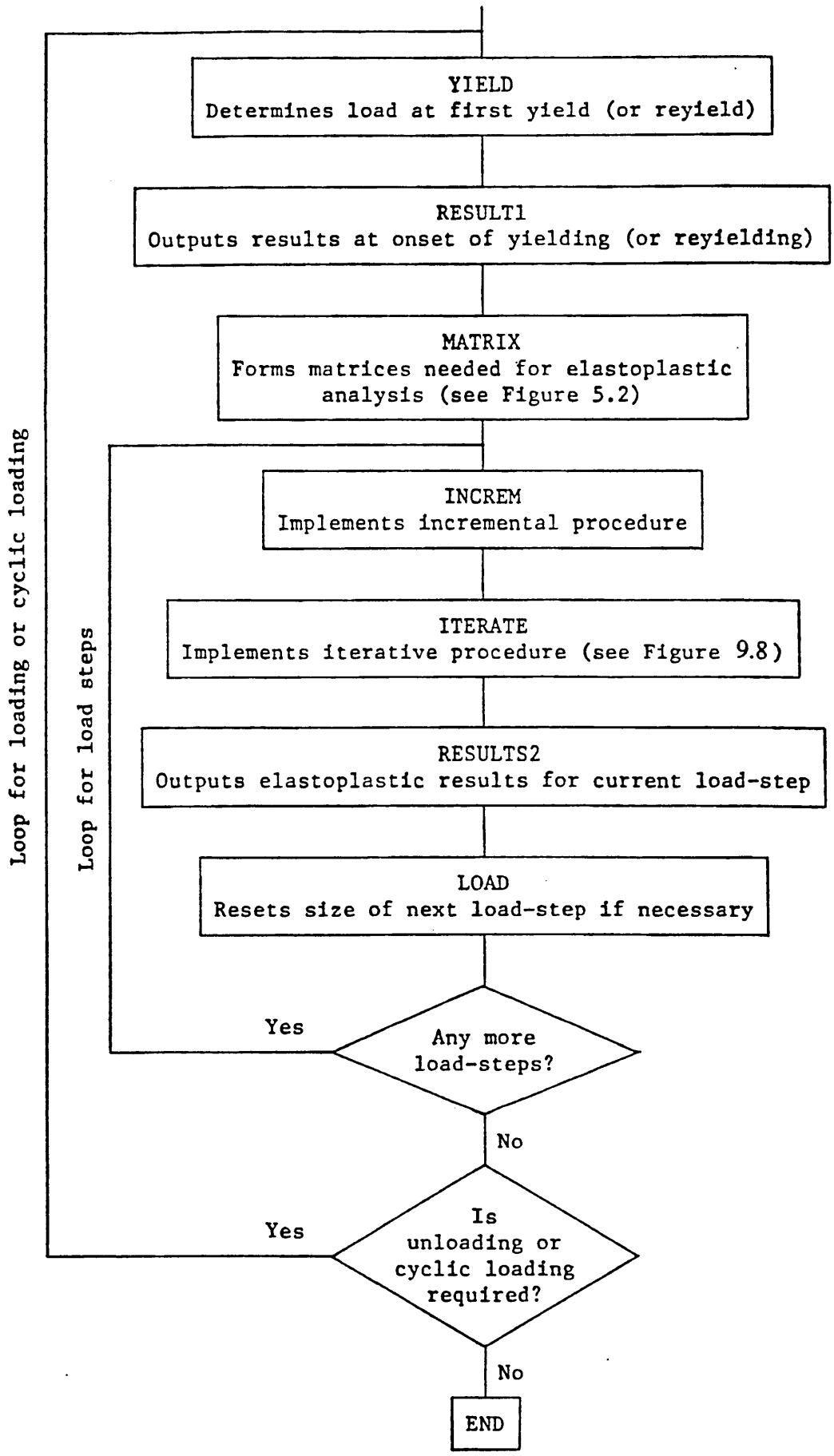


Figure 9.7 Flowchart for main program organization (B.I.E.)

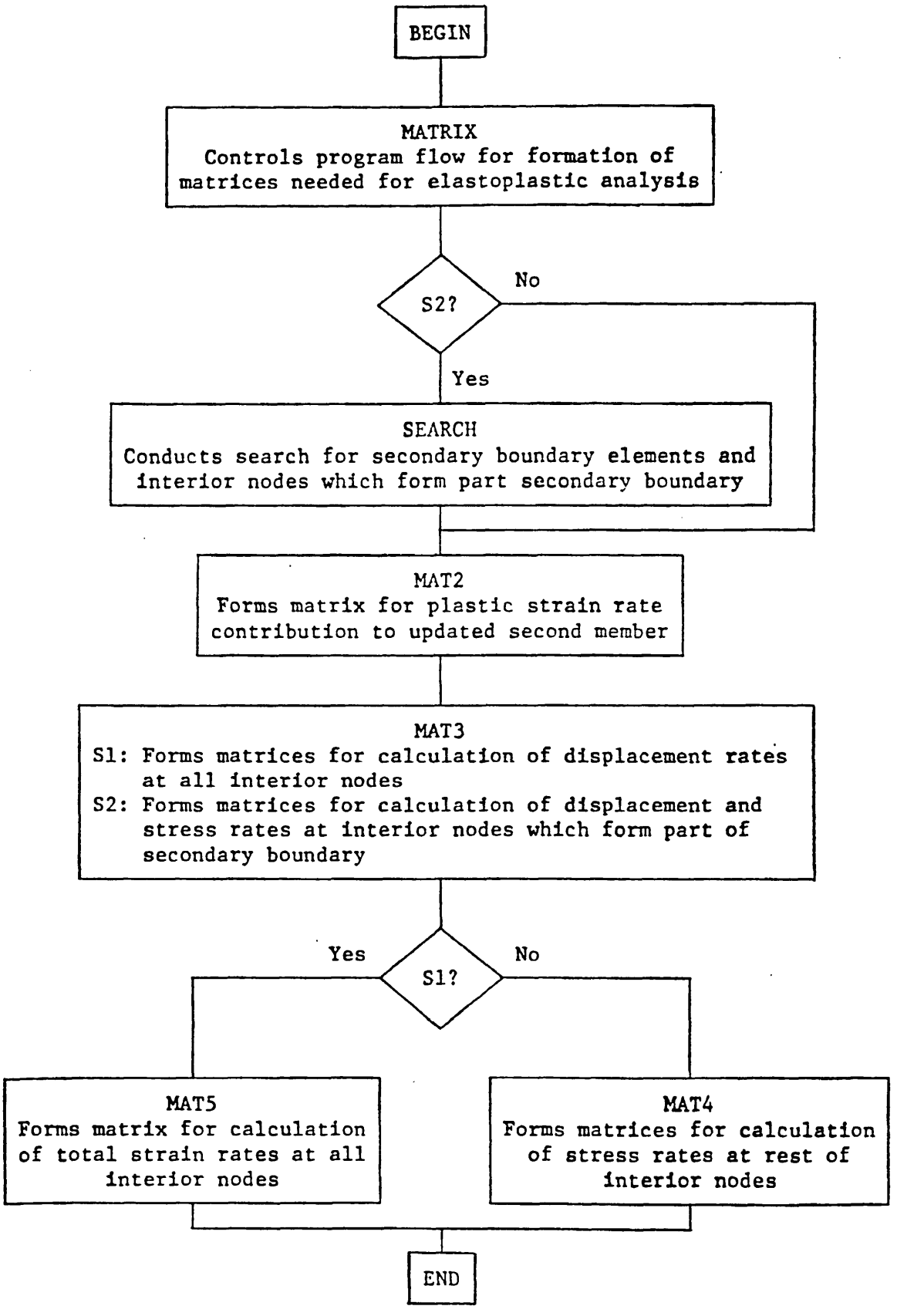


Figure 9.8 Flowchart for formation of matrices needed for elastoplastic analysis (B.I.E.)

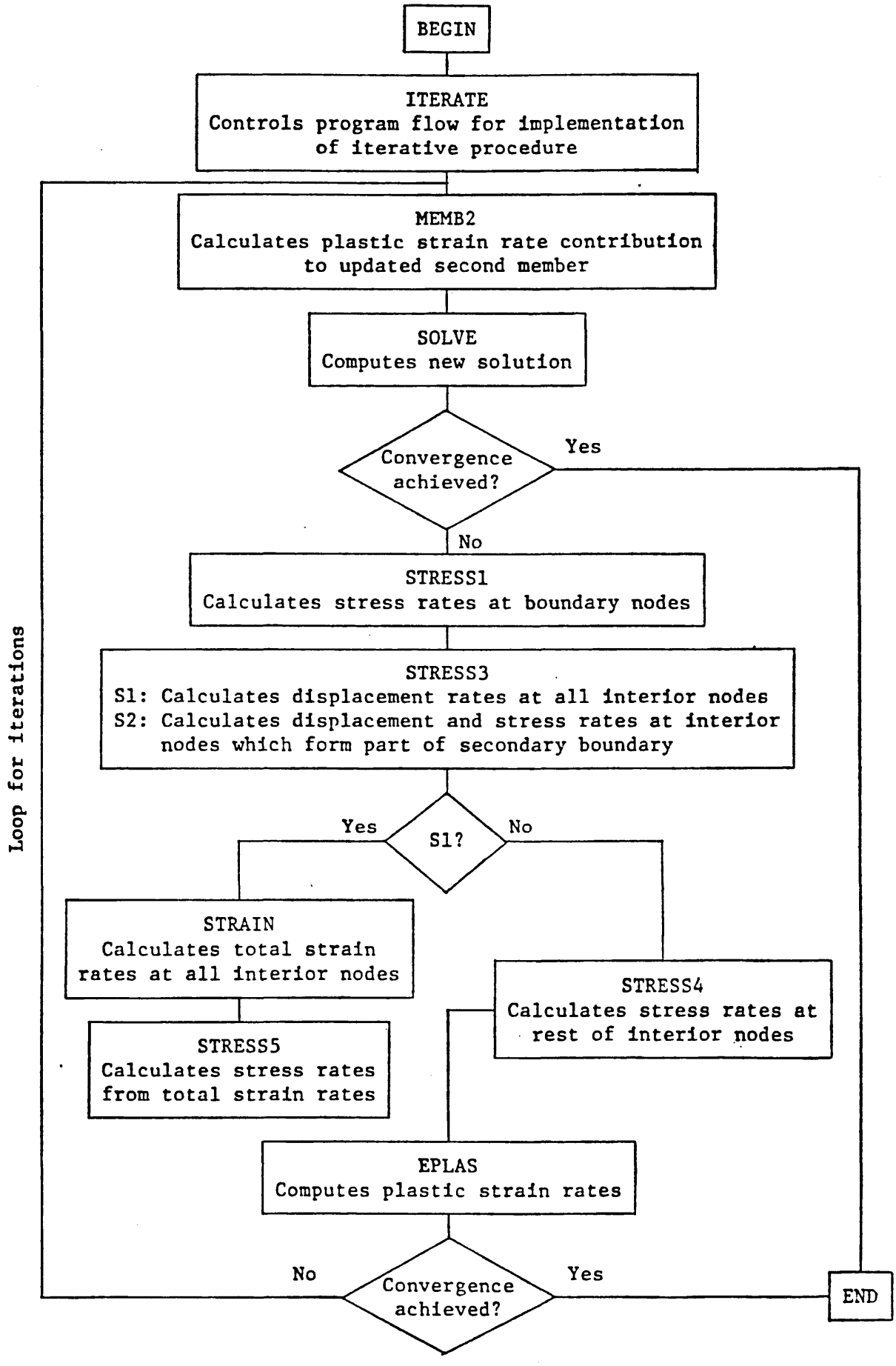


Figure 9.9 Flowchart for implementation of iterative procedure (B.I.E.).

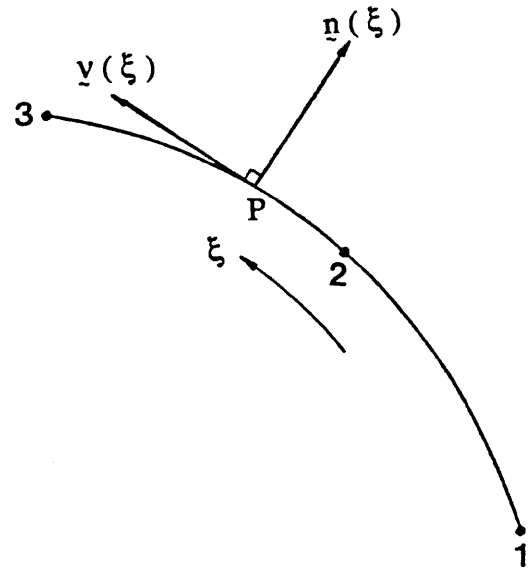


Figure 9.10 A three-noded isoparametric quadratic line or boundary element.

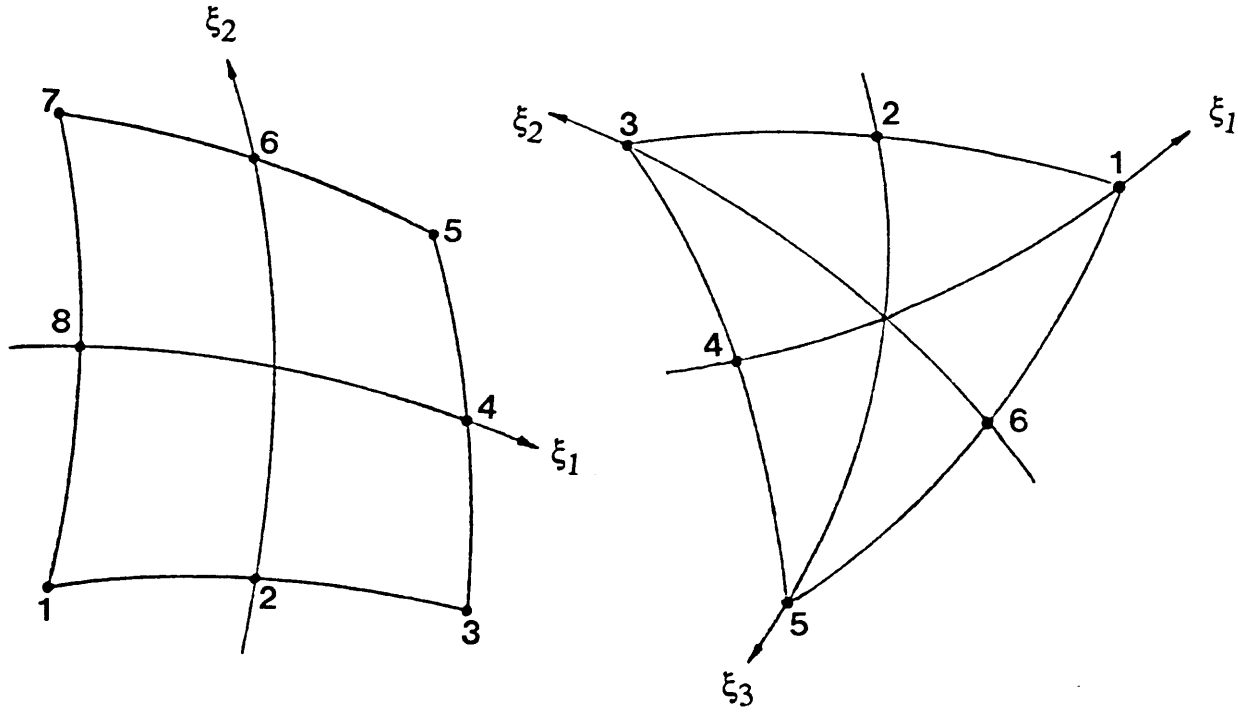


Figure 9.11 An eight - noded isoparametric quadrilateral element and a six - noded isoparametric triangular element.

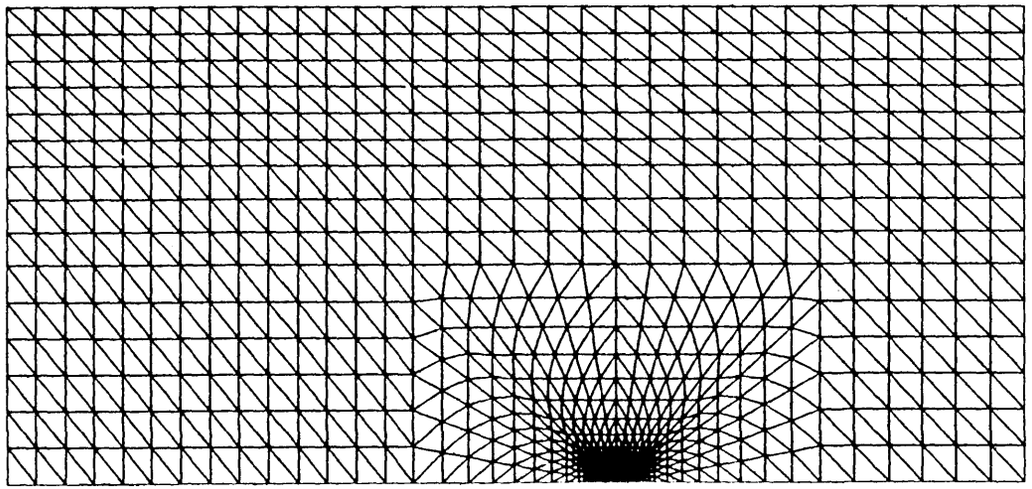


Figure 9.12 Finite element mesh of a compact tension specimen containing a relative crack length of $a / W = 0.5$.

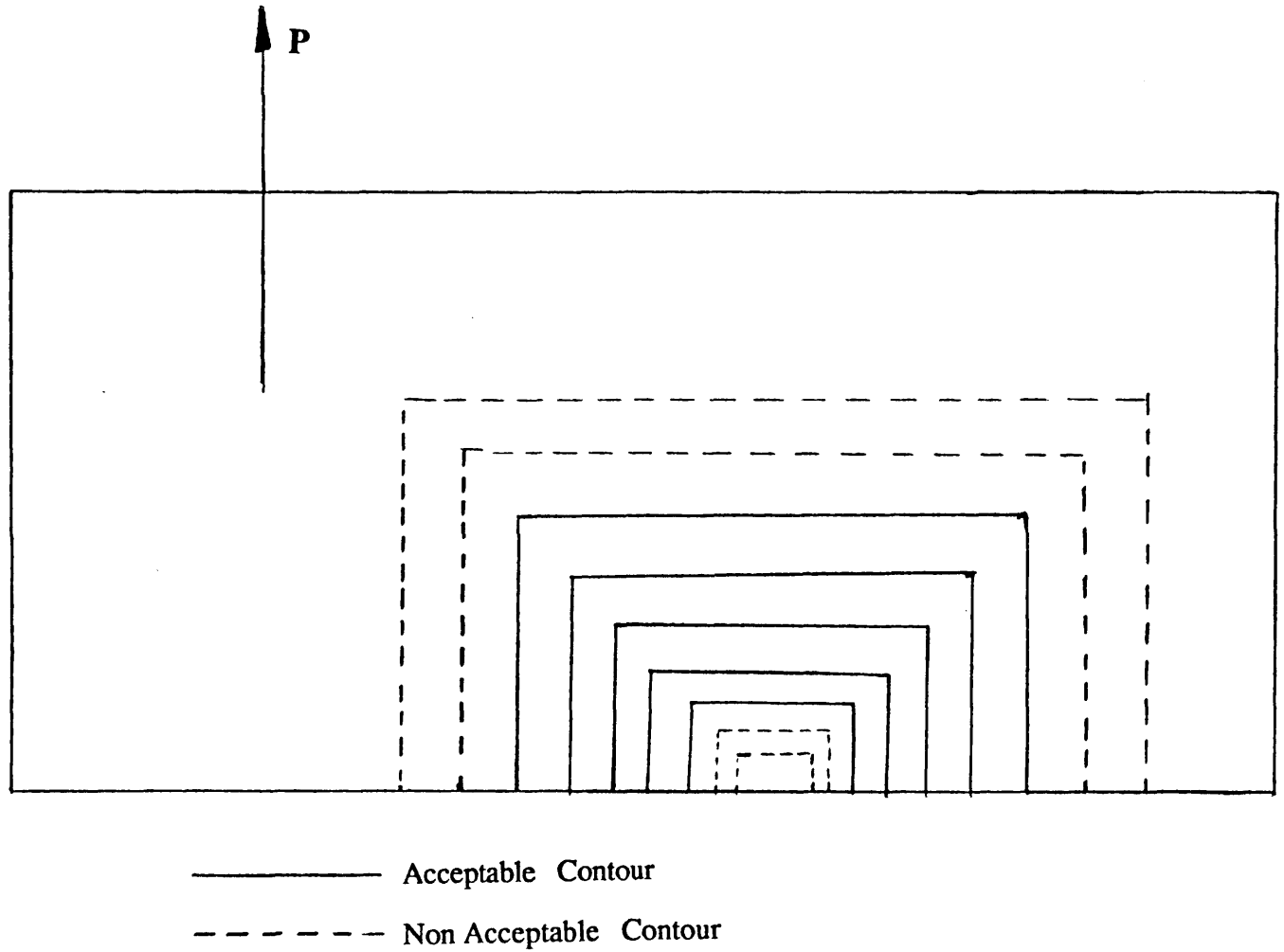


Figure 9.13 Contour paths used for the evaluation of the C* contour integral in the F.E. procedure.

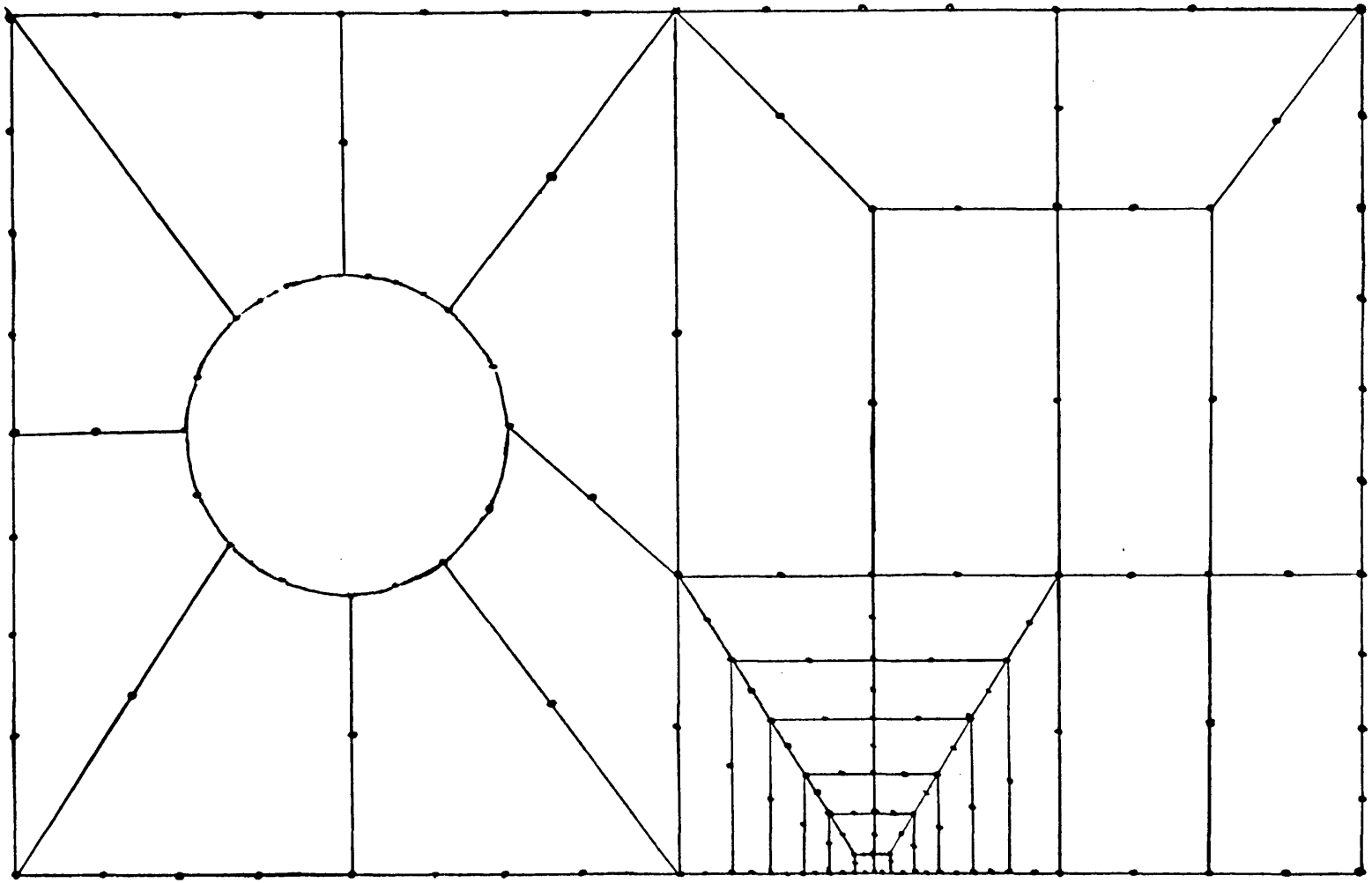


Figure 9.14 Boundary integral equation mesh of a compact tension specimen containing a relative crack length of a / W = 0.5.

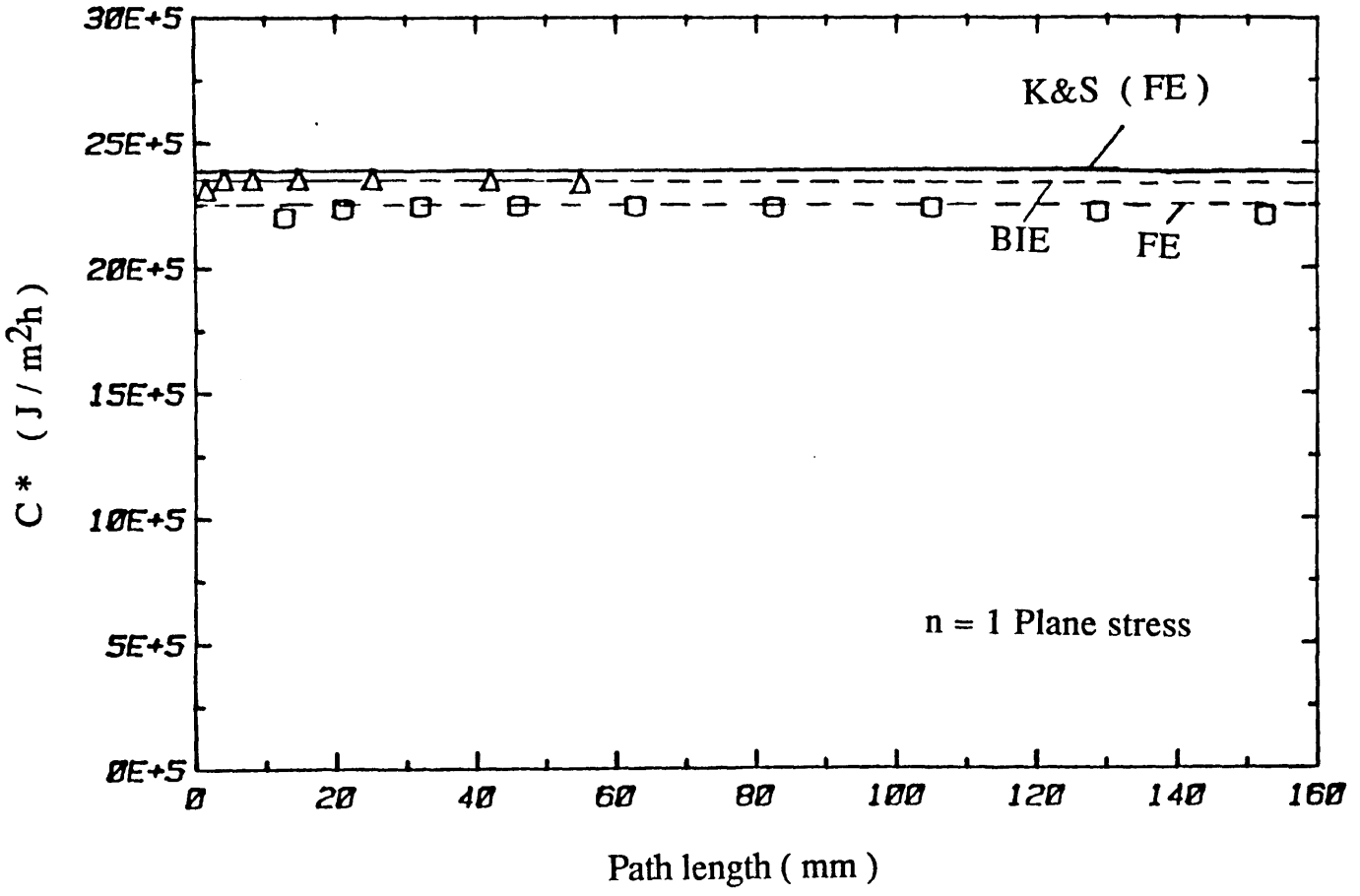


Figure 9.15 C* integral as a function of path length for n = 1 and plane stress.

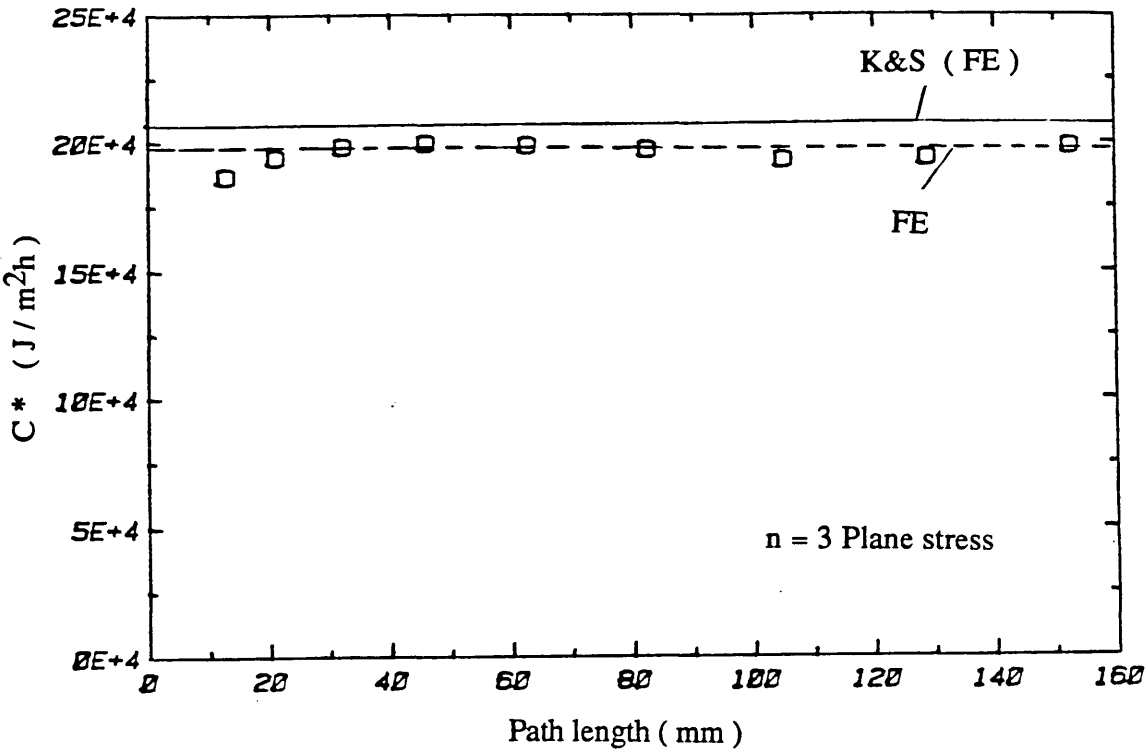


Figure 9.16 C* integral as a function of path length for n = 3 and plane stress.

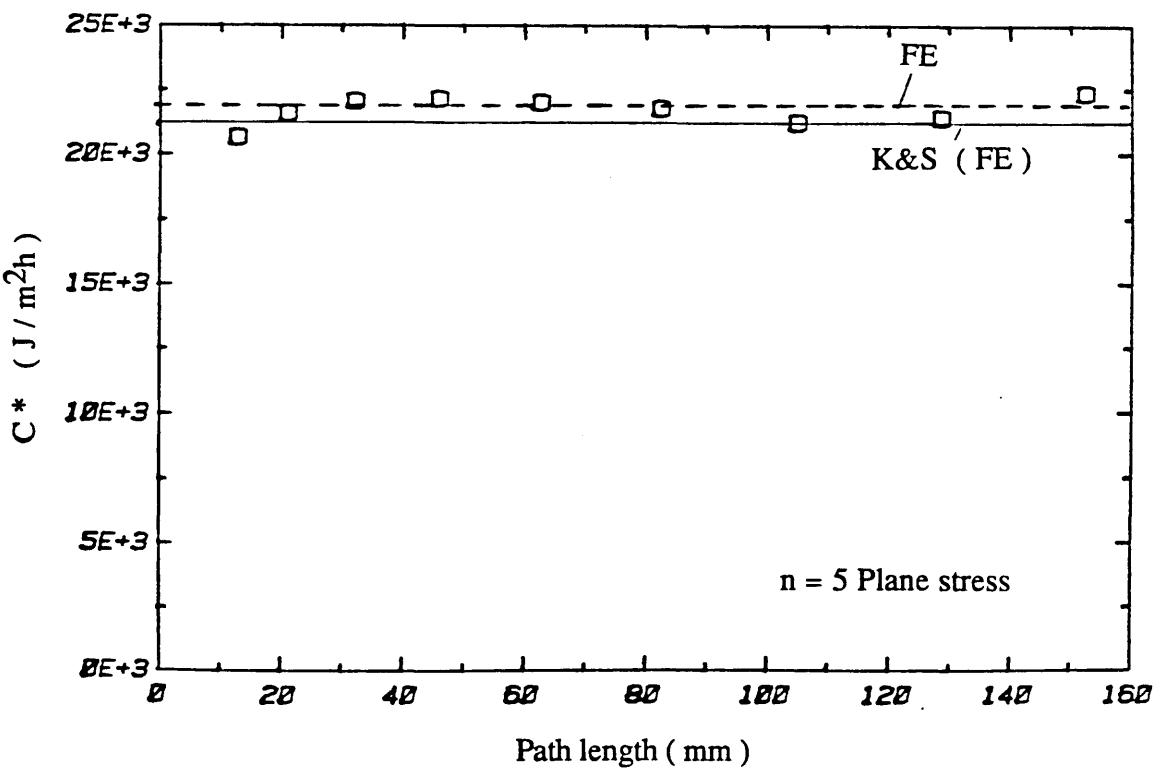


Figure 9.17 C* integral as a function of path length for n = 5 and plane stress.

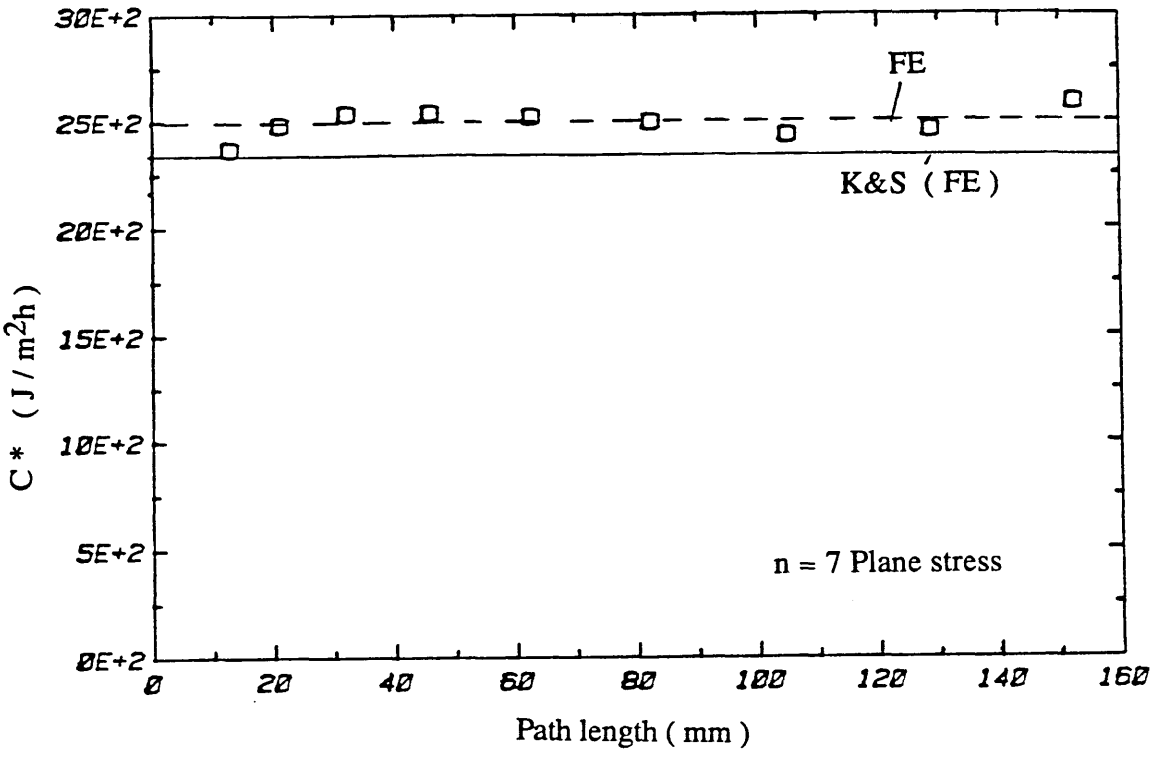


Figure 9.18 C* integral as a function of path length for n = 7 and plane stress.

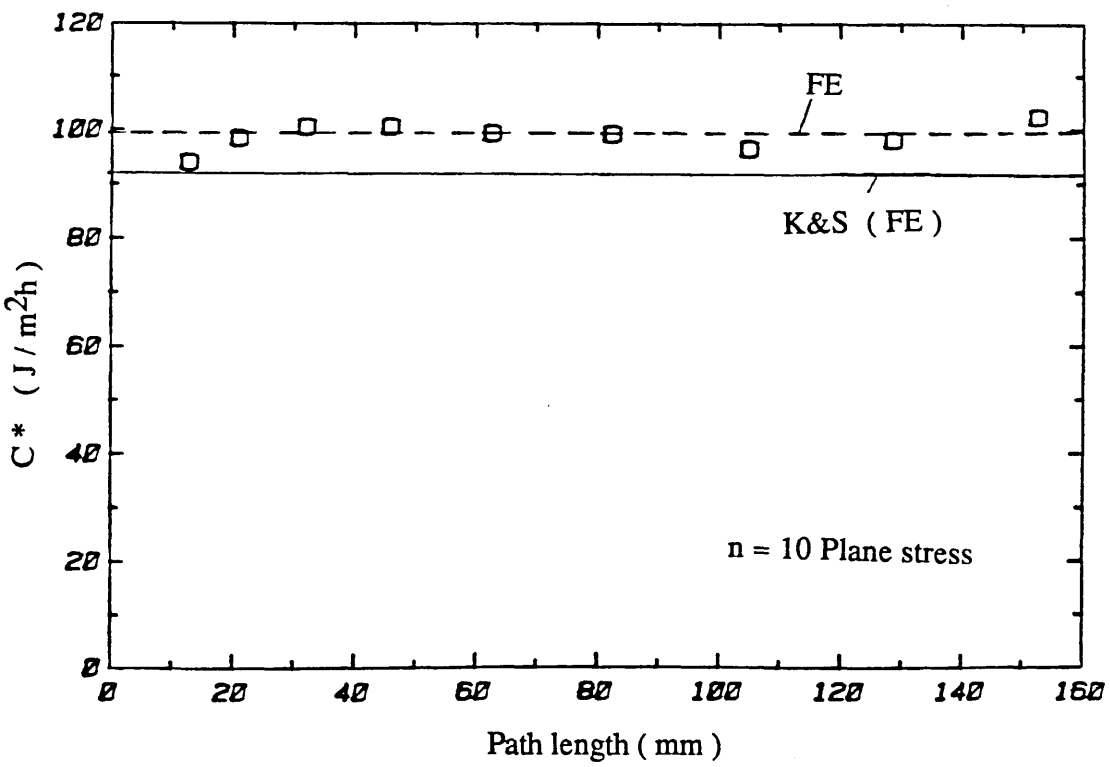


Figure 9.19 C* integral as a function of path length for n = 10 and plane stress.

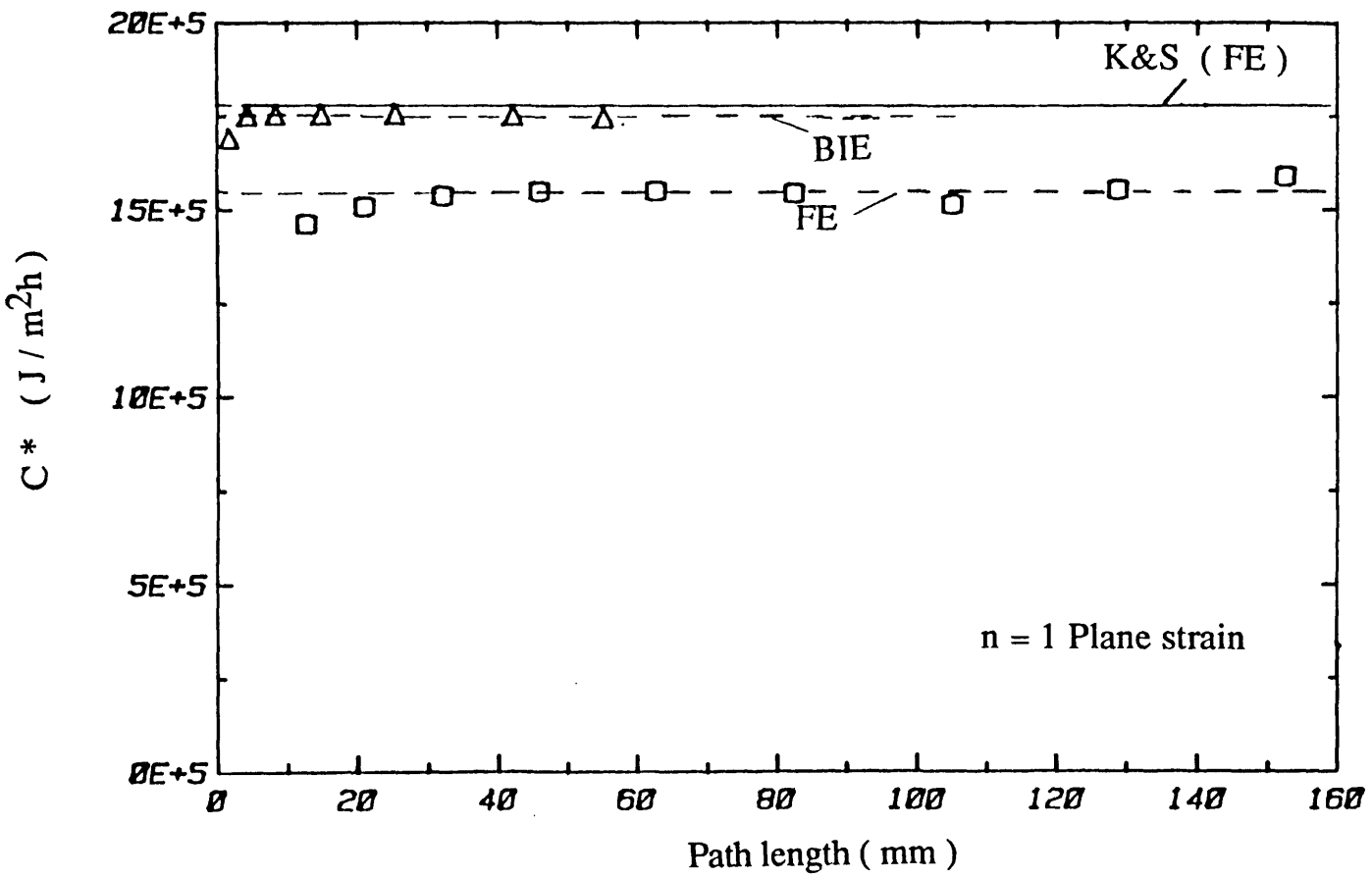


Figure 9.20 C* integral as a function of path length for n = 1 and plane strain.

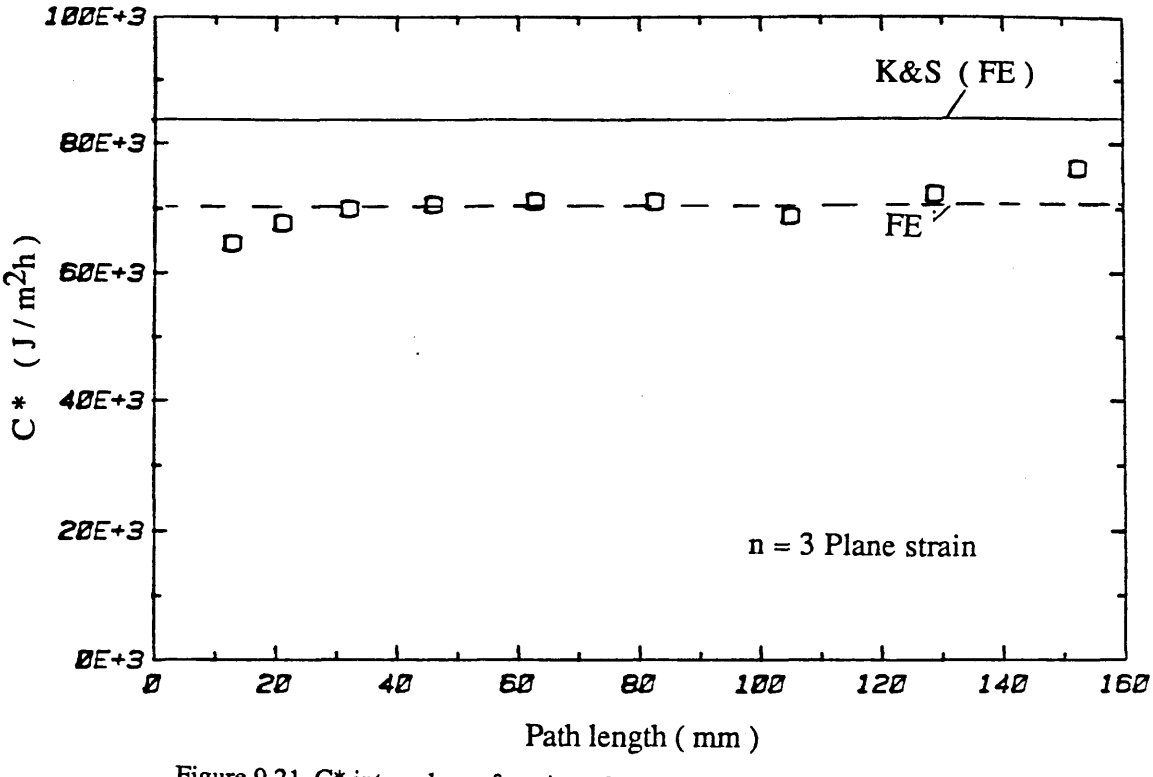


Figure 9.21 C* integral as a function of path length for n = 3 and plane strain.

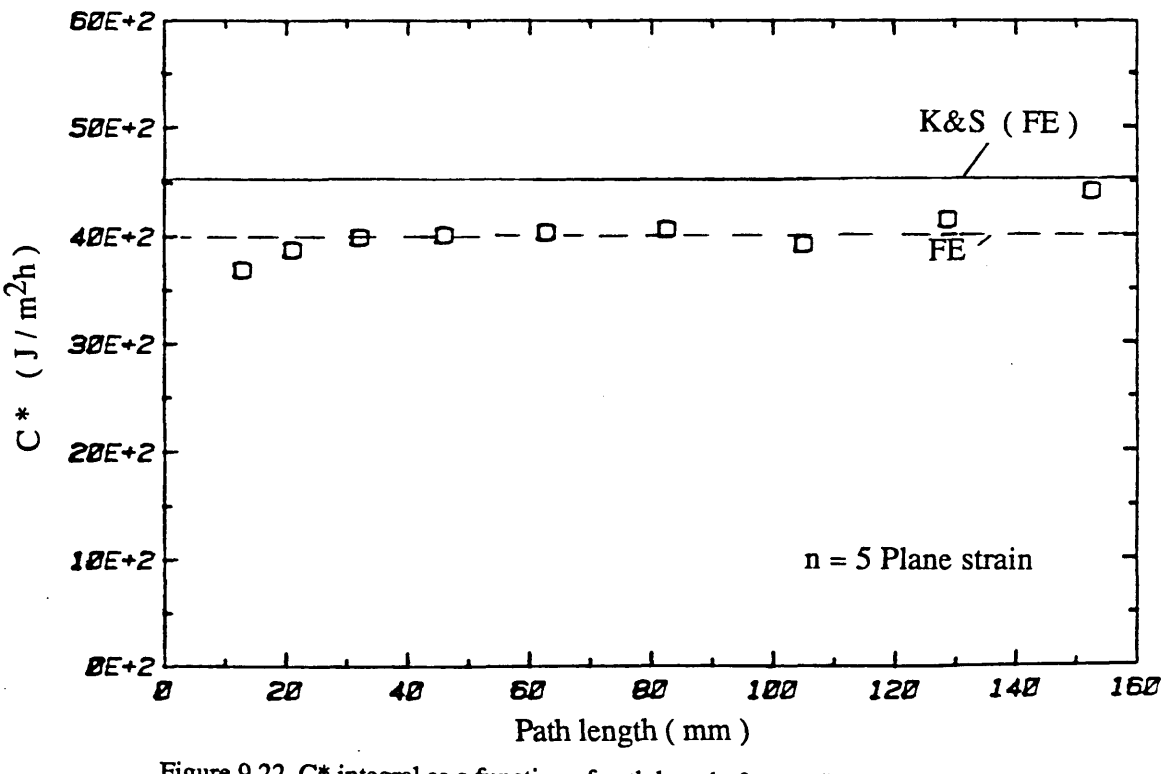


Figure 9.22 C* integral as a function of path length for n = 5 and plane strain.

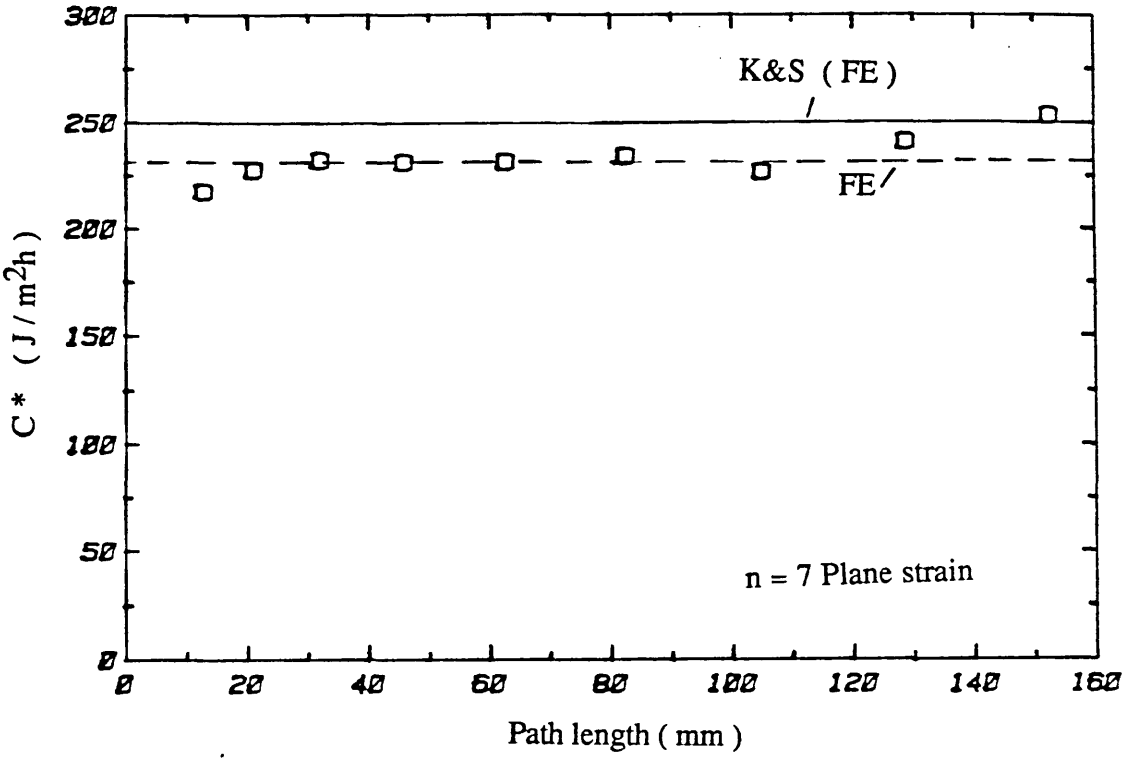


Figure 9.23 C* integral as a function of path length for n = 7 and plane strain.

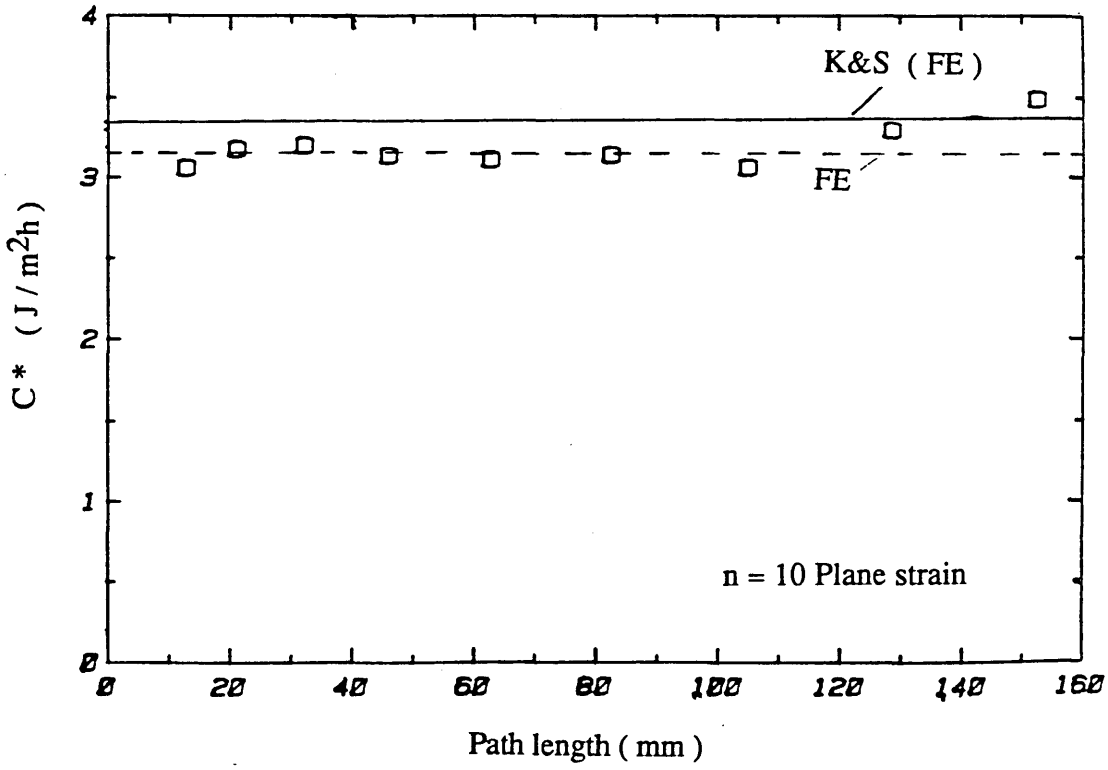


Figure 9.24 C* integral as a function of path length for n = 10 and plane strain.

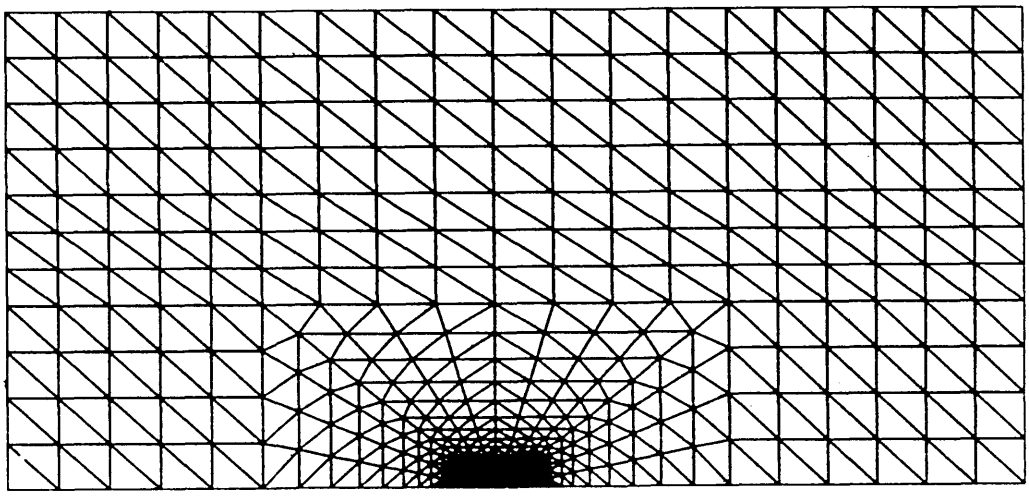


Figure 9.25 CT310 . Hole diameter = 0mm. Starter crack at a / W = 0.31.

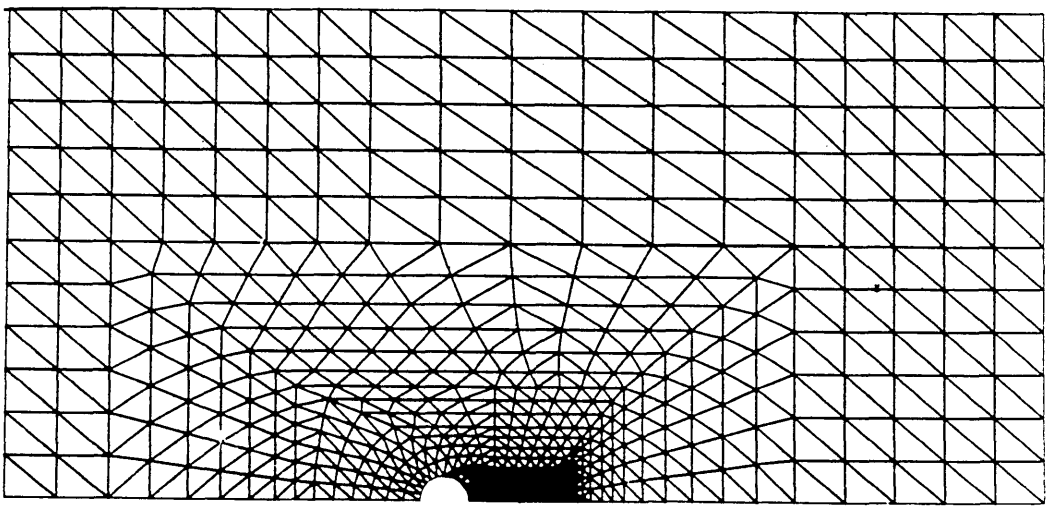


Figure 9.26 CT313 . Hole diameter = 3mm. Starter crack at a / W = 0.31.

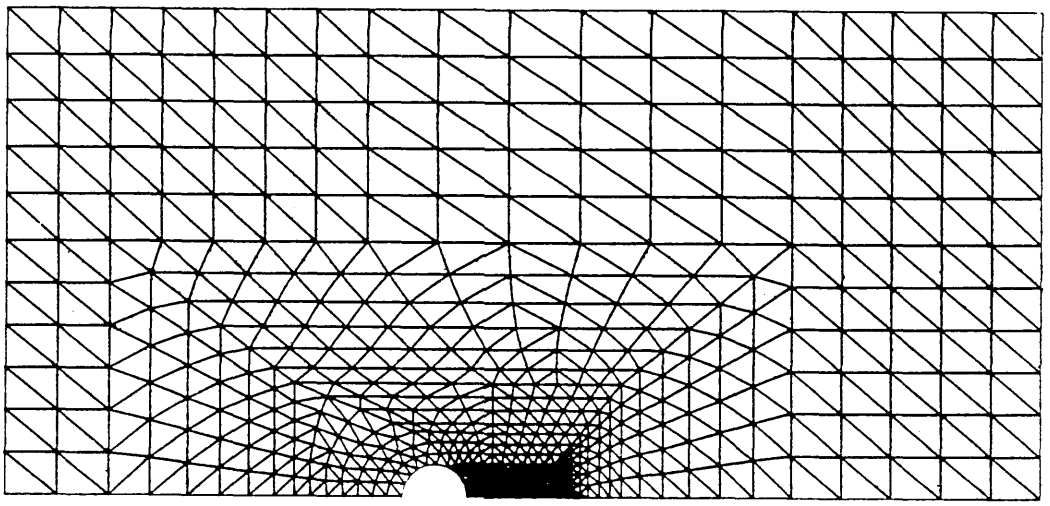


Figure 9.27 CT314 . Hole diameter = 4mm. Starter crack at a / W = 0.31.

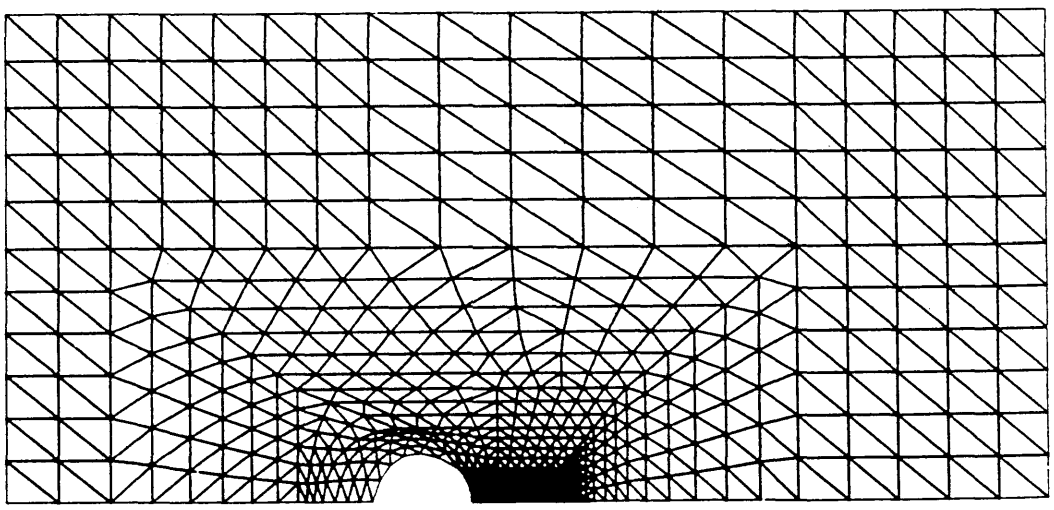


Figure 9.28 CT316 . Hole diameter = 6mm. Starter crack at a / W = 0.31.

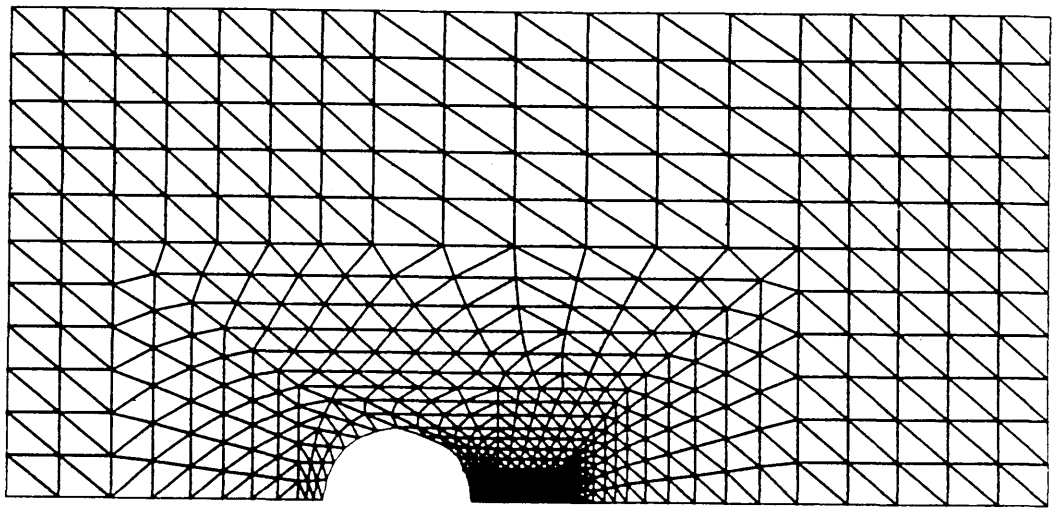


Figure 9.29 CT319 . Hole diameter = 9mm. Starter crack at a / W = 0.31.

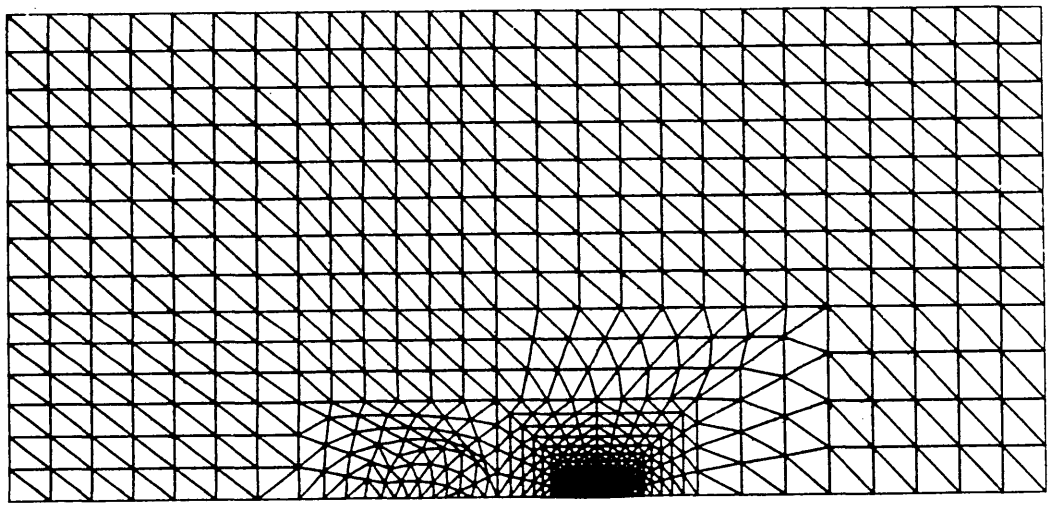


Figure 9.30 CT4260 . Hole diameter = 0mm. Starter crack at a / W = 0.426.

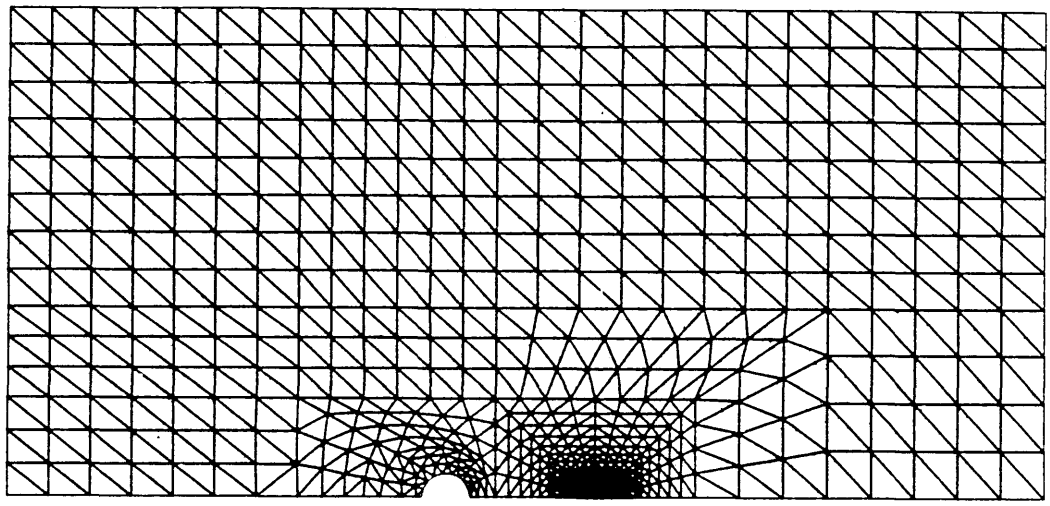


Figure 9.31 CT4263 . Hole diameter = 3mm. Starter crack at a / W = 0.426.

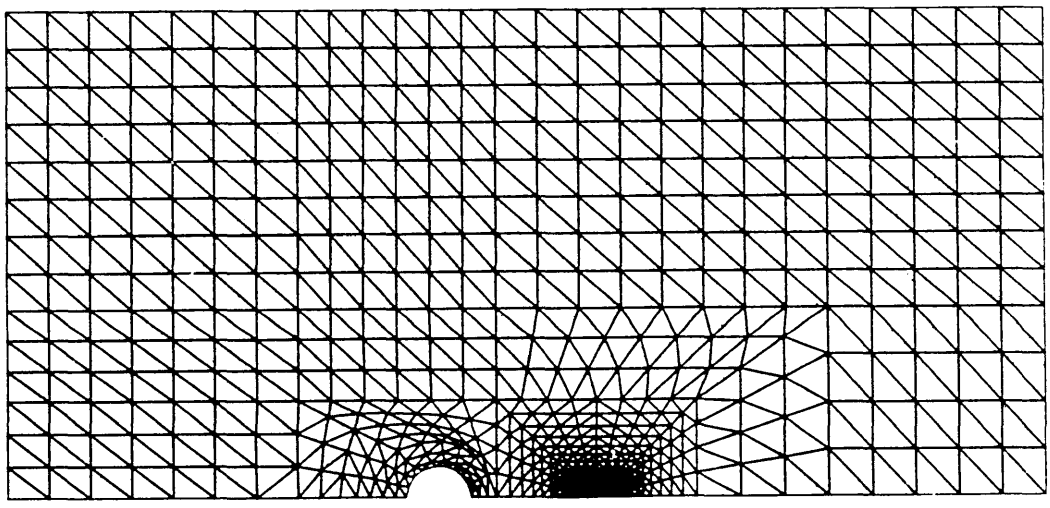


Figure 9.32 CT4264 . Hole diameter = 4mm. Starter crack at a / W = 0.426.

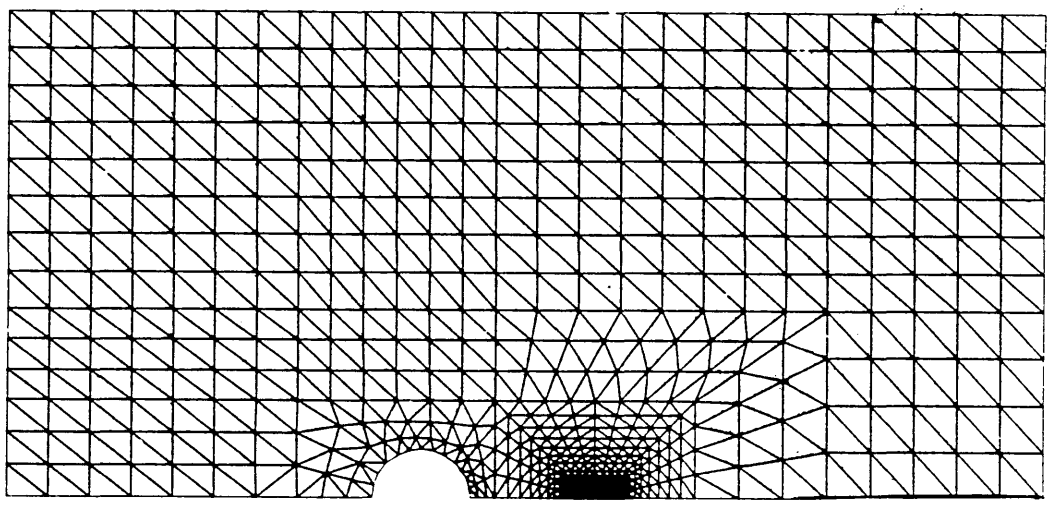


Figure 9.33 CT4266 . Hole diameter = 6mm. Starter crack at a / W = 0.426.

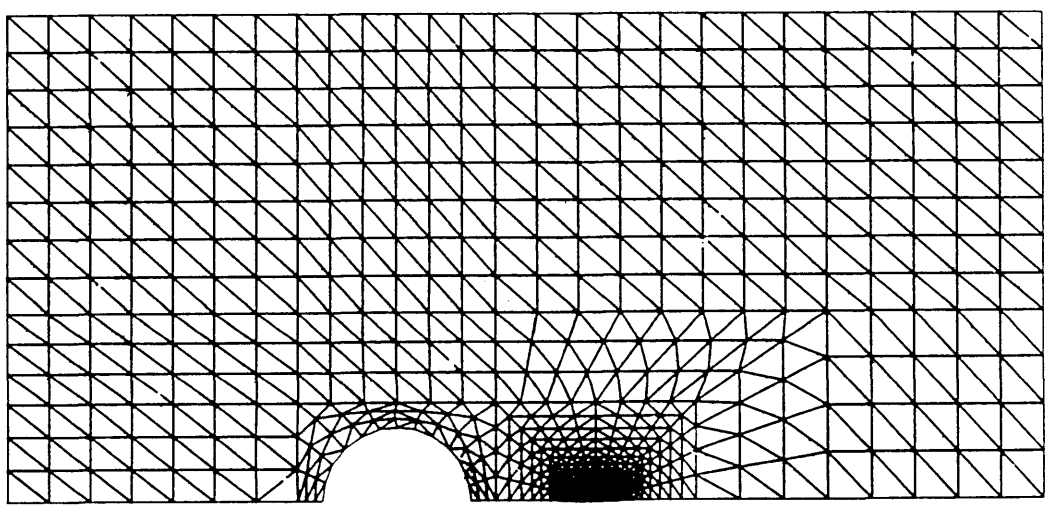


Figure 9.34 CT4269 . Hole diameter = 9mm. Starter crack at a / W = 0.426.

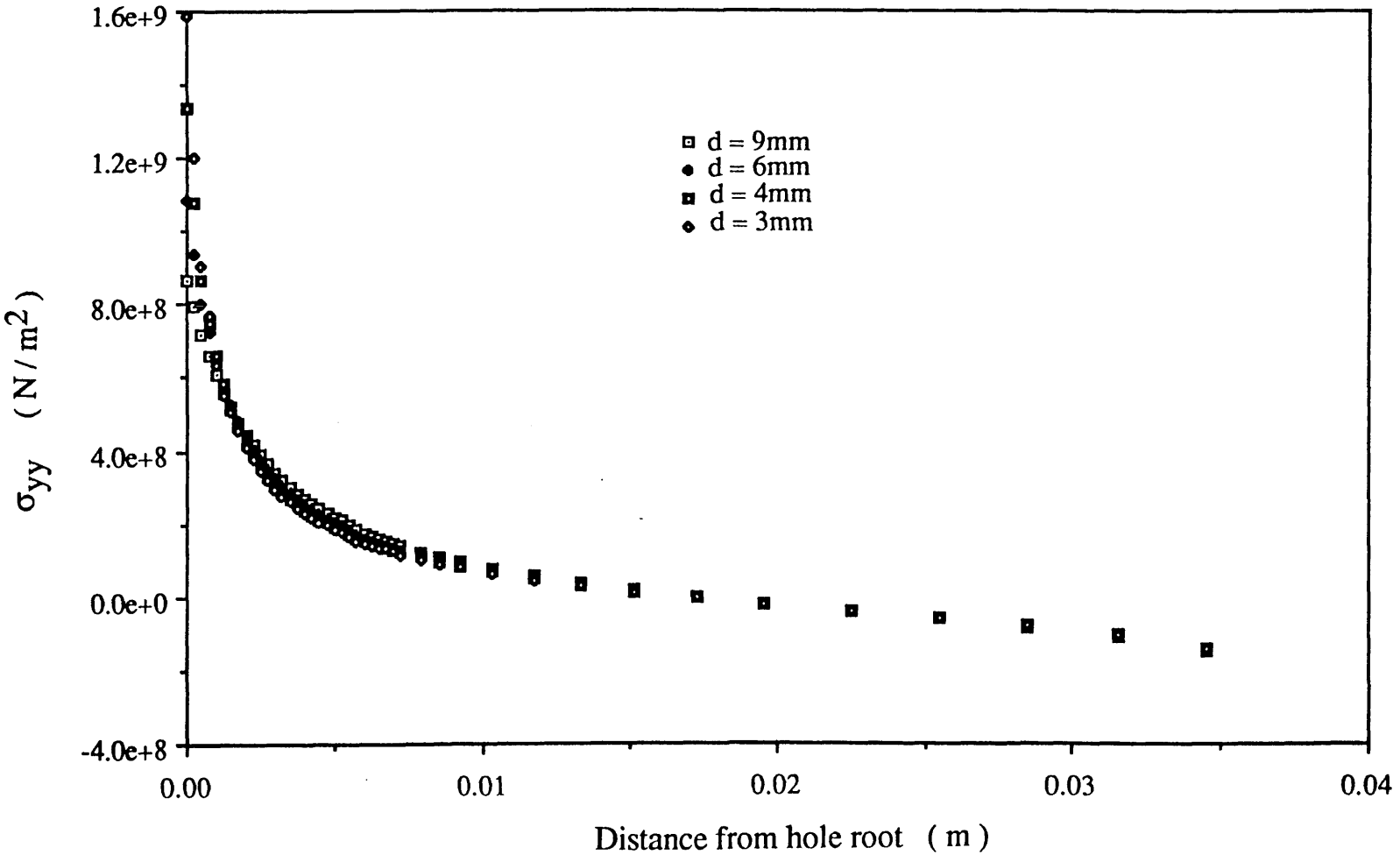


Figure 9.35 Elastic stress distribution across section ahead of a blunt hole in a compact tension geometry.

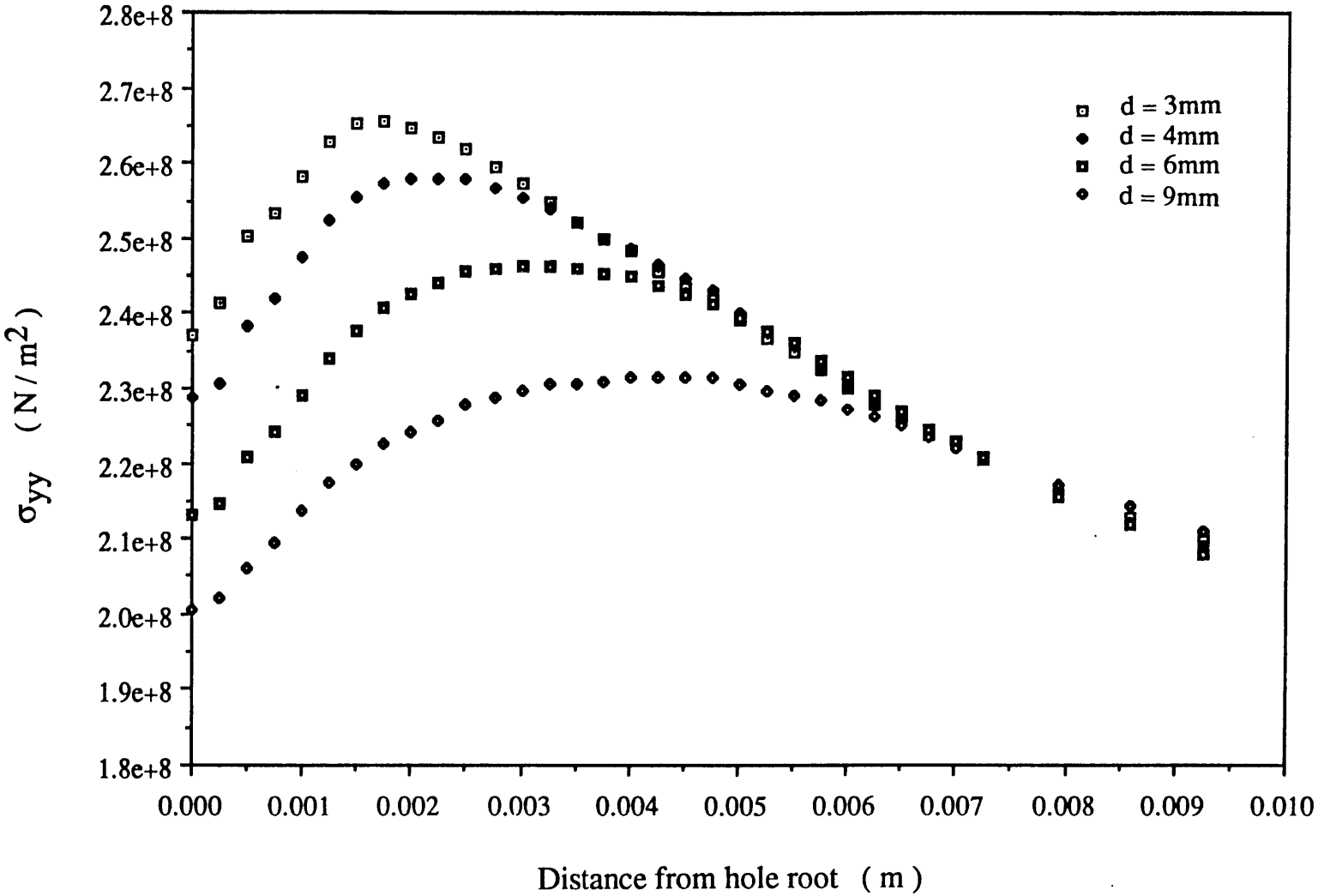


Figure 9.36 Steady state creep stress distribution close to a blunt hole in a compact tension geometry (n = 10).

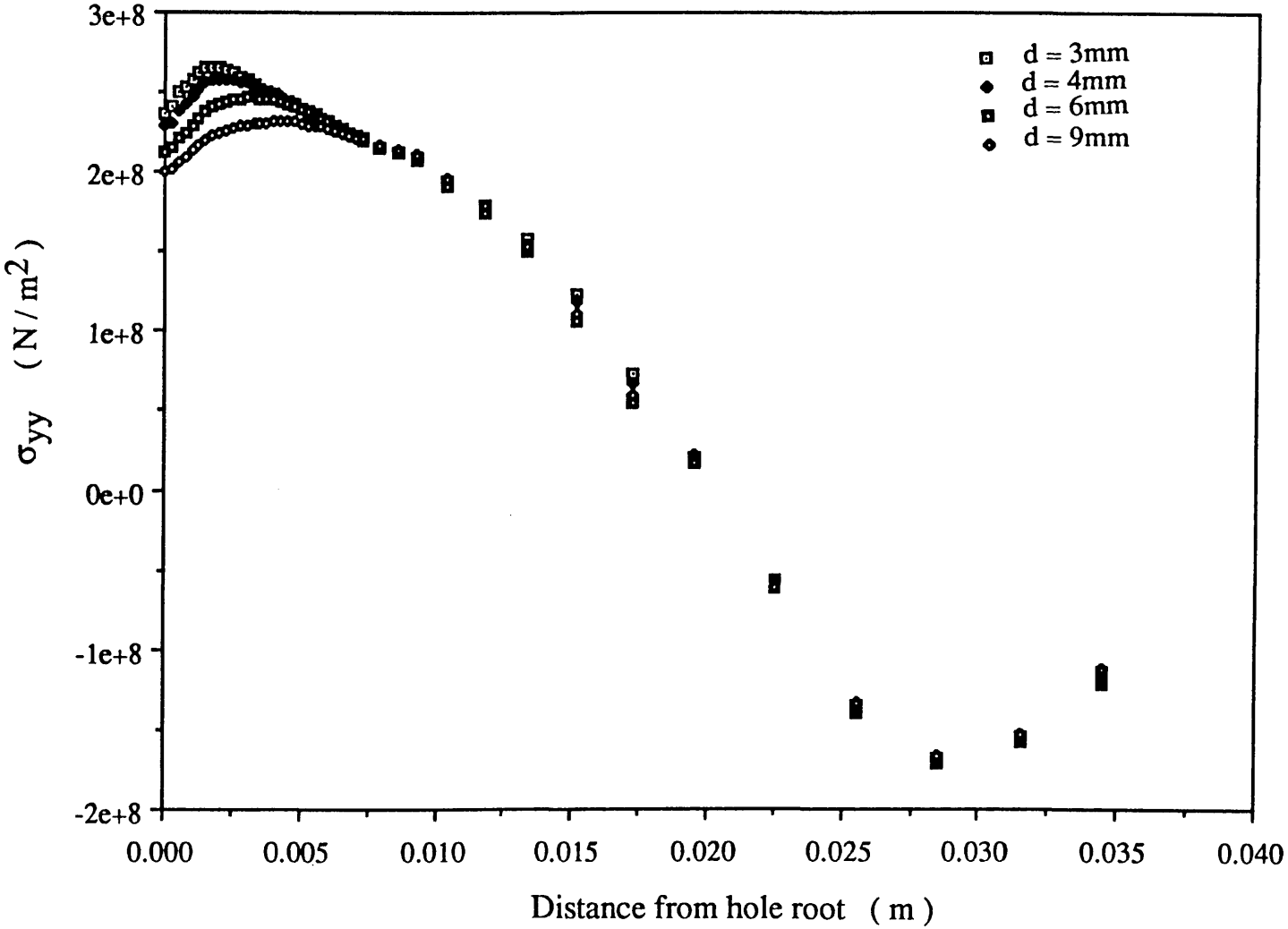


Figure 9.37 Steady state creep stress distribution across section ahead of a blunt hole in a compact tension geometry (n = 10).

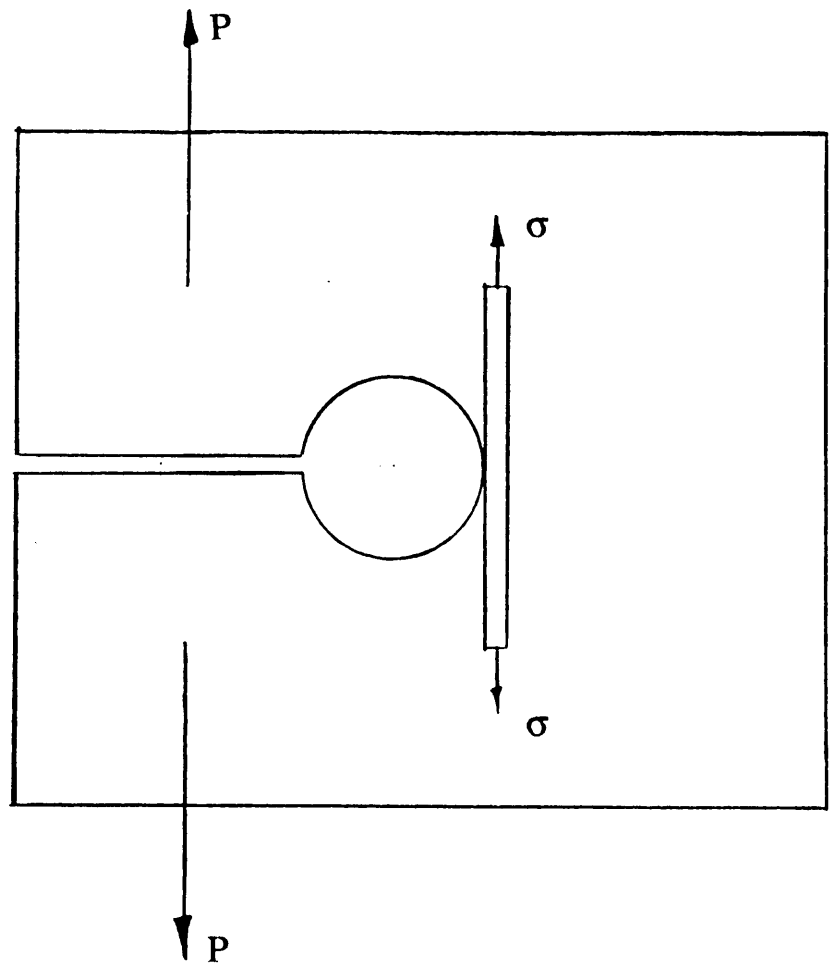


Figure 9.38 Schematic representation of a column of material just ahead of the hole root in a compact tension specimen containing a blunt hole.

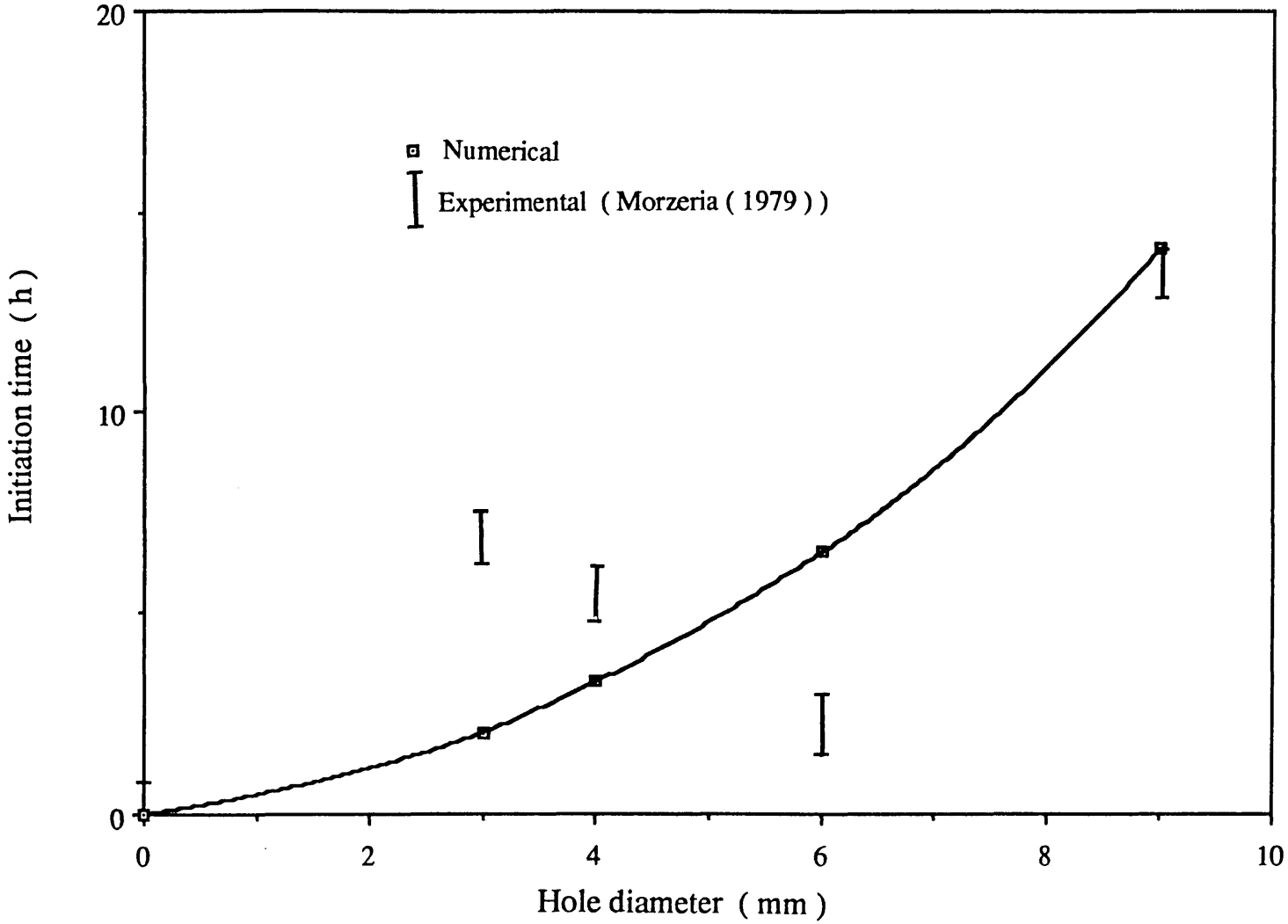


Figure 9.39 Comparison of the predicted and numerical crack initiation times.

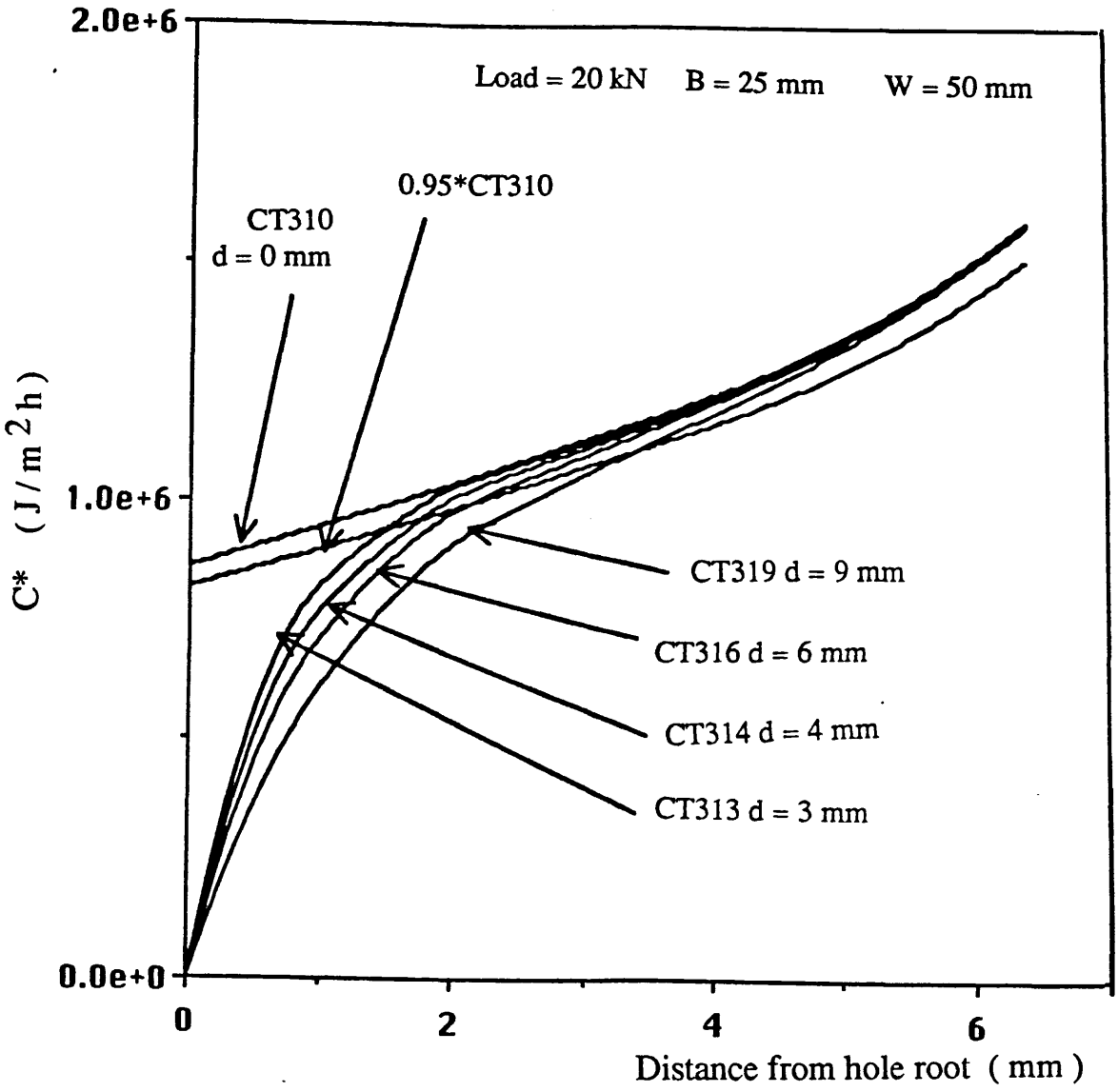


Figure 9.40 C* versus distance from hole root for various hole diameters for the compact tension geometry (n = 1).

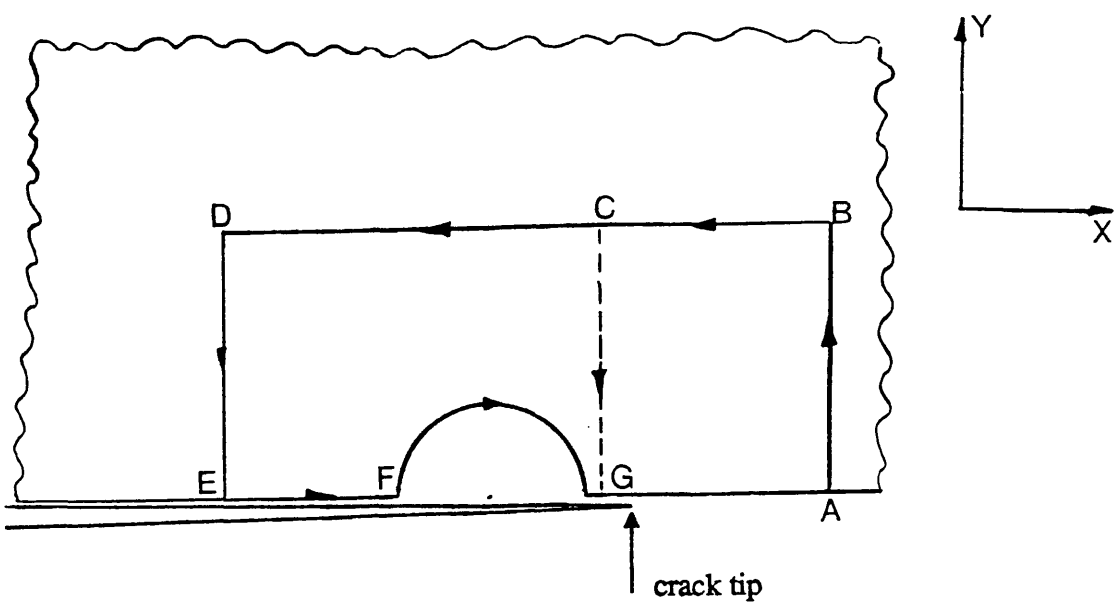


Figure 9.41 Suitable contours for the evaluation of contour integrals in a geometry containing a blunt hole.

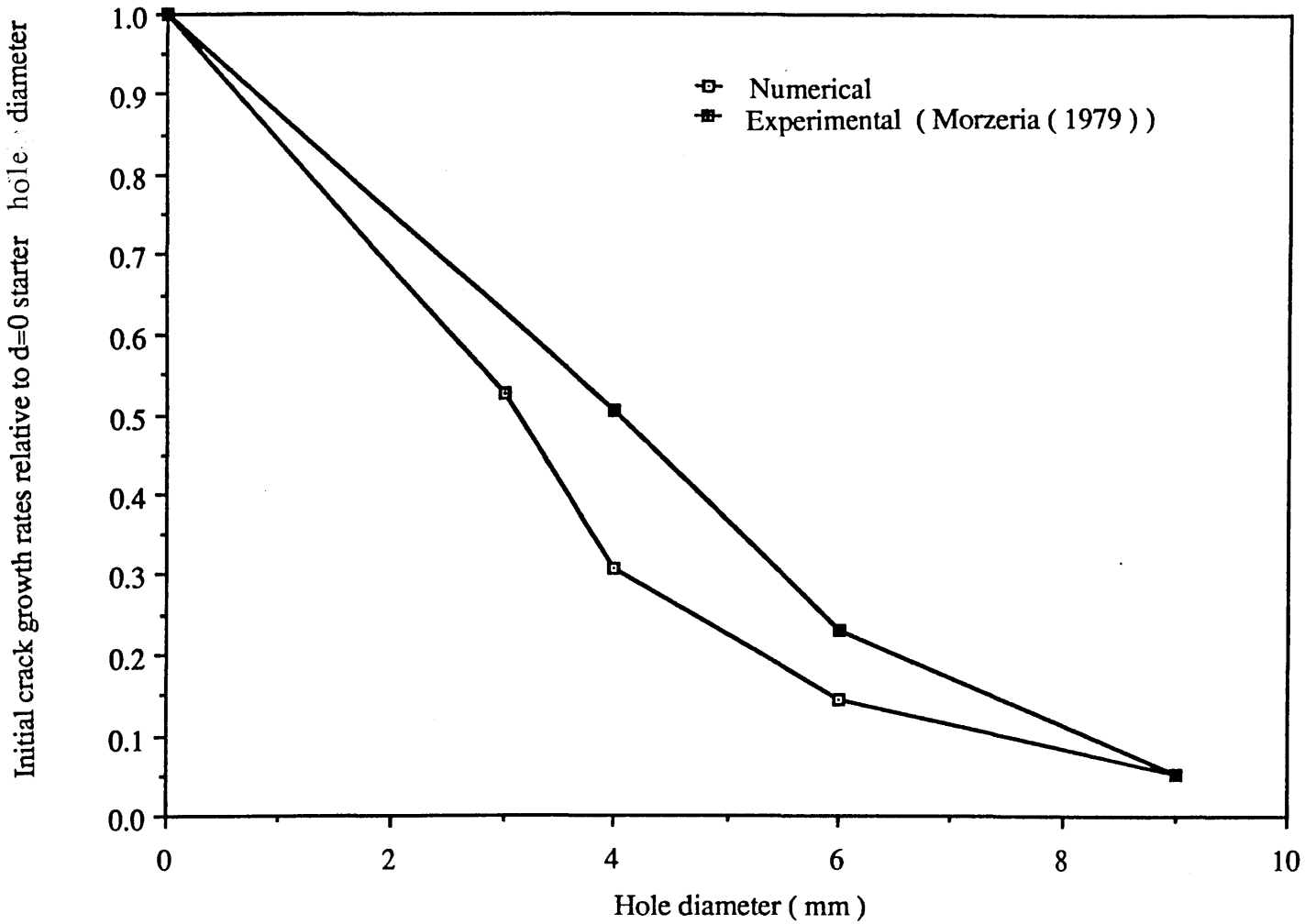


Figure 9.42 Initial relative crack growth rates for a crack emanating from blunt holes in a compact tension specimen when the crack growth is characterized in terms of the stress intensity factor K.

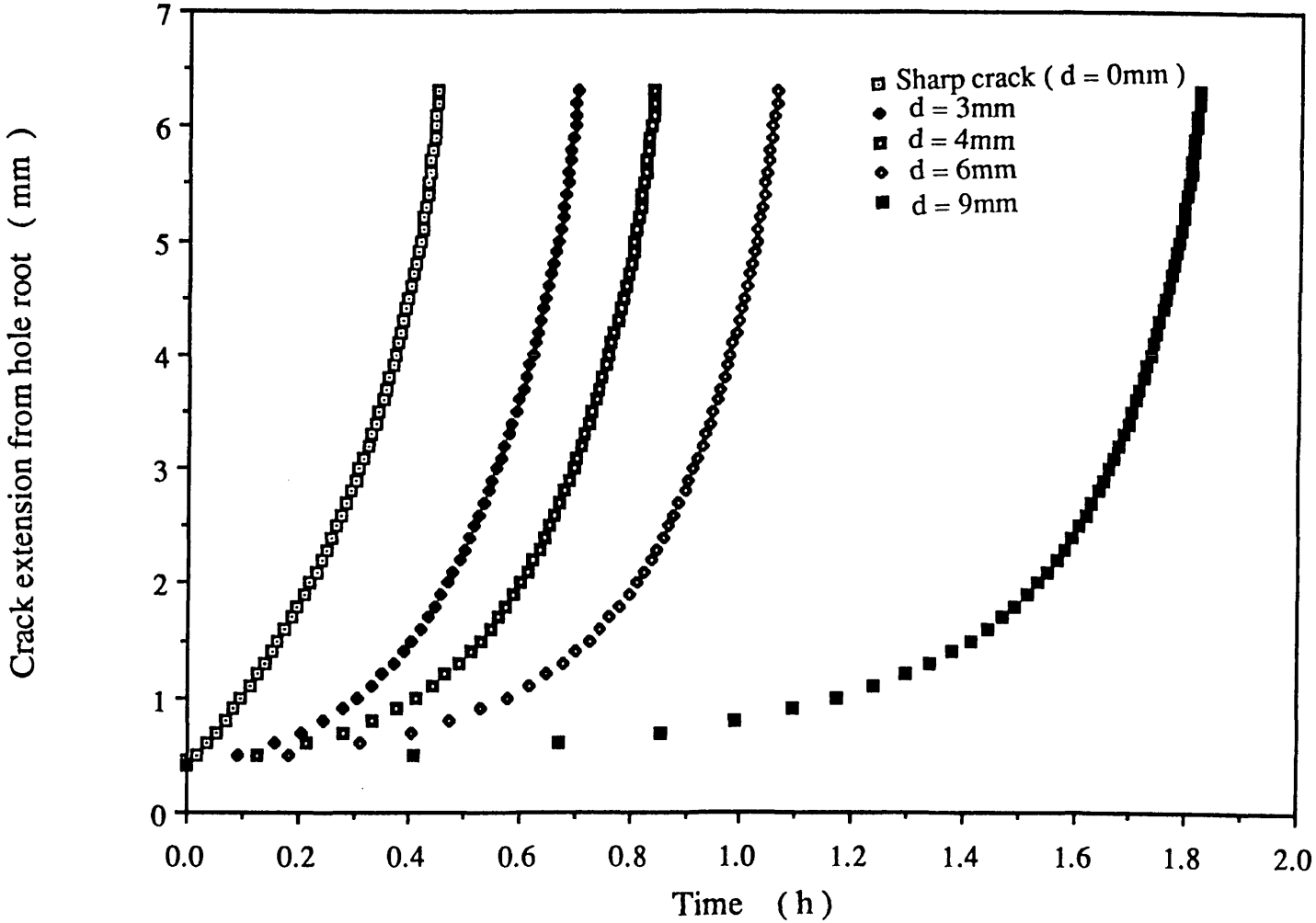


Figure 9.42a Effect of increasing the hole diameter on the evolution of a crack emanating from a blunt hole in a compact tension specimen , when the crack growth is characterized in terms of the stress intensity factor K.

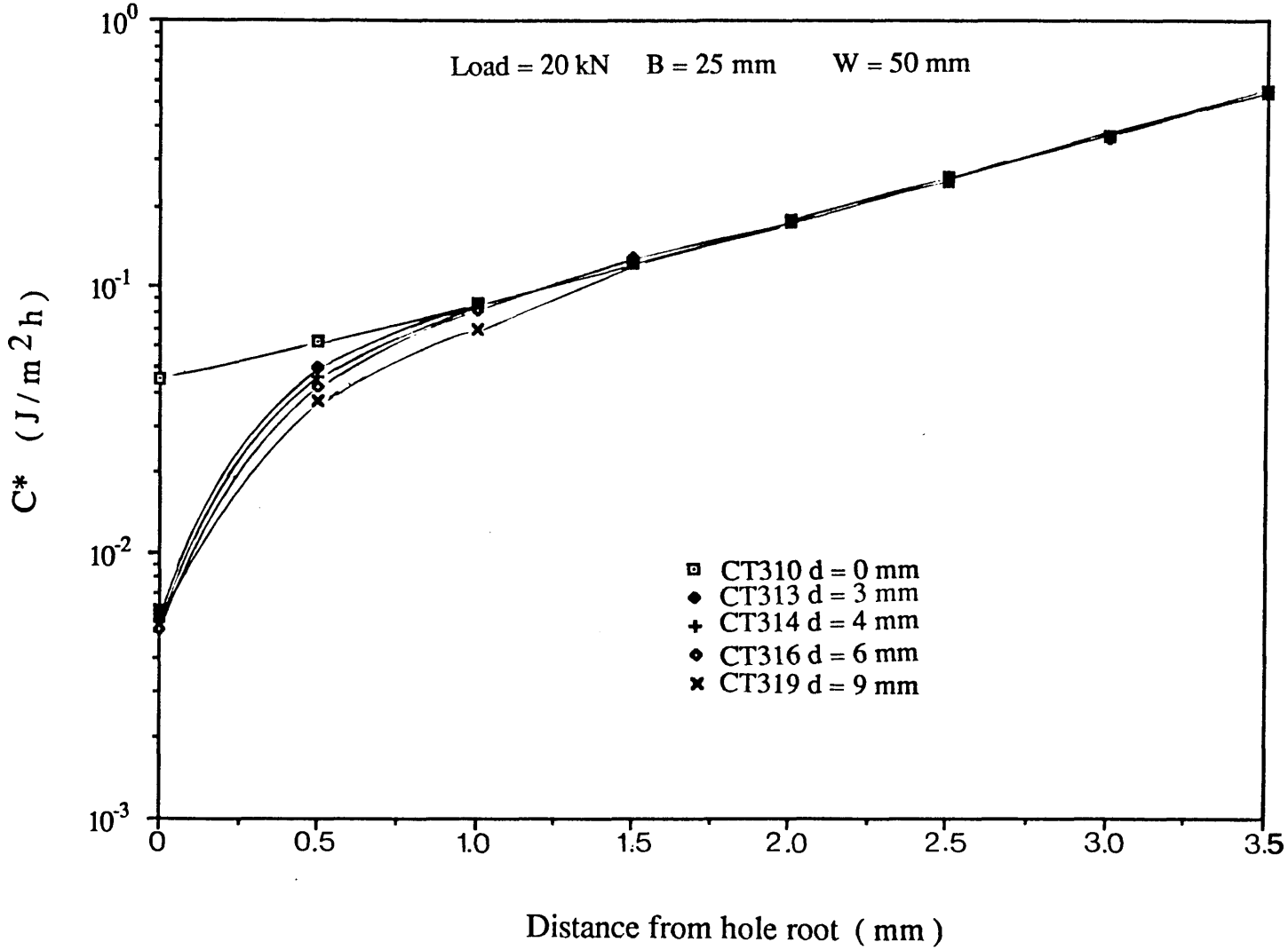


Figure 9.43 C* versus distance from hole root for various hole diameters for the compact tension geometry (n = 10).

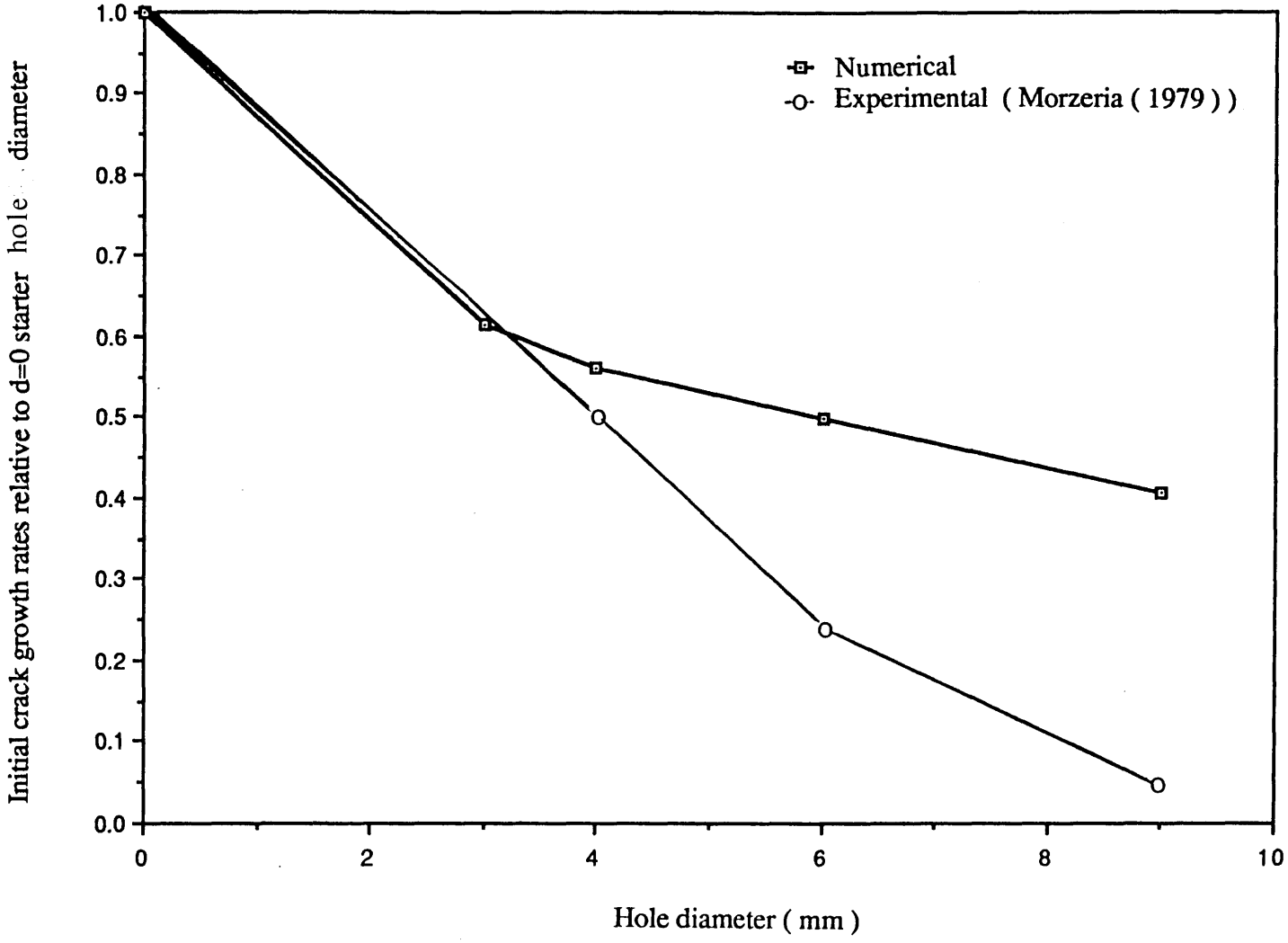


Figure 9.44 Initial relative crack growth rates for a crack emanating from blunt holes in a compact tension specimen when the crack growth is characterized in terms of the steady state creep contour integral C*

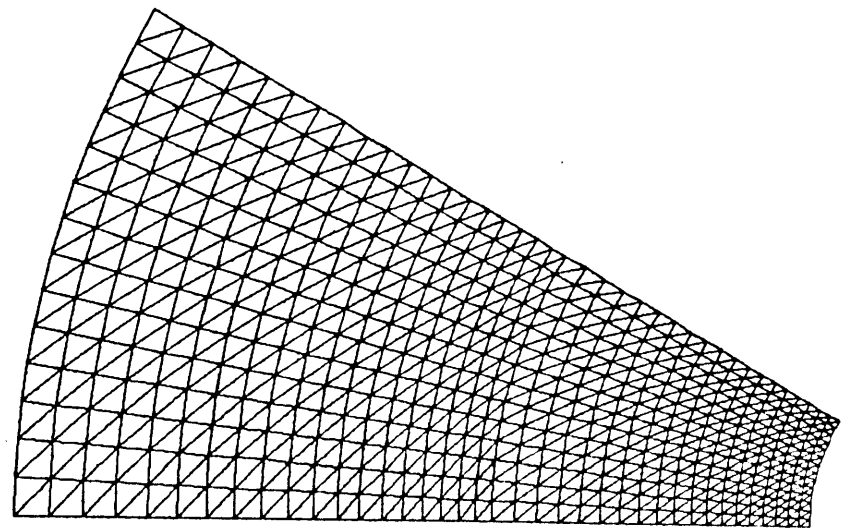


Figure 9.45 Finite Element mesh of a rotating disk containing a central hole only.

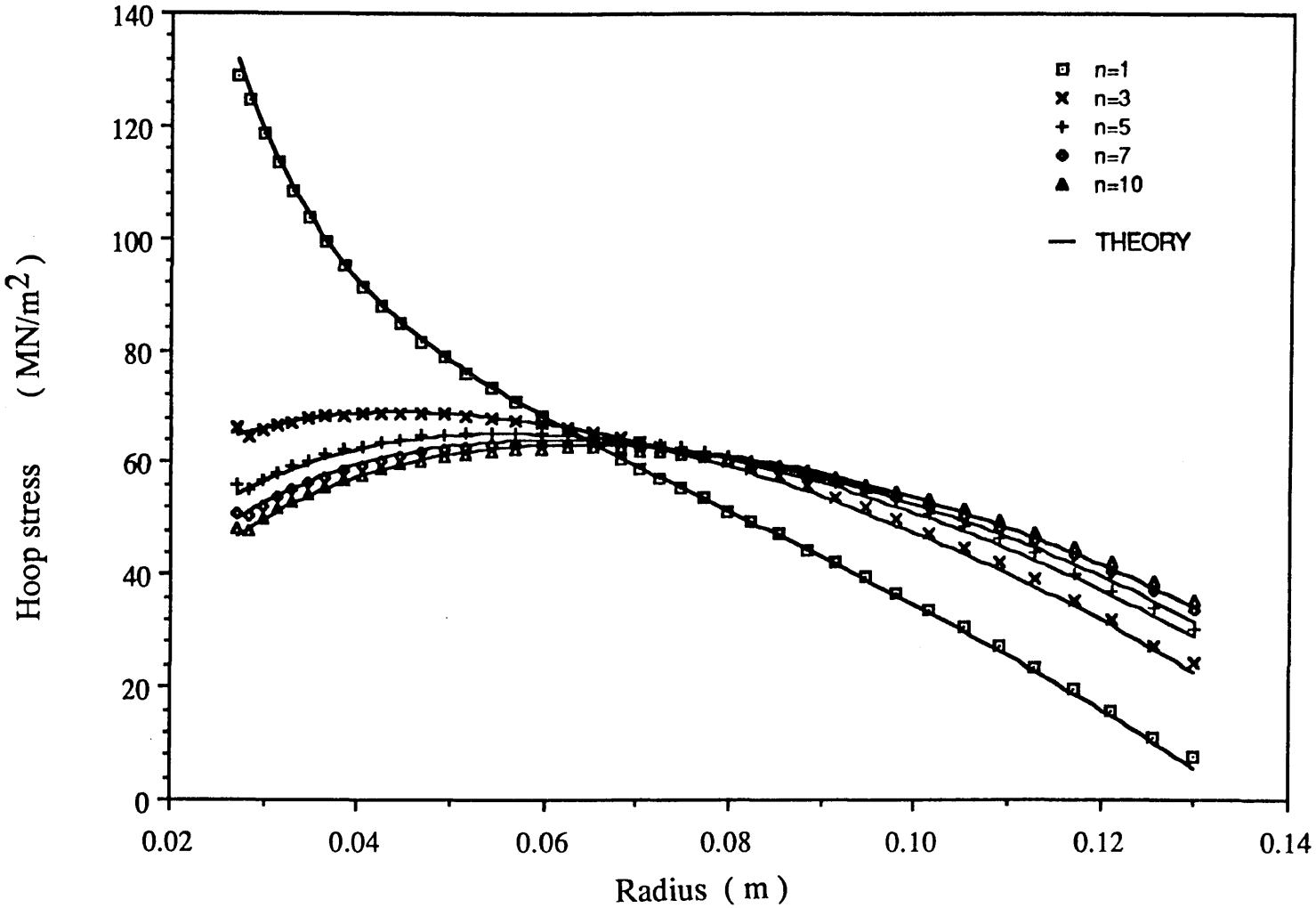


Figure 9.46 Comparison between numerical and analytical creep stress distributions for plane strain for rotating disc with a central hole.

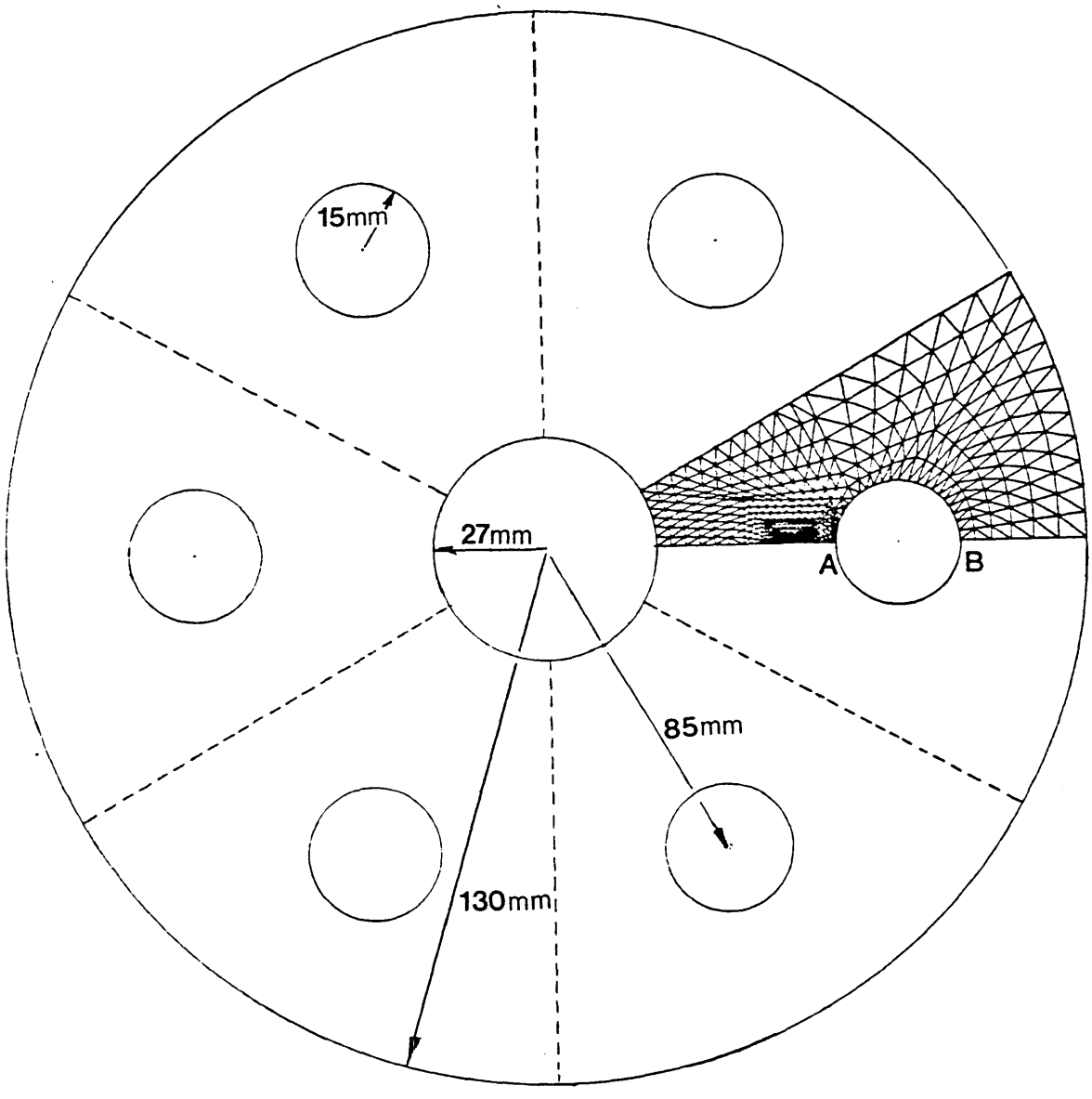


Figure 9.47 Finite Element mesh for rotating disc with central hole and six satellite holes with crack emanating from hole at point A.

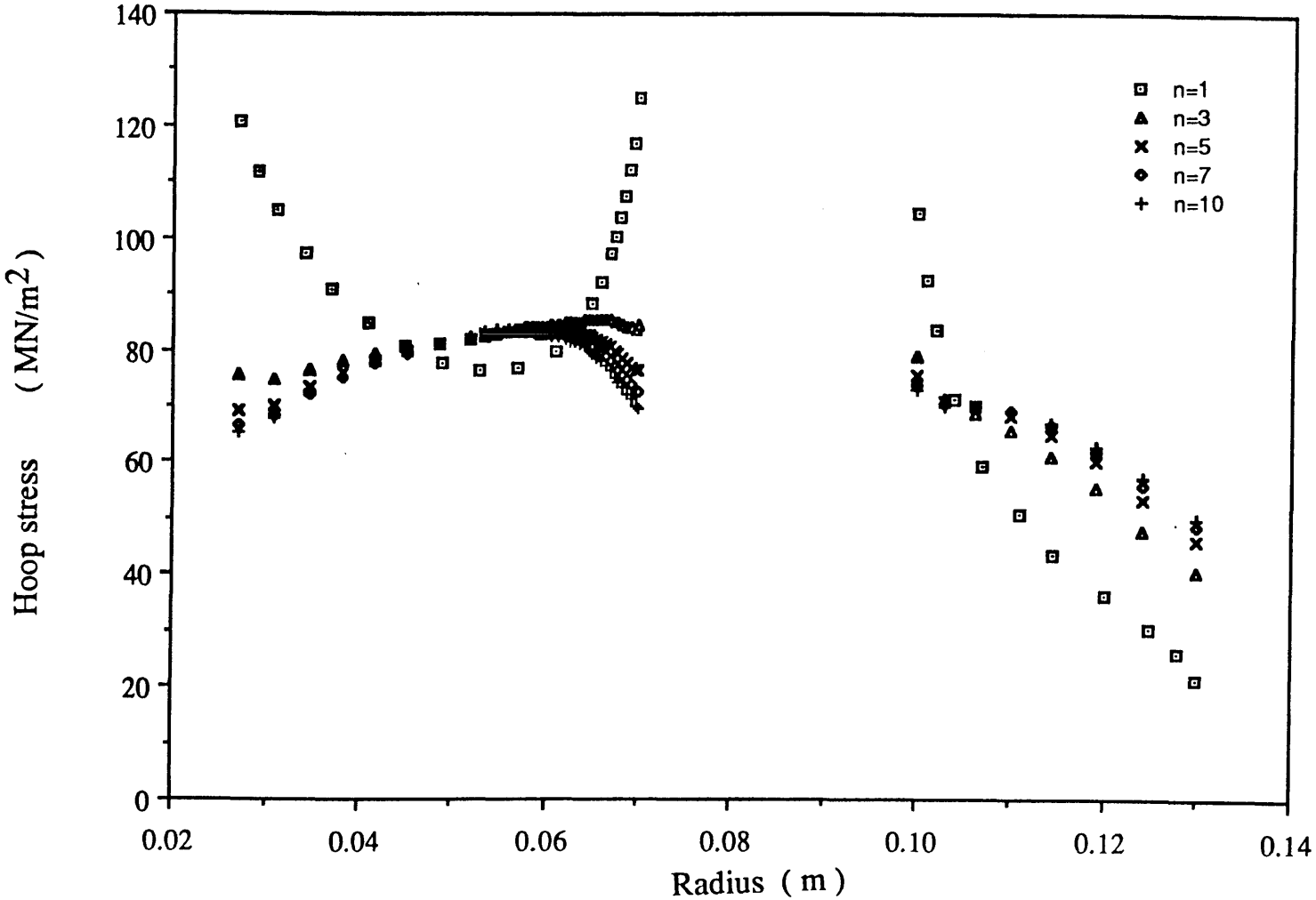


Figure 9.48 Hoop stress distribution for rotating disc with central hole and six satellite holes.

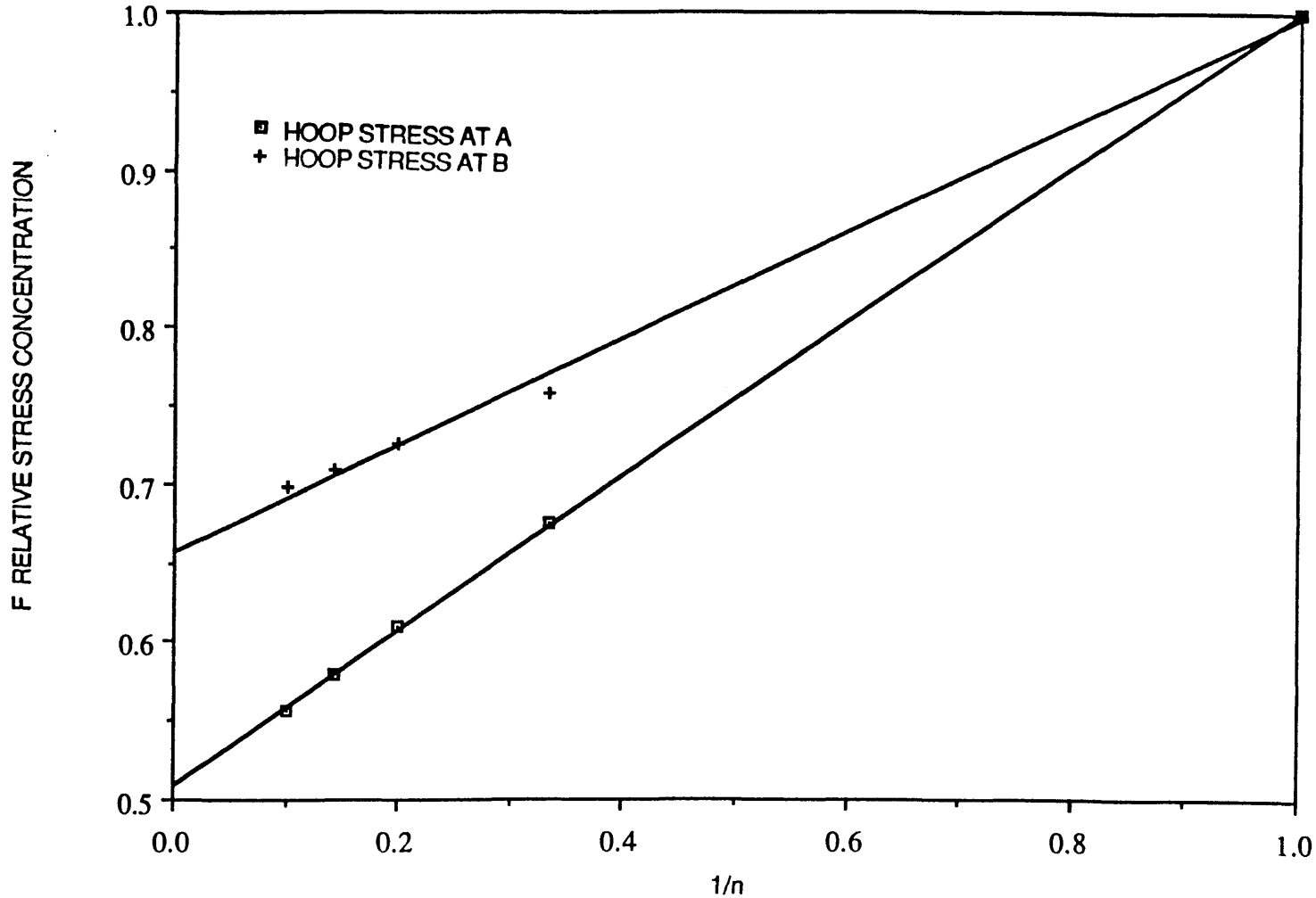


Figure 9.49 Dependence of stress concentrations at satellite hole on stress exponent n.

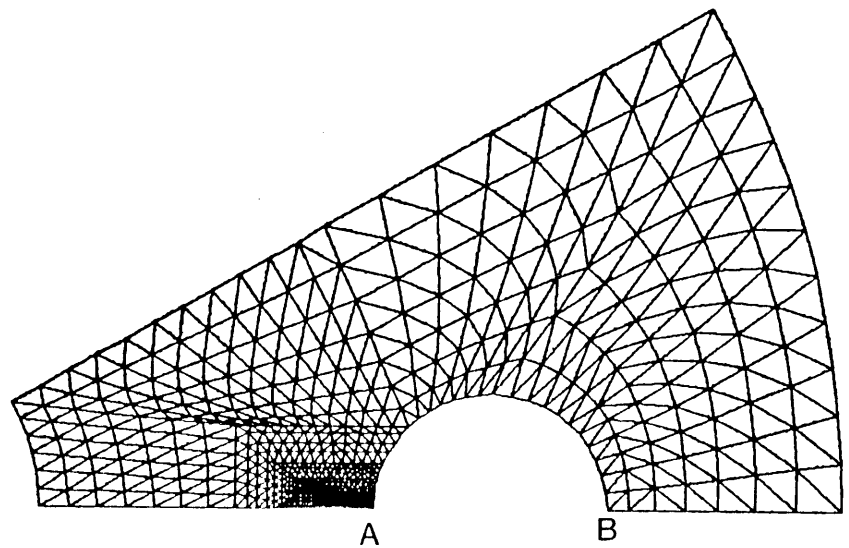


Figure 9.50 Finite Element mesh for rotating disc with central hole and six satellite holes with crack emanating from hole at point A.

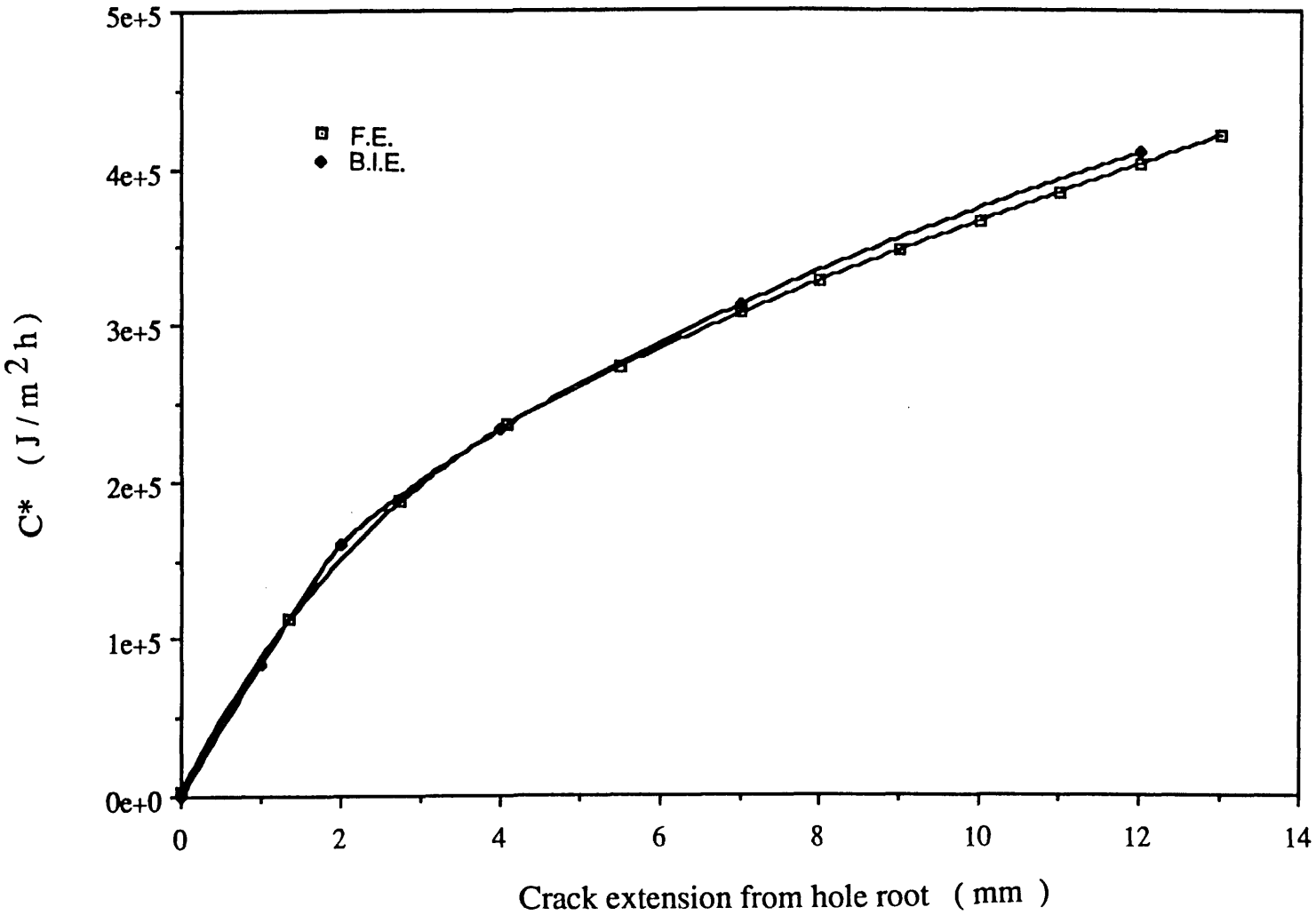


Figure 9.51 Comparison of C* at position A, determined by Finite Element and Boundary Integral Equation methods for n = 1 , plane stress.

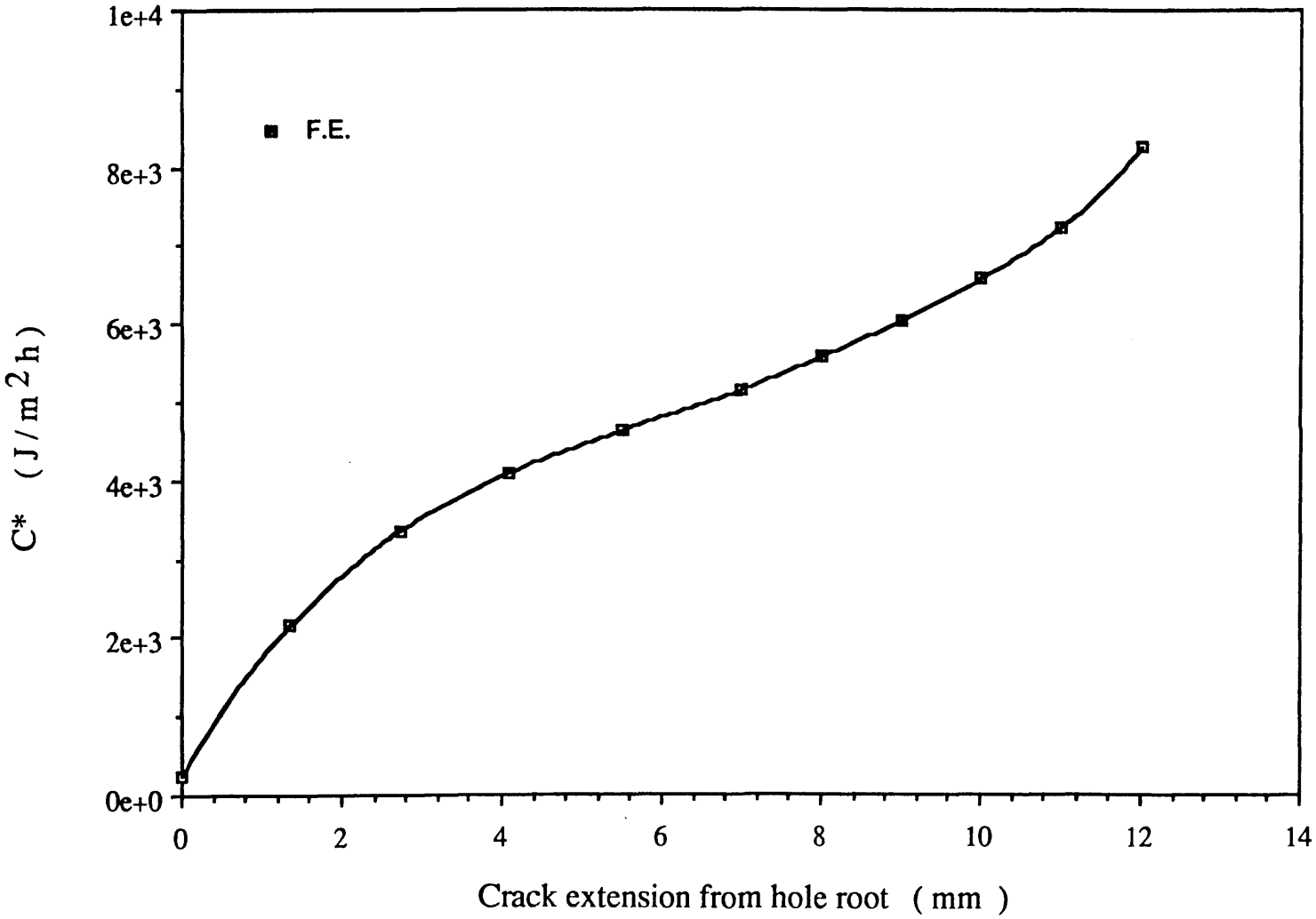


Figure 9.52 C* for n = 3 plane stress , for crack growth from point A of satellite hole.

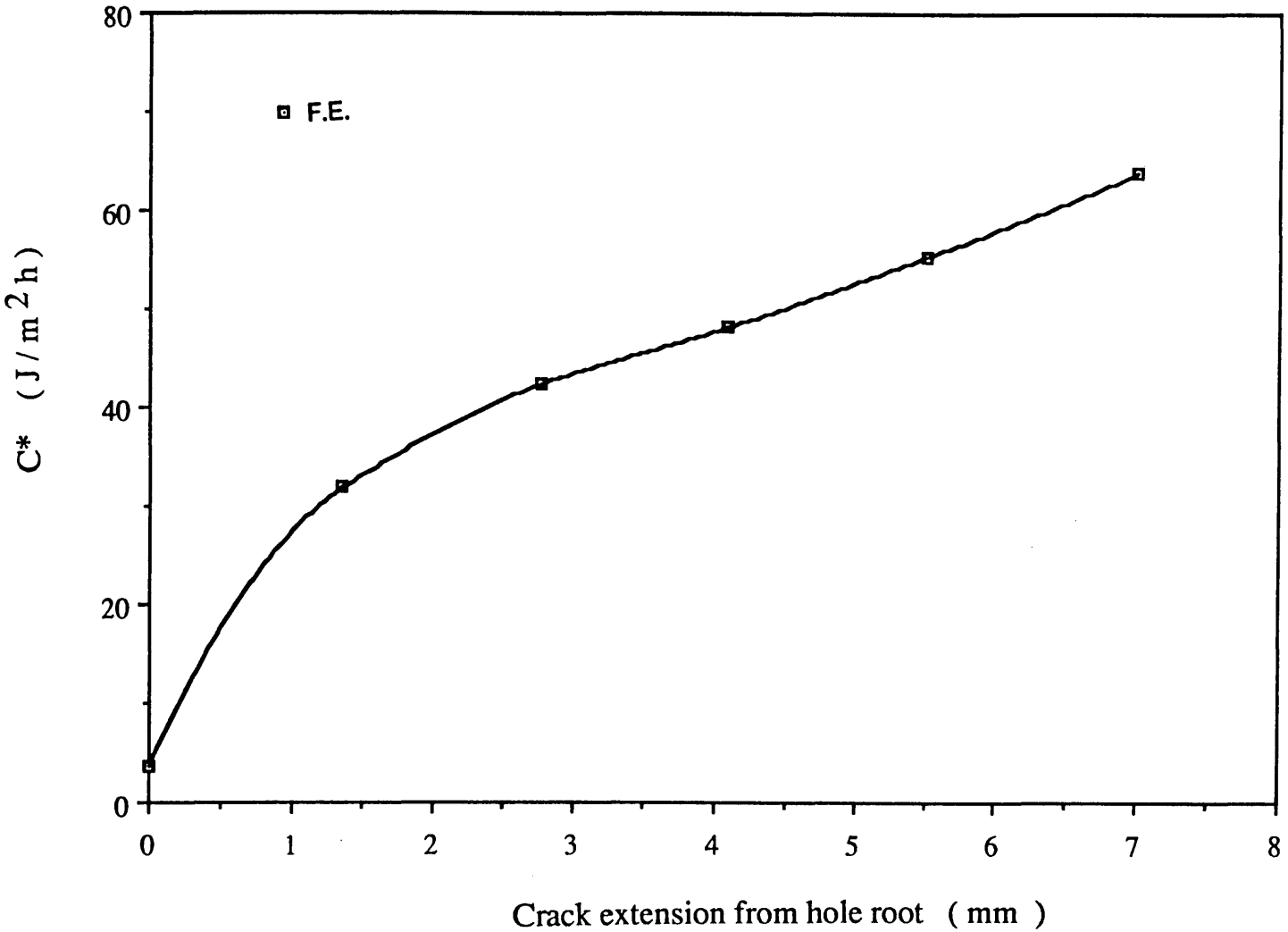


Figure 9.53 C* for n = 5 plane stress , for crack growth from point A of satellite hole.

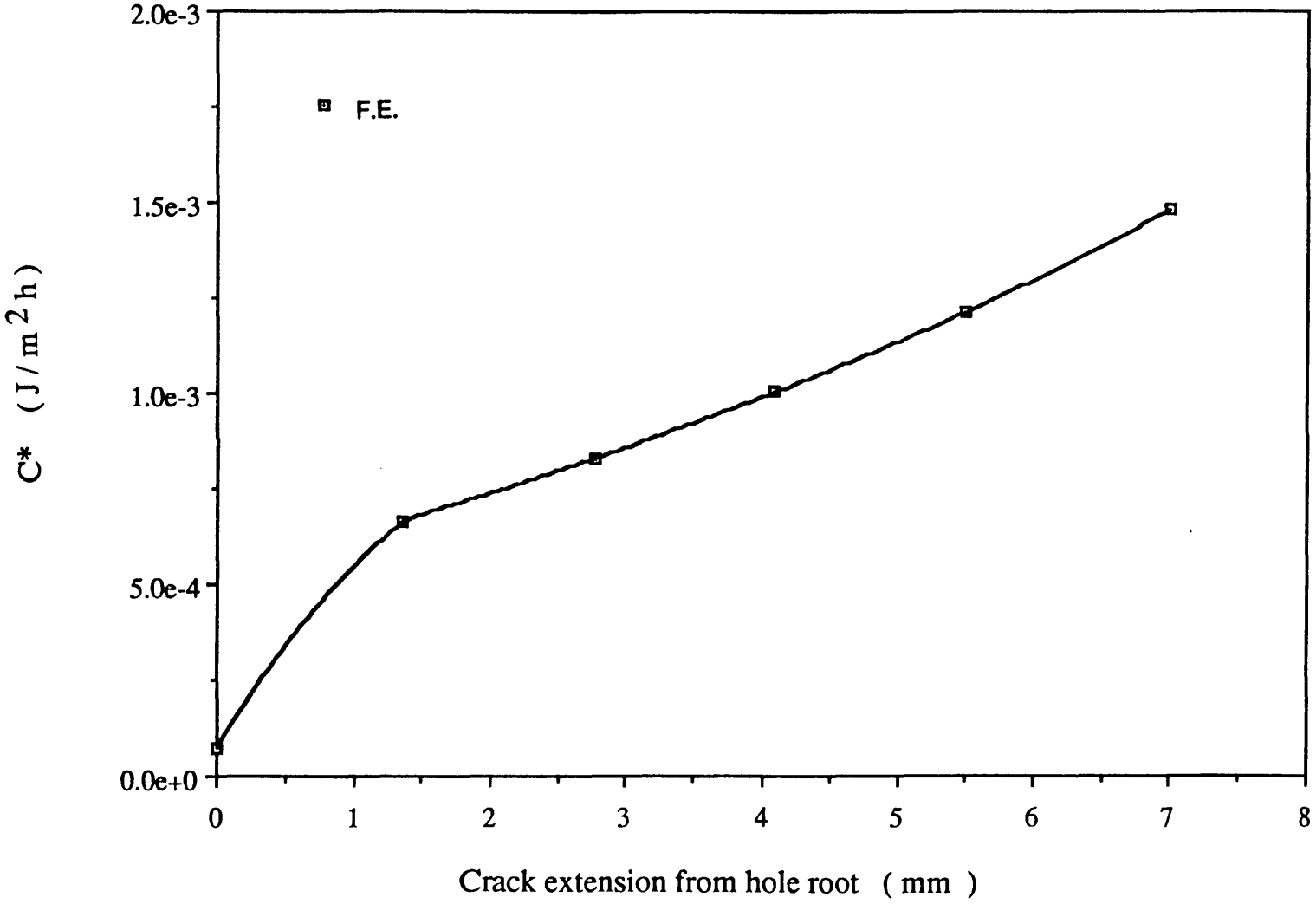


Figure 9.54 C* for n = 10 plane stress ,for crack growth from point A of satellite hole.

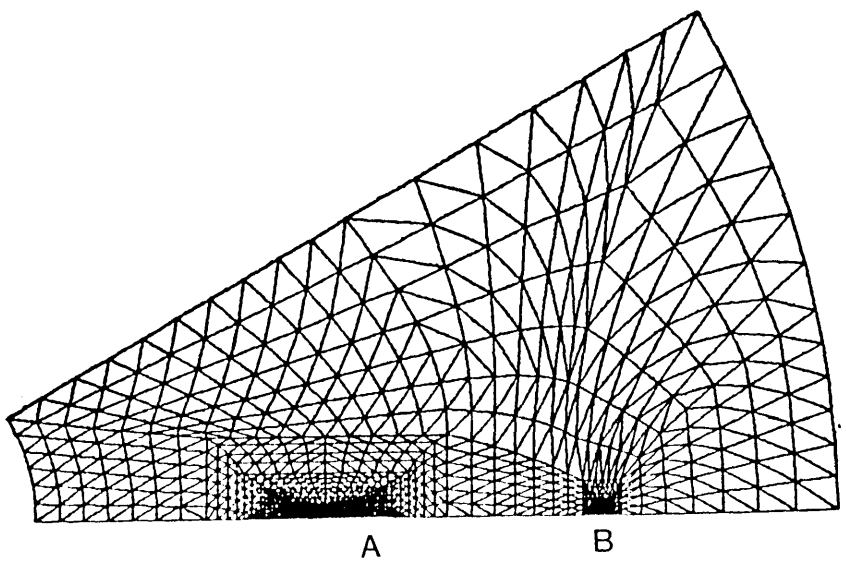


Figure 9.55 Finite Element mesh for rotating disc containing a crack aligned in the radial direction and with the crack emanating from point A.

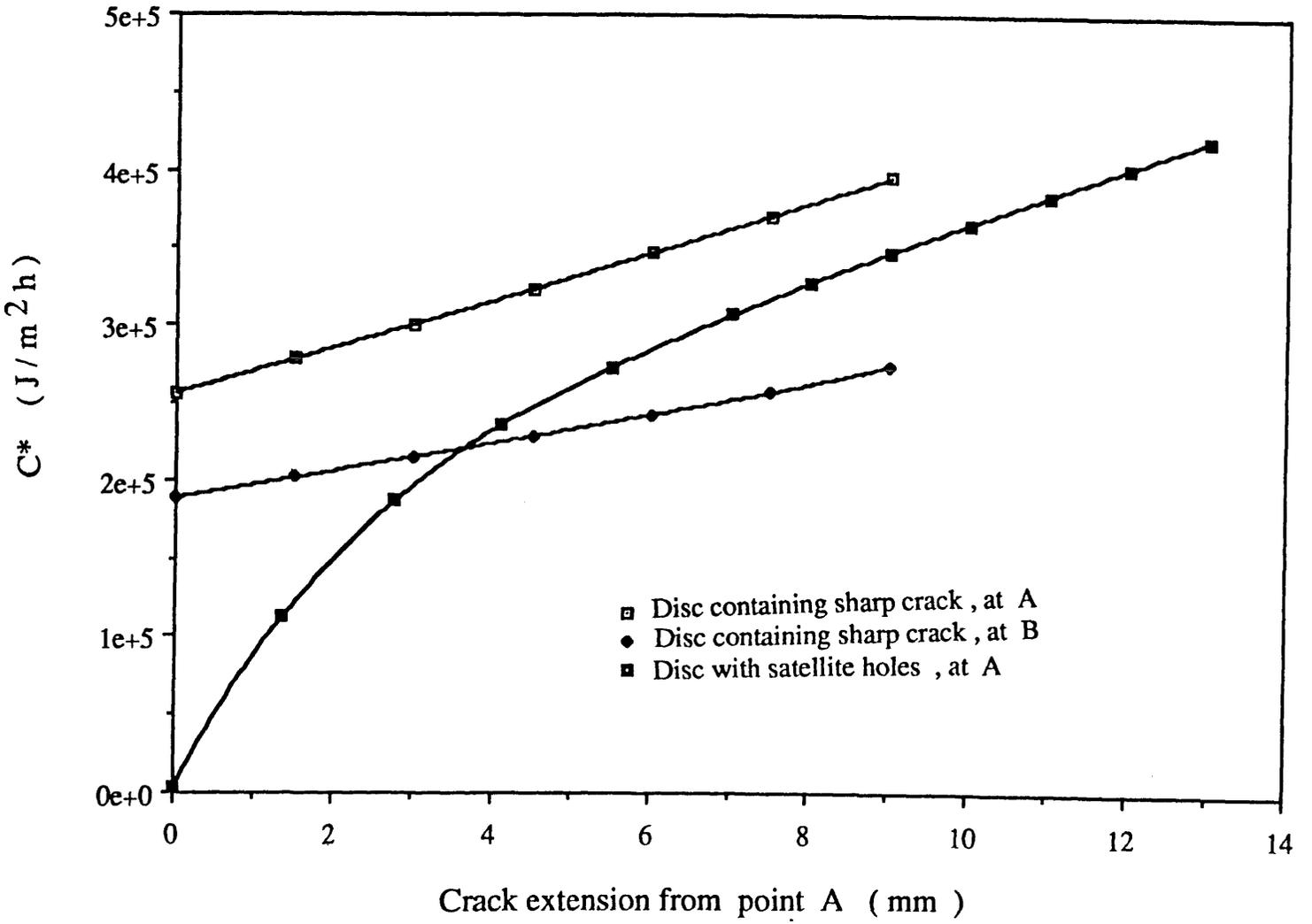


Figure 9.56 C* for n = 1 , plane stress . Comparison between disc with central hole and six satellite holes (figure 9.50) ,and, disc with sharp crack (figure 9.55).

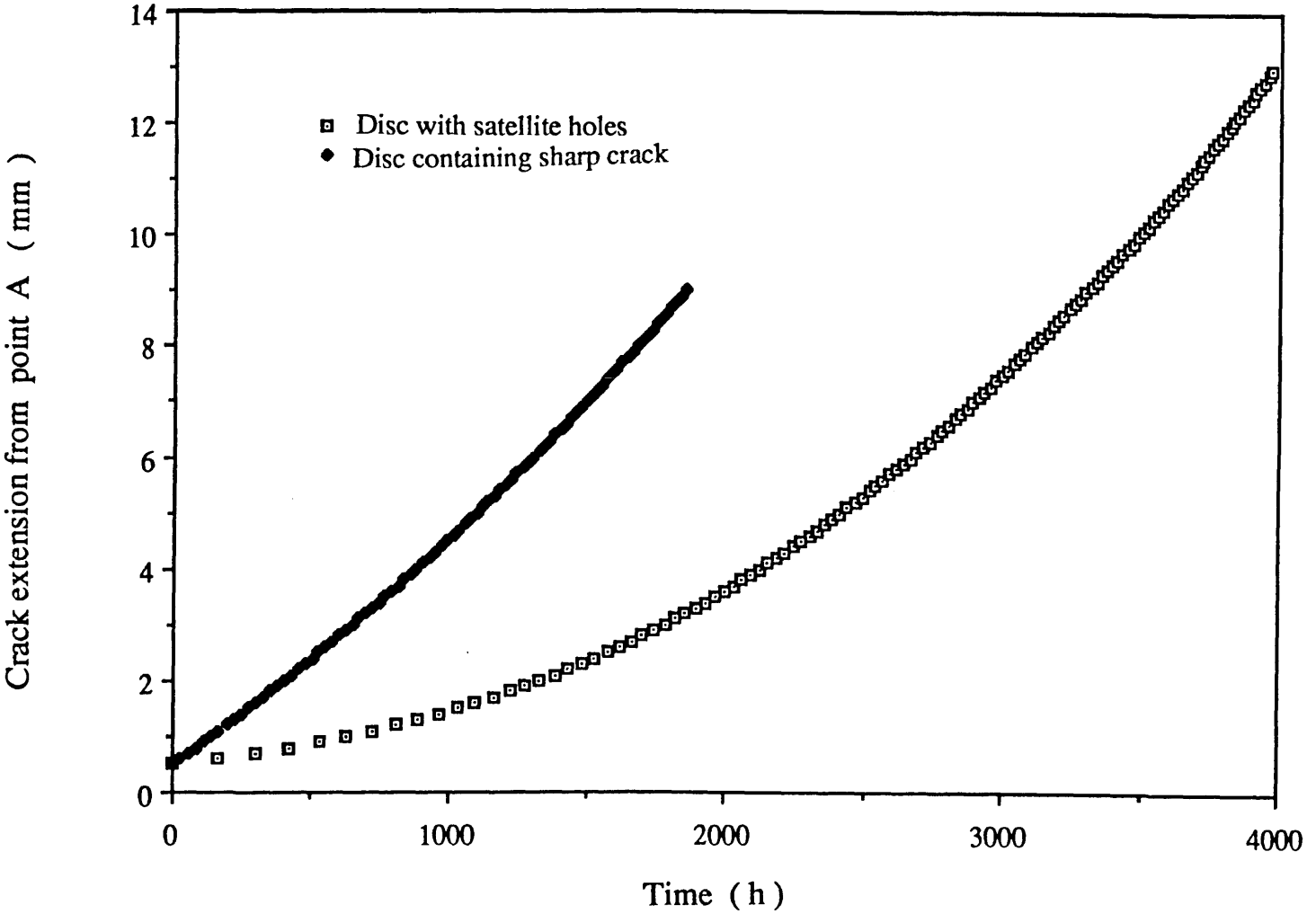


Figure 9.56a Evolution of crack length as a function of time in a rotating disc when the crack growth is characterized in terms of the stress intensity factor K.

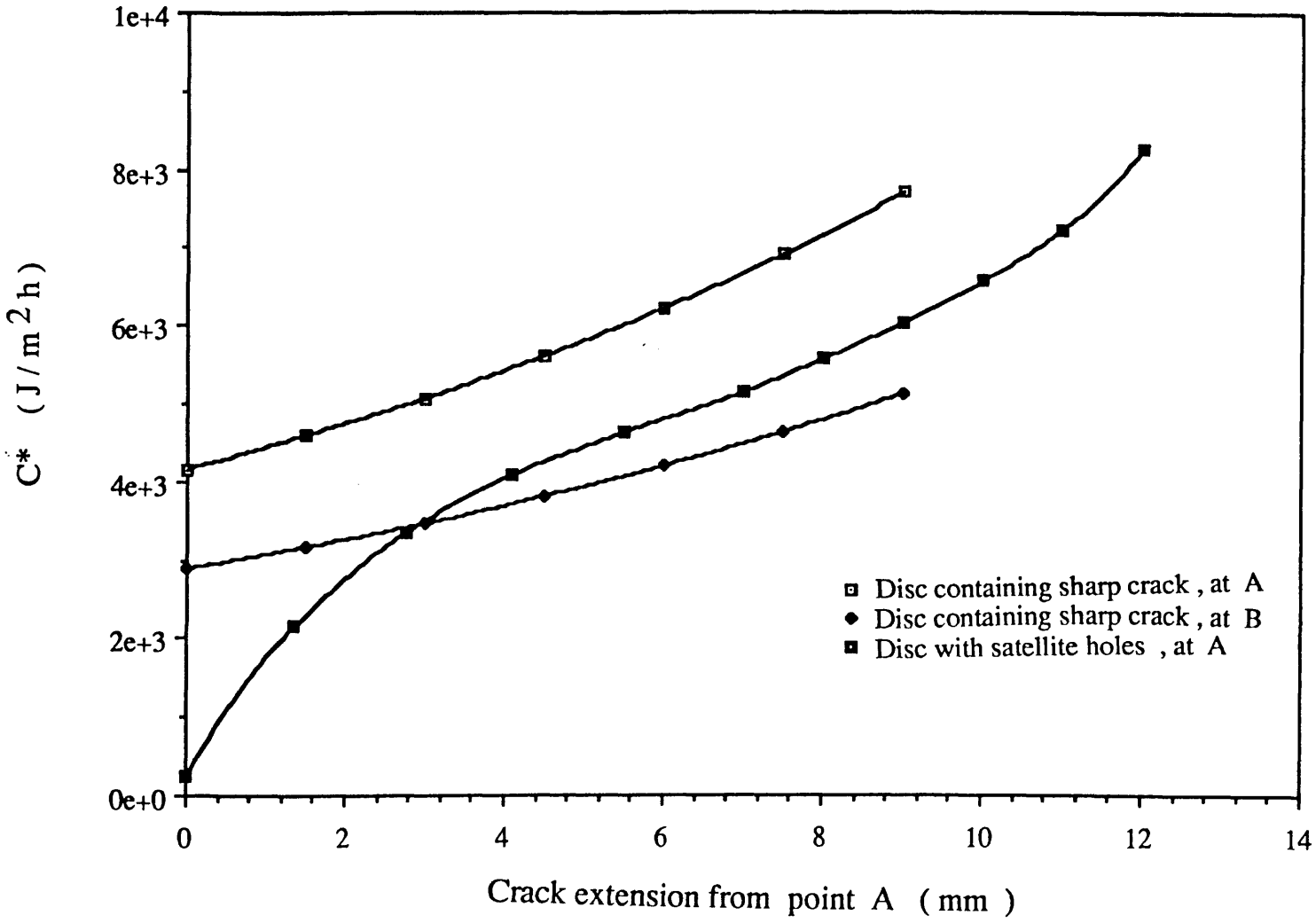


Figure 9.57 C* for n = 3 , plane stress . Comparison between disc with central hole and six satellite holes (figure 9.50), and, disc with sharp crack (figure 9.55).

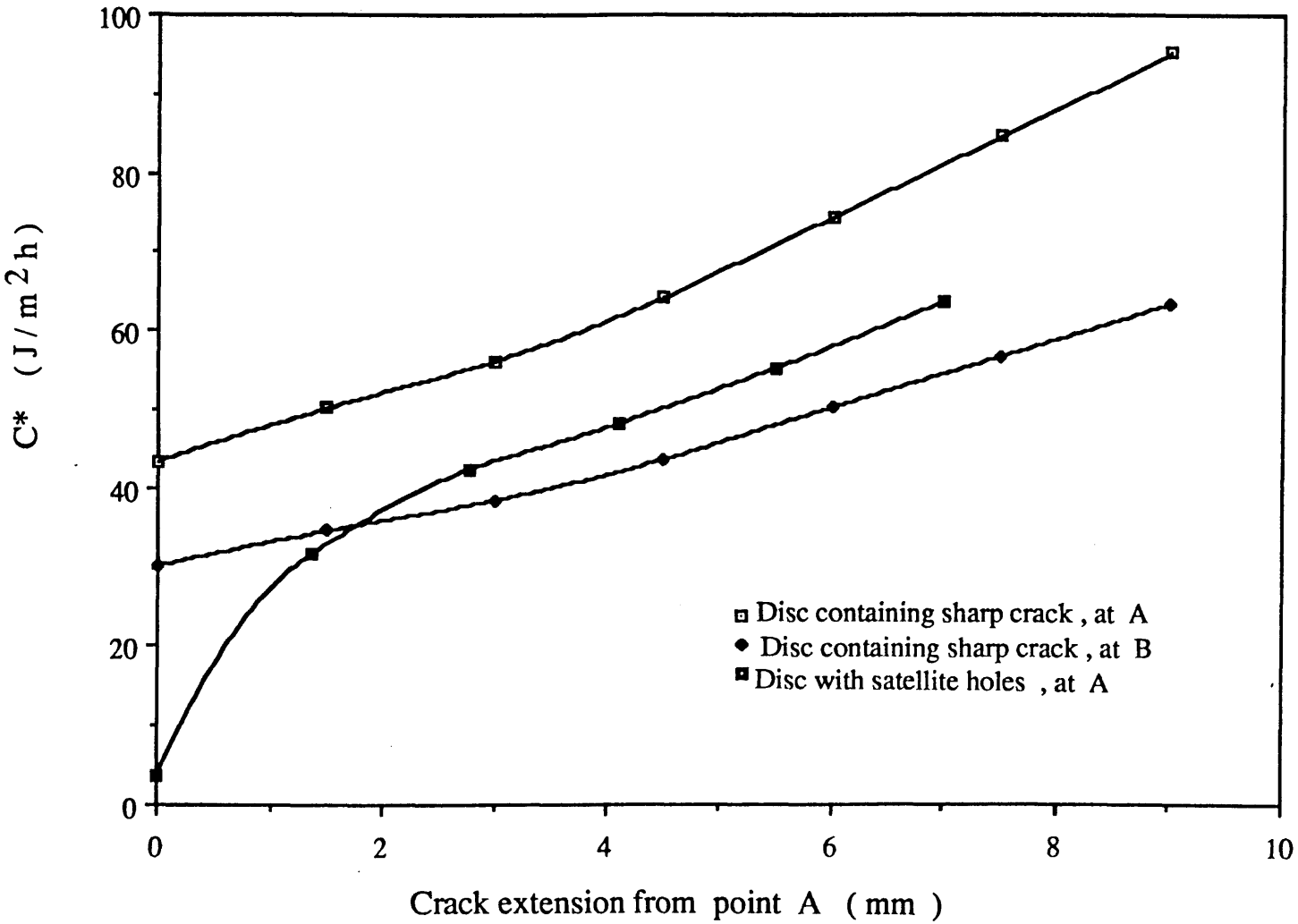


Figure 9.58 C* for n = 5 , plane stress . Comparison between disc with central hole and six satellite holes (figure 9.50), and, disc with sharp crack (figure 9.55).

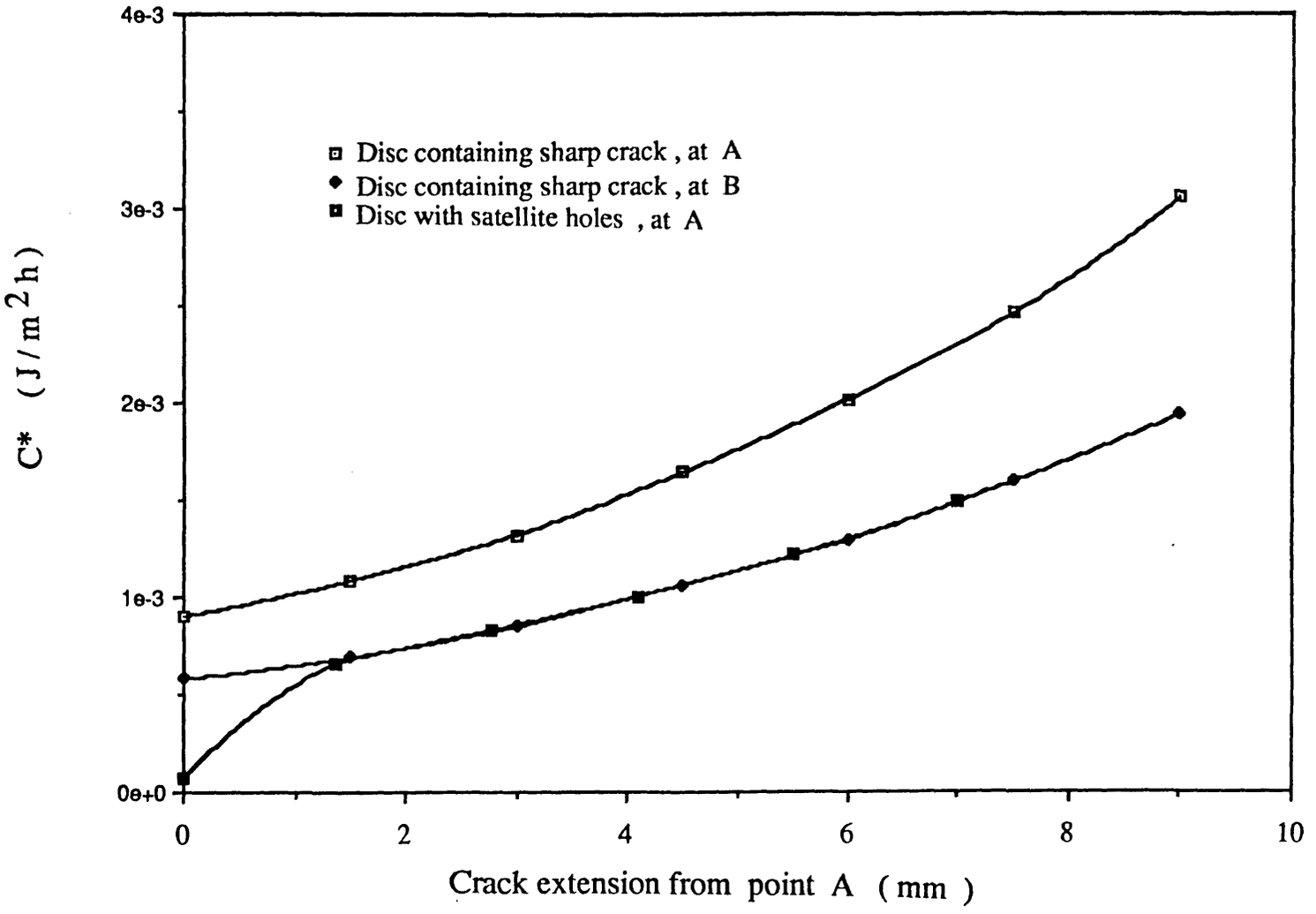


Figure 9.59 C* for n = 10, plane stress. Comparison between disc with central hole and six satellite holes (figure 9.50), and, disc with sharp crack (figure 9.55).

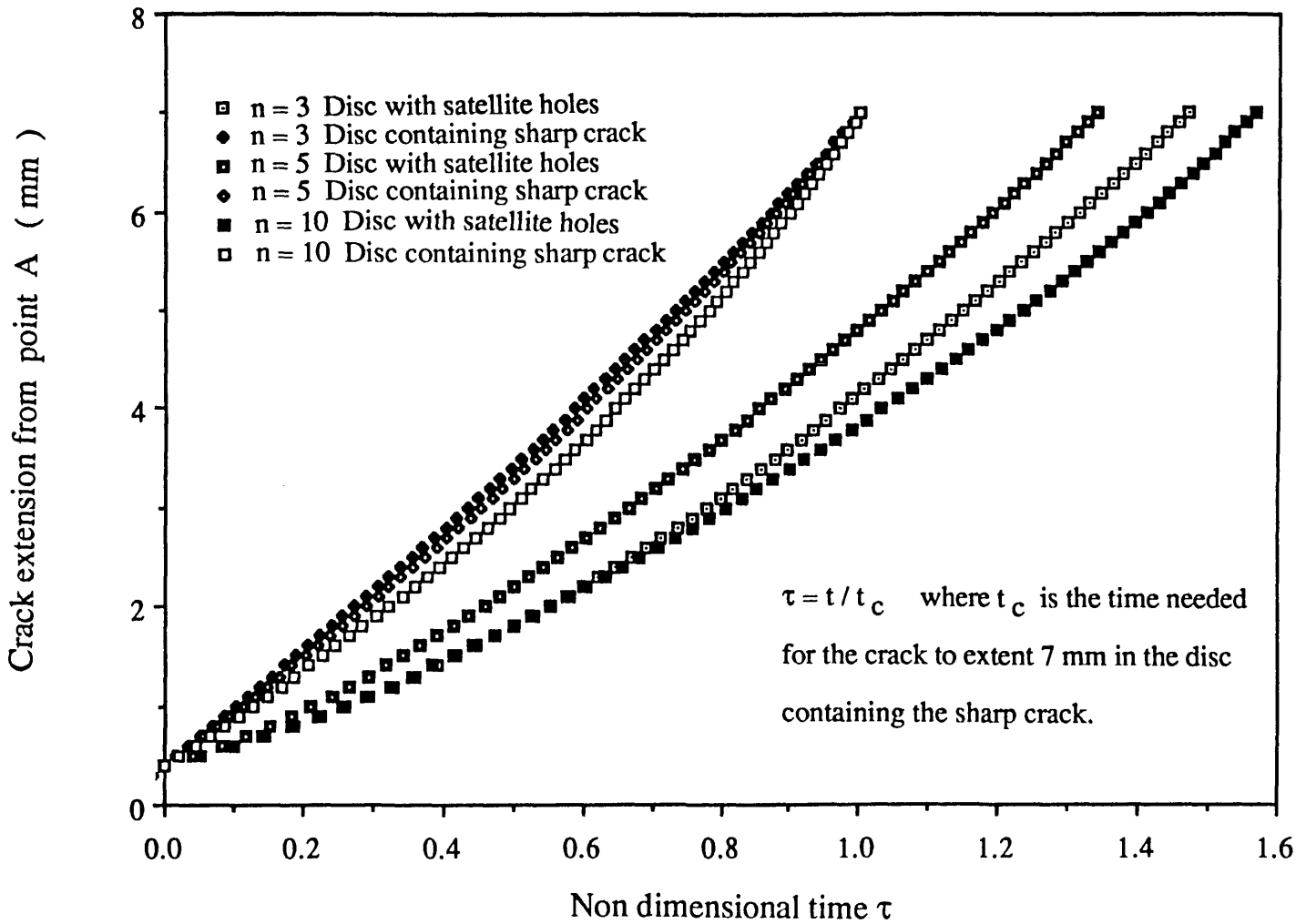


Figure 9.59a Evolution of crack length as a function of the non-dimensional time τ , in a rotating disc, when the crack growth is characterized in terms of the steady state creep contour integral C*

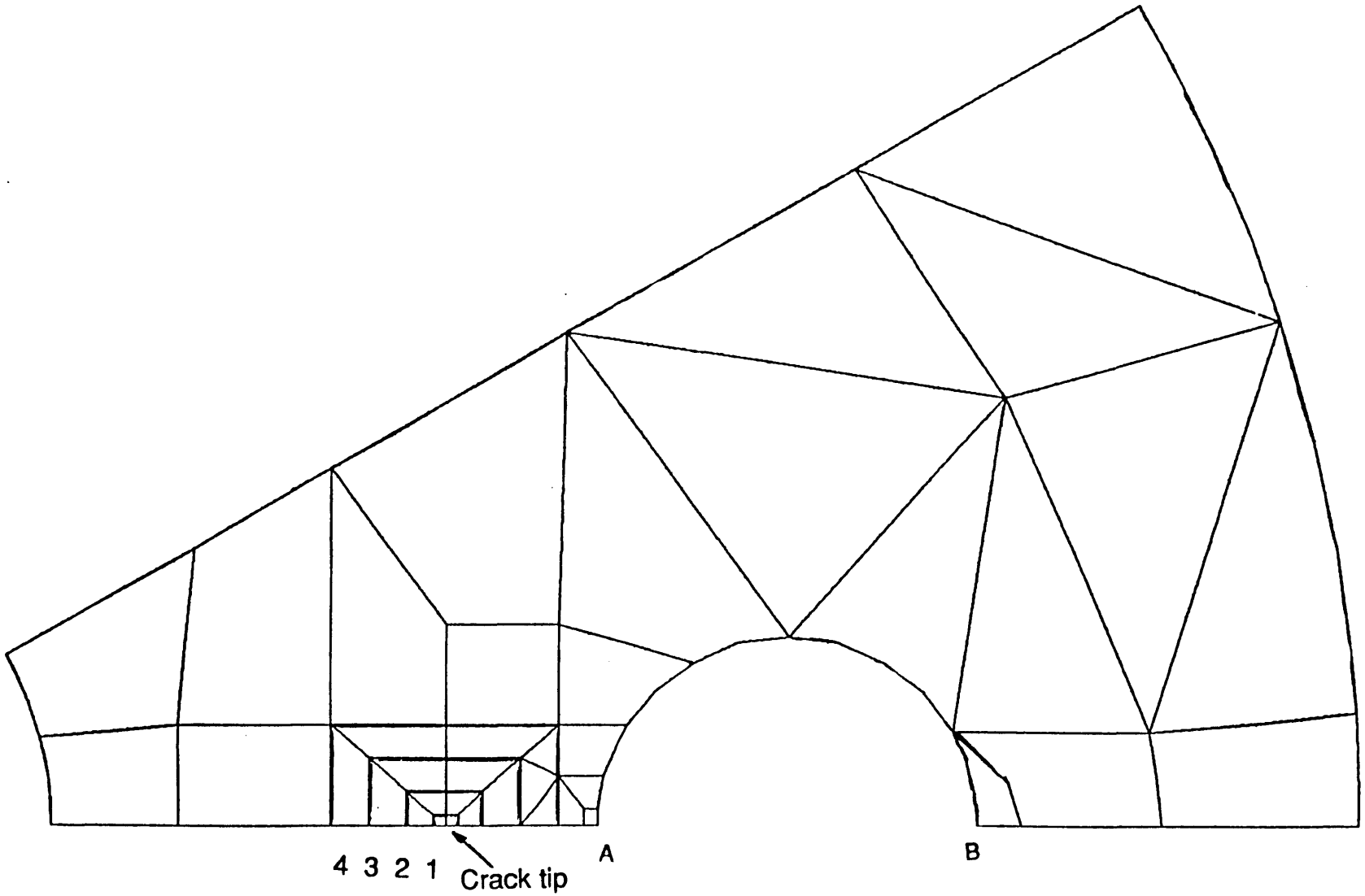


Figure 9.60 Boundary integral equation mesh of a cracked rotating disc containing a crack of 10mm from point A.

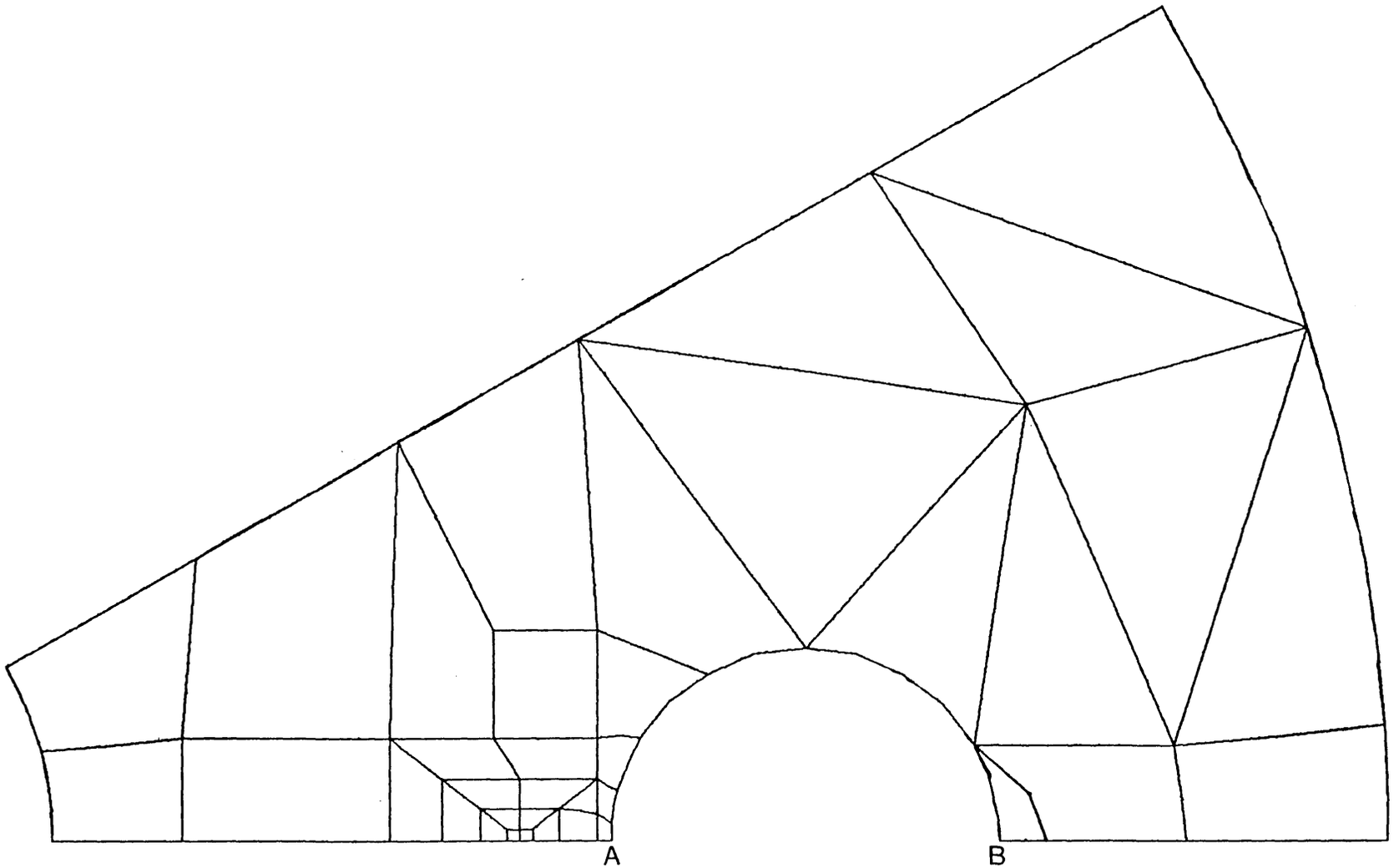


Figure 9.61 Boundary integral equation mesh of a cracked rotating disc containing a crack of 7mm from point A.

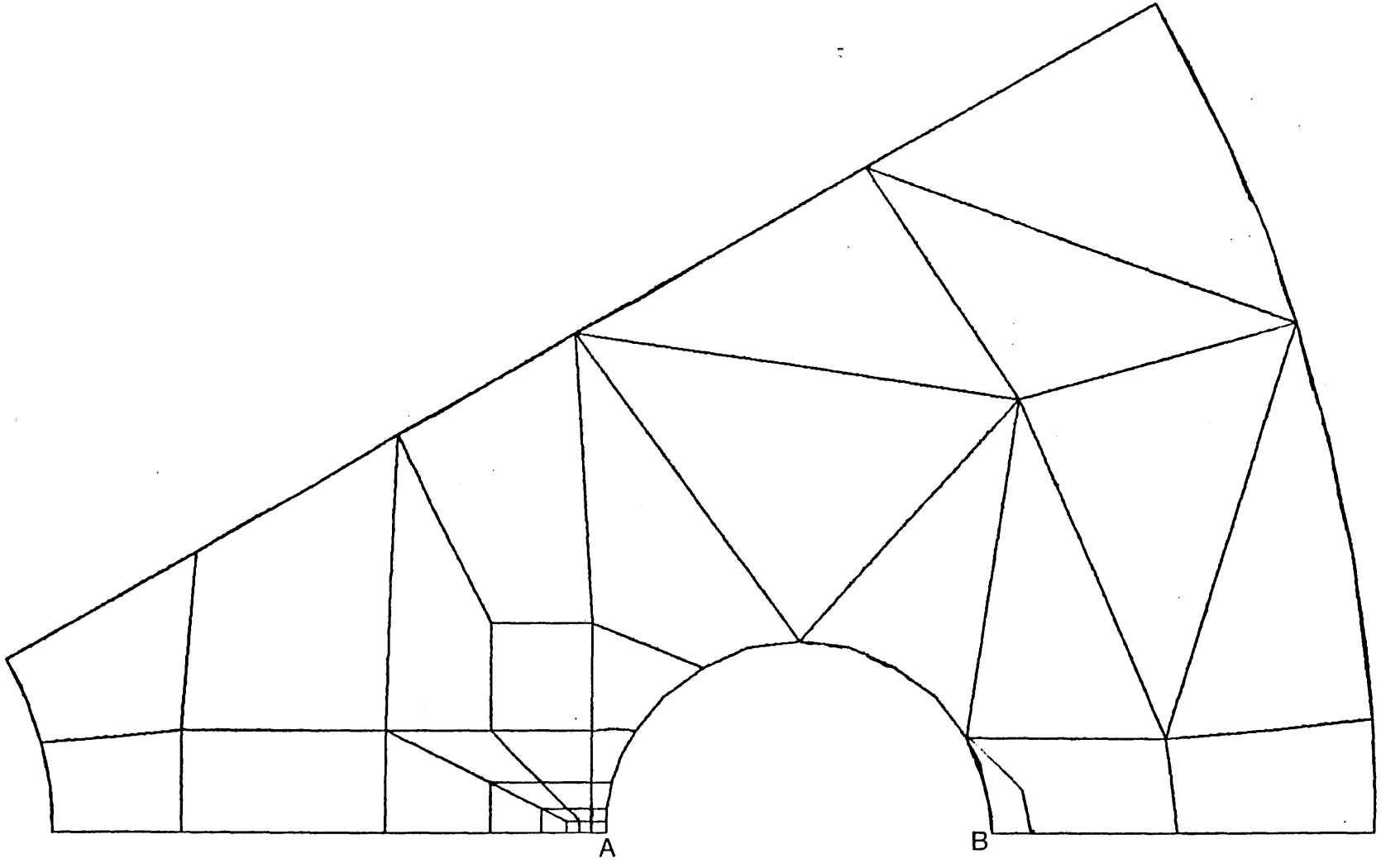


Figure 9.61a Boundary integral equation mesh of a cracked rotating disc containing a crack of 1 or 2mm from point A.

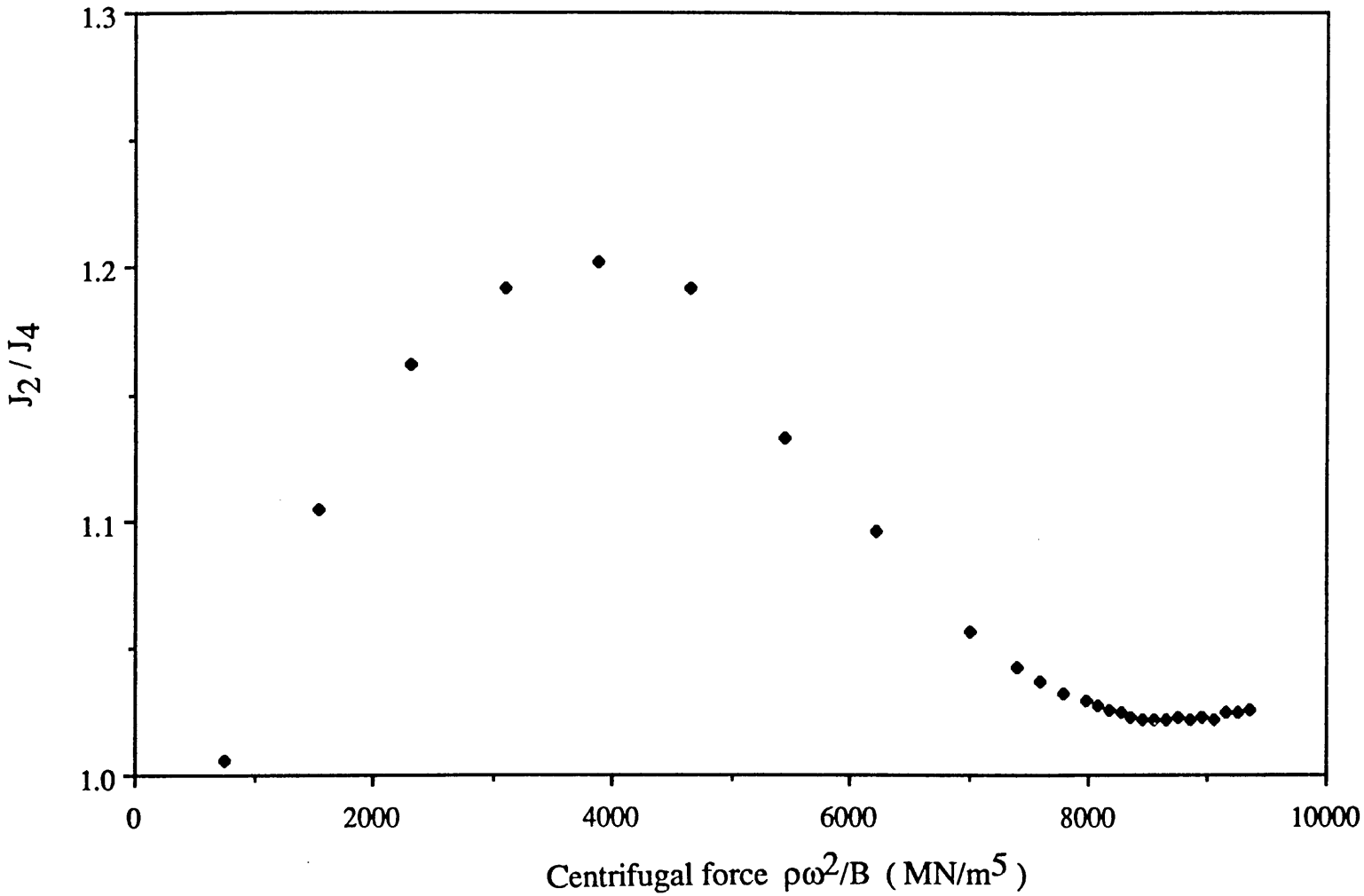


Figure 9.62 Non dimensional ratio of J obtained for path2 (J_2) and J obtained for path4 (J_4) , as a function of the increase in centrifugal force , for the disc geometry of figure 9.61 , for n = 3 plane stress

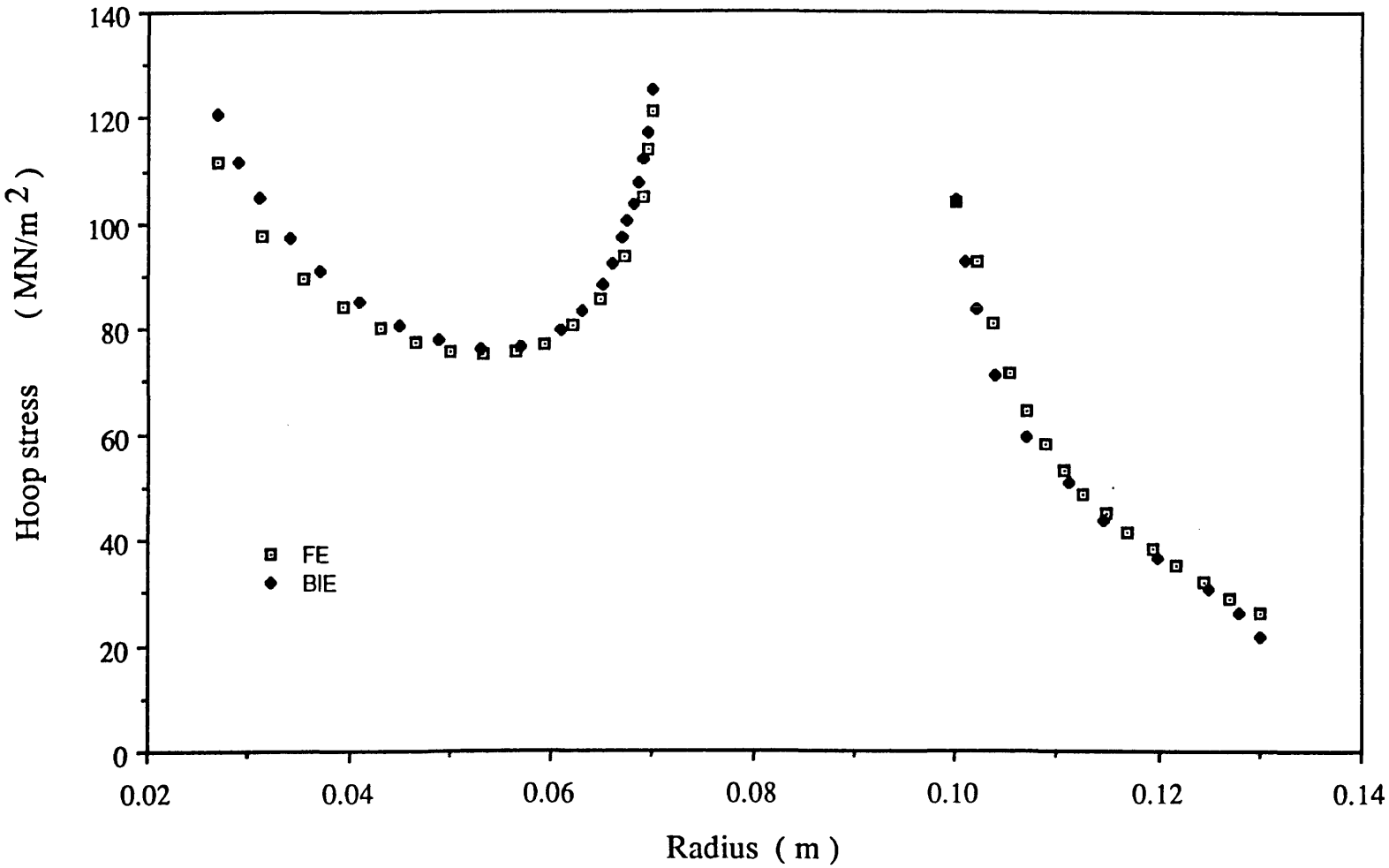


Figure 9.63 Comparison of Hoop - stress distributions , determined by F.E and B.I.E. methods for n = 1 plane stress

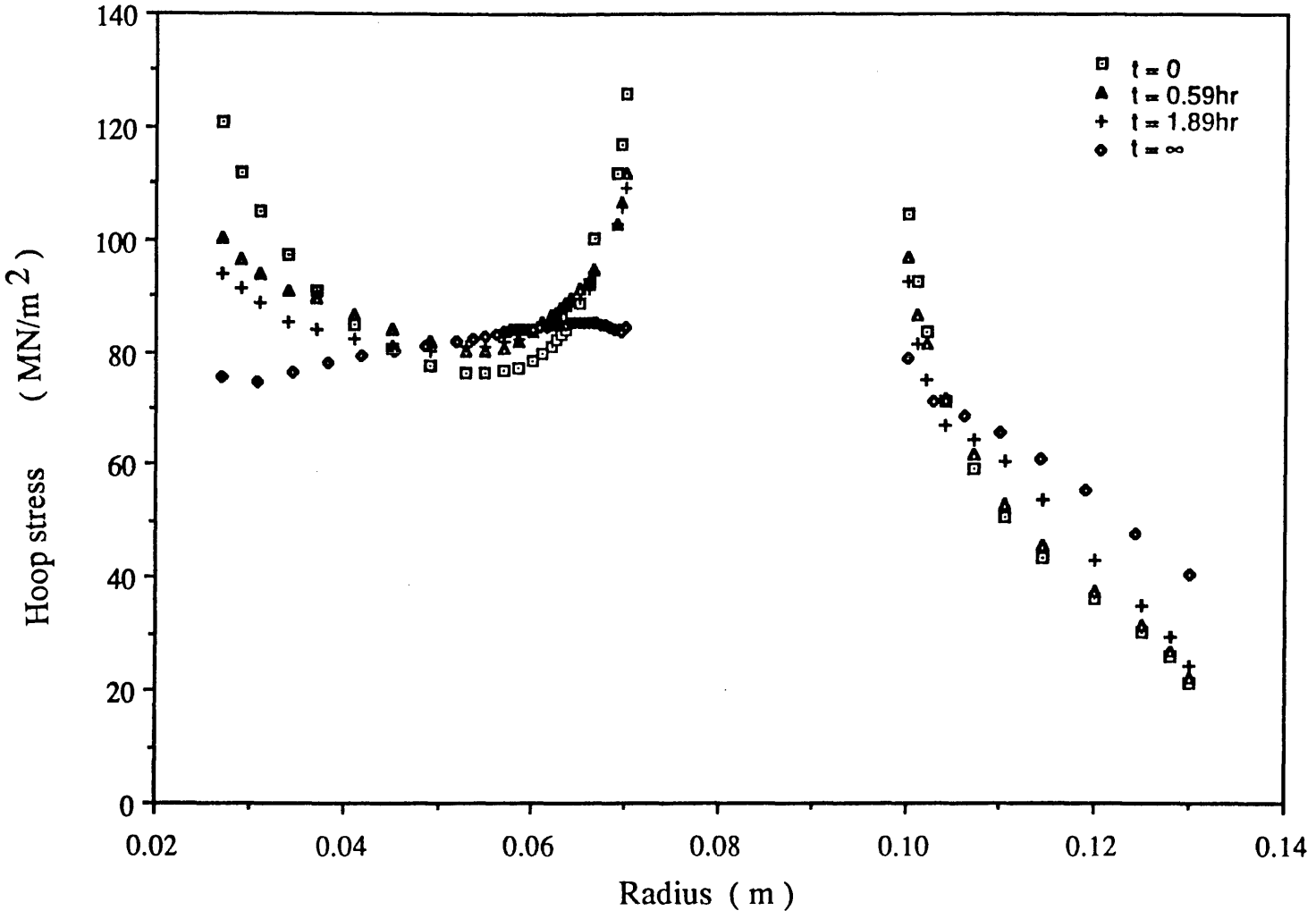


Figure 9.64 Stress redistribution by B.I.E. method due to plastic (creep) strain.

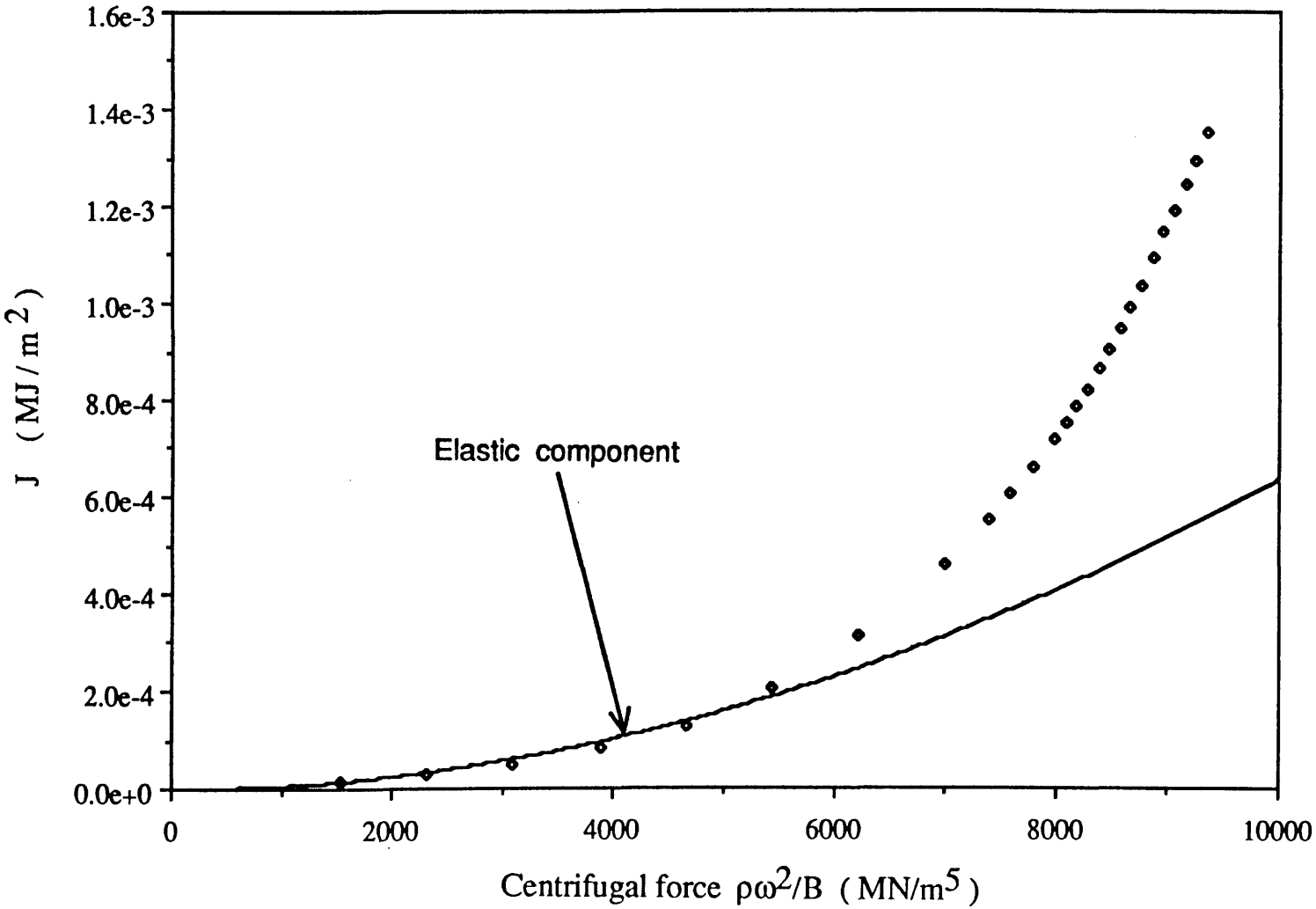


Figure 9.65 Estimate of J for increase in centrifugal force for 7mm crack and N= 3 plane stress

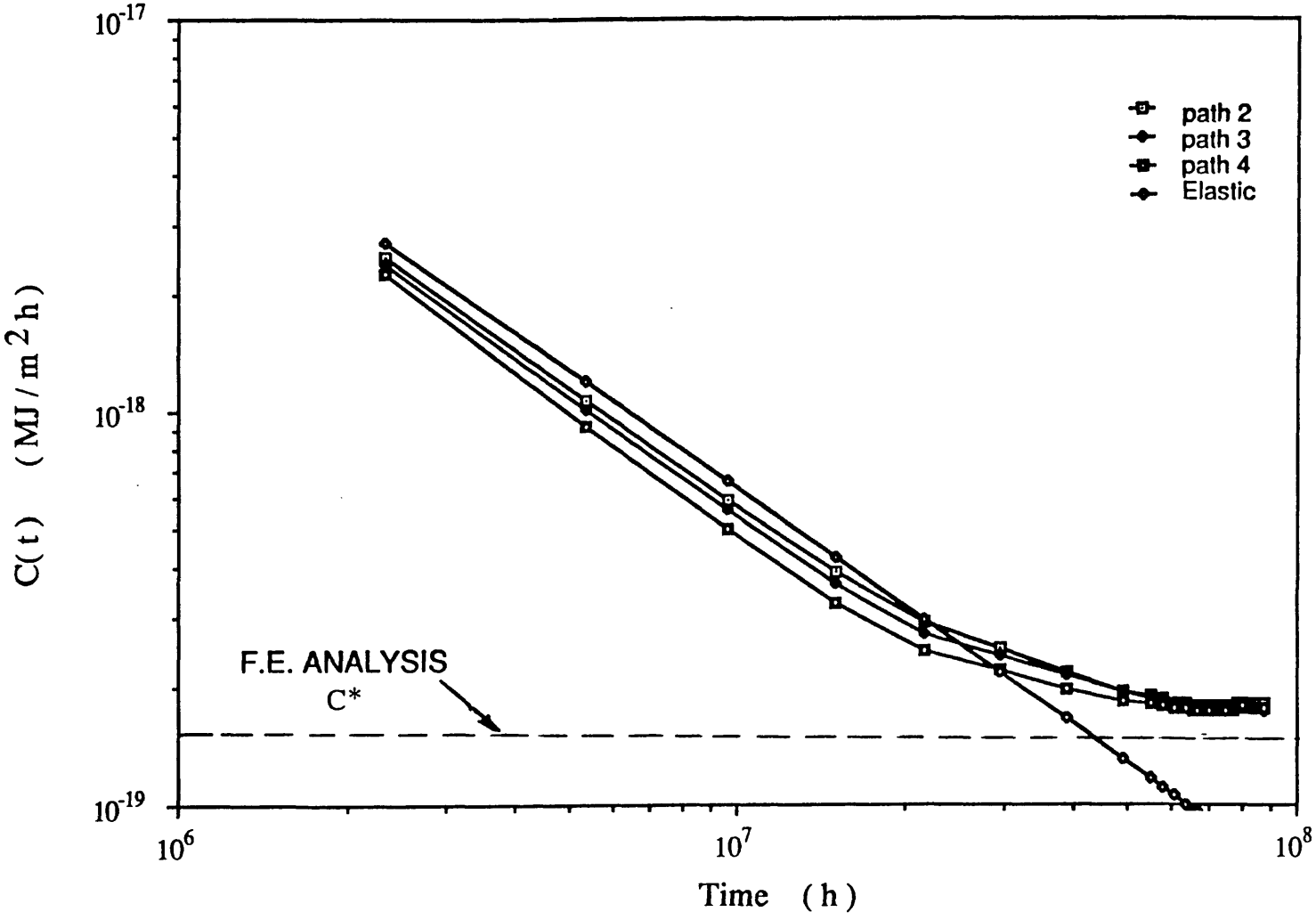


Figure 9.66 Sensitivity of C (t) to path length and time for crack length of 7mm and n = 3 plane stress , and , for a centrifugal force of $\rho\omega^2/B = 1$ MN/m^5 .

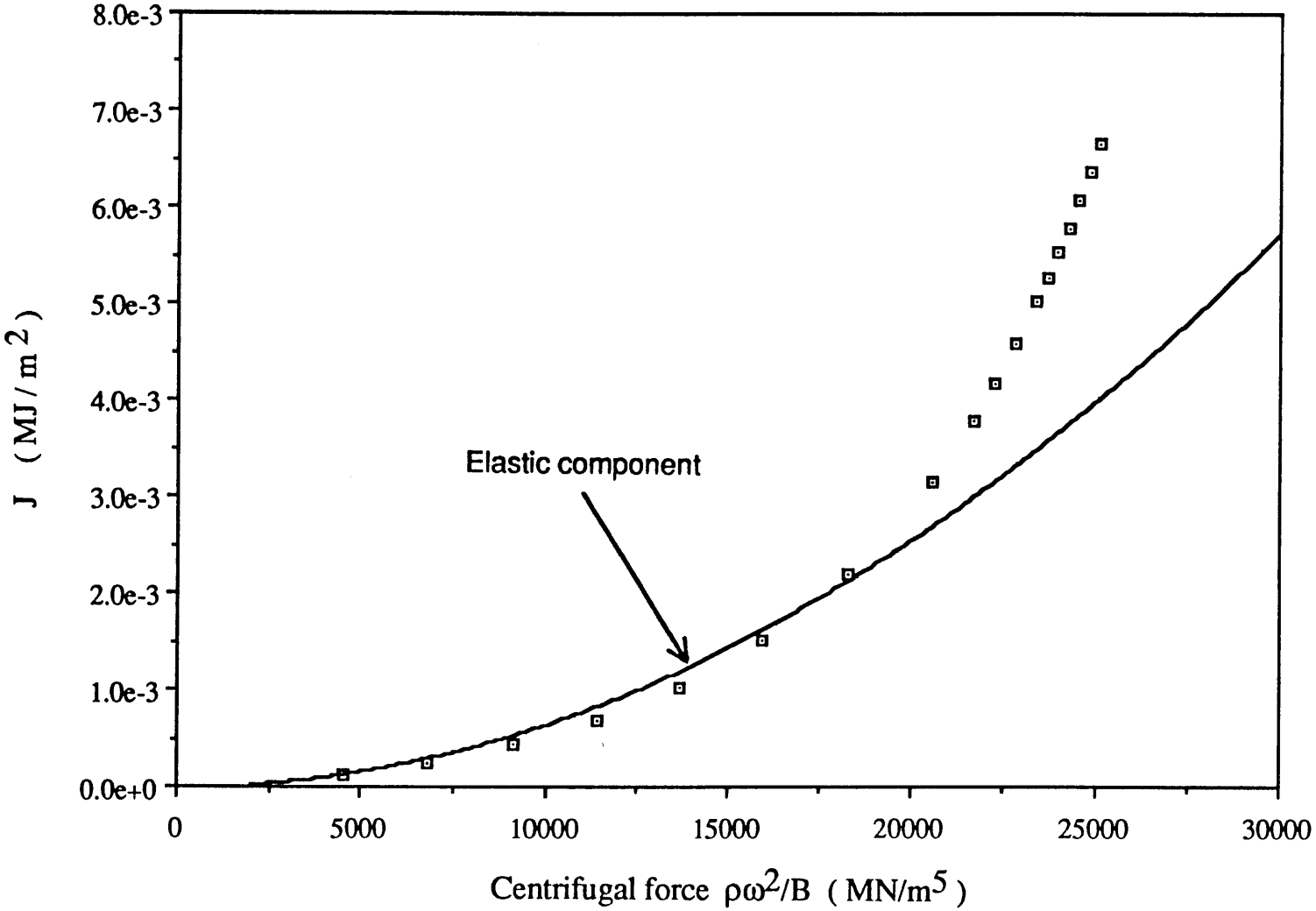


Figure 9.67 Estimate of J for increase in centrifugal force for 7mm crack and N= 5 plane stress

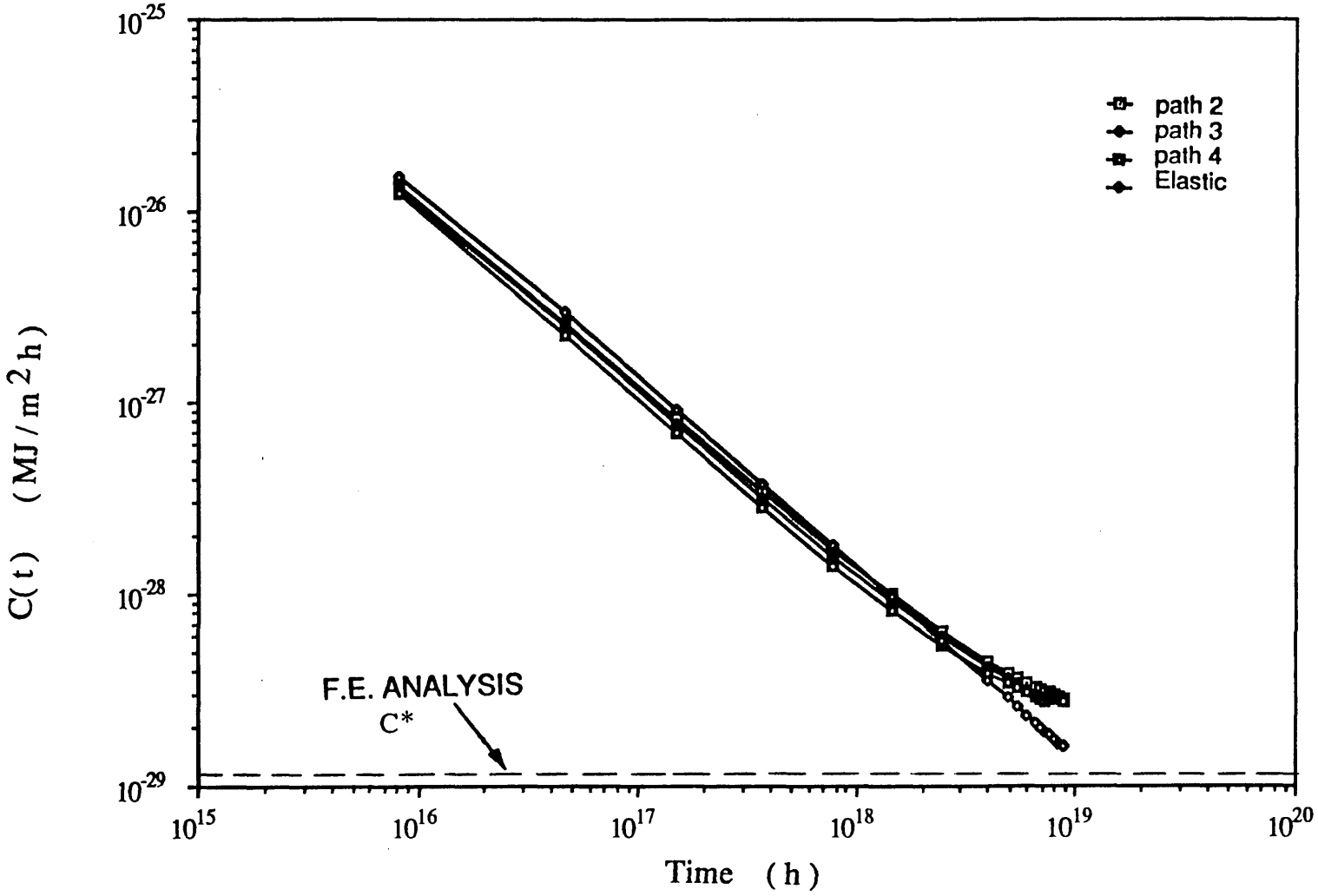


Figure 9.68 Sensitivity of C (t) to path length and time for crack length of 7mm and n = 5 plane stress , and , for a centrifugal force of $\rho\omega^2/B = 1$ MN/m^5 .

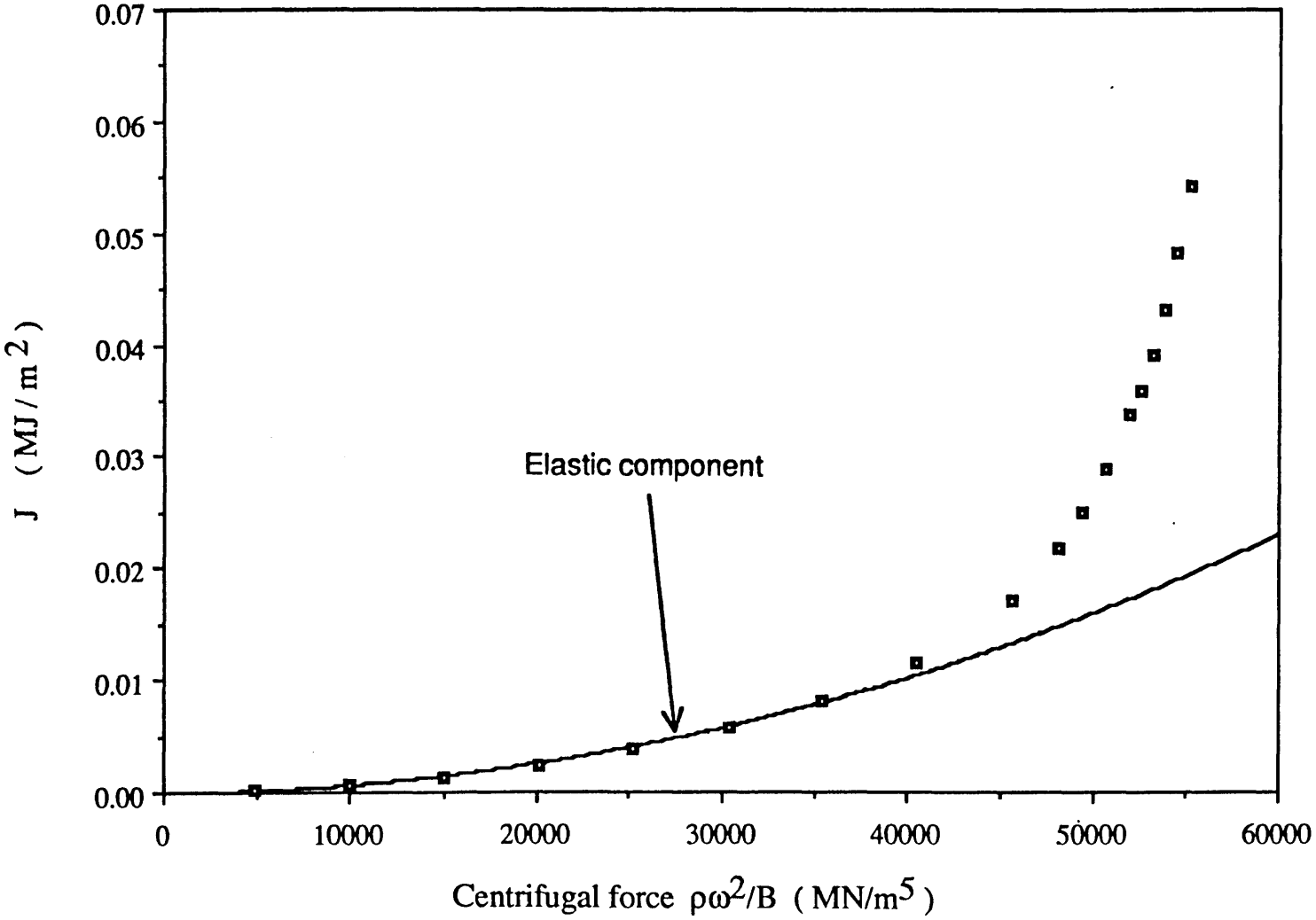


Figure 9.69 Estimate of J for increase in centrifugal force for 7mm crack and N= 10 plane stress

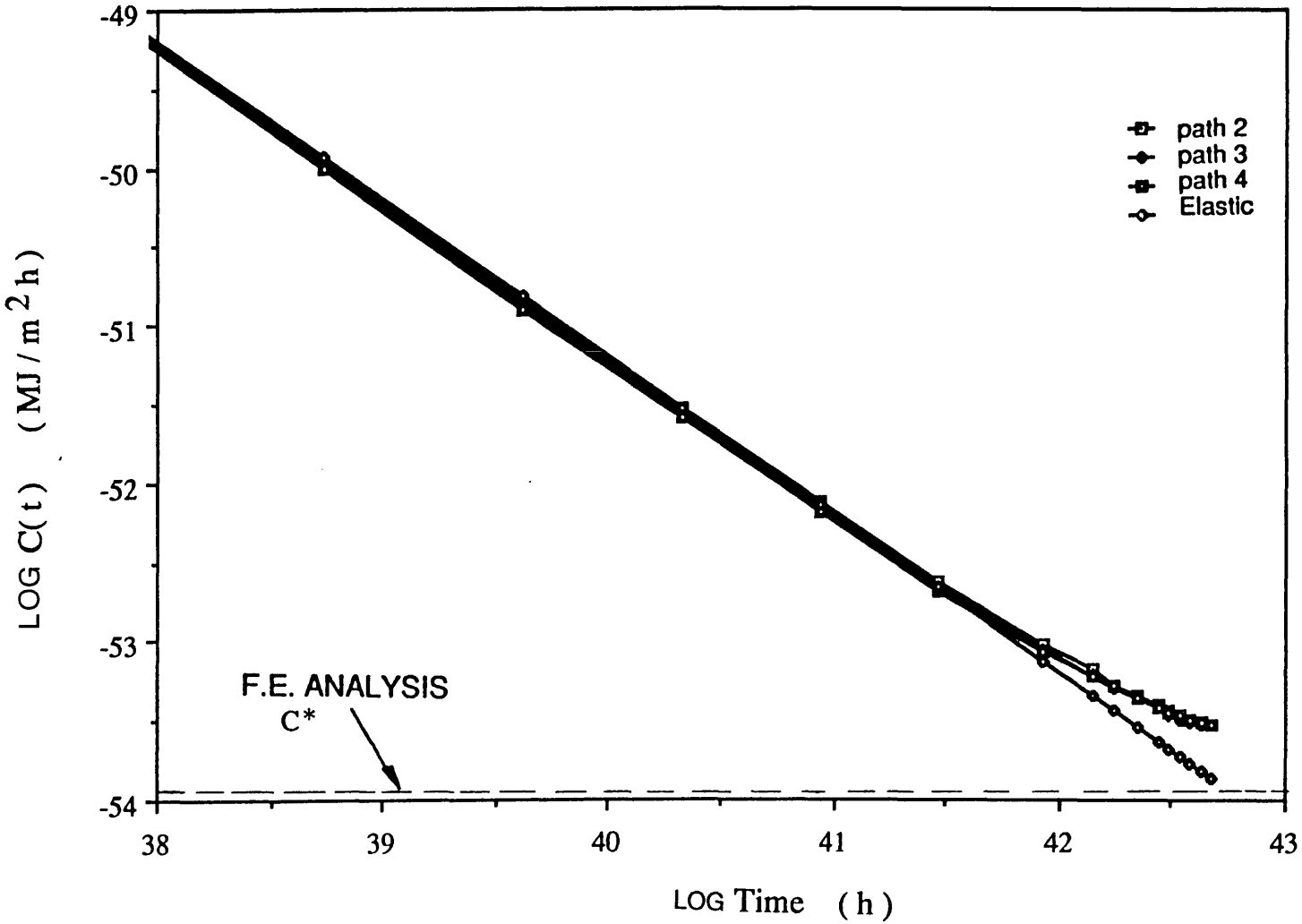


Figure 9.70 Sensitivity of C (t) to path length and time for crack length of 7mm and n = 10 plane stress , and , for a centrifugal force of $\rho\omega^2/B = 1\ MN/m^5$.

APPENDIX 9A

A good estimate for J in an elasto-plastic problem is given by simply adding the elastic and plastic terms (Kumar et.at. (1981)). It can be deduced from equation (9.21) that the plastic term it will be given by

$$J = \frac{\sigma_{op}\varepsilon_o\, a}{\sigma_{op}^{N+1}}\left[\frac{P}{f(a/W)}\right]^{N+1} \hat{J}^p(a/W,N) \qquad (9A.1)$$

which can be simplified to

$$J = \frac{\varepsilon_o}{\sigma_{op}^{N}}\, g(a/W,N)\, P^{N+1} \qquad (9A.2)$$

with g(a/W,N) given by

$$g(a/W,N) = a\, f(a/W)^{-(N+1)}\, \hat{J}^p(a/W,N) \qquad (9A.3)$$

Similarly the elastic term will be given by

$$J = \frac{\varepsilon_o}{\sigma_{op}}\, g(a/W,1)\, P^2 \qquad (9A.4)$$

or

$$J = \frac{1}{E}\, g(a/W,1)\, P^2 \qquad (9A.5)$$

So the total value of J for an elasto-plastic case will be

$$J = \frac{1}{E}\, g(a/W,1)\, P^2 + \frac{\varepsilon_o}{\sigma_{op}^{N}}\, g(a/W,N)\, P^{N+1} \qquad (9A.6)$$

or

$$J = A_p P^2 + B_p P^{N+1} \qquad (9A.7)$$

with

$$A_p = \frac{1}{E}\, g(a/W,1) \quad , \quad B_p = \frac{\varepsilon_o}{\sigma_{op}^{N}}\, g(a/W,N) \qquad (9A.8)$$

Ehlers and Riedel (1981) found that a very good approximation for C(t) can

be obtained in the whole range from short to long times by simply adding the short and long time limits to give (equation (5.29)).

$$C(t)=\frac{G}{(n+1)t}+C^{*} \qquad (9A.10)$$

Following the same procedure as for J

$$C^{*}=\frac{\dot{\varepsilon}_0}{\sigma_0^{n}}\, g(a/W,n)\, P^{n+1} \qquad (9A.11)$$

with g(a/W,n) given by

$$g(a/W,n)=a\, f(a/W)^{-(n+1)}\, \hat{J}^{c}(a/W,n) \qquad (9.A12)$$

G is equal to the elastic term of J found for the elasto-plastic case above , so C(t) it will be given by

$$C(t)=\frac{1}{(n+1)E}\, g(a/W,1)\frac{P^2}{t}+\frac{\dot{\varepsilon}_0}{\sigma_0^{n}}\, g(a/W,n)\, P^{n+1} \qquad (9A.13)$$

or

$$C(t)=A_c\,\frac{P^2}{t}+B_c P^{n+1} \qquad (9A.14)$$

with

$$A_c=\frac{1}{(n+1)E}g(a/W,1) \quad , B_c=\frac{\dot{\varepsilon}_0}{\sigma_0^{n}}\, g(a/W,n) \qquad (9A.15)$$

Consider an elasto-plastic body loaded with a load P_1. Then J it will be given by

$$J=A_p P_1^2+B_p P_1^{N+1} \qquad (9A.16)$$

Consider an elasto-creep body of with identical geometry loaded with a load P_2. C(t) it will then be given by

$$C(t)=A_c\,\frac{P_2^2}{t}+B_c P_2^{n+1} \qquad (9A.17)$$

The difficulty in obtaining numerical estimates of C(t) from numerical

estimates of J, by simulating a time increment by a load increment, is that both the elastic and the plastic terms in the evaluation of J (equation (9A.7)) change with the load increment , whereas only the short time limit changes with time in equation (9A.14) for the evaluation of C(t). However there will be a time t that makes equation (9A.16) identically equal to a fraction of equation (9A.17). At that time

$$\alpha J \equiv C(t) \qquad (9A.18)$$

so that

$$\alpha A_p P_1^2 = A_c \frac{P_2^2}{t} \qquad (9A.19)$$

and

$$\alpha B_p P_1^{N+1} = B_c P_2^{n+1} \qquad (9A.20)$$

For $N = n$ (9A.19) and (9A.20) can be solved for α and t to give

$$t = \frac{A_c}{A_p} \frac{B_p}{B_c} \left[\frac{P_1}{P_2} \right]^{n-1} \qquad (9A.21)$$

and

$$\alpha = \frac{B_c}{B_p} \left[\frac{P_2}{P_1} \right]^{n+1} \qquad (9A.22)$$

From (9A.8) and (9A.15) it can be deduced that

$$A_c = \frac{1}{n+1} A_p \qquad (9A.23)$$

Also for n=N and identical geometries g(a/W,n)=g(a/W,N) so if the material properties for the elasto-plastic and the elasto-creep bodies are such that

$$\frac{\dot{\varepsilon}_o}{\sigma_o^n} = \frac{\varepsilon_o}{\sigma_{op}^N} \qquad (9A.24)$$

the numerical values of B_c and B_p are the same. So that

$$t = \frac{1}{n+1} \left[\frac{P_1}{P_2} \right]^{n-1} \qquad (9A.25)$$

If $\dot{\varepsilon}_0$=1/h then t is in hours . From (9A.18) and (9A.22)

$$C(t) = \left[\frac{P_2}{P_1}\right]^{n+1} J \qquad (9A.26)$$

If $\dot{\varepsilon}_0$=1/h then C(t) will have the units of J divided by hours.

CHAPTER 10

ANALYSIS FOR, AND THE INTERPRETATION OF, THE EXPERIMENTAL DATA

10.1 INTRODUCTION

In chapter 5 several field parameters were proposed for characterising the creep crack growth behaviour of metals. The conditions under which each of these parameters will characterise the crack growth rate of the materials tested, are fully investigated in this chapter.

If crack growth is to be associated with a certain stress field, the crack growth rate in a particular circumstance, will be most accurately characterised with the parameter that most accurately describes the stress fields ahead of the crack tip. So the relative success of a particular parameter in characterising the crack growth rates will depend upon the amount of stress redistribution that has taken place in the region of the crack tip. If no appreciable stress redistribution has taken place, then the stress fields can accurately be described by the stress intensity factor K (in the absence of plasticity). Under these conditions K will describe the crack growth rate. If the stress fields relax to their steady state, then C* will describe the magnitude of the stress fields and so the crack growth rate.

Equations (5.27) and (5.43) give expressions for the characteristic time needed for the stress fields to relax from their elastic distribution to their steady state creep stress distribution. However these times give only a general idea of the material behaviour. To fully examine the material behaviour, the amount of stress redistribution ahead of the crack tip at a particular time must be evaluated.

The time needed for the stress to relax from its elastic state to its steady creep state is a function of the distance ahead of the crack tip. If crack growth is assumed to take place at a damage process zone ahead of the crack tip then the relaxation times for the stresses within this zone need to be investigated. A method has been developed in

section 10.2 for the time needed for the stresses to relax from their elastic state to some fraction between the elastic and creep state.

Prior to the characterisation of the crack growth data, the method by which the crack growth, displacement, and, load rates are obtained from the experimental results is presented.

The crack growth rates for the various materials are related in section 5.8 to various parameters such as K, C*, and, C^*_{exp}. In the latter case C^*_{exp} has been evaluated via the displacement rate, calculated from the experimental results. For the evaluation of C* the finite element solutions of Kumar et. al. (1981) have been used. The results from the cyclic tests are additionally investigated, particularly in relation to creep and fatigue dominated crack growth.

10.2 STRESS REDISTRIBUTION MODEL

In chapter 5 r* was defined as the distance ahead of the crack tip where the elastic and creep stress have the same magnitude equal to σ^*. An expression for r* is given by equation (5.37). Figure 10.1 considers two cylindrical columns of material one a distance r* and the other a distance r ahead of a crack tip. An expression for σ^* can be found if r* is substituted for r in (5.35) to give:

$$\sigma^* = \frac{K}{\left[2\pi \left[\frac{K^2}{2\pi} \right]^{(n+1)/(n-1)} \left[\frac{I_n C}{C^*} \right]^{2/(n-1)} \right]^{1/2}} \qquad (10.1)$$

which can be simplified to

$$\sigma^* = \left[\frac{2\pi C^*}{C K^2 I_n} \right]^{1/(n-1)} \qquad (10.2)$$

The strain rate at which the column at distance r* is deforming is the sum of the elastic strain rate, plus, the creep strain rate.

$$\dot{\varepsilon}^* = \dot{\varepsilon}^*_e + \dot{\varepsilon}^*_c \qquad \text{but } \dot{\varepsilon}^*_e = 0 \text{ so } \dot{\varepsilon}^* = \dot{\varepsilon}^*_c \qquad (10.3)$$

The strain rate at which the column at distance r is deforming is α times than the stain rate of the column at distance r* (where α is to be determined later) so:

$$\alpha \dot{\varepsilon}^* = \dot{\varepsilon}_e + \dot{\varepsilon}_c \qquad (10.4)$$

If a relationship of the form

$$\dot{\varepsilon}_c = C \sigma^n F'(t) \qquad (10.5)$$

is assumed then

$$\alpha C \sigma^{*n} F'(t) = \frac{1}{E} \frac{d\sigma}{dt} + C \sigma^n F'(t) \qquad (10.6)$$

where F(t) is a function of time. Equation (10.6) can not be solved analytically. For numerical solution (10.6) may be written as:

$$d\sigma = (\alpha \sigma^{*n} - \sigma^{n}) E C F' (t) dt \qquad (10.7)$$

The procedure for the numerical solution is schematically illustrated in figure 10.2. Equation (10.7) may be written as

$$\Delta\sigma = (\alpha \sigma^{*n} - \sigma^{n}) E C F' (t) \Delta t \qquad (10.8)$$

with the boundary condition, $\sigma=\sigma_e$ at $t=0$

at $t = t_1$, $t_1 = \Delta t_1 + 0$

$$\Delta\sigma_1 = (\alpha \sigma^{*n} - \sigma_e^{n}) E C F' (t_1 / 2) \Delta t_1 \qquad (10.9)$$

at $t = t_2$, $t_2 = t_1 + \Delta t_2$

$$\Delta\sigma_2 = (\alpha \sigma^{*n} - \sigma_1^{n}) E C F' (t_1 + (t_2 - t_1) / 2) \Delta t_2 \qquad (10.10)$$

where $$\sigma_1 = \sigma_e + \Delta\sigma_1 \qquad (10.11)$$

at $t = t_i$

$$\Delta\sigma_i = (\alpha \sigma^{*n} - \sigma_{i-1}^{n}) E C F' (t_{i-1} + (t_i - t_{i-1}) / 2) \Delta t_i \qquad (10.12)$$

where $$\Delta t_i = t_i - t_{i-1} \qquad (10.13)$$

and $$\sigma_{i-1} = \sigma_{i-2} + \Delta\sigma_{i-1} \qquad (10.14)$$

With this method the amount of stress redistribution that has taken place can be evaluated at any time and microstructural distance ahead of the crack tip. For secondary creep $F(t) = t$ and $F'(t) = 1$, so, equation (10.12) becomes:

$$\Delta\sigma_i = (\alpha \sigma^{*n} - \sigma_{i-1}^{n}) E C \Delta t_i \qquad (10.15)$$

with $\sigma = \sigma_e$ at $t = 0$

Equation (10.15) has variables separable and so it can be integrated to give:

$$t = \int_{\sigma_e}^{\sigma_i} \frac{1}{E C} \frac{d\sigma}{\alpha \sigma^{*n} - \sigma^{n}} \qquad (10.16)$$

where $\sigma_e \geq \sigma_i \geq \sigma_c$. Equation (10.16) can not be solved analytically so numerical

integration (such as Simpson's rule) is necessary.

The stress will relax to its creep value when $\Delta\sigma_i$ as given by (10.12) will become negligible. In the limit $\Delta\sigma_i = 0$. By examining (10.12) this is only possible if

$$\alpha\,\sigma^{*n} - \sigma_{i-1}{}^{n} = 0 \qquad (10.17)$$

So for big enough time $(t\to\infty)$ $\alpha\,\sigma^{*n} = \sigma_{i-1}{}^{n} = \sigma_c{}^{n}$ (10.18) must be satisfied, i.e. equation (10.18) is a necessary condition for the stress to relax to its creep value at $t\to\infty$. This can be demonstrated as follows.

α was defined as the ratio of the strain rate at r over the strain rate at r*, so:

$$\alpha = \frac{\dot{\varepsilon}_r}{\dot{\varepsilon}_{r*}} = \frac{\dot{\varepsilon}}{\dot{\varepsilon}^*} \qquad (10.19)$$

At time t=0 when the stress distribution is elastic

$$\alpha_e = \frac{\dot{\varepsilon}}{\dot{\varepsilon}^*} = \left[\frac{r^*}{r}\right]^{1/2} \qquad (10.20)$$

and at time $t\to\infty$ when the stress distribution is steady state creep

$$\alpha_c = \frac{\dot{\varepsilon}}{\dot{\varepsilon}^*} = \left[\frac{r^*}{r}\right]^{n/(n+1)} \qquad (10.21)$$

But when $\alpha=\alpha_c$ at $t\to\infty$, the ratio of the creep stresses at distances r and r* ahead of the crack tip will be given by

$$\frac{\sigma_c}{\sigma^*} = \left[\frac{r^*}{r}\right]^{1/(n+1)} \qquad (10.22)$$

$$\text{so}\quad \alpha_c\,\sigma^{*n} = \left[\frac{r^*}{r}\right]^{n/(n+1)} \left[\sigma_c\left[\frac{r}{r^*}\right]^{1/(n+1)}\right]^{n} \quad \text{or}$$

$$\alpha_c\,\sigma^{*n} = \sigma_c{}^{n} \qquad (10.23)$$

but this is the necessary condition, equation (10.18), for $\alpha=\alpha_c$, for the stress σ to relax to its creep state σ_c at $t\to\infty$, when (10.12) is used.

Numerical experimentation for specimen A76 (800H superalloy , n=6.5,

r*=3.4mm), has shown that the value of α makes a difference in the stress relaxation time when $(\sigma - \sigma_c)/(\sigma_e - \sigma_c) < 0.4$. In fact this difference is very small. When $\alpha=\alpha_e$ was used throughout the stress redistribution process the time for stress redistribution at r = 500μm to within 10% of full stress relaxation was $2.3 * 10^{-2} t_1$, where t_1 is the Riedel and Rice (1980) redistribution time, and when $\alpha=\alpha_c$ was used the time was $2.7*10^{-2} t_1$ a ratio of 1.2 (see figure 10.3). It is observed that when the value of α becomes important the stress approaches its steady state value, so α approaches α_c. So the error in using α_c throughout the stress relaxation process is very small. Another good reason for using α_c throughout, is that in the range $\alpha_e \leq \alpha \leq \alpha_c$, $\alpha = \alpha_c$ will give bigger times for stress relaxation, i.e it will be more conservative in predicting crack growth rates, although this conservatism is small.

Figure 10.4 shows the application of this model for specimen A76 (800H superalloy) at the initial a/W (=0.57), for distances 100μm, 500μm, and, 1000μm ahead of the crack tip, for $\alpha=\alpha_c$. The non dimentional factor α_c is shown in figure 10.4a as a function of n for various values of r*/r.

10.2.1 r* POSITIONS FOR THE COMPACT TENSION GEOMETRY.

Equation (5.37) gives a relationship between the C* contour integral, the stress intensity factor K, and r*, as

$$r^* = \left[\frac{K^2}{2\pi}\right]^{\frac{n+1}{n-1}} \left[\frac{I_n C}{C^*}\right]^{\frac{1}{n-1}} \qquad (5.37)$$

if C*, and K, are evaluated through equation (6.58), which gives the values of characterising parameters from finite element solutions of Kumar et. al. (1981) then it may be proved that (for proof see appendix 10A)

$$\frac{r^*}{W} = \left[1 - \frac{a}{W}\right]\left[\left[\frac{h_{1,1}}{2\pi}\right]^{n+1}\left[\frac{I_n}{h_{1,n}}\right]^2\right]^{\frac{1}{n-1}} \qquad (10.24)$$

In (10.24) above with $h_{1,1}$ is denoted the value of h_1 at n=1, and with $h_{1,n}$

the value of h_1 at n=n. $h_{1,1}$ and $h_{1,n}$ may be substituted from table 6.1

In terms of the Haigh and Richards collapse load solution it may be proved that (for proof see appendix 10A)

$$\frac{r^*}{W} = \frac{h_{1,1}}{2\pi}\left[\frac{m}{1.455\,\eta}\right]^2 \frac{1}{1-a/W} \qquad (10.25)$$

where η is given by (6.62), and, m is given by (5.92) for plane stress conditions.

Figure 10.4b shows the relationship of r*/W versus a/W for the compact tension specimen, for plane stress conditions and n ranging from 2 to 20. Also included in this figure are the collapse load solutions (Haigh and Richards (1974)). It may be argued that for a/W≥0.375 and n≥5, conditions that are satisfied for all the experimental tests conducted, there is an approximate relationship between r*/W and a/W for all n. The Haigh and Richards collapse load solutions lead to smaller r* for n≥3, so that shorter distances are predicted for the cross-over of the elastic and creep stress fields. As indicated by the dotted line at the bottom of figure 10.4b, for W=50mm, r* is greater than 500μm, which is the biggest grain size for the materials tested, up to about a/W=0.95. In general all specimens tested failed at a/W < 0.95, so that r* is greater than the grain size throughout all tests. So it may be argued that the reference position r* may be used to describe the dissipation rate ahead of the crack tip at any time.

10.3 CHARACTERISATION OF CREEP CRACK GROWTH

From figure 10.4 it is evident that for relatively small times the stress intensity factor K will characterize the stress fields since the stress redistribution is very small, and, at relatively big times when full stress redistribution has taken place C* will characterize the stress fields. However especially close to the crack tip there can be significant interval between the time that K will characterise the stress fields and the time where C* will characterise the stress fields.

If in a particular test, the cracking occurs after stress redistribution but before a stationary state has been reached, then the crack growth rate can not be characterized

with K or C*. Under these non-steady-conditions the crack tip stress distribution is a function of time even when the crack is considered stationary. A parameter that can characterise the crack growth rate in these circumstances, must take into account these non-steady-state (or transient) conditions.

Parameters that can characterise the crack growth under transient creep conditions have been discussed in chapter 5, and they are, the C(t) parameter suggested by Rice and Riedel (1980) and the C_t parameter proposed by Saxena (1986). These parameters degenerate to G (=K^2/E') for small times (when crack growth is fast for significant stress redistribution to take place) and to C* for long times (when stress redistribution takes place without any significant increase in the crack length). For a stationary crack C(t) and C_t, can easily be evaluated from equations (5.29a) and (5.54) respectively.

$$C(t) = \left[1 + \frac{t_1}{t} \right] C^* \qquad (5.29a)$$

$$C_t = \left[\left[\frac{t_1}{t} \right]^{\frac{n-3}{n-1}} + 1 \right] C^* \qquad (5.54)$$

If the crack is allowed to grow the reference time from which t is measured is lost. This makes it difficult to determine these parameters analytically. It may be argued however (Saxena (1986)), that the effect of the crack growth on the transient fields is included in the measured displacement rate so C_t can be determined experimentally. If the creep displacement rate is measured throughout the test then C_t can be evaluated using (5.51)

$$C_t = \frac{P \dot{\Delta}_c}{B W} \frac{H}{H'} \qquad (5.51)$$

$$\text{where } \frac{H'}{H} = \left[\frac{1}{1 + a/W} + \frac{3}{2} \frac{1}{1 - a/W} \right] + \frac{g_1}{g}$$

$$g = 0.886 + 4.64 \left[\frac{a}{W} \right] - 13.32 \left[\frac{a}{W} \right]^2 + 14.72 \left[\frac{a}{W} \right]^3 - 5.6 \left[\frac{a}{W} \right]^4$$

$$g_1 = 4.64 - 26.64\left[\frac{a}{W}\right] + 44.16\left[\frac{a}{W}\right]^2 - 22.4\left[\frac{a}{W}\right]^3$$

for the compact tension geometry.

Equation (5.51) is very similar to the equation (5.13) suggested for the experimental determination of C*

$$C^*_{exp} = \frac{P\dot{\Delta}_c}{BW} F \qquad (5.13)$$

where $\dot{\Delta}$ has been replaced with $\dot{\Delta}_c$ since it represents creep, rather than total displacement rate. The only difference in the numerical values of C_t and C^*_{exp} is in the non dimensional factors H'/H and F. The ratio C^*_{exp}/C_t for the compact tension geometry, is shown in figure 10.5 as a function of a/W. It can be seen that the maximum ratio is about 1.4. So although the definition of C_t and C^*_{exp} is quite different, and, C_t is more appropriate for small scale yielding whereas C^*_{exp} is more appropriate when extensive creep conditions are approached, the error in using just one of these parameters for conditions extending from small scale creep to steady state creep will be insignificant. In this thesis C^*_{exp} was chosen to correlate the crack growth rates.

When the specimens are side grooved then the thickness B in equation (5.13) must be replaced with the net thickness B_n (see for example Smith (1983)).So equation (5.13) becomes.

$$C^*_{exp} = \frac{P\dot{\Delta}_c}{B_n W} F \qquad (10.26)$$

The method of evaluating $\dot{\Delta}_c$ as well as the crack growth rate and the load rate from the experimental results is presented in the next section

10.4 RATE DATA EVALUATION

Initial investigators (Nikbin (1976), Kenyon (1976)), analysed their experimental work by a manual process, to obtain information of the rates of change, with respect to time, of certain variables, such as crack length and displacement. This process consists of plotting in linear scales the relevant variable with respect to time. A smooth curve is drawn as near as possible to all the data points using french-curves or a flexi-rule. The rate of change of the variable with respect to time, is estimated by constructing geometrically a tangent or a normal to the curve at the selected points. This method of processing is very time-consuming in evaluating the required information.

McCartney and Cooper (1977) investigated the use of numerical processes to obtain rate information. They concluded that using least squares high order polynomials on the complete data set, the fitted curve oscillates about the experimental data and thereby gives gradients which similarly oscillate to give values that are in error. On the other hand they indicate that by using a spline technique, that is using low order polynomial functions each fitted to a subset of data, this problem can be overcomed. To preserve continuity, that is to preserve smoothness, the end points of the adjacent polynomials must, for example, have identical values of the first and second differentials.

Smith (1983) indicates that using a spline technique in data containing considerable noise may result to unrealistic results for the gradient. To overcome this problem Smith (1983) used a combined manual and numerical technique. A complete data set of for the particular variable was plotted as a function of time in linear scales and, as in the manual process described earlier, a smooth curve was drawn as close as possible to all data points. The data points associated with the smoothed curve were taken as being exact and used as data input to a curve fitting technique. This technique developed by Fritsh and Carlson (1980) is essentially a method of fitting a cubic spline to monotone data in such a way that the convexity or concavity of the data is preserved at all intermediate points between the data. The monotone spline technique however, can

produce fluctuations in the rate data in the rising portion of the crack length (or displacement) curve, as a consequence of the technique using the data points exactly rather than a mean value.

In this thesis a combined manual and numerical technique was used. The manual technique is the same as the one used by Smith (1983), and the numerical technique used for calculating the crack length, displacement, and, load rates, from the experimental observations of the crack length, displacement, and, load respectively was the seven-point incremental polynomial method recommended in the ASTM standard E-647 (1982) for calculating rates from fatigue crack growth data.

The seven point polynomial involves fitting a second order polynomial through a group of seven successive data points. The rates are then obtained by differentiating the fitted equation. The characteristic equations for this procedure are:

$$\hat{p}_i = b_0 + b_1\left[\frac{t_i - C_1}{C_2}\right] + b_2\left[\frac{t_i - C_1}{C_2}\right]^2 \qquad (10.27)$$

$$\text{where} \quad -1 \le \frac{t_i - C_1}{C_2} \le +1 \qquad (10.27a)$$

$\hat{p}_i$ is the fitted value of p_i corresponding to time t_i. p_i can be crack length, displacement or load. b_o, b_1 and b_2 are regression parameters which are determined by the least square method (that is the minimization of the squares of the deviations between the observed and the fitted values) over the range $p_{i-3} \le p \le p_{i+3}$. The parameters

$$C_1 = \frac{1}{2}\left[t_{i-3} + t_{i+3}\right] \quad \text{and} \quad C_2 = \frac{1}{2}\left[t_{i-3} - t_{i+3}\right]$$

are used to scale the input data. The crack growth, displacement or load rates at any time, t_i, are obtained from the derivative of equation (10.27) as:

$$\frac{d\hat{p}_i}{dt} = \dot{p} = \frac{b_1}{C_2} + \frac{2b_2}{C_2^2}\left[t_i - C_1\right] \qquad (10.28)$$

The advantage of this method to that used by Smith (1983) is that the fitted data points, rather than the exact data points are used to obtain the rates with respect to time and fluctuations of the rate data in parts where the parameter versus time curve is very steep can be avoided.

10.5 EFFECT OF CRACK GROWTH ON THE MEASURED DISPLACEMENT RATE.

The measured load-line deflection rate for a growing crack includes contributions from changing the elastic compliances of the specimens. These contributions may be small for creeping materials but they should be subtracted from the measured displacement rate to obtain the correct value of $\dot{\Delta}_c$. In general in the absence of instantaneous plasticity the measured displacement rate will be the sum of the creep displacement rate plus the elastic displacement rate

$$\dot{\Delta} = \dot{\Delta}_e + \dot{\Delta}_c \qquad (10.29)$$

Here it is important to note that in (10.29) $\dot{\Delta}_c$ is the displacement rate due to development of creep, and, is not just the displacement due to steady state creep but includes contributions due to transient creep behaviour as the stresses relax from their elastic state to their steady creep state.

The elastic compliance of a cracked body is given by:

$$c = \frac{\Delta_e}{P} \qquad (10.30)$$

Solving (10.30) for Δ_e and differentiating with respect to time:

$$\dot{\Delta}_e = c\left[\frac{\partial P}{\partial t}\right]_c + P\left[\frac{\partial c}{\partial t}\right]_P \qquad (10.30a)$$

$$\text{but } \left[\frac{\partial c}{\partial t}\right]_P = \frac{da}{dt}\left[\frac{\partial c}{\partial a}\right]_P = \dot{a}\left[\frac{\partial c}{\partial a}\right]_P = \dot{a}\,\frac{2BK^2}{E'P^2} \qquad (10.31)$$

where $(\partial c/\partial a)_P$ is substituted from equation (5.49). E' is the effective modulus as defined by (4.32) and (4.33). Substituting (10.31) in (10.30a)

$$\dot{\Delta}_e = c\dot{P} + \dot{a}\frac{2BK^2}{E'P} \qquad (10.32)$$

Substitution of (10.32) in (10.29) leads to the creep displacement rate

$$\dot{\Delta}_c = \dot{\Delta} - \left[c\dot{P} + \dot{a}\frac{2BK^2}{E'P} \right] \qquad (10.33)$$

For constant load tests the load rate is zero so:

$$\dot{\Delta}_c = \dot{\Delta} - \dot{a}\frac{2BK^2}{E'P} \qquad (10.34)$$

For constant displacement tests the total displacement rate is zero so:

$$\dot{\Delta}_c = -\left[c\dot{P} + \dot{a}\frac{2BK^2}{E'P} \right] \qquad (10.35)$$

For tests where both the load and displacement at the specimen change with time, for example when the displacement of the testing machine is kept constant, equation (10.33) must be used to calculate the creep displacement rate.

10.6 STATIC CRACK GROWTH OF THE 800H MATERIAL

10.6.1 INTRODUCTION

As it can be seen from figure 10.4, when a cracked specimen is subjected to a load which is held constant, there will be a period of time during which stress redistribution occurs ahead of the crack tip as the stresses change from their initial elastic values to their stationary steady state creep values. When correlations with the analytical form of C* are applied it is necessary that the initial stress redistribution is essentially complete. Thus the stress redistribution time (equation (5.27)) must be much less than the test duration. Then the creep strains are expected to dominate the elastic and hence the transient effects during the stress redistribution to be negligible, and, C^*_{exp} calculated from the experimental load line displacement to approach C* calculated analytically

through equation (6.58).

In the next section the stress redistribution times for the material 800H are compared with the test duration, and, the crack growth rate is correlated with both C^*_{exp} and C* calculated analytically through (6.58).

10.6.2 800H RESULTS AND DISCUSSION.

Table 10.1 gives the non-dimentional time t_1/t_f, where t_1 is the Riedel and Rice (1980) redistribution time calculated through equation (5.27) and t_f is the failure time. It is evident that for all 800H static tests, the non-dimentional time t_1/t_f is much less than 1, so that crack redistribution occurs before any significant crack extension and hence it is expected that both C^*_{exp} calculated through the experimental displacement rates and the analytical form of C* will characterize the crack growth rates. On the other hand due to small redistribution times the stress intensity factor K is not expected to correlate the crack growth rate data.

Figure 10.6 shows the da/dt versus K correlation for the 800H material. As it was expected the correlation is inadequate as da/dt for the same stress intensity factor K may vary by as much as a factor of 100.

Figure 10.7 shows the da/dt correlation with C^*_{exp}, and, figure 10.8 the da/dt correlation with C^*_{exp}, and, the analytical form of C* calculated through equation (6.58) for plane stress conditions, for n=6.5 and σ_o=225MPa for $\dot{\varepsilon}_o$=1/h. In the determination of the analytical form of C*, the effective specimen thickness B_{eff} as defined by Shih et. al. (1977) has been used

$$B_{eff} = B - \frac{(B - B_n)^2}{B} \qquad (10.35a)$$

Both parameters give good correlation with the crack growth data. There is no any significant trend due to specimen size, indicating the applicability of both parameters in characterising creep crack growth. However there are deviations from the overall linearity at low crack growth rates so there is a doubt as to whether there is a unique

correlation of da/dt with C* or C^*_{exp}. This behaviour is discussed in detail in the next section.

It is important to note that in service a numerical estimation of C* will be required since the measured load line displacement rates will not generally be available. The parameter C* contains geometric factors, crack length a, and material crack properties, and it is in these material behaviour properties where the difficulties may lie. The C* parameter as given by equation (6.58) is proportional to σ^{n+1} and if n is high, an accurate calculation of the stress is essential if a reliable estimate of C* is to be obtained. This in turn demands an accurate knowledge of the constitutive equations describing the material behaviour. In the present analysis the stress exponent n for the 800H material is low (n=6.5) and so no large discrepancies between the calculated C* and C^*_{exp} have been found.

10.7 INITIAL TRANSIENT CRACK GROWTH BEHAVIOUR.

10.7.1 INTRODUCTION

The C^*_{exp} and C* versus da/dt correlations, exhibit at low cracking rates deviations from the overall linearity, as shown in figures 10.7 and 10.8 for the 800H alloy. In the literature (Harper and Ellison (1977), Maas and Pineau (1985), Ellison (1987)) this region is referred to as "stage 1" crack growth, and it has been identified as a low crack growth transient regime which strongly depends on the initial conditions, and during which da/dt increases very rapidly while C^*_{exp} remains essentially constant. No unique correlation can thus be established between stage 1 da/dt and C^*_{exp} (or C*).

On the other hand good correlations are found to exist between high crack growth rates and C^*_{exp}. This is referred to as "stage 2" crack growth, and is independent of specimen size and initial conditions.

It may be argued (Harper and Ellison (1977)) that stage 1 crack growth is due to the relaxation of the initial elastic stresses, and, transition from stage 1 crack growth to

stage 2 crack growth occurs when the stresses stop redistributing near the crack tip and have reached a steady state. But this is unlikely to be the reason for low crack growth rates, since the transient stress fields associated with the stress relaxation process will give higher, rather than lower crack growth rates, and in any case the effect of the transient fields during stress redistribution is included in the measured displacement rates (Saxena (1986), Saxena and Han (1986)). Also t_1, the stress redistribution time is very small (see table 10.1)

Otherwise it may be argued that sufficient time has not elapsed to allow creep strains or damage to accumulate and thereby promote propagation of the crack. Thus while relatively higher values of C^*_{exp} are obtained compared with the extrapolated linear part of the C^*_{exp} and da/dt curve, low crack propagation rates are observed. A model has been developed based on the ductility exhaustion on the crack tip and is discussed in detail in the next section.

10.7.2 REMAINING DUCTILITY MODEL.

In chapter 5 expressions for models predicting crack growth rates by postulating a process zone at the crack tip in which creep damage accumulates, have been presented. One of these expressions is given by Nikbin et. al. (1983) as :

$$\dot{a} = (n+1)\frac{\dot{\varepsilon}_o}{\varepsilon^*_f}\left[\frac{C^*}{I_n \sigma_o \dot{\varepsilon}_o}\right]^{n/(n+1)} r_c^{1/(n+1)} \qquad (5.65)$$

where r_c is the size of the process zone and ε^*_f is the creep ductility appropriate to the state of stress at the crack tip.

Nikbin et. al. (1984) suggest that, ε^*_f is equal to the uniaxial ductility ε_{fo} for plane stress conditions and equal to $\varepsilon_{fo}/50$ for plane strain conditions. (ε_{fo} has been defined in equation 5.72).

In general the initiation and growth of a creep crack at a notch, may be viewed as a process of local damage accumulation and ductility exhaustion, in the region ahead

of the notch. That is in order for a crack to propagate, the ductility at the crack tip must be exhausted.

All previous investigations have assumed that the creep damage process zone is always present at the crack tip. However immediately after loading there is no damage ahead of the crack tip, so any model which ignores this fact will end in predicting higher crack growth rates, at least for the initial part of the components life, so the life of a component can be significantly underestimated.

A new model is proposed, which takes into account the initial stages of damage accumulation.

The model

Immediately upon loading there is no damage in the process zone. Let the initial crack length be a_o, and let dr be a small distance ahead of the crack tip.

The crack will advance when $\varepsilon=\varepsilon^*_f$ at dr.

$$\varepsilon^*_f = \dot{\varepsilon}\, dt = \dot{\varepsilon}_o \left[\frac{C^*}{I_n \sigma_o \dot{\varepsilon}_o\, dr} \right]^{n/(n+1)} dt \qquad (10.36)$$

The initial cracking rate will be given by :

$$\dot{a}_o = \frac{dr}{dt} \qquad (10.37)$$

Solving (10.36) for dt and substituting into (10.37)

$$\dot{a}_o = \frac{1}{\varepsilon^*_f} \dot{\varepsilon}_o \left[\frac{C^*}{I_n \sigma_o \dot{\varepsilon}_o} \right]^{n/(n+1)} (dr)^{1/(n+1)} \qquad (10.38)$$

After time dt i.e. when the crack has grown from a_o to a_o+ dr, the damage at a_o+2dr is:

$$\varepsilon = \dot{\varepsilon}_o \left[\frac{C^*}{I_n \sigma_o \dot{\varepsilon}_o\, 2\,dr} \right]^{n/(n+1)} dt = \frac{\varepsilon^*_f}{2^{n/(n+1)}} \qquad (10.39)$$

So when the crack is propagating from a_o+dr to a_o+2dr, some of the

ductility has been used due to damage accumulation during the period when the crack grew from a_o to a_o+dr. If the used ductility is denoted as ε^*_u, and, the remaining ductility as ε^*_r then:

$$\varepsilon^*_{u2} = \varepsilon^*_f \frac{1}{2^{n/(n+1)}} \qquad (10.40)$$

$$\varepsilon^*_{r2} = \varepsilon^*_f - \varepsilon^*_{u2} = \varepsilon^*_f \left[1 - \frac{1}{2^{n/(n+1)}} \right] \qquad (10.41)$$

In general the remaining ductility at $a_o + \alpha\, dr$ is

$$\varepsilon^*_{r\alpha} = \varepsilon^*_f \left[1 - \frac{1}{\alpha^{n/(n+1)}} \right] \qquad (10.42)$$

The crack growth rate from a_o+dr to a_o+2dr it will given by :

$$\dot{a}_1 = \frac{1}{\varepsilon^*_{r2}} \dot{\varepsilon}_o \left[\frac{C^*}{I_n \sigma_o \dot{\varepsilon}_o} \right]^{n/(n+1)} (dr)^{1/(n+1)} \qquad (10.43)$$

When the crack is at a_o+2dr, the ductility used at a_o+3dr is due to damage accumulating, for the period of the crack growth from a_o to a_o+dr, and, the period of the crack growth from a_o+ dr to a_o+2dr i.e.

$$\varepsilon^*_{u3} = \frac{\varepsilon^*_f}{3^{n/(n+1)}} + \frac{\varepsilon^*_{r2}}{2^{n/(n+1)}} \qquad (10.44)$$

and the remaining ductility is :

$$\varepsilon^*_{r3} = \varepsilon^*_f - \varepsilon^*_{u3} \qquad (10.45)$$

In general the used ductility at $a_o + \alpha\, dr$ will be :

$$\varepsilon^*_{u\alpha} = \frac{\varepsilon^*_f}{\alpha^{n/(n+1)}} + \frac{\varepsilon^*_{r2}}{(\alpha-1)^{n/(n+1)}} \qquad (10.46)$$

The crack growth rate for the crack to grow from a_o+2dr to a_o+3dr it will be given by :

$$\dot{a}_2 = \frac{1}{\varepsilon^*_{r3}} \dot{\varepsilon}_o \left[\frac{C^*}{I_n \sigma_o \dot{\varepsilon}_o} \right]^{n/(n+1)} (dr)^{1/(n+1)} \qquad (10.47)$$

In general it may be proved that the remaining ductility for a crack to grow from $a_o+(i-1)dr$ to $a_o+i\,dr$ is :

$$\varepsilon^*_{ri} = \varepsilon^*_f - \sum_{m=0}^{m=i-2} \frac{\varepsilon^*_r(m+1)}{(i-m)^{n/(n+1)}} \qquad (10.48)$$

with $\varepsilon^*_{r1} = \varepsilon^*_f$, and, i an integer, $i \geq 2$, and the crack growth rate is :

$$\dot{a}_{i-1} = \frac{1}{\varepsilon^*_{ri}} \dot{\varepsilon}_o \left[\frac{C^*}{I_n \sigma_o \dot{\varepsilon}_o} \right]^{n/(n+1)} (dr)^{1/(n+1)} \qquad (10.49)$$

It must be stated here that the relevant C* for the current crack length must be used, i.e. for a crack increment from $a_o+(i-1)\,dr$ to $a_o+i\,dr$, C* at $a_o+(i-1/2)\,dr$ must be used.

An application of this model to a real situation is presented in figure 10.9 for specimen A76 of the 800H superalloy. To directly compare the model with the experimental results, C^*_{exp} calculated from the experimental displacement rate, rather than the analytical form of C*, was used. Also in the same graph the prediction from the Nikbin et. al. (1983) model, equation (5.65) is shown for comparison. Compared with the Nikbin et. al. model, the present model gives lower crack growth rates at low C*, but at high values of C* both models predict the same crack growth rate. The present model is in very good agreement with the experimental crack growth rates, especially at the beginning of the test were there is a deviation from overall linearity. The close agreement of the experimental results with the present model give additional support to the view that, the initial deviations from the overall linearity, or stage 1 cracking, are due to damage accumulation at the crack tip, and not due to failure of C* to describe small crack growth rates.

An important characteristic of equation (10.49) is the relative insensitivity on the choice of dr (since dr is raised to a very small power 1/(n+1)). This is illustrated on figure 10.10 for specimen A76.

10.8 INFLUENCE OF AGING ON CRACK GROWTH IN TYPE 304H STAINLESS STEEL

10.8.1 INTRODUCTION.

The useful lives of engineering components which are used at elevated temperatures may be different to those predicted at the initial design stage, because of assumptions in the analysis, material variability and changes in the operating procedures. Assessment of the reliability of high temperature components, such as stainless steel internals in fluid catalytic cracking units (FCCU) in the petroleum industry, is receiving increasing attention due to the higher operating temperatures and longer run times to improve efficiency and utilization.

The traditional industry approach to high temperature design has been directed towards preventing failure by stress rupture in nominally defect free structures. However, this approach is not relevant to situations where, as has been observed in a number of FCCU components, failure occurs by crack growth. The mechanism of crack advance is believed to be creep crack growth with possible environmental contributions.

To study the life of elevated temperature FCCU internals containing cracks or crack like defects, creep crack growth experiments were conducted on compact tension test specimens and the results analysed in terms of non linear fracture mechanics concepts using the C^*_{exp} parameter. The material has been tested both in the virgin and naturally aged conditions.

10.8.2 RESULTS AND DISCUSSION.

Figure 10.11 gives the da /dt versus C^*_{exp} correlation for the new material at a temperature of 760° C. There is no significant trend with specimen size or side-groove depth demonstrating that any of the specimen geometries can be used to measure the cracking behaviour.

Corresponding results for the aged material are shown in figure 10.12. As it

was explained in chapter 8 insufficient aged material was available to make monobloc specimens and a sandwich construction was employed with aged material electron beam welded between two layers of unaged material, and the crack was then propagated through the aged material. No trends are apparent with the height H of the aged layer implying no influence of the welding procedure on the results. The tests conducted on the aged material indicate a cracking rate about an order of magnitude faster than is measured on the new material at the same value of C^*_{exp}. This is consistent with less deformation accompanying cracking in the aged material than in the unaged. It may be deduced therefore that aging has embrittled the 304H stainless-steel and made it more prone to cracking. Further evidence of embrittlement can be obtained by comparing broken aged and unaged specimens. The unaged tests were terminated after excessive deformation whereas the aged specimens cracked right through with little evidence of necking. The increased crack growth rate in the aged material can be explained as follows.

Tests conducted by Buchheim et al. (1986) on smooth and notched uniaxial specimens indicate a creep ductility of about half for the aged material compared to new material. A model which predicts creep crack growth in terms of damage accumulation in a process zone at the crack tip has been discussed in detail in section 5.5. Equation 5.65 was

$$\dot{a} = (n+1)\frac{\dot{\varepsilon}_o}{\varepsilon^*_f}\left[\frac{C^*}{I_n \sigma_o \dot{\varepsilon}_o}\right]^{\frac{n}{n+1}} r_c^{1/(n+1)} \qquad (5.65)$$

which can be approximated for a wide range of material as

$$\dot{a} = \frac{300}{\varepsilon^*_f}(C^*)^{0.85} \qquad (5.67)$$

where $\dot{a}$ is in millimeters per hour with ε^*_f as a percentage and C* in units of megajoules per square meter per hour. ε^*_f is the creep ductility appropriate to the state of stress at the crack tip and as was explained in section 5.5 is equal to the uniaxial creep

ductility for plane stress conditions and 1/50 of this value for plane strain conditions. Buchheim et al. (1986) estimate a uniaxial creep ductility for the new material of 50%, and, a uniaxial creep ductility for the aged material of 25%.

The application of equation 5.67 for the new material is shown figure 10.11 for plane stress conditions. The correspondence between this equation and the experimental results, despite the use of deep side-grooves, indicates that the data agree with the predictions assuming plane stress conditions prevailed in the tests. Further evidence of plane stress behaviour was demonstrated by the observation that appreciable necking accompanied the cracking and the tests were terminated due to excessive deformation before a crack had passed through the specimens.

The appropriate expressions for plane stress and plane strain loading for the aged material are shown in figure 10.12. In this case the data lie roughly in the middle of the two predictions, suggesting that plane stress conditions are not developed at the crack tip for this material. Additional support for this view was provided by the observation that these specimens failed by the passage of the crack right through them with little indication of necking.

Application of the simplified crack growth law equation 5.67 implies that at a constant state of stress, a halving in the creep ductility should result in a doubling of the creep crack growth rate. However as is indicated with the present experimental results a decrease in ductility in a given thickness of material may cause, in addition a change from plane stress conditions towards plane strain conditions and a very significant increase in the sensitivity to crack growth. The increase in crack growth of about 10 times in the aged material may therefore be attributed to the combined effects of material embrittlement and the move towards plane strain conditions. This effect can not be investigated by uniaxial rupture tests alone.

10.9 R - RATIO AND FREQUENCY EFFECTS ON CRACK GROWTH RATES FOR THE CYCLIC TESTS

10.9.1 INTRODUCTION

Most engineering components which operate at elevated temperatures are subjected to non-steady loading service. Depending upon the material of manufacture and operating conditions creep, fatigue and environmental processes may contribute to failure. The dominating mode of failure in a particular circumstance will depend upon such factors as material composition, heat treatment, cyclic to mean load ratio, frequency, temperature and operating environment.

Tests were conducted so that the behaviour of components which may contain cracks under superimposed cyclic and steady loading, can be investigated. Attention is focused on the so-called intermediate (stage 2) region of cracking. Near threshold behaviour is not examined. The materials considered are the 1/2CMV steel the 21/4CM steel and the AP1 superalloy, which are materials of interest to the gas turbine, chemical and electrical power generation industries. Most emphasis will be given to examining the influence of cyclic to mean load ratio and the effects of frequency of loading on crack growth rate.

10.9.2 RESULTS AND DISCUSSION.

The effects of minimum to maximum load ratio R and frequency f were examined separately. Attention was confined to intermediate crack propagation rates; near threshold behaviour was not considered.

Figures 10.13 and 10.14 show the da/dN versus ΔK dependence, for the 1/2CMV steel and the AP1 superalloy over a range of frequencies at a constant R-ratio of 0.8 and 0.7 respectively. Similar figures have been obtained for other R-ratios, and the 21/4CM steel. These figures indicate that for all materials tested, at a given value of R-ratio and at high frequencies da/dN is approximately insensitive to frequency whereas

below this frequency range da/dN increases with decrease in frequency indicating time dependent effects at low frequencies. Careful examination of the fractured specimens indicates that the frequency insensitive region is associated with transgranular fractures and the time dependent region with intergranular failures (see figure 10.23). This is in agreement with results from other researchers (Nikbin and Webster (1987), Smith (1983), Winstone et al. (1985)).

The dependence of crack growth on R-ratio in the high and the low frequency regions is shown in figures 10.15 and 10.16 for the AP1 superalloy. An increase in da/dN with R-ratio at a given value of ΔK is apparent in both regions. Similar trends were obtained for the 1/2CMV and the 21/4CM steels and they are shown in figures 10.17 to 10.20 although the sensitivity to R appears to be greater in the low alloy steels than in the nickel base superalloy.

Examination of the experimental data in figures 10.14, 10.15 and 10.16 for the AP1 superalloy indicates that the crack growth rate can be correlated by an expression of the form of equation (7.1) with m=2.5. This value appears to be satisfactory for all the test conditions examined for this material and is within the range normally observed for room temperature fatigue cracking.

Corresponding results for the 1/2CMV and the 21/4CM steels are shown in figures 10.13 and 10.17 to 10.20. Equation (7.1) can still be applied to correlate the crack growth but higher values of m are required to fit the data. Generally (Sadananda and Shahinian (1981), Nikbin et. al. (1983), Nikbin et. al. (1984)) high values of m, consistent with those recorded here, are required when attempts are made to correlate creep crack growth data in terms of K. A value of m=8 has been employed to fit the 1/2CMV steel results in figures 10.13, 10.17 and 10.18, and, m = 5 those for the 21/4CM steel in figure 10.19. The same value of m appears to be satisfactory for all tests conditions for the 1/2CMV steel but there is some tendency for a higher m to be needed at the low frequencies (figure10.20) for the 21/4CM steel.

The sensitivity of da/dN to R-ratio and frequency for alloy AP1 at constant

ΔK and constant maximum stress intensity factor K_{max}, are shown in figures 10.21 and 10.22 respectively. Similar dependences on frequency are demonstrated on both figures. The influence of frequency on crack growth rate can be explained in terms of the relationship between da/dN and the crack growth rate $\dot{a}$ from

$$\frac{da}{dN} = \frac{1}{3600\,f}\,\dot{a} \qquad (10.50)$$

(where da/dN is measured in mm/cycle, f in Hz and $\dot{a}$ in mm/h), and by making use of cumulative damage concepts. A horizontal line in figures 10.21 and 10.22 corresponds with where da/dN is constant and therefore cycle dependent fatigue processes may be expected to control. When time dependent processes dominate $\dot{a}$ should be constant so that from equation (10.50), da/dN should be inversely proportional to frequency and a slope of -1 will be expected in the figures as it is observed at the low frequencies. When both processes act together then the combined crack growth per cycle it will given by (7.10) as explained in section 7.4.

$$\frac{da}{dN} = \left[\frac{da}{dN}\right]_t + \left[\frac{da}{dN}\right]_f \qquad (10.51)$$

in (10.51) above subscript "c" has been replaced by "t" to represent time dependent, rather than just creep damage, since creep damage and environmental damage are both time dependent and they can not be separated. Subscript "f" refers to fatigue damage. The predictions of this formula are shown in figures 10.21 and 10.22. The close agreement with the experimental results demonstrates the applicability of equation (10.51) and the validity of using a linear cumulative law approach. Equation (10.51) predicts that either one mechanism or the other controls except over a narrow frequency range between about 0.1 and 1Hz for alloy AP1. Further confirmation of the applicability of the cumulative damage approach was obtained from scanning electron microscopy examinations of the fracture surfaces (figure 10.23). Exclusively transgranular cracking is observed at a frequency of 10Hz (figure 10.23a), intergranular cracking at 0.001Hz (figure 10.23d) and mixed intergranular and transgranular cracking at intermediate frequencies of 1Hz (figure 10.23b) and 0.1Hz (figure 10.23c) with the

proportion of intergranular cracking increasing with decrease in frequency. These features clearly demonstrate that fatigue processes dominate at high frequencies, intergranular time dependent mechanisms govern at low frequencies and both processes act together at intermediate frequencies. Mechanistically, both types of cracking are likely to progress intermittently through or around individual grains so that at intermediate frequencies when one mechanism becomes arrested temporarily locally the other may take over to allow cracking to progress at a rate equal to the sum of the individual rates.

Figure 10.21 indicates that at constant ΔK an increase in R from 0.1 to 0.7 increases da/dN by about an order of magnitude at low frequencies and by about 3 at high frequencies. In contrast figure 10.22, which shows the results plotted at constant K_{max}, only demonstrates an R-atio effect at high frequencies with da/dN decreasing with increase in R. Both figures indicate that the transition from time dependent to fatigue dominated crack growth occurs at a higher frequency with increase in R. This trend can be interpreted in terms of mean load and crack closure effects.

An increase in R at constant ΔK or K_{max} corresponds with an increase in the mean load. It may be expected that an increase in the mean load may enhance creep and environmental attack mechanisms relative to fatigue processes. The extension of time dependent controlled cracking to higher frequencies with increase in R-ratio, as is observed in figures 10.21 and 10.22, may therefore be attributed to creep and/or environmental attack processes contributing to failure under the test conditions applied to AP1 alloy. This is demonstrated further in figure 10.24 which indicates a satisfactory correlation of crack growth rate da/dt with K_{max} at the low frequencies where time dependent processes dominate. The relative insensitivity of crack growth to R at low frequencies shown in figures 10.22 and 10.24 implies that crack extension in this region occurs predominantly at maximum load each cycle.

The frequency and R dependence of crack growth at constant K_{max} for a corresponding da/dN range for the 1/2CMV and the 21/4CM steels are shown in figures

10.25 and 10.26. As for the nickel base superalloy, regions of cycle and time dependent dominated cracking can be identified. Equation (10.51) can still be used to describe da/dN but a sensitivity to R is apparent at all frequencies, which is most pronounced for the 21/4CM steel (figure 10.26) and which suggests that K_{max} is not the most appropriate parameter for correlating the crack growth rate in these materials. Careful examination of figures 10.25 and 10.26 suggests that the crack growth rate is faster at lower R ratios. From these figures it can be also seen that the transition from time dependent to cycle controlled cracking is extended to higher frequencies with decrease in material creep ductility. (The 1/2CMV steel has the lowest ductility, the 21/4CM steel the highest, and the AP1 supperalloy has an intermediate ductility). This trend is explained later in 10.8.2(c) in terms of equation (5.65)

The influence of R-ratio on the crack growth rates when a K correlation is used, at frequencies were time dependent processes dominate, and, at frequencies where fatigue processes dominate, is examined in detail in sections 10.9.2(a) and 10.9.2(b) respectively.

(a) R - RATIO EFFECTS AT LOW FREQUENCIES

The stress fields σ_{ij}^- and σ_{ij}^+ immediately before and immediately after the load step in a cyclic test, are related by:

$$\sigma_{ij}^+ = \sigma_{ij}^- + \Delta\sigma_{ij} \qquad (10.52)$$

where $\Delta\sigma_{ij}$ is the elastic field associated with the load range ΔP (Riedel (1983)).

Near the crack tip, the elastic field $\Delta\sigma_{ij}$, dominates asymptotically since the elastic $1/\sqrt{r}$ singularity is stronger than the $1/r^{1/(n+1)}$ HRR type singularity of σ_{ij}^-. Hence the initial condition for the crack tip field after a load step is the same as that after a step load, and the short time solution after the load step is given by equation (5.22) with ΔK substituted for K.

$$\frac{\sigma_{ij}}{\sigma_o} = \left[\frac{\Delta K^2}{(n+1) I_n \sigma_o \dot{\varepsilon}_o E' r t} \right]^{\frac{1}{n+1}} \tilde{\sigma}_{ij}(\theta, n) \qquad (10.53)$$

but $$\Delta K = K_{max}\,(1 - R) \qquad (10.54)$$

substituting (10.54) in (10.53)

$$\frac{\sigma_{ij}}{\sigma_o} = \left[\frac{K_{max}^2}{(n+1) I_n \sigma_o \dot{\varepsilon}_o E' r t}\right]^{\frac{1}{n+1}} \tilde{\sigma}_{ij}(\theta, n)\left[1 - R\right]^{\frac{2}{n-1}} \qquad (10.55)$$

or

$$\frac{\sigma_{ij}}{\sigma_o \tilde{\sigma}_{ij}(\theta, n)\left[\frac{K_{max}^2}{(n+1) I_n \sigma_o \dot{\varepsilon}_o E' r t}\right]^{\frac{1}{n+1}}} = \left[1 - R\right]^{\frac{2}{n+1}} \qquad (10.56)$$

The LHS of equation (10.56) gives the non-dimentional value of the stress peak after a load step. From (10.56) it can be deduced that this non-dimentional value is a function of the R-ratio and the stress exponent n. Figure 10.27 shows the LHS of equation (10.56) plotted versus the R-ratio ($0 \leq R \leq 1$) for various values of n. The magnitude of the stress peak is maximum at R=0 and is monotonicaly decreasing with increasing R, becoming zero at R=1. This is indicating that faster crack growth rates are expected at lower R-ratios for the same K_{max}.

However if n is high, the magnitude of the stress peak after the load step, and so the crack growth rate, is relatively insensitive to R. This may explain the reason of relatively insensitivity of R-ratio, when crack growth rates are correlated with K_{max}, for the AP1 superalloy (n=15), and the progressively pronounced effect of faster crack growth rates for a lower R-ratio, for the 1/2 CMV steel (n=10) and the 21/4CM steel (n=9).

(b) R - RATIO EFFECTS AT HIGH FREQUENCIES

The influence of R-ratio on fatigue crack growth at room temperature has been attributed (see section 7.1.3) to fracture surface roughness, build up of oxide scale on the fracture surface and the development of plastic deformation at the crack tip. All these factors will help the crack close before the minimum load of the cycle is reached so that the whole of the applied stress intensity factor range is not available for propagating the crack. Elber (1971) has defined an effective stress intensity factor range ΔK_{eff} to account for when the crack is open and modified (7.1) to

$$\frac{da}{dN} = C \Delta K_{eff}^{m} \qquad (10.57)$$

to make C a constant in the frequency insensitive region and

$$\frac{\Delta K_{eff}}{\Delta K} = U = f(R) \qquad (10.58)$$

Various empirical expressions have been used for U. The form that is employed here is

$$U = b + cR + (1 - b - c) R^{2} \qquad (10.59)$$

which allows ΔK_{eff} to equal ΔK as R approaches one. The coefficients b and c are fractions which are chosen to give the best fit to the data. Application of equation (10.59) to the experimental results at 10Hz for the AP1 superalloy the 1/2CMV and the 21/4CM steels is shown in figure 10.28. The correlation achieved with da/dN for AP1 is indicated in figure 10.29. Also included in figure 10.28 is the prediction for room temperature fatigue data on a aluminium alloy (Schijve (1979)). It is apparent that the U ratio is less at elevated temperatures that it is at room temperature. This may be expected as the enhanced oxidation at elevated temperatures and accumulation of creep, as well, as plastic, deformation at the crack tip will each cause closure to occur at a higher load in each cycle and ΔK_{eff} to be reduced.

(c) LOW FREQUENCY CRACK GROWTH CORRELATION IN TERMS OF C^*_{exp}

Any load change influences the local stress state at the crack tip, as it will cause an instantaneous elastic stress distribution to be superimposed, and time will be needed for stress redistribution to occur and a new state to be developed. An enhanced cracking and displacement rate can be obtained after a load increase, and, when the load is reduced a prolonged incubation is observed before measurable crack extension and displacement are detected (Nikbin (1976)).

In section 7.3 all possible types of cyclic loading were discussed in detail. It was deduced that the only case where cycling will have no effect on the crack growth rate is when the rise time, t_r, from minimum to maximum load, is much greater than the transition time t_1. Otherwise the near crack tip stress field will exhibit a peak at the end of the rise time, and even if the cycling is too slow so that steady state conditions are reached during the cycle, cracking will occur at an enhanced rate so C* calculated analytically through (6.58) can not correlate the crack growth rates. It may be argued however that, as far as the mechanism of failure is dominated by time dependent creep, this will be reflected in the measured displacement rate, in the same way that transient field effects are included in the measured displacement of the static tests, when stress redistribution times are significant relatively to the specimen life and small scale creep conditions prevail. Higher crack growth rates will be reflected in higher measured displacement rates.

Figures 10.30 to 10.32 show the correlation of the crack growth rate da/dt for each material against the creep fracture parameter C^*_{exp} calculated at the maximum load of the cycle since most of the damage takes place at maximum load. Also included in these figures are static load creep crack growth data. Although environmental attack and creep processes cannot be separated in this investigation as all the experiments were performed in air, it can be seen that the cyclic data can be predicted satisfactorily from creep crack propagation rates using the expression

$$\dot{a} = D C^{*\Phi}_{exp} \qquad (10.60)$$

where D and Φ are material dependent parameters which can be obtained from figures 10.30 to 10.32. The implication is that a similar stress distribution to that formed ahead of a crack in static creep tests is developed at maximum load in the cyclic tests irrespective of the periodic elastic unloadings and reloadings. Substitution of equation (10.60) into the cumulative damage law (equation (10.51)) allows crack growth under combined static and cyclic loading to be obtained from

$$\frac{da}{dN} = \frac{D C^{*\Phi}_{exp}}{3600 f} + C \Delta K^{m}_{eff} \qquad (10.61)$$

Equation (10.61) implies that crack growth results obtained under creep/fatigue loading conditions in the alloys examined can be determined from tests carried out under a static load and a rapid cyclic frequency only, to identify the time dependent and fatigue components of failure. The form of equation (10.61) indicates little interaction so that either one mechanism or the other will be expected to control, except over a narrow frequency range as indicated in figures 10.21, 10.22, 10.25 and 10.26. Furthermore examination of the Nikbin et. al. model (equation (5.67))

$$\dot{a} = \frac{300 C^{*\,0.85}}{\varepsilon^{*}_{f}} \qquad (5.67)$$

where $\dot{a}$ is in mm/hr, C* in MJ/m^2hr and ε^{*}_{f} is creep ductility as a percentage appropriate to the state of stress at the crack tip, shows that the 21/4CM steel should therefore be more resistant the nickel-base superalloy in between, and the 1/2CMV steel least resistant to creep and low frequency creep-fatigue crack growth at elevated temperatures. The transition in figures 10.21, 10.22, 10.25 and 10.26 from time to fatigue controlled behaviour at progressively higher frequencies for the 21/4CM, the AP1 alloy and the 1/2CMV steel, consistent with their decreasing creep ductilities (45%, 15% and 0.1-5% respectively), confirms this prediction.

10.10 CONSTANT DISPLACEMENT TESTS

10.10.1 INTRODUCTION

Low crack growth rate correlations between da/dt and C* are of particular importance, since crack growth in industrial components will take place at very small crack growth rates. As is discussed in section 10.7 initiation effects prevent valid data to be obtained until significant crack growth has occurred and, since rates, in a constant load test, continually increase throughout the test, valid data at low crack growth rates can only be obtained from long-duration, low-load tests, when the specimens are tested under constant load conditions.

An incidental result from constant amplitude tests, is that the cracking rate da/dt decreases, in general, with crack extension, so that correlations between da/dt and C* can be obtained at low crack growth rates without any initiation effects, and, in shorter times than possible in constant load tests. Good correlation between da/dt and C* at low crack growth rates, away from any initiation effects will remove any doubt for using C*, as a characterising parameter to predict crack growth rates.

Figure 10.32a shows the prediction of da/dt versus C* for a test where the crack growth rates decrease throughout the test, which is typical of a constant displacement test, by using the model of section 10.7. Also shown for comparison in the same figure are the corresponding prediction of the Nikbin et. al. model equation (5.65), and, the prediction of the model of section 10.7 with da/dt increasing through the test, which is typical of a constant load test. It is observed that the "stage 1" cracking is at the high values of da/dt for a constant displacement test, so that correlations of da/dt with C* can be obtained at low da/dt away from any initiation effects.

Another advantage of conducting tests under both displacement and load-control is that the applicability of the crack growth parameters under different combinations of crack length, load, frequency and R-atio can be more critically assessed.

Cyclic loading between fixed displacement amplitudes represents more closely

the conditions experienced in low cycle fatigue and thermal fatigue situations, than cycling between fixed load amplitudes.

10.10.2 DISPLACEMENT CONTROLLED TESTS, RESULTS AND DISCUSSION.

The crack growth in the specimens subject to displacement controlled loading, is seen to be determined by the balance achieved between the rate at which the applied loading is relieved and the rate with which the crack is growing (or the rate the damage is accumulating ahead of the crack tip).

Figure 10.33 considers an infinite body containing a crack and loaded at points A and B. If the displacement between the points A and B is kept constant, then, if the body is loaded in the creep regime, the crack will advance and the load relax due to the combined effect of stress relaxation and crack extension. The amount by which the crack will advance depends upon the time taken for the stress to relax from its initial elastic state to its steady state creep state. Initially at t=0 the strains between A and B are elastic. If the stress relaxation is fast, the load relaxation will be fast, and, the elastic strains will be replaced with creep strains with negligible crack extension taking place. Under these conditions the crack opening will remain the same, and, little crack extension will occur. However if the stress relaxation is slow then significant crack extension will occur before the stress is redistributed. The elastic strains between A and B will be significant and as the load drops, mainly due to crack extension, the elastic strains become smaller, and for the distance AB to remain constant the crack must open to balance the decrease in the elastic strains. This crack opening will force the crack to propagate, the amount of crack extension depending upon the crack opening, hence redistribution time.

In the case of 21/4CM steel and 304H stainless steel where stress redistribution is fast, the load relaxation was fast, and, the crack extension was very small as illustrated in figures 8.17 and 8.19. Only about 0.4 mm of crack extension was

observed for the 21/4CM steel and 0.5mm for the 304H stainless steel, before cracking ceased.

For the 1/2 CMV steel the time taken for stress relaxation is considerably longer and this is reflected in the rate of load relaxation and crack extension (figure 8.20). A 5mm crack extension was observed before cracking ceased.

In the case of AP1 superalloy the stress relaxation is even slower. This is indicated in all constant displacement AP1 tests. An example is given in figure 8.22. The rate at which the load relaxed was constant indicating that the load relaxation was mainly due to crack extension, rather than stress redistribution at the crack tip. The rate of crack growth rate was about constant and the crack extension enough for the specimen to fail.

The implication is that short range residual stresses arising from thermal transient loading or welding operations are expected to have a significant effect in promoting cracking in components which are made from high creep strength materials, like the AP1 superalloy and in weld heat affected zones. (The 1/2CMV steel is heat treated to represent heat affected zone). Thus in this case account needs to be taken of the presence of such stresses when assessing the significance of cracking.

The presence of residual stresses in components made from ductile parent materials will be of less significance. In ductile, relatively low creep strength parent materials like the 21/4CM steel and the 304 stainless steel, the relaxation is rapid, and only small crack extensions are possible.

However in the case of elastic follow-up occurring larger crack extensions may be expected. This phenomenon may occur to a considerable degree in large components and, to model the effect adequately in a test, it may be necessary to control displacements between points across the loading train rather than on the specimen itself.

Figures 8.18 and 8.19 show crack growth data from tests EXW11 and EXW13, under displacement controlled cycling with and without elastic follow-up. The effect of elastic follow-up was simulated by keeping the displacement amplitude of the

fatigue machine constant instead of the displacement amplitude of the loading pins. The load decays more rapidly and less crack growth is observed for specimen EXW11 than for specimen EXW13. This is attributed to the compliance of the test machine resulting in elastic follow-up and therefore some increase in the displacement at the test-piece loading points during the hold-time for this test.

In the tests where cracking ceased, it was found that if the initial load was regenerated cracking can be reactivated and the whole process repeated. This is illustrated in figure 8.19 for specimen EXW13. Load regeneration may be induced in service during a plant start-up or shut-down cycle (Becht (1983)).

Figures 10.34 and 10.35 show the da/dt versus C^*_{exp} correlation for the 1/2CMV steel and the 21/4CM steel respectively for the constant amplitude range tests. Also in these figures data from constant load range tests are included. Good correlation is observed between the cyclic load and cyclic displacement cracking results, adding further support in using C^*_{exp} as a parameter to characterise crack growth rates. It is also observed from these graphs, that "stage 1" cracking is not present at low crack growth rates, as crack growth rates decrease rather than increase through the tests and any initiation effects are eliminated. So reliable data can be collected at very low crack growth rates. This is indicated in figure 10.35 for the 21/4CM steel. Data without any initiation effects is correlated for crack growth rates as low as $1*10^{-4}$ mm/hr for the constant displacement range tests, whereas, the lowest crack growth rate correlation from the constant load range tests is $5*10^{-3}$ mm/hr.

Figure 10.36 shows the da/dt versus C^*_{exp} correlation for the 304H aged material. In this figure are also included the bounds for aged static load data. Cyclic tests under constant load range were not performed due to shortage of material, but comparison of the constant load static tests with the constant displacement range cyclic tests, does not show any significant effect of cycling on crack growth. Crack growth rate correlations as low as $5*10^{-4}$ mm/hr were obtained for the constant displacement range tests, compared to $5*10^{-3}$ mm/hr for the static load tests. In figure 10.36 some evidence

of "stage 1" cracking at high crack growth rates, similar to that predicted in figure 10.32a is evident.

Figures 10.37 and 10.38 show the crack growth rate versus C^*_{exp} correlation for the AP1 superalloy for specimens of thickness 12.5 mm and 25 mm respectively. Also included in these figures are corresponding constant load range data. Good correlation is observed irrespective of R-ratio and frequency, and irrespective of constant load range or constant displacement amplitude conditions. Constant displacement amplitude results from specimens tested at a frequency of 1Hz, and, R=0.1 and R=0.7 (not included in these figures since only slow cycling is considered), indicate that the mechanism of failure at this frequency is dominated by fatigue, which is in agreement with the corresponding results from the constant load range tests.

10.11 HR ZONE SIZES DUE TO GROWING CRACK.

In section 5.4 it has been shown that for a growing crack there exists a stress field next to the crack tip referred to as the HR field. For small scale (or transient creep) C^*_{exp} will control the crack growth rate if the extent of this field is negligible. Saxena and Han (1986) give the extent of this field by the following equation:

$$R_{HR,HRR} = \frac{\sigma_o^n}{\dot{\varepsilon}_o}\left[\frac{\dot{a}}{E}\right]^{(n+1)/2}\left[\frac{1}{C^*_{exp}}\right]^{(n-1)/2} \qquad (10.62)$$

Finite element analysis by Hawk and Bassani (1986) shows that equation (10.62) gives good approximation for the region of dominance of the HR field.

Nikbin et. al. (1983) shown that there is an approximate relation between the crack growth rate and the C* integral as:

$$\dot{a} = D\, C^*_{exp}{}^{n/(n+1)} \qquad (10.63)$$

Substituting (10.63) into (10.62) it may be deduced that:

$$R_{HR,HRR} = \frac{\sigma_o^n}{\dot{\varepsilon}_o}\left[\frac{D}{E}\right]^{n/(n-1)} C^*_{exp}{}^{1/2} \qquad (10.64)$$

From (10.64) it can be deduced that the size of the HR zone increases with C^*_{exp}. So its maximum size will be at the maximum value of C^*_{exp} and it can be evaluated by substituting the corresponding values of da/dt and C^*_{exp} in (10.62). The maximum size of this zone for all materials tested is given in table 10.2. Since the size of this zone is negligible so it will be its effect on the crack growth rates, and, the use of C^*_{exp} for characterising da/dt is valid for all materials tested.

TABLE 10.1

Comparison between stress redistribution time and failure time for material 800H.

Specimen No	t_1 p-stress /h	t_1 p-strain /h	t_f /h	t_1/t_f p-stress	t_1/t_f p-strain
A64	0.026	0.204	189.34	1.37E-4	1.08E-3
A66	0.057	0.452	308.85	1.86E-4	1.46E-3
A76	0.094	0.728	944.00	9.96E-5	7.71E-4
A77	0.024	0.192	98.00	2.52E-4	1.96E-3
A89	0.009	0.066	31.83	2.68E-4	2.06E-3
G208	0.043	0.333	193.60	2.23E-4	1.72E-3
G209	0.091	0.706	388.50	2.35E-4	1.81E-3

t_1 is the Riedel and Rice (1980) redistribution time, t_f is the failure time.

TABLE 10.2

Maximum HR zone sizes due to crack growth

Material	Zone size (mm)
1/2CMV	2.2E-10
21/4CM	5.3E-13
AP1	1.5E-06
304H	1.1E/-12
800H	1.3E-10

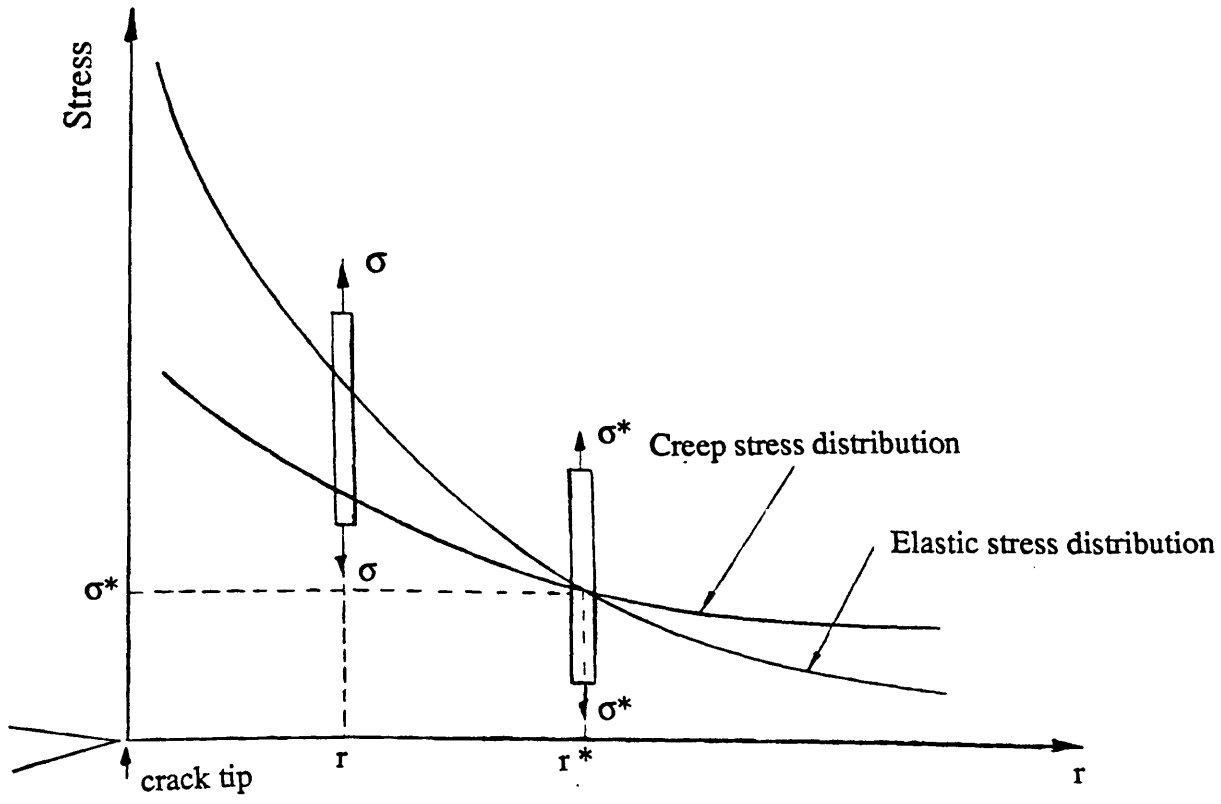


Figure 10.1 Elastic and steady state creep stress distributions ahead of a crack tip.

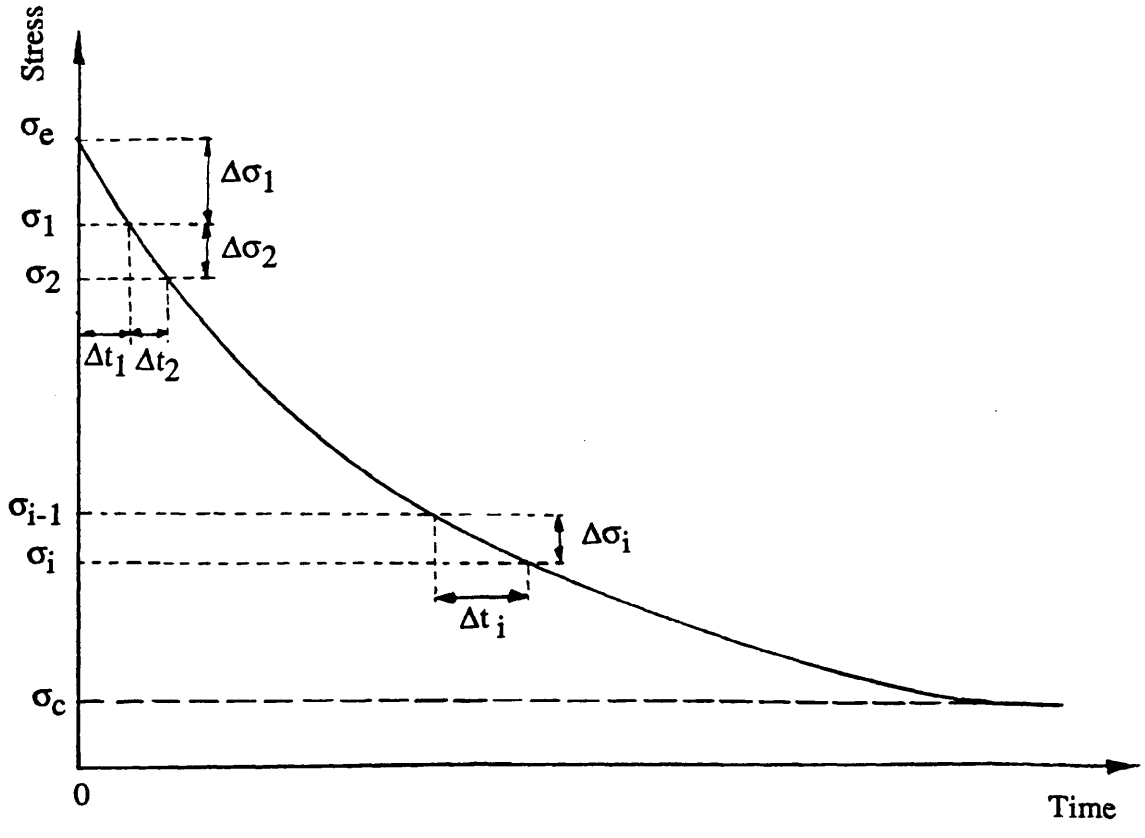


Figure 10.2 Schematic illustration of the numerical procedure employed for the calculation of stress redistribution times.

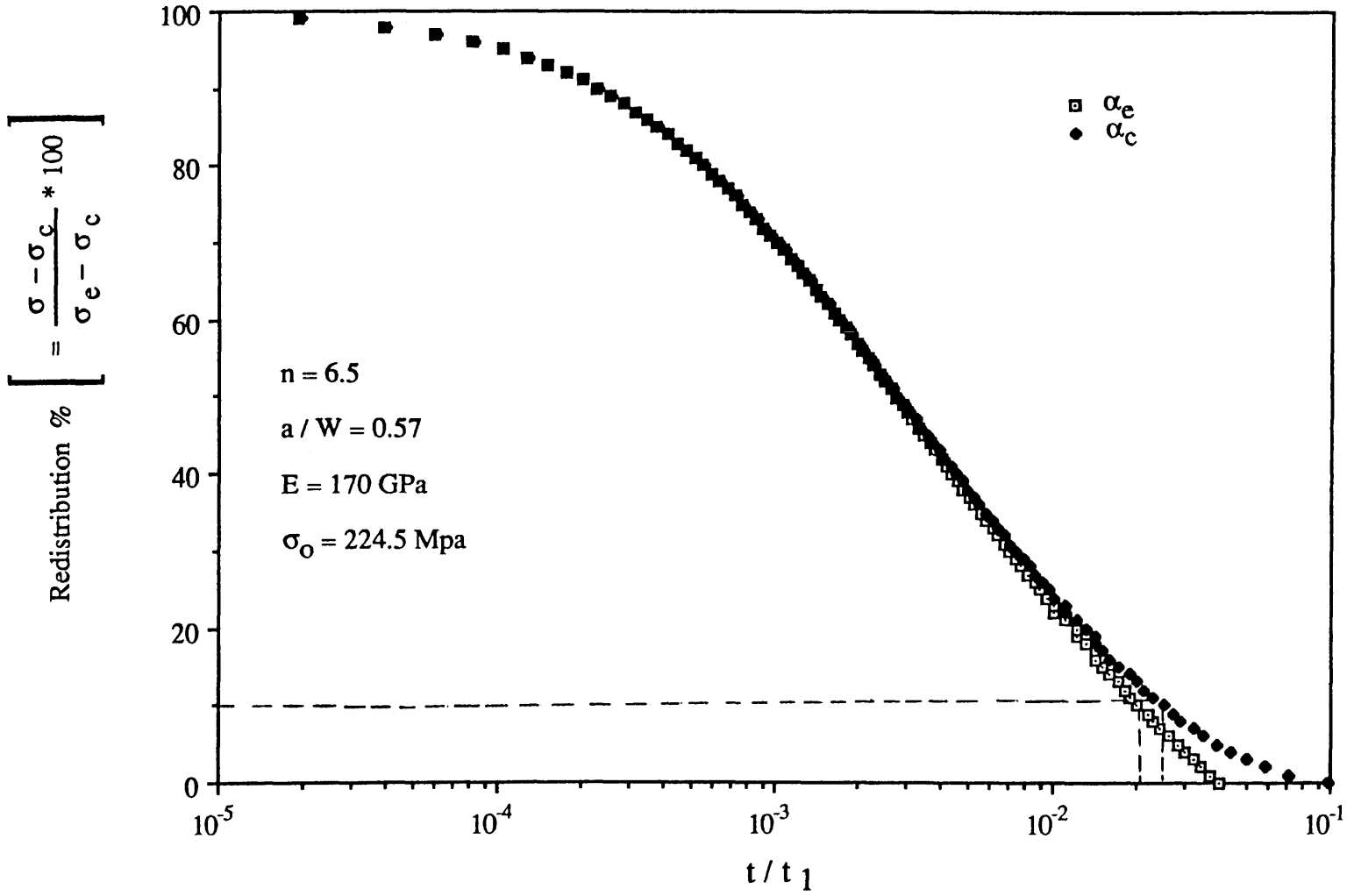


Figure 10.3 Effect of using different α on the stress redistribution as a function of the non dimensional time t / t_1 , at a distance of 500μm ahead of the crack tip , for specimen A76 (800H material).

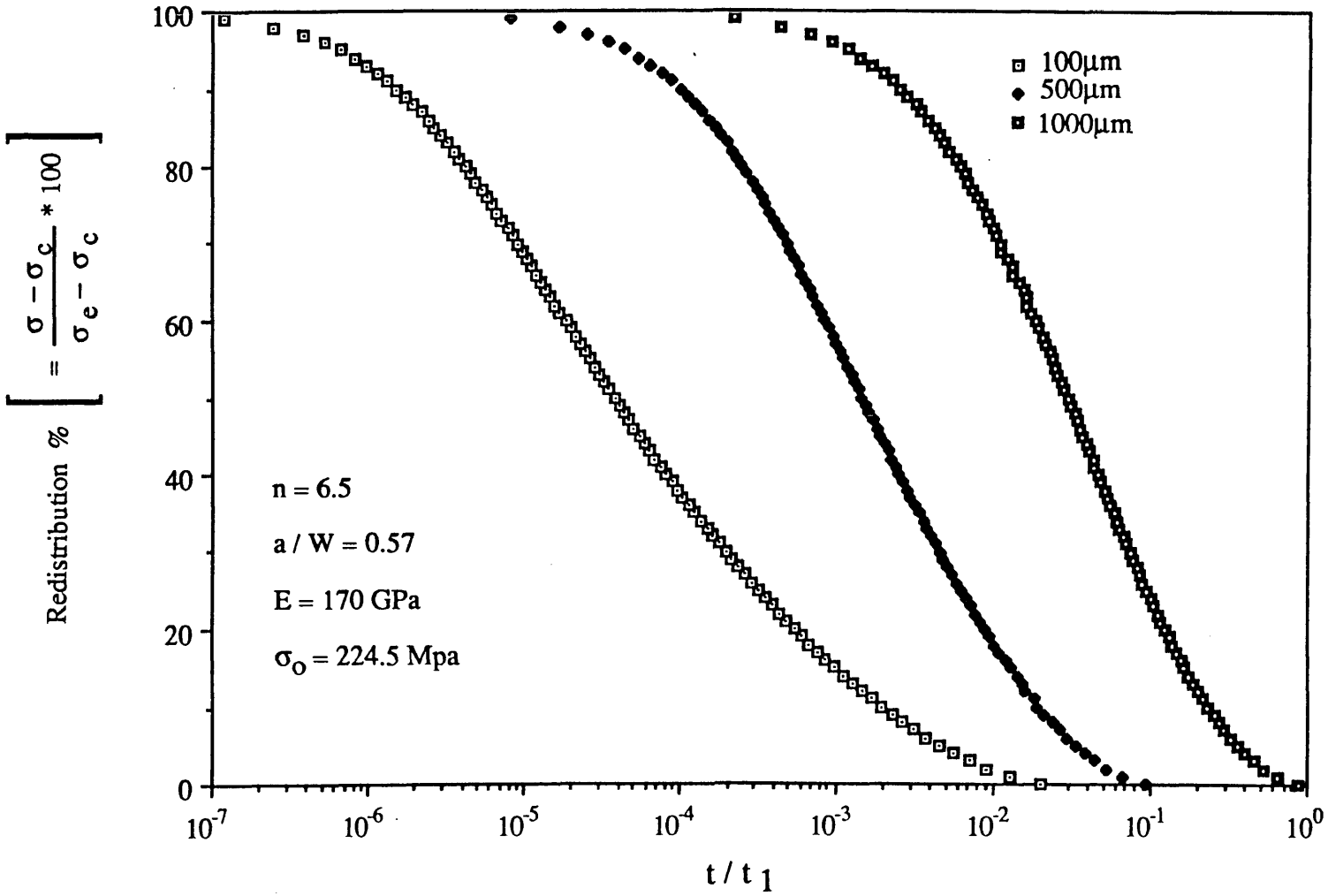


Figure 10.4 Stress redistribution as a function of the non dimensional time t / t_1 , at various distances ahead of the crack tip , for specimen A76 (800H material)

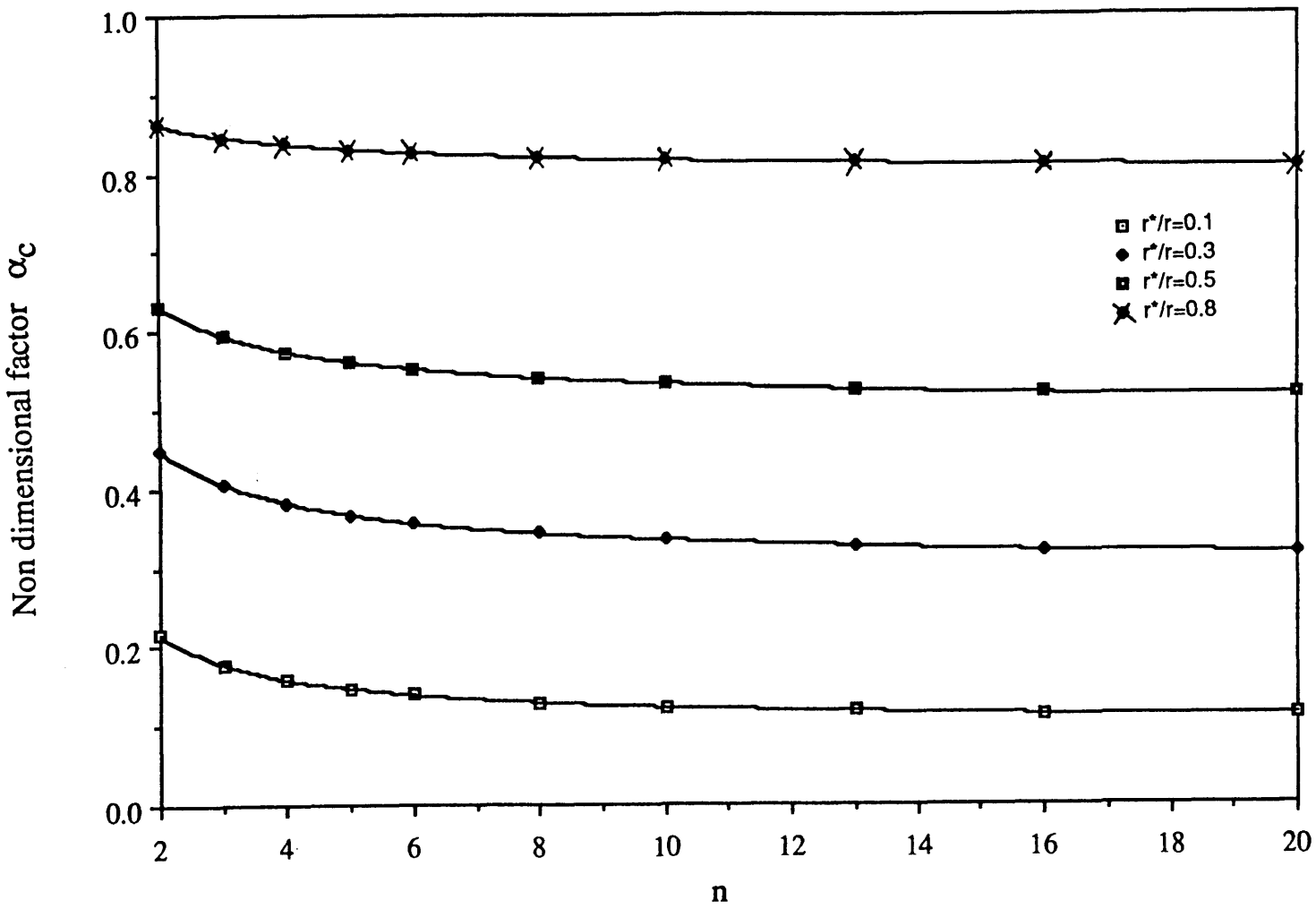


Figure 10.4a Non dimensionless factor α_c as a function of the creep index n for various values of r * / r.

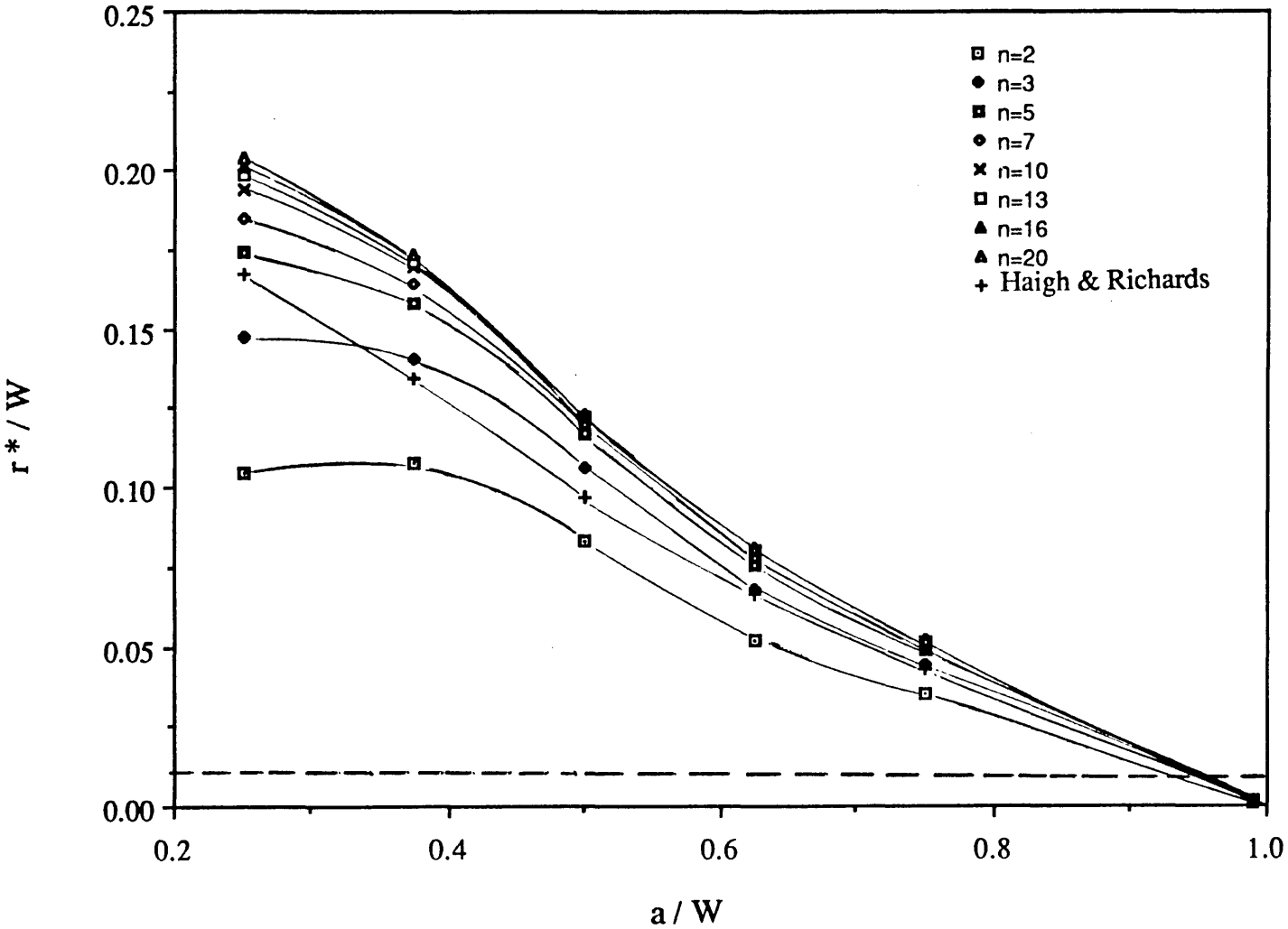


Figure 10.4b r * positions for the compact tension specimen in plane stress.

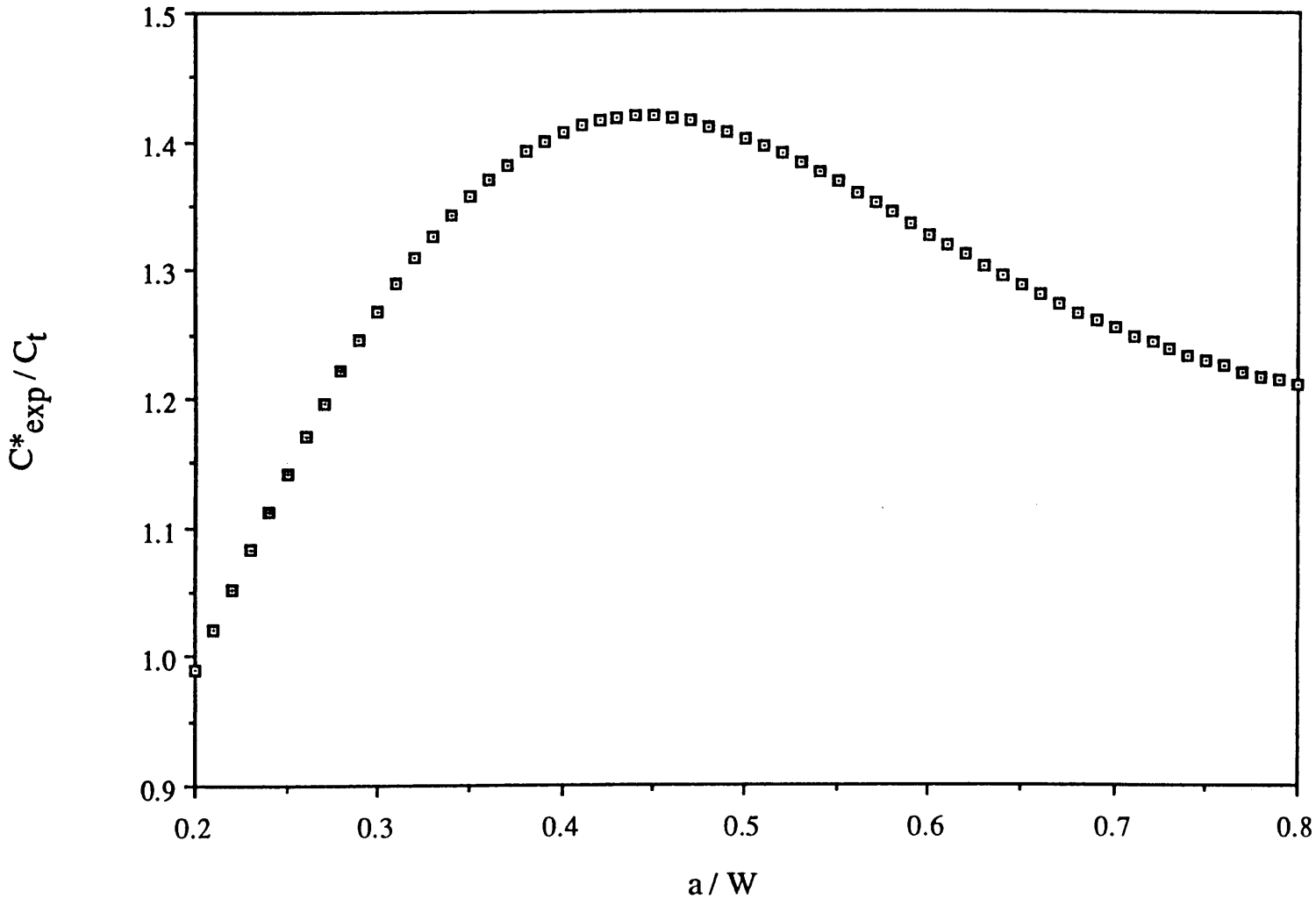


Figure 10.5 Non dimensionless ratio C^*_{exp} / C_t as a function of the non dimensionless crack length a / W.

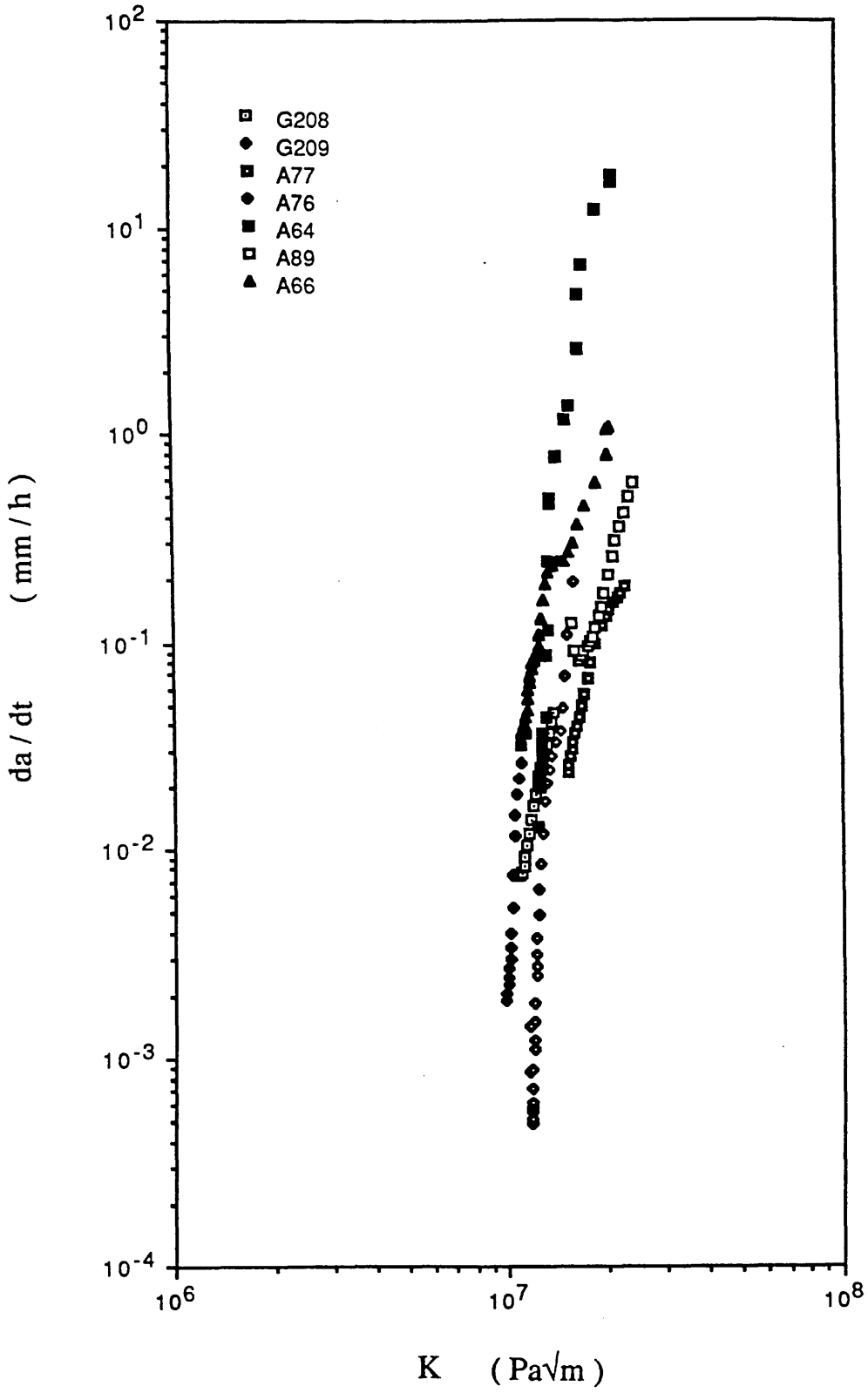


Figure 10.6 Dependence of crack growth rate da / dt on the stress intensity factor K for 800H at 800° C.

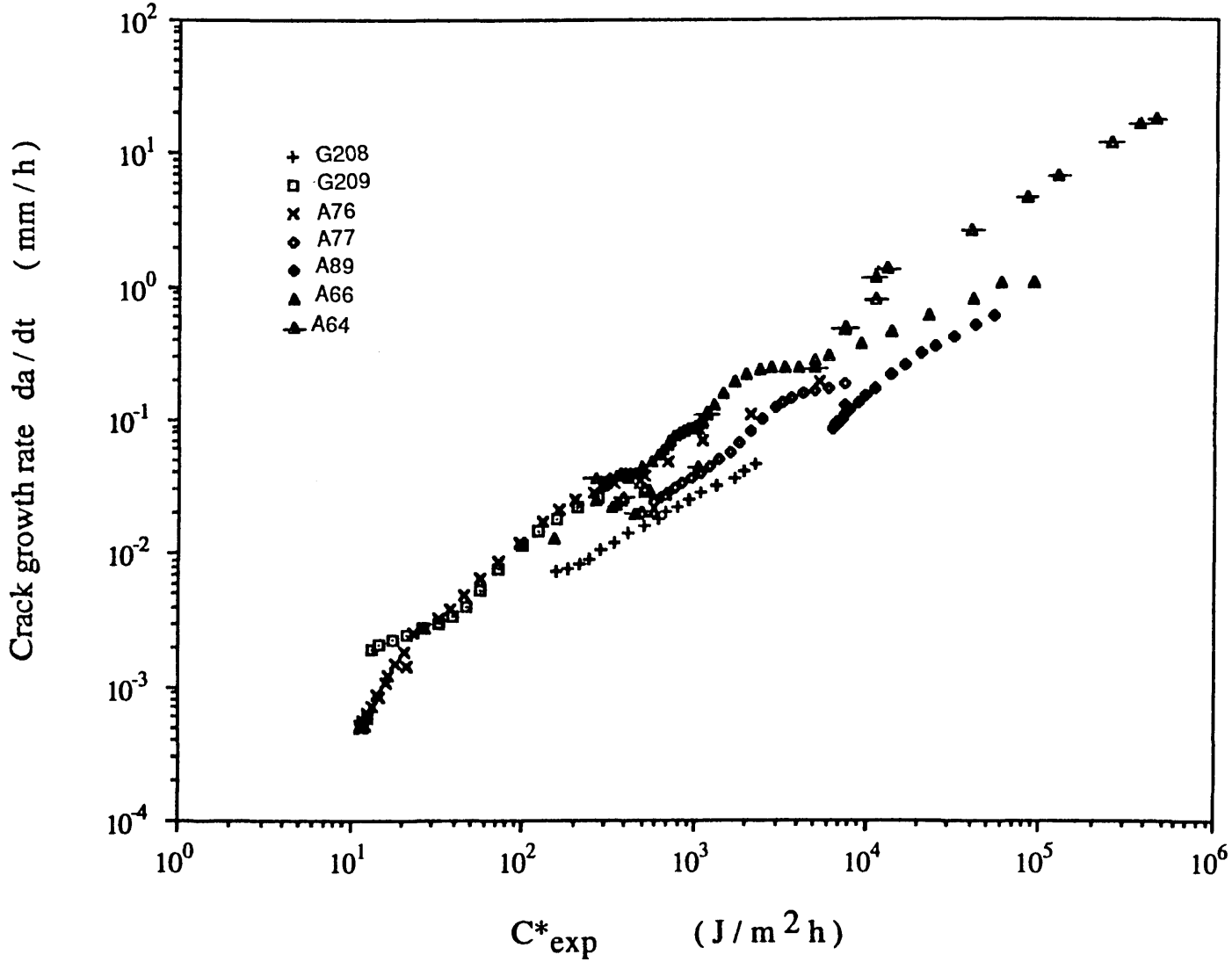


Figure 10.7 Sensitivity of crack growth rate to C^*_{exp} for 800H superalloy at 800° C.

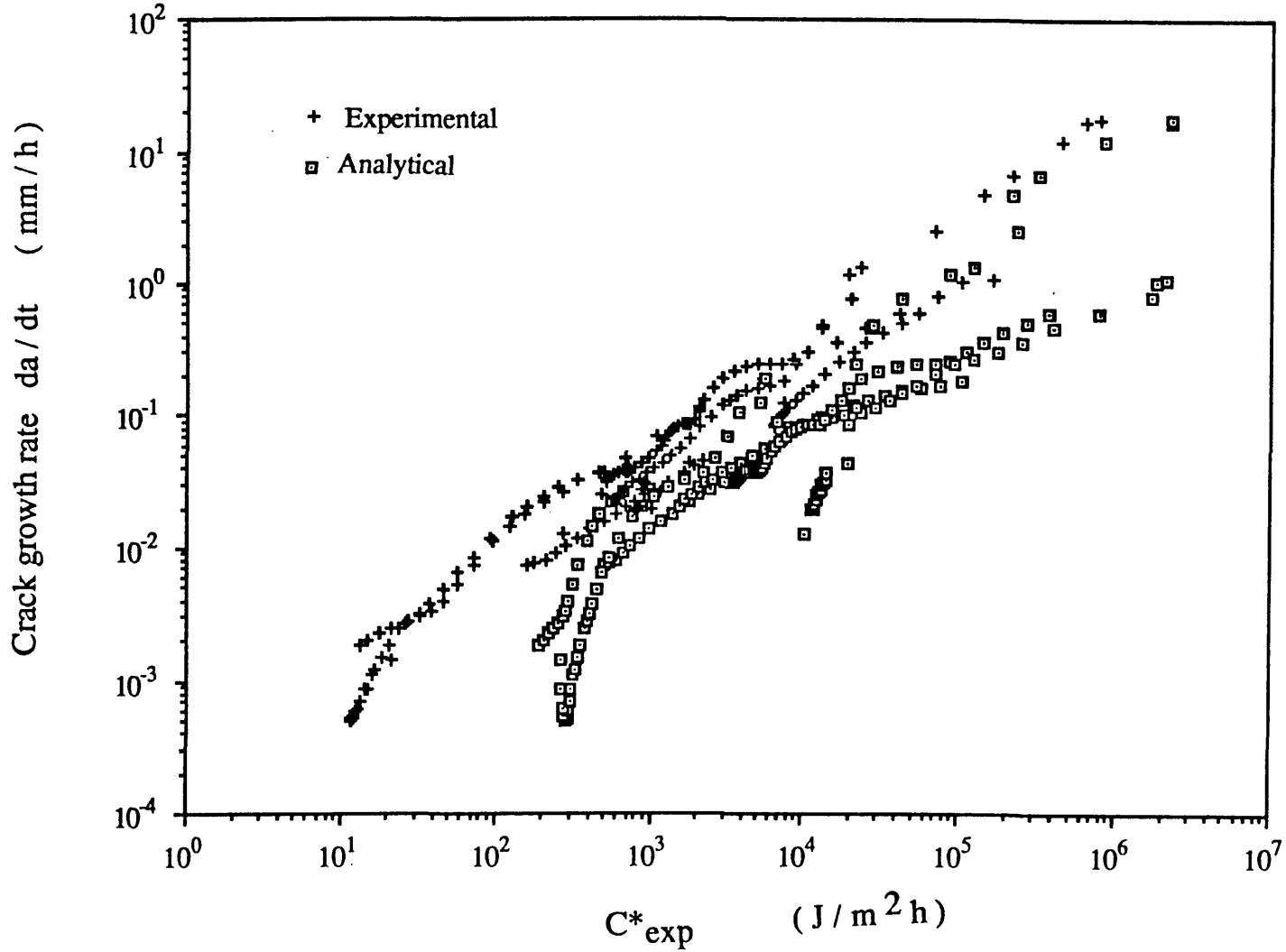


Figure 10.8 Sensitivity of crack growth rate to C^*_{exp} and C* analytical (plane stress), for 800H superalloy at 800° C.

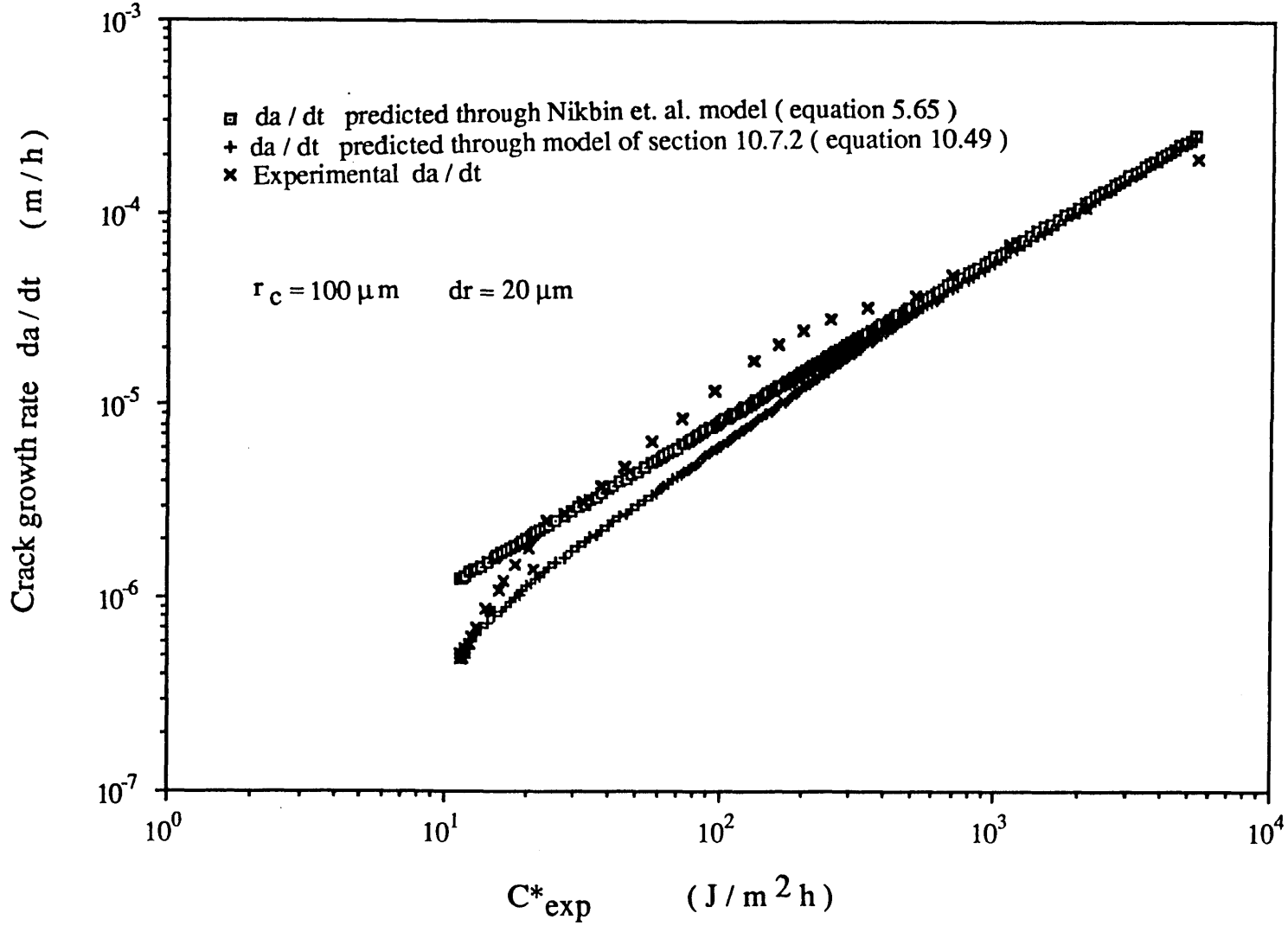


Figure 10.9 Sensitivity of crack growth rate to C^*_{exp} for specimen A76 (800H material) at 800° C.

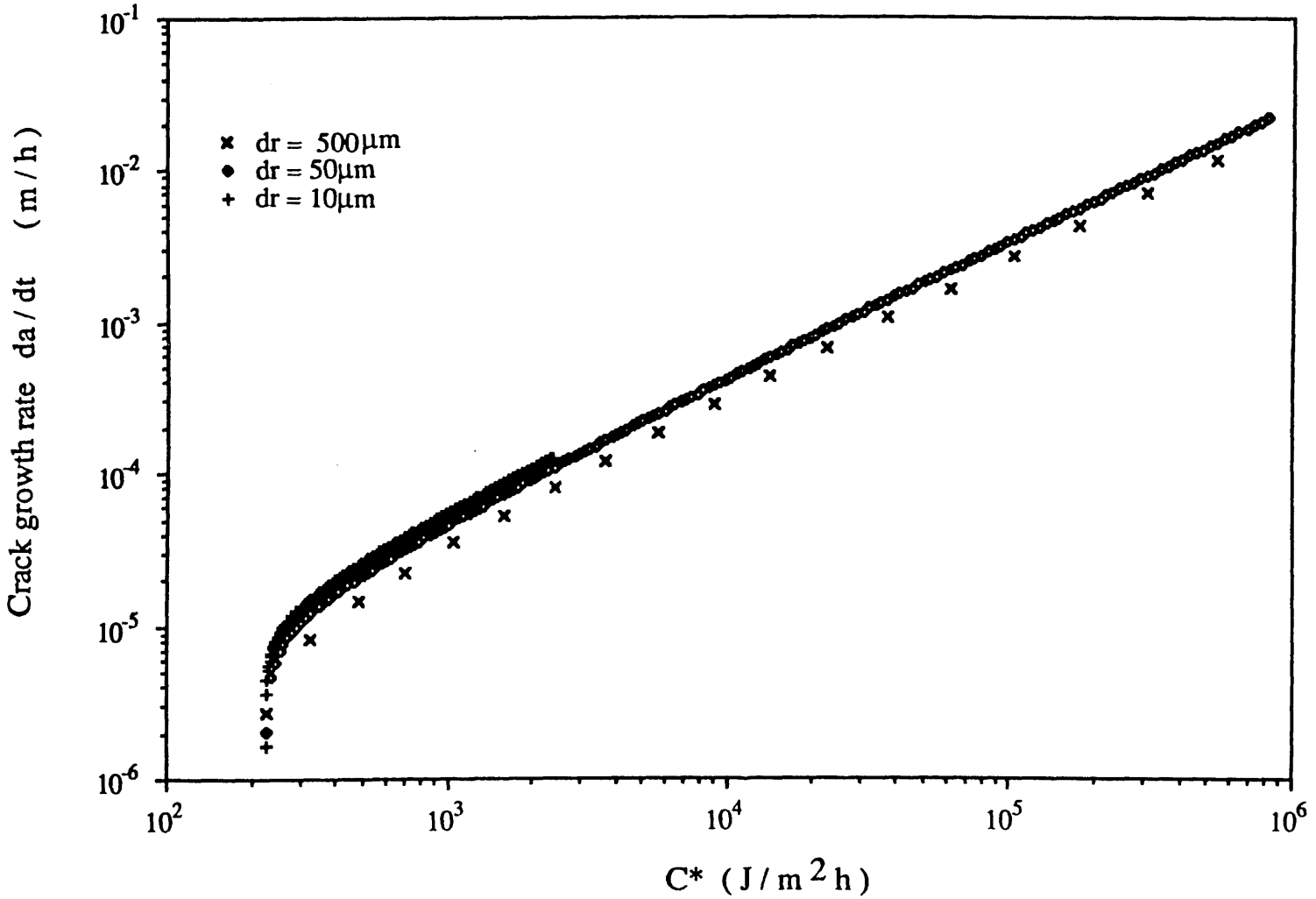


Figure 10.10 Sensitivity of crack growth rate to the analytical form of C* , with da / dt predicted through model of section 10.7.2 (equation 10.49). Effect of increasing dr

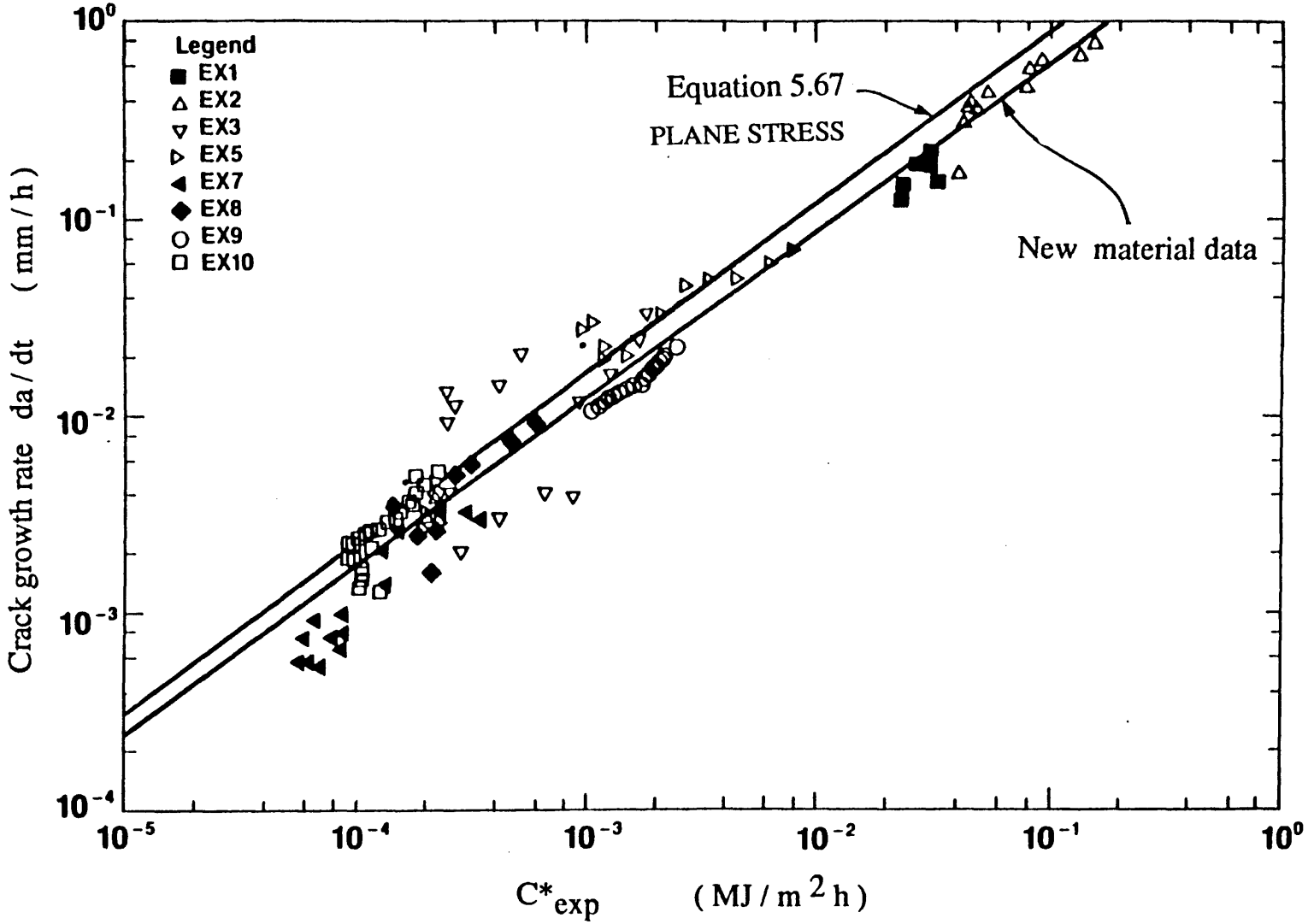


Figure 10.11 Creep crack growth rate as a function of the C^*_{exp} parameter for type 304H stainless steel new material , at 760° C.

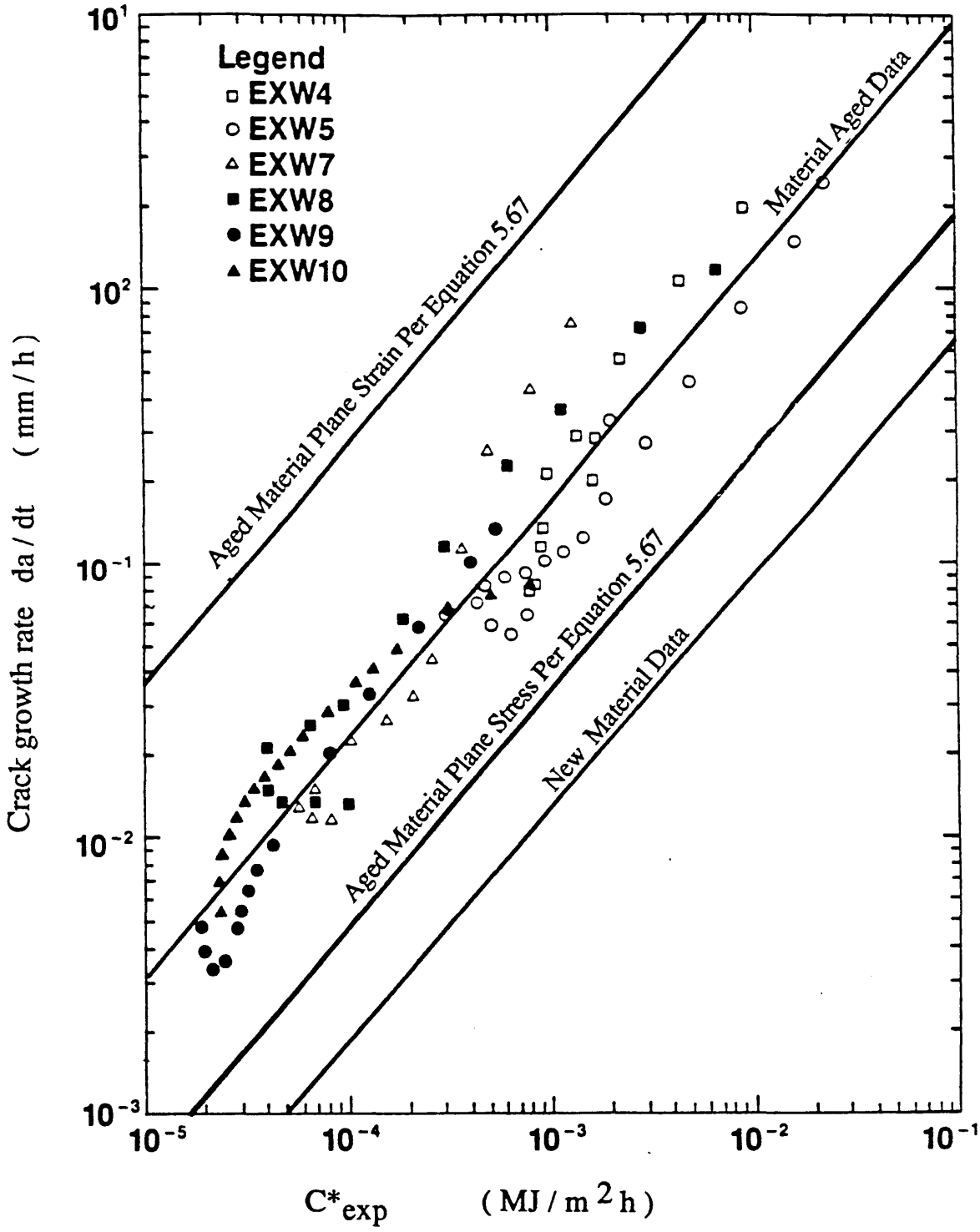


Figure 10.12 Creep crack growth rate as a function of the C^*_{exp} parameter for type 304H stainless steel aged material , at 760° C.

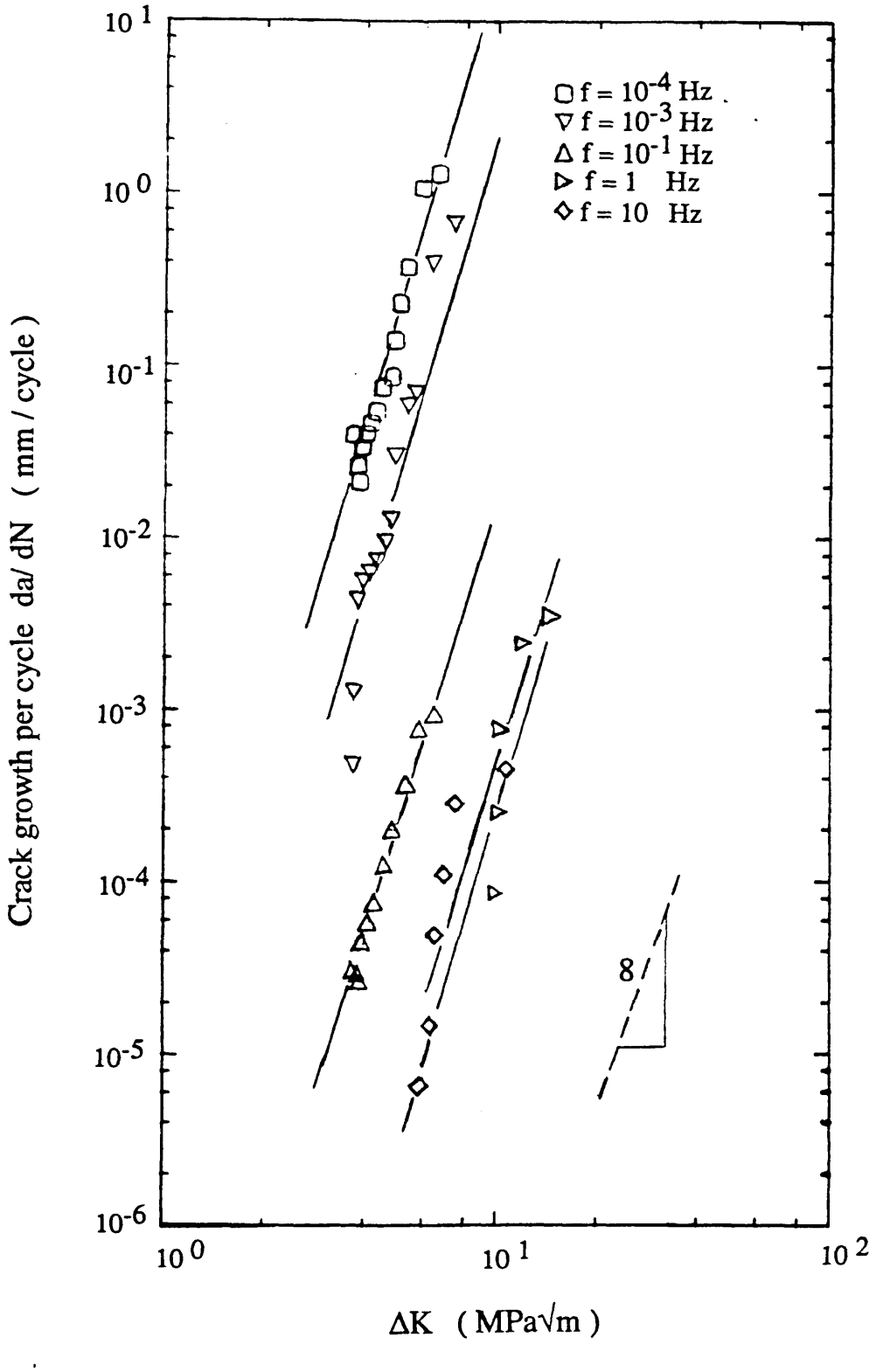


Figure 10.13 Dependence of crack growth/cycle on ΔK for 1/2CMV at 565° C, R = 0.8 and various frequencies.

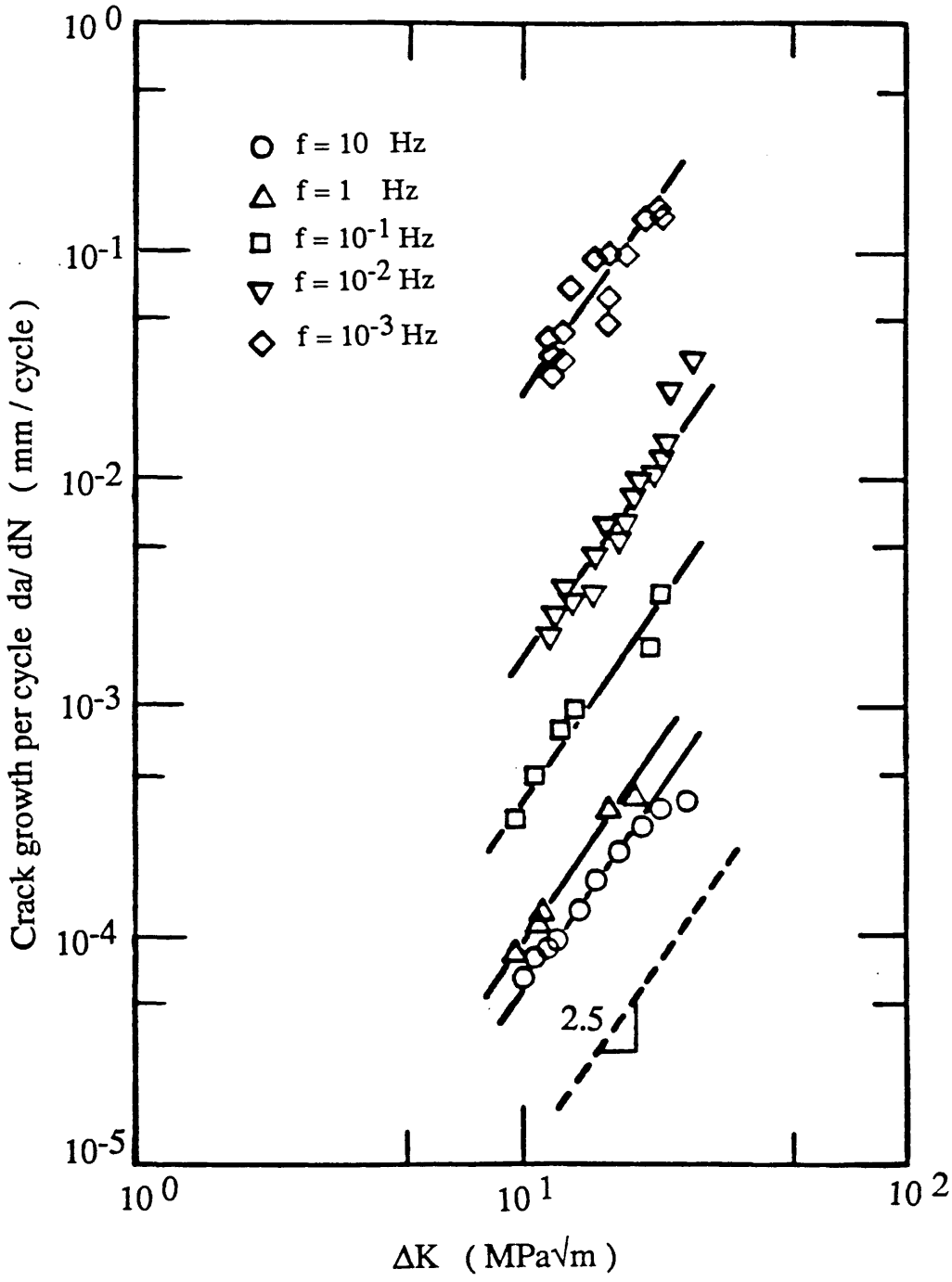


Figure 10.14 Dependence of crack growth/cycle on ΔK for AP1 at 700° C, R = 0.7 and various frequencies.

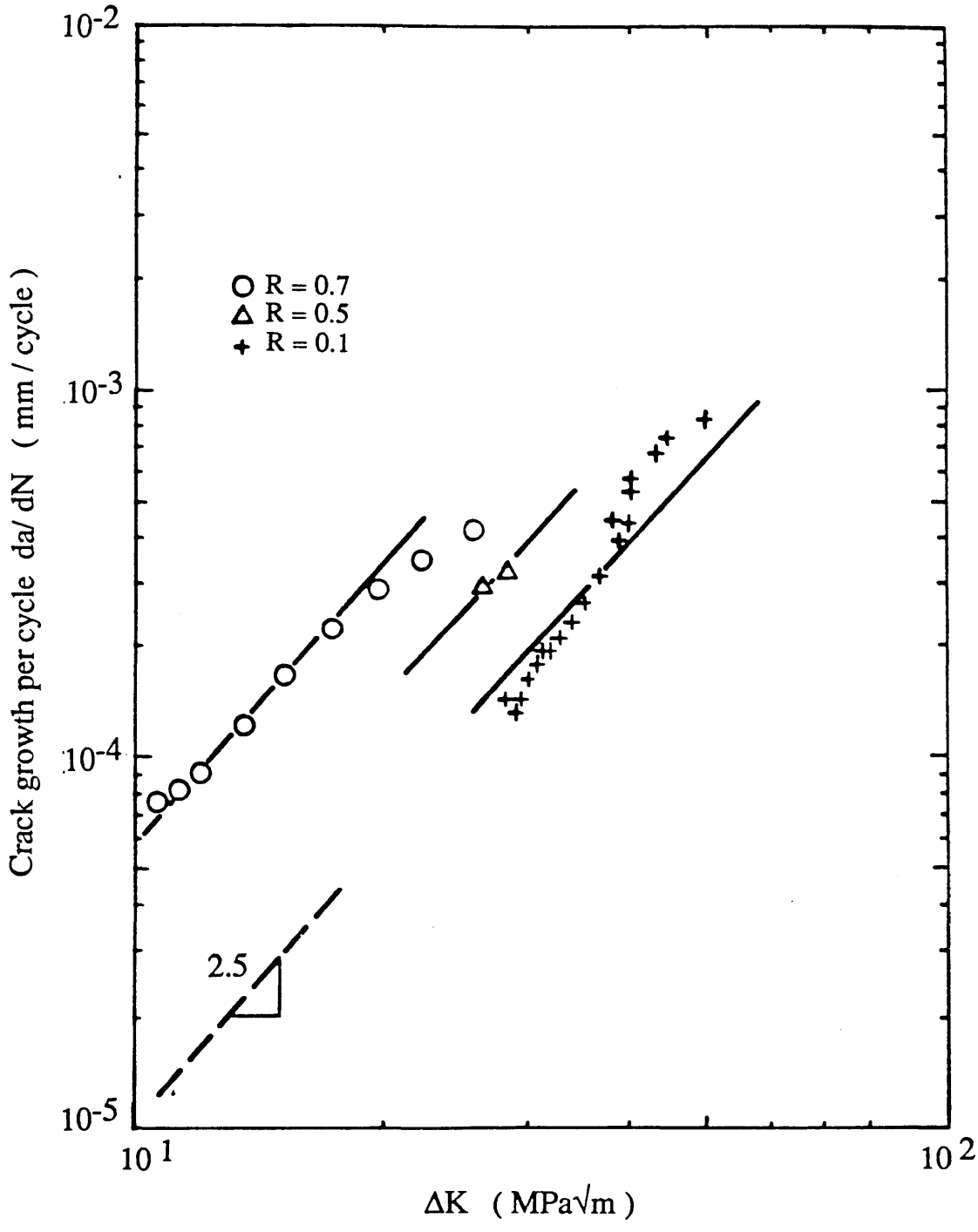


Figure 10.15 Influence of R on crack growth/cycle for AP1 at 700° C for f = 10 Hz

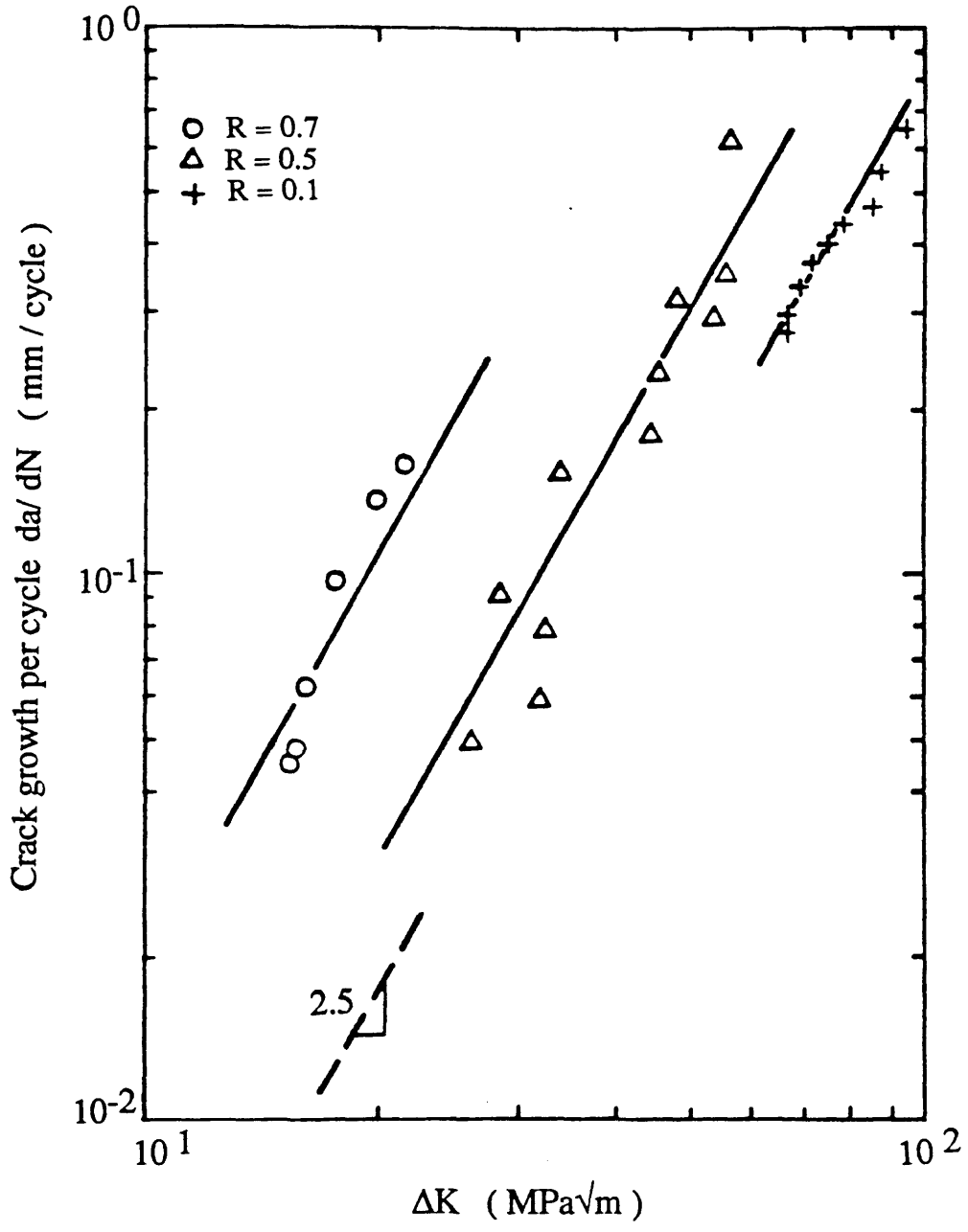


Figure 10.16 Influence of R on crack growth/cycle for AP1 at 700° C for f = 10^{-3} Hz

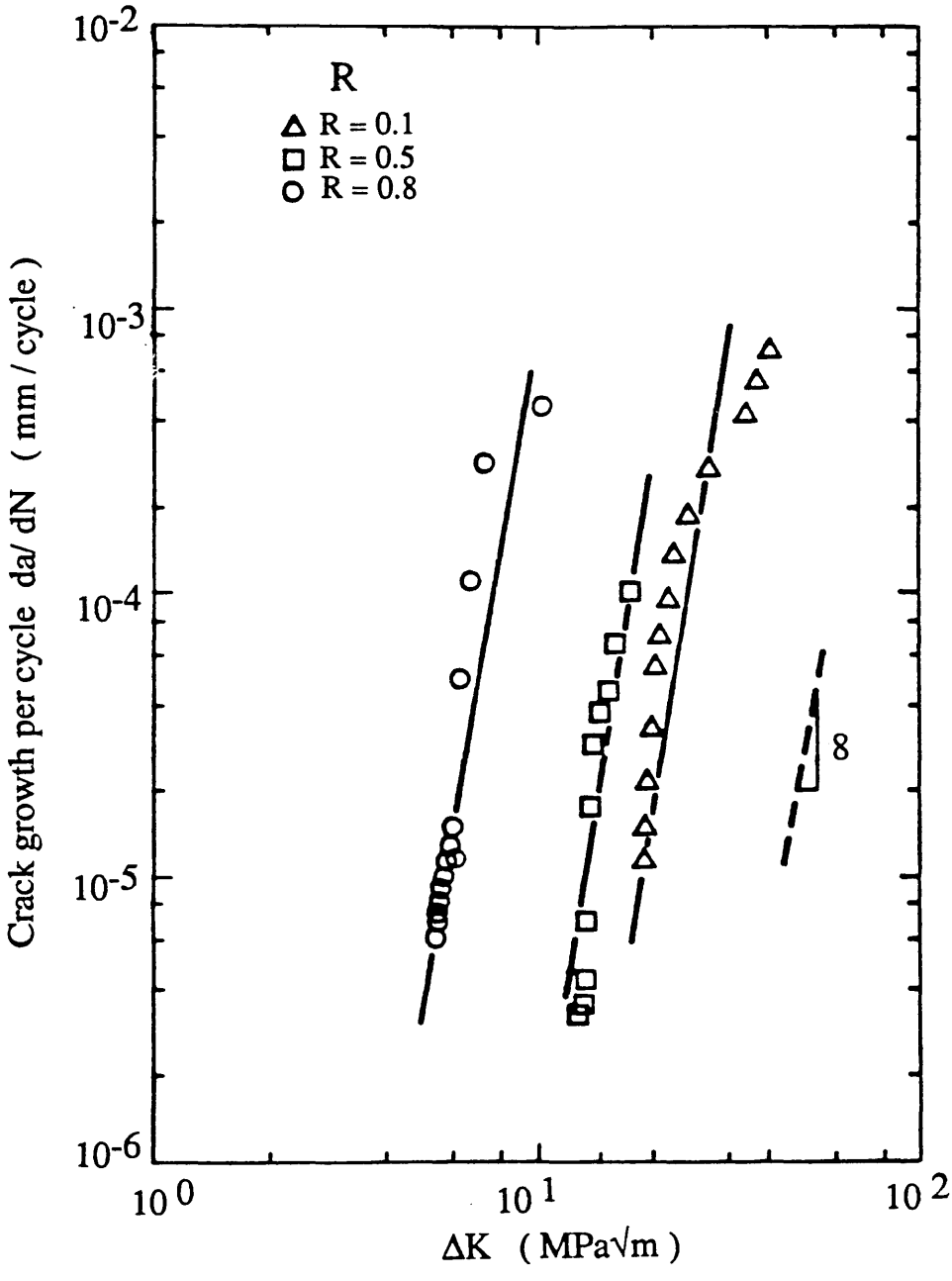


Figure 10.17 Influence of R on crack growth/cycle for 1/2CMV at 565° C for f = 10 Hz

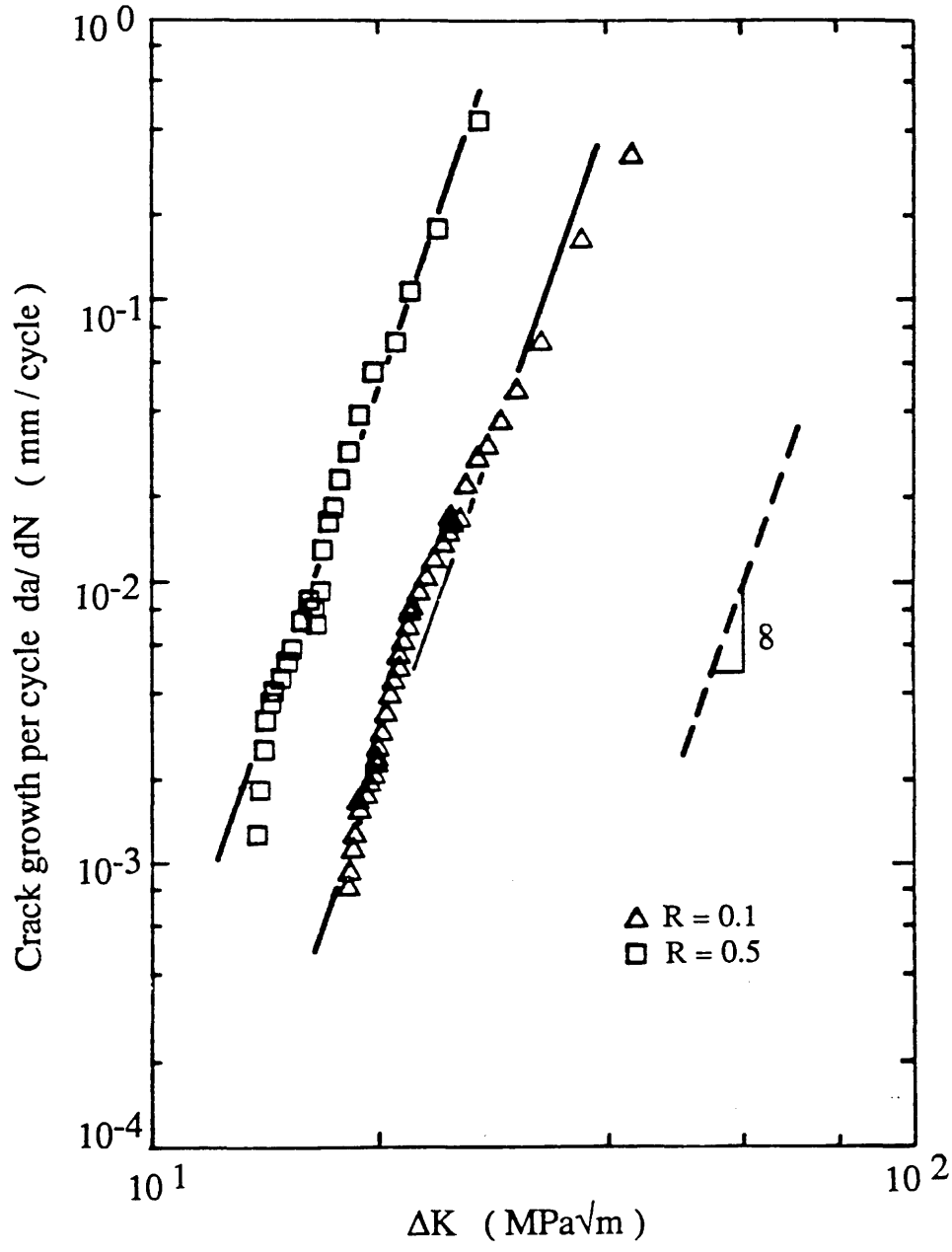


Figure 10.18 Influence of R on crack growth/cycle for 1/2CMV at 565° C for $f = 10^{-2}$ Hz.

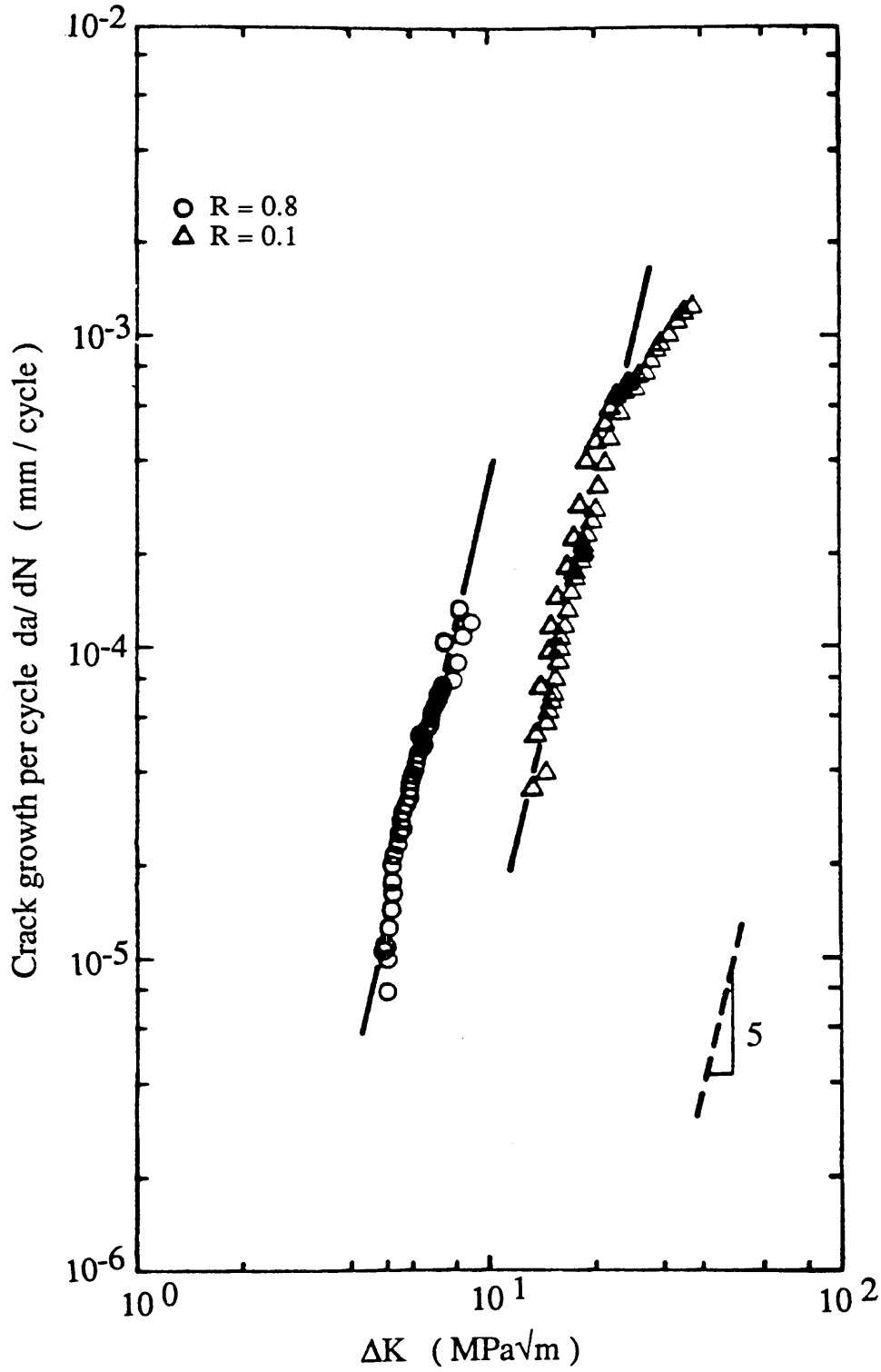


Figure 10.19 Influence of R on crack growth/cycle for 21/4CM at 538° C for f = 10 Hz

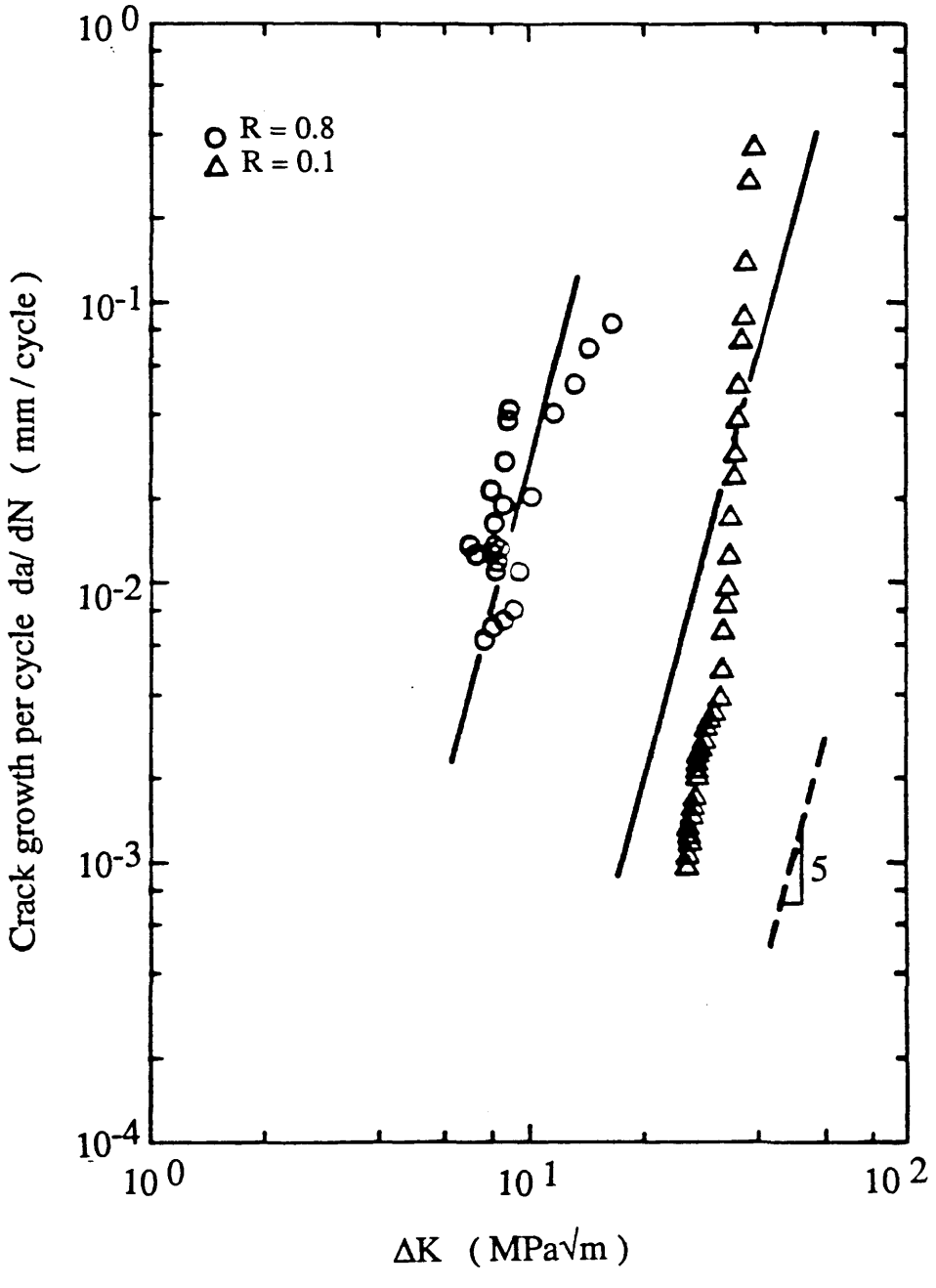


Figure 10.20 Influence of R on crack growth/cycle for 21/4CM at 538° C for $f = 10^{-3}$ Hz

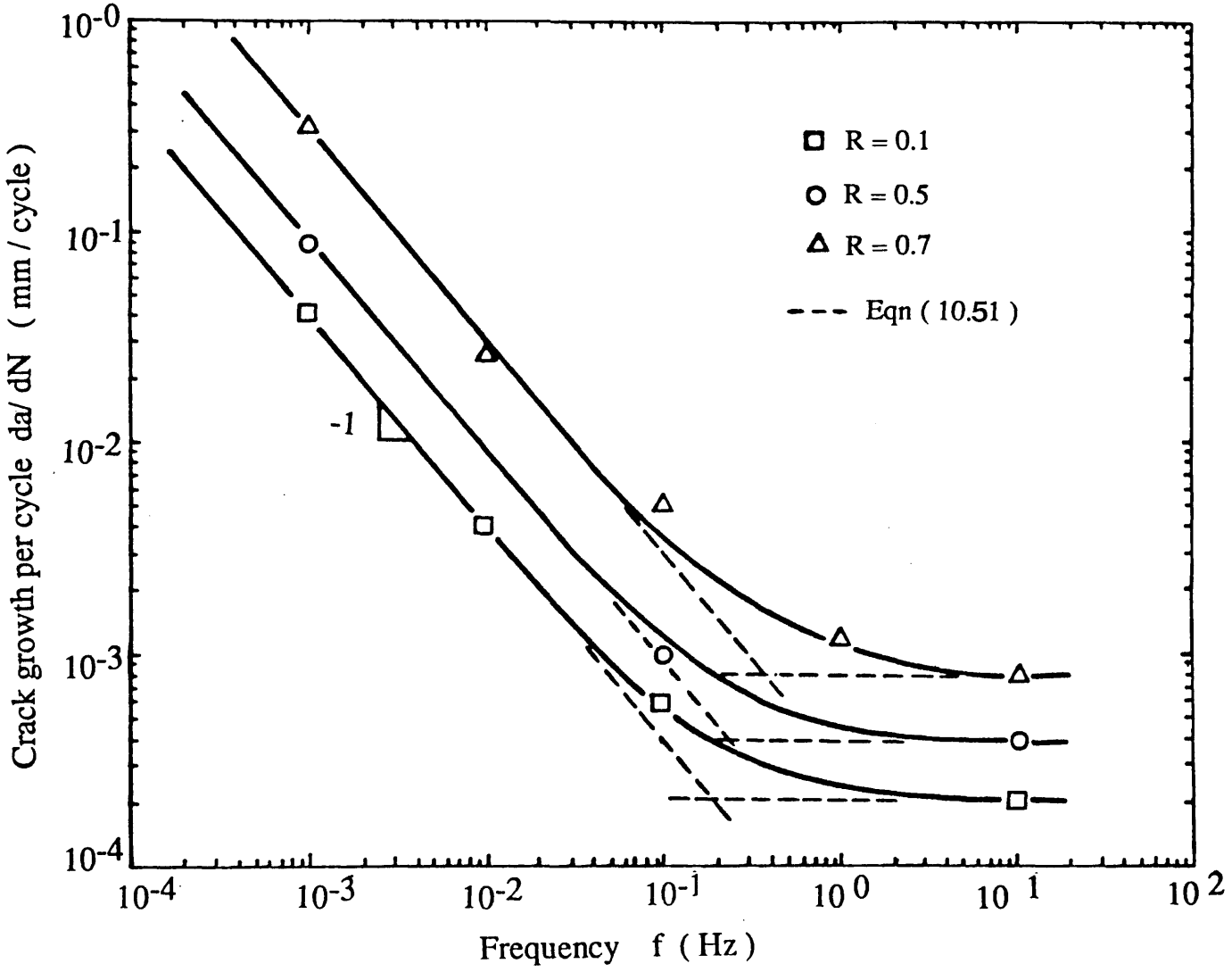


Figure 10.21 Dependence of crack growth/cycle for AP1 at 700° C on frequency and R at a constant ΔK of 30 MPa√m.

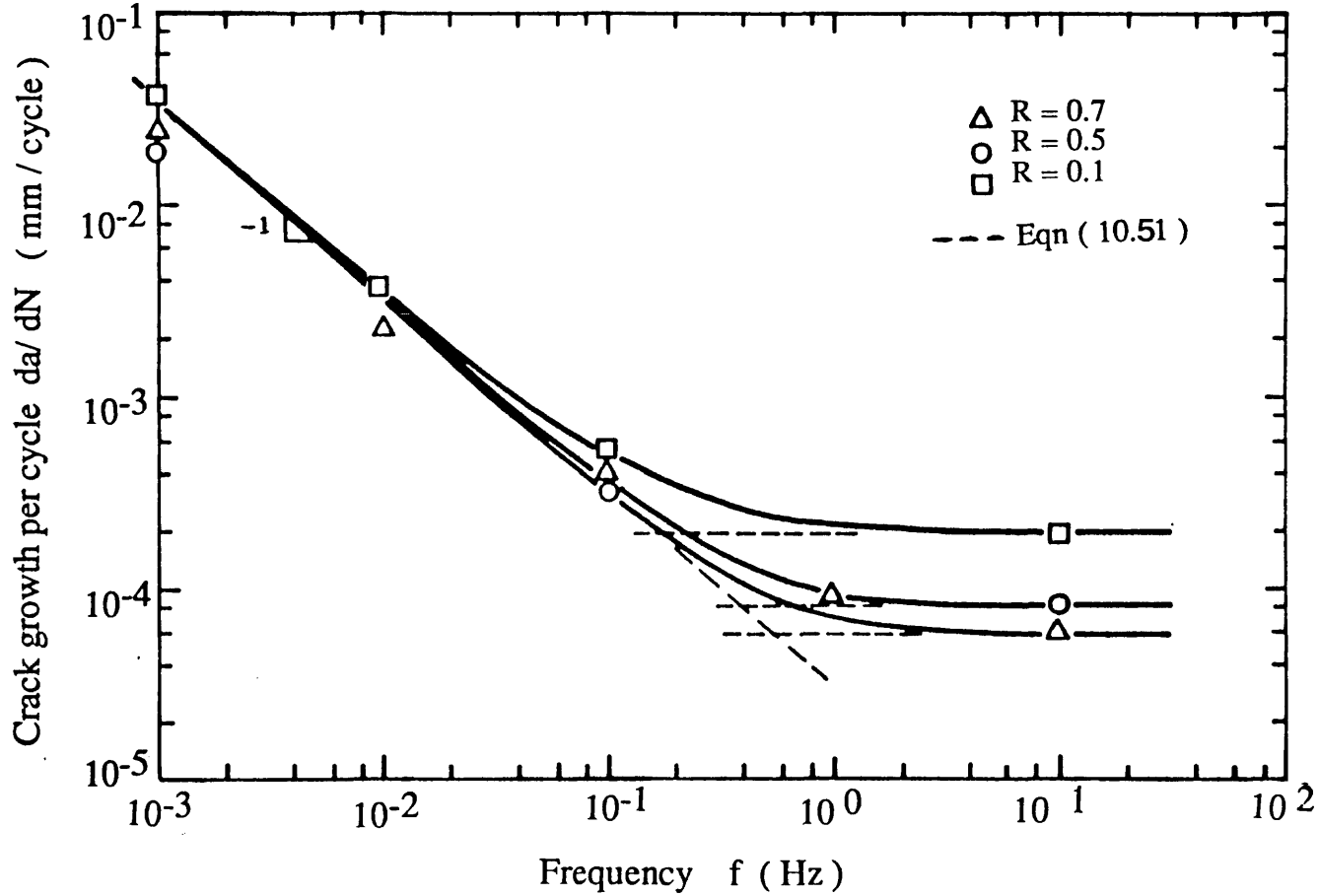


Figure 10.22 Dependence of crack growth/cycle for AP1 at 700° C on frequency and R at a constant K_{max} of 33.3 MPa$\sqrt{m}$.

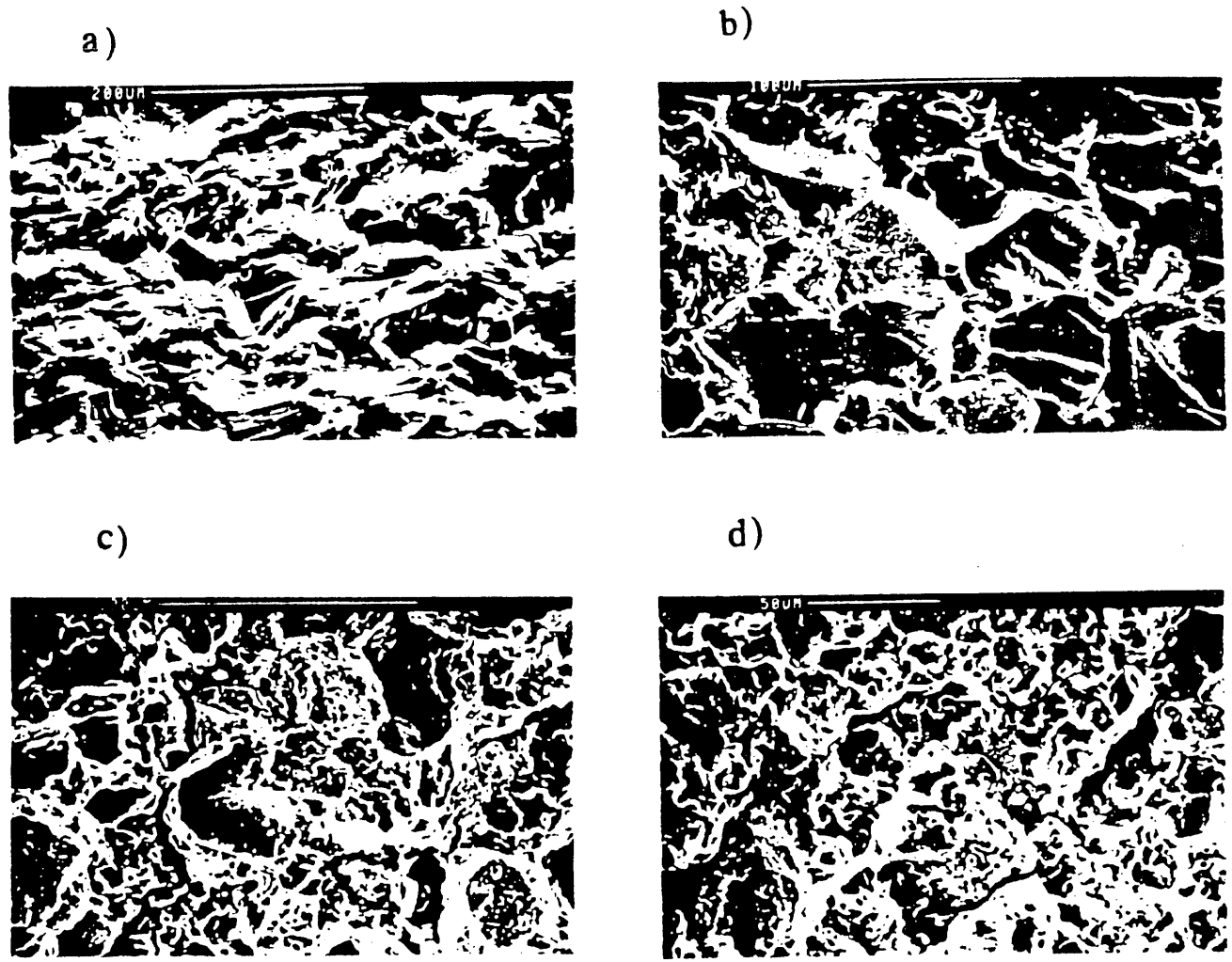


Figure 10.23 Fracture surfaces for AP1 at R = 0.7 for a) 10Hz , b) 1Hz , c) 0.1Hz and d) 0.001Hz.

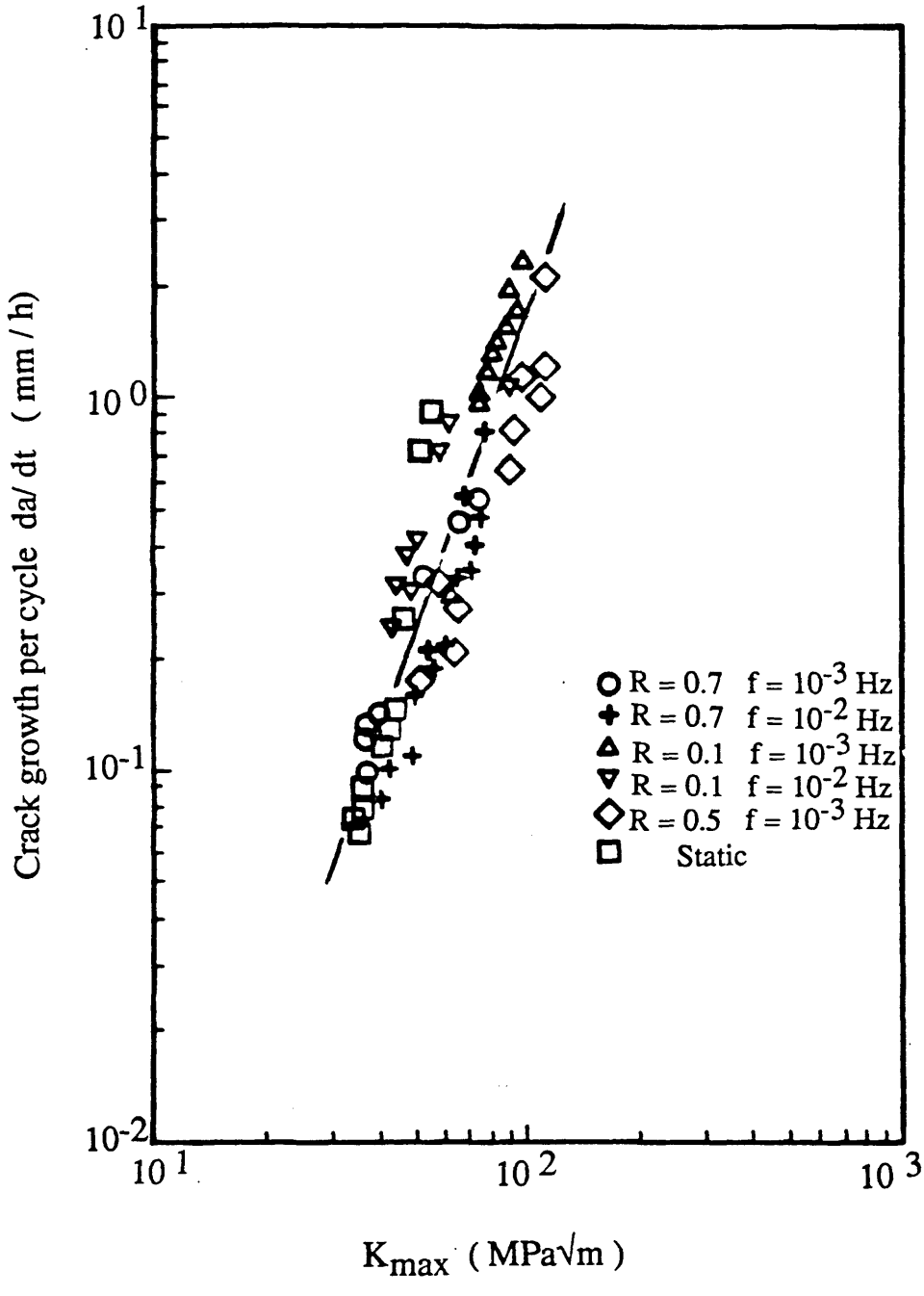


Figure 10.24 Dependence of crack growth rate for AP1 at 700° C on K_{max} at low frequencies.

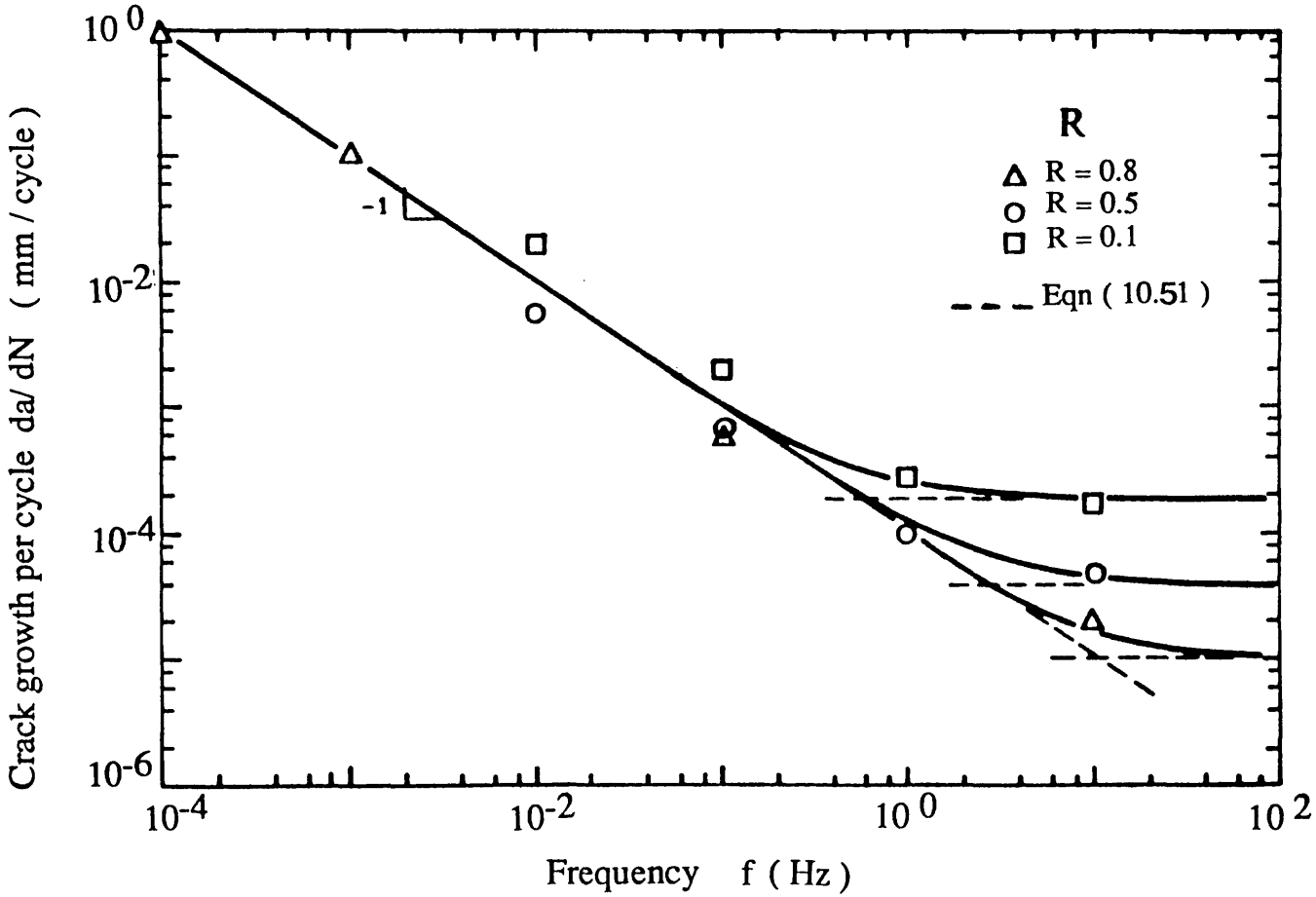


Figure 10.25 Dependence of crack growth/cycle for 1/2CMV at 565° C on frequency and R at a constant K_{max} of 30 MPa√m.

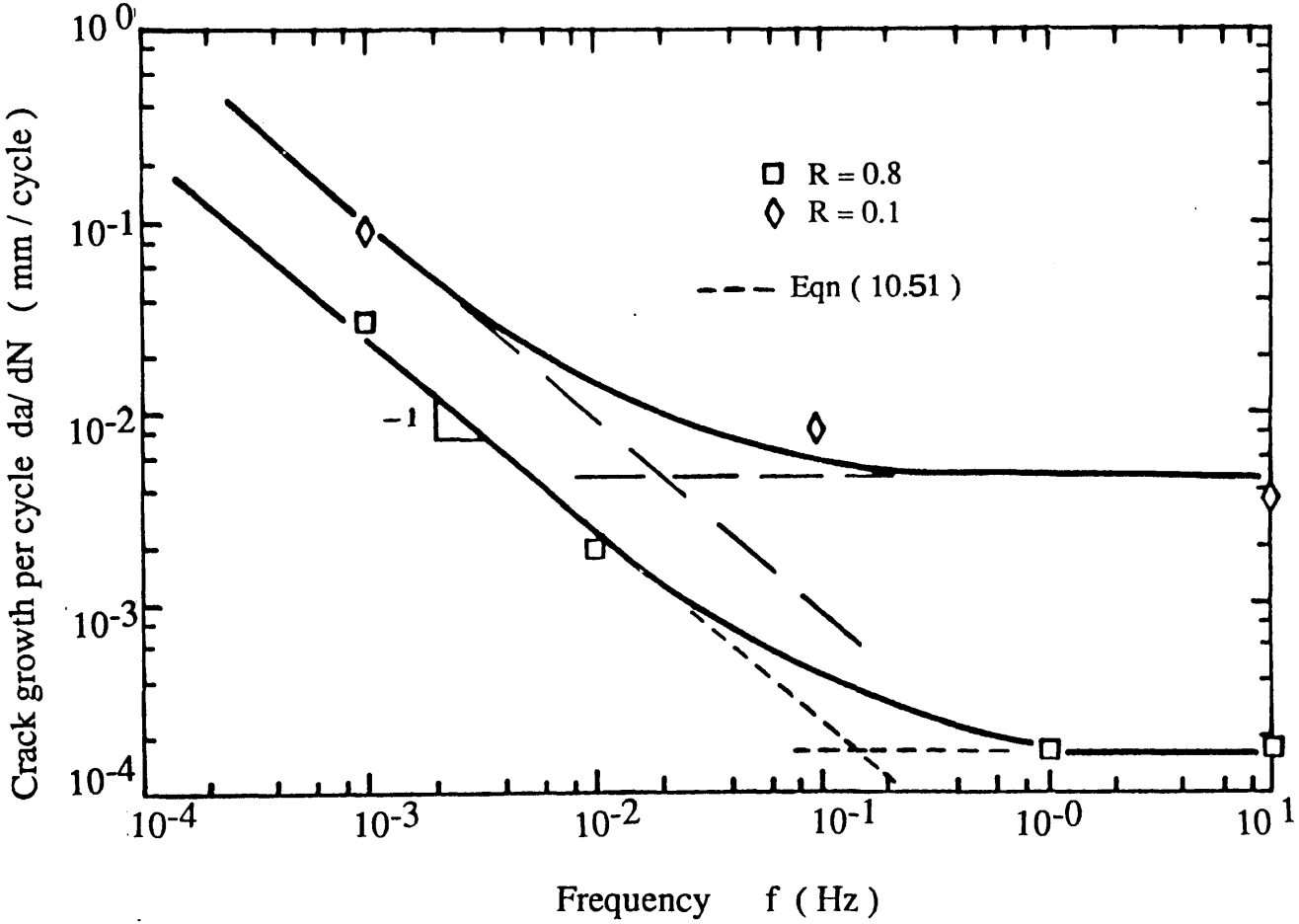


Figure 10.26 Dependence of crack growth/cycle for 21/4CM at 538° C on frequency and R at a constant K_{max} of 50 MPa$\sqrt{m}$.

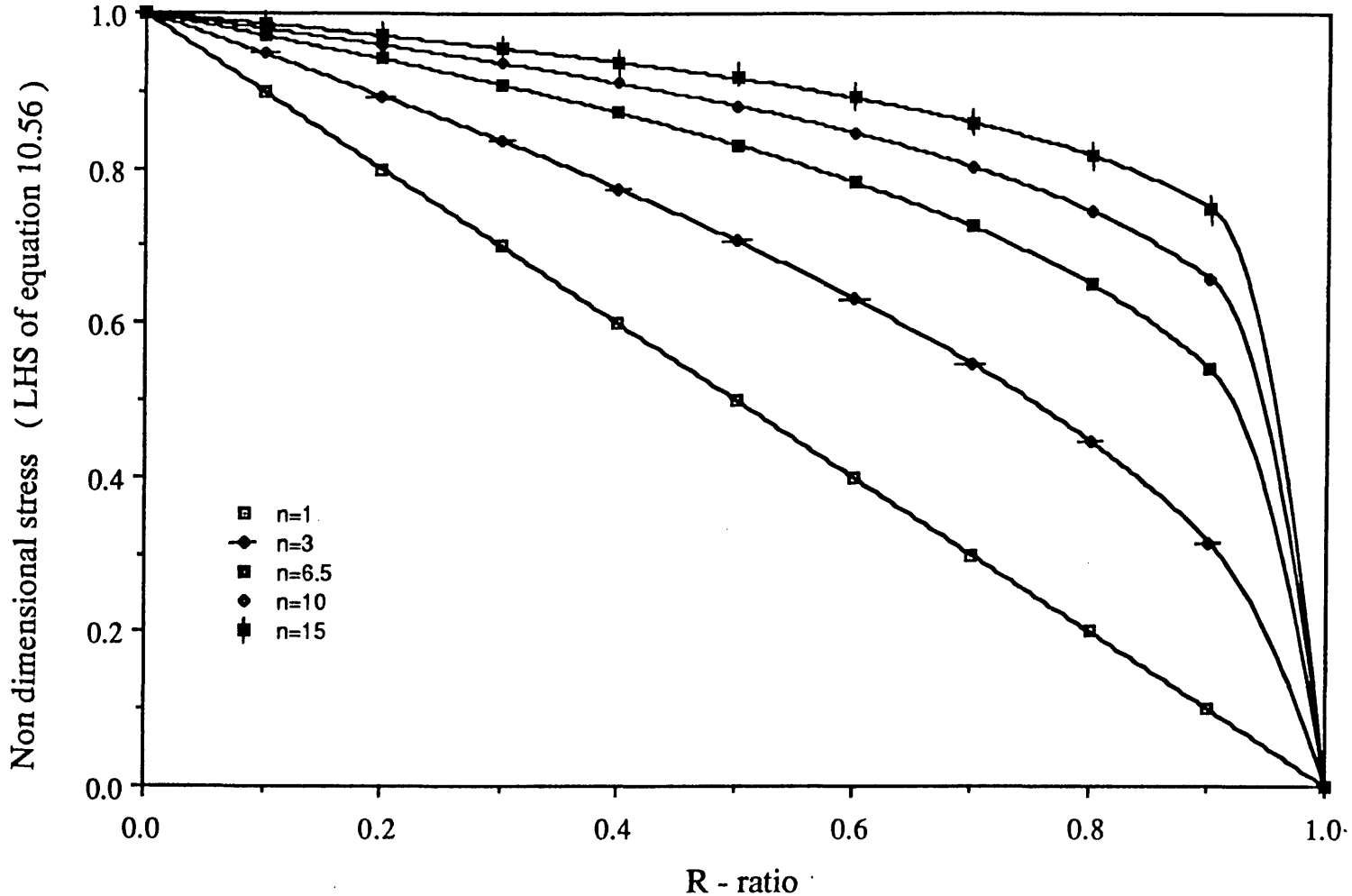


Figure 10.27 R - ratio effect on the superimposed elastic field after the load step in a square wave cyclic test , for various values of n.

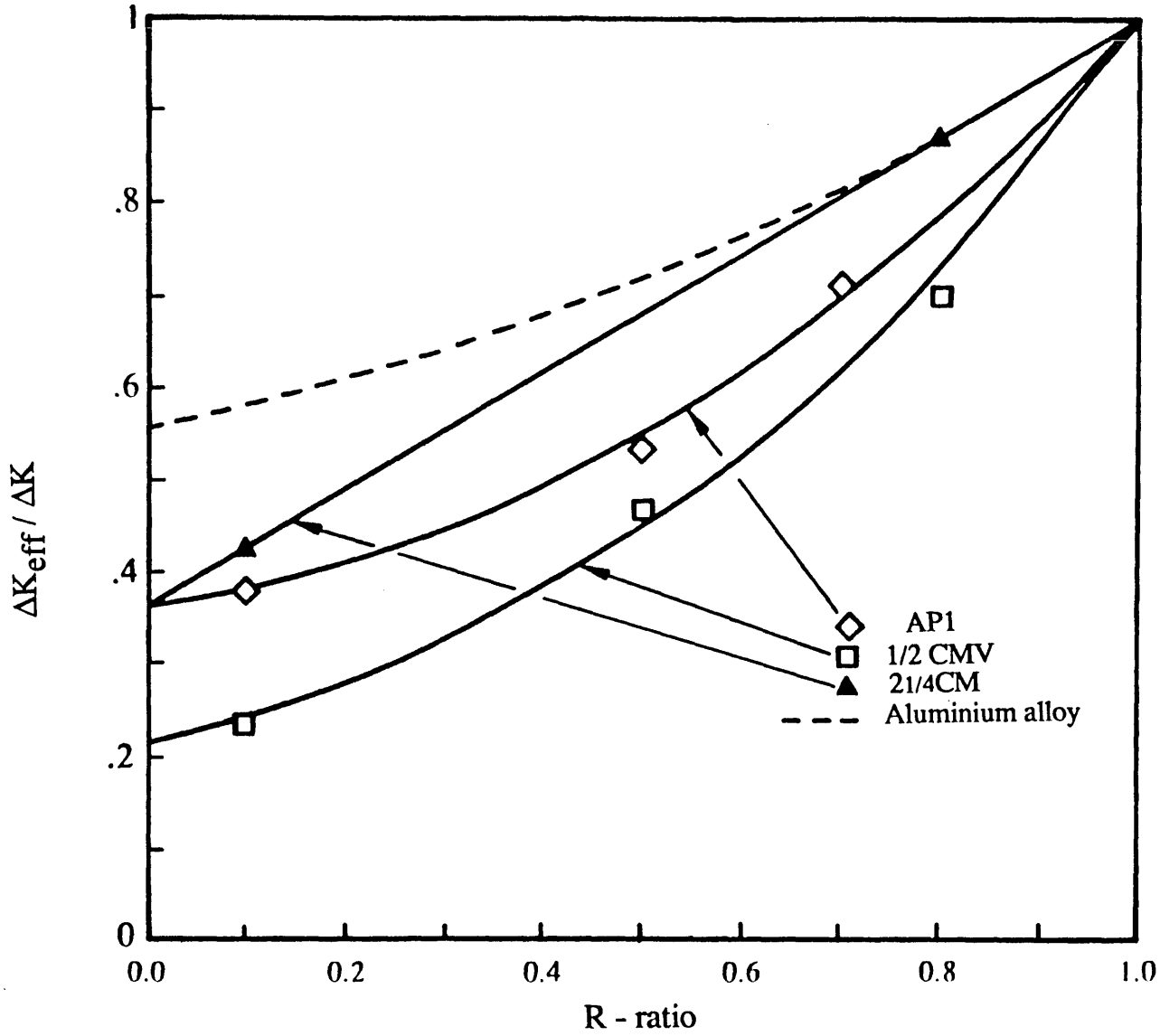


Figure 10.28 Relationship of $\Delta K_{eff} / \Delta K$ to R for AP1, 1/2CMV steel , 21/4CM steel and an aluminium alloy (Schijve (1979)).

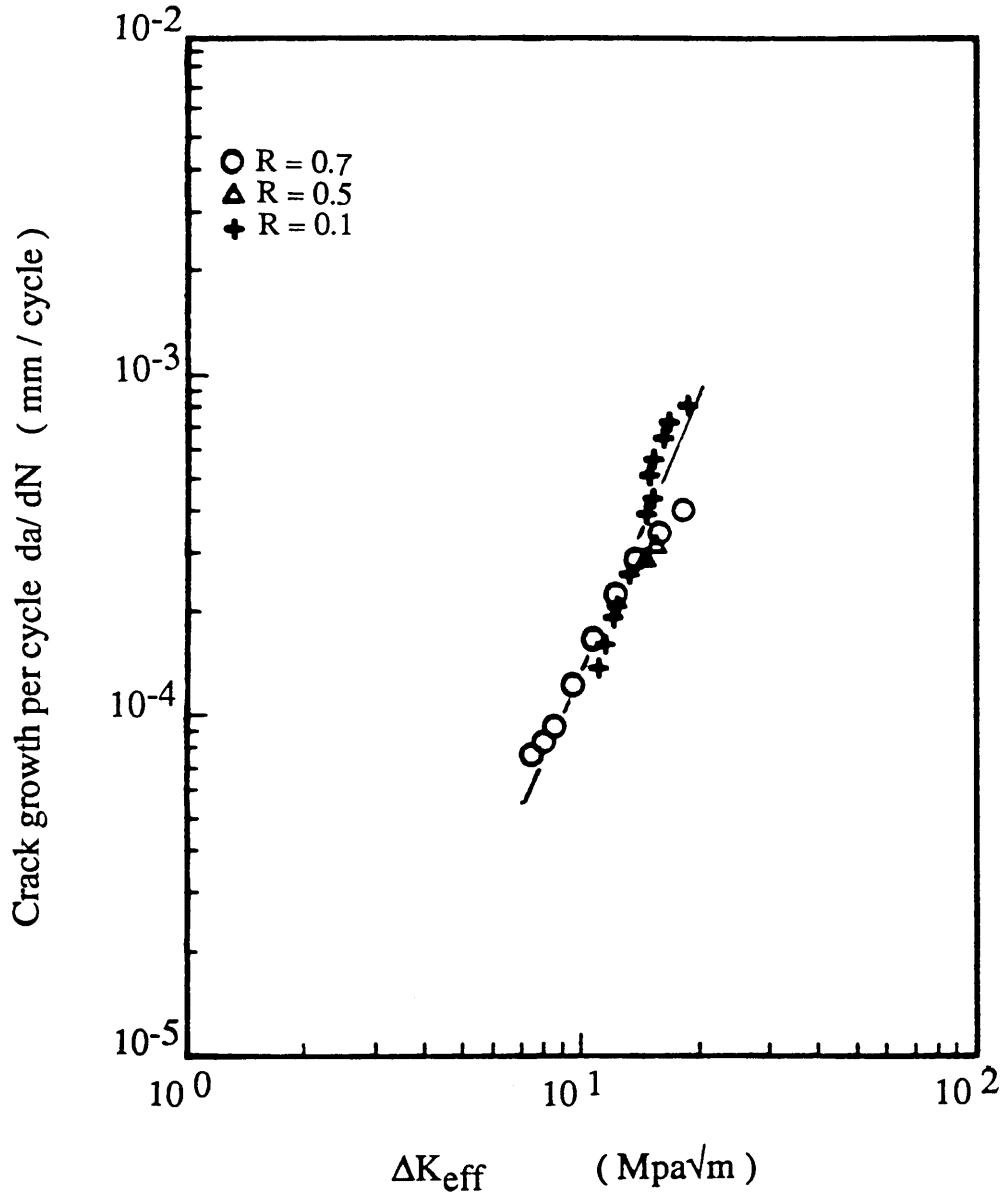


Figure 10.29 Dependence of crack growth/cycle on ΔK_{eff} for AP1 at 700° C and 10Hz

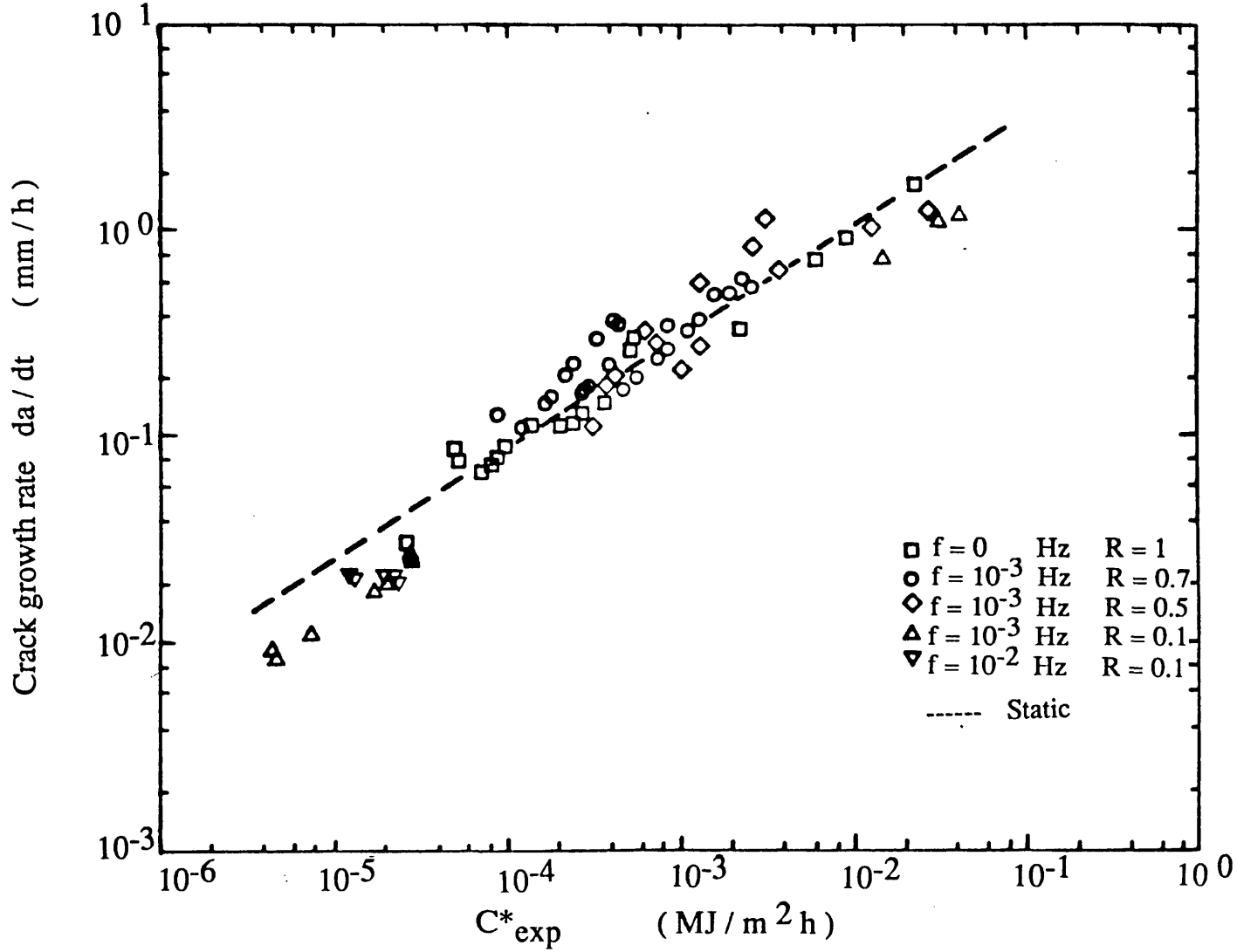


Figure 10.30 Sensitivity of crack growth rate at low frequencies to C^*_{exp} for AP1 at 700° C.

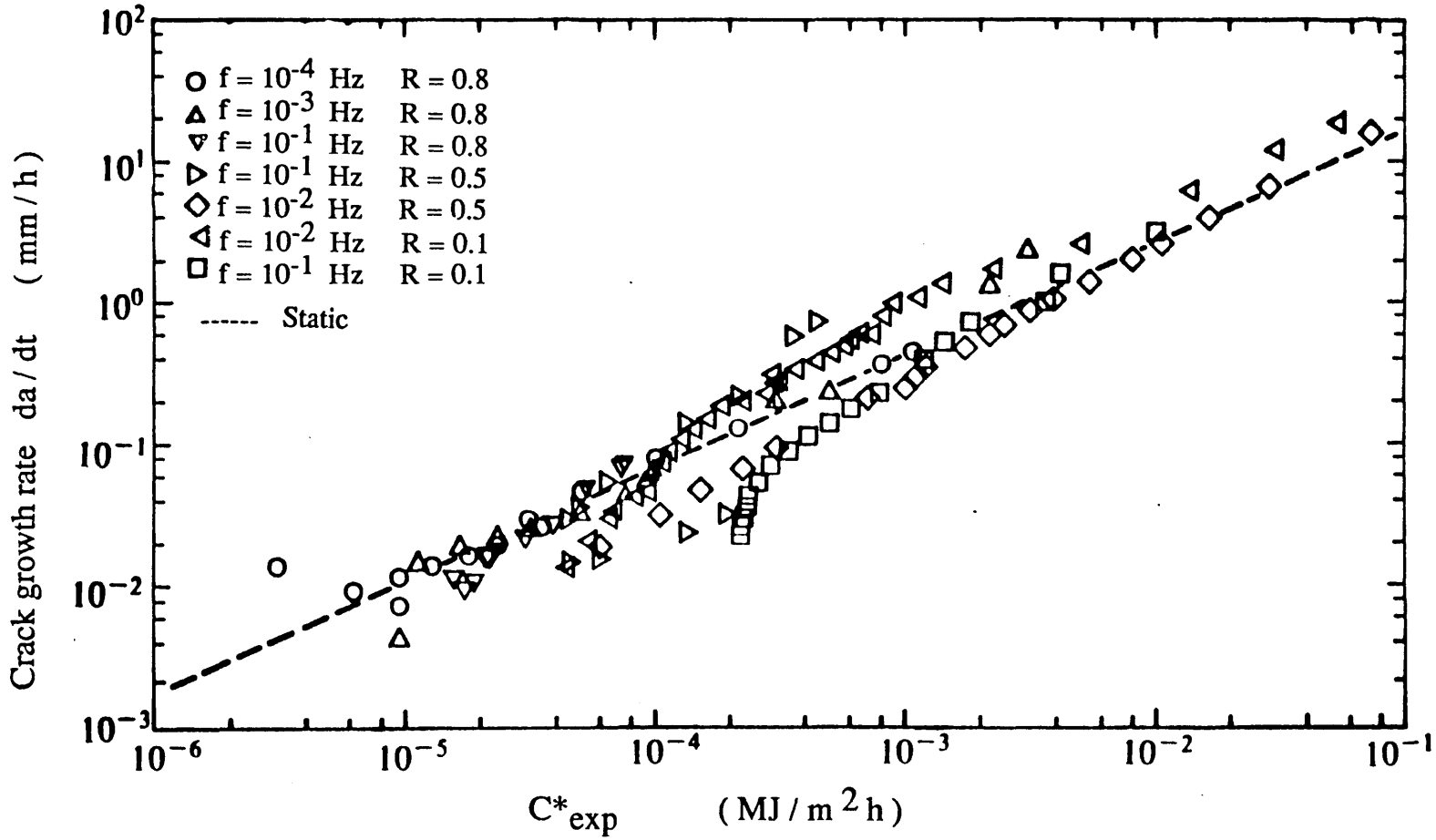


Figure 10.31 Sensitivity of crack growth rate at low frequencies to C^*_{exp} for 1/2CMV at 565° C.

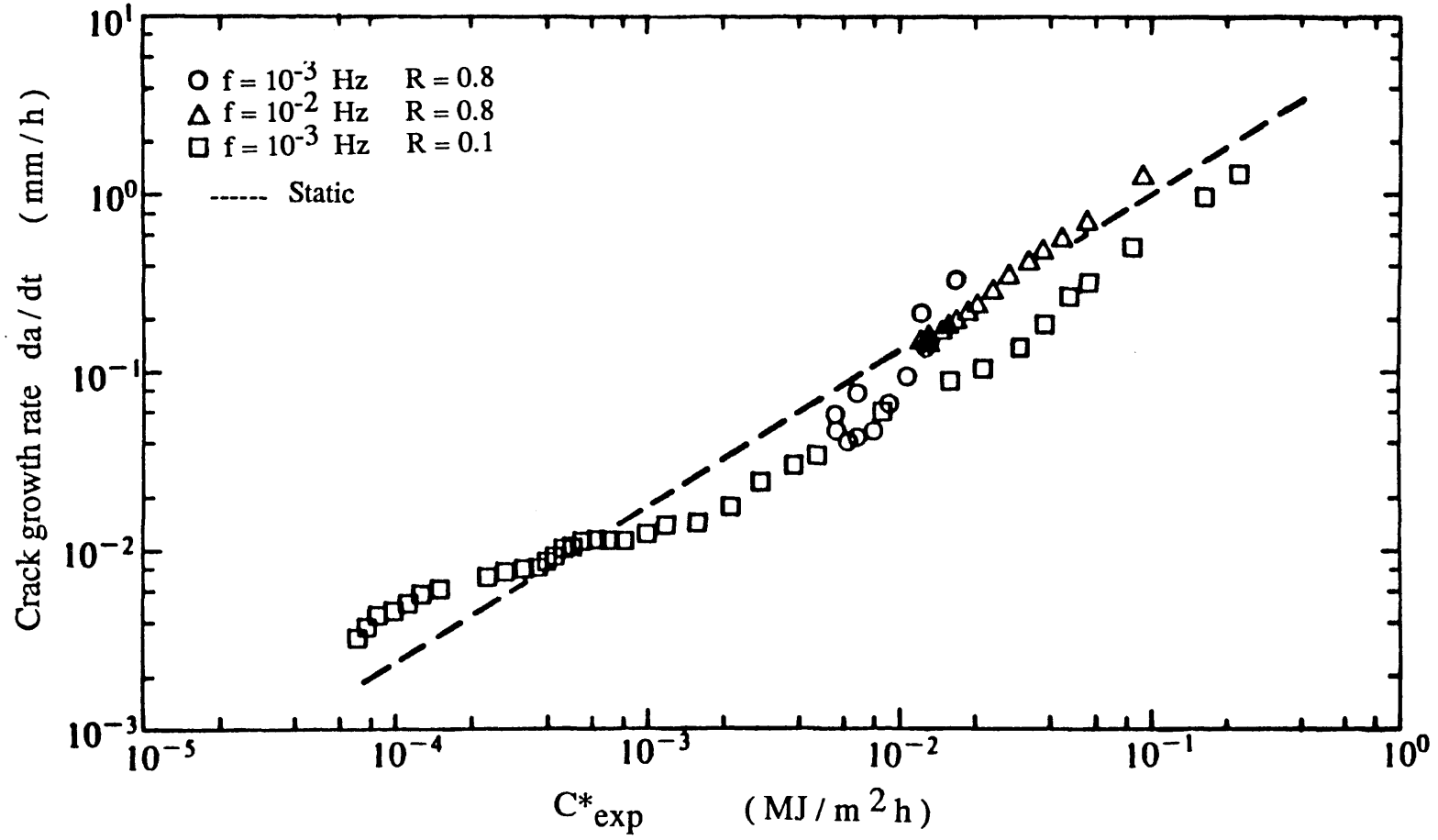


Figure 10.32 Sensitivity of crack growth rate at low frequencies to C^*_{exp} for 21/4CM at 538° C.

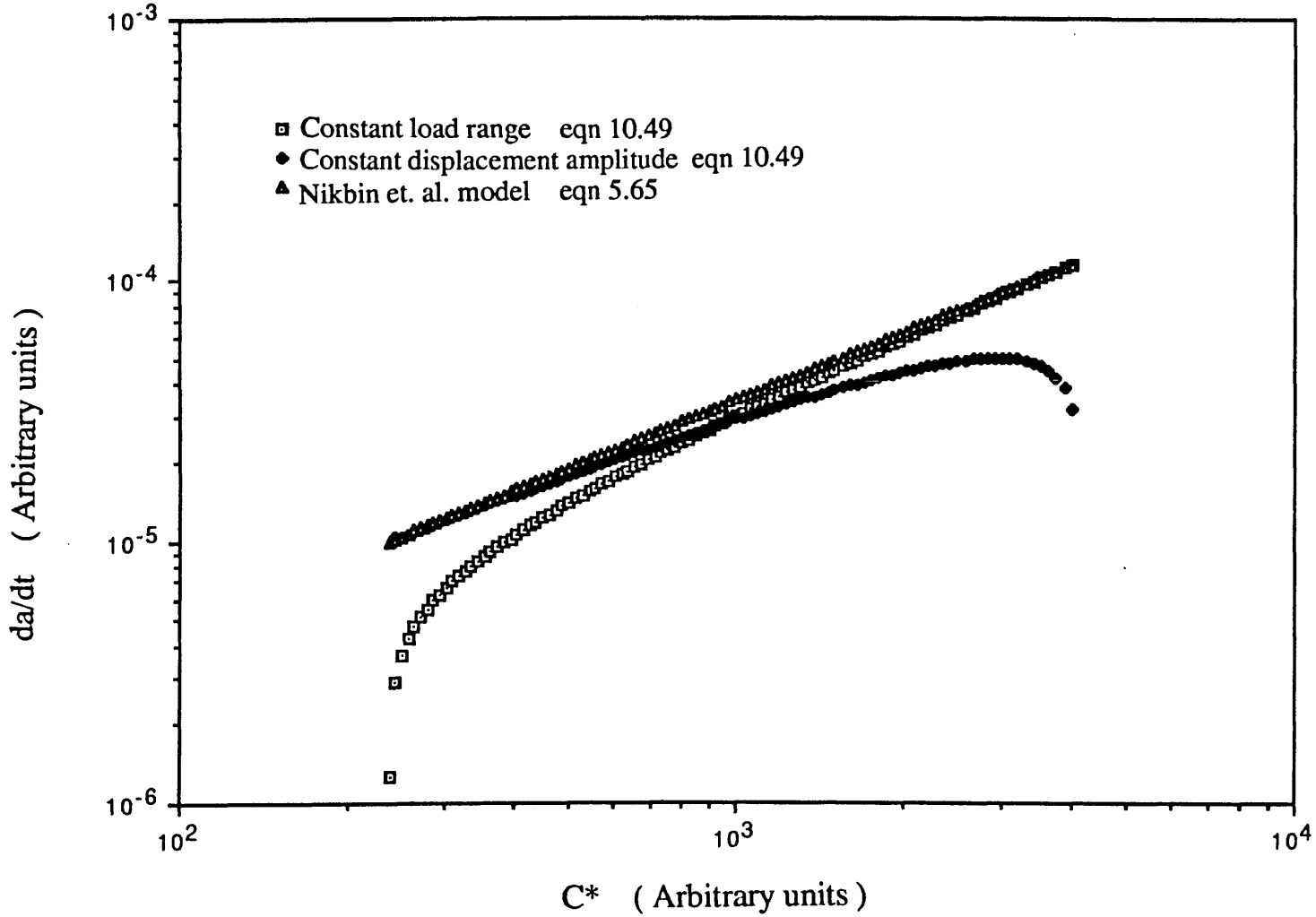


Figure 10.32a Prediction of crack growth rates for constant load range and constant displacement amplitute tests in terms of model of section 10.7.2 (equation 10.49)

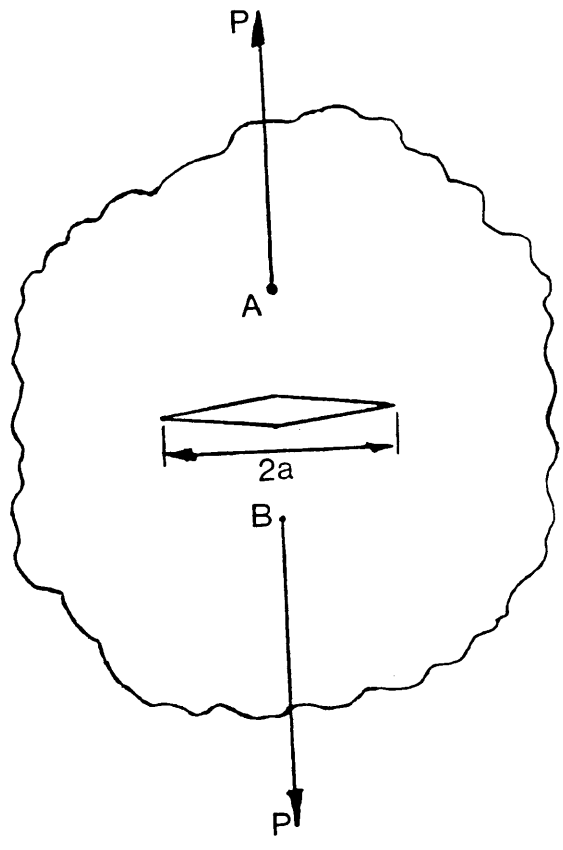


Figure 10.33 Arbitrary body containing a crack of length 2a and loaded at points A and B

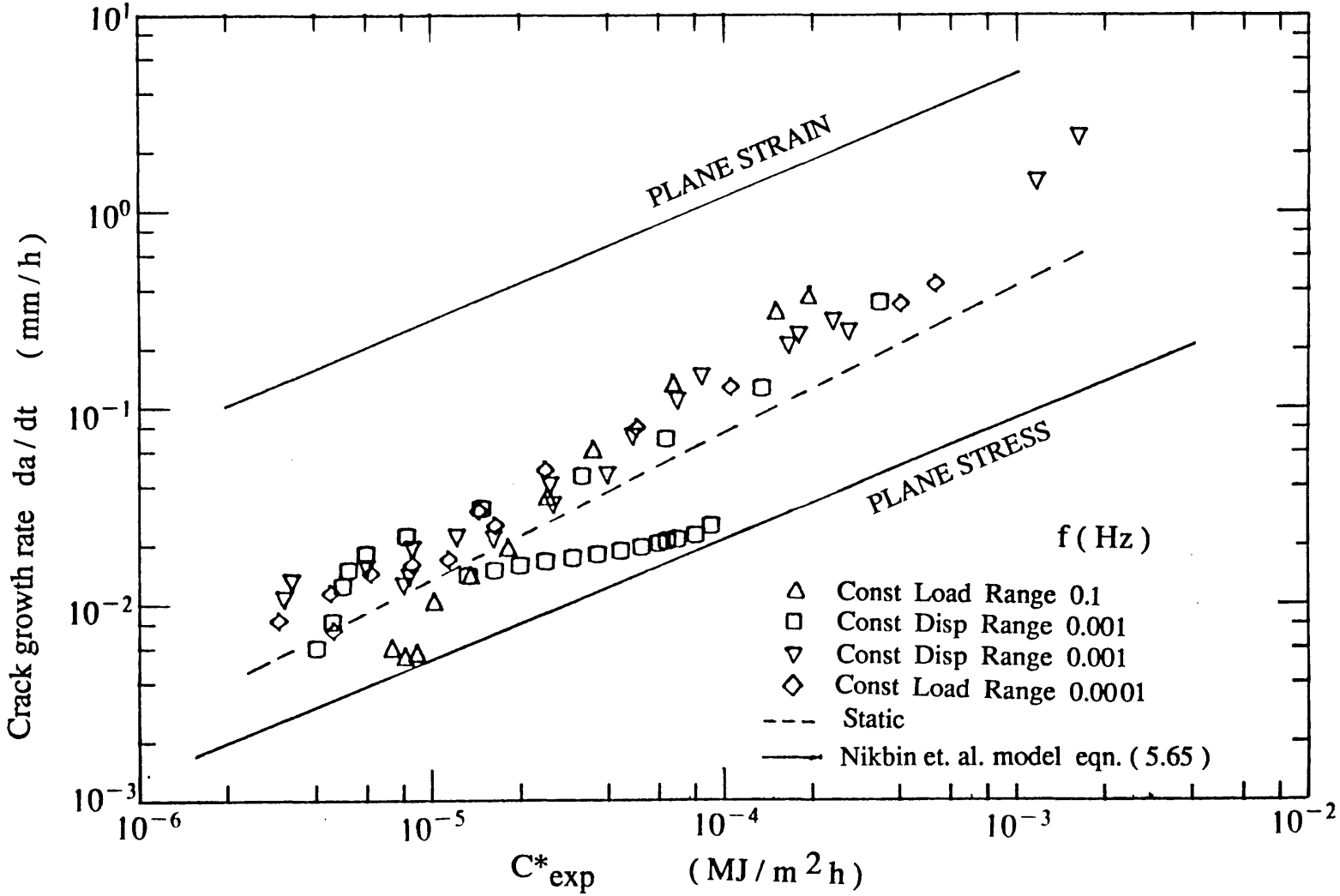


Figure 10.34 Crack growth rate versus C^*_{exp} for 1/2CMV steel , for low frequency constant load range and constant displacement amplitude tests.

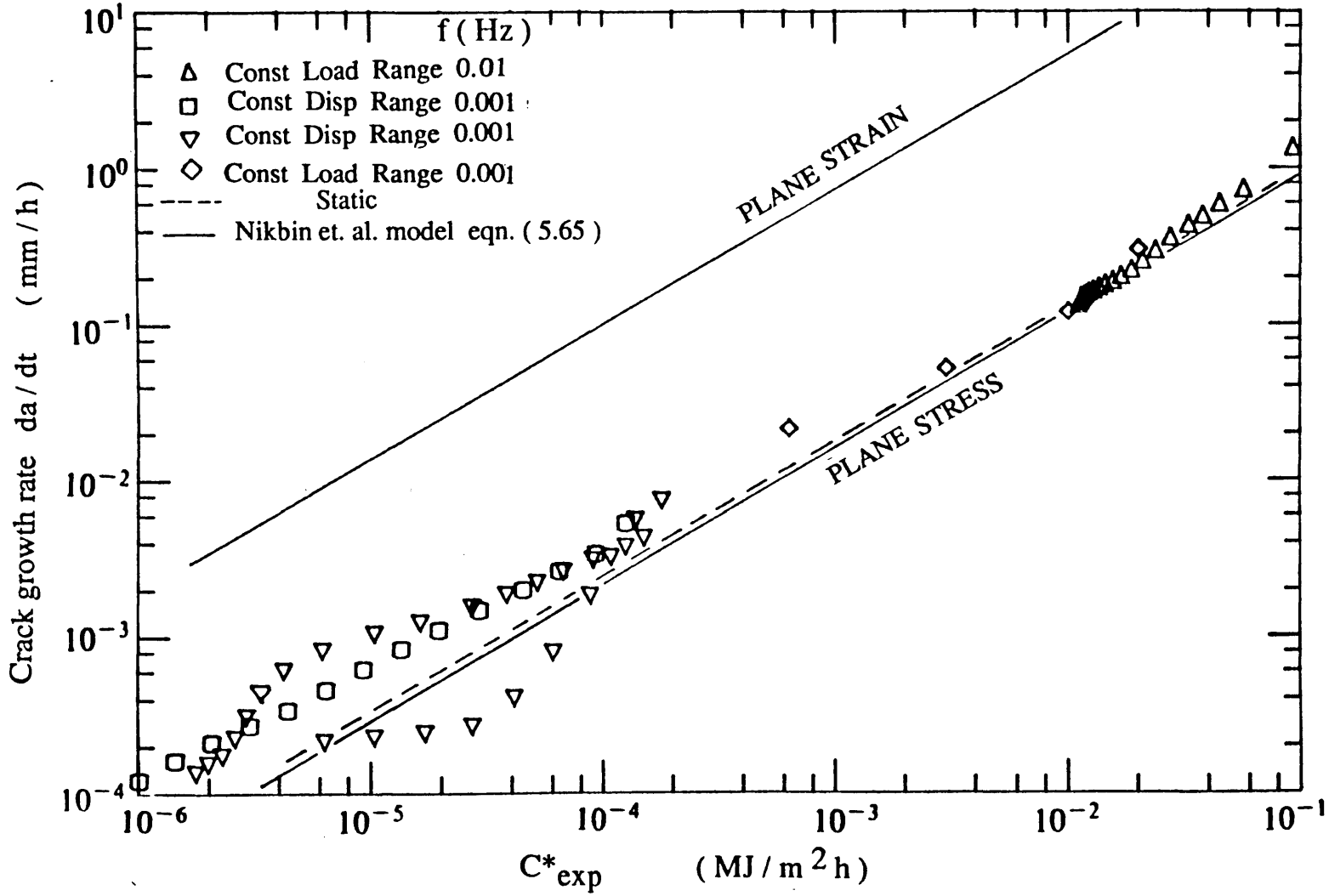


Figure 10.35 Crack growth rate versus C^*_{exp} for 21/4CM steel , for low frequency constant load range and constant displacement amplitude tests.

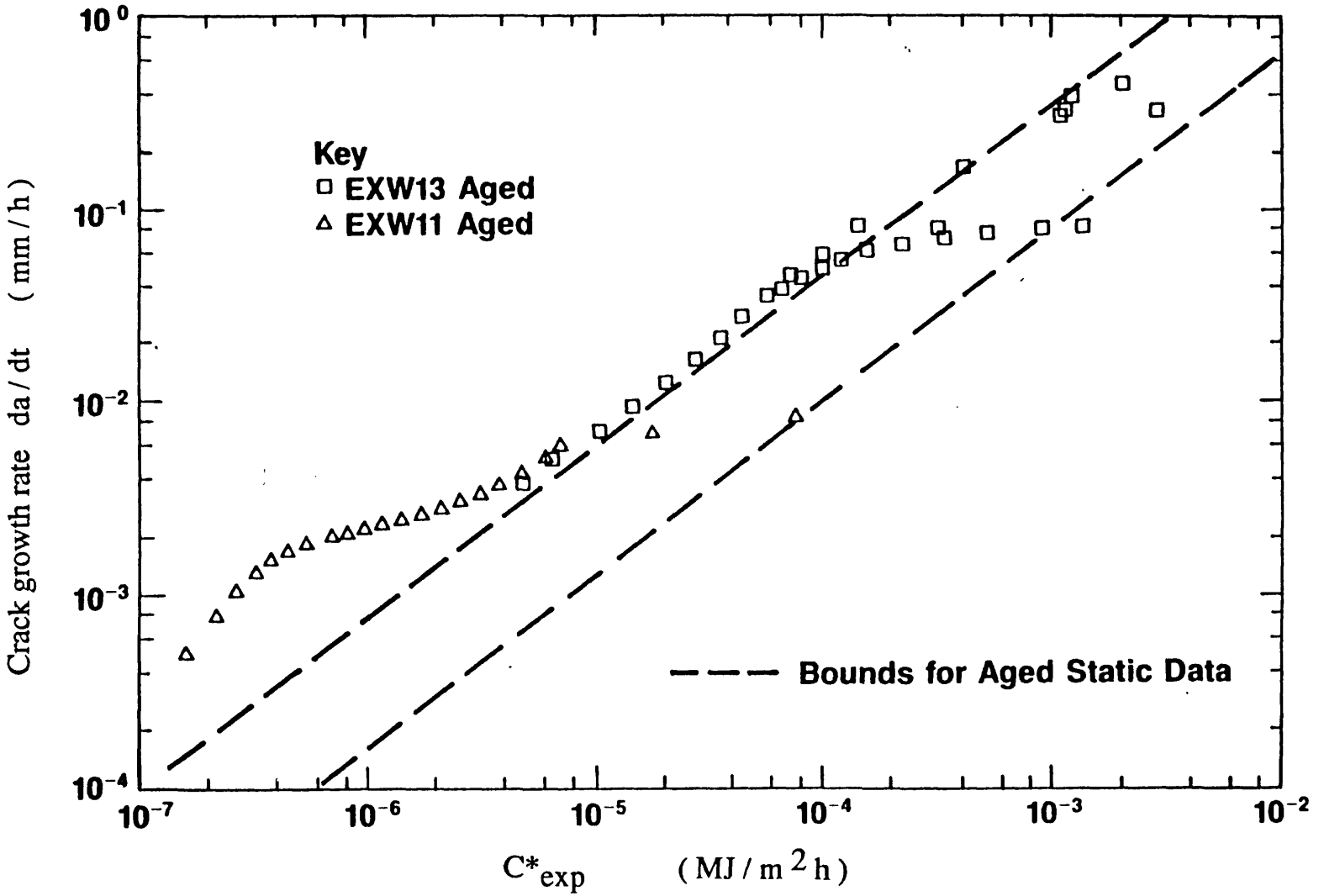


Figure 10.36 Crack growth rate versus C^*_{exp} for cyclic tests on aged material

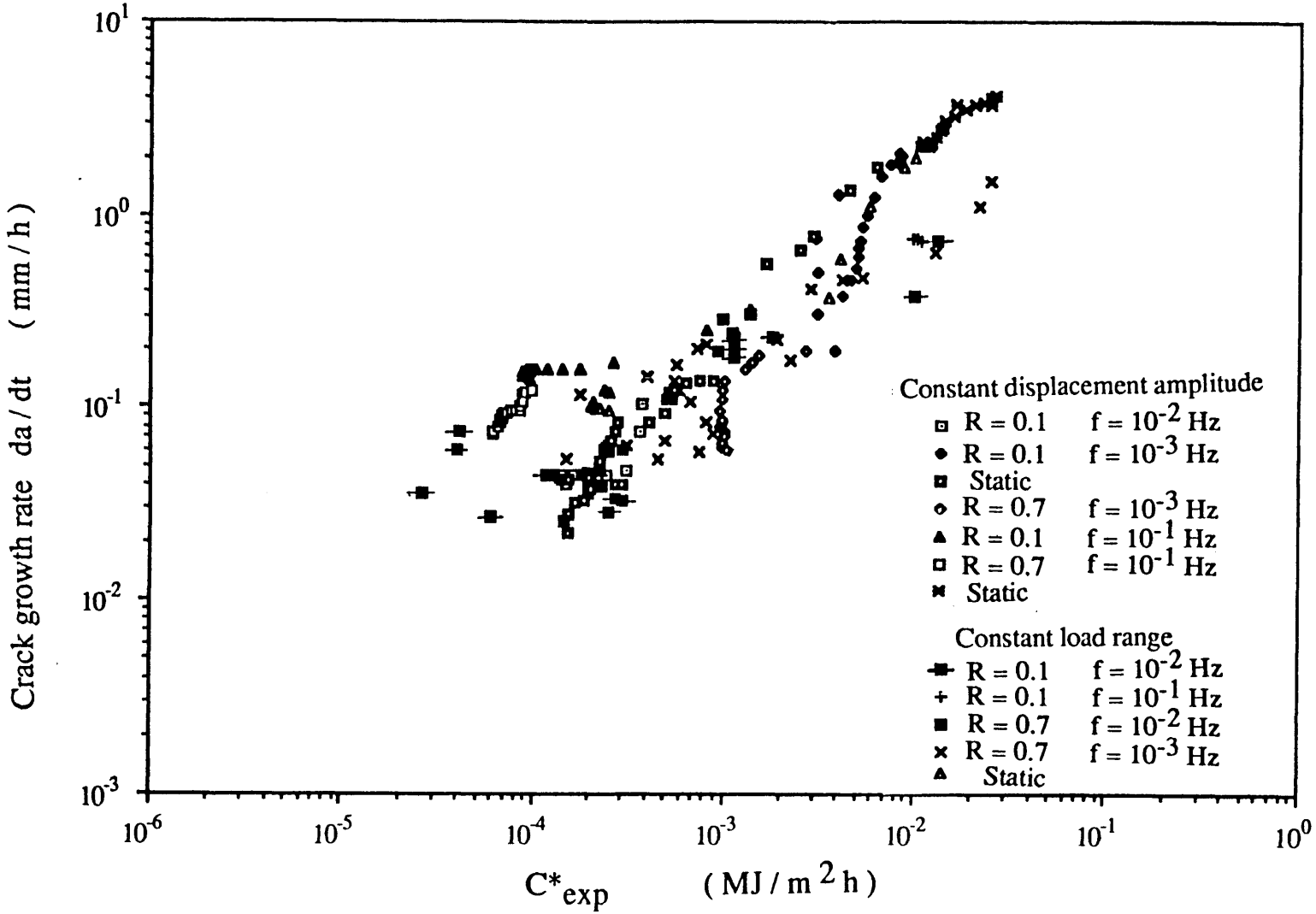


Figure 10.37 Crack growth rate versus C^{*}_{exp} for AP1 12.5mm thick specimens , for low frequency constant load range and constant displacement amplitude tests.

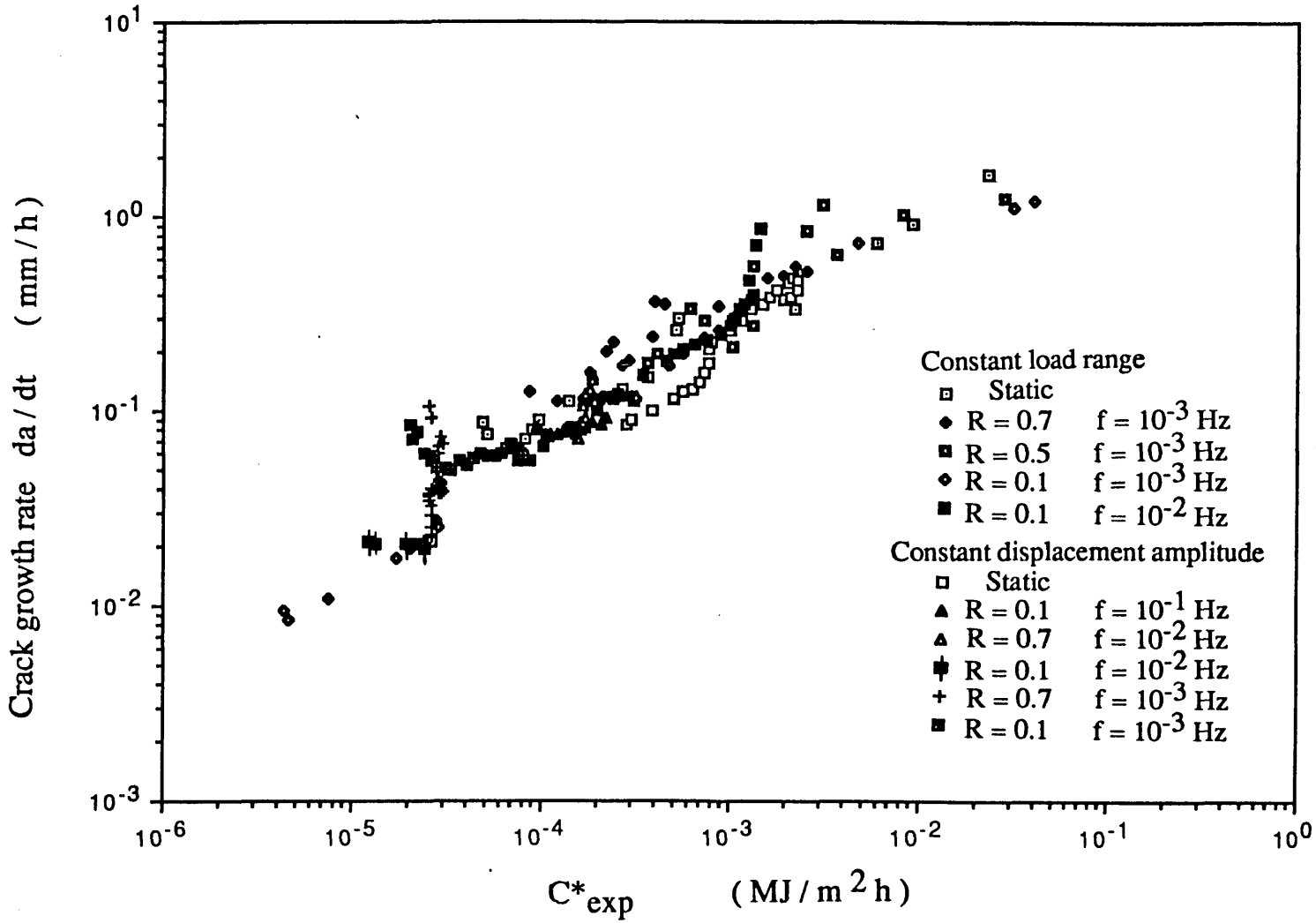


Figure 10.38 Crack growth rate versus C^*_{exp} for AP1 25mm thick specimens , for low frequency constant load range and constant displacement amplitude tests.

APPENDIX 10A.

Equation 5.37 was

$$r^* = \left[\frac{K^2}{2\pi}\right]^{\frac{n+1}{n-1}} \left[\frac{I_n C}{C^*}\right]^{\frac{2}{n-1}} \qquad (10A.1)$$

In terms of the Kumar et. al. (1981) finite element solutions K can be evaluated for the compact tension geometry and plane stress conditions through equation (6.58) as

$$G = \frac{K^2}{E} = \sigma_o \varepsilon_o h_{1,1}(W-a)\left[\frac{P}{\beta\eta(W-a)\sigma_o}\right]^2$$

$$= \frac{\varepsilon_o}{\sigma_o} h_{1,1}(W-a)\left[\frac{P}{\beta\eta(W-a)}\right]^2$$

$$= \frac{1}{E} h_{1,1}(W-a)\left[\frac{P}{\beta\eta(W-a)}\right]^2$$

Therefore

$$K^2 = h_{1,1}(W-a)\left[\frac{P}{\beta\eta(W-a)}\right]^2 \qquad (10A.2)$$

Similarly C* will be given as

$$C^* = \sigma_o \dot{\varepsilon}_o (W-a) h_{1,n}\left[\frac{P}{\beta\eta(W-a)\sigma_o}\right]^{n+1}$$

$$= \frac{\dot{\varepsilon}_o}{\sigma_o^n}(W-a) h_{1,n}\left[\frac{P}{\beta\eta(W-a)}\right]^{n+1}$$

$$= C\,(W-a) h_{1,n}\left[\frac{P}{\beta\eta(W-a)}\right]^{n+1} \qquad (10A.3)$$

or

$$\frac{C}{C^*} = \frac{1}{(W-a)\,h_{1,n}\left[\dfrac{P}{\beta\eta(W-a)}\right]^{n+1}} \qquad (10A.4)$$

Substitution of (10A.4) and (10A.2) into (10A.1) gives

$$r^* = \left[\frac{h_{1,1}(W-a)}{2\pi}\left[\frac{P}{\beta\eta(W-a)}\right]^2\right]^{\frac{n+1}{n-1}}\left[\frac{I_n}{(W-a)\,h_{1,n}\left[\dfrac{P}{\beta\eta(W-a)}\right]^{n+1}}\right]^{\frac{2}{n-1}}$$

which can be simplified to

$$r^* = (W-a)\left[\frac{h_{1,1}}{2\pi}\right]^{\frac{n+1}{n-1}}\left[\frac{I_n}{h_{1,n}}\right]^{\frac{2}{n-1}}$$

therefore

$$\frac{r^*}{W} = \left[1-\frac{a}{W}\right]\left[\left[\frac{h_{1,1}}{2\pi}\right]^{n+1}\left[\frac{I_n}{h_{1,n}}\right]^2\right]^{\frac{1}{n-1}} \qquad (10A.5)$$

In terms of Haigh and Richards (1974) collapse load solution r^* can be evaluated by equating the elastic stress with the reference stress

$$\frac{K}{\sqrt{2\pi r^*}} = \sigma_R = \frac{P}{m\,B\,W} \qquad (10A.6)$$

or

$$r^* = \frac{K^2}{2\pi}\left[\frac{m\,B\,W}{P}\right]^2 \qquad (10A.7)$$

Substituting for K from (10A.2) and solving for r*/W

$$\frac{r^*}{W} = \frac{h_{1,1}}{2\pi}\left[\frac{m}{\beta\eta}\right]^2\frac{1}{1-a/W} \qquad (10.A8)$$

where $\beta = 1.455$ for plane stress conditions

CHAPTER 11

GENERAL DISCUSSIONS, CONCLUSIONS AND RECOMMENDATIONS.

The main attention in this thesis is applied to crack growth use of fracture mechanics concepts, in particular on the use of the C* parameter (analytical or derived from experimental measurements) for creeping materials. In the following the validity of using the C* parameter is discussed in detail.

For C* to characterize the behaviour of components containing cracks, it must be path independent. C* will be path independent if there is a unique relationship between the stress and strain independent of r and θ. So only in the initial elastic state and the steady state creep state is C* path independent. For other conditions C* will be path dependent. However in the small scale-creep case approximate path-independence, as shown by Riedel and Rice (1980), can be obtained. It is expected that path independence can be obtained if it is assumed that the creep strain rates dominate the elastic rates. However the degree to which path-dependence occurs cannot be determined without resorting to numerical techniques.

Power law functions were used in order to obtain numerical estimates of contour integrals in this thesis. Other functions, such as exponential or the hyperbolic sine law (Bassani (1983)) can be also used. However the nature of the singularities in stress and strain rate, will be different compared with the Norton law creep expression. The numerical Finite Element analysis in chapter 9 shows that for all geometries examined, in the elastic and steady state creep state, C* is path independent within the numerical errors. The numerical Boundary Integral Equation analysis of the rotating disc shows that for small deformation, i.e. at loads where the elastic strains dominate the plastic, and for large amounts of plastic deformation, i.e. at loads where the plastic strains dominate the elastic, approximate path independence is obtained, but, for intermediate amounts of plastic deformation where both the elastic and creep strains are significant, C* evaluated along different paths may vary by as much as 20%. Similarly,

it is expected that, analogous to the elastic incremental plastic case, the elastic incremental creep case will give C* values which are approximately path-independent where the elastic or creep strains dominate, but when both the elastic and creep strains are significant, C* is not completely path independent. So when stress redistribution takes place C* is not path-independent.

The problems associated with a continuously growing crack in relation to C* path independence, need to be investigated too. If the crack grows in a "steady" manner in which the material history does not alter substantially in the increment Δa, the earlier arguments with regard to the static crack and path-independence or dependence are the same. As it was discussed in chapter 5 the behaviour of the material local to a continually growing crack can be entirely governed by the crack speed (Hui and Riedel (1981), Hawk and Bassani (1986)). However from the experimental investigations of the materials tested it was found that the region over which this occurs is very small (of the order of 10^{-10}m). So the zone, governed by $\dot{a}$, does not significantly affect the remaining stress field. The deformation of the body outside the zone remains governed by the stationary crack parameters.

11.1 GENERAL DISCUSSION AND CONCLUSIONS CHAPTER 9.

In chapter 9 the effect of the presence of a blunt hole on the stress distributions, and, the crack growth characterising parameters hence the crack growth rates, was examined in detail. For zero (or negligibly small) crack extension from the hole root characterising parameters such as K and C* are zero (or negligibly small). Characterising parameters such as K and C* will describe the crack growth rates after the crack has initiated. During the period of crack initiation damage accumulates at a critical distance ahead of the hole root until the material ductility is exhausted and the material over this critical distance ruptures.

For the compact tension geometry good correlation between the experimental (Morzeria (1979)) and the F.E. analytical crack initiation times has been found, by

assuming that the crack initiates after the ductility at a distance of 500μm ahead of the hole root has been exhausted. The experimental results of Morzeria (1979) are on the 1/2CMV material which is relatively creep brittle and exhibits only small stress redistribution during cracking. So the stress intensity factor K rather than the analytical form of C* will be the most appropriate parameter to describe the crack growth rates. This is indicated in figures 9.42 and 9.44. Whereas good agreement has been found between the experimental and the analytical initial crack growth rates when the crack growth is assumed to be characterised by the stress intensity K, there is poor agreement when the crack growth is assumed to be characterised by C*. For ductile materials where substantial stress redistribution occurs with crack extension, C* may be more relevant than K in characterising crack growth rates. As is illustrated in figures 9.40 and 9.43 the effect of the hole on the characterising parameters hence the crack growth rates is retained at a longer distance from the hole root for the elastic case than the steady state creep case. A higher sensitivity to hole diameter may therefore be anticipated for the elastic case than for the steady state creep case.

A bigger amount of stress redistribution will be anticipated for a higher value of n. This is clearly shown in figures 9.46 and 9.48 for a rotating disc containing a central hole only and a disc containing a central hole and six satellite holes respectively. For the disc containing a central hole and six satellite holes the relative stress concentration factor F at the points A and B (see figure 9.47), increases approximately linearly with 1/n, as illustrated in figure 9.49, and the maximum hoop stress migrates away from point A at the in-board radius of the satellite hole towards the disc bore indicating that in this circumstance failure may be expected to initiate away from the satellite hole. Calculations of the creep contour integral C* for cracks of different lengths emanating from A at the satellite hole (figures 9.51 to 9.54) indicate that there is a rapid increase in C* for short crack lengths close to a satellite hole which is most pronounced for high values of n, indicating that the effect of the hole becomes less significant for increasing n. Results for the cracked disc geometry containing a sharp crack in the radial

direction (figure 9.55), indicate that for the range of values of n examined here (n=1 to 10), C* is bigger for the crack emanating from the point A than it is at point B (figures (9.56) to (9.59)), so that for a crack aligned in the radial direction of a rotating disc, the crack growth rate is expected to be greater towards the bore than towards the outer radius.

Good agreement between the F.E. and the B.I.E. method has been found for the elastic stress distribution (figure 9.63) and the C* creep contour integral for n=1 (figure 9.51), for the disc containing a central hole and six satellite holes (figure 9.50). The non-linear B.I.E. results indicate that for small times there is an approximately linear decay on logarithmic scales in C(t) with time and that at long times asymptotic approach to the F.E steady state solution C* is obtained (figures 9.66, 9.68 and 9.70).

11.2 GENERAL DISCUSSION AND CONCLUSIONS CHAPTER 10

11.2.1 STATIC CONSTANT LOAD TESTS

The stress intensity factor K and the C* contour integral analytically calculated assuming steady state secondary creep, will not always give successful correlations with the crack growth rate. Small amounts of stress redistribution are enough to change the elastic fields in a way that K will not characterise the crack growth. Similarly full relaxation of the stress field does not occur in the 1/2CMV and AP1 materials for the life times of each of the specimens, avoiding a unique correlation to be obtained with the theoretical solutions of C*. So similar conditions, which must be satisfied as to whether either one or another parameter governs the creep crack growth rates, cannot be attained even in laboratory test pieces. The results point towards the adoption of a parameter which includes the effect of the relaxing stress fields, from the elastic to the steady state creep state. Analytical estimates for characterising parameters (like C_t or C(t) as defined in chapter 5) during transient (or small scale) creep can easily be determined for a stationary crack, but their evaluation for a growing crack is difficult, since the reference

from which the time is measured is lost. However, in adopting a parameter measured at the loading pin, where it is assumed that this parameter does give a direct measure of the state of the component during crack growth, successful characterisation of the crack growth rates is obtained, as the correlations of the crack growth rate with C^*_{exp} calculated using the measured displacement rates at the loading pin indicate.

For the 800H superalloy both C^*_{exp} and C* calculated analytically, give good correlation to the crack growth data since the stress redistribution times for this material are very small. There is no significant tread due to specimen size, indicating the applicability of both parameters in characterising the creep crack growth of this material. In service an analytical estimation of C* will be required since the measured load line displacement will not generally be available. However the C* parameter is proportional to σ^{n+1} and if n is high, an accurate estimation of the stress is essential if a reliable estimate of the analytical C* is to be obtained. This in turn demands that the constitutive equations describing the material behaviour must be accurately known.

Deviations from the overall linearity on the correlation between da/dt and C^*_{exp} or C* at low crack growth rates is observed. So there is a doubt whether there is a unique correlation of da/dt with C* or C^*_{exp}. It is argued that this is due to that sufficient time has not elapsed to allow creep strains to accumulate and thereby promote propagation of the crack. A model has been developed in section 10.7 based on the ductility exhaustion on the crack tip, which accurately predicts this behaviour.

Static tests on new and naturally aged 304H stainless steel material, show that aging can have a significant effect on resistance to crack growth. It was found that C^*_{exp} could satisfactorily characterize creep crack growth for the tests conducted. The crack growth rate was approximately an order of magnitude faster at a given value of C^*_{exp} in the aged material than in the new material. This is rationalized in terms of the creep ductilities of the material and the state of stress at the crack tip. For this type of material, data obtained from uniaxial tests, can be used to obtain approximate expressions for the bounding cases of plane stress and plane strain for crack growth rate

as a function of the C^*_{exp} parameter (see figures 10.11 and 10.12). Engineering judgements can then be made regarding to the relevant state of stress for the components being analysed and thus an approximate crack growth behaviour within the plane stress and plane strain boundaries can be estimated.

11.2.2 CYCLIC CONSTANT LOAD RANGE TESTS.

The cyclic crack growth tests on the 1/2CMV, 21/4CM and the AP1 steels illustrate that, for a wide range of loading conditions there is no major interaction between the creep and the fatigue mechanisms. From the da/dN versus frequency graphs at constant K_{max}, a sharp transition from one mechanism to the other is observed, at a frequency depending on the R-ratio and material creep ductility. For lower R-ratio transition occurs at a lower frequency, as higher amplitude of loading will enhance creep and environmental attack mechanisms relative to fatigue processes.

In the creep dominated region the contribution due to the fatigue mechanism is minor, and a -1 slope is obtained in the da/dN versus frequency graph at constant K_{max}. There is a small R-ratio effect, due to the superimposed elastic fields after each load step which is most pronounced for the 21/4CM ductile steel, but this is attributed to the different magnitude of the superimposed elastic fields for a different R-ratio, rather than to a contribution of the fatigue mechanism on the crack growth.

In the high frequency region where fatigue processes dominate, the influence of R-ratio can be accounted for by crack closure effects caused by fracture surface roughness, oxidation and creep and plastic strains developed at the crack tip. All these factors will help the crack to close before the minimum load of the cycle is reached, so that the whole of the applied stress intensity factor is not available for propagating the crack. These effects appear to be more pronounced at elevated temperatures than at room temperature. As it is stressed in section 7.3.1 the transition from the creep to fatigue mechanism, has nothing to do with the transition from creep dominated to elastically dominated overall specimen behaviour which will, in general occur at another

characteristic frequency, as the failure mechanism may be dominated by creep even for small-scale-creep behaviour.

In terms of C^*_{exp} calculated at the maximum load (since most of the damage occurs at maximum load), as far as creep processes dominate good correlation is found between the static and cyclic data. No significant trend was found due to frequency or R-ratio, showing that the measuring response takes into account the stress peaks at the end of each load step in the cycle. A faster crack growth rate in the cyclic tests due to the superimposed elastic field, will be reflected in a faster displacement rate at the loading pins, in the same way as small scale (or transient) creep during stress relaxation in a static test, is reflected at the loading pins.

The small interaction of creep and fatigue mechanisms, under creep/fatigue loading conditions in the alloys examined, allows crack growth results to be obtained from tests carried out under static and high frequency loading only, to identify the time dependent and fatigue dependent components of failure, if a relationship of the form

$$\frac{da}{dN} = \frac{D C^{*\Phi}_{exp}}{3600\, f} + C\, \Delta K^{m}_{eff}$$

is assumed.

11.2.3 CONSTANT DISPLACEMENT TESTS

The applicability of C^*_{exp} parameter in describing crack growth rates, was more critically assessed by conducting tests under constant displacement loading. In the constant load tests the crack growth and displacement rates both accelerate with crack advance and time, as the magnitude of the stress fields ahead of the crack tip rises continuously as growth proceeds. In the constant displacement tests relaxation of the load takes place with crack extension, and the magnitude of the stress fields ahead of the crack tip may remain essentially unchanged throughout the test resulting in an approximately constant crack growth rate, as it was observed in the case of the AP1 superalloy, or more generally reduce with time and crack extention resulting in a

decelerating crack growth rate. When the crack growth rates decrease with time good correlation between da/dt and C^*_{exp} can be obtained at low crack growth rates, away from any initiation effects. Low crack growth correlations between da/dt and C* are of particular importance, since this is the region where crack growth in industrial components will take place. The good correlation between the constant load range results and the constant displacement range results indicates the applicability of C^*_{exp} in describing crack growth under different loading conditions.

It is observed that the amount of crack extension in a constant displacement range test depends on the stress redistribution time. For relatively ductile materials (21/4CM steel and 304H stainless steel) the stress redistribution times are relatively small and only small crack extensions are possible, whereas for relatively brittle materials (1/2CMV steel and AP1 superalloy) where stress redistribution times are significant, large crack extensions are possible. It is unlikely that a component made out of the 21/4CM steel or the 304H stainless steel will fracture under this type of loading, except if there is a mechanism that regenerates the load, or significant amount of elastic follow-up.

11.3 RECOMMENDATIONS FOR FURTHER WORK

Although certain areas of crack growth at elevated temperatures have been specifically investigated in this thesis, it was inevitable that not all aspects could be covered. To this end, areas for further work are briefly presented below for investigation.

(1) Conduct laboratory tests in an inert environment to investigate whether environmental effects influence the creep and creep-fatigue crack propagation.

(2) Develop the analysis suggested in section 10.9 to use the data collected in the laboratory to predict the behaviour of industrial components, under combined creep-fatigue loading.

(3) Conduct laboratory tests on crack growth specimens with various hole diameters using the 800H superalloy material , which is characterized by C* rather than the stress intensity factor K, to confirm the predictions of the crack growth rates and crack initiation near to a stress concentration.

(4) Conduct laboratory tests on 800H superalloy and 304H stainless steel specimens under cyclic loading, to compare with the behaviour of the cyclic load data of the 1/2CMV and 21/4CM steels and the AP1 superalloy.

(5) Evaluation of the C* parameter from experimental load-displacement rates and numerical techniques, for exponential and hyperbolic creep stress laws rather than the Norton power law.

(6) Obtain estimates of the C* parameter, using numerical methods, for a growing crack.

(7) Repeat the numerical analysis conducted on the rotating disc containing six satellite holes, for different hole sizes, to study the effect of the hole size on the crack growth rates and hence the expected life.

REFERENCES

AINSWORTH, R.A. [1982]. Int. Journ. of Fracture 20 , 1982, pp. 147-159.

AINSWORTH, R.A. [1987]. "Reference Stress Estimates of C*", presented at "High Temperature Component Life Assesment", 17-19 June 1987, held at Imperial College of Science and Technology.

AL-FADDAGH, K.D., FENNER, R.T. and WEBSTER, G.A. [1982]. J. Strain Analysis, 17, pp. 123-132.

AL-FADDAGH, K.D. [1983]. PhD Thesis University of London, 1983.

ANDERSON, R.G. [1980]. "Some observations on reference stresses, skeletal points, limit loads and finite elements", presented at "Creep in Structures", IUTAM 3rd Symposium, Leicester, September 1980.

ASHBY, M.F. and TOMKINS, B. [1979]. "Micromechanisms of fracture and elevated temperature fracture mechanics". 3rd Inter. conf. on Mech. Behaviour of Materials, Cambridge, England, August 1979.

BASSANI, J.L. [1983]. "Cracks in Materials with Hyperbolic-Sine-Law Creep Behaviour". American Society for Testing and Materials, ASTM STP 803 Volume I, pp. I-532-I-550 ,1983.

BASSANI, J.L., HAWK, D.E. and SAXENA, A. [1986] "Evaluation of the C_t parameter for Characterizing Creep Crack Growth Rate in the Transient Regime". Private communication, to be published in A.S.M.E.

BECHT, C. [1983]. "A Simplified Approach for Evaluating Secondary Stresses in Elevated Temperature Design", 83-PVP-51. The American Society of Mechanical Engineers, 1983.

BEGLEY, J.A. and LANDES, J.D. [1972]. American Society for Testing and Materials, ASTM STP 514, pp. 24-29, 1972.

BROWN, L.M., and EMBURY, J.D. [1973]. Proc. 3rd Int. Conf. on the Strengh of Metals and Alloys, Institute of Metals, London.

BUCHHEIM, G.M., BECHT, C., NIKBIN, K.M., DIMOPULOS, V., WEBSTER,

G.A., and SMITH, D.J. [1986]. Third International Symposium on Nonlinear Fracture Mechanics, October 6-8, 1986, Knoxville, TN, to be published in ASTM STP.

BURKE, M.A., and NIX, W.D. [1975]. Acta Met. 23, 793.

CHAN, S.K., TUBA, I.S. AND WILSON, W.K. [1970]. Eng. Fracture Mech., vol. 2, 1970, pp. 1-17.

CHANG, T.C., POPELAR C.H. and STAAB G.H. [1987]. Inter. Jour. of Fracture 33 pp. 31-45, 1987.

COCKS, A.F.C. and ASHBY, M.F. [1980]. Metal Sci., 14, pp. 395-402, 1980.

COCKS, A.F.C. and ASHBY, M.F. [1982a]. Metal Sci., 16, pp. 465-474, 1982.

COCKS, A.F.C. and ASHBY, M.F. [1982b]. "On Creep by Void Growth", Progress in Metal Science, 27, 1982, pp. 189.

COCKS, A.F.C. and ASHBY, M.F. [1982c]. Scr. Metall., 16, pp. 109-114

CROSSMAN, F.W., and ASHBY, M.F. [1975]. Acta Met. 23, 425.

DELORENZI, H.G. and SHIH, C.D. [1983]. Int. Journ. of Fracture 21, 1983, pp. 195 - 220

DESAI, C.S., and ABEL, J.F. [1972]. "Introduction to the Finite Element Method", Van Nostrand Rheinhold, New York, 1972.

DIMOPULOS, V., NIKBIN, K.M. and WEBSTER, G.A. [1986]. ASME Materials Week, 1986, Lake Buena Vista, Florida, 4-9 Oct, 1986, to be published in A.S.M.E.

DORN, J.E., ORR, R.L. and SHERBY,O.D. [1954]. "Correlations of Rupture Data for Metals at Eleveted Temperatures" Trans. A.S.M.E. 46, 113, 1954.

EDWARD, G.H. and ASHBY, M.F. [1979]. Acta Metall., 27, pp.1505-1518, 1979.

EHLERS, R. [1981]. PhD thesis (in German). Fakultar fur Bergbau und Huttenwesen der Rheinisch-Westfalischen Technischen Hochschule Aachen.

EHLERS, R. and RIEDEL, H. [1981]. "Advances in Fracture Research, Rroceedings of ICF5", vol.2, D Francois et al, Eds., Pergamon Press, Oxford and New York, pp. 691-698.

ELBER, W., [1971]. American Society for Testing and Materials, ASTM STP 486 pp. 230-242, 1971.

ELLIS, F.V., HILTON, S.O., HENRY, J.F., and BYNUM, J.E. [1982]. J. Pressure Vessel Tech., 104, pp. 120-129.

ELLISON, E.G. [1987]. "Prediction of fracture at high temperature", presented at a Seminar on "High temperature crack growth", held at Imperial College of Science and Technology on 10November 1987. (published by I. Mech E.).

ELLISON, E.G. and HARPER M.R. [1978]. J. Strain Analysis, 13 (1), pp.35-51.

ELLISON, E.G. and WALTON, D. [1974]. "Fatigue, creep and cyclic creep crack propagation in a 1CrMoV steel", presented at Int. Conference on "Creep and Fatigue in Eleveted Temperature Applications", Philadelphia, September 1973, Sheffield, April 1974 (published by I. Mech E.).

FENNER, R.T. [1975]. "Finite Element Method for Engineers", Macmillan, London, 1975.

FINNIE, I. and HELLER, W.R. [1959]. "Creep of Engineering Materials", McGraw-Hill, New York, 1959.

FLOREEN, S. [1975]. Met. Trans. A., 6A, pp. 1741-1749, 1975.

FORMAN, R.G., KEARNEY, V.E. and ENGLE, R.M. [1967]. J. of Basic Eng., Sept 1967, pp. 459-464

FRITSCH, F.N. and CARLSON, R.E. [1980]. J. Numer. Anal., 17 (2), 1980, pp. 238-426.

GANDHI, C., and ASHBY, M.F. [1979]. Overview 4, Acta Metall. 27, 1979.

GAROFALO, F. [1965]. "Fundamentals of Creep and Creep-Rupture in Metals", McMillan, 1965.

GOLDMAN, N.L., and HUTCHINSON, J.W. [1975]. International Journal of Solids and Structures. Vol. 11,1975, pp. 575-591.

GOODS, S.H., and BROWN L.M. [1979]. Overview 1, Acta Met. 27, 1.

HAIGH, J.R., and RICHARDS, C.E. [1974]. "Yield point loads and compliance functions of fracture mechanics specimens", CEGB CERL Memo NO.

RD/L/M/461, 1974.

HAIGH, J.R. [1975]. Met. Sci. Eng., 20, 1975, pp.225-235.

HARPER, M. [1976]. "Creep, Cyclic Creep and Fatigue Fracture in a Low Alloy Steel", PhD Thesis, University of Bristol.

HARPER, H.P. and ELLISON, E.G. [1977]. J. Strain Analysis, 12, 3, 1977, pp.167-179.

HARRISON, C.B. and SANDOR, G.N [1971]. Eng. Fracture Mechanics, 3, pp. 403-420, 1971.

HAWK, D.E. AND BASSANI, J.L. [1986]. Jour. of Mech. and Physics of Solids, vol. 34, No 3, 1986, pp. 191-212

HAYES, D.J., [1970]. "Some Applications of Elastic-Plastic Analysis to Fracture Mechanics". PhD Thesis, University of London, 1970.

HAYHURST, D.R. and HENDERSON, J.T. [1977]. "Creep Stress redistribution in notched bars", Int. J. Mech. Sci., 1977, 19, pp. 147-159.

HILTON, P. D. [1977]. "A specialized finite element approach for three-dimentional crack problems". From: Mechanics of Fracture, vol. 3, Plates and Shells with Cracks, Ed. Shih, G.C., pp. 273-298 (Noordhoff International Publishing).

HUI, C.Y. and RIEDEL, H. [1981]. Int. Journ. of Fracture, Vol. 17, 1981, pp. 409-425.

HUI, C.Y.and WU, K.C. [1986]. Int. Journ. of Fracture, 31, 1986, pp. 3-16.

HUTCHINSON, J.W. [1968]. J. Mech. Phys. Solids, 1968, Vol. 16 , pp. 13 - 31.

HYDE, T.H, LOW, K.C. and WEBSTER J.J. [1983] "Elastic-Plastic-Creep behaviour of a compact -tension specimen". J. of Strain Analysis, Vol 18, No 3, 1983, pp. 157-166.

HYDE, T.H, LOW, K.C. and WEBSTER J.J. [1984] "Comparison of finite element predictions of creep crack growth with experimental data". J. of Strain Analysis, Vol 19, No 2, 1984, pp. 103-109.

IRWIN, G.R. [1957]. J. Appl. Mech., 24, pp. 361-364, 1957.

IRWIN, G.R. [1960]. Trans. ASME, Journal of Applied Mech., 24, 1960, pp. 361

IRWIN, G.R.and KIES, J.A. [1952]. Weld. J. Res. Suppl., 17, pp. 95-100

ILYUSHIN, A.A. [1946]. Prikadnaia Mathematika i Mechanika, 10, 347.

KACHANOV, L.M. [1958]. Izv. Ak. Nauk. SSSR Otdel.Tekh, Nauk., 8, pp. 26-31, 1958, (in Russian).

KELLY, A., TYSON, W.R., and COTTRELL, A.H. [1967]. Phil. Mag.15, pp. 567.

KENYON, J.L. [1976]. "Application of Linear Elastic Fracture Mechanics to Creep Cracking", PhD Thesis University of London, 1976.

KLINTWORTH, G.C. [1977]. MSc Thesis University of London, 1977.

KLINTWORTH, G.C. and WEBSTER, G.A. [1979]. J. Strain Analysis, 14, 1979, pp.187.

KLINTWORTH, G.C. [1981]. PhD Thesis University of London, 1981.

KUMAR, V., GERMAN, M.D. and SHIH, C.F. [1981]. "Estimation technique for the prediction of elastic-plastic fracture of structural components of nuclear systems", Report No. SRD-80-094, EPRI, June 1981.

LADLES, J.D., and BEGLEY, J.A. [1974]. Report 74-1E7-FESGT-P1, Westinghouse Research Laboratory, 1974.

LADLES, J.D., and BEGLEY, J.A. [1976]. American Society for Testing and Materials, ASTM STP 590, pp. 128-148, 1976.

LAIRD, C. [1967]. American Society for Testing and Materials, ASTM STP 415, pp.131, 1967.

LARSON, F.R. and MILLER, J. [1952]. "A time-temperature relationship for rupture and creep stresses". Trans. A.S.M.E., 174, 5, 1952.

LEE, K.H. [1983]. "A Boundary Integral Equation Method for Two-Dimensional Elastoplastic Analysis". PhD Thesis University of London, 1983.

LERCKIE, F.A., and HAYHURST, D.R. [1974]. Pro. R. Soc. Lond. A. 340 pp. 323-347, 1974.

MAAS, E. and PINEAU, A. [1985]. Eng. Fracture Mechanics, vol. 22, No. 2, 1985, pp. 307-325.

MACHENZIE, A.C. [1968]. Int. J. Mech. Sci., 10, pp.441-453, 1968.

MACMILLAN, N.H., [1972]. J. Mat. Sci. Eng. 7, 239.

MARRIOTT, D.L. [1970]. "A review of reference stress methods for estimating creep deformation", presented at 2nd Int. Symposium on Creep in Structures, Ed. Hult, J., pp. 137-152, Gothenberg, Sweden 17-21 August, 1970.

McCARTNEY, L.N. and COOPER, P.M. [1977]. Eng. Fracture Mech., 19, 1977, pp. 265-272.

McCLINTOCK, F.A. [1977]. "Mechanics in Alloy Design", Fundamental Aspects of Structural Alloy Design. Eds. Jaffee, R.I. and Wilcox, B.A. Plenum, New York, 1977.

McCLINTOCK, F.A. and BASSANI, J.L [1981]. Inter. Jour. of Solids and Structures, vol .7, 1981, pp.479-492

MERKLE J.G. and CORTEN, H.T. [1974]. J. Pressure Vessel Tech., 96, 1974, pp. 286-292.

MORZERIA, A.M. [1979]. "Creep Crack Growth from Blunt and Sharp Notches", Third Year Project Report, 1979, Imperial College of Science and Technology, Mechanical Engineering Department.

MYERS, J., and PRICE, A.T. [1977]. Metals Tech., August 1977, 406-410.

NEWMAN, J.C. [1974]. American Society for Testing and Materials, ASTM STP 560 pp. 105-121, 1974.

NIKBIN, K.M. [1976]. "Relevance of Fracture Mechanics to Creep Crack Growth", PhD Thesis, University of London, 1976.

NIKBIN, K.M., WEBSTER, G.A. and TURNER, C.E. [1976]. ASTM STP 601, American Society for Testing and Materials pp. 47-62, 1976.

NIKBIN, K.M. and WEBSTER, G.A. [1982]. In: "Micro and macro mechanics of crack growth", (ed. K. Sadananda, B.B. Rath and D.J. Michel), Conf. Proc. Metall. Soc., AIME, pp. 137-147

NIKBIN, K.M., SMITH, D.J. and WEBSTER, G.A. [1983]."Advances in Life Prediction Methods at Eleveted Temperatures", Ed. D.A. Woodford and J.R. Whitehead, Conf. Proc., ASME, 1983, pp.249-258.

NIKBIN, K.M., SMITH, D.J. and WEBSTER, G.A. [1984]. Rroc. R. Soc. Lond. A. 396, pp. 183 - 197, 1984

NIKBIN, K.M., SMITH, D.J. and WEBSTER, G.A. [1986]. J. Eng. Mat. and Tech., Trans. ASME, 108, 1986, pp. 186-191.

NIKBIN, K.M. [1986]. Private communication.

NIKBIN, K.M. and WEBSTER, G.A. [1987]. American Society for Testing and Materials, ASTM STP 942,1987.

NORTON, F.H. [1929]. "The Creep of Steels at High Temperatures", McGraw-Hill, 1929.

ORR, R.L., SHERBY, O.D. and DORN, J.E. [1954]. Trans. ASME, 76, pp. 113.

PARIS, P.C., and ERDOCAN, F. [1963]. Trans. ASME, J. Basic Eng., 85, pp. 528.

PENNY, R.K., and MARRIOT, D.L. [1971]. "Design for Creep", McGraw-Hill, 1971.

RABOTNOV,Y.N. [1969]. "Creep Problems in Structural Members". North-Holland Publishers, 1969.

RAJ, R., and ASHBY, M.F. [1975]. Acta Met. 23, 653.

RAJU, I.S. and NEWMAN, J. C. [1979]. Eng. Fracture Mechanics, vol. 11, No. 4, 1979, pp. 817-829.

REMZI, E.M. [1981]. "Boundary Integral Equation Stress Analysis of Incompressible and Nearly Incompressible Materials". PhD Thesis, Unversity of London, 1981.

RICE, J.R. [1968a]. J. Appl. Mech., 35, pp. 379-386, 1968.

RICE, J.R. [1968b]. "Mathematical Analysis in the Mechanics of Fracture", Treatise on Fracture, vol.2, Ed. Liebowitz, H., Academic Press, New York,1968.

RICE, J.R., and ROSENGREN, G.F. [1968]. J. Mech. Phys. Solids, 1968, Vol. 16 pp. 1- 12.

RICE, J.R. and TRACEY, D.M [1969] J. Mech. Phys. Solids, 1969, Vol. 17, pp. 201-217.

RIEDEL, H., and RICE J.R. [1980]. "Tensile Cracks in Creeping Solids", Fracture

Mechanics: Twelfth Conference, ASTM STP 700, 1980, pp. 112-130.

RIEDEL, H. [1981]. J. Mech. Phys. Solids Vol. 29, pp. 35- 49

RIEDEL, H. and WAGNER, W. [1981]. Proceedings of the Fifth International Conference on Fracture, Cannes, 1981, pp.683-690.

RIEDEL, H. [1983]. American Society for Testing and Materials, ASTM STP 803 Volume I, pp. I-505-I-520, 1983.

RITCHIE, R.O., GARRET, G.G., and KNOTT, J.F. [1971]. Int. J. Fracture, 7, 1971, pp. 462-467.

RITCHIE, R.O., SURESH, S. and MOSS, C.M. [1980]. J. Eng. Mat. Tech., Trans. ASME Series H, 1980, vol 102, pp. 293.

ROOKE, D.P., and CARTWRIGHT, D.J. [1976]. "Compendium of Stress Intensity Factors", HMSO, London, 1976.

SADANANDA, K. and SHAHINIAN, P. [1978]. "Application of fracture mechanics techniques to high temperature crack growth", in Fracture Mechanics, (Eds. N. Perrone, et al.), 10th Symposium on Naval Structural Mechanics, Washington, published by the university Press of Virginia.

SADANANDA, K. and SHAHINIAN, P. [1981]. "Cavities and Cracks in Creep and Fatigue", Ed. J.H. Gittus, Applied Sci., London, 1981, pp. 109-196.

SAXENA, A. and HUDAK, S.J. [1978]. Int. J. Fracture, vol. 14, No. 5, 1978 pp. 453.

SAXENA, A., [1986]. "Creep Crack Growth under Non-Steady-State Conditions", Fracture Mechanics: VOL. 17, ASTM STP 905, 1986, pp. 185-201.

SAXENA, A. and HAN, J. [1986]. "Evaluation of crack tip parameters for characterizing crack growth behaviour in creeping materials", ASTM task group report, E24.08.07/E24.04.08, 1986.

SAXENA, A. and LIAW, J. [1986]. "Remaining Life Estimation of Boiler Pressure Parts - Crack Growth Studies", Final Report EPRI contract 2253-7, Westinghouse R&D Center, 1986.

SCHIJVE, J. [1979]. "The stress Ratio Effect on Fatigue Crack Growth in 2024-T3

Alclad and the relation to crack closure", Delft Univ. Aerospace Eng. Memo. M-336, Aug 1979.

SCHIJVE, J. [1980]. American Society for Testing and Materials, ASTM STP 700 pp. 3-34, 1980.

SEGERLIND, L.J. [1976]. "Applied Finite Element Analysis", Willey, New York, 1976.

SHIH, C.F., [1974]. "Small-Scale Yielding of Mixed Mode Plane-Strain Crack Problems", Fracture Analysis, ASTM STP 560, 1974, pp. 187 - 210.

SHIH, C.F. and HUTCHINSON, J.W. [1976]. Trans. of ASME, J. of Engin. Mater. and Tech., Series H, vol. 98, No 4, 1976, pp. 289-295.

SHIH, C.F., DeLORENZI, H.G., and ANDREWS, W.R. [1977]. Int. J. Fracture, 13, 1977, pp. 544-548.

SIM, R.G. [1968]. PhD Thesis, University of Cambridge.

SIVERS, M.L. and PRICE, A.T. [1973]. Int. J. of Fracture, 9 (2), pp.199-207.

SMITH, D.J. [1983]. "Creep Crack Growth in Low Alloy Steels Under Steady and Cyclic Loading". PhD Thesis, University of London, 1983.

SMITH, D.J. and WEBSTER G.A. [1981]. J. Strain Analysis, 16(2), 1981, pp.137-143.

SMITH, D.J. and WEBSTER G.A. [1983]. " Estimates of the C* Parameter for Crack Growth in Creeping Materials". American Society for Testing and Materials, ASTM STP803 Volume I, pp. I-654-I-674, 1983.

SMITH, D.J. and WEBSTER G.A. [1985]. Materials Science and Technology, Volume 1, 1985, pp. 366-372.

STEWART, A.T. [1980]. Eng. Fract. Mech., 1980, vol. 13, pp. 463.

SURESH, S., and RITCHIE, R.O. [1982]. Metallurgical Transactions A, Volume 13A ,September 1982, pp. 1627.

SURESH, S., ZAMISKI, G.F., and RITCHIE, R.O. [1981]. Metallurgical Transactions A, Volume 12A , August 1981, pp. 1435.

TADA, H., PARIS, P.C. AND IRWIN, G.R. [1973]. "The Stress Analysis of

Cracks Handbook", Del Research, Hellertown, Pa., 1973.

WALKER, K. [1970]. American Society for Testing and Materials, ASTM STP 462, pp. 1-14, 1970.

WEBSTER, G.A [1981]. "Methods of measuring crack growth at eleveted temperatures", presented at NPL Conference on "Measurement of High Temperature Mechanical Properties of materials", June 1981, HMSO.

WILLIAMS, J.G. [1977]. J. Mater. Sci. 12, 1977, pp. 2525.

WELLS, C.H., SULLIVAN, C.P., and GELL, M. [1971]. American Society for Testing and Materials, ASTM STP 495, 1971, pp. 61-122.

WILSON, W.K., and YU, I.W. [1979]. "The use of the J-Integral in Thermal Stress Crack Problems", Int. J. Fracture, 15, pp. 377-387.

WINSTONE, M.R., NIKBIN, K.M. and WEBSTER, G.A. [1985]. J. Mat. Sci., 20, 1985, pp. 2471

WU, F.H., BASSANI, J.L. and VITEK, V. [1986] Jour. of Mech. and Physics of Solids, vol. 34, 1986, pp. 455-475

WU, D. CHRISTIAN, E.M. and ELLISON, E.G. [1984]. "Evaluation of Creep Crack C* Integrals", J. Strain Analysis, Vol. 19, No. 3, 1984, pp. 185-195.

PUBLISHED WORK- ABSTRACTS

1. Dimopulos, V., Nikbin, K.M., and Webster G.A. [1986]

" Influence of cyclic to mean load ratio on creep/fatigue crack growth". Presented at ASME Materials Week, 1986, Lake Buena Vista, Florida, 4-9 October, 1986, to be published in A.S.M.E.

Abstract: Crack growth data under combined creep and fatigue loading conditions are presented on a nickel base superalloy and a brittle and ductile low alloy steel. The main variables that have been examined are minimum to maximum load ratio R and frequency. It is shown that at high frequencies transgranular fatigue failure dominates and at low frequencies time dependent mechanisms govern. Where fatigue processes control, it is demonstrated that crack growth/cycle can be described by the Paris law and that the influence of R ratio can be accounted for by crack closure caused by fracture surface roughness, oxidation and creep and plastic strain developed at the crack tip. At the low frequencies where time dependent processes dominate, it is shown that crack growth can be characterized satisfactorily in terms of the creep fracture mechanics parameter C* using a model of crack extension based on ductility exhaustion in the creep damage zone at the crack tip. This model leads to enhanced resistance to creep/fatigue crack growth with increase in material creep ductility.

2. Buchheim, G.M., Becht, C., Nikbin, K.M., Dimopulos, V., Webster, G.A. and Smith, D.J. [1986].

"Influence of aging on high temperature creep crack growth in type 304H stainless steel". Presented at the Third International Symposium on Non-Linear Fracture Mechanics, October 6-8, 1986, Knoxville, TN, to be published in ASTM STP.

Abstract: Stress rupture tests on smooth and notched tensile bars creep crack growth measurements under both static and cyclic loading have been made on virgin (new) solution annealed and "naturally aged" Type 304H stainless steel (SS) at 760° C. The

naturally aged material was taken from a component which had been in service for 15 years at temperatures in the range 690 to 725° C. It is known that some deterioration in properties occurs with aging in Type 304H SS and that could affect sensitivity to cracking. This paper shows that crack growth rate can be characterized in terms of the creep fracture mechanics parameter C* and that the behaviour of the new and aged materials can be rationalized in terms of their creep ductilities and the influence of ductility on the state of stress developed at the crack tip. Furthermore, it is demonstrated that lower and upper bound crack growth rates can be estimated approximately from uniaxial creep rupture data.